

https://dspace.org/

Fabrication of a composite nanofibrous platform for enhanced neurocompatibility

Lategan, Michelle

2022

https://hdl.handle.net/10539/34838

Downloaded from a DSpace repository. https://dspace.org/

FABRICATION OF A COMPOSITE NANOFIBROUS PLATFORM FOR ENHANCED NEUROCOMPATIBILITY

MICHELLE LATEGAN

A dissertation submitted to The Faculty of Health Sciences, University of the Witwatersrand, Johannesburg, in fulfilment of the requirements for the degree of Master of Pharmacy.



UNIVERSITY OF THE
WITWATERSRAND,
JOHANNESBURG

Supervisors

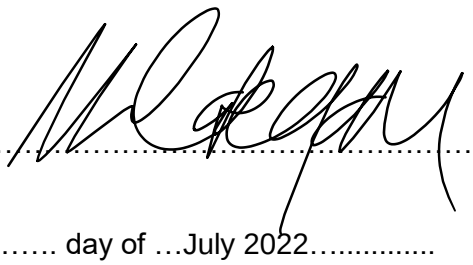
Professor Yahya. E. Choonara
University of the Witwatersrand, Department of Pharmacy and Pharmacology, Johannesburg, South Africa

Associate Professor Pradeep Kumar
University of the Witwatersrand, Department of Pharmacy and Pharmacology, Johannesburg, South Africa

Johannesburg, 2022

DECLARATION

I, Michelle Lategan, declare that this dissertation is my own work. It is being submitted for the degree of Master of Pharmacy in the Faculty of Health Sciences at the University of the Witwatersrand, Johannesburg, South Africa. It has not been submitted before for any degree or examination at this or any other University.

Signature …………

This …….2nd……. day of …July 2022…..

DEDICATIONS

This research is dedicated to my husband, Yasar.

RESEARCH PRESENTATIONS ARISING FROM THIS WORK

1. Michelle Lategan, Pradeep Kumar, and Yahya E Choonara. Two-Dimensional Nanofibrous and Non-fibrous Thin Films for Potential Neuro-regeneration. University of the Witwatersrand, BRICS Multi-national Research Presentation Day, Johannesburg, South Africa (Podium Presentation).

RESEARCH PUBLICATIONS ARISING FROM THIS WORK

1. Lategan, M., Kumar, P. and Choonara, Y.E. (2022). Functionalizing Nanofibrous Platforms for Neural Tissue Engineering Applications. Drug Discovery Today. https://doi.org/10.1016/j.drudis.2022.01.005.

2. Lategan, M., Kumar, P. and Choonara, Y.E. (2022). Ultra-thin polymeric films for enhanced neurocompatibility. In progress.

3. Lategan, M., Kumar, P. and Choonara, Y.E. (2022). Polycaprolactone/ cellulose acetate phthalate nanofibrous platforms for neural tissue engineering. In progress.

RESEARCH ACCOLADES

1. Postgraduate Research Scholarship Awards

- Grant holder-linked bursary as part of the National Research Foundation's Chair Grant Program. 2020-2021.
- Ernst and Ethel Ericksen Trust Postgraduate Scholarship. 2020-2021.
- Faculty Research Committee Individual Research Grant 2021 from the Faculty of Health Science, University of the Witwatersrand, Johannesburg.

ACKNOWLEDGEMENTS

I would like to express my deepest thanks and gratitude to individuals who have offered me their kind assistance and support that has enabled my completion of this degree. Firstly, and most importantly, I thank God for guiding me to this specific point in my life. I attribute this entire opportunity and achievement to Him. The last two years have changed drastically for me, and it has all been a result of Your supreme guidance and wisdom. I would like to thank my family, who have always encouraged me to achieve my goals, work hard and become an independent woman. I thank my parents for providing me with the opportunity to pursue my degree. To my dear husband, who encouraged me to pursue this master's degree, if it wasn't for your persuasiveness, I would never have enrolled for this degree. For this I am eternally grateful as it will provide me with endless opportunities. Thank you for your encouragement. You encouraged me to stay when I was about to quit. You uplifted me when I was at my lowest and provided me with immeasurable support when I was having difficulty throughout these two years. You believed in me when I did not believe in myself and sparked an enthusiasm and passion for life in me that I did not know I had. You taught me confidence, self-belief, and an unbelievable work ethic. You taught me to enjoy research and more importantly, how to enjoy life.

To my supervisor, Professor Yahya Choonara, thank you for providing me with the opportunity to pursue this degree, the opportunity to publish a paper and to work within your department. I will always look up to you and your achievements, you are an outstanding leader, and I can only hope to follow in your footsteps and become a confident leader like yourself. It is a privilege to be given the opportunity to conduct research with you both and the esteemed Wits Advanced Drug Delivery Platform Research Unit. I will always look up to you both as role models and I will always draw inspiration from you throughout my life.

To my supervisor, Professor Pradeep Kumar, thank you for supporting me throughout my research and showing me how to be an independent researcher. You pushed me out of my comfort zone by throwing me in the deep end, which I did not understand at first, but it has made me become an independent thinker and has helped shape me into a mature professional. I would like to thank you for your help with procuring my research funding, without which, I would not have been able to pursue this degree. Thank you for believing in me. Your door was always open to me, and you always provided me with excellent advice and great inside tips through your advanced expertise and experience. Thank you for being patient with me and giving me so much of your time and effort (and never becoming tired of my silly questions). Thank you for tolerating me when I walked into your office crying and complaining about silly things!

I would like to acknowledge my good friend, Ayesha Suleman, for always lending a kind word when you could see I was down. Thank you for always being willing to assist and support me. You never got tired of my outbursts after failure, and you always encouraged me to continue persevere. You taught me about integrity and truthfulness, and I will always draw inspiration from you. Thank you for sharing your locker and entire inventory with me! I am fortunate to have met you in undergrad and I am so lucky to have shared this experience with you. I would like to thank Onyinye Uwaezuoke for your patience with me in the lab and sharing your expertise, knowledge, and humour with me. Your laugh was always contagious.

To Mr Sello Ramarumo and Mrs Matshidiso Mosete, thank you for always ensuring that we always had what we needed. Your efforts never went unnoticed. Mr Kleinbooi Mohlabi, Mr Bafana Temba, Dr Hillary Mndlovu and Mr Siyabonga Maphumulo, thank you for being there for me, you went above and beyond for me and all of us in the department. To the cleaning staff of the University, thank you for ensuring a clean and optimum working environment daily. I would like to thank and acknowledge Dr Philemon Ubanako, for your patience in teaching me such great cell work techniques. Your patience with me was astounding. Your time and effort to teach me superior cell lab techniques will always be appreciated. To Mrs Petra Dinham, your advanced knowledge and expertise with SEM has made all the difference in my project. I am grateful for all your time and patience. Your willingness to go out of your way to ensure my images were world-class is highly appreciated. I could never have achieved this without you. A special thanks for all our chats and conversations while working.

The financial assistance of the National Research Foundation of South Africa and the Erick and Ethel Erickson Trust towards my research is hereby acknowledged. This research would not be possible without this funding. Their support is highly appreciated.

TABLE OF CONTENTS

Cover page……..i
Declaration……....ii
Dedications……....iii
Research presentations arising from this work……...iv
Research publications arising from this work……...v
Research accolades……....vi
Acknowledgements……..….vii-viii
Table of contents……ix-xii
List of figures……..…xiii-xx
List of tables…….....xxi
List of abbreviations…….xxiii-xxiv
Abstract……..….xxv
Chapter 1: Introduction....27
1.1 Background to the study....27
1.2 Rationale and motivation....30
1.3 Aims and objectives....31
1.4 Overview of dissertation....32
1.5 Concluding remarks....33
1.6 References....33
Chapter 2: Functionalizing nanofibrous platforms for neural tissue engineering applications35
2.1 Introduction....35
2.2 Wet chemical functionalization....37
2.3 Plasma modification....41
2.4 Surface adsorption of drugs or biomolecules....43
2.5 Layer-by-layer multilayer assembly....45
2.6 Blend electrospinning....47
2.7 Co-axial electrospinning....49
2.8 Emulsion electrospinning....52
2.9 Electrically conductive nanofibrous platforms....56
2.10 Piezoelectric nanofibrous platforms....59
2.11 Challenges and future prospects....63
2.12 Concluding remarks....63
2.13 References....63
Chapter 3: Fabrication of 2D thin films for neural tissue engineering applications....73
3.1 Introduction....73

3.2 Materials and Methods 75
3.2.1 Pre-formulation research 76
3.2.1.1 Method employed to identify the ideal polymer ratio to form thin films 76
3.2.1.2 Method employed to determine the optimal total polymer 76
3.2.1.3 Method employed to determine the optimal drying method……..... 76
3.2.2 Method employed to fabricate the unfunctionalized thin films 77
3.2.3 Hydrolysis of the thin films 77
3.2.4 Aminolysis of the thin films 77
3.2.5 Method employed for chemical integrity characterization 78
3.2.6 Method employed for thermodynamic behavior analysis using 78
3.2.7 Method employed for phase transition assessments utilizing x-ray diffraction..... 78
3.2.8 Method employed for thermal stability evaluation……..79
3.2.9 Method employed for surface topography characterizations 79
3.2.10 Method employed for porosimetric and surface area analysis..... 79
3.2.11 Method employed for surface topography analysis using atomic force microscopy... 80
3.2.12 Method employed for spectrophotometric mapping of amine group attachment..... 80
3.2.13 Method employed for evaluating mechanical properties……..80
3.2.14 Method employed for wettability analysis 81
3.2.15 Method employed for In Vitro degradation analysis 81
3.2.16 Method employed for In Vitro water-uptake analysis..... 81
3.2.17 Method employed for PC12 and A172 cell culture and cell viability quantification..... 82
3.2.18 Method employed for the qualitative assessment of 82
3.2.19 Method employed for the quantification of cell attachment..... 83
3.3 Results and discussions 83
3.3.1 Pre-formulation research 83
3.3.1.1 Determination of the optimal polymer ratio in terms of qualitative outcomes 83
3.3.1.2 Determination of the optimal total polymer concentration..... 84
3.3.2 Visual appearance of the thin films 86
3.3.3 Chemical integrity characterization employing Fourier-transform infrared analysis 87
3.3.4 Analysis of the thermodynamic behavior of the thin films..... 89
3.3.5 Phase transitions assessment utilizing x-ray diffraction analysis..... 94
3.3.6 Thermogravimetric analysis of the thin films 96
3.3.7 Surface topography characterizations by scanning electron microscopy analysis..... 100
3.3.8 Surface topography mapping analysis by atomic force microscopy 104
3.3.9 Porosimetric and surface area evaluation of the thin films using BET analysis 107
3.3.10 Spectrophotometric mapping of amine group attachment to thin films 112
3.3.11 Determination of the mechanical properties of the thin films 114

3.3.12 Determination of the hydrophilicity of the thin films 117
3.3.13 In Vitro degradation behavior of the thin films 118
3.3.14 In Vitro water-uptake behavior of thin films 121
3.3.15 PC12 and A172 cell culture and cell viability quantification 123
3.3.16 Qualitative assessment of cell attachment utilizing light microscopy 125
3.3.17 Quantification of cell attachment using trypan blue exclusion method 127
3.4 Concluding remarks 130
3.5 References 130
Chapter 4: Fabrication of 2D bioactive thin films for enhanced neurocompatibility 135
4.1 Introduction 135
4.2 Materials and Methods 136
4.2.1 Method of bio-active thin film fabrication 137
4.2.2 Method of chemical integrity characterization employing FT-IR spectroscopy 137
4.2.3 Method of thermodynamic behavior analysis 138
4.2.4 Method of phase transition assessment utilizing x-ray diffraction analysis 138
4.2.5 Method of thermal stability evaluation utilizing thermogravimetric analysis 138
4.2.6 Method of surface topography characterization 138
4.2.7 Method of porosimetric and surface area characterization 138
4.2.8 Method of mechanical characterizations using texture analyser analysis 139
4.2.9 Method of hydrophilicity characterization 139
4.2.10 Method of In Vitro degradation analysis 139
4.2.11 Method of In Vitro water-uptake analysis 140
4.2.12 Method of biomolecule attachment quantification using BCA protein assay 140
4.2.13 Method of PC12 and A172 cell culture and cell viability quantification 140
4.2.14 Method of cell attachment visualization utilizing light microscopy 141
4.2.15 Method of cell attachment quantification using the trypan blue exclusion method 141
4.3.1 Visual appearance of the bio-active thin films 142
4.3.2 Chemical integrity characterization of the thin films utilizing FT-IR 143
4.3.3. Analysis of the thermodynamic behavior of the thin films 148
4.3.4. Assessment of phase transitions of thin films utilizing x-ray diffraction analysis 151
4.3.5. Thermogravimetric analysis for thermal stability evaluation of the thin films 155
4.3.6. Surface topography characterizations by scanning electron microscopy analysis 160
4.3.7 Porosimetric and surface area analysis of the thin films using BET analysis 162
4.3.8 Determination of the mechanical properties of the thin films 163
4.3.9 Determination of the hydrophilicity of the thin films 165
4.3.10 In Vitro degradation study 167
4.3.11 In Vitro water-uptake study 168

4.3.12 Quantification of biomolecule attachment onto the films 170
4.3.13 PC12 and A172 cell culture and and quantification of cell viability 173
4.3.14 Qualitative assessment of cell attachment onto the bioactive thin films 175
4.3.15 Quantification of cell attachment using the trypan blue exclusion assay 176
4.4 Concluding remarks 178
4.5 References 179
Chapter 5: Fabrication of 2D nanofibrous platform for enhanced neurocompatibility 185
5.1. Introduction 185
5.2 Materials and Methods 186
5.2.1 Method of bioactive nanofibrous platform fabrication 186
5.2.1.1 Electrospinning of the polymeric solutions to form nanofibers 186
5.2.1.2 Method of determining the optimal total polymer concentration 187
5.2.1.3 Method of optimal aminolysis conditions determination 187
5.2.2 Surface topography mapping method by atomic force microscopy 188
5.2.3 Method of chemical integrity characterizations employing FT-IR 188
5.2.4 Analysis of the thermodynamic behavior of the nanofibrous platforms 188
5.2.5 Method of phase transition assessment utilizing x-ray diffraction analysis 189
5.2.6 Method of thermal stability analysis utilizing thermogravimetric analysis 189
5.2.7 Method of porosimetric and surface area characterization 189
5.2.8 Method of mechanical characterization using texture analyser analysis 189
5.2.9 Method of hydrophilicity characterization 189
5.2.10 Method of biomolecule immobilization quantification using BCA protein assay 190
5.2.11 Method of PC12 and A172 cell culture and cell viability quantification 190
5.2.12 Method of cell attachment quantification using the trypan blue exclusion method 191
5.3 Results and discussions 191
5.3.1 Fabrication of the bioactive nanofibrous platforms 191
5.3.1.1 Determination of the optimal total polymer concentration 191
5.3.2 Surface topography mapping analysis by atomic force microscopy 196
5.3.3 Chemical integrity characterizations of the nanofibrous platforms 197
5.3.4 Analysis of the thermodynamic behavior of the nanofibrous platforms 204
5.3.5 Assessment of phase transitions of nanofibrous films 208
5.3.6 Thermogravimetric analysis of the nanofibrous platforms 212
5.3.7 Porosimetric and surface area analysis of the nanofibrous platforms 220
5.3.8 Determination of the mechanical properties of the nanofibrous platforms 222
5.3.9 Determination of the hydrophilicity of the nanofibrous platforms 223
5.3.10 Quantification of biomolecule attachment using BCA protein assay 226
5.3.11 PC12 and A172 cell culture and quantification of cell viability 229

5.3.12 Quantification of cell attachment utilizing trypan blue exclusion assay 233
5.4 Conclusion 235
5.5 References 236
Chapter 6: Conclusions and recommendations 240
6.1 Conclusions 240
6.2 Limitations and recommendations 242
6.3 References 244
Chapter 7: Appendices 225
A1: Published literature review 246
A2:Podium presentation 247
A3: Individual TGA thermograms (Chapter 3) 248
A4: Parameters employed during bet porosity and surface area analysis (all chapters) 251
A5: Adsorption-desorption isotherms (Chapter 3) 252
A6: TGA thermograms (Chapter 4) 253
A7: Adsorption-desorption isotherms (Chapter 4) 255
A8: TGA thermograms (Chapter 5) 256

LIST OF FIGURES

Figure 1. 1 Some key requirements of an ideal nerve guide (Ramburrun et al., 2014)…….....29
Figure 1. 2 Polymeric thin film or electrospun nanofibrous platform for potential neural regeneration. Polymeric nerve guides with cell-interactive moieties (represented by purple stars) offer the required optimal mechanical, chemical, and biological cues for developing neurites differentiating into fully matured neurons. They regulate biological cues to guide axonal growth and sprouting, to promote the regeneration of the nerve tissue. Modified with permission from Boni (2018)……..31

Figure 2. 1 Characterization of aligned and bioactive nanofibers. Scanning electron microscopy images of (a) random poly(l-lactic acid) nanofibers, (b) aligned poly(l-lactic acid) nanofibers, (c) immobilization of basic fibroblast growth factor and laminin on poly(l-lactic acid) nanofibers, (d) a modified ELISA technique was used to show relative levels of basic fibroblast growth factor attachment on untreated, linker-modified, and heparin-functionalized poly(l-lactic acid) nanofibers, (e) immunostaining of immobilized laminin and (f) immunostaining of immobilized basic fibroblast growth factor. Reproduced with permission from Patel (2007)…….39
Figure 2. 2 Scanning electron microscope images of (a) untreated polycaprolactone nanofibrous platforms, (b) polycaprolactone nanofibrous platforms cold atmospheric plasma treated for 1 min, (c) 3 min, (d) 5 min, and (e) 7 min. Reproduced with permission from Meghdadi (2019)……..43
Figure 2. 3 Scanning electron microscopy and transmission electron microscopy images of the polyacrylic acid/polyvinyl alcohol electrospun nanofibers assembled with (a, b) small gold nanoparticles, (c, d) small gold nanoparticles-big gold nanoparticles. Reproduced with permission from Liu (2018)…….44
Figure 2. 4 Transmission electron microscopy of a core–shell fiber prepared by co-axial electrospinning. A 10 % w/v aqueous polyvinyl alcohol was used as the core, whereas 8 % w/v polyvinylpyrrolidone dissolved in dimethylformamide was used as the shell. Reproduced with permission from Sahay (2011)……...49
Figure 2. 5 Cell morphologies and alignment of HT-22 mouse hippocampal neuronal cells on the random polydioxanone, aligned polydioxanone, aligned polydioxanone/collagen, and aligned laminin-polydioxanone/collagen core/shell matrices. Two-photon excitation fluorescence images of HT-22 mouse hippocampal neuronal cells on the random polydioxanone, aligned polydioxanone, aligned polydioxanone/collagen, and aligned laminin-polydioxanone/collagen core/shell matrices at five days of culture. (i-iv). Magnified images of the region enclosed by the dashed white square in (v-viii). Reproduced with permission from Song (2018)……..50
Figure 2. 6 Schematic representation of the different spinnerets loaded with polymeric solutions for (a) blend, (b) co-axial, and (c) emulsion electrospinning. Reproduced with permission from Nikmaram (2017)……53
Figure 2. 7 (a) Representative images of neurite outgrowth from dorsal root ganglion cells co-cultured with induced bone marrow-derived stem cells on nanofibrous scaffolds. Neurites were immunofluorescent stained with Tuj1 primary antibodies and 568-conjugated second antibodies (red) and the transdifferentiated Schwann cells were derived from green fluorescent protein rats and show green fluorescence, (b) quantification of the average and maximum neurite length. Reproduced with permission from Yan (2020). (R) randpmly orientated nanofibers, (RC) randomly orientated conductive nanofibers, (A) aligned nanofibers, (AC) aligned conductive nanofibers……58

Figure 3. 1 Aminolysis reaction of polycaprolactone with 1,6-hexanediamine. Reproduced with permission from Zhu (2013). Copyright 2012, Springer…….75
Figure 3. 2 Photographic image illustrating the visual appearance of the films (a) polycaprolactone, (b) polycaprolactone/cellulose acetate phthalate, (c) sodium hydroxide-functionalized films, (d) potassium hydroxide-functionalized films, (e) ethylenediamine-functionalized films……..86

Figure 3. 3 Fourier-transform infrared spectroscopy of pristine (a) polycaprolactone, (b) cellulose acetate phthalate and (c) polycaprolactone/cellulose acetate phthalate……87
Figure 3. 4 Fourier-transform infrared spectroscopy of (a) sodium hydroxide-hydrolyzed films, (b) potassium hydroxide-hydrolyzed films and (c) aminolyzed films. Regions A and B have been highlighted as areas of interest……88
Figure 3. 5 Differential scanning calorimetry thermogram of (PCL) pristine polycaprolactone and (PCL FILM) polycaprolactone film……..90
Figure 3. 6 Differential scanning calorimetry thermogram of (CAP) pristine cellulose acetate phthalate and (CAP FILM) cellulose acetate phthalate film……..91
Figure 3. 7 Differential scanning calorimetry thermogram of (PCL) pristine polycaprolactone, (CAP) cellulose acetate phthalate and (PCL/CAP) polycaprolactone/cellulose acetate phthalate film……92
Figure 3. 8 Differential scanning calorimetry thermogram of (PCL/CAP) polycaprolactone/cellulose acetate phthalate film, (PCL/CAP-NaOH) sodium hydroxide and (PCL/CAP-KOH) potassium hydroxide hydrolyzed films and (PCL/CAP-EDA) aminolyzed film……..93
Figure 3. 9 X-ray diffractograms of (PCL) polycaprolactone film, (CAP) cellulose acetate phthalate film, (PCL/CAP) polycaprolactone/cellulose acetate film……95
Figure 3. 10 Comparison of the X-ray diffractograms of (PCL/CAP) polycaprolactone/cellulose acetate phthalate film, (PCL/CAP-NaOH) sodium hydroxide hydrolyzed film, (PCL/CAP-KOH) potassium hydroxide hydrolyzed film, (PCL/CAP-EDA) aminolyzed film……95
Figure 3. 11 Thermogravimetric analysis of (PCL) pristine polycaprolactone, (CAP) pristine cellulose acetate phthalate, (PCL/CAP) polycaprolactone/cellulose acetate phthalate film…97
Figure 3. 12 Thermogravimetric analysis of (PCL/CAP) polycaprolactone/cellulose acetate phthalate film, (PCL/CAP-NaOH) sodium hydroxide hydrolyzed film, (PCL/CAP-KOH) potassium hydroxide hydrolyzed film, (PCL/CAP-EDA) aminolyzed film……99
Figure 3. 13 Scanning electron microscopy images of (a) polycaprolactone film, (b) cellulose acetate phthalate film and (c) polycaprolactone/cellulose acetate phthalate film……100
Figure 3. 14 Scanning electron microscopy of the polycaprolactone/cellulose acetate phthalate film (a) objective lens and (b) in-lens highlighting the lamellar-like morphology of the films…101
Figure 3. 15 Scanning electron microscopy imagery of an acellular peripheral nerve (Borschel et al., 2003). Reproduced with permission from Elsevier, UK……...101
Figure 3. 16 Scanning electron microscopy images of polycaprolactone/cellulose acetate phthalate film (glass) at (a) 500X and (b) 5000X; the aminolyzed film (air) at (c) 500X and (d) 5000X; the sodium hydroxide-hydrolyzed film (glass) at (e) 500X and (f) 5000X……102
Figure 3. 17 Scanning electron microscopy images of the potassium hydroxide-hydrolyzed film (air) at (a) 500X and (b) 5000X; the potassium hydroxide-hydrolyzed film (glass) at (c) 500X and (d) 5000X; the aminolyzed film (air) at (e) 500X and (f) 5000X; the aminolyzed film (glass) at (g) 500X and (h) 5000X……...103
Figure 3. 18 3D atomic force microscopy images of polycaprolactone film (a) air and (b) glass; cellulose acetate phthalate film (c) air and (d) glass; polycaprolactone/cellulose acetate phthalate film (e) air and (f) glass demonstrating the difference in surface topography of the films……..……..106
Figure 3. 19 3D atomic force microscopy images of the sodium hydroxide-hydrolyzed film (a) air and (b) glass; the potassium hydroxide-hydrolyzed film (c) air and (d) glass; the aminolyzed film (e) air and (f) glass demonstrating the difference in surface topography of the various surface modified films……...107
Figure 3. 20 International Union of Pure and Applied Chemistry classification of (a) nitrogen adsorption isotherms (b) and hysteresis loops (S. Yang et al., 2018). Figure reproduced with permission from SAGE Journals……108
Figure 3. 21 adsorption-desorption isotherm for the sodium hydroxide-hydrolyzed film……..110
Figure 3. 22 Photographic image of the samples during the ninhydrin assay (a) before heating and (b) after heating, showing the color change from yellow to purple proving the presence of amine groups……..113
Figure 3. 23 Calibration curve used for amine group quantification on the surface ……113

Figure 3. 24 Stress-strain curve generated for (PCL) polycaprolactone films, (CAP) cellulose acetate phthalate films and (PCL/CAP) polycaprolactone/cellulose acetate phthalate film..114
Figure 3. 25 Stress-strain curves of (PCL/CAP) polycaprolactone/cellulose acetate phthalate films, (PCL/CAP-NaOH) sodium hydroxide hydrolyzed films, (PCL/CAP-KOH) potassium hydroxide hydrolyzed films, (PCL/CAP-EDA) aminolyzed films…….115
Figure 3. 26 Water contact angles of (PCL) polycaprolactone film, (CAP) cellulose acetate phthalate films, (PCL/CAP) polycaprolactone/cellulose acetate phthalate films, (PCL/CAP-NaOH) sodium hydroxide hydrolyzed films, (PCL/CAP-KOH) potassium hydroxide hydrolyzed films, (PCL/CAP-EDA) aminolyzed films……117
Figure 3. 27 Photographic images of water drops on (a) polycaprolactone/cellulose acetate phthalate film, (b) aminolyzed film, (c) potassium hydroxide-hydrolyzed film and (d) sodium hydroxide-hydrolyzed film…….118
Figure 3. 28 Percentage degradation of the films over the 30-day period. (PCL) polycaprolactone film, (PCL/CAP) polycaprolactone/cellulose acetate phthalate film. (PCLCAP-NaOH) sodium hydroxide hydrolyzed film, (PCL/CAP-KOH) potassium hydroxide hydrolyzed film, (PCL/CAP-EDA) aminolyzed film……...119
Figure 3. 29 *In Vitro* degradation rate of the film samples over the 30 day period. (PCL) polycaprolactone film, (PCL/CAP) polycaprolactone/cellulose acetate phthalate film. (PCLCAP-NaOH) sodium hydroxide hydrolyzed film, (PCL/CAP-KOH) potassium hydroxide hydrolyzed film, (PCL/CAP-EDA) aminolyzed film……...120
Figure 3. 30 *In Vitro* water-uptake behavior of (PCL) polycaprolactone film, (PCL/CAP) polycaprolactone/cellulose acetate phthalate film. (PCLCAP-NaOH) sodium hydroxide hydrolyzed film, (PCL/CAP-KOH) potassium hydroxide hydrolyzed film, (PCL/CAP-EDA) aminolyzed film……..122
Figure 3. 31 PC12 cell viability results after 48 and 72 h of exposure to extraction media. (PCL) polycaprolactone film, (PCL/CAP) blend film, (NaOH) sodium hydroxide-hydrolyzed film, (KOH) potassium hydroxide-hydrolyzed film, (EDA) aminolyzed film, (+) positive control, (-) negative control. An unpaired, two-tailed student T-test was conducted comparing the cell viability obtained from the unfunctionalized sample and the functionalized samples, which showed statistical significance after the 48 h exposure of P=0.001, 0.16 and 0.002, respectively, and after 72 h exposure of P=0.073, 0.009 and 0.08, respectively……..123
Figure 3. 32 A172 cell viability results after 48 and 72 h of exposure to extraction media. (PCL) polycaprolactone film, (PCL/CAP) blend film, (NaOH) sodium hydroxide-hydrolyzed film, (KOH) potassium hydroxide-hydrolyzed film, (EDA) aminolyzed film, (+) positive control, (-) negative control. An unpaired, two-tailed student T-test was conducted comparing the cell viability obtained from the unfunctionalized sample and the functionalized samples, which showed statistical significance after the 48 h exposure of p= 0.56, 0.86, and 0.01, respectively, and after 72 h exposure of P= 0.74, 0.79 and 0.42, respectively……124
Figure 3. 33 Light microscopy images of confluent (a) PC12 and (b) A172 cells……125
Figure 3. 34 Light microscopy image of the polycaprolactone/cellulose acetate phthalate film demonstrating the branched/lamellar-like morphology of the films which hinders the visualization of cell attachment……126
Figure 3. 35 PC12 cells attached onto the polycaprolactone/cellulose acetate phthalate film126
Figure 3. 36 PC12 cells attached onto polycaprolactone/cellulose acetate phthalate film….127
Figure 3. 37 Quantification of cell attachment of PC12 cells to the films. (PCL) polycaprolactone film, (PCL/CAP) polycaprolactone/cellulose acetate phthalate film. (PCLCAP-NaOH) sodium hydroxide hydrolyzed film, (PCL/CAP-KOH) potassium hydroxide hydrolyzed film, (PCL/CAP-EDA) aminolyzed film……128
Figure 3. 38 Quantification of A172 cell attachment to the films. (PCL) polycaprolactone film, (PCL/CAP) polycaprolactone/cellulose acetate phthalate film. (PCLCAP-NaOH) sodium hydroxide hydrolyzed film, (PCL/CAP-KOH) potassium hydroxide hydrolyzed film, (PCL/CAP-EDA) aminolyzed film……129

Figure 4. 1 Photographic image of the films secured in well plates (a) the aminolyzed film (b) the genipin crosslinked film, (c) the collagen crosslinked film, (d) the sodium alginate crosslinked film, (e) the gelatin crosslinked film……142

Figure 4. 2 Fourier-transform infrared spectra of (a) genipin, (b) collagen, (c) sodium alginate and (d) gelatin pristine powders showing two regions of interest: A and B……..144
Figure 4. 3 Fourier-transfer infrared spectra spectra of (PCL/CAP-EDA) aminolyzed film, (PCL/CAP-EDA-GEN) genipin crosslinked film, (PCL/CAP-EDA-GEN-COLL) collagen crosslinked film, (PCL/CAP-EDA-GEN-SA) so films, the genipin crosslinked films, the collagen crosslinked films, the sodium alginate crosslinked films and the gelatin crosslinked films…145
Figure 4. 4 Fourier-transform infrared spectra of (a) collagen coated and (b) collagen crosslinked films…….146
Figure 4. 5 Fourier-transform infrared spectra of (a) sodium alginate coated and (b) sodium alginate crosslinked film……146
Figure 4. 6 Fourier-transform infrared spectra of (a) gelatin coated film and (b) gelatin crosslinked film……..147
Figure 4. 7 Differential scanning calorimetry thermogram comparing pristine genipin, collagen, sodium alginate and gelatin……..149
Figure 4. 8 Differential scanning calorimetry thermograms of (PCL/CAP-EDA) aminolyzed film, (PCL/CAP-EDA-GEN) genipin crosslinked film, (PCL/CAP-EDA-COLL) collagen coated film, (PCL/CAP-EDA-GEN-COLL) collagen crosslinked film……...149
Figure 4. 9 DSC thermograms of (PCL/CAP-EDA) aminolyzed film, (PCL/CAP-EDA-GEN) genipin crosslinked film, (PCL/CAP-EDA-SA) sodium alginate crosslinked film, (PCL/CAP-EDA-GEN-SA) sodium alginate crosslinked film……..150
Figure 4. 10 DSC thermograms of (PCL/CAP-EDA) aminolyzed film, (PCL/CAP-EDA-GEN) genipin crosslinked film, (PCL/CAP-EDA-GEL) gelatin coated film, (PCL/CAP-EDA-GEN-GEL) gelatin crosslinked film……..151
Figure 4. 11 X-ray diffraction pattern of pristine collagen, sodium alginate and gelatin…….153
Figure 4. 12 X-ray diffraction pattern of (PCL/CAP-EDA) aminolyzed film, (PCL/CAP-EDA-GEN) genipin crosslinked film, (PCL/CAP-EDA-COLL) collagen coated film, (PCL/CAP-EDA-GEN-COLL) collagen crosslinked film……153
Figure 4. 13 X-ray diffraction patterns of (PCL/CAP-EDA) aminolyzed film, (PCL/CAP-EDA-GEN) genipin crosslinked film, (PCL/CAP-EDA-SA) coated film, (PCL/CAP-EDA-GEN-SA) sodium alginate crosslinked film……..154
Figure 5. 14 X-ray diffractogram of (PCL/CAP-EDA) aminolyzed film, (PCL/CAP-EDA-GEN) genipin crosslinked film, (PCL/CAP-EDA-GEL) gelatin coated film, (PCL/CAP-EDA-GEN-GEL) gelatin crosslinked film……..154
Figure 4. 15 Thermogravimetric analysis of (PCL/CAP-EDA) aminolyzed film, (PCL/CAP-EDA-GEN) genipin crosslinked film, (PCL/CAP-EDA-COLL) collagen coated film, (PCL/CAP-EDA-GEN-COLL) collagen crosslinked film……157
Figure 4. 16 Region C of Figure 4.15, highlighting the thermogravimetric analysis of the samples from 300-900 °C…….158
Figure 4. 17 Thermogravimetric analysis of (PCL/CAP-EDA) aminolyzed film, (PCL/CAP-EDA-GEN) genipin crosslinked film, (PCL/CAP-EDA-SA) sodium alginate coated film, (PCL/CAP-EDA-GEN-SA) sodium alginate crosslinked film……..158
Figure 4. 18 Region C of Figure 4.17, highlighting the thermogravimetric analysis of the samples from 350-900 °C…….159
Figure 4. 19 Thermogravimetric analysis of (PCL/CAP-EDA) aminolyzed film, (PCL/CAP-EDA-GEN) genipin crosslinked film, (PCL/CAP-EDA-GEL) gelatin coated film, (PCL/CAP-EDA-GEN-GEL) gelatin crosslinked film……..159
Figure 4. 20 Scanning electron microscopy of the aminolyzed films at (a) 500X and (b) 5000X, the collagen crosslinked films at (c) 500X and (d) 5000X, the sodium alginate crosslinked films at (e) 500X and (f) 5000X and the gelatin crosslinked films at (g) 500X and (h) 5000X……161
Figure 4. 21 Adsorption-desorption isotherm for the aminolyzed films……..162
Figure 4. 22 Adsorption-desorption isotherm for the biomolecule-crosslinked films……162
Figure 4. 23 Stress-strain curves comparing the aminolyzed films and the biomolecule-crosslinked films. (PCL/CAP-EDA) aminolyzed films, (PCL/CAP-EDA-GEN) genipin crosslinked films, (PCL/CAP-EDA-GEN-GEL) gelatin crosslinked films, (PCL/CAP-EDA-GEN-COLL) collagen crosslinked films, (PCL/CAP-EDA-GEN-SA) sodium alginate crosslinked films…….164

Figure 4. 24 Water contact angles for (E) the aminolyzed films, (EC) collagen coated films, (ES) sodium alginate coated films, (EG) gelatin coated films, (EGEN) genipin crosslinked films, (EGC) collagen crosslinked films, (EGS) sodium alginate crosslinked films, (EGG) gelatin crosslinked films…….165
Figure 4. 25 Photographic image of water droplets on (a) the aminolyzed films, (b) the sodium alginate crosslinked films, (c) the gelatin crosslinked films and (d) the collagen crosslinked films…….166
Figure 4. 26 *In Vitro* degradation behavior of the biomolecule-immobilized samples in comparison with the aminolyzed films. (PCL/CAP-EDA) aminolyzed films, (PCL/CAP-EDA-GEN) genipin crosslinked films, (PCL/CAP-EDA-GEN-GEL) gelatin crosslinked films, (PCL/CAP-EDA-GEN-COLL) collagen crosslinked films, (PCL/CAP-EDA-GEN-SA) sodium alginate crosslinked films……..167
Figure 4. 27 Water-uptake behavior of the biomolecule-immobilized films compared to the aminolyzed films. (PCL/CAP-EDA) aminolyzed films, (PCL/CAP-EDA-GEN) genipin crosslinked films, (PCL/CAP-EDA-GEN-GEL) gelatin crosslinked films, (PCL/CAP-EDA-GEN-COLL) collagen crosslinked films, (PCL/CAP-EDA-GEN-SA) sodium alginate crosslinked films…….169
Figure 4. 28 Calibration curve used for the quantification of collagen on the films…….170
Figure 4. 29 Bar graph representing the collagen concentration detected on the surface of the (EDA-COLL) collagen coated films and the (EDA-GEN-COLL) collagen crosslinked films.170
Figure 4. 30 Calibration curve used for the quantification of sodium alginate on the films. 171
Figure 4. 31 Bar graph representing the concentration detected on the (EDA-SA) sodium alginate coated films and the (EDA-GEN-SA) sodium alginate crosslinked films……171
Figure 4. 32 Calibration curve used for the quantification of gelatin on the surface of the films…….172
Figure 4. 33 Bar graph representing the concentration detected on the surface of the (EDA-GEL) gelatin coated films and the (EDA-GEN-GEL) gelatin crosslinked films……172
Figure 4. 34 Cytocompatibility results for PC12 cells after 48 and 72 h. (E) aminolyzed films, (EC) collagen coated films, (ES) sodium alginate coated films, (EG) gelatin coated films, (EGEN) genipin crosslinked films, (EGC) collagen crosslinked films, (EGS) sodium alginate crosslinked films, (EGG) gelatin crosslinked films, (+) positive control and (-) negative control. An unpaired, two-tailed student T-test was conducted comparing the cell viability obtained from the aminolyzed sample and the biomolecule crosslinked samples, which showed statistical significance after the 48 h exposure of P= 0.03, 0.99 and 0.36, respectively, and after 72 h exposure of P= 0.74, 0.31 and 0.52 respectively……..174
Figure 4. 35 PC12 cells attached to a collagen coated film……176
Figure 4. 36 PC12 cells attached to a gelatin crosslinked film circled in red……176
Figure 4. 37 Quantification of cell attachment of PC12 cells after 72 h incubation. (E) aminolyzed film, (EC) collagen coated film, (ES) sodium alginate coated film, (EG) gelatin coated film, (EGEN) genipin crosslinked film, (EGC) collagen crosslinked film, (EGS) sodium alginate crosslinked film, (EGG) gelatin crosslinked film…….177
Figure 4. 38 Quantification of cell attachment results for A172 cells after 72 h incubation. (E) aminolyzed film, (EC) collagen coated film, (ES) sodium alginate coated film, (EG) gelatin coated film, (EGEN) genipin crosslinked film, (EGC) collagen crosslinked film, (EGS) sodium alginate crosslinked film, (EGG) gelatin crosslinked film…….178

Figure 5. 1 Polycaprolactone/cellulose acetate phthalate (9% w/v) nanofibrous film showing a large variation in fiber diameter……192
Figure 5. 2 Polycaprolactone/cellulose acetate phthalate (9% w/v) nanofibrous film showing a large variation in fiber diameter……192
Figure 5. 3 Polycaprolactone/cellulose acetate phthalate (9% w/v) nanofibrous film showing a large variation in fiber diameter……193
Figure 5. 4 polycaprolactone/cellulose acetate phthalate (6% w/v) nanofibers, showing a more uniform fiber diameter distribution……...193
Figure 5. 5 Polycaprolactone (4% w/v) nanofibers (no cellulose acetate phthalate), showing the presence of many beads……194

Figure 5. 6 Scanning electron microscopy images of polycaprolactone/cellulose acetate phthalate nanofibrous platforms aminolyzed for (a) 0, (b) 7.5, (c) 15, (d) 30, (e) 60 and (f) 90 mins…….195
Figure 5. 7 3D atomic force microscopy images of polycaprolactone/cellulose acetate phthalate nanofibrous platforms showing the fibrillar surface topography of the platforms…….196
Figure 5. 8 3D atomic force microscopy images of aminolyzed nanofibrous platforms demonstrating the fibrillar nature of the surface…….196
Figure 5. 9 Fourier-transform infrared spectra of (a) pristine polycaprolactone and (b) polycaprolactone nanofibrous platform……..198
Figure 5. 10 Fourier-transform infrared spectra of (a) pristine polycaprolactone, (b) pristine cellulose acetate phthalate and (c) polycaprolactone/cellulose acetate phthalate nanofibrous platform……...198
Figure 5. 11 Fourier-transform infrared spectra of (PCL/CAP) polycaprolactone/cellulose acetate phthalate and the (PCL/CAP-EDA) aminolyzed nanofibers using 20% v/v ethylenediamine for 30 mins……199
Figure 5. 12 Fourier-transform infrared spectra of pristine (a) genipin, (b) collagen, (c) sodium alginate and (d) gelatin…….200
Figure 5. 13 Fourier-transform infrared spectra of (PCL/CAP-EDA) aminolyzed film, (PCL/CAP-EDA-GEN) genipin crosslinked film, (PCL/CAP-GEN-COLL) collagen crosslinked film, (PCL/CAP-EDA-GEN-SA) sodium alginate crosslinked film, (PCL/CAP-EDA-GEN-GEL) gelatin crosslinked film……..201
Figure 5. 14 Fourier-transform infrared spectra of (a) collagen coated nanofibers and (b) collagen crosslinked nanofibers……..203
Figure 5. 15 Fourier-transform infrared spectra of (a) sodium alginate coated nanofibers and (b) sodium alginate crosslinked nanofibers……203
Figure 5. 16 Fourier-transform infrared spectra of (a) gelatin coated nanofibers and (b) gelatin crosslinked nanofibers……..204
Figure 5. 17 Differential scanning calorimetry of (PCL) pristine polycaprolactone nanofibers, (PCL/CAP) polycaprolactone/cellulose acetate phthalate nanofibers and (PCL/CAP-EDA) the aminolyzed nanofibers……..207
Figure 5. 18 Differential scanning calorimetry of (PCL/CAP-EDA) aminolyzed nanofibers, (PCL/CAP-EDA-GEN) genipin crosslinked nanofibers, (PCL/CAP-EDA-COLL) collagen coated nanofibers and (PCL/CAP-EDA-GEN-COLL) collagen crosslinked nanofibers……..207
Figure 5. 19 Differential scanning calorimetry of (PCL/CAP-EDA) aminolyzed, (PCL/CAP-EDA-GEN) genipin crosslinked, (PCL/CAP-EDA-SA) sodium alginate coated, (PCL/CAP-EDA-GEN-SA) sodium alginate crosslinked nanofibers……207
Figure 5. 20 Differential scanning calorimetry of (PCL/CAP-EDA) aminolyzed, (PCL/CAP-EDA-GEN) genipin crosslinked, (PCL/CAP-EDA-GEL) gelatin coated, (PCL/CAP-EDA-GEN-GEL) gelatin crosslinked nanofibers…….208
Figure 5. 21 X-ray diffraction patterns of (PCL) polycaprolactone nanofibers, (PCL/CAP) polycaprolactone/cellulose acetate phthalate nanofibers, (PCL/CAP-EDA) aminolyzed nanofibers……...211
Figure 5. 22 X-ray diffraction patterns of (PCL/CAP-EDA) aminolyzed, (PCL/CAP-EDA-GEN) genipin crosslinked, (PCL/CAP-EDA-COLL) collagen coated, (PCL/CAP-EDA-GEN-COLL) collagen crosslinked nanofibers……..211
Figure 5. 23 X-ray diffraction patterns (PCL/CAP-EDA) aminolyzed, (PCL/CAP-EDA-GEN) genipin crosslinked, (PCL/CAP-EDA-SA) sodium alginate coated, (PCL/CAP-EDA-GEN-SA) sodium alginate crosslinked nanofibers…….211
Figure 5. 24 X-ray diffraction patterns of (PCL/CAP-EDA) aminolyzed, (PCL/CAP-EDA-GEN) genipin crosslinked, (PCL/CAP-EDA-GEL) gelatin coated, (PCL/CAP-EDA-GEN-GEL) gelatin crosslinked nanofibers……..212
Figure 5. 25 Thermogravimetric analysis of (PCL) pristine polycaprolactone and (CAP) cellulose acetate phthalate, (PCL NF) polycaprolactone nanofibers and (PCL/CAP NF) polycaprolactone/cellulose acetate phthalate nanofibers……214
Figure 5. 26 Thermogravimetric analysis of (PCL/CAP) polycaprolactone/cellulose acetate phthalate, (PCL/CAP-EDA) aminolyzed nanofibers, pristine collagen, pristine genipin, (PCL/CAP-EDA-COLL) collagen coated nanofibers, (PCL/CAP-EDA-GEN) genipin

crosslinked nanofibers and (PCL/CAP-EDA-GEN-COLL) collagen crosslinked nanofibers……...216
Figure 5. 27 Thermogravimetric analysis of (PCL/CAP) polycaprolactone/cellulose acetate phthalate nanofibers, (PCL/CAP-EDA) aminolyzed nanofibers, pristine sodium alginate, pristine genipin, (PCL/CAP-EDA-SA) sodium alginate coated nanofibers, (PCL/CAP-EDA-GEN) genipin crosslinked nanofibers and (PCL/CAP-EDA-GEN-SA) sodium alginate crosslinked nanofibers……..218
Figure 5. 28 Thermogravimetric analysis of (a) region A, (b) region B and (c) region C of Figure 5.27……..219
Figure 5. 29 Thermogravimetric analysis of (PCL/CAP-EDA) aminolyzed, (PCL/CAP-EDA-GEN) genipin crosslinked, (PCL/CAP-EDA-GEL) gelatin coated, (PCL/CAP-EDA-GEN-GEL) gelatin crosslinked nanofibers…….218
Figure 5. 30 Nitrogen adsorption-desorption isotherm for polycaprolactone/cellulose acetate phthalate nanofibrous platforms……..222
Figure 5. 31 Stress-strain curves generated to compare the mechanical properties of (PCL) polycaprolactone nanofibers, (PCL/CAP) polycaprolactone/cellulose acetate phthalate nanofibers, (PCL/CAP-EDA) aminolyzed nanofibers, (PCL/CAP-EDA-GEN) genipin crosslinked nanofibers and (PCL/CAP-EDA-GEN-BM) biomolecule crosslinked samples…223
Figure 5. 32 Bar graph representing the water contact angle values of the nanofibrous platforms. (P) polycaprolactone, (PC) polycaprolactone/cellulose acetate phthalate, (E) aminolyzed, (EC) collagen coated, (ES) sodium alginate coated, (EG) gelatin coated, (EGEN) genipin crosslinked, (EGC) collagen crosslinked, (EGS) sodium alginate crosslinked, (EGG) gelatin crosslinked nanofibrous platforms……..224
Figure 5. 33 Water drop images on (a) polycaprolactone/cellulose acetate phthalate, (b) aminolyzed, (c) genipin crosslinked, (d) gelatin crosslinked, (e) collagen crosslinked and (f) sodium alginate crosslinked nanofibrous platforms…….225
Figure 5. 34 Calibration curve used for the quantification of collagen on the nanofibrous surface……..226
Figure 5. 35 Concentration of collagen detected on the nanofibrous surfaces of (EDA-COLL) collagen coated nanofibers and (EDA-GEN-COLL) collagen crosslinked nanofibers…….227
Figure 5. 36 Calibration curve used in the quantification of sodium alginate on the nanofibrous surface……..227
Figure 5. 37 Concentration of sodium alginate detected on the surface of the (EDA-SA) sodium alginate coated nanofibers and (EDA-GEN-SA) sodium alginate crosslinked nanofibers….228
Figure 5. 38 Calibration curve used in the quantification of gelatin on the nanofibrous samples……...228
Figure 5. 39 Concentration of gelatin quantified on the nanofibrous surfaces of (EDA-GEL) gelatin coated nanofibers and (EDA-GEN-GEL) gelatin crosslinked nanofibers…….229
Figure 5. 40 PC12 Cytocompatibility results for 48 and 72 h for all the nanofibrous samples. (P) polycaprolactone, (PC) polycaprolactone/cellulose acetate ptthhalate, (E) aminolyzed, (EC) collagen coated, (ES) sodium alginate coated, (EG) gelatin coated, (EGEN) genipin coated, (EGC) collagen crosslinked, (EGS) sodium alginate crosslinked, (EGG) gelatin crosslinked, (+) positive control and (-) negative control. An unpaired, two-tailed student T-test was conducted comparing the cell viability obtained from the unfunctionalized sample, the aminolyzed sample and the biomolecule crosslinked samples, which showed statistical significance after the 48 h exposure of P= 0.45, 0.51, 0.19 and 0.24, respectively, and after 72 h exposure of P= 0.27, 0.14, 0.02 and 0.07, respectively…….230
Figure 5. 41 A172 Cytocompatibility results for 48 and 72 h for all the nanofibrous samples. (P) polycaprolactone, (PC) polycaprolactone/cellulose acetate ptthhalate, (E) aminolyzed, (EC) collagen coated, (ES) sodium alginate coated, (EG) gelatin coated, (EGEN) genipin coated, (EGC) collagen crosslinked, (EGS) sodium alginate crosslinked, (EGG) gelatin crosslinked, (+) positive control and (-) negative control. An unpaired, two-tailed student T-test was conducted comparing the cell viability obtained from the aminolyzed sample and the biomolecule crosslinked samples, which showed statistical significance after the 48 h exposure of P= 0.11, 0.03, 0.82 and 0.13, respectively, and after 72 h exposure of P= 0.15, 0.48, 0.99 and 0.43, respectively……...232

Figure 5. 42 Quantification of cell attachment for PC12 cells after 72 h. (P) polycaprolactone, (PC) polycaprolactone/cellulose acetate phthalate, (E) aminolyzed, (EC) collagen coated, (ES) sodium alginate coated, (EG) gelatin coated, (EGEN) genipin coated, (EGC) collagen crosslinked, (EGS) sodium alginate crosslinked, (EGG) gelatin crosslinked nanofibers……233
Figure 5. 43 Quantification of cell attachment results for A172 cells after 72 h. (P) polycaprolactone, (PC) polycaprolactone/cellulose acetate pththalate, (E) aminolyzed, (EC) collagen coated, (ES) sodium alginate coated, (EG) gelatin coated, (EGEN) genipin coated, (EGC) collagen crosslinked, (EGS) sodium alginate crosslinked, (EGG) gelatin crosslinked……..235

LIST OF TABLES

Table 1. 1 Neural guide fabrication techniques……...29

Table 2. 1. Summary of *In Vitro* studies on wet chemical functionalized nanofibrous platforms for application in neural tissue engineering……..40
Table 2. 2 Summary of *In Vitro* and *In Vivo* studies of plasma-functionalized nanofibrous platforms for application in neural tissue engineering……42
Table 2. 3 Summary of *In Vitro* and *In Vivo* studies on nanofibrous platforms for application in neural tissue engineering based on physical adsorption for drug/biomolecule delivery……45
Table 2. 4 Summary of *In Vitro* and *In Vivo* studies on nanofibrous platforms for application in neural tissue engineering based on layer-by-layer multilayer assembly……..48
Table 2. 5 Summary of *In Vitro* studies of blend electrospun nanofibers for application in neural tissue engineering……51
Table 2. 6 Summary of *In Vitro* and *In Vivo* studies on nanofibrous platforms for application in neural tissue engineering based on co-axial electrospinning……54
Table 2. 7 Summary of *In Vitro* studies on nanofibrous platforms for application in neural tissue engineering based on emulsion electrospinning……55
Table 2. 8 Summary of *In Vitro* and *In Vivo* studies of electrically conductive and piezoelectric electrospun nanofibers for application in neural tissue engineering……..61

Table 3. 1 Drying conditions evaluated for suitability in the film formation process……..53

Table 4. 1 Sample abbreviations and relative compositions……137
Table 4. 2 Thermal profiles of the modified samples compared with the unmodified sample.148
Table 4. 3 Full width at half maximum values ……...152
Table 4. 4 $T_{5\%}$ and T_{max} values for each sample derived from individual……156
Table 4. 5 Average tensile strength, Young's modulus and toughness……164

Table 5. 1 Electrospinning conditions employed to fabricate the nanofibrous platforms…….187
Table 5. 2 Abbreviations of all samples with their respective constituents……188
Table 5. 3 Differential scanning calorimetry profiles of samples……205
Table 5. 4 Full width at half maximum values for the samples……209
Table 5. 5 T_{max} and $T_{5\%}$ for pristine polymers and nanofibers……213
Table 5. 6 T_{max} and $T_{5\%}$ for each sample……214
Table 5. 7 Porosity analysis of the nanofibrous samples……221
Table 5. 8 Comparison of the tensile strengths of the samples……223

LIST OF EQUATIONS

Equation 3. 1 % Crystallinity= (area of crystalline peak/total area) x 100 ……...54

Equation 3. 2 Π=Ky/βcosϴ..……..54

Equation 3. 3 % Degradation= [(wi-wf)/wi] x 100 ……...……...……..57

Equation 3. 4 Dry mass ratio= wf/wi……..57

Equation 3. 5 % Water-uptake= [(wh-wi)/wi] x 100…….....57

Equation 3. 6 % Cell attachment= (number of live cells on sample/number of live cells on control) x 100 ……..…….....59

Equation 4. 1 % Degradation= [(wi-wf)/wi] x 100……..115

Equation 4. 2 % Water-uptake= [(wh-wi)/wi] x 100……..…..…116

Equation 4. 3 % Cell attachment= (number of live cells on sample/number of live cells on control) x 100……..…….....118

Equation 5. 1 % Cell attachment= (number of live cells on sample/number of live cells on control) x 100……....123

∆hd- enthalpy of degradation

∆hm- enthalpy of melting

A172- Cellosaurus cell line

AFM- atomic force microscopy

APTES- 3-Aminopropyl)triethoxysilane

AUC- area under the curve

BCA- Bicinchoninic acid

BET- Brunaeur-Emmet-Teller

BJH- Barrett-Joyner-Halender

BSA- bovine serum albumin

CAP- cellulose acetate phthalate

CI- crystallinity index

CRISPR- clustered regularly interspaced short palindromic repeats

D/B- drugs or biomolecules

DES- donor equine serum

DMEM- Dulbecco's Modified Eagle Medium

DRG- dorsal root ganglion

DSC- differential scanning calorimetry

EDA-ethylenediamine

EDC/NHS- 1-Ethyl-3-[3-dimethylami- nopropyl]-carbodiimide hydrochloride/m-hydroxysuccimide

FBS- fetal bovine serum

FT-IR- Fourier Transform Infrared

FWHM- full width half maximum

HDA- hexamethyldiamine

KOH- potassium hydroxide

LBL-layer-by-layer

MWCNT- multi-walled carbon nanotubes

NaOH- sodium hydroxide

NGF- nerve growth factor

NSC- neural stem cell

PBS- phosphate buffered saline

PC12- Pheocytochroma cell line

PCL- poly(caprolactone)

PHB- poly(hydroxybutyrate)

PLGA- Poly(lactic-co-glycolic acid)

PLLA- poly(l-lactic acid)

Poly(ATMA-CO-DOPAMA-CO-PEGMA)- poly{[aniline tetramer methacrylamide]-co-[dopamine methacrylamide]-co-[poly(ethylene glycol) methyl ether methacrylate]}

Ra- Average surface roughness derived from AFM data

RGD- Arg-Gly-Asp amino acid sequence

Rq- Root square of surface roughness derived from AFM data

Rz- maximum height of the surface roughness profile derived from AFM data

SDS- sodium dodecyl sulfate

SEM- scanning electron microscopy

$T_{5\%}$- initiation of degradation temperature

Td- degradation temperature

Tg- glass transition temperature

TGA- thermo-gravimetric analysis

Tm- melting temperature

Tmax- Temperature of maximum decomposition rate

XRD- x-ray diffraction

XTT- (sodium 3′-[1-[(phenylamino)-carbony]-3,4-tetrazolium]-bis(4-methoxy-6-nitro)benzene-sulfonic acid hydrate)

ABSTRACT

The lack of treatment options for traumatic brain injury has inspired great interest in the neural tissue engineering arena, which is streamlined by the use of polymeric-engineered nerve guidance conduits. The complex and intricate nature of the neural regeneration process has posed as an immense challenge in tissue engineering, despite recent advances in the field. Herein, an innovative mechanistic forecast to augment the regeneration of transected nerves, independently of drug therapy is described, through the use of two dimensional polycaprolactone/cellulose acetate phthalate thin polymeric films and nanofibrous platforms. These scaffolds were modified to impart favourable morphological, chemical, and biological cues to facilitate enhanced neural cell attachment and proliferation by firstly chemically modifying the films utilizing sodium hydroxide, potassium hydroxide and ethylenediamine to impart hydroxyl and amine moieties onto the surface of the films. Thereafter, biomolecules were immobilized on the film surface via genipin crosslinking. Various characterization analyses were undertaken to prove the suitability of the modified scaffolds for neural tissue engineering, such as FT-IR, DSC, XRD, TGA, SEM, porosimetric and surface area analyses, mechanical integrity testing, hydrophilicity analyses, biomolecule quantification, *In Vitro* degradation and water-uptake, *In Vitro* cytotoxicity and finally, cell attachment quantification. The hydrolysis and aminolysis treatments successfully reduced the water contact angle of the films from 71.60 to 50.64, 55.37 and 67.68°, respectively. An enhanced surface roughness is advantageous for neural tissue engineering scaffolds and was enhanced upon chemical functionalization from 35.43 to 53.03, 74.73 and 55.17, respectively. The mechanical tensile strength of the chemical functionalized films was reduced from 8.01 MPa to 6.78, 7.87 and 5.43 MPa, respectively. However, these values still fell within the range of acceptable tensile strengths for nerve tissue engineering. The BET surface area was increased from -0.40 to 6.49, 1.47 and 4.05 m^2/g. The BET cumulative volume of pores was also increased upon chemical functionalization. *In Vitro* cell attachment was quantified using a trypan blue exclusion assay and the results indicated that chemical functionalization enhanced cell attachment from 29.30 to 36.62, 41.58 and 55.44%, respectively. Biomolecules were immobilized on the aminolyzed films which resulted in an increase in all of the parameters discussed above: the water contact angles were reduced to <40°, the tensile strength was enhanced to >10 MPa, the BET surface area was increased to 33.14 m^2/g and the cell attachment was significantly improved to 123.72%. A BCA protein assay proved the presence of each biomolecule on the films. The fabrication of the biomolecule modified nanofibrous platforms resulted in an even further improvement of scaffold properties due to the extracellular matrix-mimicking nature of nanofibers. The surface roughness of the nanofibrous platforms was improved to 448.33 m^2/g. A BCA protein assay quantified the concentration of attached biomolecule on the nanofibrous platform, proving successful biomolecule immobilization. The BET surface area was improved to 16.33 m^2/g. The BET cumulative volume of pores was improved to 125.45 m^2/g, with an interconnected pore system with parallel slit-like pores which can facilitate the permeability of the nanofibrous platform to aid the efflux of wastes and influx of nutrients for attached cells. This investigation ultimately highlighted the success of the enhancement of neurocompatibility of the films and nanofibers using chemical functionalization as well as biomolecule immobilization.

CHAPTER 1:
INTRODUCTION

1.1 Background to the study

Damage to the nervous system often results in serious and potentially lethal consequences (Boni et al., 2018). Successful nerve regeneration is dependent on two critical events. Firstly, the transected neuron must initiate a program of gene expression that supports axon elongation (Purves et al., 2008). When neuronal damage occurs in the peripheral nervous system, some of these genes are re-expressed. The second factor that supports successful nerve regeneration is that the emerging growth cones must come into direct contact with an environment that is able to guide and support re-growing axons (Purves et al., 2008). This favourable environment is usually created in the peripheral nervous system after neurotrauma (Purves et al., 2008). In addition, adhesion molecules, extracellular matrix components, multiple neurotrophins and other signal molecules that support axon growth are signalled by Schwann cells and other non-neuronal cells after an injury has occurred (Nagajaran et al., 2019). Another important process that occurs in the peripheral nervous system that allows axon regrowth is that macrophages readily invade peripheral nerves to remove remains of degenerating axons and myelin that inhibit their regeneration (Purves et al., 2008). When damage to the axonal tracts in the adult central nervous system occurs, the remnants of axons and their myelin sheaths are not efficiently cleared, which impedes regeneration (Evans, 2001). In addition, the astrocytes that react to central nervous system injury, express additional inhibitors of axon extension. These factors combined impede the regeneration of axons in the central nervous system, thus making brain and spinal cord injury difficult to treat (Purves et al., 2008).

Traumatic brain injury, in specific, is a major concern globally that affects sixty-nine million individuals each year (Dewan et al., 2019). Traumatic brain injury occurs when neuropathologic damage and dysfunction occurs from an injury to the head (Mckee & Daneshvar, 2015). The damage can be caused by both primary and secondary mechanisms. Primary injury is caused by the immediate mechanical impact, while secondary injury evolves over a period after the injury has occurred (Kaur & Sharma, 2017). The current treatment for traumatic brain injury aims to minimise secondary injury and includes interventions such as calcium channel blockers, osmotherapy, amantadine, erythropoietin, and hypothermia (Galgano et al., 2017).The lack of treatment options has inspired great interest in the neural tissue engineering arena, which is streamlined by the use of polymeric-engineered nerve guidance conduits or nerve guides. These detour the limitations of conventional autologous and allogenic nerve grafts, such as the scarcity of donor nerves and the risk of immunological

rejection, respectively (Evans, 2001). Despite advances in this field, neural tissue engineering still poses an immense challenge in tissue engineering as a result of the complex nature of the neural regeneration process (Liu et al., 2015). As a result, initiatives in the fabrication of nerve guidance conduits have been widely explored, with the aim of improving neurocompatibility by optimizing biochemical, mechanical, electrical, and topographical signals; allowing for the regulation of cellular responses and ultimately promoting targeted neuron dendrite regeneration (Cao et al., 2019).

The restorative properties of both natural and synthetic polymers have been extensively evaluated in neural tissue engineering (Nagajaran et al., 2019). Polymers offer versatility in terms of shape and mechanical characteristics, with an unmatched biocompatibility in comparison to ceramics and metals (Boni et al., 2018). Research has proven that polymeric materials have an excellent capacity to be formed into scaffolds, such nerve guides, films and electrospun matrices, with the ability to improve the neural regeneration process (Boni et al., 2018). Natural polymers are advantageous in terms of their excellent biocompatibility and bioactivity, whereas synthetic polymers are hallmarked by superior mechanical and structural properties (Cao et al., 2019). Often, the combination of the two allow for the development of composite polymeric conduits or scaffolds that are able to mimic the native physiological environment of healthy neural tissues and, consequently, regulate cell behavior and offer support to transected nerves (Nagajaran et al.,2019).Many studies have described methods to fabricate neural guides using a range of manufacturing techniques, some of which have been compared in Table 1.1. Various materials have been studied for suitability in the development of nerve guides (Huang & Huang, 2006). Collagen based conduits have been developed commercially by Integra™ such as NeuraGen™ (Archibald et al., 1995). Yoshii and Oka also investigated a collagen filament nerve guide without the external tube (Yoshii & Oka, 2001). Synthetic polymer conduits are often fabricated with hydrolysable polyesters, such as polylactic-co-glycolic acid (Golafshan et al., 2017) and poly ε-caprolactone (Oh et al., 2008). The design of thin films with precise control of their structures and properties for targeted biomedical applications is an emerging topic due to the vast potential applications as well as the wide range of adaptability of these scaffolds (Jang et al., 2011).

Nanofibers have the capacity to mimic the inherent nature of the fibrillar extracellular matrix and have featured extensively in the fabrication of nerve guidance conduits (Nagarajan et al., 2019). These conduits are aimed at the recapitulation of the essential biological and structural features of the native extracellular matrix to provide a viable environment to guide the regrowth or repair transected nerves (Nagarajan et al., 2019). Furthermore, these fibrillar structures are able to provide favourable topographical and chemical cues to neural cells in addition to providing a means for the influx of nutrients and efflux of waste (Valmikinathan et al., 2011).

Table 1. 1 Neural guide fabrication techniques.

Fabrication technique	Advantages	Disadvantages	Reference
Electrospinning	Superior mechanical properties	Solvents may be toxic; difficult to fabricate three-dimensional structures	(Vasita & Katti, 2006)
Solvent casting	Cost-effective, porosity can be achieved easily	Time-consuming process; solvent removal may be problematic; batch-to-batch variation	(W. Liu et al., 2012)
Thermal induced phase separation	Excellent porosity and surface-to-volume ratio is achievable; thermoplastic crystalline polymer scaffolds can be fabricated	Can only be used for only thermoplastic materials	(Lu et al., 2013)
Freeze-drying	A versatile technique; pore size can be regulated; high temperatures can be obtained	Irregular pore size is often problematic; high energy consumption; cytotoxic solvents are often used; time-consuming	(Sultana & Wang, 2012)
Bioprinting	Less time-consuming; low production cost; high batch-to-batch homogeneity	Equipment is costly; polymers with ideal printability must be determined	(Do et al., 2015)

The fabrication of an ideal nerve guide which promotes functional recovery involves the close interplay of the following properties highlighted in Figure1.1.

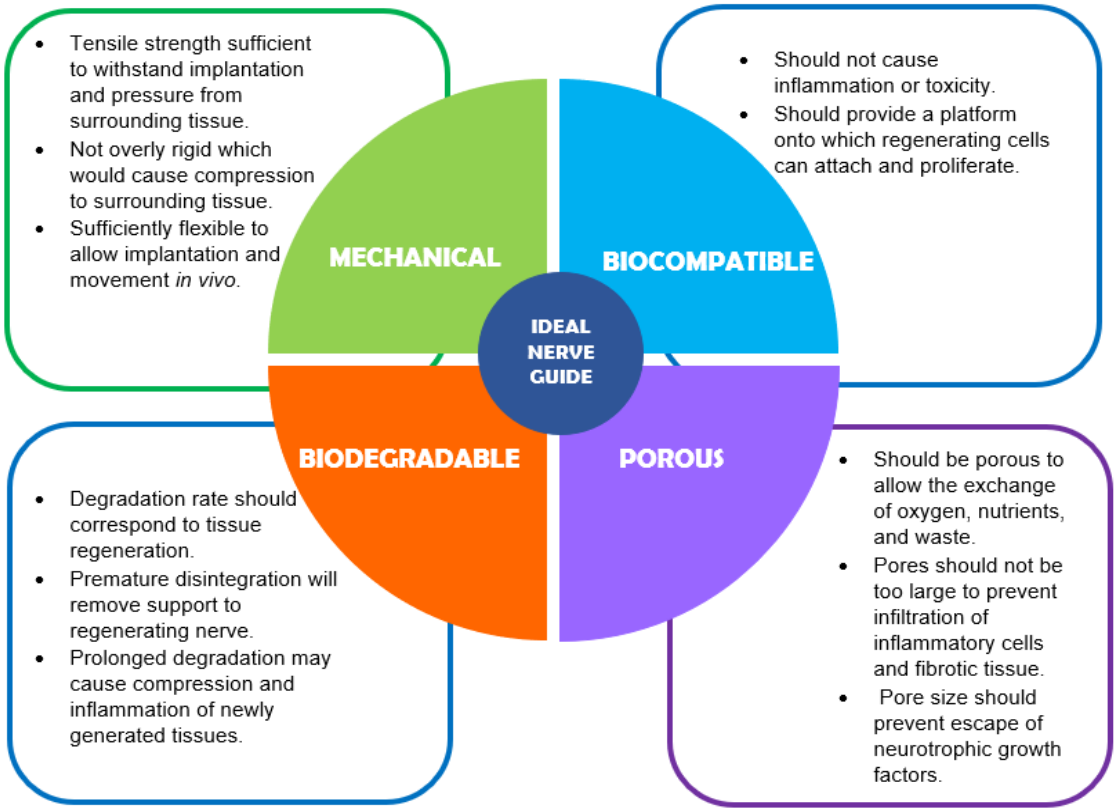


Figure 1. 1 Some key requirements of an ideal nerve guide (Ramburrun et al., 2014).

Electrospinning has gleaned considerable interest in the production of nanofibers due to its appreciably efficient, reproducible, simple and highly adaptable nature (Doshi & Reneker, 1995). Attempts to optimise the chemical and biological cues of nerve guides has initiated the incorporation of surface functionalities, biomolecules, or drugs in the bulk of, or on the surface of polymeric neural guides (Doshi & Reneker, 1995). Methods to achieve this include but are not limited to chemical surface functionalization, covalent bonding, crosslinking, layer-by-layer multilayer assembly and nanoparticle incorporation.

1.2 Rationale and motivation

Polymeric thin films and electrospun nanofibrous platforms have been well studied and widely used in regenerative medicine. The rationale behind this study is the creation of a composite polymeric thin film and an electrospun nanofibrous platform with enhanced neurocompatibility. The term ‘composite’ refers to the use of a number of polymers to form hybrid nanofibers, which may provide the film and nanofibrous platform with desirable qualities from all constituent polymers (Jiang et al., 2018). To enhance the neurocompatibility of the films and nanofibers, the biological, chemical, and physical properties of the scaffolds must be optimised. The physical cues that will be optimised include, but are not limited to fiber diameter, porosity, and mechanical strength. The chemical cues to be optimised could include, for example, the chemical functionalization of the surface of the films and fibers during or after the solution casting and electrospinning processes. The biological cues to be optimised could include the addition of drugs and/or biomolecules in and/or onto the scaffolds via various methods which could include surface crosslinking, nanoparticle deposition or incorporation, blending, emulsification or co-axial electrospinning. The schematic in Figure 1.2 demonstrates how the polymeric thin film and electrospun nanofibrous platform may be altered to enhance neurocompatibility.

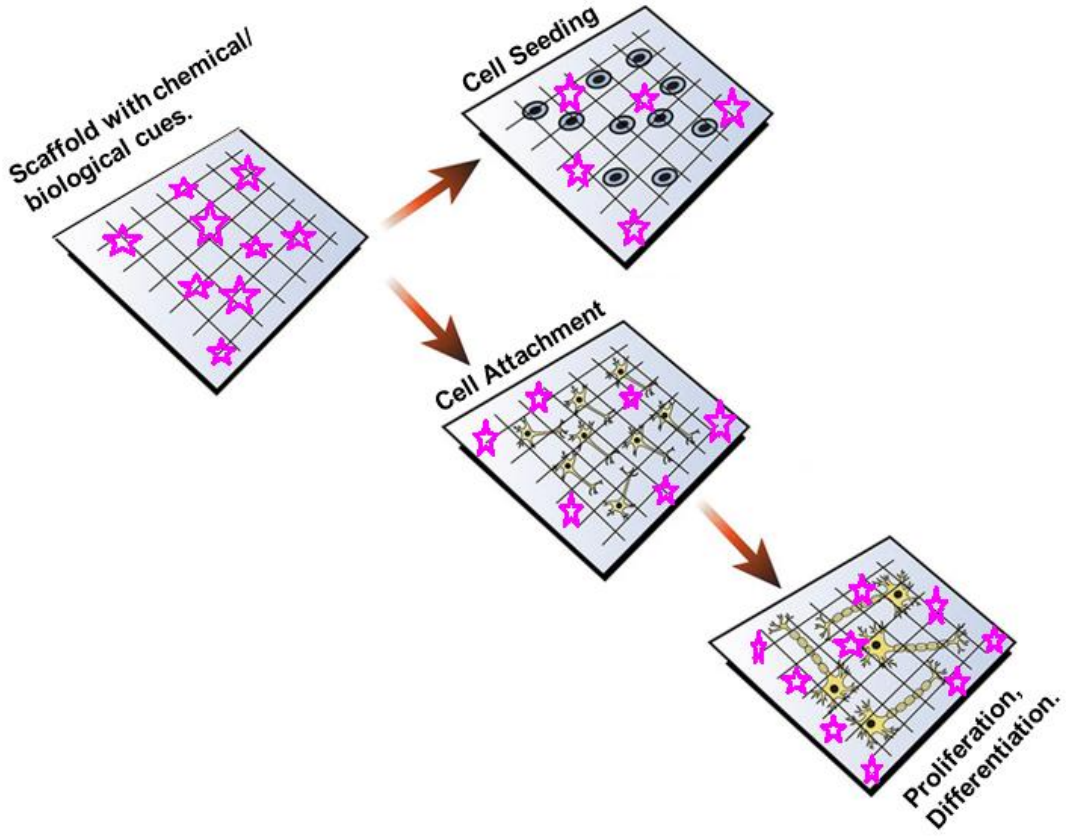


Figure 1. 2 Polymeric thin film or electrospun nanofibrous platform for potential neural regeneration. Polymeric nerve guides with cell-interactive moieties (represented by purple stars) offer the required optimal mechanical, chemical, and biological cues for developing neurites differentiating into fully matured neurons. They regulate biological cues to guide axonal growth and sprouting, to promote the regeneration of the nerve tissue. Modified with permission from Boni (2018).

1.3 Aims and objectives

The aim of this research is to develop a composite polymeric thin film and nanofibrous platform for enhanced neurocompatibility. In order to achieve this aim, the following objectives will be undertaken:

1. To optimize size, strength, and composition of the thin films and nanofibrous platforms for enhanced neurocompatibility.
2. To characterise the physicochemical, physio-mechanical, and morphological characteristics of the platforms by evaluating the chemical integrity, thermal stability, tensile strength, surface morphology, wettability, degradation, porosity, water retention, and weight loss of the platforms.
3. To evaluate the *In Vitro* effectiveness of the composite nanofibrous structure in supporting nerve regeneration by evaluating the neuronal cell cytocompatibility, proliferation, attachment, and morphology on the platforms.
4. To quantify the drug/biomolecule release/immobilization from/on the platforms by performing the relevant drug/protein release/quantification assay(s).

1.4 Overview of dissertation

Chapter One of this dissertation provides an introduction and background to the study, including epidemiological information and current therapeutic approaches. This chapter describes current advances and limitations of neural tissue engineering and highlights the advantages of the scaffold design chosen for this study. The rationale, aims, and objectives of the study are addressed.

Chapter Two of this dissertation is an in-depth literature review exploring the various methods available for the functionalization of nanofibrous platforms for neural tissue engineering purposes, including wet chemical functionalization, plasma modification, surface adsorption, layer-by-layer multilayer assembly, blend electrospinning, emulsion electrospinning, electrically active scaffolds, and piezoelectric scaffolds. This chapter ends with a discussion of the limitations and future approaches in the neural tissue engineering and electrospinning arenas.

Chapter Three of this dissertation includes a preliminary study in which the ideal ratio composition and the total polymer concentration are investigated quantitatively based on mechanical strength testing. Thereafter the drying conditions are assessed quantitively based on mechanical strength testing and an optimal film formulation is identified to be used in the proceeding chapters. This chapter contains a detailed study of the effects of surface chemical functionalization on the polymeric thin films in the form of surface hydrolysis and aminolysis. The effects of these surface functionalization techniques are investigated through an evaluation of physio-chemical characteristics, the morphological characteristics such as scanning electron microscopy and atomic force microscopy, the porosimetric characteristics, the mechanical characteristics, the hydrophilicity, and *In Vitro* assessments such as degradation and water-uptake, cytocompatibility quantification as well as the quantification of cell attachment.

Chapter Four of this dissertation explores the effects of the surface immobilization of collagen, sodium alginate and gelatin to the surface of the polymeric thin films using genipin as the crosslinker. An extensive physicochemical, morphological, mechanical, porosimetric and hydrophilicity evaluation is undertaken. The effects of the presence of these biomolecules are investigated *In Vitro* through cytocompatibility studies and cell attachment quantification, as well as degradation and water-uptake analysis.

Chapter Five of this dissertation introduces the electrospun nanofibrous platform, which is fabricated using the same optimized techniques and constituents identified in the preceding chapters. The nanofibrous platforms are characterized using the same physicochemical,

mechanical, morphological and porosimetric characterizations from the preceding chapters, as well as *In Vitro* cytocompatibility and cell attachment studies to establish the effect of an interconnected nanofibrous network structure on the performance of the scaffold in comparison to the thin film.

Lastly, **Chapter six** discusses the applications of two-dimensional polymeric thin films and nanofibrous platforms in neural tissue engineering, as well as a presentation of the scope of the study. A summary of results of Chapter 4 is presented, discussing the limitations and methods to enhance the neurocompatibility of the thin films which are undertaken in the proceeding chapters. Thereafter, the results from chapters 5 and 6 are summarized, including the physiochemical, mechanical, thermodynamic, cytotoxicity and cell attachment results. The conceptual desirability of the bioactive platforms for neural tissue engineering are proposed. The progression of the neurocompatibility of the scaffolds throughout the dissertation is graphically highlighted and discussed.

1.5 Concluding remarks

This chapter highlights the challenges associated with traumatic brain injury intervention and outlines strategies based on physical and chemical guidance cues for the potential overall improvement of regeneration of transected neurons following traumatic brain injury. It entails the proposed mechanism of action of the polymeric thin film and the electrospun nanofibrous platform in terms of architectural structure and the required implementations for the successful fabrication and functioning. In addition, this chapter presents the rationale, aim and objectives of the research study, as well as a dissertation summary.

1.6 References

Archibald, S. J., Shefner, J., Krarup, C., & Madison, R. D. (1995). Monkey median nerve repaired by nerve graft or collagen nerve guide tube. Journal of neuroscience, 15(5), 4109-4123.

Boni, R., Ali, A., Shavandi, A., & Clarkson, A. N. (2018). Current and novel polymeric biomaterials for neural tissue engineering. Journal of biomedical science, 25(90), 102-115.

Dewan, M. C., Rattani, A., Gupta, S., Baticulon, R. E., Hung, Y. C., Punchak, M., Agrawal, A., Adeleye, A. O., Shrime, M. G., Rubiano, A. M., Rosenfeld, J. V., & Park, K. B. (2019). Estimating the global incidence of traumatic brain injury. Journal of neurosurgery, 2018(1),1-18.

Do, A. V., Khorsand, B., Geary, S. M., & Salem, A. K. (2015). 3D printing of scaffolds for tissue regeneration applications. Advanced healthcare materials, 4(12), 1742-1762.

Doshi, J., & Reneker, D. H. (1995). Electrospinning process and applications of electrospun fibers. Journal of electrostatics, 35(2-3),151-160.

Galgano, M., Toshkezi, G., Qiu, X., Russell, T., Chin,T. and Zhao, L. (2017). Traumatic brain injury-current treatment strategies and future endeavors. Sage journals, 26(7), 1118-1130.

Golafshan, N., Kharaziha, M., & Fathi, M. (2017). Tough and conductive hybrid graphene-PVA: Alginate fibrous scaffolds for engineering neural construct. Carbon, 111(2), 257-263.

Huang, Y. C., & Huang, Y. Y. (2006). Biomaterials and strategies for nerve regeneration. Artificial organs, 30(7), 514-522.

Jang, Y., Park, S., & Char, K. (2011). Functionalization of polymer multilayer thin films for novel biomedical applications. Korean journal of chemical engineering, 28(5), 1149-1160.

Kaur, P., & Sharma, S. (2017). Recent advances in pathophysiology of traumatic brain injury. Current neuropharmacology, 16(8), 1224-1238.

Li, X., Lee, S. C., Zhang, S., & Akasaka, T. (2015). Biocompatibility and toxicity of nanobiomaterials. Journal of nanomaterials, 2012(special issue), 2-6.

Liu, Y.X., Zhang, Y.R., Bogaerts, A., & Wang, Y.N. (2015). Electromagnetic effects in high-frequency large-area capacitive discharges: a review. Journal of vacuum science & technology A: vacuum, surfaces, and films, 33(2), 20801-20808.

Lu, T., Li, Y., & Chen, T. (2013). Techniques for fabrication and construction of three-dimensional scaffolds for tissue engineering. International journal of nanomedicine, 8(8), 337-350.

Mckee, A. C., & Daneshvar, D. H. (2015). The neuropathology of traumatic brain injury. Handbook of clinical neurology, 127(2), 45-66.

Nagarajan, S., Bechelany, M., Kalkura, N. S., Miele, P., Bohatier, C. P., & Balme, S. (2019). Electrospun nanofibers for drug delivery in regenerative medicine. Applications of targeted nano drugs and delivery systems, 9(3), 595-626.

Oh, S. H., Kim, J. H., Song, K. S., Jeon, B. H., Yoon, J. H., Seo, T. B., Namgung, U., Lee, I. W., & Lee, J. H. (2008). Peripheral nerve regeneration within an asymmetrically porous PLGA/pluronic F127 nerve guide conduit. Biomaterials, 29(11), 1601-1609.

Purves, D., Augustine, G., Fitzpatrick, D., Hall, W., LaMantia, A., McNamara, J., & White, L. (2008). Neuroscience. Sunderland (MA): Sinauer Associates, 4.

Schaub, N. J., Johnson, C. D., Cooper, B., & Gilbert, R. J. (2016). Electrospun fibers for spinal cord injury research and regeneration. Journal of neurotrauma, 1(33), 1405-1415.

Sultana, N., & Wang, M. (2012). PHBV/PLLA-based composite scaffolds fabricated using an emulsion freezing/freeze-drying technique for bone tissue engineering: Surface modification and *In Vitro* biological evaluation. Bio fabrication, 4(1), 15003-15009.

Valmikinathan, C. M., Hoffman, J., & Yu, X. (2011). Impact of scaffold micro and macro architecture on Schwann cell proliferation under dynamic conditions in a rotating wall vessel bioreactor. Materials science and engineering C, 31(1), 22-39.

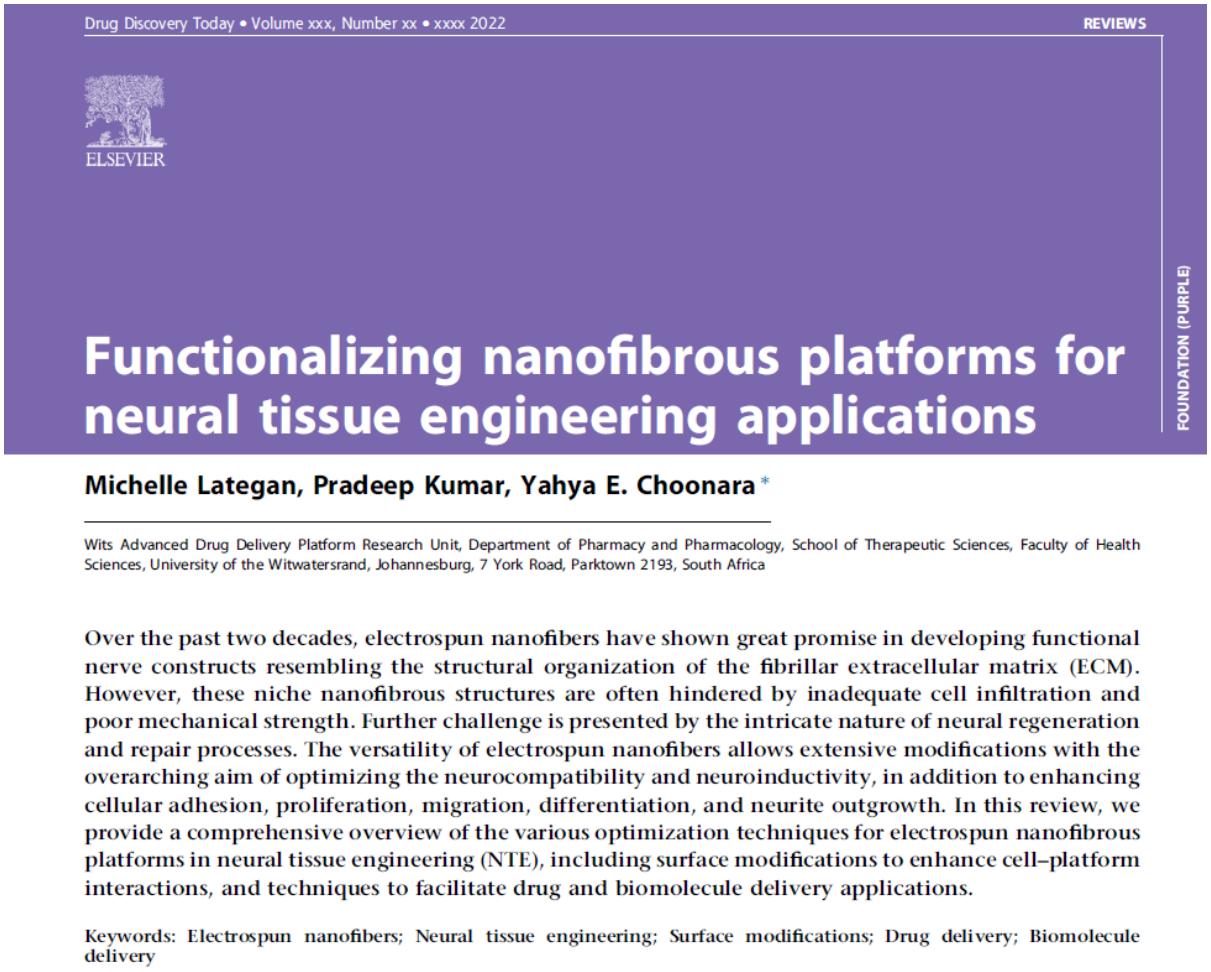
Vasita, R., & Katti, D. S. (2006). Nanofibers and their applications in tissue engineering. International journal of nanomedicine, 1(1), 15-30.

Yoshii, S., & Oka, M. (2001). Peripheral nerve regeneration along collagen filaments. Brain research, 888(1), 158-162.

CHAPTER 2:

FUNCTIONALIZING NANOFIBROUS PLATFORMS FOR NEURAL TISSUE ENGINEERING APPLICATIONS

(Available Online https://doi.org/10.1016/j.drudis.2022.01.005)



Drug Discovery Today • Volume xxx, Number xx • xxxx 2022 REVIEWS

ELSEVIER

FOUNDATION (PURPLE)

Functionalizing nanofibrous platforms for neural tissue engineering applications

Michelle Lategan, Pradeep Kumar, Yahya E. Choonara *

Wits Advanced Drug Delivery Platform Research Unit, Department of Pharmacy and Pharmacology, School of Therapeutic Sciences, Faculty of Health Sciences, University of the Witwatersrand, Johannesburg, 7 York Road, Parktown 2193, South Africa

Over the past two decades, electrospun nanofibers have shown great promise in developing functional nerve constructs resembling the structural organization of the fibrillar extracellular matrix (ECM). However, these niche nanofibrous structures are often hindered by inadequate cell infiltration and poor mechanical strength. Further challenge is presented by the intricate nature of neural regeneration and repair processes. The versatility of electrospun nanofibers allows extensive modifications with the overarching aim of optimizing the neurocompatibility and neuroinductivity, in addition to enhancing cellular adhesion, proliferation, migration, differentiation, and neurite outgrowth. In this review, we provide a comprehensive overview of the various optimization techniques for electrospun nanofibrous platforms in neural tissue engineering (NTE), including surface modifications to enhance cell–platform interactions, and techniques to facilitate drug and biomolecule delivery applications.

Keywords: Electrospun nanofibers; Neural tissue engineering; Surface modifications; Drug delivery; Biomolecule delivery

2.1 Introduction

Neural damage from brain, spinal cord, or peripheral nerve injury can lead to permanent and incapacitating conditions, as a result of a lack of the innate ability to regenerate the nervous system (Steward et al., 2013). This has inspired great interest in the neural tissue engineering arena, which is streamlined by the use of polymeric-engineered nerve guidance conduits (Steward et al., 2013). These detour the limitations of conventional autologous and allogenic nerve grafts, such as the scarcity of donor nerves and the risk of immunological rejection, respectively (Evans, 2001). Despite advances in this field, neural tissue engineering still poses an immense challenge in tissue engineering as a result of the complex nature of the neural regeneration process (Liu et al., 2015). As a result, initiatives in the fabrication of nerve guidance conduits have been widely explored, with the aim of improving biocompatibility, biodegradability, neuro-conductivity, and neuro-inductivity by optimizing biochemical,

mechanical, electrical, and topographical signals, allowing for the regulation of cellular responses, and ultimately promoting targeted neuron dendrite regeneration (Cao et al., 2019).

Nanofibers have the capacity to imitate the inherent structure of the fibrillar extracellular matrix and have featured extensively in the fabrication of nerve guidance conduits (Nagajaran et al., 2019). These conduits aim to recapitulate the essential biological and structural features of the native extracellular matrix to provide a viable environment to guide the regrowth or repair of transected nerves (Nagajaran et al., 2019). Furthermore, these fibrillar structures provide favorable topographical and chemical cues to neural cells, in addition to providing a means for the influx of nutrients and efflux of waste (Valmikinathan et al., 2011; Doshi & Reneker, 1995; Schaub et al., 2016; Li et al., 2012). A host of natural and synthetic polymers have been electrospun for application in neural tissue engineering, known for their inherent viscoelastic nature (Nagajaran et al., 2019). Natural polymers are innately bioactive, presenting vast domains of cellular interactive moieties on their backbones (Bhattarai et al., 2018). Nanofibrous platforms prepared from natural polymers exhibit a niche promotion of cell-platform interactions, such as cell adhesion, proliferation, and differentiation, but are often limited by poor processability, inadequate mechanical strength, and rapid degradation (Bhattarai et al., 2018). Synthetic polymers have been used to great effect in neural tissue engineering due to their flexible processing, synthesis, and remarkable mechanical strength (Amani et al., 2019). Hydrophobicity and low surface energy are a few of the hallmark traits of most synthetic polymers, which hinder cell attachment and proliferation on the nanofibrous platforms (Muthiah et al., 2012). Accordingly, a combination of natural and synthetic polymers is frequently used to exploit the individual favorable traits to achieve optimal physical properties and excellent bioactivity (Bhattarai et al., 2018).

Regardless, a significant push has been made toward improving the performance of platforms *In Vitro* and *In Vivo*. The versatility of nanofibrous platforms allows for extensive modifications to further improve neurocompatibility, cell-platform interactions, and neurite outgrowth by conferring surface functionalization and facilitating the surface attachment and/or incorporation of drugs or biomolecules (D/B) (Zhan et al.,2012). In addition, the incorporation of D/B within the bulk of nanofibers has been widely performed, creating nanofibrous platforms with biomimicking surface characteristics as well as tailorable release properties (Balogh-Weiser et al., 2019). The choice between loading D/B onto the surface or within nanofibers is dependent on the application of the platform as well as the molecule type (Balogh-Weiser et al., 2018). The encapsulation of D/B within the bulk of fibers enables efficient release, contingent on diffusion and degradation mechanisms, allowing for the regulation of release by manipulating the chemical and morphological composition of the fibers (Buzgo et al., 2015). However, this method has proven to be unsuitable for molecules that are sensitive to the conditions of the

electrospinning process because the addition of D/B occurs before processing (Buzgo et al., 2015).

Several methods exist to attach D/B to the surface or incorporate them within the bulk of platforms. The choice of method is dependent on factors such as the type of drug (small molecule, protein, or gene) and its physicochemical properties (hydrophobicity, hydrophilicity, and molecular weight) (Nagajaran et al., 2019). In this review, we present an overview of the various applications of platform modifications, which are classified into chemical approaches (wet chemical functionalization), physicochemical approaches (plasma treatment), and physical approaches (physical adsorption, layer-by-layer multilayer assembly, blend electrospinning, co-axial electrospinning, and emulsion electrospinning, with particular emphasis on enhancing neural cell-platform interactions). The emerging field of electrically conductive and piezoelectric nanofibrous platforms is also introduced, highlighting the various methods available to optimize nanofibers and the unexplored potential within the field. Finally, conclusion is drawn to the current challenges and future directions in the domain of nanofibrous platforms for neural tissue engineering.

2.2 Wet chemical functionalization

Wet chemistry entails the immersion of nanofibrous platforms into strong acids or alkalis, enabling the grafting of hydroxyl, carboxylic, or amino groups via hydrolysis or aminolysis (Lavrov, 2002). The effect of surface hydrophilicity on cell adhesion was investigated by Lee and co-workers, who found that nanofibrous platforms with an increased surface hydrophilicity exhibited enhanced cell adhesion (Lee et al., 2002). Imani and co-workers hydrolyzed polylactic acid electrospun nanofibers with sodium hydroxide to enable the covalent attachment of polypyrrole-grafted gelatin onto the surface of the nanofibrous mat. The group found that surface hydrolysis improved the hydrophilicity of the platform, which had a positive effect on pheochromocytoma (PC12) cell adhesion, viability, and proliferation. In addition, this surface modification facilitated the attachment of the bioactive molecule gelatin, grafted with polypyrrole, which increased cell-binding moieties on the platform as well as the addition of conductive properties to the platform, which further enhanced nanofibrous platform-cell interactions (Imani et al., 2021). De Sousa and co-workers aminolyzed poly(ε-caprolactone) (PCL) nanofibers with 1,6-hexanediamine (HDA) to impart amine moieties to the fibers. Laminin and the synthetic linear integrin inhibitor peptide Gly-Arg-Gly-Asp-Ser-Pro were crosslinked to these amine moieties using glutaraldehyde. The cells that attached to the modified nanofibrous platforms showed enhanced average cell eccentricities, differentiation efficiency, and enhanced neurite length compared with the unfunctionalized PCL nanofibers. These results suggest that the adhesion of peptides or proteins with biological motifs on the nanofibrous platforms establishes important cell interactions (de Sousa et al., 2020). Borah

and co-workers, fabricated poly[2-methoxy-5-(2-ethylhexyloxy)-1,4-phenylenevinylene] electrospun mats aminolyzed with 3-aminopropyltriethoxysilane (APTES) and HDA. The group suggested this as an alternative to costly biomolecule coating to improve platform-cell interactions. The aminated nanofibrous platforms exhibited enhanced PC12 cell attachment and differentiation compared with unfunctionalized controls. Aminolysis coupled with the electrical stimulation of the nanofibrous mats demonstrated enhanced neurite formation and elongation compared with collagen-coated mats without electrical stimulation. These findings indicate that the combination of surface amination and electrical stimulation is an advanced strategy for augmented nerve regeneration (Borah et al., 2021).

Sangsanoh and co-workers compared aminolysis and hydrolysis as surface treatments on poly(3-hydroxybutyrate) (PHB) nanofibrous platforms using HDA and sodium hydroxide, respectively. Both treatments enhanced the surface roughness of the fibers and decreased the water contact angle. Although the aminolysis and hydrolysis of the nanofibrous platforms facilitated the grafting of laminin onto the surface using *N*-(3-dimethylaminopropyl)-*N*¢-ethylcarbodiimidehydrochloride/*N*-hydroxysuccinimide (EDC/NHS) activation, the hydrolyzed samples enabled a higher amount of laminin immobilization. The laminin-immobilized nanofibrous platforms enhanced Neuro2a cell attachment and proliferation, although mouse brain-derived neural stem cells (NSCs) were unable to proliferate on the neat PHB, hydrolyzed PHB, and hydrolyzed PHB with immobilized laminin nanofibrous platforms (Sangsanoh et al., 2018). This study highlights the cell line variability in neural tissue engineering.

Patel and co-workers developed a novel technique based on wet chemistry to immobilize laminin and basic fibroblast growth factor on the surface of poly(l-lactic acid) (PLLA) nanofibrous platforms. First, the nanofibrous platforms were treated with sodium hydroxide to increase the number of carboxylic moieties on the nanofibers. Then, the linker molecule, di-amino-poly(ethylene glycol), was used to create heparin-functionalized nanofibrous platforms. The di-amino-poly(ethylene glycol) molecules were covalently attached to the carboxylic groups on the PLLA nanofibers using EDC/NHS activation. Thereafter, heparin molecules were covalently attached to the free amines on the di-amino-poly(ethylene glycol) molecules via EDC and sulfo-NHS. Then, basic fibroblast growth factor and laminin were able to bind heparin, enabling their immobilization on the surface of the nanofibers, enhancing neurite outgrowth from dorsal root ganglion (DRG) tissue (Figure 2.1) (Patel et al., 2007). Chen and co-workers compared the effectiveness of wet chemical functionalization and physical adsorption techniques in binding laminin to the surface of silica nanofibrous platforms, which demonstrated superior results in terms of biocompatibility, bioactivity, and biodegradability compared with nanofibrous platforms modified by physical adsorption (Chen et al., 2018).

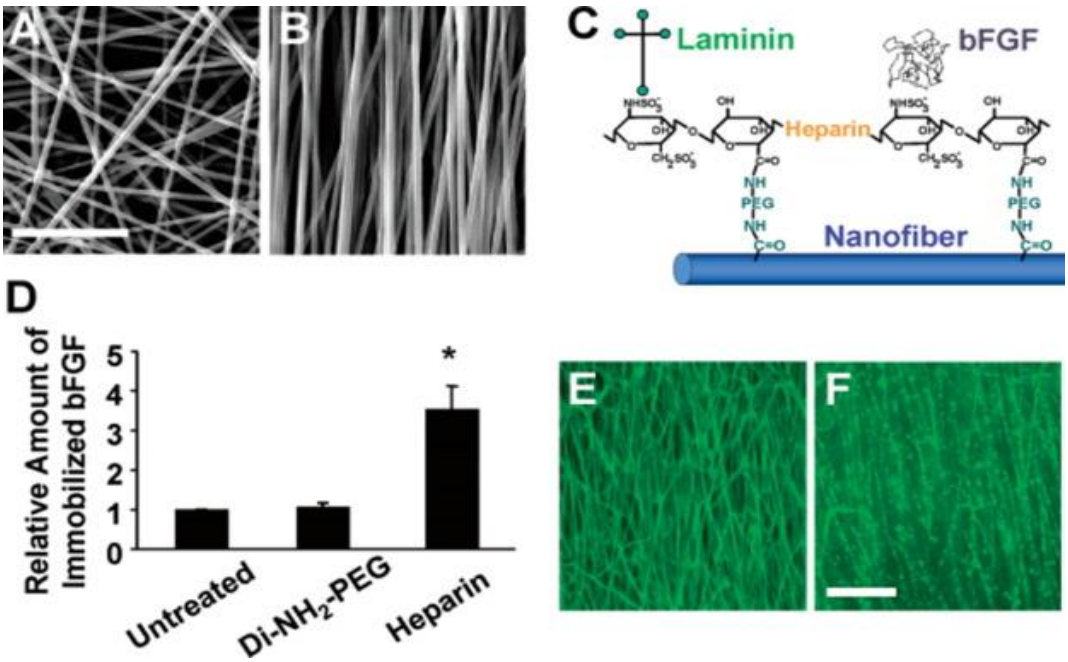


Figure 2. 1 Characterization of aligned and bioactive nanofibers. Scanning electron microscopy images of (a) random poly(l-lactic acid) nanofibers, (b) aligned poly(l-lactic acid) nanofibers, (c) immobilization of basic fibroblast growth factor and laminin on poly(l-lactic acid) nanofibers, (d) a modified ELISA technique was used to show relative levels of basic fibroblast growth factor attachment on untreated, linker-modified, and heparin-functionalized poly(l-lactic acid) nanofibers, (e) immunostaining of immobilized laminin and (f) immunostaining of immobilized basic fibroblast growth factor. Reproduced with permission from Patel (2007).

In addition, PC12 cells were seeded onto the covalently modified nanofibrous platforms and demonstrated significantly longer neurite extensions compared with those seeded onto the physical adsorption-modified platform (Chen et al., 2018).Table 2.1 summarizes recent relevant studies on the use of aminolysis and hydrolysis as a means to hydrophilize nanofibrous platforms and facilitate the surface attachment of bioactive moieties. The covalent attachment of these biomolecules renders chemical immobilization of D/B on the surface of nanofibrous platforms advantageous in neural tissue engineering because it prevents the leaching of these chemicals from the nanofibers when incubated over an extended period (Yoo et al., 2009). Furthermore, the enhanced hydrophilicity is advantageous for cell-platform interactions. However, scission of the polymer backbone as well as partial inactivation of the immobilized molecules can occur, thus somewhat limiting this method of D/B immobilization (Yoo et al., 2009). In addition, if these cytotoxic residual chemicals are not entirely removed from the scaffold which can negatively impact *In Vitro* and *In Vivo* interactions in terms of toxicity (Yoo et al., 2009).

Table 2. 1. Summary of *In Vitro* studies on wet chemical functionalized nanofibrous platforms for application in neural tissue engineering.

Aminolysis				
Substrate	**Chemical agent**	**Outcomes**	***In Vitro* observations**	**Reference**
Poly(l-lactic) acid	Hexamethylenediamine	Amine groups enabled graphene oxide coating; decreased water contact angle; produced uneven surface roughness of nanofibers	Enhanced PC12 cell proliferation and neurite outgrowth	Zhang et al., 2016)
Iron chloride-doped polycaprolactone	(3-aminopropyl) triethoxysilane/ hexamethylenediamine	Enhanced mechanical properties after surface functionalization	Enhancement in PC12 cell attachment, differentiation, and neurite outgrowth	(Borah et al., 2021)
Polycaprolactone	Ethylenediamine/ hexamethylenediamine	Fibers changed to 'glued morphology', which reduced porosity, yet still fell within acceptable range; decreased water contact angle, crystallinity, and Young's modulus	Increase in cell-covered area	(Toledo et al., 2021)
Polylactic acid	Polyacrylamide/ polyvinylaminde	All altered average fiber diameter and porosity; facilitated chemical grafting of recombinant human epidermal growth factor	Polyvinylamide-aminolyzed mats with grafted epidermal growth factor enhanced cell viability and proliferation	(Haddad et al., 2016)
Polycaprolactone	Ethylenediamine/ tetra-acetic acid	Facilitated immobilization of brain-derived neurotrophic factor	Enhanced cell attachment, differentiation, and proliferation	(Horne et al., 2010)
Hydrolysis				
Substrate	**Outcomes**		***In Vitro* observations**	**Reference**
Polylactic acid	Facilitated grafting of pyrrole/ gelatin copolymer on to surface of scaffold using ethyl(dimethylamino propyl)carbodiimide/N-hydroxysuccinimide; reduced contact angle		Increased intercellular attachment and proliferation	(Imani et al., 2021)
Polycaprolactone	Enabled covalent attachment of matrigel to polycaprolactone nanofibrous platform using ethyl(dimethylamino propyl)carbodiimide/ N-hydroxysuccinimide; decreasing contact angle and tensile strength with increasing treatment time		Enhanced cell proliferation, cell surface contact area, and differentiation	(Ghasemi et al., 2010)
Polyhydroxybutyrate/ poly(3-hydroxybutyrate-co-3-hydroxyvalerate)	Facilitated immobilization of various proteins and peptides		Increased Schwann cell proliferation and neural gene expression	(Masaeli et al., 2014)
Poly(l-lactic) acid/ poly lactic-co-glycolic acid	Reduced surface tension at lower potassium hydroxide concentrations, but enhanced surface tension at higher concentrations		Enhanced neurite extension	(Nosbet et al., 2007)
Polycaprolactone	Reduced water contact angle, tensile strength and mass, 1 M sodium hydroxide; 4 h was optimal for both aligned and random samples		Increased protein adsorption, improved cell attachment	(Bosworth et al., 2019)

2.3 Plasma modification

Plasma is defined as an ionized gas comprising an equal density of positive and negative charges (Asadian et al., 2019). The two categories of plasma are thermal and non-thermal plasma (Samal, 2017). For the application of surface modifications of nanofibrous platforms, nonthermal plasma, also known as nonequilibrium or cold plasma, is preferred (Chu et al., 2002). Dielectric barrier discharges or radiofrequency discharges are most frequently used to generate plasma in the tissue-engineering domain, with radio frequency-generated plasma being the most widely used in neural tissue engineering (Samal, 2017)

Although plasma treatment alone might not always directly enhance neural cell adhesion or neurite outgrowth, it can enhance hydrophilicity and provide a means of introducing binding sites for D/B, similar to wet chemistry (Patel et al., 2007). Meghdadi and co-workers used direct barrier discharge-generated helium plasma treatment to introduce hydroxyl and carboxyl groups onto a nanofibrous platform surface, which decreased the water contact angle and improved the hydrophilicity of the platforms. In addition, the plasma treatment facilitated the covalent attachment of gelatin onto the nanofibrous platform surface, which further improved the hydrophilicity and enhanced cell attachment, adhesion, proliferation, and viability compared with the control without gelatin grafting. The modified platforms revealed uniform nanofibrous morphology, with an increased average fiber diameter (Meghdadi et al., 2019). The effect of plasma exposure time was evaluated and revealed no change in morphology of the nanofibrous platforms with an exposure time of up to 3 min. However, after 3 min, the fibers began to aggregate (Figure 2.2(a–e)) (Meghdadi et al., 2019). This highlights the importance of plasma exposure time in maintaining the morphology of the nanofibrous platforms. Table 2.2 highlights recent relevant studies utilizing plasma modification in neural tissue engineering.

Plasma treatment is performed in the gaseous phase and often avoids the use of harsh chemicals, reducing the risk of chemical contamination, as is the case in wet chemical modifications (Yoshida et al., 2013). Plasma modifications are simple, cost-effective, and habitually limited to the first few subsurface layers of nanofibrous platforms; therefore, the bulk of the platform is not influenced (Wagner et al., 2003). If correct plasma conditions are utilized, minimal heating of the platform occurs, avoiding thermal damage to fibers (Wagner et al., 2003). The studies presented in Table 2.2 provide insight into the usefulness of both direct barrier discharge- and radio frequency-generated plasma surface modifications in enhancing the neurocompatibility of nanofibrous platforms. plasma modifications are effective in enhancing surface properties of nanofibers, thereby promoting cell-platform interactions, or facilitating the surface attachment of D/B (Yoshida et al., 2013).

Table 2. 2 Summary of *In Vitro* and *In Vivo* studies of plasma-functionalized nanofibrous platforms for application in neural tissue engineering.

Gas	Substrate	Outcomes	*In Vitro/In Vivo* observations	Reference
Air	Polycaprolactone/ collagen	Decreased water contact angle; decreased tensile strength; no surface morphology changes	Enhanced attachment and proliferation of Schwann cells compared with controls	(Prabhakaran et al., 2008)
	Poly(lactic-co-glycolic) acid/ carboxyl-modified multi-walled carbon nanotubes	Decreased water contact angle; no morphological changes with plasma exposure time <60 s; plasma exposure time >60 s showed curls in fibers; no mechanical strength changes; improved fiber toughness	Improved PC12 cell, Schwann cells, and dorsal root ganglion neuron attachment, proliferation, differentiation, maturation, and neurite extension *In Vitro*	(Wang et al., 2017)
	Polylactic acid/ silk fibroin	Decreased water contact angle; smoother fiber surface	Increased PC12 cell attachment, differentiation, and enhanced neurite length	(Tian et al., 2015)
Argon	Polycaprolactone	Increased surface area; facilitated attachment of Schwann cell-derived conditioned medium	Enhanced motor coordination, muscle activity and remyelination; increased myelin sheath thickness, number of motoneurons, neuroglial cells and volume of anterior horn of spinal cord in male Wistar rats	Raoofi et al., 2019)
	Polycaprolactone/ polyethylene oxide	Enabled coating of cyclopropylamine; enhanced stiffness; decreased ductility; enhanced water stability	–	(Kupka et al., 2020)
Oxygen	Polylactic acid	No reported effect on fiber morphology	Positively supported differentiation of stem cells into neural lineage; encouraged appropriate cell adhesion, proliferation, and differentiation	(Miri et al., 2021)
	Polyvinylidene fluoride	Enabled binding of nanorods on the surface; reduced contact angle; controlled release of iron	Promoted cell attachment, spread, proliferation, and migration and differentiation; upregulation of neural-specific genes	(Zhang et al., 2021)
	Silk fibroin/ polyethylene oxide	Decreased water contact angle	Improved Schwann cell proliferation *In Vitro*	(Rajabi et al., 2018)
Oxygen, Helium, Argon	Polyurethane	Decreased fiber diameter of oxygen-nanofibers; no fiber diameter changes for helium and argon plasma-treated platforms	Improved neural stem cell adhesion *In Vitro*, with no effect on neuronal differentiation of neural stem cells	(Zanden et al., 2014)

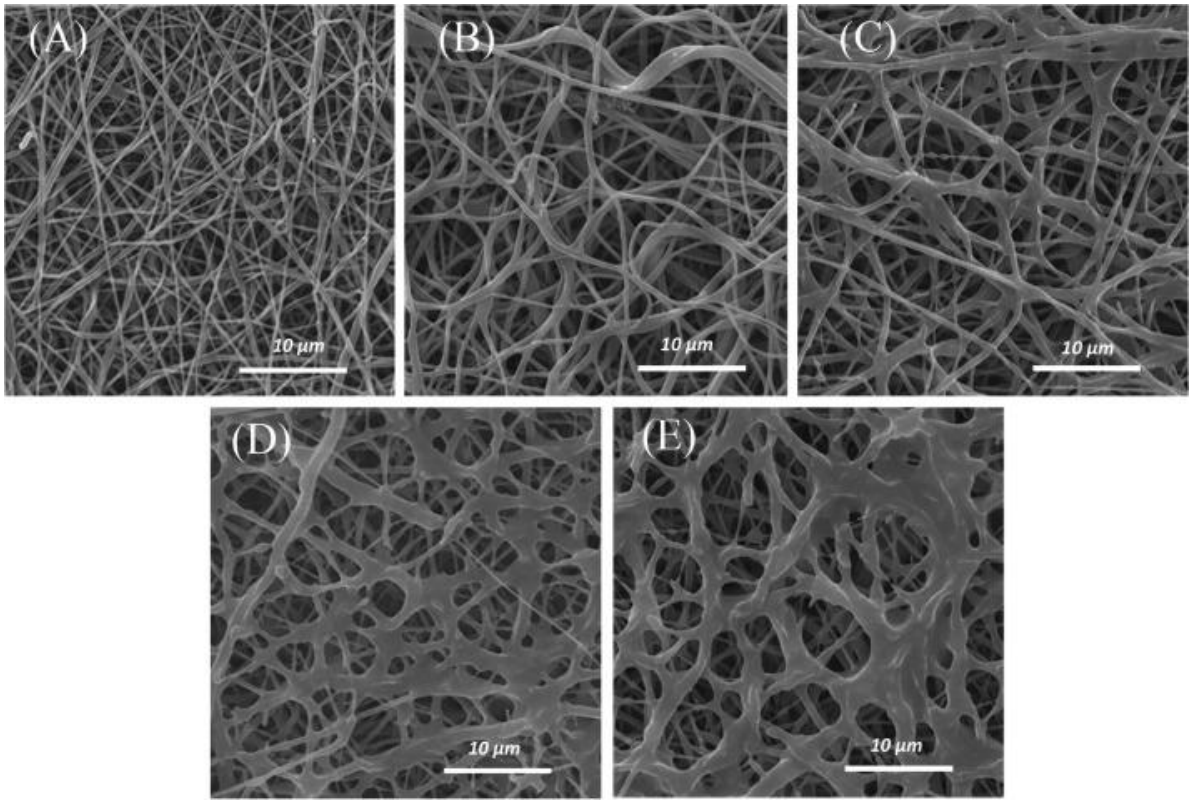


Figure 2. 2 Scanning electron microscope images of (a) untreated polycaprolactone nanofibrous platforms, (b) polycaprolactone nanofibrous platforms cold atmospheric plasma treated for 1 min, (c) 3 min, (d) 5 min, and (e) 7 min. Reproduced with permission from Meghdadi (2019).

2.4 Surface adsorption of drugs or biomolecules

Drug-or biomolecule-loaded nanoparticles can be adsorbed onto the nanofibrous platform surface before or after the electrospinning process (Kim et al., 2005; Liu et al., 2018) (Figure 2.3). The pre-processing addition of nanoparticles can improve fiber hydrophilicity (Kurusu et al., 2019). A prerequisite for this to occur is the homogenous location of the nanoparticles on the surface of the fibers (Kurusu et al., 2019). Even if homogenous dispersion is achieved, the nanoparticles can still aggregate in the bulk of the fibers, however, this phenomenon can be curbed by tailoring the surface energy of the polymeric composite and the nanoparticles (Zhang et al., 2015). If the surface energy of the nanoparticles is higher than the surface energy of the polymer, they are likely to be buried within the bulk of the polymer. By contrast, nanoparticles with a relatively low surface energy have an affinity to the air interface and, consequently, can be used to change the surface properties of the fibers (Kurusu et al., 2019; Jiang et al., 2004). Guo and co-workers compared composite keratin/polyvinyl alcohol nanofibers formed by blend electrospinning (discussed in Section 2.6) and polyvinyl alcohol nanofibers surface-functionalized with keratin nanoparticles formed by electrospray deposition after electrospinning. The finding was that the addition of keratin into the blend nanofibers

decreased the mechanical properties of the nanofibers as a result of the poor spinnability of keratin, leading to a heterogenous distribution of keratin within the fibers.

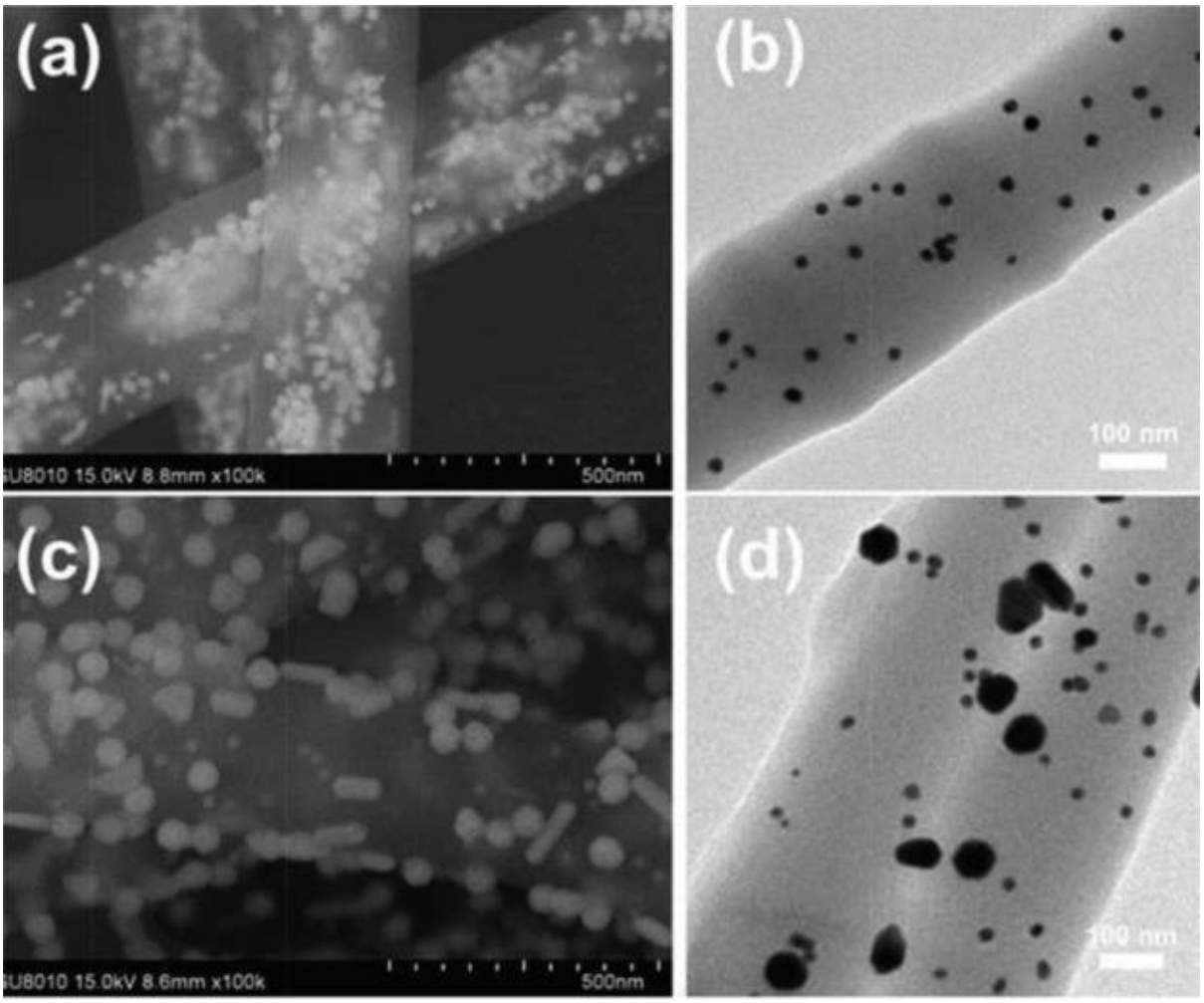


Figure 2. 3 Scanning electron microscopy and transmission electron microscopy images of the polyacrylic acid/polyvinyl alcohol electrospun nanofibers assembled with (a, b) small gold nanoparticles, (c, d) small gold nanoparticles-big gold nanoparticles. Reproduced with permission from Liu (2018).

The attachment of keratin nanoparticles to the surface of the polyvinyl alcohol nanofibers improved the hydrophilicity and mechanical strength of the nanofibers, thereby improving the PC12 and Cellosaurus cell line cellular adhesion and proliferation compared with the blend keratin/polyvinyl alcohol nanofibers (Guo et al., 2019). Christopherson and co-workers cultured rat hippocampus-derived adult NSCs on laminin-coated polyether sulfone electrospun nanofibers, with average fiber diameters of 283 ± 45 nm, 749 ± 153 nm, and 1452 ± 312 nm. The study highlighted the dependency of neural stem cell behavior on average fiber diameter. The stem cells demonstrated a substantial increase in oligodendrocyte differentiation on the 283 nm fibers and an increase in neuronal differentiation on the 749 nm fibers compared with controls (Christophersen et al., 2009). Du and co-workers compared the effect of nanofiber composition on cell interactions by fabricating polyether sulfone, chitosan, and cellulose

acetate nanofibers. Experiments involving PC12 cells were coated with collagen, whereas those involving human-derived NSCs were coated with poly-d-lysine. The polysaccharide-derived materials (cellulose acetate and chitosan) inhibited proliferation to a lesser extent compared with polyether sulfone. The 3D nanofibrillar architecture enhanced NSC differentiation compared with the 2D controls (Du et al., 2014). This study illustrated the importance of the incorporation of bioactive materials in the fabrication of nanofibrous platforms for neural tissue engineering. Table 2.3 highlights recent studies illustrating the effectiveness of physical surface adsorption of D/B for neural tissue engineering.

Table 2. 3 Summary of *In Vitro* and *In Vivo* studies on nanofibrous platforms for application in neural tissue engineering based on physical adsorption for drug and biomolecule delivery.

Substrate	Adsorbed constituent	Outcomes	*In Vitro/In Vivo* observations	Reference
Poly(lactic-co-glycolic) acid/ multi-walled carbon nanotubes	Dopamine, laminin and dopamine-laminin	Coatings reduced water contact angle to 0 ; enhanced degradation rate	Enhanced cell attachment, viability, and neurite outgrowth	(Nazeri et al., 2021)
Polyamide	Tenascin C-derived peptides	–	Promoted growth of neuronal processes, neurite attachment, generation and outgrowth	(Ahmed et al., 2006)
Polyethylene glycol conjugated to polycaprolactone	Nerve growth factor	Conjugated nerve growth factor scaffold=sustained release; physically absorbed nerve growth factor= burst release	Conjugation of nerve growth factor increased expression levels of marker proteins for neuron cells	(Choi et al., 2010)
Polylactic acid/ nerve growth factor emulsion	Vascular endothelial growth factor	Decreased water contact angle; controlled release of the growth factors; slightly decreased Young's modulus	Promoted nerve differentiation of stem cells; improved neovascularization and nerve healing post-operation for 3 months	(Xia et al., 2018)

Although the addition of nanoparticles to the electrospinning solution is an effective and simple method to alter surface properties or to incorporate D/B within the fibers, complex aspects, such as nanoparticle dispersion and segregation in solution, must be taken into careful consideration (Du et al., 2014).

2.5 Layer-by-layer multilayer assembly

The layer-by-layer (LbL) multilayer assembly technique can also be used to attach D/B to the surface of electrospun nanofibrous platforms, avoiding denaturation and loss of activity

(Thierry et al., 2005). This technique involves the fabrication of a multiple layer coating on nanofibers with tailorable qualities, such as thickness, charge, porosity, and functionality, driven by the alternating adsorption of polymers with opposing charges (Kim et al., 2008). Alternatively, each polymer solution can be electrospun from separate outlets and subsequently collected on the same target collector in alternating layers (Kidoaki et al., 2005). Zhang and co-workers fabricated a nanofibrous platform designed for the localized delivery of clustered regularly interspaced short palindromic repeat (CRISPR) and the dead Cas9 plasmid via a LbL self-assembling peptide coating on the nanofibers for application in neural tissue engineering. These CRISPR systems have emerged as frontiers in precise genome editing for diverse biological applications. The group created two oppositely charged amphiphilic self-assembling peptides. First, the negatively charged self-assembling peptide was coated onto a PCL nanofibrous platform via hydrophobic interactions, which allowed electrostatic adsorption of the positively charged peptide bound to arginylglycylaspartic acid onto the platform. The peptide-coated scaffolds facilitated efficient loading and sustained release of pDNA complexes, while enhancing human mesenchymal stem cell adhesion and proliferation. The local delivery of CRISPR/dead Cas9 system activated glial cell line-derived neurotrophic factor expression in mammalian cells, which promoted neurite outgrowth *In Vitro* (Hsu et al., 2014).

He and co-workers used laminin and chitosan to modify the surface of electrospun PLLA nanofibrous platforms by LbL self-assembly. Briefly, the PLLA nanofibers were activated by polyethyleneimine to obtain a stable charged surface, achieving a multilayer build-up of laminin and chitosan by alternatively dipping the platforms in the respective solutions. The LbL self-assembly was triggered by the static electrostatic interactions between the negatively charged laminin and positively charged chitosan. Laminin-coated nanofibrous platforms using the physical adsorption method was used as a comparison. This technique led to more laminin being deposited on the fibers and more uniform fibers, enhancing biocompatibility, neuron growth, and neurite outgrowth compared with the laminin-coated nanofibrous platforms via physical adsorption (He et al., 2013). Zhou and co-workers used LbL assembly to coat PCL nanofibrous platforms with PLLA/heparin/graphene. The authors demonstrated that the imparted electrical conductivity enhanced neuronal attachment and neurite outgrowth and the incorporation of multilayers did not disturb the inherent fiber morphology or porosity, rendering LbL assembly a simple, effective, and inexpensive method of preparing multi-layered nanofibrous platforms for neural tissue engineering (Zhou et al., 2012). Table 2.4 highlights recent relevant studies based on LbL deposition for neural tissue engineering applications.

Despite the many advantages of this technique, LbL systems utilizing hydrogen bonding are often unstable at neutral pH ranges, which significantly enhances their degradation, hindering

controlled release of D/B. Therefore, these systems would be most suited for burst-release applications (Wood et al., 2005).

2.6 Blend electrospinning

Blend electrospinning involves the mixing of D/B with a polymeric solution before electrospinning (Maderuelo et al., 2011). The molecule is dissolved or dispersed within the solution, which can lead to surface modification of nanofibers, surface attachment, or D/B encapsulation (Maderuelo et al., 2011). The incorporation of a second polymer can alter the chemical composition, conductivity, viscosity, and surface tension of the polymeric solution, which can affect the electrospinnability of the solution (Kurusu et al.,2019). The surface energy of the constituent polymers is crucial for controlling the surface morphology of the resultant nanofibrous platforms. Bhutto and co-workers created a composite nanofibrous platform comprising vitamin B5, PCL, and silk fibroin using blend electrospinning. The addition of vitamin B5 improved the hydrophilicity of the platform, which enhanced the adhesion and proliferation of Schwann cells. Vitamin B5 exhibited sustained release from the fibers, which has been shown to improve the cellular mitochondrial metabolic activity (Bhutto et al., 2016). Saadatkish and co-workers fabricated a PCL, gelatin, and fibrinogen system. The incorporation of PCL improved the mechanical properties of the platform, whereas gelatin and fibrinogen improved the hydrophilicity and cell proliferation (Saadatkish et al., 2018). Motamedi and co-workers created hybrid nanofibrous platforms by blending gold nanoparticles with polyvinylidene difluoride. The combination supported the adhesion and proliferation of seeded PC12 cells, which mimicked the morphology of native neural cells (Motamedi et al., 2017). Thipkaew and co-workers fabricated blend-electrospun nanofibers incorporating zein and quercetin for the recovery of focal entrapment neuropathy in streptazocin-induced diabetes. Walking track analysis, measurements of foot withdrawal reflex, nerve conduction velocity, and morphological analysis were used to assess functional recovery in an *In Vivo* rodent model. The results demonstrated that the drug-loaded nanofibers improved the sciatic function index, significantly reduced the foot withdrawal reflex latencies, enhanced nerve conduction velocities, axonal densities, and phosphorylated extracellular regulated-kinase 1 and 2 levels in the lesioned nerve, which are associated with neurite extension and plasticity (Thipkaew et al., 2017).

These and other studies outlined in Table 2.5 demonstrate the effectiveness of blend electrospinning in the creation of hybrid nanofibrous platforms combining the unique properties of the constituents. Furthermore, blend electrospinning avoids the harsh morphological changes often imparted by the wet chemical method or plasma etching.

Table 2. 4 Summary of *In Vitro* and *In Vivo* studies on nanofibrous platforms for application in neural tissue engineering based on layer-by-layer multilayer assembly.

Constituent layers	Outcomes	*In VitroIn Vivo* observations	Reference
Polycaprolactone/ deferoxamine	Layer-by-layer assembly achieved through aminolysis; rapid burst release; aminolysis caused no change in mechanical strength	Accelerated transition from acute inflammation phase to repair phase in 14 mm sciatic nerve defect; enhanced removal of myelin degradation products	(Quan et al., 2021)
Heparin/ poly(l-lysine) on polycaprolactone	Growth factors immobilized on surface	Enhanced proliferation, neurite outgrowth, longer neurites, and larger cell numbers of neural progenitor cells	(Zhou et al., 2014)
Heparin/ poly(l-lysine) on polycaprolactone	Surface activation using polyethyleneimine.	Enhanced mesenchymal stem cell adhesion, networking of monolayers containing nestin-positive presumptive neurons	(Thouas et al., 2008)
Chitosan/ gelatin on polylactic acid	Surface activation via aminolysis nanofibrous platforms maintained porous and fibrous nature	Enhanced cell viability and neurite outgrowth; longer, branched neurite outgrowth; enhanced cell viability	(He at al., 2012)
Heparin/ collagen/ nerve growth factor on polylactic acid	Enhanced surface roughness; development of ‘net-like’ protuberances; decreased water contact angle; nerve growth factor presented sustained release for two weeks	Enhanced Schwann cell proliferation and neurite outgrowth along fiber orientation; enhanced PC12 differentiation	(Zhang et al., 2017)
Vascular endothelial growth factor-loaded poly(allylamine hydrochloride)/ polystyrene sulfonate multilayers on polycaprolactone	Increased surface roughness	Neuroprotective effects by inhibiting oxidative stress, suggesting therapeutic value in ischemic cerebrovascular diseases	(Wang et al., 2021)
Nerve growth factor-coated polycaprolactone; temozolomide-doped polycaprolactone and sodium alginate hydrogel	‘Sandwich scaffold’ fabricated by attaching sodium alginate hydrogel on top of nerve growth factor-coated polycaprolactone; enabled attachment of temozolomide-loaded polycaprolactone nanofibrous platform; reduced water contact angle	Inhibited growth of glioma cells and improved differentiation of neuronal cells	(Huang et al., 2016)

2.7 Co-axial electrospinning

Co-axial electrospinning is based on simultaneous fiber formation from two polymeric solutions, using two co-axially placed needles, as opposed to one in the conventional electrospinning set-up (Briggs et al., 2014). This results in the formation of a composite polymeric solution comprising an inner core, pumped through the internal needle, and the outer shell, pumped through the external needle (Briggs et al., 2014). This core/shell morphology (Figure 2.4) allows for tailorable pharmaceutical release profiles without altering surface chemistry, while also enabling the electrospinning of non-spinnable or hardly spinnable materials (Briggs et al., 2014).

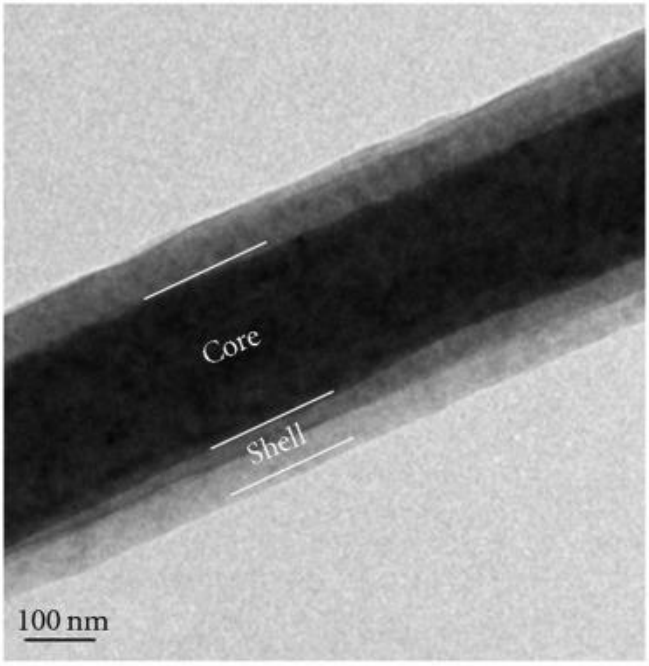


Figure 2. 4 Transmission electron microscopy of a core–shell fiber prepared by co-axial electrospinning. A 10 % w/v aqueous polyvinyl alcohol was used as the core, whereas 8 % w/v polyvinylpyrrolidone dissolved in dimethylformamide was used as the shell. Reproduced with permission from Sahay (2011).

Some of the defining limitations of this technique include its complex set-up, as a co-axial needle and an array of syringe pumps is required (Motamedi et al., 2017). It is further limited by a low production rate and the formation of fibers with differing properties across the interwoven polymeric matrix (Buzgo et al., 2018). Nonetheless, nanofibers with a core/shell morphology have paved the way for eliminating burst-release drug elution profiles, which are observed in single component fibers (Zhang et al., 2006). Ma and co-workers created an oxygen-enriched core/shell nanofibrous platform using perfluorotributylamine as the core and PCL as the shell. The core/shell morphology provided a ‘reservoir’ for the controlled delivery of oxygen using perfluorotributylamine. *In Vitro*, the scaffold was found to enhance the

expression of nerve growth factor (NGF), brain-derived neurotropic factor, and vascular endothelial growth factor.

Furthermore, the synergistic effects of the polymeric-enriched gel and the encapsulated fibers enhanced Schwann cell survival in 3D cultures under hypoxic conditions. *In Vivo*, the results indicated that perfluorotributylamine in core/shell fibers and hydrogel synergistically enhanced the survival of Schwann cells following *In Vivo* implantation (Ma et al., 2020). Sun and co-workers fabricated core/shell electrospun nanofibers using a polylactide-co-poly(caprolactone) and silk fibroin blend as the shell and a combination of NGF and monosialoganglioside as the core. The system enhanced PC12 and Schwann cell differentiation and proliferation, demonstrating that co-axial electrospinning is a useful technique for the dual encapsulation of neurotrophins (Sun et al., 2016). Song and co-workers successfully fabricated core/shell co-axially electrospun nanofibers, with a laminin core and a polydioxanone/collagen shell. Laminin was steadily and continuously released from the fiber core, providing enhanced neurite outgrowth and neurogenic differentiation (Figure 2.5) as a combination of biochemical and topographical cues provided by the sustained release of laminin and the aligned nanofibrous structure (Song et al., 2018). The yellow lines indicate the direction of neurite outgrowth.

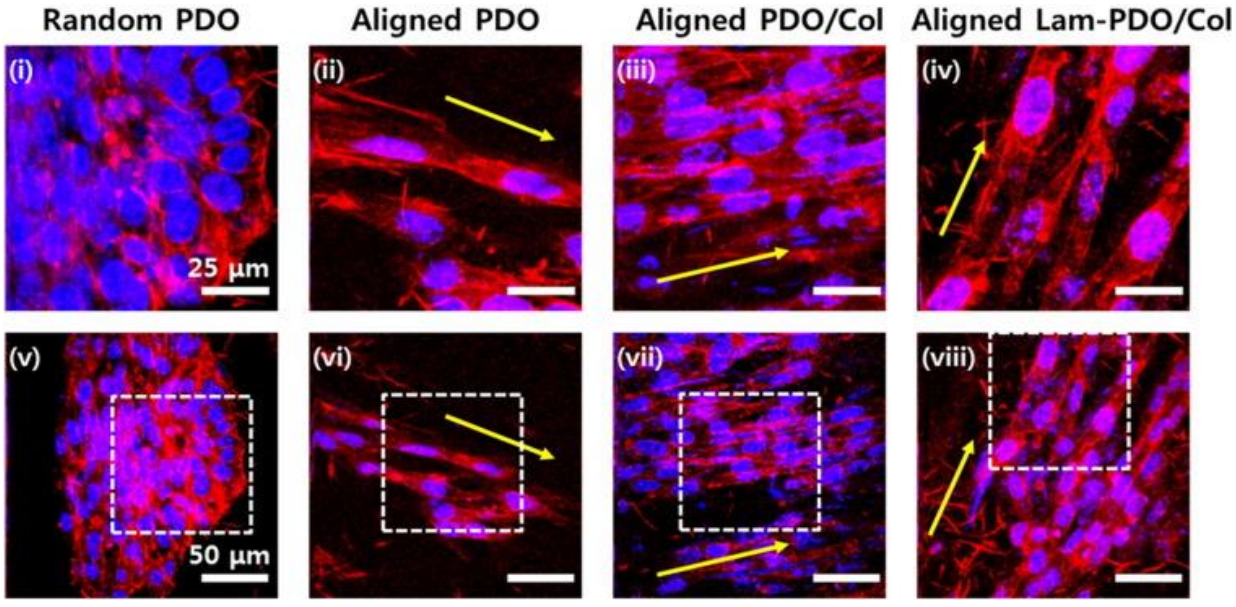


Figure 2. 5 Cell morphologies and alignment of HT-22 mouse hippocampal neuronal cells on the random polydioxanone, aligned polydioxanone, aligned polydioxanone/collagen, and aligned laminin-polydioxanone/collagen core/shell matrices. Two-photon excitation fluorescence images of HT-22 mouse hippocampal neuronal cells on the random polydioxanone, aligned polydioxanone, aligned polydioxanone/collagen, and aligned laminin-polydioxanone/collagen core/shell matrices at five days of culture. (i-iv). Magnified images of the region enclosed by the dashed white square in (v-viii). Reproduced with permission from Song (2018).

Table 2. 5 Summary of *In Vitro* studies of blend electrospun nanofibers for application in neural tissue engineering.

Blend	Constituent attributes			*In Vitro* observations	Reference
Gelatin/ polycaprolactone/ graphene		Polycaprolactone: Hydrophobic; lack of cell-recognition sites; good electrospinnability; good mechanical properties; biodegradable		Antibacterial activity and enhanced hydrophilicity due to graphene; enhanced PC12 cell migration, proliferation, and differentiation; controlled drug release	(Schnell et al., 2007)
Gelatin/ polycaprolactone	Gelatin: Poor mechanical properties; biodegradability; biocompatibility; commercial availability at low cost			Enhanced Schwann cell attachment, viability and proliferation, and differentiation into neural lineages; controlled release of citicoline	(Alvarez-Perez et al., 2010)
Gelatin/ hyaluronan		Hyaluronan: Provides hydration and porosity; conceals encapsulated cells from other cells and humoral factors; keeps stem/progenitor cells in quiescent state; silences inflammation		Schwann cells displayed better organized F-actin; improved expression of genes, such as those encoding neuregulin 1, glial fibrillary acidic protein	(Liou et al., 2013)
poly(l-lactic acid-co-epsilon-caprolactone) polylactide-co-polycaprolactone/ collagen I and III	Polylactide-co-polycaprolactone: Good mechanical properties; the degradation rate of the scaffold can be altered by varying the ratios of lactic acid and caprolactone; neuro-compatible	Collagen I and III: Constituents of many peripheral nerve tissues. This study utilized both type I and type III collagen for fabrication of nerve graft to mimic structure and composition of native nerve as much as possible		Improved cell proliferation and neurofilament protein expression; accelerated nerve regeneration	(Kijenska et al., 2012)
Elastin/ polycaprolactone	Elastin: Promotion of cell attachment and scaffold elasticity	Polycaprolactone: Provides controlled degradation rate under physiological conditions		Improved cell attachment and neurite extension of embryonic chick dorsal root ganglia	(Swindle-Reiley et al., 2014)
Polypyrrole/ poly(d,l-lactic acid)	Polypyrrole: Electrical properties; cell and tissue compatibility; easy to synthesize	Poly(d,l-lactic acid): Good biodegradability; cyto-compatible; good mechanical properties		Increase in both percentage of neurite-bearing cells and median neurite length	(Xu et al., 2014)
Silk fibroin/ polyethylene oxide electrospun on reduced graphene oxide sheet	Silk fibroin: Biocompatible, biodegradableextracellular matrix-mimicking topography; promotes cell attachment and proliferation	Polyethylene oxide: Good electrospinnability	Reduced graphene oxide: Electrical conductivity; enhances neuronal differentiation	Could induce oriented growth of SH-SY5Y cells; enhancement of neuronal differentiation, and formation of neural networks.	(Thampi et al., 2020)

Binan and co-workers created a core/shell nanofibrous platform with a PLLA core, and a gelatin shell, loaded with retinoic acid and purmorphamine. The use of retinoic acid and purmorphamine enabled the differentiation of NSCs into motor neurons (Binan et al., 2014). This unique core/shell platform presented sufficient mechanical strength and was able to distribute sustained instructive cues, enabling the advanced proliferation and differentiation of non-small cell lung carcinoma cells into motor neurons. The study concluded that the platform could offer the necessary chemical and mechanical cues for the development of motor nerve grafts from non-small cell lung carcinoma cells, either *In Vitro* or *In Situ* (Binan et al., 2014). Table 2.6 summarizes recent studies utilizing co-axial electrospinning to fabricate unique core/shell nanofibers with tailorable release properties and enhanced cell-platform interactions.

Co-axial electrospinning is a useful, high-throughput, and reproducible technique to create nanofibers with precise control over the positioning of the D/B within the nanofibers as well as tailorable release properties. A notable drawback of core/shell fibers is that their primary release mechanism is reliant on the diffusion of D/B through the shell, thereby limiting their ability to efficiently respond to physiological triggers, such as pH (Wood et al., 2005).

2.8 Emulsion electrospinning

Emulsion electrospinning is a promising and flexible technique to curb the vast limitations of co-axial and blend electrospinning (Nikmaram et al., 2017). Figure 2.6 depicts the difference between blend, co-axial, and emulsion electrospinning (Nikmaram et al., 2017). This mechanistic approach exploits the advantages of the core/shell morphology as with co-axial electrospinning, however, this is achieved by electrospinning a stable emulsion, as opposed to the use of a multi-nozzle spinneret (Buzgo et al., 2018). The emulsion is formed by mixing two immiscible phases stabilized by surfactants (Buzgo et al., 2018). The continuous phase of the emulsion forms the shell of the fibers, whereas the droplet phase forms the core (Buzgo et al., 2018). Emulsion electrospinning enables the encapsulation of lipophilic compounds while avoiding the use of organic solvents, if required (Arecchi et al., 2010).

Emulsion electrospinning has pioneered the fabrication of nanofibrous platforms with tailorable release properties achieved by adjusting the emulsifier, water, and oil ratio (Wu et al., 2015). Water-in-oil emulsions are typically used for encapsulating polar and hydrophilic molecules, such as proteins, stabilized by surfactants with low hydrophilic-lipophilic balance values (Tadros et al., 2006). Hu and co-workers used emulsion electrospinning to fabricate PCL, NGF, and bovine serum albumin nanofibrous platforms, protecting the two proteins within the core with a PCL shell. Emulsion electrospinning was favoured because it allowed the polymer to encapsulate the protein, thus protecting its bioactivity while simultaneously providing extended

release, imparted by bovine serum albumin. This proved the cytocompatibility of the platforms as well as their superiority to the control (Nikmaram et al., 2017). In this study, emulsion electrospinning proved as an effective technique to encapsulate and provide controlled release of proteins within electrospun polymeric nanofibers (Nikmaram et al., 2017).

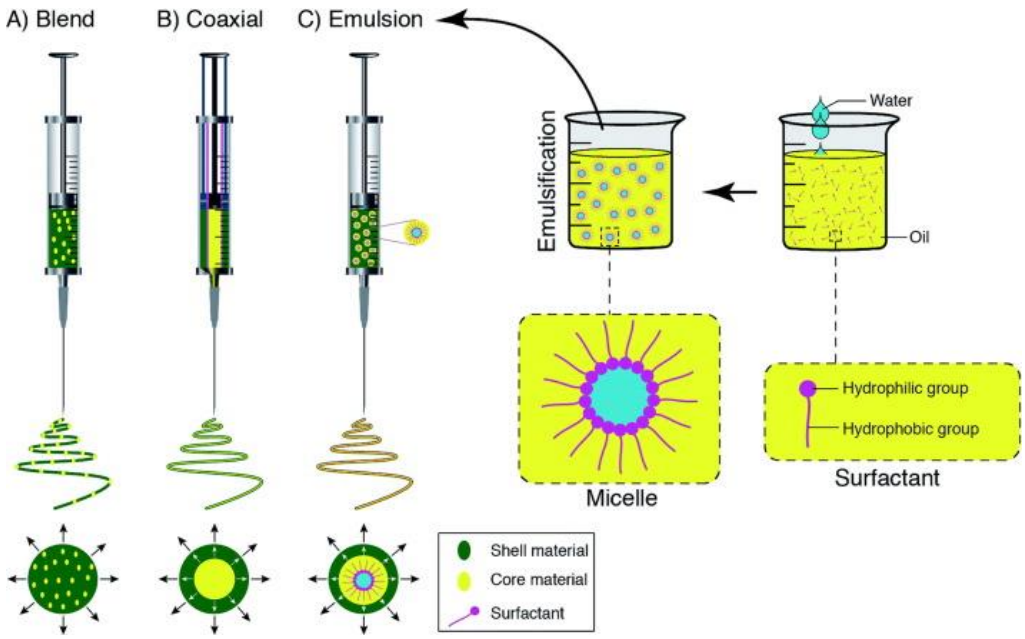


Figure 2. 6 Schematic representation of the different spinnerets loaded with polymeric solutions for (a) blend, (b) co-axial, and (c) emulsion electrospinning. Reproduced with permission from Nikmaram (2017).

Xia and co-workers created a dual-delivery nanofibers using emulsion electrospinning. The platform contained vascular endothelial growth factor loaded onto the surface of the platform and NGF within the core of the PLLA nanofibers. The system demonstrated a sequential release pattern in which most of the vascular endothelial growth factor was released over the first few days, whereas NGF was continuously released for more than one month. In addition, the platform enhanced the neural differentiation of induced pluripotent stem cell-derived neural crest stem cells *In Vitro*. *In Vivo*, the dual-delivery system improved neovascularization and nerve healing three months post-operation (Xia et al., 2018). Other recent studies have used the emulsion electrospinning technique to preserve the bioactivity or control the release of D/B (Chu et al., 2005; Zhang et al., 2006). Xie and co-workers formulated a functional pH-responsive immunoregulation-assisted nanofibers to suppress the release of inflammatory cytokines for the neural differentiation of mesenchymal stem cells *In Vitro*. The group loaded interleukin-4 plasmid-loaded liposomes into nanofibers, which conferred immunoregulatory features. The nanofibers also provided sustained release of NGF through the use of a microsol core/shell structure.

Table 2. 6 Summary of *In Vitro* and *In Vivo* studies on nanofibrous platforms for application in neural tissue engineering based on co-axial electrospinning.

Core	Shell	Outcomes	*In Vivo*/*In Vitro* observations	Reference
Polylactic acid	Polyglycerol sebacate	Reduction in fiber diameter, water contact angle and Young's modulus; increase in stretchability	Enhanced A59 nerve cell attachment and proliferation with enhanced establishment of intercellular contact	(Yan et al., 2017)
Platelet-derived growth factor/ bovine serum albumin	Polycaprolactone/ polyethylene glycol	Uniform protein distribution; enhanced fiber swelling, porosity and protein release rate	Enhanced proliferation rate of NIH 3T3 cells	(Liao et al., 2006)
Gelatin/ polyvinyl alcohol	Polycaprolactone	Surface of nanofibers etched using chloroform/methanol to expose gelatin; increased average fiber diameter when flow rate increased	Enhanced adhesion and proliferation of NIH 3T3 cells	(Park et al., 2020)
Valproic acid	Poly(lactic-co-glycolic) acid	Produced smooth and bead-free surface with uniform fiber diameters; rapid drug release, followed by sustained release; increased Young's modulus, maximal elongation, and tensile strength	Enhanced PC12 attachment, differentiation, and proliferation; no morphological differences between samples/controls; inhibited cell growth (useful for treatment of pheocytochromas)	(Reis et al., 2020)
Nerve growth factor	Poly(lactic-co-glycolic) acid	Improved viscosity and no bead formation; increased average fiber diameter; smooth core/shell interface; nerve growth factor exhibited an initial burst release, followed by steady release for 29 days	Promoted vascularization; increased myelin sheath thickness, nerve fiber percentage, muscle weight recovery, nerve conduction velocity and compound motor action potential	(Wang et al., 2012)
Laminin	Poly(l-lactide-co-ε-caprolactone)	Production of randomly orientated bead-free, uniform and porous fibers; enhanced fiber diameter, reduced water contact angle; increased ultimate tensile strength	Increased Schwann cell proliferation, cell proliferation on day 3 and 7 attributed to controlled release of laminin	(Kijenska et al., 2014)
Polycaprolactone/ silk fibroin/ carbon nanotubes	Gelatin methacryloyl hydrogel	Increased collector rotation rate produced fibers with a smaller diameter	Desirable neurocompatibility; PC12 and dorsal root gaglion neurites were aligned with fiber orientation; enhanced neurite length;	(Wang et al., 2019)

The combination of PH responsiveness, immunoregulation, NGF, and appropriate topographical signals downregulated acute inflammation responses, reduced scar tissue formation, and promoted angiogenesis at the lesion site. In addition, *In Vivo* studies showed that the microenvironment-responsive fibrous system significantly decreased scar tissue formation, downregulated the inflammatory response and glial fiber acidic protein secretion, and promoted angiogenesis, neurogenesis, and motor function recovery (Xi et al., 2020). Table 2.7 highlights relevant studies on the use of emulsion electrospinning to incorporate desirable D/B.

Table 2. 7 Summary of *In Vitro* studies on nanofibrous platforms for application in neural tissue engineering based on emulsion electrospinning.

Dispersed phase	Continuous phase	Outcomes	*In Vitro* observations	Reference
Silk fibroin	Polycaprolactone	Reduced contact angle, fiber diameter, tensile strength; increased mean roughness, elastic modulus	70:30: cell adherence in clusters; 50:50: cell cluster formation with monolayer of cell sheet observed after five days	(Roy et al., 1985)
Chitosan/ polyvinyl alcohol	Poly(lactic-co-glycolic) acid	Reduced contact angle; adequate tensile strength	Enhanced cell attachment and proliferation	(Ajalloueian et al., 2014)
Nerve growth factor/ bovine serum albumin	Polylactide-co-polycaprolactone	Reduced contact angle; stable, sustained protein release	Enhanced neurite extension	(Li et al., 2010)
Nerve growth factor	Polylactic acid/ graphene oxide	Stable, sustained release of nerve growth factor; enhanced porosity, hydrophilicity, tensile strength, and elongation at break	Nerve growth factor retained its bioactivity for 3 weeks; enhanced PC12 proliferation and differentiation	(Haixing et al., 2020)
1: Nerve growth factor, 2: Glial cell-derived growth factor	1: Poly(d,l-lactic acid), 2: poly(lactic-co-glycolic) acid	Reduced average fiber diameter; initial burst release then sustained release over 42 days	Enhanced PC12 adhesion, proliferation, neurite outgrowth and differentiation; growth factors induced dose-dependent extensions independently	(Liu et al., 2021)

Although the incorporation of D/B onto, and within, the bulk of nanofibers imparts desired and often valuable characteristics to nanofibers, it might affect fiber morphology, which, in turn, affects crucial cell-platform interactions, such as cell adherence, proliferation, and growth (Wang et al., 2011). Additionally, care has to be taken when preparing these emulsions because mechanical mixing or ultrasonication processes can affect the structure of the embedded molecules or polymers (Jiang et al., 2012).

2.9 Electrically conductive nanofibrous platforms

The discovery of piezoelectricity, endogenous electric fields, and transmembrane potentials in neural tissues has led to extensive research into the role of electric fields in cellular function and, in turn, the research and development of electrically active engineered scaffolds (Cellot et al., 2009). Electrical charge and charge transfer are vital to numerous physiological processes, particularly at cell membrane interfaces. These processes can be facilitated by the use of applied currents to directly stimulate neurons (Cellot et al., 2009). The passive conductivity of a substrate has the potential to influence cellular responses, such as cell adhesion, proliferation, differentiation, and cellular signalling (Cellot et al., 2006). Electrically active polymers allow the delivery of an electrical stimulus through the use of an external power source. Typical electrically conductive polymers in neural tissue engineering include polyaniline, polypyrrole, polythiophene, polyacetylene, and polyphenylene, as well as carbon-based materials, such as carbon nanotubes, graphite, graphene, fullerene, and nano-diamond (Abidian et al., 2009). The incorporation of electrically active polymers into nanofibers can be achieved through various methods, including LbL multilayer assembly, blend, co-axial, or emulsion electrospinning.

Even without the use of an electric current, cells have shown enhanced neurite extension and proliferation on electrically conductive platforms compared with control samples with no conductive properties (Sahay et al., 2011; Badami et al., 2006). Granato and co-workers combined the electrical conductivity of polypyrrole and the excellent biodegradability and mechanical properties of poly(butylene adipate-co-terephthalate) via blend electrospinning to enhance cellular adhesion and neurite outgrowth compared with the control [pristine poly(butylene adipate-co-terephthalate)] (Granato et al., 2008).

Sadeghi and co-workers fabricated a composite electrospun nanofibrous platform comprising PCL, polypyrrole, and chitosan. The PCL/polypyrrole formulations demonstrated a 2.75-fold increase in the PC12 proliferation rate because of the electrically charged nature of polypyrrole. PCL and polypyrrole are both hydrophobic in nature, yet the addition of chitosan to the formulations improved the hydrophilicity of the platforms, thereby augmenting cell attachment. The blend composition of these three polymers worked synergistically to produce optimized

nanofibers for neural tissue engineering (Sadeghi et al., 2019). Yan and co-workers developed a micropatterned conductive electrospun nanofibrillar scaffold using poly{[aniline tetramer methacrylamide]-co-[dopamine methacrylamide]-co-[poly(ethylene glycol) methyl ether methacrylate]} [poly(ATMA-co-DOPAMA-co-PEGMA] and PCL and electrospinning technology based on a rotation mechanism. The nanofibers were then coated with NGF. The authors investigated the synergism between electrical stimulation and a micropatterned conductive electrospun nanofibrillar topography on the differentiation of rat nerve stem cells. They concluded that the addition of poly(ATMA-co-DOPAMA-co-PEGMA) reduced the average fiber diameter and hydrophilicity but increased the conductivity and electroactivity. Each component had a role in the upregulation of Tuj1 expression and downregulation of the gene encoding glial fibrillary acidic protein, thereby synergistically promoting NSC proliferation and differentiation (Yan et al., 2020).

Zha and co-workers modified electrospun cellulose electrospun nanofibrous platforms with four types of soluble conductive polymer derivatives: poly [*N*-(methacryl ethyl) pyrrole], poly [*N*-(2-hydroxyethyl) pyrrole], poly [3-(ethoxycarbonyl) thiophene], and poly (3-thiophenethanol) by an *In Situ* polymerization method. The group found that PC12 cells demonstrated enhanced cell growth, viability, and proliferation compared with pristine cellulose fiber mats. The authors concluded that conductive coatings on nanofibers act as an active interface for cell interactions, which can further be used to regulate cell activity through electrical stimulations (Zha et al., 2021). Hu and co-workers hypothesized that, because Schwann cells are electrically conductive axons, conductivity might have a role in their differentiation and could then facilitate nerve regeneration. Therefore, the authors fabricated PCL and gelatin nanofibrous platforms that had electrically conductive properties imparted by the incorporation of amine-functionalized multi-walled carbon nanotubes (MWCNTs), seeded with human bone-derived mesenchymal stem cells. When the DRG cells were cultured on randomly orientated nanofibers (R), randomly orientated conductive nanofibers (RC), or bare culture plate (control), the length and orientation of their neurites were similar, and neurite outgrowth occurred in all directions (Figure 2.7) (Wu et al., 2020). However, on the aligned (A) or aligned conductive nanofibers (AC), the neurites projected from the DRG cells were longer and grew parallel to the orientation of the fiber. Statistically, both the average neurite length and maximum neurite length were longest in the AC, second in the A, and there was no significant difference among the R, RC, and control groups (Figure 2.7). During an *In Vivo* study, green fluorescent protein-bone marrow stem cells were seeded on nanofibrous platforms and induced *In Vitro* for 2 weeks. The nanofibrous platforms were subsequently rolled up and inserted into a PCL nerve guidance conduit. The conduits, in addition to a segment of sciatic nerve, were used to bridge a 10 mm rat sciatic nerve gap. 12 weeks after transplantation, the results indicated that the grafted cells had differentiated into mature Schwann cells and participated in myelin formation.

The conduit significantly improved axonal regeneration compared with controls. The study showed that the nanofibrous platform had a significant role in the differentiation of mesenchymal stem cells into Schwann cells and the promise of conductive polymers in peripheral nerve tissue engineering (Wu et al., 2020). Ghorbani and co-workers fabricated PLLA nanofibrous platforms coated with alginate, gelatin, and MWCNTs. They highlighted the ability of the platform to support the growth of Human Wharton Jelly-derived mesenchymal stem cells in 3D culture. Through the addition of valproic acid as the inducer for 21 days *In Vitro*, mesenchymal stem cells differentiated into neural lineages, highlighting the potential of the platform in neural tissue engineering (Ghorbani et al., 2018).

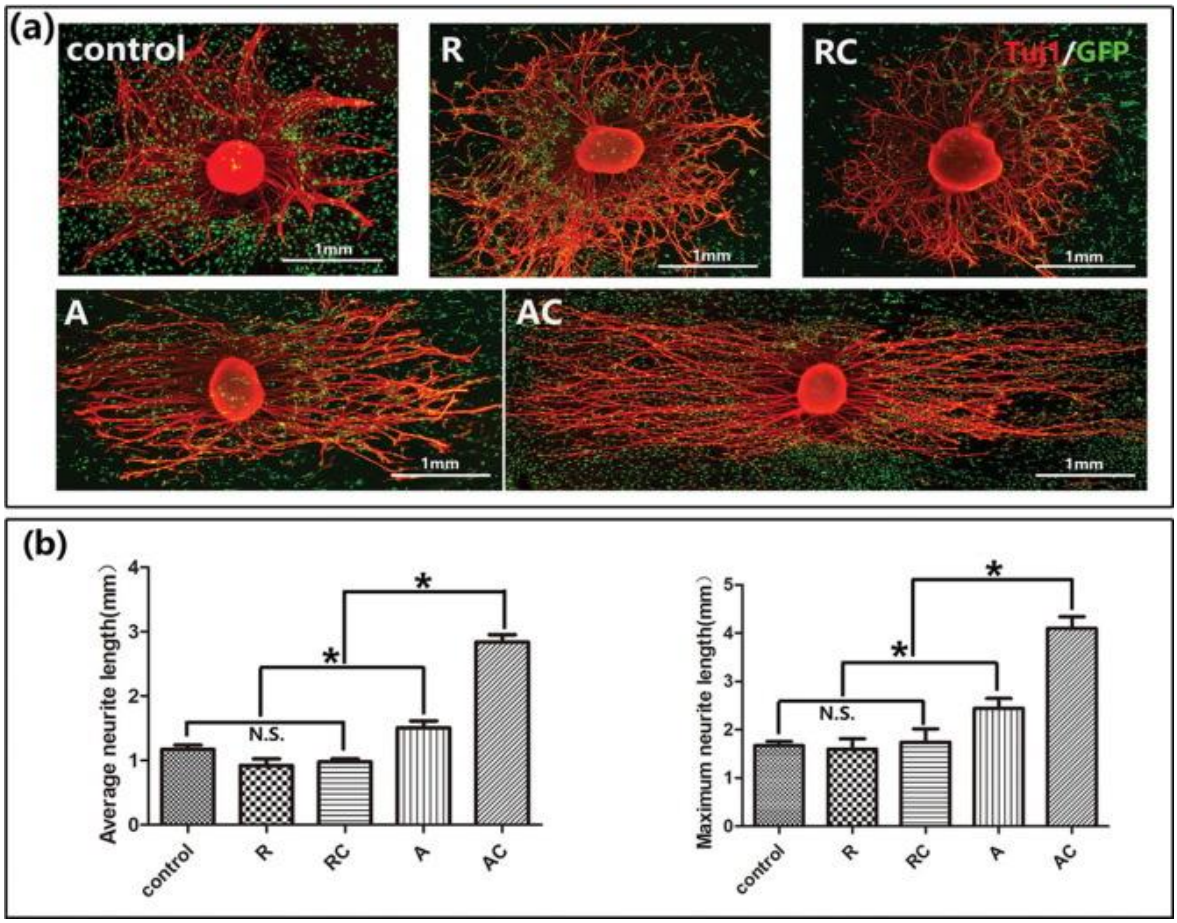


Figure 2. 7 (a) Representative images of neurite outgrowth from dorsal root ganglion cells co-cultured with induced bone marrow-derived stem cells on nanofibrous scaffolds. Neurites were immunofluorescent stained with Tuj1 primary antibodies and 568-conjugated second antibodies (red) and the transdifferentiated Schwann cells were derived from green fluorescent protein rats and show green fluorescence, (b) quantification of the average and maximum neurite length. Reproduced with permission from Yan (2020). (R) randomly orientated nanofibers, (RC) randomly orientated conductive nanofibers, (A) aligned nanofibers, (AC) aligned conductive nanofibers.

Table 2.8 highlights the effectiveness of electrically active constituents in nanofibrous platforms for neural tissue engineering in enhancing neurite outgrowth *In Vitro* and functional recovery

In Vivo. One of the major drawbacks of electrically active polymers is that they are inherently non-biodegradable, which could induce chronic inflammation and require surgical removal *In Vivo* (Huang et al., 2017). However, they often trump piezoelectric polymers in the sense that the electrical stimulus can be controlled, whereas there is no control over the electric stimulus with the use of piezoelectric polymers. Furthermore, electrically conductive polymers have excellent electrical and optical properties, a high conductivity: weight ratio, and tailorable biocompatibility, biodegradability, and porosity, making them an attractive choice for incorporation in nanofibers in the neurogenesis domain (Balant et al., 2014).

2.10 Piezoelectric nanofibrous platforms

Piezoelectric materials have the innate ability to generate electrical activity when deformed, therefore eradicating the need for an external source to supply electrical stimulation, as required with electrically conductive materials in the preceding section (Satyanarayana et al., 2012). This proves advantageous because it eliminates the potential for the accumulation of products of electrolysis (Satyanarayana et al., 2012). When a piezoelectric polymer is deformed, a change in electric polarization is induced by the asymmetric shift in charges, thereby generating electricity. Piezoelectric polymers have gleaned considerable interest in the neural tissue engineering arena because electric pulses can stimulate neurite directional outgrowth to repair nervous tissue injuries (Satyanarayana et al., 2012). Polyvinylidene fluoride is an attractive piezoelectric polymer for application in neural tissue engineering because of its cytocompatibility and flexibility, an advantage over piezoceramics, which are inherently cytotoxic. Polyvinylidene fluoride crystalizes in various phases: α-PVDF is non-piezoelectric because it has a trans-gauche conformation without a net dipole moment, whereas β-polyvinylidene fluoride exhibits an all-trans conformation, a net dipole moment, and, thus, is piezoelectric (Satyanarayana et al., 2012). Poly[(vinylidene fluoride-co-trifluoro ethylene] is a copolymer with an all-trans conformation, excellent piezoelectricity, and high electromechanical coupling (Koga et al., 2011). The copolymerization increased the β-phase content; therefore, polyvinylidene-co-trifluoro ethylene exhibits superior piezoelectricity compared with polyvinylidene fluoride (Koga et al., 2011). Motamedi and co-workers developed a polyvinylidene fluoride nanofibrous platform and found that cells attached and spread well on the entire scaffold. The cell shape changed from their original circular shape to an elongated shape, with the direction of neurite elongation parallel to fiber orientation. On day seven, the cell viability was higher than that of the control group, but lower on day 14 (Gryshkov et al., 2021).

Gryshkov and co-workers compared the two polymers in the form of electrospun nanofibers in terms of their structural and piezoelectric properties as well as their *In Vitro* performance, to show that polyvinylidene fluoride could be used as an alternative to the costly co-polymer.

Electrical poling and shearing occur during the electrospinning process as a result of the application of the electric field, force of the ejection from the needle, and its subsequent transport onto the collector drum. These processes yield the orientation of dipole moments and phase transformation, thereby enhancing the β-phase content and surface charge of polyvinylidene fluoride (Koga et al., 2011). Schwann cells were cultured on the nanofibers and revealed no distinct differences in the cell growth patterns, proving the similarity of the two. Schwann cells cultivated on both piezoelectric nanofibers showed cell-specific bipolar or polygonal morphology with enhanced neurite outgrowth compared with nonpiezoelectric controls, indicating that they could be used as comparative alternatives (Gryshkov et al., 2021).

The discovery of the piezoelectricity of PLLA inspired great interest in this biodegradable and biocompatible polymer in neural tissue engineering because most of the focus on PLLA has placed little emphasis on its innate piezoelectric potential. Yang and co-workers constructed a nanofibrous platform based on the electrospinning and phase separation of PLLA, which facilitated the attachment and differentiation of NSCs (Koh et al., 2008). Tai and co-workers fabricated PLLA nanofibrous platforms and found that the transverse and longitudinal piezoelectric voltage outputs of the nanofibrous platforms were dependent on fiber diameter and heat treatment temperature. As the heat treatment temperature rose above the glass transition point of PLLA nanofibers, there was a significant reduction in the transverse voltage output, but an increase in longitudinal voltage output. Such modulation of piezoelectric properties in PLLA nanofibers significantly affected the differentiation behaviors of stem cells, whereby neurogenesis was enhanced by orthogonal piezoelectricity, whereas osteogenesis was enhanced by shear piezoelectricity. This study demonstrated that the electrospun PLLA nanofibrous platforms, with tailorable piezoelectric properties, have the potential to develop self-powered stem cell engineering platforms that are specific to target tissues (Tai et al., 2021). Table 2.8 highlights various studies including piezoelectric materials for use in neural tissue engineering. Piezoelectric materials are an attractive choice for neural tissue engineering because they do not require an external stimulus, as is the case with electrically conductive polymers. However, this implies a lack of control over this electric stimulus.

Table 2. 8 Summary of *In Vitro* and *In Vivo* studies of electrically conductive and piezoelectric electrospun nanofibers for application in neural tissue engineering.

Constituents	Outcomes	*In VitroIn Vivo* observations	Reference
Electrically conductive polymers			
Polyaniline/ graphene nanoparticles in polyvinylidene fluoride/Mobil Composition of Matter No. 41 nanofibers/ gelatin-gellan scaffold	Reduced contact angle; enhanced electrical conductivity and storage modulus	Cyto-compatible; enhanced PC12 cell attachment and proliferation	(Mohseni et al., 2010)
Polyacrylonitrile/ polyaniline and nickel nanoparticles	Resemblance to tensile strength of acellularized rat nerve; super hydrophilic; enhanced electrical conductivity	Enhanced Schwann cell proliferation	(Wang et al., 2021)
Polylactic acid/ reduced graphene oxide/ polypyrrole	Increased electrical conductivity; reduced contact angle	Enhanced PC12 proliferation and differentiation	(Liu et al., 2021)
Silk fibroin/ reduced graphene oxide	Enhanced electrical conductivity; enhanced surface roughness and protein adsorption	Enhanced cell proliferation, neurite extension, metabolic activity	(Magaz et al., 2021)
Polypyrrole-coated poly(lactic-co-glycolid acid) fibers deposited into a poly(lactic-co-glycolic acid)/ polypyrrole film	Decreased elasticity and degradation rate	Enhanced attachment, differentiation, and proliferation of PC12 cells; enhanced sciatic function index values and conduction velocity *In Vivo*	(Lee et al., 2009)
Graphene/ collagen/ polycaprolactone suspension	No significant change in Young's modulus; decrease in tensile strength and percentage elongation at break; enhanced electrical conductivity and hydrophilicity	Promoted migration and secretion of neurogenic factors and enhanced functional recovery, recovery of gastrocnemius muscle, regeneration and remyelination of injured sciatic nerve comparable to gold standard *In Vivo*	(Dong et al., 2020)
Polyaniline nanoparticles/ polyhydroxybutyrate	Decreased tensile strength and contact angle; increased surface roughness	Enhanced fibroblast cell attachment; longer neurite outgrowth after electrical conductivity; enhanced proliferation and migration	(Zamanifari et al., 2020)
Polycaprolactone/ collagen/ polypyrrole	Decreased contact angle	Elongation of PC12 cells along direction of fibers; enhanced neurite outgrowth and neurogenesis	(Tang et al., 2020)
Polycaprolactone /gelatin/ polypyrrole/ graphene	Graphene enhanced electrical conductivity and mechanical properties; reduced fiber diameter and contact angle	Enhanced human fibroblast cell adhesion and proliferation	(Talebi et al., 2021)

Reduced graphene oxide/ gelatin methacroylyl/ polycaprolactone	Enhanced electrical conductivity and biocompatibility	Enhanced Schwann cell proliferation; promoted both sensory & motor nerve regeneration and functional recovery *In Vivo*	(Fang et al., 2020)
polyaniline nanoneedles in polycaprolactone/ gelatin	Reduced fiber diameter; more efficient alignment of fibers	Enhanced cell adhesion and growth; supports actin cytoskeleton rearrangement	(Saracino et al., 2021)
Polyaniline/ polyethersulfone	Increased electrical conductivity	Enhanced cell infiltration; exhibits time/dose-dependent cytotoxicity	(Daraeinejad et al., 2021)
Gold nanoparticles/ polyvinylidene fluoride	Homogenous nanoparticle dispersion; enhanced electrical conductivity and piezoelectricity	Enhanced PC12 cell adhesion and morphology	(Motamedi et al., 2017)
Piezoelectric polymers			
Polylactic acid	The electrospinning process increased hydrophobicity: nanofibers were induced with a laboratory-built corona poling system, which reduced contact angle	Polarization potentiates retinoic acid-induced neuronal differentiation in SH-SY5Y cells; increased proliferation; neurite outgrowth	(Barroca et al., 2018)
Polyvinylidine fluoride-trifluoroethylene	Piezoelectricity and porosity enhanced by annealing	Radial neurite outgrowth on random fiber orientation; directed neurite outgrowth on aligned fiber orientation	(Lee et al., 2011)
Polylactic acid/ gelatin/ polypyrrole	Increased average fiber diameter, hydrophilicity and electrical conductivity	Enhanced PC12 cell viability after gelatin addition	(Imani et al., 2021)
Polyvinylidene fluoride/ chitosan/ gelatin filled with *In Situ* gellan gum containing polyaniline/ graphene	Adequate output voltage; gellan gum imparted orientated pore structure and thermosensitive properties; decreased water contact angle	Supports PC12 cell attachment and proliferation	(Mohseni et al., 2021)
Polyvinylidene fluoride-trifluoroethylene	Electrospinning process increased crystallinity and enhanced piezoelectricity	Supported human skin fibroblast cell spreading and increased cell numbers over time	(Weber et al., 2010)
Iron (III) oxide-hydroxide nanorods on polyvinylidene fluoride	Oxygen plasma treatment facilitated cell attachment; reduced water contact angle	Induced neural differentiation	(Zhang et al., 2021)
Molybdenum disulphide/ polyvinylidene fluoride	Slow degradation rate; porous nanostructure; electrical conductivity	Enhanced neural stem cellattachment, differentiation, proliferation and cytocompatibility	(Wang et al., 2017)

2.11 Challenges and future prospects

Despite the countless diverse positive and promising results of electrospun nanofibers in nerve tissue engineering, most nanofibrous platforms have a pseudo-2D geometry, which somewhat limits their use in tissue engineering in general. By adapting the collector plate, some researchers have found alternate methods to deposit the fibers in a tubular fashion, adapting their geometry. In addition, there is the potential for combining electrospinning with additional manufacturing technologies, such as the LbL deposition of nanofibrous platforms to form a 3D platform. Further investigations are being conducted to modify the nozzle configuration and collector design to significantly improve fiber properties and simplify the manufacturing process. Furthermore, *In Vivo* studies around central nervous repair in particular are scarce compared with *In Vivo* studies; therefore, more efforts should be directed toward testing conduits based on electrospun nanofibers for central nerve injury repair *In Vivo*.

2.12 Concluding remarks

Inspired by the fibrous architecture of the extracellular matrix, the fabrication of nanoscale polymeric fibers with tailorable dimensions and robust surface modifications have gained considerable interest in the neural tissue engineering arena in recent years. In this review, methods to modify the surface of nanofibrous platforms were discussed, in addition to techniques used to attach, enclose, and/or control release rates of D/B for specific applications in neural tissue engineering. These optimization techniques aim to improve the neurocompatibility and cell-platform interactions of the scaffolds. The use of electrospun nanofibrous platforms to promote the differentiation of stem cells into neural lineages can be considered a promising technique for NSC culture and nerve regeneration strategies because of their favorable topographical cues and tailorable characteristics. One of the major problems that nanofibrous platforms present is their inability to maintain cellular viability *In Vivo*. However, the studies discussed herein highlight the importance of functional nerve constructs, such as electrospun nanofibrous platforms, in attempt to promote targeted neuron dendrite regeneration.

2.13 References

Abidian, M.R., Ludwig, K.A., Marzullo, C., Martin, D.C., Kipke. D.R. (2009). Interfacing conducting polymer nanotubes with the central nervous system: chronic neural recording using poly(3,4-ethylenedioxythiophene) nanotubes. Advanced materials, 21(3), 3764-3770.

Ahmed, I., Liu, H.Y., Mamiya, P.C., Ponery, A.S., Babu, A.N., Weik, T. et al.(2006). Three-dimensional nanofibrillar surfaces covalently modified with tenascin-C-derived peptides enhance neuronal growth *In Vitro*. Journal of biomedical materials research-part A, 76(4), 851-860.

Ajalloueian, F., Tavanai, H., Hilborn, J., Donzel-Gargand, O., Leifer, K., Wickham, A. et al. (2014). Emulsion electrospinning as an approach to Fabricate PLGA/chitosan nanofibers for biomedical applications. Biomedical research international, 2014(1), 475-481.

Alvarez-Perez, M.A., Guarino, V., Cirillo, V., Ambrosio, L. (2010). Influence of gelatin cues in PCL electrospun membranes on nerve outgrowth. Biomacromolecules, 11(9), 2238-2246.

Amani, H., Kazerooni, H., Hassanpoor, H., Akbarzadeh, A., & Pazoki-Toroudi, H. (2019). Tailoring synthetic polymeric biomaterials towards nerve tissue engineering: a review. Artificial cells, nanomedicine, and biotechnology, 47(1), 3524-3539.

Amores de Sousa, M. C., Rodrigues, C. A. V., Ferreira, I. A. F., Diogo, M. M., Linhardt, R. J., Cabral, J. M. S., & Ferreira, F. C. (2020). Functionalization of electrospun nanofibers and fiber alignment enhance neural stem cell proliferation and neuronal differentiation. Frontiers in bioengineering and biotechnology, 8.

Arecchi, A., Mannino, S., Weiss, J. (2010). Electrospinning of poly(vinyl alcohol) nanofibers loaded with hexadecane nanodroplets. Journal of food science, 75(6), 80-88.

Asadian, M. Dhaenens, M., Onyshchenko I. (2018). Plasma functionalization of polycaprolactone nanofibers changes protein interactions with cells, resulting in increased cell viability. ACS applied material interfaces,10(49), 41962-41977.

Badami, A.S., Kreke, M.R. Thompson, M.S., Riffle, J.S., Goldstein, M. (2006). Effect of fiber diameter on spreading, proliferation, and differentiation of osteoblastic cells on electrospun poly(lactic acid) substrates. Biomaterials, 27(4), 596-606.

Balint, R., Cassidy, N.J., Cartmell, S.H. (2014). Conductive polymers: towards a smart biomaterial for tissue engineering. Acta biomaterialia, 10(6), 2341-2353.

Barroca, N., Marote, A., Vieira, S.I., Almeid, A., Fernandes, M.H.V., Vilarinho, P.H. et al (2018). Electrically polarized PLLA nanofibers as neural tissue engineering scaffolds with improved neuritogenesis. Colloids surfaces B biointerfaces, 167, 93-103.

Bhattarai, D. P., Aguilar, L. E., Park, C. H., & Kim, C. S. (2018). A review on properties of natural and synthetic based electrospun fibrous materials for bone tissue engineering. Membranes, 8(3), 62-67.

Bhutto, M.A., Wu, T., Sun, B., EI-Hamshary, H., Al-Deyab, S.S., Mo, X (2016). Fabrication and characterization of vitamin B5 loaded poly (l-lactide-co-caprolactone)/silk fiber aligned electrospun nanofibers for schwann cell proliferation. Colloids surfaces B biointerfaces, 144(2), 108-117.

Binan, L.,Tendey, C., De Crescenzo, G., El Ayoubi, R., Ajji, A., Jolicoeur, M. (2014). Differentiation of neuronal stem cells into motor neurons using electrospun poly-l-lactic acid/ gelatin scaffold. Biomaterials, 35(2), 664-674.

Borah, R., Ingavle, G.C., Kumar, A., Sandeman, S.R., Mikhalovsky, S.V. (2021) Surface-functionalized conducting nanofibers for electrically stimulated neural cell function. Biomacromolecules, 22 (2021), 594-611.

Bosworth, L.A., Hu, W., Shi, Y., Cartmell, S.H. (2019). Enhancing biocompatibility without compromising material properties: an optimised NaOH treatment for electrospun polycaprolactone fibres. Journal of nanomaterials, 2019(1), 11-22.

Briggs, T., and Arinzeh, T.L. (2014). Examining the formulation of emulsion electrospinning for improving the release of bioactive proteins from electrospun fibers. Journal of biomedical materials research-part A, 102(3), 674-684.

Buzgo, M., Mickova, A., Rampichova, M., Doupnik, M. (2018). Blend electrospinning, coaxial electrospinning, and emulsion electrospinning techniques. In Focarete, M., and Tampieri, A. (2018). Core-shell nanostructures for drug delivery and theranostics: challenges, strategies, and prospects for novel carrier systems, Elsevier, 325-347.

Cellot, G., Cilia, E., Cipollone, S., Rancic, V., Sucapane, A., Giordani, S. et al. (2009). Carbon nanotubes might improve neuronal performance by favouring electrical shortcuts. Nature nanotechnology, 4(2), 126-133.

Chen, W.S., Guo, L.Y.,Tang, C.C., Tsai, C.Y., Huang, H.H., Chin,T.Y. et al. (2018). The effect of laminin surface modification of electrospun silica nanofiber substrate on neuronal tissue engineering. Nanomaterials, 8(3), 165-171.

Chew, S.Y., Wen, J.,Yim, E.K.F., Leong, K.W. (2005). Sustained release of proteins from electrospun biodegradable fibers. Biomacromolecules, 6(4), 2017-2024.

Christopherson, G.T., Song, H., Mao H.Q. (2009). The influence of fiber diameter of electrospun substrates on neural stem cell differentiation and proliferation. Biomaterials, 30(4), 556-564.

Chu, P.K., Chen, J.Y. Wang, L.P., Huang, N. (2002). Plasma-surface modification of biomaterials. Material science engineering reports, 36(3), 143-206.

Daraeinejad, Z. and Shabani, I. (2021). Enhancing cellular infiltration on fluffy polyaniline-based electrospun nanofibers. Frontiers bioengineering biotechnology, 9(1), 641371.

Dębski, T., Kijeńska- Gawrońska, E., Zołocińska, A., Siennicka, K., Słysz, A., Paskal, W. et al. (2021). Bioactive nanofiber-based conduits in a peripheral nerve gap management-an animal model study. International journal of molecular sciences, 22(11), 5588-5594.

Dong, C., Qiao, F., Wensheng Hou, L.L.Y. (2020). Graphene-based conductive fibrous scaffold boosts sciatic nerve regeneration and functional recovery upon electrical stimulation. Applied materials today, 21(1), 100870-100884.

Doshi, J., & Reneker, D. H. (1995). Electrospinning process and applications of electrospun fibers. Journal of electrostatics, 35 (2-3),151-160.

Du, J., Tan, E., Kim, H.J. Zhang, A., Bhattacharya, R., Yarema, K.J (2014). Comparative evaluation of chitosan, cellulose acetate, and polyethersulfone nanofiber scaffolds for neural differentiation. Carbohydrate polymers, 99(2), 483-490.

Evans, G.R.D (2013). Peripheral nerve injury: a review and approach to tissue engineered constructs. Anatomical records, 263(2013), 396-404.

Fang, X., Guo, H., Zhang, W., Fang, F. (2020). Reduced graphene oxide-GelMA-PCL hybrid nanofibers for peripheral nerve regeneration. Journal of material chemistry B, 8(1), 10593-10601.

Ganesh, V.A., Nair, A.S., Raut, H.K., Tan, T.S.Y., Chaobin, H., Ramakrishna, S. et al. (2012). Superhydrophobic fluorinated POSS-PVDF-HFP nanocomposite coating on glass by electrospinning. Journal of material chemistry, 22(2),18479-18485.

Ghasemi-Mobarakeh, L., Prabhakaran, M.P., Morshed, M., Nasr-Esfahani, M.H., Ramakrishna, S. (2008). Electrospun poly(ε-caprolactone)/gelatin nanofibrous scaffolds for nerve tissue engineering. Biomaterials, 29(34), 4532-4539.

Ghasemi-Mobarakeh, L., Prabhakaran, M.P.,Morshed, M., Nasr-Esfahani, M.H., Ramakrishna, S. (2010). Bio-functionalized PCL nanofibrous scaffolds for nerve tissue engineering. Material science engineering C, 30(8), 1129-1136.

Ghorbani, S., Tiraihi, T., Soleimani, M. (2018). Differentiation of mesenchymal stem cells into neuron-like cells using composite 3D scaffold combined with valproic acid induction. Journal of biomaterial applications, 32(6), 702-715.

Granato, A.E.C., Ribeiro, A., Marciano, F.R., Rodrigues, B.V.M.,Lobo, O., Porcionatt, M. (2018). Polypyrrole increases branching and neurite extension by Neuro2A cells on PBAT ultrathin fibers. Nanomedicine, nanotechnology, biology, and medicine, 14(3), 1753-1763.

Gryshkov, O., Halabi, F.A.L., Kuhn, A.I., Leal-Marin, S., Freund, L.J., Förthmann, M. et al.(2021). PVDF and P(VDF-TrFE) electrospun scaffolds for nerve graft engineering: a comparative study on piezoelectric and structural properties, and In Vitro biocompatibility. International journal of molecular science, 22(21), 11373-11379.

Guo, X., Xia, B., Lu, X., Zhang, Z., Li, Z., Li, W., Deng, L., Tan, M., & Huang, Y. (2016). Grafting of mesenchymal stem cell-seeded small intestinal submucosa to repair the deep partial-thickness burns. Connective tissue research, 57(5), 388-397.

Haddad, T., Noel, S., Liberelle, B., El Ayoubi, R., Ajji, A., De Crescenzo, G. (2016). Fabrication and surface modification of poly lactic acid (PLA) scaffolds with epidermal growth factor for neural tissue engineering. Biomatter, 6(1), e1231276.

Haixing, X.U., Rui, L.I., Yiping, L.I., He, Q., Yan, X., Shu, T. et al.(2020). Preparation and characterization of poly lactic acid/ graphene oxide/ nerve growth factor scaffold with electrical stimulation for peripheral nerve regeneration In Vitro. Journal of Wuhan university technology -material science edition, 35(5), 1149-1161.

He, L., Liao, S., Quan, D., Ma, K., Chan, C., Ramakrishna, S., & Lu, J. (2010). Synergistic effects of electrospun PLLA fiber dimension and pattern on neonatal mouse cerebellum C17.2 stem cells. Acta biomaterialia, 6(8), 2960-2969.

He, L., Shi, Y.,Han, Q., Zuo, Q., Ramakrishna, S., Xue, W. et al.(2012). Surface modification of electrospun nanofibrous scaffolds via polysaccharide-protein assembly multilayer for neurite outgrowth. Journal of material chemistry, 22(26),13187-13196.

Horne, M.K., Nisbet, D.R., Forsythe, S., Parish, L. (2010). Three-dimensional nanofibrous scaffolds incorporating immobilized BDNF promote proliferation and differentiation of cortical neural stem cells. Stem cells development, 19(6), 843-852.

Hsu, P.D., Lander, E.S., Zhang, F. (2014). Development and applications of CRISPR-Cas9 for genome engineering. Cell, 157(6), 1262-1278.

Hu, J., Prabhakaran, M.P., Tian, L.,Ding, X., Ramakrishna, S. (2015). Drug-loaded emulsion electrospun nanofibers: Characterization, drug release and In Vitro biocompatibility. RSC advances, 5(121), 100256-100267.

Hu, W., Wang, X., Xu, Y., Li, L., Liu, J., He, L. et al. (2020). Electric conductivity on aligned nanofibers facilitates the trans differentiation of mesenchymal stem cells into Schwann cells and regeneration of injured peripheral nerve. Advanced healthcare materials, 9(11), 1901570-1901581.

Huang, D., Lin, L., Wen, X., Gu, S., Zhao, P. (2016). A potential nanofiber membrane device for filling surgical residual cavity to prevent glioma recurrence and improve local neural tissue reconstruction. PLoS ONE, 11(8), e0161435.

Huang, L., Hu, J., Lang, L., Wang, X., Zhang, P., Jing, X. et al. (2007). Synthesis and characterization of electroactive and biodegradable ABA block copolymer of polylactide and aniline pentamer. Biomaterials, 28(10), 1741-1751.

Imani, F., Karimi-Soflou,R., Shabani, I. and Karkhaneh, A. (2021). PLA electrospun nanofibers modified with polypyrrole-grafted gelatin as bioactive electroconductive scaffold. Polymer, 218(1), 123487-123492.

Ji, W. Sun, Y., Yang, F., van der Beuken, J.J.P., Mi, F., Chen, Z. et al (2011). Bioactive electrospun scaffolds delivering growth factors and genes for tissue engineering applications. Pharmaceutical research, 28(6), 1259-1272.

Jiang, L., Zhao, Y., Zhai, J. A lotus-leaf-like superhydrophobic surface: a porous microsphere/nanofiber composite film prepared by electrohydrodynamics. Angew chemie-International edition, 43(33), 4338-4341.

Jiang, Y.N., Mo, H.Y., Yu, D.G. (2012). Electrospun drug-loaded core-sheath PVP/zein nanofibers for biphasic drug release. International journal of pharmaceutics, 438(1-2), 232-239.

Kidoaki, S., Kwon, I.K., Matsuda, T. (2005). Mesoscopic spatial designs of nano- and microfiber meshes for tissue-engineering matrix and scaffold based on newly devised multilayering and mixing electrospinning techniques. Biomaterials, 26(1), 37-46.

Kijeńska, E., Prabhakaran, M.P., Swieszkowski, E., Kurzydlowski, J., Ramakrishna, S. (2014). Interaction of Schwann cells with laminin encapsulated PLCL core-shell nanofibers for nerve tissue engineering. European polymer journal, 50(4), 30-38.

Kijeńska, E., Prabhakaran, M.P.,Swieszkowski, W., Kurzydlowski, K.J., Ramakrishna, S. (2012). Electrospun bio-composite P(LLA-CL)/ collagen I/ collagen III scaffolds for nerve tissue engineering. Journal of biomedical material research-part B applied biomaterials, 100(1), 1093-1102.

Kim, B.S., Park, S.W., Hammond, P.T. (2008). Hydrogen-bonding layer-by-layer-assembled biodegradable polymeric micelles as drug delivery vehicles from surfaces. ACS nano, 2(2), 386-392.

Kim, H.W., Song, J.H., Kim, H.E. (1994). Nanofiber generation of gelatin-hydroxyapatite biomimetics for guided tissue regeneration. Advanced functional materials, 15(12),1988-1994.

Koga, K., Suzuki, M., Nakanishi, T., Kimura, K., Hashimoto, N. (2011). Applications to biomedical instrumentation: piezoelectric and ferroelectric properties of P(VDF-TrFE) copolymers and their application to ultrasonic transducers. Ferroelectrics, 60(1), 263-276.

Koh, H.S., Yong, T., Chan, C.K., Ramakrishna, T. (2008). Enhancement of neurite outgrowth using nano-structured scaffolds coupled with laminin. Biomaterials, 29(26), 3574-3582.

Kupka, V., Dvoˇráková, E., Manakhov, A., Michlíek, M., Petruš, J. (2020). Well-blended PCL/PEO Electrospun nanofibers with functional properties enhanced by plasma processing. Polymers (Basel), 12(6), 1403-1410.

Kurusu, R.S. and Demarquette, N.R. (2019). Surface modification to control the water wettability of electrospun mats. International material reviews, 64(5), 249-287.

Lavrov, N.A. (2002).Characteristics of the alkaline hydrolysis of N-vinyl and acrylic polymers. International polymer science technology, 29(11), 38-45.

Lee, S. J., Khang, G., Lee, Y. M., & Lee, H. B. (2002). Interaction of human chondrocytes and NIH/3T3 fibroblasts on chloric acid-treated biodegradable polymer surfaces. Journal of biomaterials science, polymer edition, 13(2), 197-212.

Lee, J.Y., Bashur, C.A., Goldstein, A.S., Schmidt, A.E. (2009). Polypyrrole-coated electrospun PLGA nanofibers for neural tissue applications. Biomaterials, 30(26), 4325-4335.

Lee, Y.S., Collins, G., Livingston, A.T. (2011). Neurite extension of primary neurons on electrospun piezoelectric scaffolds. Acta biomaterialia, 7(11), 3877-3886.

Li, X., Lee, S. C., Zhang, S. & Akasaka, T. (2015). Biocompatibility and toxicity of nanobiomaterials. Journal of nanomaterials, 2012(special issue), 2-4.

Li, W., Guo, Y., Wang, H., Shi, P., Liang, C., Ye, Z. et al. (2008). Electrospun nanofibers immobilized with collagen for neural stem cells culture. Journal of material science material medicine, 19(2), 847-854.

Li, X., Su, Y., Liu, S., Tan, L., Mo, X., Ramakrishna, S. (2010). Encapsulation of proteins in poly(l-lactide-co-caprolactone) fibers by emulsion electrospinning. Colloids surfaces B biointerfaces, 75(2), 418-424.

Liao, C.I., Chew, S.Y., Leong, K.W. (2006). Aligned core-shell nanofibers delivering bioactive proteins. Nanomedicine, 1(4), 465-471.

Liou, H.M., Rau, L.M., Huang, C.C., Lu, M.R., Hsu, F.R. (2013). Electrospun hyaluronan–gelatin nanofibrous matrix for nerve tissue engineering. Journal of nanomaterials, 2013(1), 163638-163643.

Liu, C., Wang C, Zhao Q, X. (2018). Incorporation and release of dual growth factors for nerve tissue engineering using nanofibrous bicomponent scaffolds. Biomedical materials, 13(4), 4412-4418.

Liu, C. (2021). Nanofibrous bicomponent scaffolds for the dual delivery of NGF and GDNF: controlled release of growth factors and their biological effects. Journal of material science material medicine, 32(4), 9-13.

Liu, X.Y., Zhang, Y.R., Bogaerts, A., Wang Y.N (2015). Electromagnetic effects in high-frequency large-area capacitive discharges: a review. Journal of vacuum science & technology A, 33(2), 1116-1119.

Liu, R., Huang, X., Wang, X. (2021). Electrical stimulation mediated the neurite outgrowth of PC-12 cells on the conductive polylactic acid/reduced graphene oxide/polypyrrole composite nanofibers. Applied surface science, 560(1), 149965-149971.

Liu, Z. Yan, Z., Bai L. (2018). Electrospun nanofiber templated assembly of hybrid nanoparticles. RSC advances, 8(1), 9344-9352.

Ma, T., Yang, Y., Quan, X (2020). Oxygen carrier in core-shell fibers synthesized by coaxial electrospinning enhances Schwann cell survival and nerve regeneration. Theranostics, 10(3), 8957-8973.

Maderuelo, C., Zarzuelo, A., Lanao, J.M.(2011). Critical factors in the release of drugs from sustained release hydrophilic matrices. Journal of control release, 154(1), 2-19.

Magaz, A., Li, X., Gough, E., Blaker, E.E. (2021). Graphene oxide and electroactive reduced graphene oxide-based composite fibrous scaffolds for engineering excitable nerve tissue. Material science engineering C, 119(1), 111632-111641.

Masaeli, E., Wieringa, M., Nasr-Esfahani, MH., Sadri, S., van Blitterswijk, C.A and Moroni, L. (2014). Nanomedicine: nanotechnology, biology, and medicine, 10(7), 1559-1569.

Meghdadi, M., Atyabi, S.M., Pezeshki-Modaress, M., Irani, S., Noormohammadi, Z., & Zandi, M. (2019). Cold atmospheric plasma as a promising approach for gelatin immobilization on poly(ε-caprolactone) electrospun scaffolds. Progress in biomaterials, 8(2), 65-75.

Miri, V., Asadi, A., Sagha, M., Najafzadeh, N., Golmohammadi, M.G. (2021). Poly (l-lactic acid) nanofibrous scaffolds support the proliferation and neural differentiation of mouse neural stem and progenitor cells. International journal of developmental neuroscience, 81(5), 438-447.

Mohseni, M., Shirazi, F., Nemati, N.H.(2020). Preparation and characterization of self-electrical stimuli conductive gellan based nano scaffold for nerve regeneration containing chopped short spun nanofibers of PVDF/MCM41 and polyaniline/graphene nanoparticles: physical, mechanical, and morphological studies. International journal of biological macromolecules, 167(2), 881-893.

Mohseni, M. and Ramazani, S.A. (2021). Highly conductive self-electrical stimuli core-shell conduit based on PVDF-chitosan-filled with in-situ gellan gum as a possible candidate for nerve regeneration: a rheological, electrical, and structural study. Applied nanoscience, 11(4), 2199-2213.

Motamedi, A.S., Mirzadeh, H., Hajiesmaeilbaigi, F., Bagheri-houlenjani, S., Shokrgozar, M.A. (2017). Piezoelectric electrospun nanocomposite comprising Au NPs/PVDF for nerve tissue engineering. Journal of biomedical materials research- part A, 105(7), 1984-1993.

Muthiah, P., Hoppe, S. M., Boyle, T. J., & Sigmund, W. (2011). Thermally tunable surface wettability of electrospun fiber mats: Polystyrene/ poly(N-isopropylacrylamide) blended versus crosslinked poly[(N-isopropylacrylamide)-co-(methacrylic acid)]. Macromolecular rapid communications, 32(21), 1716-1721.

Nagarajan S., Bechelany M., Kalkura N.S., Miele P., Bohatier C.P., Balme S (2019). Electrospun nanofibers for drug delivery in regenerative medicine. Applications of targeted nano drugs and delivery systems, 4(3), 595-625.

Nazeri, N., Karimi, R., Ghanbari, H. (2021). The effect of surface modification of poly-lactide-co-glycolide/carbon nanotube nanofibrous scaffolds by laminin protein on nerve tissue engineering. Journal of biomedical materials research-part A, 109(2), 159-169.

Nikmaram, S., Roohinejad, S., Hashemi, S., Kouba, M., Barba, K.J., Abbaspourrad, M. et al. (2017). Emulsion-based systems for fabrication of electrospun nanofibers: food, pharmaceutical and biomedical applications. RSC advances, 7(2), 28951-28964.

Nisbet, D.R., Pattanawong, S., Ritchie, N.E., Shen, W., Finkelstein, D.I., Horne, L. et al. (2007). Interaction of embryonic cortical neurons on nanofibrous scaffolds for neural tissue engineering. Journal of neural engineering, 4(2), 35-41.

Ochanda, F.O., Samaha, M.A., Tafreshi, H.V., Tepper, G., Gad-El-Hak, M. (2012). Fabrication of superhydrophobic fiber coatings by DC-biased AC-electrospinning. Journal of applied polymer science, 123(2), 1112-1119.

Park, J.K., Pham-Nguyen, O.K., Yoo, H.S. (2020). Coaxial electrospun nanofibers with different shell contents to control cell adhesion and viability. ACS omega, 5(1), 28178-28185.

Patel, S., Kurpinski, K., Quigley, R.C., Gao, H., Hsiao, B.S. Poo, M.M. et al. (2007). Bioactive nanofibers: Synergistic effects of nanotopography and chemical signaling on cell guidance. Nano letters, 7(4), 2122-2128.

Prabhakaran, M.P., Venugopal, J., Chan, C.K., Ramakrishna, S. (2008). Surface modified electrospun nanofibrous scaffolds for nerve tissue engineering. Nanotechnology, 19(2), 455102-455113.

Quan, Q., Hong, L., Wang, Y., Li, R., Yin, X., Cheng, X. et al. (2021). Hybrid material mimics a hypoxic environment to promote regeneration of peripheral nerves. Biomaterials, 277(1),121068-121072.

Rajabi, M., Firouzi, M., Hassannejad, Z., Haririan, I., Zahedi, P. (2018). Fabrication and characterization of electrospun laminin-functionalized silk fibroin/poly(ethylene oxide) nanofibrous scaffolds for peripheral nerve regeneration. Journal of biomedical material research-part B applied biomaterials, 106(3), 1595-1604.

Raoofi, A., Sadeghi, Y., Piryaei, A., Sajadi, E., Aliaghaei, A., Rashidabadi-Rashidiani, A. et al. (2021). Bone marrow mesenchymal stem cell condition medium loaded on PCL nanofibrous scaffold promoted nerve regeneration after sciatic nerve transection in male rats. Neurotoxicity research, 39(3),1470-1486.

Reis, K.P., Sperling, C., Teixeira, C., Sommer, L., Colombo, M., Koester, L.S. et al. (2020). VPA/PLGA microfibers produced by coaxial electrospinning for the treatment of central nervous system injury. Brazilian journal of medical biological research, 53(4), 1-9.

Roy, T., Maity, P.P., Rameshbabu, R.P., Das, D., John, A., Dutta, A. et al. (1995). Core-shell nanofibrous scaffold based on polycaprolactone-silk fibroin emulsion electrospinning for tissue engineering applications. Bioengineering (Basel), 5(3), 68-75.

Saadatkish, N., Nouri Khorasani, S., Morshed, N. (2018). A ternary nanofibrous scaffold potential for central nerve system tissue engineering. Journal of biomedical materials research-part A, 106(9), 2394-2401.

Sadeghi, A., Moztarzadeh, F., Aghazadeh, M.J. (2019). Investigating the effect of chitosan on hydrophilicity and bioactivity of conductive electrospun composite scaffold for neural tissue engineering. International journal of biological macromolecules, 121(1), 625-632.

Sahay, R., Thavasi, V., Ramakrishna S. (2011). Design modifications in electrospinning setup for advanced applications. Journal of nanomaterials, 2011(special issue),17-32.

Samal, S. (2017). Thermal plasma technology: the prospective future in material processing. Journal of cleaner production, 142(1), 3131-3150.

Sangsanoh, P., Ekapakul, N., Israsena, N., Suwantong, O and Supaphol, P. (2018). Enhancement of biocompatibility on aligned electrospun poly(3-hydroxybutyrate) scaffold immobilized with laminin towards murine neuroblastoma Neuro2a cell line and rat brain-derived neural stem cells (mNSCs). Polymers for advanced technologies, 29(5110), 2050-2063.

Saracino, E., Zuppolini, S., Guarino, S. (2021). Polyaniline nano-needles into electrospun bio active fibres support In Vitro astrocyte response. RSC advances, 11(1), 11347-11355.

Satyanarayana, K.C., Bolton, K. (2012). Molecular dynamics simulations of α- To β-poly(vinylidene fluoride) phase change by stretching and poling polymer. Guildford journals, 53(14), 2927-2934.

Schaub, N. J., Johnson, C. D., Cooper, B., & Gilbert, R. J. (2016). Electrospun fibers for spinal cord injury research and regeneration. Journal of neurotrauma, 1(33), 1405-1415.

Schnell, E., Klinkhammer, K., Balzer, S., Brook, G., Klee, D., Dalton, P. et al. (2007). Guidance of glial cell migration and axonal growth on electrospun nanofibers of poly-ε-caprolactone and a collagen/ poly-ε-caprolactone blend. Biomaterials, 28(1), 3012-3025.

Sionkowska, A. (2011). Current research on the blends of natural and synthetic polymers as new biomaterials. Review of progress of polymer science, 36(9), 1254-1276

Song, S.J. Shin, Y.C., Kim, S.E. (2018). Aligned laminin core-polydioxanone/collagen shell fiber matrices effective for neuritogenesis. Scientific reports, 8(2), 5570.

Sperling, L.E., Reis, K.P., Pozzobon, L.G., Girardi, C.S., Pranke, P. (2017). Influence of random and oriented electrospun fibrous poly(lactic-co-glycolic acid) scaffolds on neural differentiation of mouse embryonic stem cells. Journal of biomedical material research-part A, 105(5),1333-1345.

Steward, M., Sridhar, M., Meyer, J.S (2013). Neural regeneration. Current topics in microbiology and immunology, 367(22), 594-611.

Sun, B., Wu, T., He, L., Zhang, J. (2016). Development of dual neurotrophins-encapsulated electrospun nanofibrous scaffolds for peripheral nerve regeneration. Journal of biomedical nanotechnology, 12(11), 1987-2000.

Swindle-Reilly, K.E., Paranjape, S.C., Miller, C.A. (2014). Electrospun poly(caprolactone)-elastin scaffolds for peripheral nerve regeneration. Progress in biomaterials, 3(1), 1960-1972.

Tadros, T. (2006). Principles of emulsion stabilization with special reference to polymeric surfactants. Journal of cosmetic science, 57(2), 53-169.

Tai, Y., Yang, S., Yu, S., Banerjee, A., Myung, V., Nam, J. (2021). Modulation of piezoelectric properties in electrospun PLLA nanofibers for application-specific self-powered stem cell culture platforms. Nano energy, 89(1), 106444-106449.

Talebi, A., Labbaf, S., Atari, M. Parhizkar, M. (2021). Polymeric nanocomposite structures based on functionalized graphene with tunable properties for nervous tissue replacement. ACS biomaterial science engineering, 7(9), 4591-4601.

Tang, J., Wu, C., Chen, S., Qiao, Z. (2020). Combining electrospinning and electrospraying to prepare a biomimetic neural scaffold with synergistic cues of topography and electrotransduction. ACS applied biomaterials, 3(8), 5148-5159.

Thampi, S., Thekkuveettil, A., Muthuvijayan, V., Parameswaran, R. (2020). Accelerated outgrowth of neurites on graphene oxide-based hybrid electrospun fibro-porous polymeric substrates. ACS applied biological materials, 3 (2020), 2160-2169.

Thierry, B., Kujawa, P., Tkaczyk, C., Winnik, F., Bilodeau, L., Tabrizian, M. (2005). Delivery platform for hydrophobic drugs: prodrug approach combined with self-assembled multilayers. Journal of American chemical society, 127(6), 1626-1627.

Thipkaew, C., Wattanathorn, J., Muchimapura, S. (2017). Electrospun nanofibers loaded with quercetin promote the recovery of focal entrapment neuropathy in a rat model of streptozotocin-induced diabetes. Biomedical research international, 2017(2017), 2017493.

Thouas, G.A., Contreras, K.G., Bernard, C.C., et al. (2008). Biomaterials for spinal cord regeneration: outgrowth of presumptive neuronal precursors on electrospun poly(ε)-caprolactone scaffolds microlayered with alternating polyelectrolytes. 2008 30th annual

international conference of the IEEE engineering in medicine and biology society. New York, IEEE, 1825-188.

Tian, L., Prabhakaran, M.P., Hu, J., Chen, M., Besenbacher, F., Ramakrishna, S. (2015). Coaxial electrospun poly(lactic acid)/silk fibroin nanofibers incorporated with nerve growth factor support the differentiation of neuronal stem cells RSC. Journal of advanced research, 5(62), 949-958.

Toledo, A.L., Ramalho, B.S., Picciani, P.H., Baptista, L.S., Martinez, A.M., Dias, M.L. (2021). Effect of three different amines on the surface properties of electrospun polycaprolactone mats. International journal of polymer materials: polymeric biomaterials, 70(1), 1258-1270.

Valmikinathan, C. M., Hoffman, J., & Yu, X. (2011). Impact of scaffold micro and macro architecture on Schwann cell proliferation under dynamic conditions in a rotating wall vessel bioreactor. Materials science and engineering C, 31(1), 22-39.

Wagner, H.E., Brandenburg, R., Kozlov, K.V., Sonnenfeld, A., Michel, P., Behnke, J.P. (2003). The barrier discharge: basic properties and applications to surface treatment. Vacuum, 71(2003), 417-436.

Wang, Y., Qiao, W., Wang, B., Zhang, Y., Shao, P., Yin, T. (2011). Electrospun composite nanofibers containing nanoparticles for the programmable release of dual drugs. Polymer journal, 43(4), 478-483.

Wang, C.Y., Liu, L.J., Fan, C.Y., Mo, M.X., Ruan, H.J., Li, F.F. (2012). The effect of aligned core-shell nanofibres delivering NGF on the promotion of sciatic nerve regeneration. Journal of biomaterial science polymer edition, 23(1-4), 167-184.

Wang, D.P., Jin, K.Y., Zhao, Z., Lin, Q., Kang, K., Hai, J. (2021). Neuroprotective effects of VEGF- a nanofiber membrane and FAAH inhibitor against oxygen-glucose deprivation-induced ischemic neuronal injury. International journal of nanomedicine, 16(1), 3661-3678.

Wang, J., Chen, N., Ramakrishna, S., Tian, L., o, X. (2017). The effect of plasma treated PLGA/MWCNTs-COOH composite nanofibers on nerve cell behavior. Polymers (Basel), 9(12), 713-719.

Wang, L., Wu, Y., Hu, T., Ma, P.X., Guo, B. (2019). Aligned conductive core-shell biomimetic scaffolds based on nanofiber yarns/hydrogel for enhanced 3D neurite outgrowth alignment and elongation. Acta biomaterialia, 96(4), 175-187.

Wang, M., Tremblay, P.L., Zhang, L. (2021). Optimizing the electrical conductivity of polyacrylonitrile/polyaniline with nickel nanoparticles for the enhanced electrostimulation of Schwann cells proliferation. Bioelectrochemistry, 140(3), 107750-107755.

Wang, S., Qiu, J., Guo, W., Yu, X., Nie, J. Zhang, J. et al. (2011). A Nanostructured molybdenum disulfide film for promoting neural stem cell neuronal differentiation: toward a nerve tissue-engineered 3D scaffold. Advanced biosystems, 1(5), e1600042.

Weber, Y.S. Lee, S. Shanmugasundaram, M. Jaffe, T.L. Arinzeh. (2010). Characterization and In Vitro cytocompatibility of piezoelectric electrospun scaffolds. Acta biomaterialia, 6(9), 3550-3556.

Wood, K.C., Boedicker, J.Q., Lynn, D.M., Hammond, P.T. (2005). Tunable drug release from hydrolytically degradable layer-by-layer thin films. Langmuir, 21(4), 1603-1609.

Xi, K., Gu, Y., Tang, J., Chen, H., Xu, Y., Wu, L. et al (2020). Microenvironment-responsive immunoregulatory electrospun fibers for promoting nerve function recovery. Nature communications, 11(3), 4505.

Xia, B., Lv, Y. (2018). Dual delivery of VEGF and NGF by emulsion electrospun nanofibrous scaffold for peripheral nerve regeneration. Material science engineering C, 82(2), 253-264.

Xu, H., Holzwarth, J.M., Yan, Y., Xu, P., Zheng, H., Yin, Y. et al. (2014). Conductive PPY/PDLLA conduit for peripheral nerve regeneration. Biomaterials, 35(2014), 225-235.

Yan, H., Wang, Y., Li, J., Zhou, X., Shi, X., Wei, Y. et al. (2020). A micropatterned conductive electrospun nanofiber mesh combined with electrical stimulation for synergistically enhancing differentiation of rat neural stem cells. Journal of material chemistry B, 8(2020), 2673-2688.

Yan, Y., Sencadas, V., Jin, T., Huang, Y., Chen, J., Wei, D. et al. (2017). Tailoring the wettability and mechanical properties of electrospun poly(l-lactic acid)-poly(glycerol sebacate) core-shell membranes for biomedical applications. Journal of colloid interface science, 508(1), 87-94.

Yoo, J. S., Kim, Y. J., Kim, S. H., & Choi, S. H. (2011). Study on genipin: A new alternative natural crosslinking agent for fixing heterograft tissue. Korean journal of thoracic and cardiovascular surgery, 44(3), 197-207.

Yoshida, S., Hagiwara, K., Hasebe, T.,Hotta A. (2013). Surface modification of polymers by plasma treatments for the enhancement of biocompatibility and controlled drug release. Surface coatings technologies, 233(1), 99-107.

Zamanifard, M., Khorasani, M.T., Taliri, M., Parvazinia, M. (2020). Preparation and modeling of electrospun polyhydroxybutyrate/ polyaniline composite scaffold modified by plasma and printed by an inkjet method and its cellular study. Journal of biomaterial science polymer edition, 31(2), 1515-1537.

Zandén, C., Hellström Erkenstam, N., Padel, T., Wittgenstein, J., Liu, J., Kuhn, H.G. (2014). Stem cell responses to plasma surface modified electrospun polyurethane scaffolds. Nanomedicine, 10(2014), 949-958.

Zha, F., Chen, W., Lv, G., Wu, C., Hao, L., Meng, L. et al. (2021). Effects of surface condition of conductive electrospun nanofiber mats on cell behavior for nerve tissue engineering. Material science engineering C, 120(120), 111795-111799.

Zhan, J., Singh, A., Zhang, Z., Huang, L., & Elisseeff, J. H. (2012). Multifunctional aliphatic polyester nanofibers for tissue engineering. Biomatter, 2(4), 202-212.

Zhang, C., Salick, M.R, Cordie, T.M, Ellingham, T., Dan, Y., Turng, L.S. (2015). Incorporation of poly(ethylene glycol) grafted cellulose nanocrystals in poly(lactic acid) electrospun nanocomposite fibers as potential scaffolds for bone tissue engineering. Materials science and engineering C, 49(2015), 463-71.

Zhang, K., Huang, D., Yan, Z., Wang., C. (2017). Heparin/collagen encapsulating nerve growth factor multilayers coated aligned PLLA nanofibrous scaffolds for nerve tissue engineering. Journal of biomedical materials research-part A, 105(7),1900-1910.

Zhang, R., Han, S., Liang, L., Chen, Y., Sun, B., Liang, N. et al. (2021). Ultrasonic-driven electrical signal-iron ion synergistic stimulation based on piezotronics induced neural differentiation of mesenchymal stem cells on FeOOH/PVDF nanofibrous hybrid membrane. Nano energy, 87(1), 106192-106199.

Zhang, Y., Liu, S., Li, Y. (2015). Electrospun graphene decorated MnCo2O4 composite nanofibers for glucose biosensing. Biosensing bioelectronics, 66(2015), 308-315.

Zhang, Y.Z., Wang, X., Feng, Y., Li, J., Lim, C., Ramakrishna, S. (2006). Coaxial electrospinning of (fluorescein isothiocyanate-conjugated bovine serum albumin)-encapsulated poly(ε-caprolactone) nanofibers for sustained release. Biomacromolecules, 74(2), 1049-1057.

Zhou, K., Thouas, G., Bernard, C., Forsythe, S. (2014). 3D presentation of a neurotrophic factor for the regulation of neural progenitor cells. Nanomedicine, 9(8), 1239-1251.

CHAPTER 3:
FABRICATION OF TWO-DIMENSIONAL THIN FILMS FOR NEURAL TISSUE ENGINEERING APPLICATIONS

3.1 Introduction

The development of new pharmaceutical entities has historically been a long and research-driven process. The first step in the formulation development lifecycle (pre-formulation), is vital for laying the initial framework of the formulation and translates to the ultimate success of the formulation (Jones, 2018). The pre-formulation phase involves laboratory experimentation that allows for the determination of the ideal or optimal characteristics of the desired formulation that may influence process design, performance, safety, and suitability for the application (Jones, 2018). To this end, the fabrication of a typical polymeric thin film involves the consideration of many factors such as polymer concentration, composition, speed of solvent evaporation and drying conditions. These factors considerably affect the formation of the final film and its properties (Zhe Yang et al., 2010).

Polycaprolactone (PCL) and cellulose acetate phthalate (CAP) were chosen to create the polymeric thin films for a number of reasons. PCL is a biodegradable, thermoplastic, semi-crystalline aliphatic linear polyester, making it ideal for casting very thin films (Van De Velde & Kiekens, 2002). Previous studies have shown that PCL films contain surface pores or pits with a homogenous distribution, which is advantageous for cell growth and metabolism (Sun & Downes, 2009; Tang et al., 2004). Biocompatibility studies have demonstrated that PCL films support PC12, A172 and NG108-15 cell attachment, proliferation, migration and differentiation (Sun & Downes, 2009). Cellulosic polymers are biocompatible, biodegradable and offer excellent mechanical support to cells *In Vitro*. One of the most interesting cellulosic polymers for use in tissue engineering is CAP, which is gaining research interest due to its inherent antimicrobial and antiviral activity (Olaru & Olaru, 2010). Cellulose acetate phthalate has previously been used as a pharmaceutical excipient for drug delivery as well as to reduce the risk of transmission of human immunodeficiency virus, herpes viruses, and non-viral sexually transmitted diseases (Olaru & Olaru, 2010; Stone, 2002). The combination of these two polymers into thin films are novel in the tissue engineering realm and will be chosen as the polymers for the thin film fabrication based on their unique and favourable qualities.

A long-standing challenge in the development of nerve guidance platforms is to achieve a balance between optimal mechanical properties with the ability to withstand physiological stresses whilst still mimicking natural nerve biomechanics to support endogenous peripheral nerve repair (Hsiang et al., 2011). To optimise the polymeric thin film, this preliminary chapter was developed to identify and select the optimal polymer ratio, concentration, and drying

techniques for the thin film fabrication process in terms of mechanical strength. Mechanical strength is seen as one of the most important properties of ideal nerve guides (Tang et al., 2004). This chapter includes mechanical evaluation of film samples with various ratio compositions, concentrations, and drying conditions.

The appropriate nerve guide should assume appropriate cell-substrate interactions to facilitate cell attachment, spread, proliferation and differentiation (Denis et al., 2019). Wei and co-workers found that the highest level of NIH 3T3 fibroblast attachment occurred at surfaces that were more hydrophilic, and the best results were observed for surfaces with contact angles in the range of 20-60° (Wei et al., 2020). De Sousa and co-workers hydrolyzed polylactic acid electrospun nanofibers with sodium hydroxide to facilitate the covalent attachment of polypyrrole-grafted gelatin onto the surface of the nanofibrous mat. The group found that the surface hydrolysis improved the hydrophilicity of the platform which enhanced the adhesion, viability and proliferation of PC12 cells (de Sousa et al., 2020).

Polycaprolactone is a relatively hydrophobic polymer with a water contact angle of ± 112° (Dulnik et al., 2016). This is disadvantageous in the realm of tissue engineering as hydrophilicity encourages initial cell attachment and spreading, as discussed (Dulnik et al., 2016; Guo et al., 2016). In this regard, hydrophilic functionalization of the polymeric thin films is paramount (Niemczyk-Soczynska et al., 2020). Hydrolysis is one of the most useful techniques to provide a significant improvement in hydrophilicity and thus cell attachment and proliferation (Sun & Downes, 2009). Hydrolysis leads to the formation of carboxylic groups by cleaving the ester bond of PCL, thereby enhancing the hydrophilicity of the surface (Sun & Downes, 2009). In addition, surface hydrolysis has also been found to improve surface roughness, which is an important property for nerve tissue engineering to promote cell attachment (Sun & Downes, 2009). Aminolysis serves as an additional approach to enhance hydrophilicity by cleaving the hydrophobic ester bonds of polyesters and replaces them with relatively hydrophilic amide bonds and O-H groups (Sun &Downes, 2009). The use of diamines is the most frequent technique used to introduce amine moieties to scaffold surfaces, wherein one of the two amine groups reacts with the carbonyl carbon and the other one is left free on the surface (Dulnik et al., 2016). These polar groups increase the hydrophilicity of polyester materials, exemplified by Figure 3.1, involving the aminolysis of PCL using 1,6 hexanediamine (Zhu et al., 2013). In addition, De Luca and co-workers found that the aminolysis of PCL membranes enhanced the hydrophilicity of the membrane, which encouraged the attachment and proliferation of Schwann cells (De Luca et al., 2014).

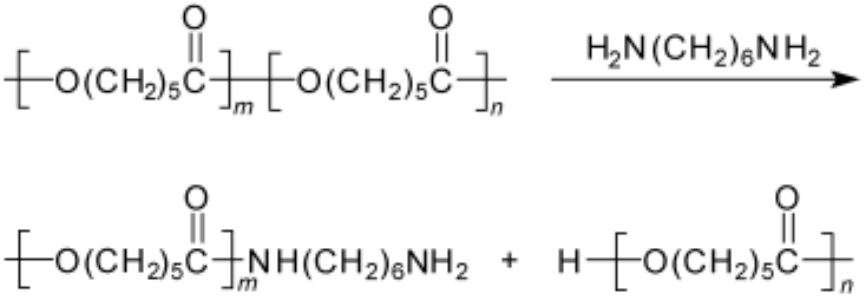


Figure 3. 1 Aminolysis reaction of polycaprolactone with 1,6-hexanediamine. Reproduced with permission from Zhu (2013). Copyright 2012, Springer.

To this end, this chapter focuses on the pre-formulation research to determine the optimal conditions for the thin film fabrication. The chapter then proceeds with the investigation of employing hydrolysis and aminolysis reactions as the main hydrophilicity probe in order to achieve structurally suited PLC/CAP films that have the ability to enhance cell-platform interactions *In Vitro*.

3.2 Materials and Methods

PCL (Mw ~ 80 g/mol), cellulose acetate phthalate (Mw ~ 2534.12 g/mol), The Kaiser Test Kit and ethylenediamine (EDA) (Mw ~ 60.1 g/mol), sodium dodecyl sulfate (SDS) and phosphate buffered saline (PBS) were purchased from Sigma-Aldrich (St. Louis, MO, USA). Ethanol (99% absolute) was purchased from LabChem, Edenvale, Johannesburg, South Africa. Chloroform, acetone, dimethyl sulfoxide (DMSO) and 2-propanol were purchased from Associated Chemical Enterprises, Southdale, Johannesburg, South Africa. NaOH and potassium hydroxide (KOH) pellets were purchased from Merck, Darmstadt, Germany. Millipore water was used for washing of preparations. Dulbecco's Modified Eagle Medium (DMEM), Trypan Blue, penicillin/streptomycin, cell culture treated well plates, flasks, Donor Equine Serum (DES), CellCrown^{TM} Inserts and Fetal Bovine Serum (FBS) were purchased from Sigma Aldrich, South Africa. The Ham's F12 Nutrient Mixture was purchased from Gibco (Thermo Fischer, South Africa). The Roche Cell Proliferation Kit II (XTT) was purchased from Sigma Aldrich, South Africa. The PC12 and A172 cells were purchased from Cellonex (Separations, South Africa). Mammoth powerful grip double sided transparent tape was purchased from Builders Warehouse, South Africa. The bicinchoninic acid (BCA) protein kit was purchased from Pierce (Thermofischer, South Africa).

3.2.1 Pre-formulation research

3.2.1.1 Method employed to identify the ideal polymer ratio to form thin films based on mechanical testing

In order to determine the ideal ratio of PCL:CAP to form a blend leading to thin film development, various polymer ratios were investigated (1:1, 1:2 and 2:1), while the total polymer concentration was kept constant. Briefly, PCL pellets were dissolved in chloroform to form a 6% w/v polymer solution. CAP pellets were dissolved in acetone: ethanol (2:3) to make a 3% w/v polymer solution. Both solutions underwent mechanical stirring at 25 °C until dissolved. Thereafter, the solutions were mixed at various ratios and were combined to form a PCL/CAP blend solution (total polymer concentration of 9% w/v). Following this, the solutions were cast onto borosilicate glass coverslips and left to dry in a Memmert drying oven under continuous air flow at 40 °C for 24 h. After the films were dried, the mechanical properties of the thin films were determined with a Texture Analyzer (TA.XTplus Texture Analyser, Stable Microsystems, Surrey, UK) fitted with two clamps. The width, height, and length of the samples were measured with digital Vernier callipers (Krafft, DV150GW, Schoellerstr Düren, Germany). Rectangular 40 x 15 mm strips of each sample were fixed at 20 mm between the two clamps. Tests were conducted at 0.167 $mm.s^{-1}$ while applying a 0.5 N trigger force to obtain resultant stress (MPa)-strain (%) curves. The ratio that produced the optimal mechanical strength for neural tissue engineering was chosen and carried over to the next evaluation in 3.2.1.2.

3.2.1.2 Method employed to determine the optimal total polymer concentration of the thin films based on quantitative mechanical evaluation

In order to assess the structural integrity of films at various total polymer concentrations, a set ratio of PCL:CAP defined in Section 3.3.1.1 was synthesized at various concentrations (3, 6 and 9% w/v). The films were dried in a Memmert drying oven under continuous air flow at 40 °C for 24 h. The films were then subjected to the same mechanical evaluation described in Section 3.2.1.1. The film that produced optimal mechanical properties was carried over to Section 3.2.1.3.

3.2.1.3 Method employed to determine the optimal drying method based on quantitative mechanical evaluation

Two different drying conditions were evaluated for their suitability for the formation of the thin films in terms of mechanical strength. The optimal ratio composition and total polymer concentration from Sections 3.3.1.1 and 3.3.1.2, were used to fabricate the films in this Section. The effect of each drying method on the mechanical properties of the films was investigated using the same mechanical evaluations described in 3.2.1.1. Table 3.1 describes the drying methods evaluated for suitability in the film formation process.

Table 3. 1 Drying conditions evaluated for suitability in the film formation process.

Drying Method	Conditions
1	Dried in fume hood at 25° C with continuous air flow.
2	Dried in oven at 40° C with continuous airflow.

3.2.2 Method employed to fabricate the unfunctionalized thin films

The following fabrication method was designed based on the results of pre-formulation research outlined in Sections 3.3.1.1-3.3.1.3. The PCL pellets were dissolved in chloroform at a concentration of 6% w/v and CAP pellets were dissolved at a concentration of 3% w/v in an acetone: ethanol mixture (2:3). The solutions were dissolved separately through mechanical stirring at 25 °C for one hour. The solutions were combined to form a blend, with a total polymer concentration of 9% w/v. Borosilicate glass coverslips were then dipped in the solutions and placed upright to dry in a Memmert drying oven at 40 °C for 24 h. Lastly, the films were placed in deionised water to remove the films from the coverslips and placed in a fume hood at 37 °C to dry until use.

3.2.3 Hydrolysis of the thin films

Briefly, film samples were immersed in 10M NaOH or 10M KOH at 37 °C with gentle shaking for 90 mins in an orbital shaking incubator (LM-530-2, MRC Laboratory Instruments Ltd, Hahistadrut, Holon, Israel). The films were then removed and rinsed in deionised water for 10 mins and placed in the fume hood under continuous air flow to dry until further characterization. Method adapted from De Luca (2014).

3.2.4 Aminolysis of the thin films

Samples were immersed in 20% v/v ethylenediamine in 2-propanol at 37 °C and gently shaken for 90 mins in an orbital shaking incubator. The films were then removed and rinsed in deionised water for 10 mins and placed in a fume hood under continuous air flow to dry until further characterization. Method adapted from De Luca (2014).

Due to the nature of the casting method, the films had two surfaces: namely, an air surface and a glass surface. For each analysis, the samples were analysed on both sides, where applicable. Table 3.2 describes the various abbreviated sample names used in this research and their meanings.

Table 3. 2 The various samples prepared in this study.

Sample	Constituents
PCL	6% w/v polycaprolactone film cast in chloroform.
CAP	3% w/v cellulose acetate phthalate film cast in acetone: ethanol (2:3).
PCL/CAP	6% w/v polycaprolactone, 3% w/v cellulose acetate phthalate film.
PCL/CAP-NaOH	Polycaprolactone/cellulose acetate phthalate film hydrolyzed with 10M NaOH, 90 min.
PCL/CAP-KOH	Polycaprolactone/cellulose acetate phthalate film hydrolyzed with 10M KOH, 90 min.
PCL/CAP-EDA	Polycaprolactone/cellulose acetate phthalate film aminolyzed with 20% v/v ethylenediamine/ 2-propanol, 90 min.

3.2.5 Method employed for chemical integrity characterization employing Fourier-transform infrared spectroscopy

The FT-IR spectroscopy detected the molecular transitions and changes in crystallinity indices of the films arising from interactions between PCL, CAP, NaOH, KOH and EDA. Samples were analysed over an FT-IR spectra of wavelengths between 4000 and 600 cm^{-1} using a PerkinElmer Spectrum 2000 ATR-FT-IR (PerkinElmer 100, Llantrisant, Wales, UK) spectrometer fitted with a single-reflection diamond MIRTGS detector.

3.2.6 Method employed for thermodynamic behavior analysis using differential scanning calorimetry

Differential scanning calorimetry (DSC) (Mettler Toledo, Schwerzernback, Switzerland) was used to reveal the thermal properties of the PCL/CAP thin films and all the native polymers used to form the composite films. Samples of 2-10 mg were sealed in aluminium crucibles and heated over a temperature range of 0-450 °C, at a rate of 10 $°C.min^{-1}$. DSC curves were obtained by plots of sample weight over sample temperature. Measurements were done in duplicate.

3.2.7 Method employed for phase transition assessments utilizing x-ray diffraction

X-ray diffraction (XRD) was employed to determine the phase changes (crystallinity or amorphous) between native polymer films, as well as the blended film and the surface modified films. This characterization technique was performed on the Rigaku MiniFlex 600 Benchtop X-ray Diffractometer (Rigaku Corporation, Tokyo, Japan). The film samples were secured on a sample holder and were scanned at a rate of 15 °C per min with a diffraction angle range of 03-90° 2θ, with a degree step of 0.02, a voltage of 40 kV and a current of 15 mA. Sample crystallinity and crystallite sizes were determined by computing the XRD diffraction measurements into the crystallinity equation (Equation 3.1) and the Scherrer equation (Equation 3.2), respectively.

Equation 3. 1 % Crystallinity= (area of crystalline peak/total area) x 100

Equation 3. 2 $\Pi = K\gamma/\beta\cos\Theta$

Where Π is the particle size of single crystallites, K is the shape factor of value 0.9 for spherical particles, β is the line broadening width (FWHM) at half maximum intensity measured in radians and cosϴ is the Bragg angle.

3.2.8 Method employed for thermal stability evaluation utilizing thermogravimetric analysis

The determination of the change of thermal stability of the samples was evaluated by observing the change in sample weight as a function of temperature. This was performed using a Thermogravimetric analyser (TGA) (PerkinElmer, TGA 4000, Llantrisant, Wales, UK). Samples were heated at a rate of 10 ˚C/min from 0-900 ˚C under continuous nitrogen purging. Thermograms were generated as percentage weight vs. temperature and analysed using Pyris TM software (PerkinElmer, Llantrisant, Wales, UK). Individual curves were plotted for each sample as well as their derivative curves to accurately determine the temperature of each degradation step.

3.2.9 Method employed for surface topography characterizations utilizing scanning electron microscopy

Scanning electron microscopy (SEM) was utilized to evaluate the surface morphology of the thin films and the changes arising from hydrolysis and aminolysis. This was performed under different magnifications using an FEI Nova NanoLab 600TM scanning electron microscopy (FEI Company, Hillsboro, OR, USA). Samples were fixed to aluminium stubs using double-sided adhesive carbon tape and then sputter coated with carbon and gold palladium for 120 s (SPI ModuleTM Sputter-Coater and Control Unit, West Chester, PA, USA).

3.2.10 Method employed for porosimetric and surface area analysis

The porosity and surface area of the samples were analysed using the Micromeritics Porositometer (Micromeritics ASAP 2020, Norcross, GA, USA). Surface areas, pore sizes, shapes, and distributions were assessed according to the parameters presented in Section A4 of the appendix and were analyzed. Prior to analysis, the samples were degassed by heating the samples while simultaneously running gas over the samples to remove impurities. The samples were then cooled with liquid nitrogen and analyzed by measuring the volume of gas adsorbed at specific pressures. The resultant nitrogen adsorption-desorption isotherms were recorded.

3.2.11 Method employed for surface topography analysis using atomic force microscopy

Atomic Force Microscopy (AFM) (Veeco CP2) was used to determine high-resolution surface mapping of thin film structures in three dimensions providing rich data regarding the film's surface topography. Imaging was done on both sides of the sample, to determine the difference in surface roughness.

3.2.12 Method employed for spectrophotometric mapping of amine group attachment to thin films using the ninhydrin assay

Effectiveness of the aminolysis functionalization was determined by evaluating the concentration of free amine groups using the ninhydrin assay. Ninhydrin reacts positively in the presence of primary amine groups resulting in Ruhemanns purple color change (Friedman, 2004). The Kaiser test kit was used as well as the instructions detailed in the kit. Firstly, 5 mg of the aminolyzed films were transferred to a 15 ml centrifuge tubes (n=3). Unfunctionalized films were used as controls (n=3). Thereafter, 1 ml ethanol, 500 µl acetone and 500 µl chloroform were added to each centrifuge tube to dissolve the films. Following this, 1 ml of each sample was aliquoted into separate centrifuge tubes and sonicated for 10 mins. These solutions containing dissolved films were then reacted with 1 ml of ninhydrin solution (made up of equal amounts of 1-500 mg ninhydrin in 10 ml ethanol, 2-80 mg phenol in 20 ml ethanol and 3-2 ml of 0.001 M solution of potassium cyanide diluted to 100 ml with pyridine) at 120 °C for 10 min before dilution with 16 ml of ethanol once cooled. Relative concentrations were determined photometrically at 570 nm using the Carry 50 Conc UV-Vis's spectrophotometer (Varian (PTY) LTD, Australia). The amount of free amine groups was calculated on the basis of the absorbance calibration curve with known concentration of ethylenediamine in isopropanol.

3.2.13 Method employed for evaluating mechanical properties using the Texture Analyser

The mechanical properties of the thin films were determined with a Texture Analyser (TA.XTplus texture analyser, Stable Microsystems, Surrey, UK) fitted with two clamps. The width, height, and length of the samples were measured with a digital Vernier calliper (Krafft, DV150GW, Schoellerstr Düren, Germany). Rectangular 40 x 15 mm strips of each sample were fixed at 20 mm between the two clamps. Tests were conducted at 0.167 $mm.s^{-1}$ while applying a 0.5 N trigger force.

3.2.14 Method employed for wettability analysis utilizing water contact angle measurements

The hydrophilicity of the films was evaluated on both sides using the DataPhysics Instruments contact angle goniometer by measuring the water contact angle using the sessile drop method. The samples were placed on the stage and secured with double-sided tape. Subsequently, a Hamilton syringe was used to dispense 2 µl of distilled water onto the surface at a dosing rate of 2 $\mu l.s^{-1}$ at three random positions on the film. The images of the water droplets were recorded by camera software after the droplet was stable. Thereafter, the water contact angles at each position were measured using the SCA202 version 4.1.12 build 1019 software and an average calculated.

3.2.15 Method employed for *In Vitro* degradation analysis

The *In Vitro* degradation study was performed by submersing 0.5 cm x 3 cm film samples in 2 ml PBS (pH 7.4) contained in 24-well plates (n=3) and placed in an orbital shaking incubator at 37 °C. Acidic degradation may result in by-products which can cause autocatalysis and speed up degradation (Mailly et al., 2003). Therefore, the PBS was replaced every alternate day in order to avoid this by simulating the physiological environment, by mimicking the elimination of degradation products. Samples were removed at predetermined time intervals and placed in the oven at 40 °C for 48 h to dry, then weighed again. Equation 3.3 was used to calculate the percentage degradation. The dry mass ratio (Equation 3.4) was used to plot a degradation rate curve.

Equation 3. 3 $\%\ \text{Degradation} = [(wi - wf)/wi] \times 100$

Equation 3. 4 $\text{Dry mass ratio} = wf/wi$

Where wi is the initial weight of the film samples and wf is the weight of the final oven-dried samples (Ramburrun et al., 2019).

3.2.16 Method employed for *In Vitro* water-uptake analysis

The water-uptake study was performed by submersing 0.5 x 3 cm film samples in 2 ml PBS (pH 7.4) contained in 24-well plates (n=3) and placed in an orbital shaking incubator at 37 °C. Samples were removed at predetermined time intervals; excess moisture was carefully removed by blotting with tissue paper and the change in mass was measured for determination of moisture absorption using Equation 3.5 (Ramburrun et al., 2019).

Equation 3. 5 $\%\ \text{Water-uptake} = [(wh - wi)/wi] \times 100$

Where wi is the initial weight of the film samples, wh is the weight of the samples after hydration (Ramburrun et al., 2019)

3.2.17 Method employed for PC12 and A172 cell culture and cell viability quantification utilizing the XTT cytocompatibility assay

Rat adrenal gland pheochromocytoma PC12 mixed adherent/suspension cells were cultured in cell culture treated T-75 flasks using Ham's F12 Nutrient Mixture supplemented with 15% v/v DES, 2.5% v/v FBS and 1% v/v penicillin/streptomycin solution. Human glioma cells (A172) were cultured in cell culture treated T-75 flasks using DMEM supplemented with 10% v/v FBS and 1% v/v penicillin/streptomycin solution. Both cell lines were cultured in a humid 5% CO_2 atmosphere at 37˚C. The culture medium was replaced at 75% confluency every two days.

For the detection of cell proliferation and cyto-compatibility of the films, The Cell Proliferation Kit II (XTT) was utilized. Thereafter, 5 mg of each sample was sterilised with 70% ethanol and rinsed three times in sterile PBS. Following this, 1 ml of the respective media was added to a 12-well plate containing the sterilised sample and incubated for 24 h at 37° C, 5% CO_2 and 97% humidity. The resultant liquids were termed 'extraction media' (Khorramnezhad et al., 2021). PC12 and A172 cells were seeded into 96-well plates at densities of 25 000 cells/ml in 90 µl cell culture media and incubated for 24 h. Thereafter, the media was replaced with 90 µl extraction media. For the negative control, 10 µl fresh media was added to a cell-containing well. The positive control was prepared by adding 10 µl of DMSO to a cell-containing well. Thereafter, all wells were incubated for 48 and 72 h. At the respective time points, activated XTT solution was prepared by combining the 5 ml XTT Reagent and the 0.1 ml Activation Reagent. Thereafter, 50 µl of the activated XTT solution was added to each well and incubated for 4 h. The absorbance was read at 450 nm and 660 nm using a multiplate reader (BioTek, USA). The 660 nm absorbance reading was used to eliminate background signal produced by cell debris or other non-specific absorbance. The average 660 nm readings were subtracted from each 450 nm absorbance result to obtain the specific absorbance of each sample. Thereafter, an average of the negative control was obtained and an average cell viability for each sample was calculated by expressing each specific absorbance as a percentage of the negative control.

3.2.18 Method employed for the qualitative assessment of cell attachment using light microscopy visualization

For the visualization of the PC12 and A172 cells on the films, the films were sterilised with 70% ethanol and cut to 1 x 1 cm strips and rinsed three times in sterile PBS. The samples were sterilized for 15 mins under UV light and transferred to 12-well plates and secured to the bottom of the plates using double sided transparent tape (Mammoth Powerful Grip Double Sided tape,

Builders Warehouse, South Africa) to prevent the films from floating in the media. PC12 and A172 cells were seeded onto each film at a density of 500 000 cells/ml and incubated for 48 h. Thereafter, light microscopy images (Olympus, DP 80,Tokyo, Japan) equipped with LCmicro Software, were taken of cells attached to the films.

3.2.19 Method employed for the quantification of cell attachment using the trypan blue exclusion method

Samples were cut to 3 cm x 3 cm strips and rinsed three times in sterile PBS. The samples (n=3) were UV sterilised for 15 mins and transferred to 6-well plates. The samples were secured to the bottom of the wells using sterile CellCrown™ Inserts to prevent the films floating in the medium. PC12 and A172 cells were each seeded at a density of 500 000 cells/ml onto the samples and incubated for 48 h. The control included cells seeded onto the bottom of the well plate in the absence of any sample. Thereafter, the media was aspirated and discarded. The samples were removed from the plates and placed in new 6-well plates. The samples were rinsed three times in sterile PBS. Thereafter, 200 µl trypsin was added to each sample to detach the cells. Following this, 500 µl media was added to stop the trypsinization and was placed in sterile centrifuge tubes and centrifuged for 10 mins at 5000 rpm. The supernatant was discarded, and the cells were re-suspended with 50 µl fresh media. Following this, 10 µl trypan blue was added to 10 µl of the cell suspension and cells were manually counted using a haemocytometer. The cell attachment was calculated by expressing the total number of counted live cells on each film as a percentage of live cells counted on the control using Equation 3.6.

Equation 3. 6 % Cell attachment= (live cells on sample/ live cells on control) x 100

Statistical analysis

All samples were analysed in triplicates and the mean standard deviations were recorded as computed. Student T-tests were performed for statistical significance for *In Vitro* studies. Samples that had P values of $P \leq 0.05$ were considered to have a significant effect on the variable being investigated. All statistics and calibration curves were analysed on Microsoft Excel. All graphs were plotted using OriginPro 8.5 Software.

3.3 Results and discussions

3.3.1 Pre-formulation research

3.3.1.1 Determination of the optimal polymer ratio in terms of qualitative outcomes

Tensile strength and modulus of toughness are vital to the translational success when choosing a material for structural purposes such as a nerve guidance conduit (Zhang et al., 2011). In order to act as a support structure for the regenerating nerve, the film needs to be

robust enough to structurally accommodate tissue repair needs and the implantation process (Tang et al., 2004). Tensile strength is defined as the maximum stress that a material can withstand when a force is applied and is calculated using the maximum stress value obtained from a stress-strain curve. Zhang and co-workers observed that the ideal tensile strength for optimal mechanical performance (comparable to that of clinical materials such as Neurolac®) is 1-7 MPa (Zhang et al., 2011).

The modulus of toughness is defined as the work done on a unit volume of material as the force is gradually increased, in $J.m^{-3}$. This is calculated as the area under the entire stress-strain curve. The toughness of a material is its ability to absorb energy without causing it to break (Zhang et al., 2011). The Young's modulus of a film is also important when designing a nerve guidance conduit (Tang et al., 2004). The Young's modulus, also known as the elastic modulus, is defined as the ratio of stress and strain (gradient) when the deformation is completely elastic and is related to the stiffness of the material (Tang et al., 2004). An ideal nerve guidance conduit should have a Young's modulus similar to that of the native neural tissue, in this case, a rat sciatic nerve was used as a reference, having a Young's modulus of 580 ± 0.015 KPa (Borschel et al., 2003).

Table 3. 3 The effect of various polymer ratios on qualitative outcomes.

Ratio of PCL:CAP	Fmax (N)	Tensile strength (MPa)	Young's modulus (KPa)	Toughness ($J.m^{-3}$)
1:1	2.10 ± 0.28	4.62 ± 0.65	406.58 ± 5.31	49.97 ± 3.77
1:2	1.49 ± 0.23	3.55 ± 0.32	306.47 ± 5.95	15.81 ± 2.31
2:1	2.10 ± 0.28	5.01 ± 0.39	535.39 ± 6.25	115 ± 2.162

From Table 3.3, it is evident that that ratio of PCL to CAP of 2:1 is the optimal ratio for neural tissue engineering as it has the highest tensile strength, Young's modulus, and toughness, which are also in-line with the standards of neural tissue engineering. This ratio is thus the formulation selected for further analysis in Sections 3.3.1.2 and 3.3.1.3. The optimal formulation is highlighted in green in each table.

3.3.1.2 Determination of the optimal total polymer concentration based on quantitative mechanical evaluation

Following polymer ratio determination, the optimal total polymer concentration was investigated as the total polymer concentration significantly affects film properties, in particular the mechanical strength of polymeric films (Tarus, 2016). Table 3.4 highlights that the higher the total polymer concentration, the higher the mechanical properties of the films.

Table 3. 4 The effect of total polymer concentrations on the mechanical properties of the films.

Total polymer concentration (% w/v)	Fmax (N)	Tensile strength (MPa)	Young's modulus (KPa)	Toughness ($J.m^{-3}$)
3	0.54 ± 0.03	1.29 ± 0.32	158.64 ± 6.99	32.135 ± 2.02
6	0.81 ± 0.17	1.55 ± 0.16	394.27 ±4.30	43.37 ± 4.63
9	3.09 ± 0.27	5.01 ± 0.39	535.39 ± 6.25	115 ± 2.16

The film with 9% w/v total polymer concentration best suits the requirements of an ideal nerve guide and is thus the optimal formulation to be used in further evaluation in Section 3.3.1.3.

3.3.1.3 Determining the optimal drying method based on quantitative mechanical evaluation

The drying method was carefully selected based on quantitative mechanical results as the drying conditions significantly affect the mechanical properties of the films (Tapa-Blàcido et al., 2013) as highlighted by Table 3.5. Different drying methods will subject films to various degrees of heat, which will in turn affect the solvent evaporation rate (Tapa-Blàcido et al., 2013).

Table 3. 5 The effect of drying conditions on the mechanical properties of the films.

Drying Method	Fmax (N)	Tensile strength (MPa)	Young's modulus (KPa)	Toughness ($J.m^{-3}$)
1	1.38 ± 0.22	4.55 ± 0.78	869.95 ± 7.69	1618.714 ± 4.68
2	3.09 ± 0.27	5.01 ± 0.39	535.39 ± 6.25	115 ± 2.16

The relative tensile strengths of the PCL/CAP films using drying method 1 and 2 are 4.55 ± 0.78 and 5.01 ± 0.39 MPa, respectively, indicating that both films have adequate tensile strength for a nerve guidance conduit in terms of the reference values discussed. However, the tensile strength for the film dried in the oven is slightly higher than the film dried in the fume hood. Drying method 2 has a Young's modulus that most suited the requirements of an ideal nerve guidance conduit. The Young's modulus of the film dried by method 1 is much higher than that of the standard, making the film too flexible, thus indicating that it may not be rigid enough to withstand the forces applied during the implantation and regeneration processes (Zhang et al., 2014). The modulus of toughness is 1618.71 ± 4.68 and 535.39± 6.25 $J.m^{-3}$, respectively, for drying method 1 and 2. The modulus of toughness greatly differs between the different drying methods, with the film formed from drying method 2 having a much higher value, which is consistent with another study by Tapia-Blàcido and co-workers (Tapia-Blàcido et al., 2013). Due to the favourable mechanical properties produced by drying method 2, this is the method chosen for the film formation throughout the dissertation.

In this pre-formulation subsection, it is evident that the polymeric film formation process is highly sensitive to constituent ratios, concentrations, and drying temperature and rate. Through evaluation of the mechanical properties of the film variations it is evident that the ratio of PCL:CAP of 2:1 is the optimal ratio for neural tissue engineering purposes. In addition, the total polymer concentration of 9% w/v yields the highest tensile strength, Young's modulus, and toughness. Further, drying method 2 is selected as the optimal condition to dry the films as it produces mechanical properties that are most in line with the standards for ideal nerve guides. Drying method 2 allows for faster solvent evaporation due to the higher temperature, thereby resulting in films with stronger mechanical attributes. This was also observed in a study by Tapia-Blàcido and co-workers in 2013 who observed tougher films at higher drying temperatures (Tapia-Blàcido et al., 2013).

This pre-formulation research highlights that the composition of films and drying conditions significantly affects the mechanical properties of films. The results from this subsection indicate that the PCL/CAP thin films for the proceeding chapters will be fabricated with a 2:1 ratio of PCL to CAP, a 9% w/v total polymer concentration and will be dried in the Memmert drying oven at 40 °C under continuous air flow.

3.3.2 Visual appearance of the thin films

Photographic images of the unfunctionalized and functionalized samples were taken to qualitatively assess the visual changes following functionalization. The unfunctionalized and functionalized films were placed in a 6-well plate and secured with CellCrown Inserts™ to secure the films in place for ease of imaging (Figure 3.2).

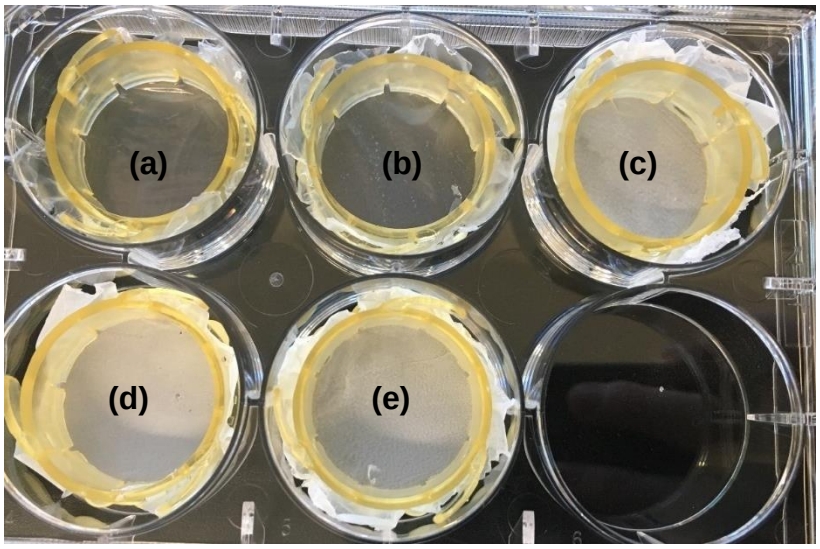


Figure 3. 2 Photographic image illustrating the visual appearance of the films (a) polycaprolactone, (b) polycaprolactone/cellulose acetate phthalate, (c) sodium hydroxide-functionalized films, (d) potassium hydroxide-functionalized films, (e) ethylenediamine-functionalized films. The yellow structures are the well plate inserts used to secure the films in place.

The functionalization of the films changes the opacity of the films as well as the color. The PCL films and the PCL/CAP unfunctionalized films are transparent while the functionalized films are opaque and whiter in color. The proposed reason for this is unknown.

3.3.3 Chemical integrity characterization employing Fourier-transform infrared analysis

Fourier-transform infrared analysis (FT-IR) was employed to assess the chemical changes that occurred following PCL and CAP blending as well as subsequent hydrolysis and aminolysis of the composite film. There are no differences observed between the two different surfaces of the thin films, namely, the air and glass surfaces. Characteristic peaks of PCL are observed which include ~ 2945, 2866, 1720, 1239 and 1160 cm^{-1}, assigned to C-H hydroxyl group asymmetric stretching, C-H hydroxyl group symmetric stretching, C=O stretching vibrations of the ester carbonyl group, C-O-C asymmetric stretching and C-O-C symmetric stretching, respectively (Pawlik et al., 2019).

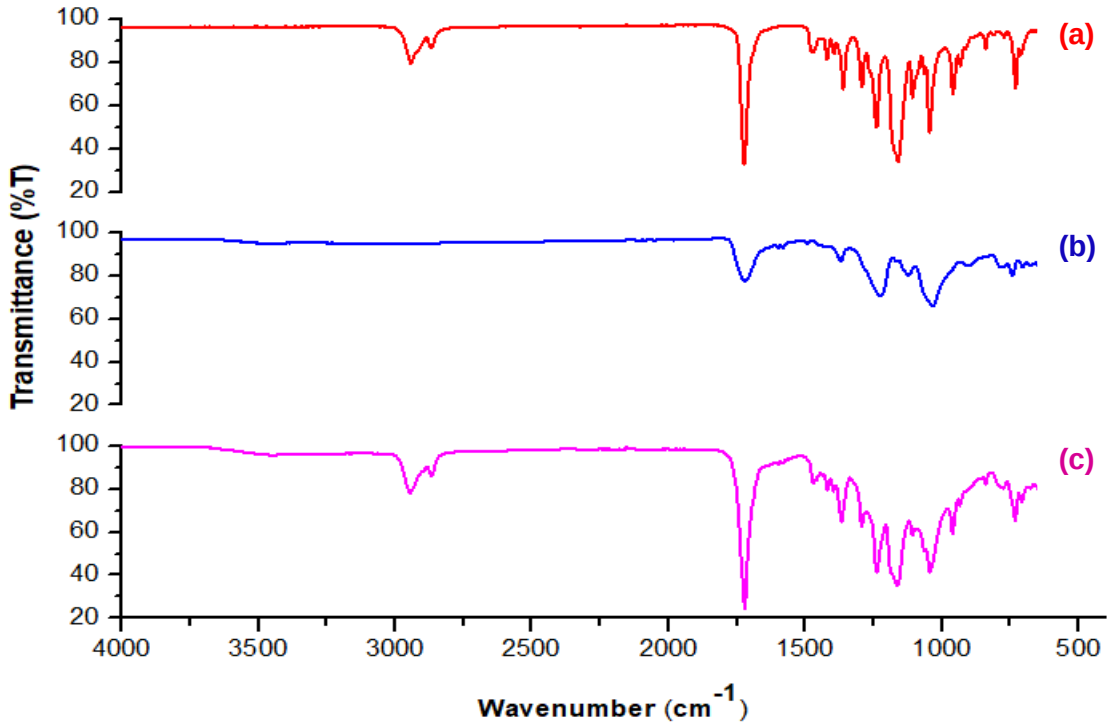


Figure 3. 3 Fourier-transform infrared spectroscopy of pristine (a) polycaprolactone, (b) cellulose acetate phthalate and (c) polycaprolactone/cellulose acetate phthalate.

The characteristic peaks of CAP include ~ 735-770 cm^{-1}, representing the ortho disubstituted benzene ring, ~ 1034, 1223, 1369, 1719, 2942, 3490 cm^{-1}, representing C-O-C stretching, the ester bond, methyl groups, the C=O carboxyl group, asymmetric and symmetric stretching of methyl C-H groups and O-H groups present in CAP, respectively (Pawlik et al., 2019). The bands at 1582 and 1598 cm^{-1} are attributed to the cyclic alkene bonds in CAP (Chaturvedi et al., 2011; Roxin et al., 1998).The spectra in (c) shows evidence of a blended formulation with a primarily PCL structure, which is a reasonable conclusion due to the relatively high

concentration used in the blend (twice that of CAP) (Parak et al., 2019). This is evidenced by the presence of the PCL-related bands at ~ 2943, 2868, 1724, 1237 and 1160 cm^{-1} which are assigned to C-H hydroxyl group asymmetric stretching, C-H hydroxyl group symmetric stretching, C=O stretching vibrations of the ester carbonyl group, C-O-C asymmetric stretching and C-O-C symmetric stretching, respectively (Pawlik et al.,2019). Characteristic CAP bands are present at ~ 3400 cm^{-1}, which indicates the presence of the asymmetric and symmetric stretching of the O-H groups in CAP (Roxin et al.,1998). The peak at ~ 1598 cm^{-1} is due to the cyclic alkene bonds in CAP (Roxin et al., 1998). The peak at ~ 1369 cm^{-1} is due to the methyl groups present in CAP (Chaturvedi et al., 2011). The slight change in shape of the bands at ~ 1164 cm^{-1} and ~ 1045 cm^{-1} indicates overlapping bands from each native polymer (Chaturvedi et al., 2011). There is an increase in intensity of the peaks at ~ 1722, 1364, 1238, 1042 and 961 cm^{-1}, as a result of the additive effect of CAP to PCL (Pawlik et al., 2019). There are no new peak appearances in the FT-IR spectrum of the respective films, which indicates the absence of any chemical bond formation between the components, proving that they combine to form a physical blend (Parak et al., 2019). Figure 3.4 presents the hydrolyzed and aminolyzed samples.

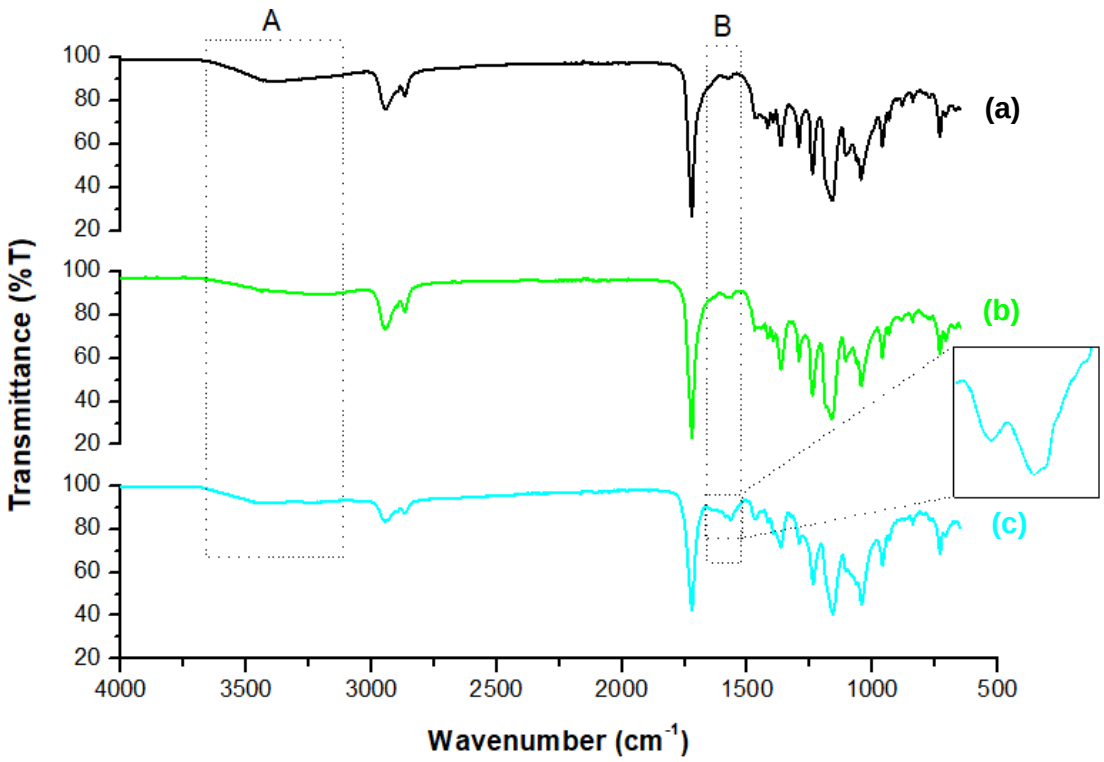


Figure 3. 4 Fourier-transform infrared spectroscopy of (a) sodium hydroxide-hydrolyzed films, (b) potassium hydroxide-hydrolyzed films and (c) aminolyzed films. Regions A and B have been highlighted as areas of interest.

The presence of the broad at ~ 3600 cm $^{-1}$ in region A proves that hydrophilicity is induced due to stretching vibrations of O-O-H bands from C-O-O-H and O-H groups, while maintaining the general spectra of the films, indicating no compromise to the polymer backbone structure (Peña et al., 2006; Zuppolini et al., 2020). It is evident that this band is more intense in (a), indicating that NaOH is more effective in hydrolyzing the films than KOH (Zuppolini et al., 2020). Spectrum (c) illustrates the successful aminolysis of the films due to the presence of the relatively strong band at ~ 1566 cm^{-1} in region B, representing the N-H bending of the amide II group (Krithica et al., 2012). The area is enlarged for clarity, showing a smaller band at ~ 1640 cm^{-1} which represents the C=O stretching of the amide I band (Krithica et al., 2012). Further, the broad band at ~ 3500 cm^{-1} in region A is due to the presence of a secondary amine group (Krithica et al., 2012). In conclusion, the FT-IR spectra prove that the films were successfully hydrolyzed and aminolyzed with no compromise to the polymer backbones.

3.3.4 Analysis of the thermodynamic behavior of the thin films utilizing differential scanning calorimetry

Differential scanning calorimetry thermograms are necessary to observe effects of surface functionalization on the thermal profile of materials (Levya-Porras et al., 2020). Table 3.6 represents the respective values for the melting temperatures (Tm), enthalpy of melting (∆hm), degradation temperature (Td) and enthalpy of degradation (∆hd).

Table 3. 6 Representing the changes to the DSC thermal profiles of the samples.

Sample	Onset of Melting (°C)	Tm[1] (°C)	∆hm [2](mW.°C)	Onset of Degradation (°C)	Td[3] (°C)	∆hd[4] (mW.°C)
Pristine polycaprolactone	34.85	64.55	280.15	331.12	408.43	-
Polycaprolactone film	34.61	61.12	82.00	321.10	405.53	731.10
Polycaprolactone/ cellulose acetate phthalate film	33.86	61.77	53.47	280.80	402.44	346.21
Sodium hydroxide hydrolyzed film	35.86	61.63	89.78	281.46	386.01	749.87
Potassium hydroxide hydrolyzed film	38.51	62.27	65.30	283.30	390.90	704.66
Aminolyzed film	34.36	60.34	110.09	353.85	406.89	507.74

[1] Melting temperature
[2] Enthalpy of melting
[3] Degradation temperature
[4] Enthalpy of degradation

Tm correlates to the endothermic peak (Levya-Porras et al., 2020). A shift in this value indicates a change in thermal stability of the sample (Labet & Thielemans, 2009). The area under the endothermic peak represents ∆hm. The energy associated with this phase of melting provides an indication of the ease of bond breaking, which similarly can be related to thermal stability (Labet & Thielemans, 2009). The temperature at which the material degrades is Td and is represented by the peak of the second endothermic peak and its corresponding area represents ∆hd (Levya-Porras et al., 2020). These values were identified and calculated from the DSC thermograms using OriginPro 8.5 Software.

Figures 3.5-3.8 represent the DSC thermograms for the pristine polymers, their corresponding films, the composite PCL/CAP film as well as the functionalized films. Figure 3.5 indicates that the onset of melting for pristine PCL is 34.85 °C and the Tm is 64.55 °C, which corresponds with literature (Dash & Konkimalla, 2012; Labet & Thielemans, 2009; Woodruff & Hutmacher, 2010). The area under the curve (AUC) of the endothermic peak is 280.149 mW.°C. The thermal degradation of PCL occurs by specific chain end scission in bulk, at 280-330 °C (Labet & Thielemans, 2009). The thermogram supports this as the onset of degradation occurs at 331.12 °C, which is within the range stipulated above. The temperature of onset of melting is similar to that of the pristine polymer.

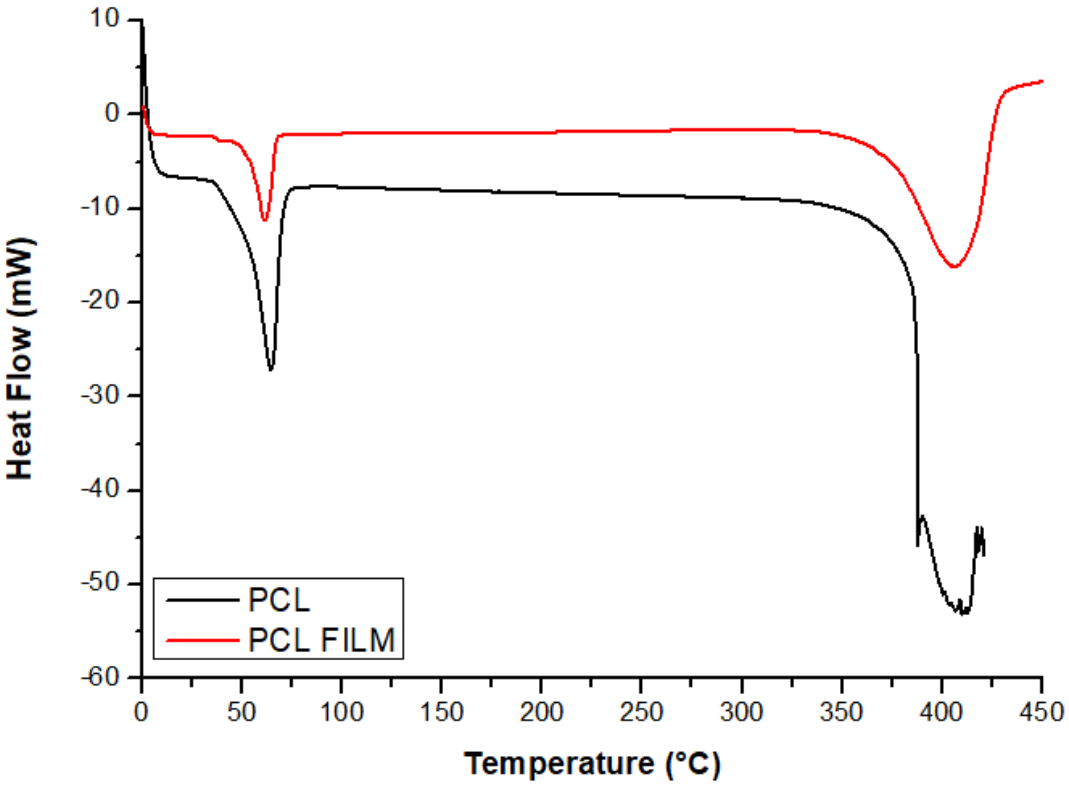


Figure 3. 5 Differential scanning calorimetry thermogram of (PCL) pristine polycaprolactone and (PCL FILM) polycaprolactone film.

However, the Tm is reduced to 61.12 °C, indicating a reduced thermal stability in comparison to the pristine polymer (da Silva et al., 2021). This is confirmed by the TGA data in Section 3.3.6. The ∆hm is reduced to 82.00 mW.°C, which indicates a decrease in release of energy during this transition phase, correlating to a decrease in bond breakage in the polymer, conferring an enhanced thermal stability during the melting phase of the film (Ramburrun et al., 2019). The onset of degradation is also reduced by ± 10 °C, indicating that the film starts to degrade at a lower temperature compared to the pristine polymer, suggesting a reduced thermal stability (Labet & Thielemans, 2009). The AUC of the second endothermic peak is much larger for the pristine polymer, which indicates an enhanced release of energy during this transition phase (Ramburrun et al., 2019). This is related to an increase in bond breakage in the polymer and a reduced thermal stability during degradation (Ramburrun et al., 2019).

It is to be noted that crystallisation and melting peaks are only observed for polymers that can form crystals, while purely amorphous polymers will only undergo a glass transition (Garg et al., 2016). The amorphous portion only undergoes the glass transition while the crystalline regions only undergo melting, indicated by the melting peak. With reference to pristine CAP in Figure 3.6, there is no defined melting peaks since CAP is amorphous, proven by the XRD data (Garg et al., 2016). The Tg is 172 °C and is reported to be between 171 °C and 175 °C in literature (Béchard et al., 1995).

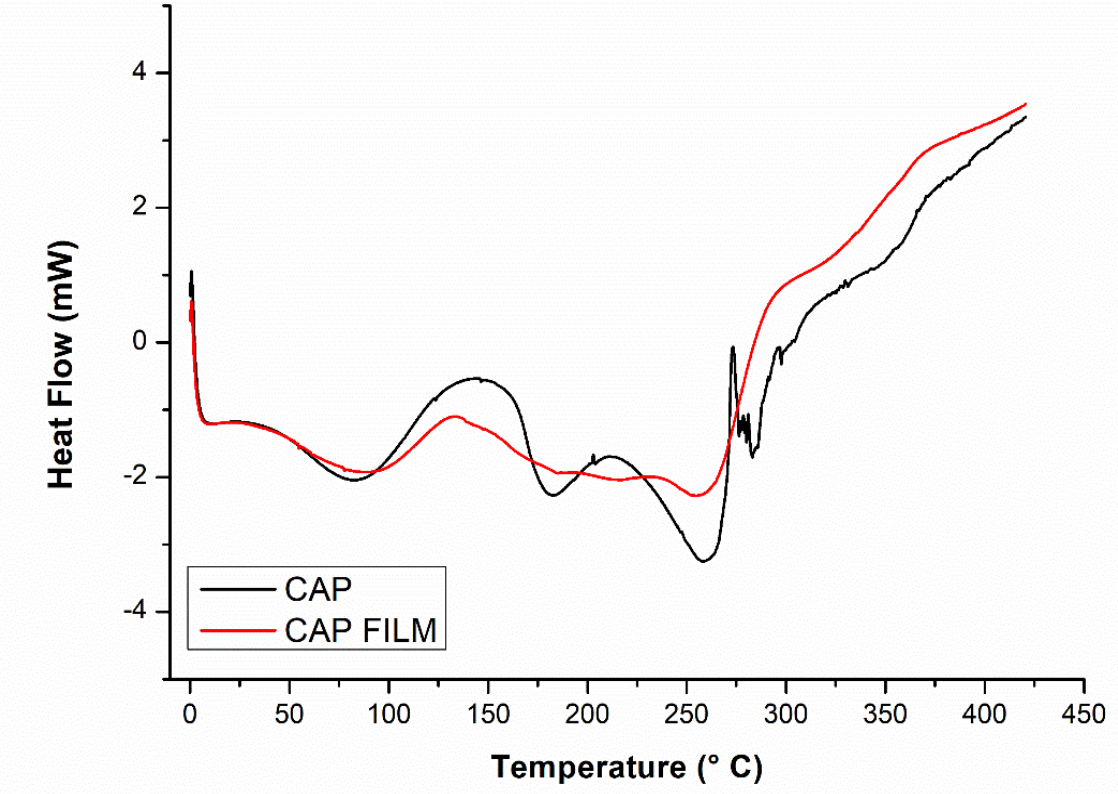


Figure 3. 6 Differential scanning calorimetry thermogram of (CAP) pristine cellulose acetate phthalate and (CAP FILM) cellulose acetate phthalate film.

It then proceeds to undergo decomposition at 266 °C, indicated by the small exothermic peak, which is analogous to the T_{max} value generated from the TGA data in Section 3.3.6. The DSC thermogram of the CAP film is similar to that of the pristine CAP sample, indicating little change to the thermal properties during the solvent-casting process.

A comparison between the pristine PCL polymer and the PCL/CAP composite film in Figure 3.7 indicates a reduced onset of degradation, corresponding to a reduced thermal stability during degradation. This is a result of the blending process (Parak et al., 2019). However, the ∆hm and ∆hd values are also reduced which indicates a decrease in release of energy during each transition phase. This correlates to decreased bond breakage in the polymer and enhanced thermal stability during the entire melting and degradation phase of the film compared to the pristine PCL polymer (Ramburrun et al., 2019).

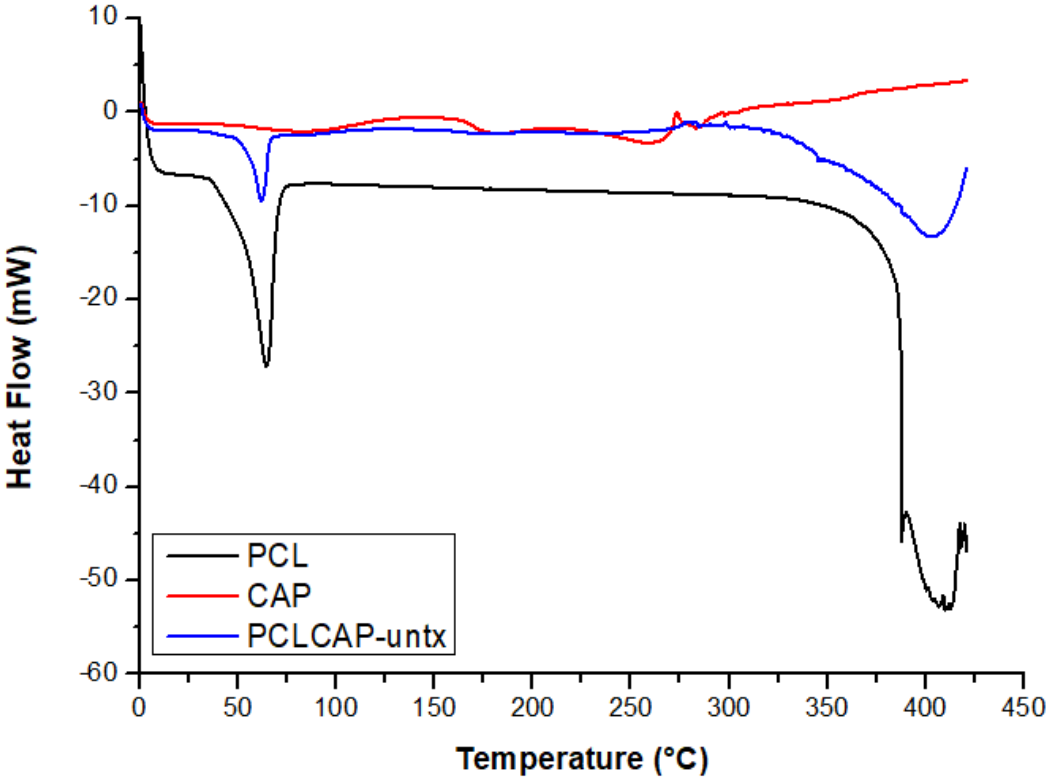


Figure 3. 7 Differential scanning calorimetry thermogram of (PCL) pristine polycaprolactone, (CAP) cellulose acetate phthalate and (PCL/CAP) polycaprolactone/cellulose acetate phthalate film.

Figure 3.8 compares the DSC thermograms of the unfunctionalized and functionalized samples. The onset of melting for the unfunctionalized film is 33.86 °C. The functionalized films all display higher onsets of melting (35.86; 38.51 and 34.36 °C). The Tm values for all samples are similar. The ∆hm of the unfunctionalized film is 53.47 mW.°C and the functionalized films all display higher ∆hm values as compared to the unfunctionalized film (89.78, 65.30 and 110.09 mW.°C, respectively). As discussed previously, a higher AUC value indicates a

reduced thermal stability during melting. In terms of degradation, the onset of degradation occurs at similar temperatures for the unfunctionalized and NaOH and KOH-hydrolyzed samples (280.80; 281.46 and 283.30 °C, respectively). However, the onset of degradation for the aminolyzed sample occurs at a much lower temperature (353.85 °C). This suggests a lower thermal stability of the aminolyzed sample during degradation in this temperature range which is analogous to the results from the TGA analysis (Kotsilkova et al., 2019).

The PCL/CAP film has a Td value of 402.244 °C. The aminolyzed film displays a similar value of 406.89 °C. However, the NaOH and KOH-hydrolyzed films demonstrate lower values of 386.00 and 390.90 °C, respectively. This leftward shift of the degradation point compared to the unfunctionalized film indicates a reduced thermal stability during degradation (Kotsilkova et al., 2019). Further, there are significant changes to the ∆hd values. The hydrolysis and aminolysis reactions all enhance the ∆hd values from 346.21 mW.°C to 749.87, 704.66 and 507.74 mW.°C, respectively, which indicates a reduced thermal stability during degradation (Ramburrun et al., 2019).

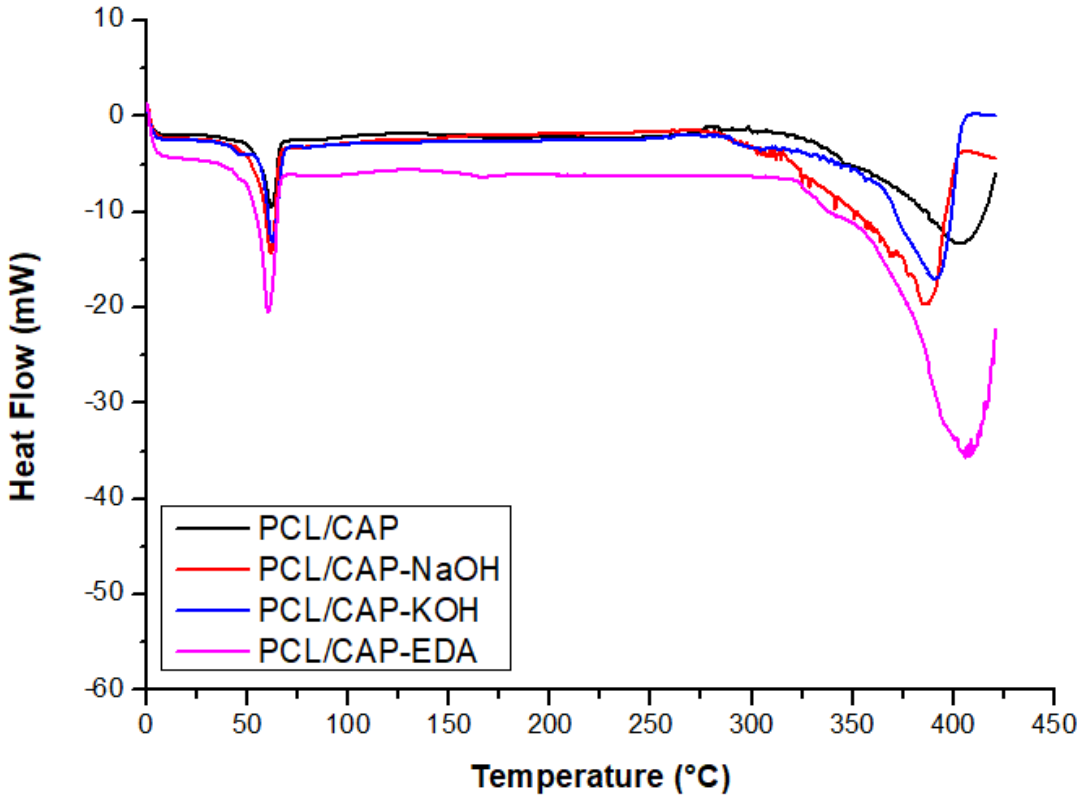


Figure 3. 8 Differential scanning calorimetry thermogram of (PCL/CAP) polycaprolactone/cellulose acetate phthalate film, (PCL/CAP-NaOH) sodium hydroxide and (PCL/CAP-KOH) potassium hydroxide hydrolyzed films and (PCL/CAP-EDA) aminolyzed films.

In conclusion, the onsets of melting are improved through functionalization, which improves thermal stability in this region, whereas the onset of degradation for the hydrolyzed films remain

unchanged. The onset of degradation is drastically reduced for the aminolyzed sample, compromising its thermal stability during degradation (Kotsilkova et al., 2019). Although the hydrolysis and aminolysis reactions slightly alter the thermal stability of the films in comparison to the unfunctionalized sample, these changes are not drastic, which is permittable due to the nature of the biomedical application (Parak et al., 2019). However, it should be noted that if further modifications under harsher conditions were to be applied, the thermal stability of the films would be compromised.

3.3.5 Phase transitions assessment utilizing x-ray diffraction analysis

X-ray diffraction characterizations are necessary to observe the changes in crystallinity of the samples following polymer blending, hydrolysis and aminolysis (Nagaraj et al., 2017). The crystallinity percentage and spherulite sizes are calculated to provide detailed information regarding the phase changes of the samples. Figures 3.9 and 3.10 highlight the minimal difference in crystallinity after surface modifications, similarly, proven in Table 3.7.

Table 3. 7 List of X-ray diffraction-derived % crystallinity and spherulite sizes for the film samples.

Sample	Crystallinity (%)	Spherulite size (nm)
Pristine polycaprolactone	64.83	0.04
Pristine cellulose acetate phthalate	47.62	0.82
Polycaprolactone/cellulose acetate phthalate film	53.66	0.81
Sodium hydroxide hydrolyzed film	54.08	0.79
Potassium hydroxide hydrolyzed film	55.21	0.79
Aminolyzed film	53.98	0.79

It can be seen that the percentage crystallinity of the unfunctionalized and functionalized samples are very similar, with PCL/CAP, the NaOH-hydrolyzed, KOH-hydrolyzed and aminolyzed films each having a percentage crystallinity of 53.66, 54.08, 55.21 and 53.98%, respectively. In addition, the spherulite sizes all decreased from 0.81 to 0.79 nm upon functionalization, which is a relatively small reduction (da Silva et al., 2021).

The XRD pattern of the pure PCL films in Figure 3.9 exhibit two significant sharp crystalline peaks at 2Θ values of ~ 21.4° and 23.7° which are assigned to the (110) and (200) orientation planes, respectively (Ravi et al., 2016). These sharp peaks are attributed to the crystalline phase of PCL, which originates from the ordering of polymer side chains due to the intermolecular interaction between PCL chains through hydrogen bonding (Ravi et al., 2016). A broad hump between 40° and 50° is also observed and is attributed to the amorphous phase

of PCL. These observations confirm that the pure PCL polymer is semi-crystalline in nature (Ravi et al., 2016).

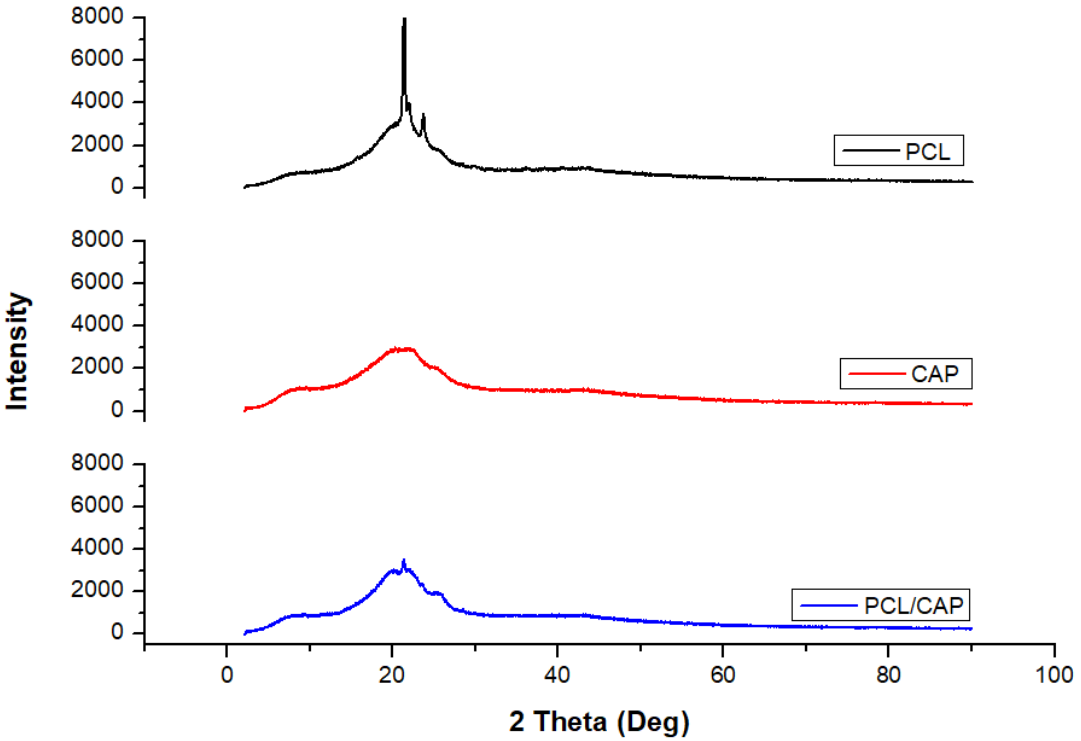


Figure 3. 9 X-ray diffractograms of (PCL) polycaprolactone film, (CAP) cellulose acetate phthalate film, (PCL/CAP) polycaprolactone/cellulose acetate film.

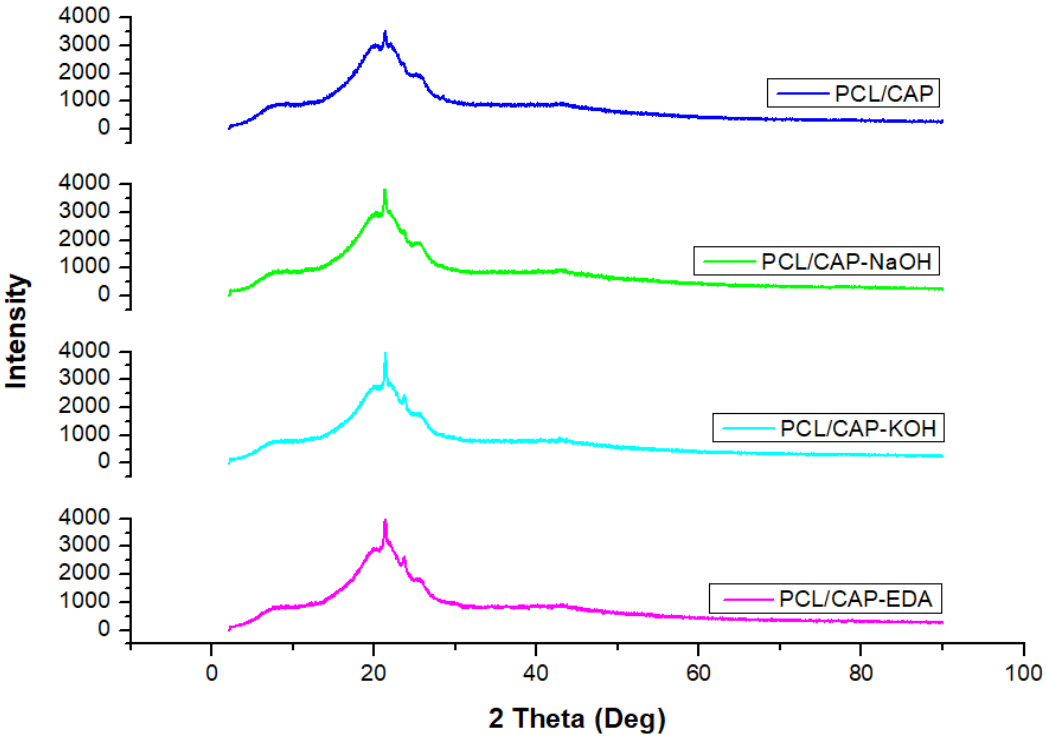


Figure 3. 10 Comparison of the X-ray diffractograms of (PCL/CAP) polycaprolactone/cellulose acetate phthalate film, (PCL/CAP-NaOH) sodium hydroxide hydrolyzed film, (PCL/CAP-KOH) potassium hydroxide hydrolyzed film, (PCL/CAP-EDA) aminolyzed film.

The XRD pattern of the CAP films (Figure 3.9) depict a broad amorphous peak at a 2θ value of ~22.038°, confirming its amorphous nature (Garg et al., 2016b). The blended PCL/CAP films show a broad amorphous peak at a 2θ value of ~22.04°, similar to the CAP films. However, the presence of the sharp peak at ~21.4°, classifies the blended films as semi-crystalline, imparted by the PCL component (Ravi et al., 2016). In terms of the hydrolyzed and aminolyzed films (Figure 3.10), there is a slight increase in crystallinity of the films indicated by the increase in size of the sharp crystalline peak at ~21.4° (Man et al., 2013).

In conclusion, the PCL/CAP films are semi-crystalline in nature which remains relatively unchanged following hydrolysis and aminolysis surface treatments, which is further confirmed by the insignificant changes observed in the crystallinity percentages and spherulite sizes in Table 4.3.

3.3.6 Thermogravimetric analysis of the thin films

The thermodynamic profiles of pristine PCL, CAP, the composite film, and the surface modified films were evaluated to derive important information regarding the thermal stability of the samples. The initiation of degradation ($T_{5\%}$) of a sample is the temperature at which five percent of the sample mass is lost during heating and is identified on the individual thermograms in A3 of the appendix (Azizi et al., 2019). The temperature at which the maximum decomposition rate occurs (T_{max}) is derived from the temperature of the main peak found in the derivative curves in A3 (Azizi et al., 2019). The individual thermograms and corresponding derivative curves for each graph were plotted and analysed. The results are compared in Table 3.8.

Table 3. 8 Comparing the thermodynamic properties of the pristine polymers, the pristine films, and the composite film.

	Thermodynamic Property		
Sample	**Number of Degradation Steps**	**Temperature at initiation of degradation (°C)**	**Temperature of maximum decomposition rate (°C)**
Polycaprolactone	1	368.97	413.84
Polycaprolactone film	3	322.82	422.53
Cellulose acetate phthalate	3	195.12	359.83
Cellulose acetate phthalate film	4	179.07	354.47
Polycaprolactone/cellulose acetate phthalate film	4	203.24	420.07

The TGA curve of neat PCL in Figure 3.11 displays a one-step degradation and a single weight loss phenomenon corresponding to polymer pyrolysis (Pan et al., 2019). The individual

thermogram of the PCL film indicates a three-step degradation, confirmed by three distinct peaks in its corresponding derivative curve. The $T_{5\%}$ occurs at 322.82 °C, which is lower than pristine PCL pellets (~ 368.97 °C). This indicates that the formation of PCL into a film reduces the thermal stability of the polymer (Azizi et al., 2019). Each degradation step results in 4.7,11.06 and 88.39% weight loss, respectively. There is no residue present at the end of the run. The TGA thermogram and corresponding derivative curve for CAP, indicates a three-step degradation mechanism that results in a 3.24, 45.81 and 44.65% weight loss, respectively. The $T_{5\%}$ occurs at 195.12 °C. There is a 6.3% residual amount remaining, which aligns with literature (Roxin et al., 1998). The TGA thermogram and derivative for the CAP film, shows a four-step degradation with each step resulting in 2.94, 19.31, 29.08 and 41.19% weight loss, respectively. With reference to PCL/CAP, the $T_{5\%}$ occurs at 208.08 °C, which is much lower than that of pristine PCL. This suggests that the addition of CAP to the PCL films decreases the thermal stability of the formulation (Azizi et al., 2019). There is a 2.42% residue left after the study, which could be residual content from CAP, since PCL left no residue.

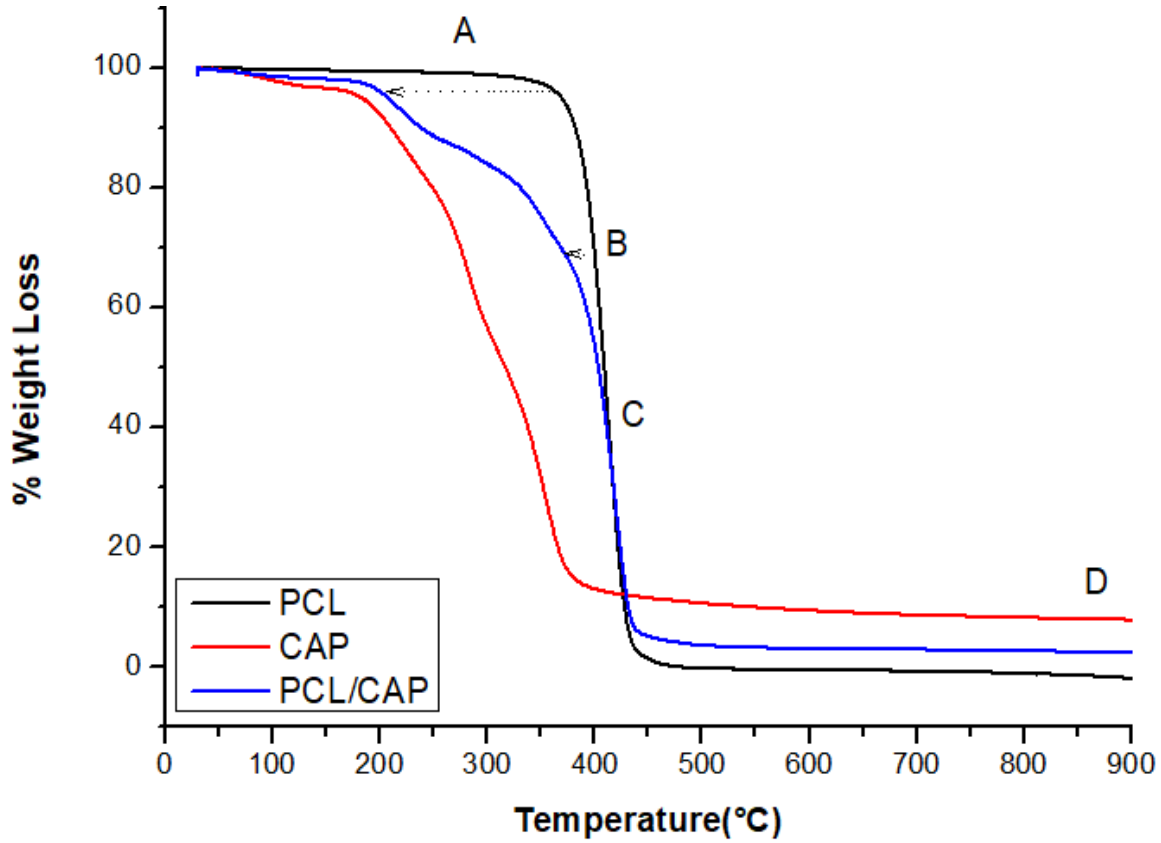


Figure 3. 11 Thermogravimetric analysis of (PCL) pristine polycaprolactone, (CAP) pristine cellulose acetate phthalate, (PCL/CAP) polycaprolactone/cellulose acetate phthalate film.

Figure 3.11 compares pristine PCL and CAP to the composite PCL/CAP film. Region A and B of Figure 3.11 shows that the addition of CAP to PCL results in a reduced thermal stability, which is further confirmed by the reduction of the $T_{5\%}$ value seen in Table 3.8 (Azizi et al., 2019). Section D highlights that more residue is left from the film in comparison to pristine PCL.

This is due to the fact that CAP has a high residual content at 900 °C. An analysis on the effects of hydrolysis and aminolysis on the thermal degradation profiles of the samples was carried out and the results are outlined in Table 3.8. The $T_{5\%}$ of the NaOH-hydrolyzed sample is 203.37 °C, which is slightly lower than that of the unfunctionalized films at 208.08 °C. This shows that NaOH hydrolysis decreases the thermal stability of the films (Azizi et al., 2019). The NaOH hydrolyzed samples demonstrate a five-step degradation behavior, with each step resulting in a 3.54, 3.99, 65.84, 15.29 and 2.23% weight loss, respectively, with 0.77% residue remaining. In terms of the TGA thermograms for the KOH-hydrolyzed PCL/CAP films, the onset of degradation is 244.09 °C, which is significantly higher than that of PCL/CAP and the NaOH-functionalized films. Each step results in 11.76, 77.83 and 10.41% weight loss, respectively. The degradation behavior of the aminolyzed samples demonstrates a four-step degradation pattern with each step resulting in 7.53, 86.52, 5.87 and 0.08% weight loss, respectively. The $T_{5\%}$ occurs at 279.46 °C which is higher than that of the unfunctionalized films as well as both hydrolyzed film samples. This proves that the aminolyzed films are more thermally stable than the unfunctionalized as well as the hydrolyzed films (Azizi et al., 2019). Figure 3.12 compares the TGA thermograms of the unfunctionalized and functionalized films.

Table 3. 9 Comparison of the thermogravimetric profiles of the unfunctionalized and functionalized polycaprolactone/cellulose acetate phthalate films.

	Thermodynamic Property		
Sample	**Number of Degradation steps**	**Temperature at initiation of degradation (°C)**	**Temperature of maximum decomposition rate (°C)**
Polycaprolactone/cellulose acetate phthalate	4	203.24	420.07
Sodium hydroxide hydrolyzed film	5	203.37	318.88
Potassium hydroxide hydrolyzed film	3	244.09	355.58
Aminolyzed film	4	279.46	360.45

Figure 3.13 demonstrates a leftward shift of the functionalized films compared to the unfunctionalized film (indicated by the arrows). This indicates that the functionalized films have a lower thermal stability in this initial temperature range due to the hydrolytic and aminolytic degradation of the PCL/CAP film (da Silva et al., 2020). Region B in Figure 3.13 depicts the slopes of the curves, the aminolyzed film displays the highest thermal stability at this temperature and a slope at 341.11 °C as shown in the derivative curve in A3 in the appendix. The slope of the KOH-hydrolyzed samples occurs at a lower temperature (241.48 °C), indicating a lower thermal stability compared to the aminolyzed films at this temperature range (225-350 °C) (Aziza et al., 2019). Further, the NaOH-hydrolyzed films show a drastic leftward shift from the KOH-hydrolyzed films occurring at 262.66 °C, confirmed by the second peak

identified in derivative curve. Figure 3.12 has three distinct portions: A, B, C and D. Each section is enlarged for ease of analysis.

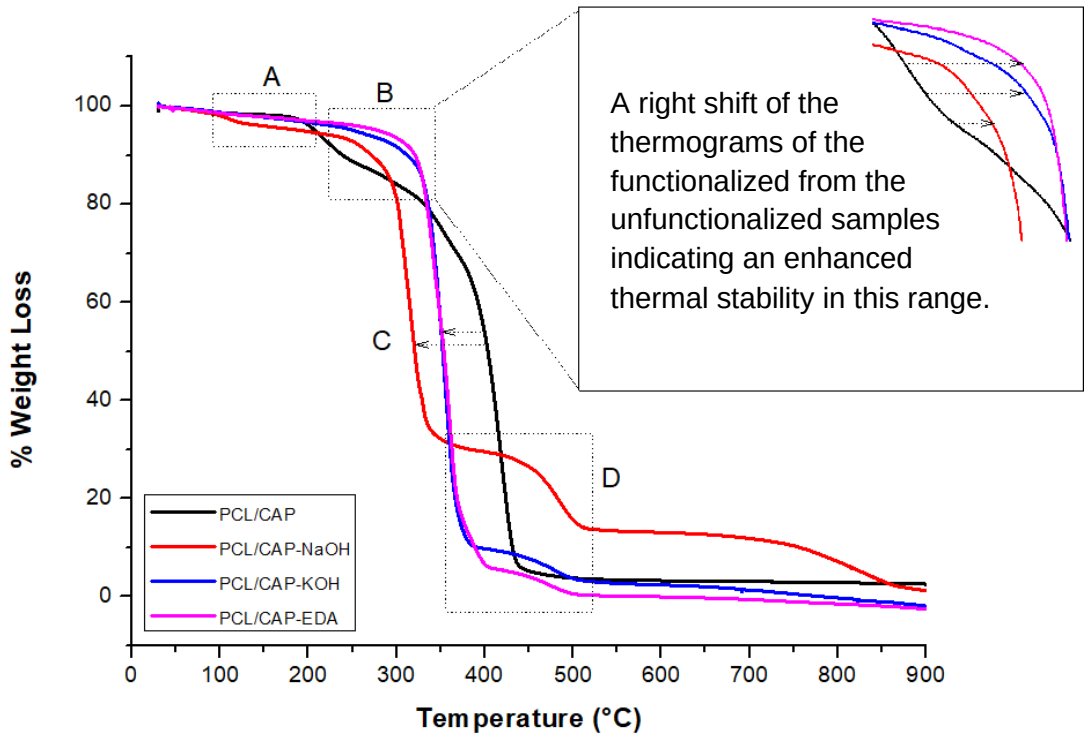


Figure 3. 12 Thermogravimetric analyses of (PCL/CAP) polycaprolactone/cellulose acetate phthalate film, (PCL/CAP-NaOH) sodium hydroxide hydrolyzed film, (PCL/CAP-KOH) potassium hydroxide hydrolyzed film, (PCL/CAP-EDA) aminolyzed film.

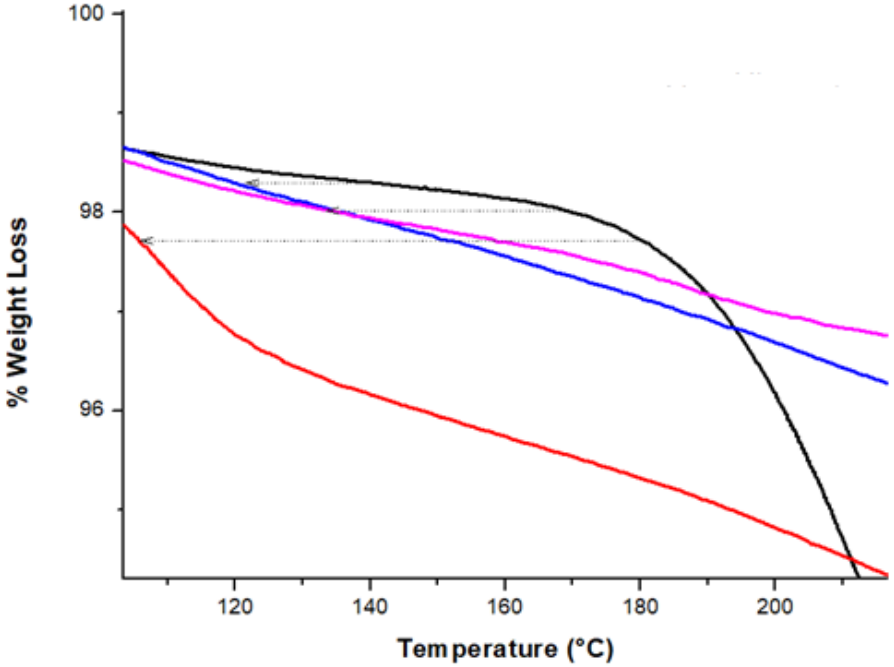


Figure 3. 13 Thermogravimetric analysis of (PCL/CAP) polycaprolactone/cellulose acetate phthalate film, (PCL/CAP-NaOH) sodium hydroxide hydrolyzed film, (PCL/CAP-KOH) potassium hydroxide hydrolyzed film, (PCL/CAP-EDA) aminolyzed film.

In conclusion, surface modifications significantly alter the TGA thermograms in comparison to the unfunctionalized film by decreasing the decomposition temperature from ~368.97 °C to ~228.184, ~273.74 and ~331.28 °C for the NaOH, KOH and EDA functionalized samples, respectively. This suggests that the functionalization of the films decreases their thermal stability in comparison to the unfunctionalized film. It is to be noted that harsher functionalization conditions could result in a substantial loss in thermal stability and could compromise scaffold integrity.

3.3.7 Surface topography characterizations by scanning electron microscopy analysis

Scanning electron microscopy images were captured of the native polymer films and the composite film to identify changes in the surface morphology upon polymer blending. In addition, the changes in surface morphology for the functionalized films were also identified.

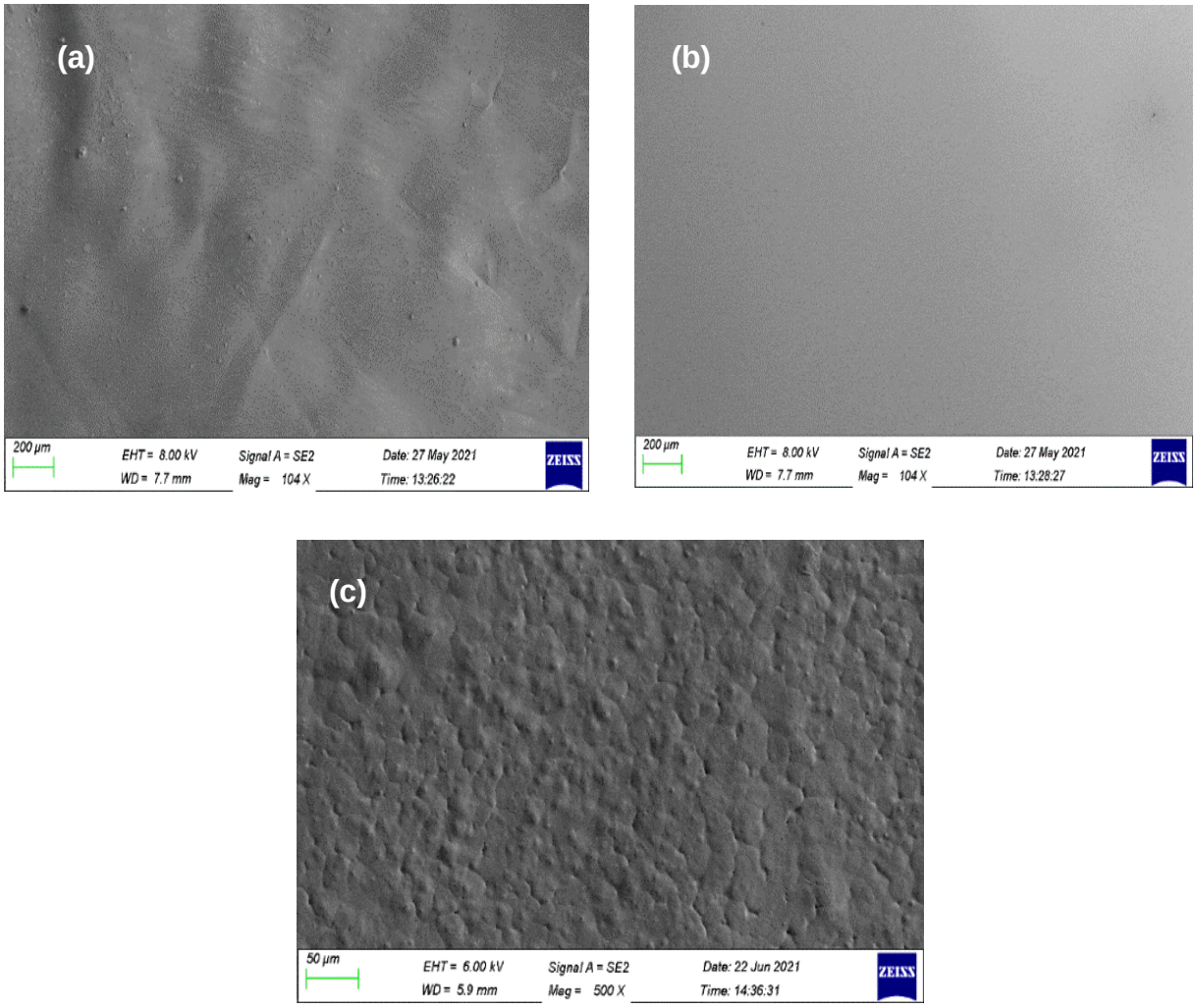


Figure 3. 14 Scanning electron microscopy images of (a) polycaprolactone film, (b) cellulose acetate phthalate film and (c) polycaprolactone/cellulose acetate phthalate film.

Figure 3.14 highlights that the PCL film contains minimal topographical cues, the CAP film (b) has almost no visible topographical cues and the PCL/CAP film (c) has vast topographical cues, which is a requirement for neural tissue engineering to enable sufficient cell attachment (Tang et al., 2004). FT-IR proves the formation of a physical blend upon PCL and CAP mixing, which is responsible for the lamellar morphology, with extremely well-defined areas (Figures 3.14(c)). This is due to phase separation of the two polymers, forming phase domains (Geoghegan et al., 1994). This suggests that PCL and CAP form an immiscible polymer blend (P. Wang & Koberstein, 2004). Figures 3.15 (a) and (b) highlight the phase domains in the film structure taken at 5000X magnification. Although an unusual morphology, it is strikingly similar to SEM imagery of acellular peripheral nerves, seen in Figure 3.16, which suggests its suitability in the recapitulation of the nerve environment during regeneration (da Silva et al., 2020). The series of SEM images in Figure 3.17 demonstrate that the films maintain their lamellar-like and porous nature following surface modifications.

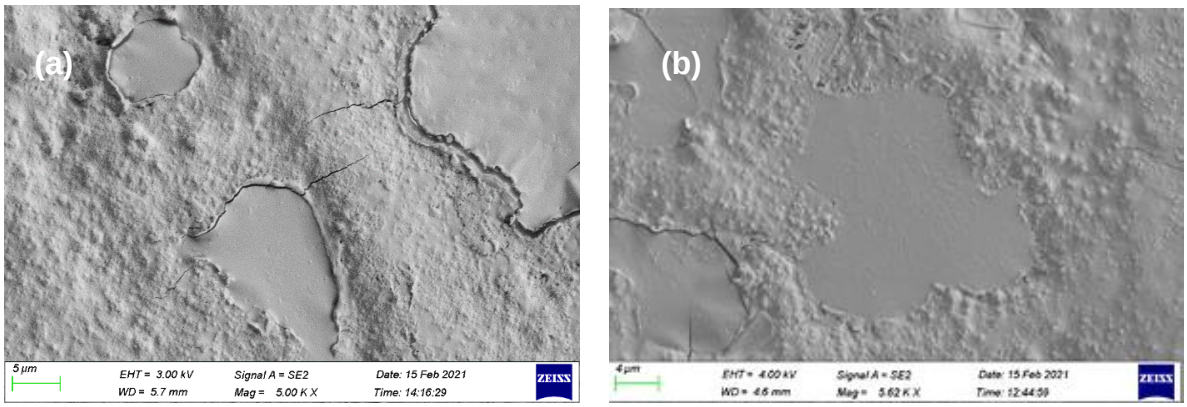


Figure 3. 15 Scanning electron microscopy of the polycaprolactone/cellulose acetate phthalate film (a) objective lens and (b) in-lens highlighting the lamellar-like morphology of the films.

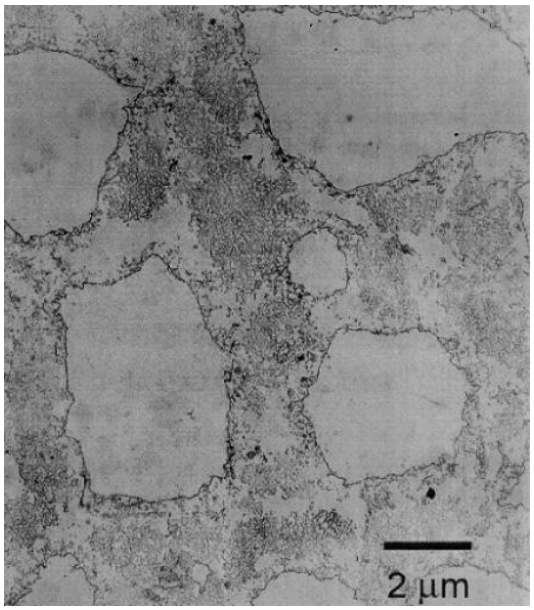


Figure 3. 126 Scanning electron microscopy imagery of an acellular peripheral nerve (Borschel et al., 2003). Reproduced with permission from Elsevier, UK.

The PCL/CAP films in Figure 3.17 (a) illustrate the porous nature of the films as seen by the pores identified under scanning electron microscopy. Figure 3.17 (a) highlights the porous nature of the films, (b) highlights the lamellar-like morphology of the films, with distinct phase domains, circled in red, (c) highlights the porous and lamellar-like nature of the films and (d-f) highlights the porous nature of the films, The series of SEM images in Figures 3.17 and 3.18 highlight that the surface modifications with NaOH, KOH and EDA do not change the porous and lamellar-like nature of the films.

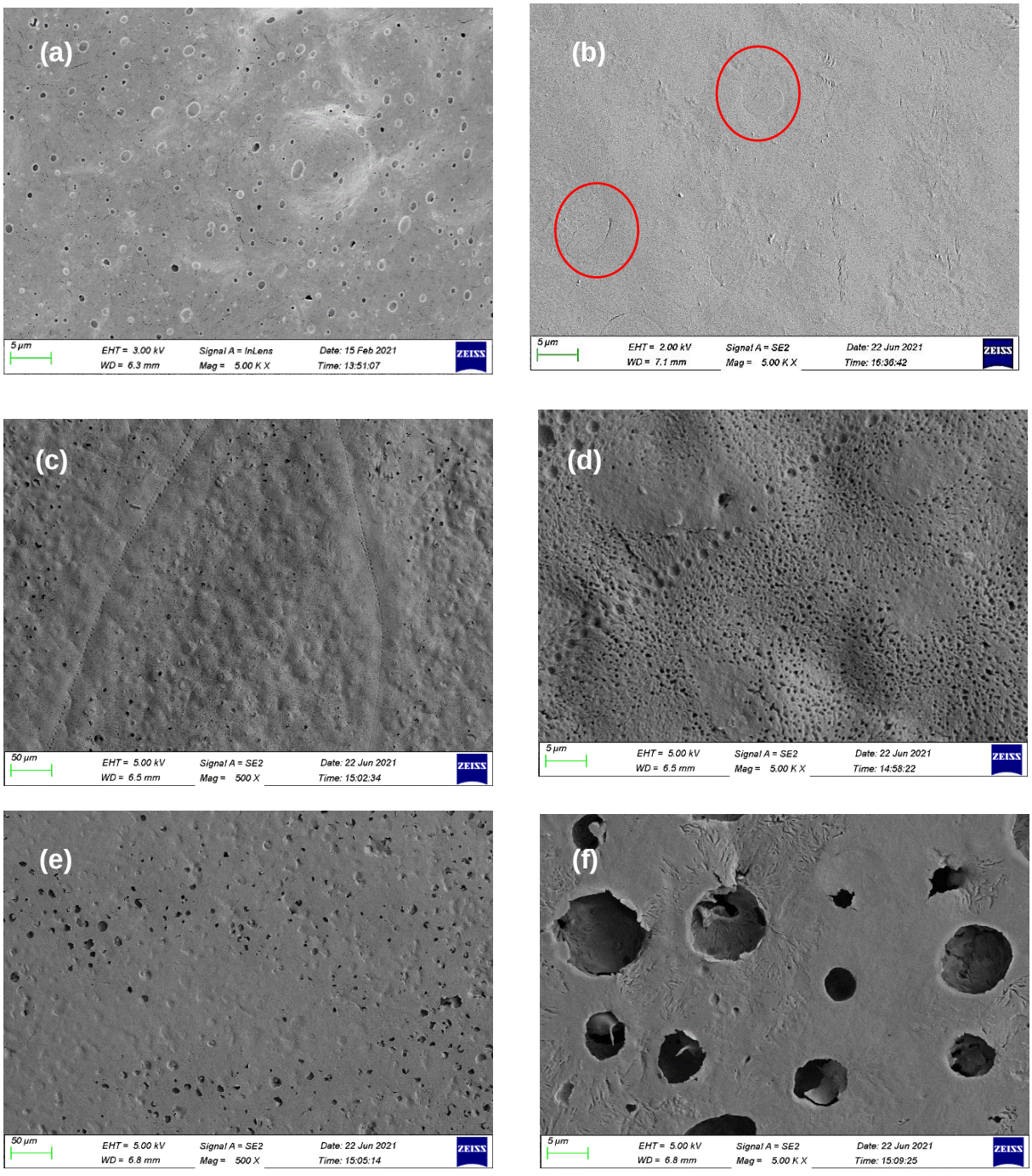


Figure 3. 17 Scanning electron microscopy images of polycaprolactone/cellulose acetate phthalate film (glass) at (a) 500X and (b) 5000X; the aminolyzed film (air) at (c) 500X and (d) 5000X; the sodium hydroxide-hydrolyzed film (glass) at (e) 500X and (f) 5000X.

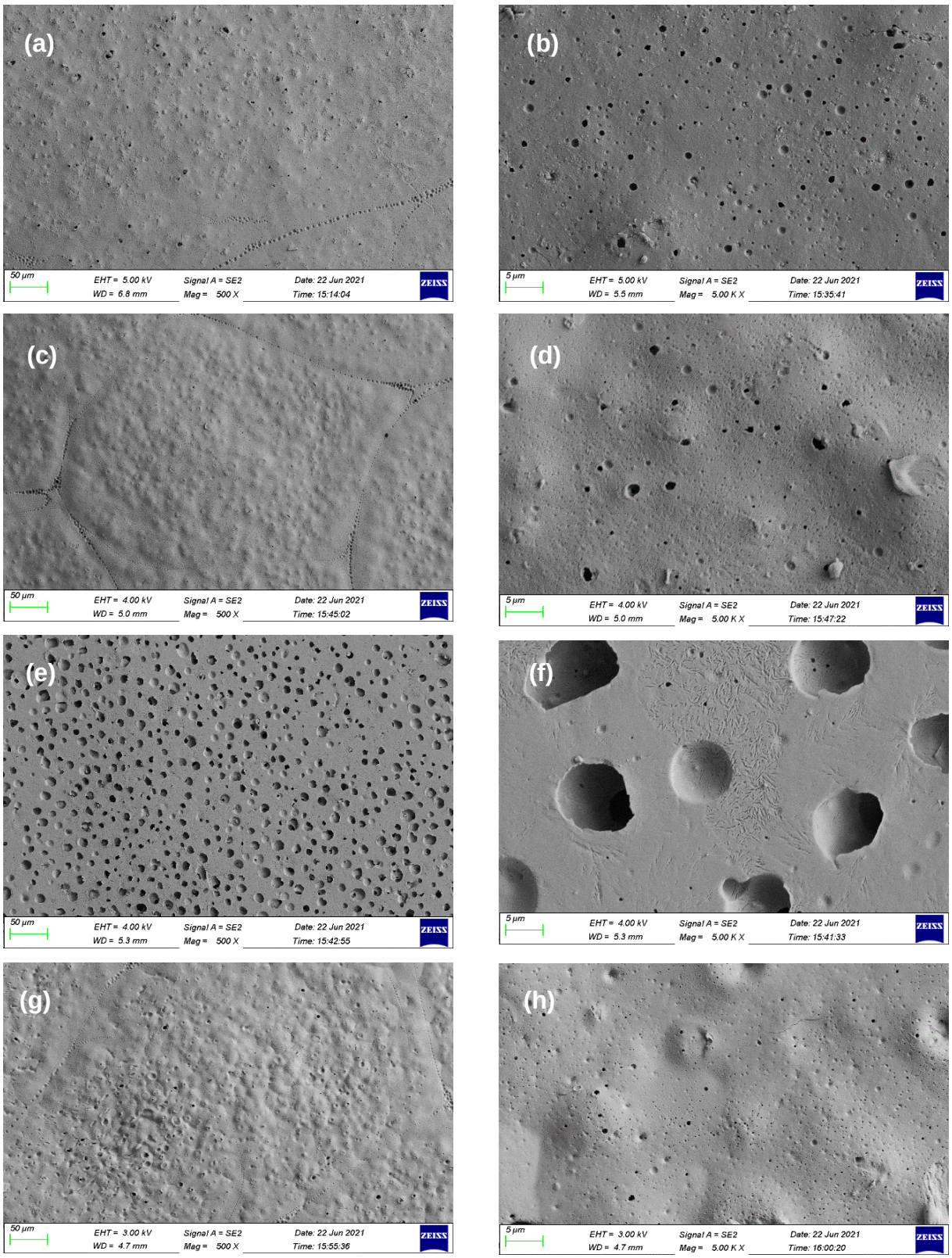


Figure 3. 18 Scanning electron microscopy images of the potassium hydroxide-hydrolyzed film (air) at (a) 500X and (b) 5000X; the potassium hydroxide-hydrolyzed film (glass) at (c) 500X and (d) 5000X; the aminolyzed film (air) at (e) 500X and (f) 5000X; the aminolyzed film (glass) at (g) 500X and (h) 5000X.

The importance of the lamellar-like morphology is that it mimics the natural morphology of the acellular peripheral nerve (Figure 3.16), which is important since nerve guides should ideally

mimic the native environment of the regenerating nerve (Sun & Downes, 2009). In addition, the porous nature of the films is important to allow the exchange of metabolites between the film and the surrounding tissues during nerve regeneration and repair (Sun & Downes, 2009).

To conclude, the films maintained their two general structural identities following surface modification. Namely, their porosity and lamellar-like structure. The series of figures presented in Figures 3.17 and 3.18 contain pores and the lamellar-like structure, proving that the surface hydrolysis and aminolysis reactions do not alter the main structural profiles of the films which are advantageous in neural issue engineering.

3.3.8 Surface topography mapping analysis by atomic force microscopy

Atomic force microscopy (AFM) analysis was conducted to qualitatively evaluate the surface topography of the samples illustrated in Figures 3.19 and 3.20. In addition, AFM was carried out to quantitatively assess the surface roughness of the samples following surface modifications (Podgornik & Viˇ, 2009). Average surface roughness (Ra), root square deviation of surface roughness (Rq), and the maximum height of the profile (Rz) are surface roughness parameters widely used in surface characterization and are all assessed during routine AFM analysis (Podgornik & Viˇ, 2009; Svahn et al., 2003). Ra indicates a general description of height variations in the sample, but does not provide any ripple information and lacks sensitivity to small changes in the profile (Podgornik & Viˇ, 2009). Rq is more sensitive to deviations from the baseline than Ra (Podgornik & Viˇ, 2009), specifically highlighting the peaks and valleys present on the surface (Svahn et al., 2003). Rz corresponds to the sum of the maximum height of the profile peaks and the highest depth of the profile valleys in the sample length (Svahn et al., 2003). The parameter Rz can generate misleading information of the surface since it detects surface defects such as pores and scratches that are not representative of the roughness (Svahn et al., 2003). It thus follows that Rq values are the most appropriate values to provide useful information regarding surface roughness and were used to compare the surface roughness of the samples (Munhoz et al., 2020). Table 3.10 compares the Image Rq values taken from the air and glass surfaces of the samples.

Table 3.10 highlights that the air surfaces of the films have higher image Rq values than the glass surfaces, indicating that the air surfaces are significantly rougher than the glass surfaces, which corresponds to literature (Sun & Downes, 2009). The pristine PCL and CAP films have relatively smooth surfaces, indicated by low Rq values as well as minimal topographical cues identified in Figure 3.19 (a-d) in comparison to the blend film, which is also confirmed by SEM data. The CAP film exhibits an almost completely smooth surface morphology. The composite film displays an increase in surface roughness of 35.43 nm as compared to the pristine films and is observed in the 3D AFM images (Figure 3.19 (e) and (f)).

Table 3. 10 The effect of hydrolysis and aminolysis treatments on the surface roughness of the films.

	Root square deviation of surface roughness (Rq) (nm)	
Sample	**Air surface**	**Glass surface**
Polycaprolactone film	20.2 ± 2.95	12.72 ± 1.78
Cellulose acetate phthalate film	2.73 ± 1.06	1.11 ± 2.59
Polycaprolactone/ cellulose acetate phthalate film	35.43 ± 7.50	13.83 ± 1.69
Sodium hydroxide hydrolyzed film	53.03 ± 7.85	21.4 ± 3.13
Potassium hydroxide hydrolyzed film	74.73 ± 9.48	46.23 ± 6.82
Aminolyzed film	55.17 ± 7.97	37.5 ± 2.98

The Figures 3.20 and 3.21 represent the 3D AFM images obtained for the film samples. The possible reason for this is the formation of pores and phase domains as seen in Figure 3.20 (e) and (f). Both hydrolysis treatments increase the surface roughness of the films, which is likely due to alkaline hydrolysis by NaOH and KOH aqueous solutions (Roux & Demoustier-champagne, 2003), which leads to carboxylate-functionalization of the PCL/CAP films, which causes surface imperfections, thereby resulting in an increased surface roughness (Gonz & Guti, 2009). NaOH hydrolysis causes an increase in surface roughness from 35.43 to 53.03 nm and KOH hydrolysis causes an even further increase in surface roughness to 74.73 nm. The aminolysis functionalization increases the surface roughness to 55.17 nm. The KOH hydrolysis causes the highest increase in surface roughness. It is known that rougher surfaces promote neuronal adhesion, extension, and proliferation (Brunetti et al., 2010; Sorkin et al., 2009). Therefore, the enhanced surface roughness imparted by hydrolysis and aminolysis is predicted to be advantageous in aiding cell-film interactions *In Vitro*.

To conclude, the PCL/CAP blend films have superior surface roughness in comparison to the native films. In addition, surface hydrolysis and aminolysis enhances the surface roughness of the films, which is advantageous for application in neural tissue engineering. Further, the surfaces in contact with air during the film casting process are rougher than those in contact with glass. Since surface roughness significantly affects cell attachment, the air surfaces are chosen as the optimal for *In Vitro* characterizations and in the proceeding chapters due to their enhanced surface roughness.

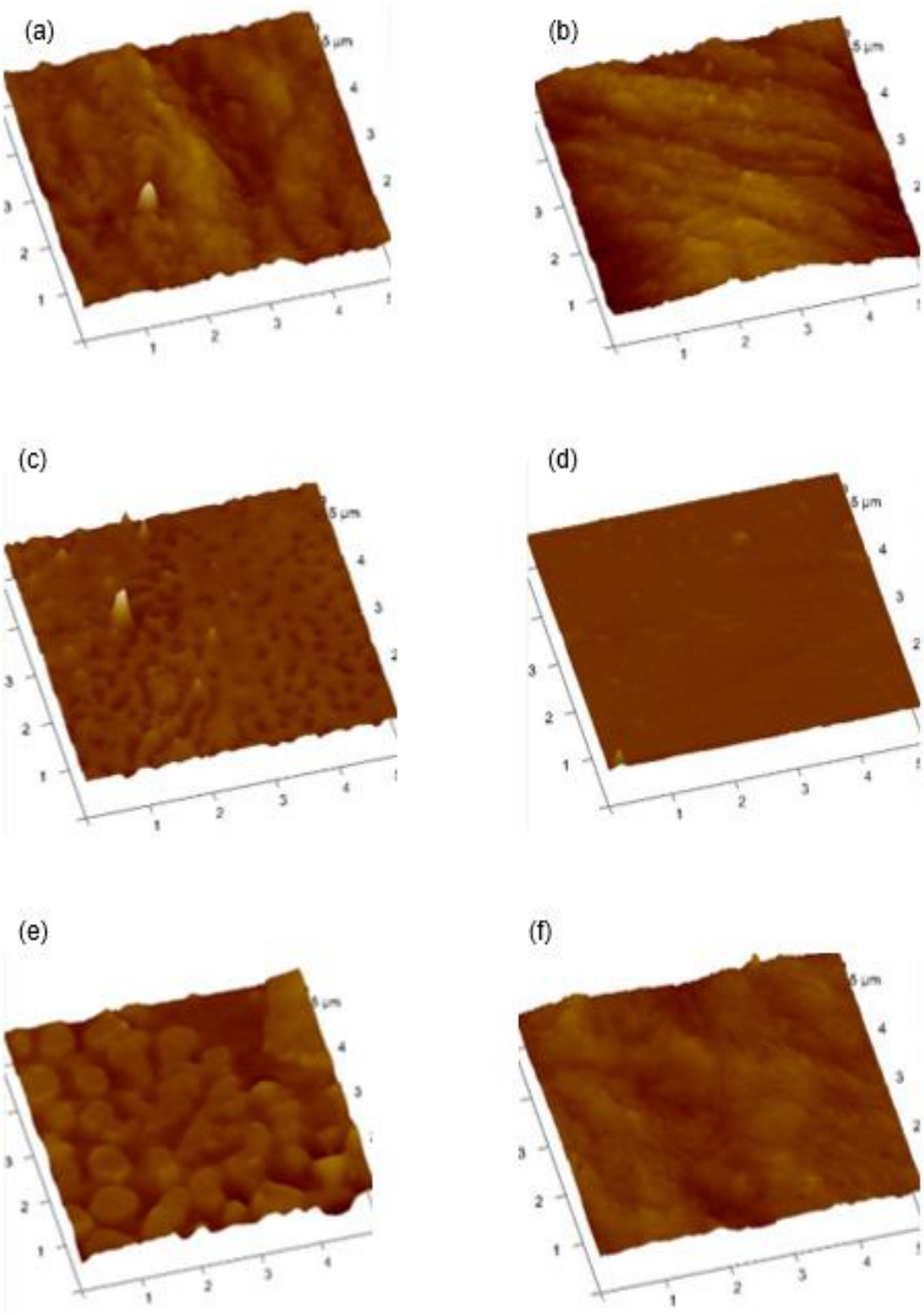


Figure 3. 13 3D atomic force microscopy images of polycaprolactone film (a) air and (b) glass; cellulose acetate phthalate film (c) air and (d) glass; polycaprolactone/cellulose acetate phthalate film (e) air and (f) glass demonstrating the difference in surface topography of the films.

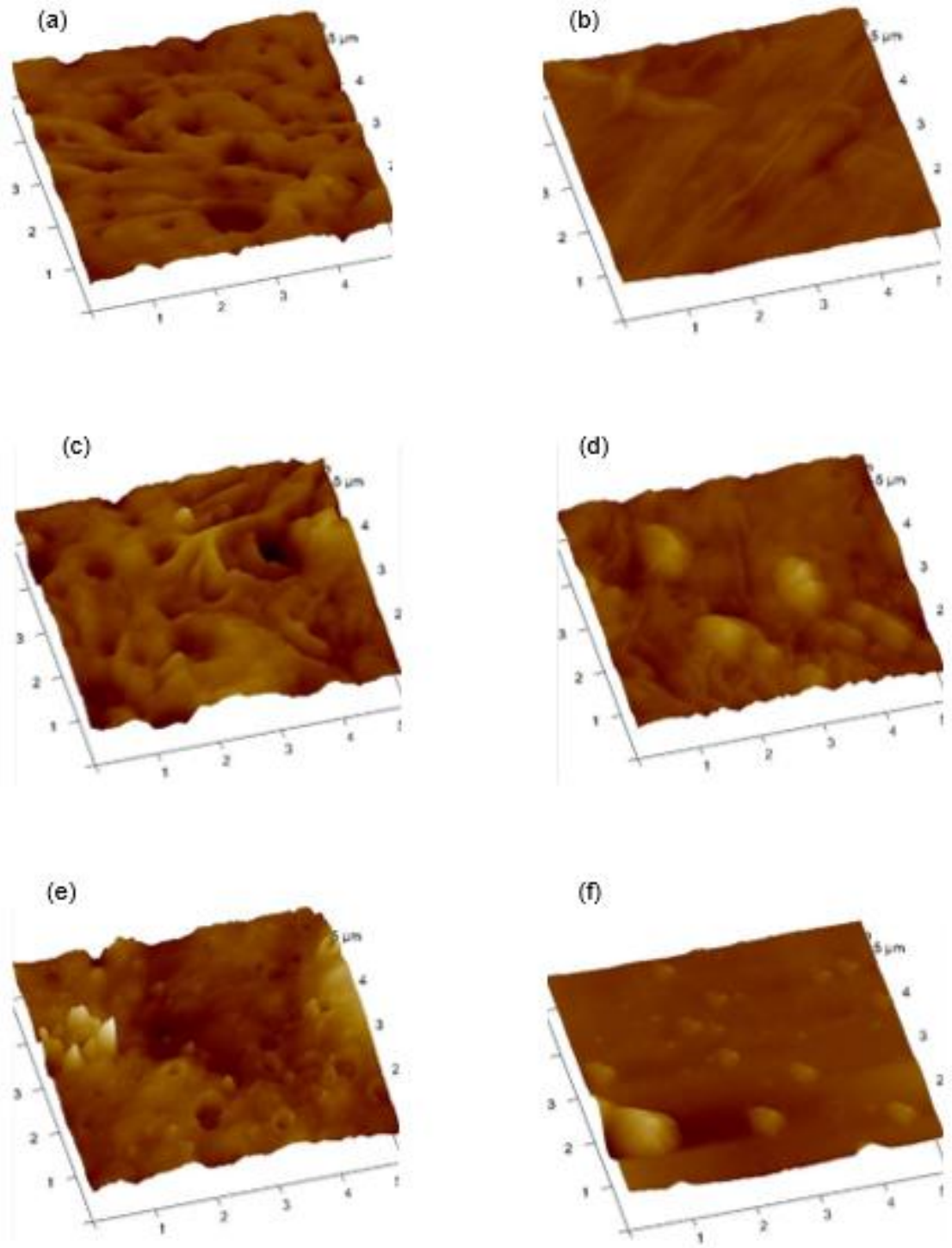


Figure 3. 14 3D atomic force microscopy images of the sodium hydroxide-hydrolyzed film (a) air and (b) glass; the potassium hydroxide-hydrolyzed film (c) air and (d) glass; the aminolyzed film (e) air and (f) glass demonstrating the difference in surface topography of the various surface modified films.

3.3.9 Porosimetric and surface area evaluation of the thin films using BET analysis

Major considerations when designing scaffolds for neural tissue engineering are porosity, pore size and surface area. Ideal nerve guides should be porous with interconnecting pores to

facilitate cell growth, migration and to facilitate the influx of externally generated growth factors, nutrients, and oxygen as well as the efflux of waste products (Yannas, 1992). If the pores of a conduit are too small, migration can be limited, resulting in a cellular capsule around the edges of the conduit, which can limit the distribution of nutrients and removal of waste products around the conduit. Conversely, large pores may result in a large specific surface area (Yannas, 1992), which reduces the availability of cell-binding ligand density (Brien et al., 2005). Cellular activity is influenced by integrin-ligand interactions between cells and the surrounding extracellular matrix (Brien et al., 2005). Initial cell adhesion mediates all subsequent events such as proliferation, migration, and differentiation on the scaffold (Brien et al., 2005). It thus follows that the mean pore size of a scaffold has a significant impact on cell adhesion, thereby affecting proliferation, migration and differentiation (Karageorgiou et al., 2005; Ma et al., 2005). The BET gas adsorption technique is extensively used for surface area and porosity quantification for a variety of materials (Sing et al., 1985). The analysis includes a detailed evaluation of pore diameter, pore volume, pore surface area and surface area of the films. In addition, nitrogen adsorption-desorption isotherms are generated which are classified according to IUPAC classifications which are depicted in Figure 3.21.

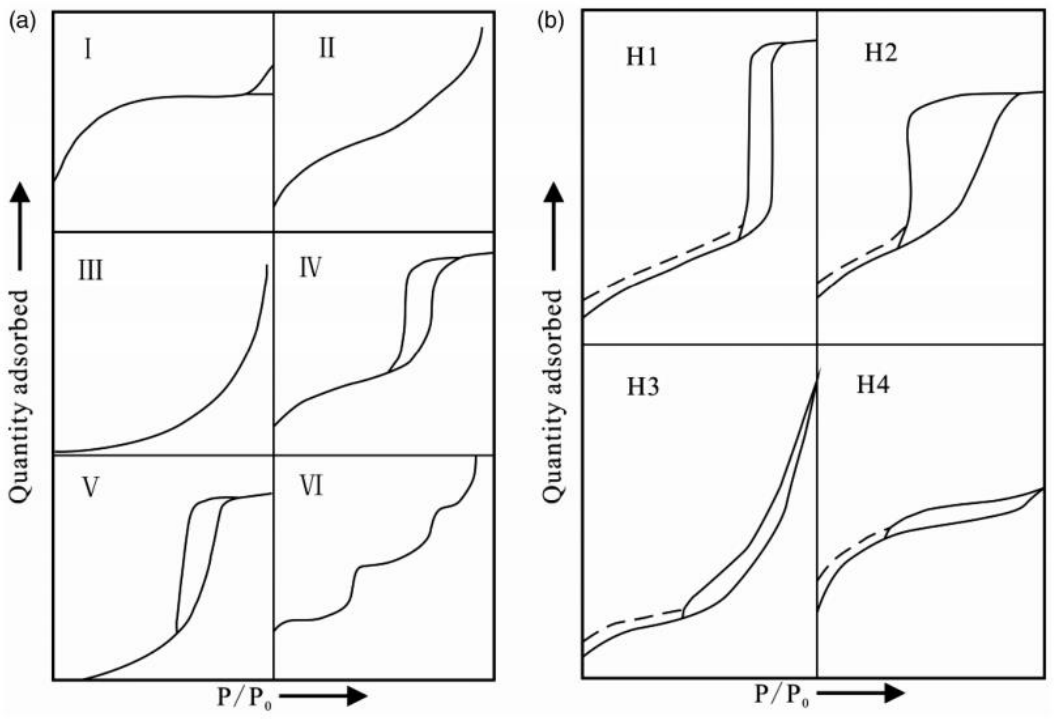


Figure 3. 151 International Union of Pure and Applied Chemistry classification of (a) nitrogen adsorption isotherms (b) and hysteresis loops (S. Yang et al., 2018). Figure reproduced with permission from SAGE Journals.

During BET analysis, adsorbents with micropores exhibit a type one (I) adsorption isotherm, where adsorption occurs via micropore filling (Sing et al., 1985). The rate of adsorption depends on the micropore volume available as opposed to the total internal surface area. Non-

porous or macroporous adsorbents with unlimited monolayer-multilayer adsorption exhibit type two (II) and type four (IV) adsorption isotherms (Sing et al., 1985). Initially, the volume of adsorption rapidly rises at low relative pressure values as a result of the contact between the adsorbate molecules with the higher energetic section, followed by the interaction with the less energetic section (Sing et al., 1985). The “sharp knee” region develops following the formation of the monolayer, known as multilayer adsorption. As the relative pressure approaches unity, a sudden rise in the curve depicts the bulk condensation of adsorbate gas to liquid. Type three (III) and five (V) isotherms exhibit exponential growth of adsorption indicating multilayer formation. The lack of the “sharp knee” indicates that the adsorbate-adsorbate interactions are stronger than the adsorbate-adsorbent interactions, therefore no monolayer is formed (Brunauer et al., 1936). Capillary condensation causes the formation of hysteresis loops, which are related to low density gas adsorption in the pores following a sufficient amount of gas supply, which then spontaneously condenses into a liquid-like state inside the pores (Brunauer et al., 1936). Hysteresis loops can be classified according to Figure 3.21 (b), where type H1 corresponds to porous channels with uniform sizes and shapes. Type H2 refers to channels with a pore mouth smaller than pore body (ink-bottle shaped pores). Type H3 relates to solids with a very wide distribution of pore size and H4 refers to limited amounts of mesopores (Brunauer et al., 1936).

Detailed information regarding pore sizes and surface areas were calculated during analysis and are presented in Table 4.9. A5 of the appendix contains nitrogen adsorption-desorption isotherm plots obtained for all the samples, which all present with the same shape, therefore all have the same classification. The curve in Figure 3.22 is a representative of the nitrogen adsorption-desorption isotherm plots for the samples. According to the classifications presented in Figure 3.21, all the samples are typical of type II isotherms, indicating that they are mesoporous in nature (Ramburrun et al., 2019). The hysteresis loops are characteristic of shape H3 which relates to solids with a very wide distribution of pore size (Sing et al., 1985). The adsorption (black) and desorption (red) curves do not form a closed loop. The proposed reason for this is that the water-uptake phenomenon has occurred, indicating the formation of narrow slip or bottle-shaped pores within the film structure (Sing et al., 1985). Table 3.11 and 3.12 define the criteria for surface area classification and porosity, respectively (Sing et al., 1985). Table 3.13 summarizes the results relating to pore size and surface area.

The average pore diameters for all samples are classified as mesoporous, which is consistent with the isotherm plot predictions. In terms of the native polymer films, the pores in the PCL film are smaller in diameter but larger in volume therefore potentially occupying a larger depth of the film, thereby having a larger BJH adsorption cumulative surface area of pores, which reduces the BET surface area as compared to the CAP film (Groen et al., 2003). The pore size

and volume reflects the cumulative surface area of pores on the sample, where pores larger in diameter and depth contribute to a larger pore surface area but result in a smaller BET total surface area (Ramburrun et al., 2019). The PCL film is classified as having a very low surface area in terms of Table 3.11 (Groen et al., 2003; Sing et al., 1985).

The CAP film has a larger pore diameter, yet a lower pore volume compared to the PCL film, indicating that the pores are limited to the surface of the film and are perhaps blind ended, as suggested in Figure 3.19 (e) and Figure 3.20 (d) and (f) of the AFM data in Section 3.3.8 (Groen et al., 2003). Due to the fact that the pores occupy a lower volume of the film (as seen by the lower BJH cumulative surface area of pores), the BET surface area increases. The PCL and CAP films are both classified as mesoporous (Groen et al., 2003; Sing et al., 1985).

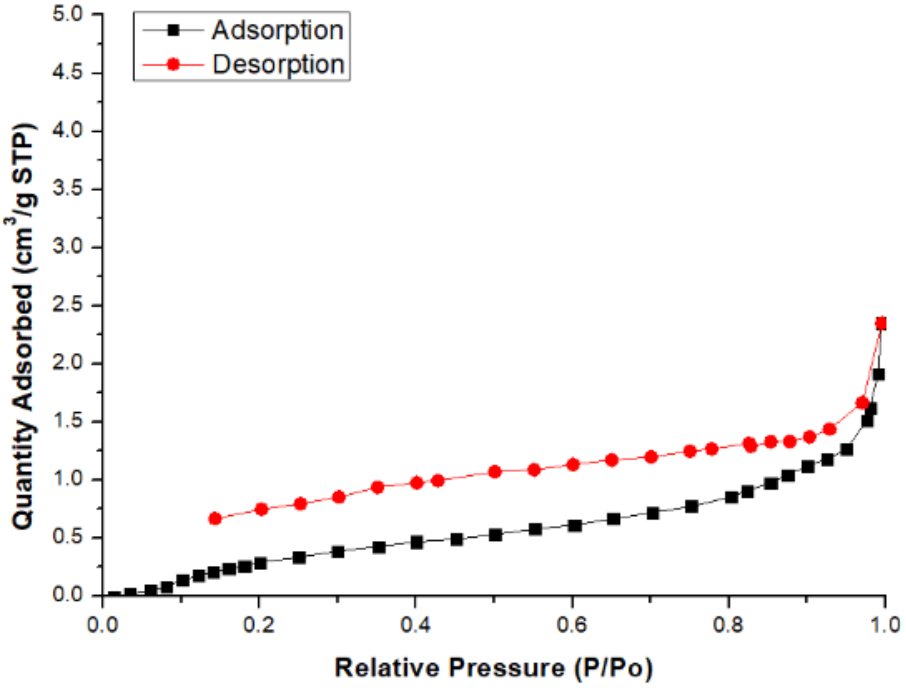


Figure 3. 16 Adsorption-desorption isotherm for the sodium hydroxide-hydrolyzed film**.**

Table 3. 11 Criteria defining surface area classifications.

Surface area	Range (m^2)
Very low surface area	< 0.01
Low surface area	< 10
High surface area	> 250

Table 3. 12 Criteria defining porosity classifications.

Porosity	Pore size (nm)
Microporous	< 2
Mesoporous	2-50
Macroporous	> 50

Compared to the PCL film, the PCL/CAP film has a larger average pore diameter and cumulative pore volume indicating that the combination of PCL and CAP increases the overall porosity of the film (Groen et al., 2003). The addition of CAP also increases the BET surface area of the films (as pore volume increases, the number of pores where nitrogen sits increases, these will finally facilitate increase in BET surface area) (Ramburrun et al., 2019). The PCL/CAP film is classified as mesoporous with a very low surface area in terms of Tables 3.11 and 3.12. The NaOH and KOH-hydrolysis of the PCL/CAP film enhances the average pore volume and the cumulative surface area of pores, however, reduces the average pore diameter. This means that the pores are smaller in diameter but occupy a larger volume in the film matrix (Groen et al., 2003). This is consistent with the findings in SEM (Figure 3.17 (f) and Figure 3.18 (e) and (f), where the hydrolyzed films clearly have larger pores in comparison to the unfunctionalized PCL/CAP films in Figure 3.17 (a) and (b)).

Table 3. 13 Porosity Analysis of the native polymer films, the composite film, and the functionalized films.

Property	Sample					
	PCL[5]	CAP[6]	PCL/CAP[7]	NaOH[8]	KOH[9]	EDA[10]
Surface Area						
BET[11] surface area (m^2/g)	-6.20	0.41	-0.40	6.49	1.47	4.05
BJH[12] adsorption cumulative surface area of pores diameter (m^2/g)	2.10	0.12	0.63	4.02	1.32	1.42
BJH desorption cumulative surface area of pores (m^2/g)	2.76	0.32	1.45	4.24	2.37	2.43
Pore Volume						
BJH Adsorption cumulative volume of pores (mm^3/g)	2.76	0.42	3.016	6.66	3.41	3.51
BJH desorption cumulative volume of pores (mm^3/g)	2.97	0.34	3.20	6.76	3.35	3.59
Pore Size						
Adsorption average pore width (4V/A by BET) (nm)	-1.78	4.42	-9.14	3.07	6.26	-2.31
BJH Adsorption average pore diameter (4V/A) (nm)	5.25	13.77	19.16	6.62	10.30	9.87
BJH desorption average pore diameter (4V/A) (nm)	4.30	4.28	8.80	6.37	5.66	5.90

[5] Polycaprolactone film
[6] Cellulose acetate phthalate film
[7] Polycaprolactone/cellulose acetate phthalate film
[8] Sodium hydroxide hydrolyzed film
[9] Potassium hydroxide hydrolyzed film
[10] Ethylenediamine aminolyzed film
[11] Brunauer-Emmet-Teller theory
[12] Barrett-Joyner-Halenda theory

Both hydrolysis treatments increase the BET surface area of the films. The aminolysis of the PCL/CAP films decreases the average pore diameter yet increases the pore volume, indicating that the pores are penetrating the film more so than in the unfunctionalized sample (Groen et al., 2003). This is also consistent with the SEM (Figure 3.18 (a)) and AFM (Figure 3.20 (e)) data. The cumulative pore surface area is also increased.

To conclude, all of the functionalized films maintain their mesoporosity following functionalization, which is advantageous in tissue engineering as mesoporous materials have been shown to promote superior bioactivity as well as excellent drug delivery capabilities (Luo et al., 2013). However, all the films have a low or very low surface areas which is disadvantageous as structures with high surface areas have been shown to improve the probability of neural cell attachment and proliferation (Vijayavenkataraman et al., 2019).

3.3.10 Spectrophotometric mapping of amine group attachment to thin films utilizing the ninhydrin assay

The quantification of the amine groups on the aminolyzed polymer films was undertaken using the ninhydrin assay. Ninhydrin reacts positively in the presence of primary amine groups resulting in Ruhemanns purple color change from yellow to purple when heated (Friedman et al. 2004). Figure 3.23 depicts the samples before and after heating highlighting the color change in the presence of primary amine groups. The calibration curve in Figure 3.24 was used to quantify the amine groups present on the films. The presence of amine groups is confirmed for all samples, with no free amino groups found on the controls, as expected. The average concentration of free amino groups detected on the aminolyzed films is 0.122 ± 0.014 moles/g, derived from Table 3.14.

Table 3. 14 Experimental data used to quantify free amine groups on the films during the ninhydrin assay.

Sample	Concentration (mg/ml)	Concentration on sample (mg/ml)	Concentration on sample (mmol)	Concentration on sample (mmol/gram)
Polycaprolactone/ cellulose acetate phthalate film	0.44 ± 0.01	2.62 ± 0.03	43 ± 0.000514	0.8 ± 0.02
Aminolyzed film	2.10 ± 0.26	33.67 ± 4.09	560 ± 0.07	112 ± 0.01

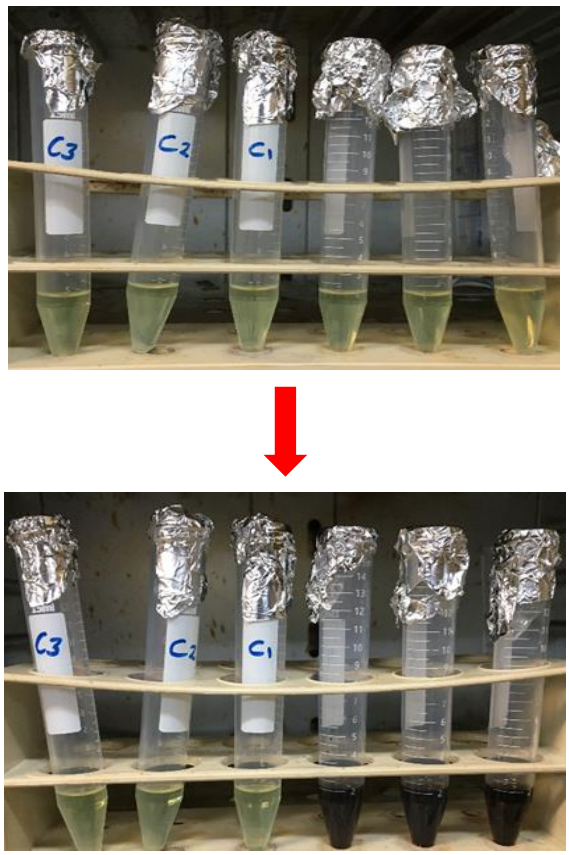


Figure 3. 23 Photographic image of the samples during the ninhydrin assay (a) before heating and (b) after heating, showing the color change from yellow to purple proving the presence of amine groups.

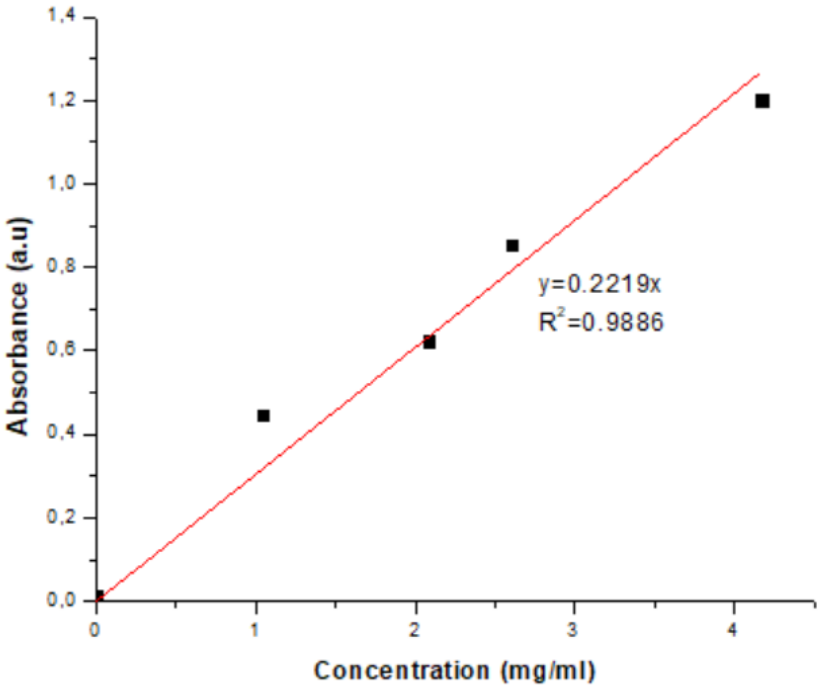


Figure 3. 174 Calibration curve used for amine group quantification on the surface of the films.

In conclusion, this ninhydrin assay proves the successful aminolysis of the PCL/CAP films and successfully quantifies the amine groups present on the films. The samples that were not aminolyzed demonstrate no color change, therefore no absorbance is detected, indicating the lack of amine groups. The aminolyzed samples produce a color change from yellow to purple, indicating the presence of amine groups.

3.3.11 Determination of the mechanical properties of the thin films using Texture Analyser analysis

Mechanical properties such as the tensile strength, Young's modulus and toughness of nerve guidance conduits play a crucial role in regulating neural cellular migration, proliferation, morphology, and neurite outgrowth (Wu et al., 2019). In order to act as a support structure for the regenerating nerve, the film needs to be robust enough to structurally accommodate tissue repair needs, as well as withstand the implantation process (Wu et al., 2019). However, little work has been done to find standard reference values as it is challenging to form direct comparisons due to variance of fabrication substrates, fabrication techniques and the difference in machinery systems adopted in individual work (Sun & Downes, 2009). For nerve tissue engineering, the nerve guidance conduit should be pliable, non-destructive to surrounding tissue and should resist structural collapse during implantation, failing which may cause additional necrosis and inflammation (Bini et al., 2005).

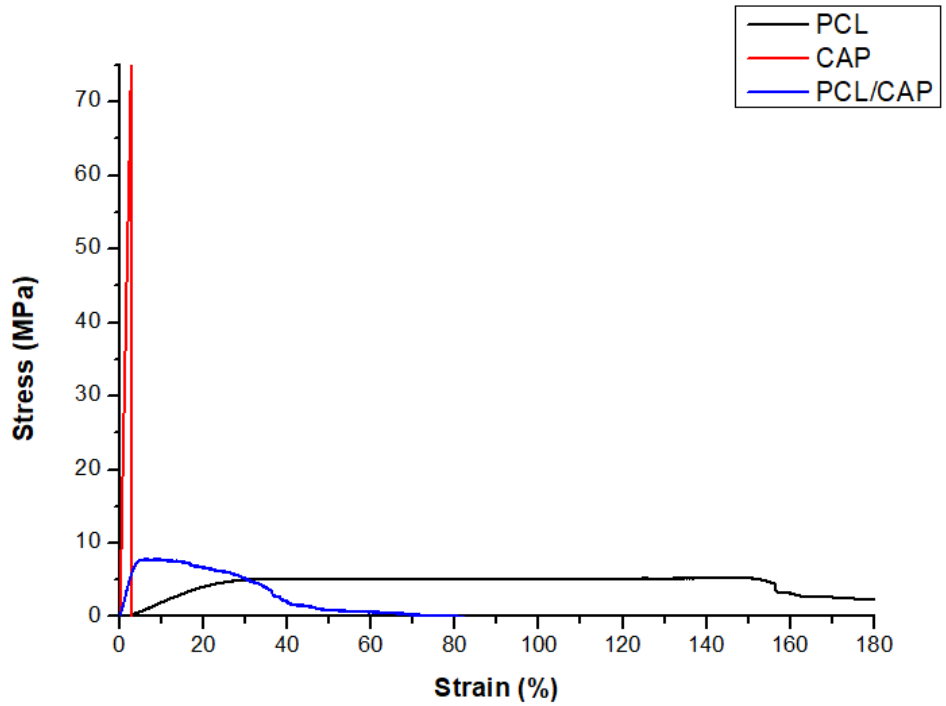


Figure 3. 185 Stress-strain curve generated for (PCL) polycaprolactone films, (CAP) cellulose acetate phthalate films and (PCL/CAP) polycaprolactone/cellulose acetate phthalate film.

Zhang and co-workers have observed that the ideal tensile strength for optimal mechanical performance (comparable to that of clinical materials such as Neurolac®) is 1-7 MPa (Zhang

et al., 2011). Borschel et al. 2003 reported that the Young's modulus of a rat sciatic nerve is 580 ± 0.015 KPa (Borschel et al., 2003). Figure 3.25 compares the stress-strain curves of the PCL, CAP and PCL/CAP film, while Table 3.15 details the values of the tensile strengths, Young's moduli, and toughness results for all samples.

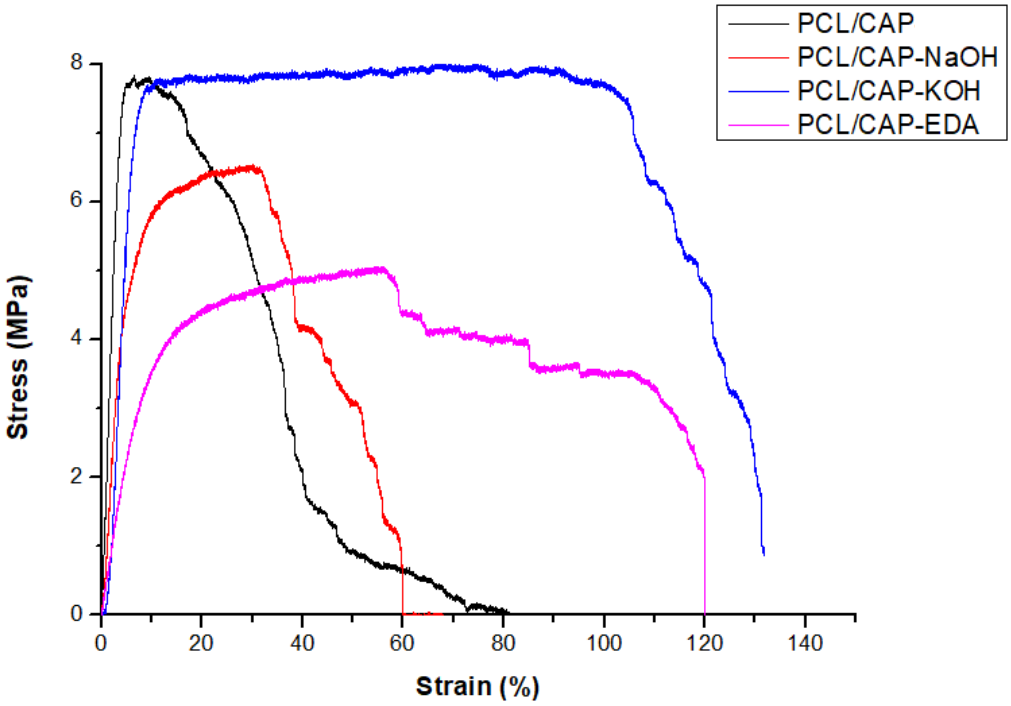


Figure 3. 196 Stress-strain curves of (PCL/CAP) polycaprolactone/cellulose acetate phthalate films, (PCL/CAP-NaOH) sodium hydroxide hydrolyzed films, (PCL/CAP-KOH) potassium hydroxide hydrolyzed films, (PCL/CAP-EDA) aminolyzed films.

The PCL films have a tensile strength of 5.47 ± 0.63 MPa, a Young's modulus of 605.23 ± 5.93 KPa and a toughness of 824.30 ± 5.15 $J.m^{-3}$. The CAP films have a higher tensile strength yet are much less flexible-as seen by the reduced Young's modulus (Wu et al., 2019). They have a lower toughness than PCL films due to the significantly lower area under the stress-strain curve in Figure 3.25 (Wu et al., 2019). The CAP films are classified as brittle, which refers to materials which break into pieces upon the application of a force without any elongation or plastic deformation (Zhang et al., 2011). However, the PCL films are more ductile, which refers to the ability of a material to withstand an applied tensile force as it undergoes plastic deformation (Zhang et al., 2011). The PCL/CAP films show characteristics of a ductile material and comply with the standards mentioned previously in terms of tensile strength and Young's modulus for neural tissue engineering. Hydrolysis and aminolysis treatments slightly reduce the maximum force that the film can withhold (Fmax). In terms of tensile strength, aminolysis produces the highest reduction in tensile strength from 8.01 ± 0.39 MPa to 5.43 ± 0.27 MPa.

Table 3. 15 The effect of aminolysis and hydrolysis on mechanical properties of the films.

Sample	Fmax (N)	Tensile strength (MPa)	Young's modulus (KPa)	Toughness ($J.m^{-3}$)
Polycaprolactone film	2.47 ± 0.29	5.47 ± 0.63	605.23 ± 5.93	824.30 ± 5.15
Cellulose acetate phthalate film	32.13 ± 2.90	71.40 ± 6.45	25.23 ± 2.85	108.24 ± 2.65
Polycaprolactone/ cellulose acetate phthalate film	3.09 ± 0.27	8.01 ± 0.39	535.39 ± 6.25	115 ± 2.16
Sodium hydroxide hydrolyzed film	3.22 ± 0.63	6.78 ± 0.40	622.54 ± 9.47	425.58 ± 4.89
Potassium hydroxide hydrolyzed film	3.12 ± 0.29	7.87 ± 0.13	662.95 ± 7.15	840.8 ± 6.84
Aminolyzed film	2.62 ± 0.36	5.43 ± 0.27	578.55 ± 7.22	580.57 ± 5.87

In terms of hydrolysis, the NaOH treatment also reduces the tensile strength of the films, while KOH treatment produces the least reduction in tensile strength. Interestingly enough, the presence of amine and hydroxyl groups significantly improves the flexibility of the films with Young's moduli of 622.54 ± 6.47, 662.95 ± 4.15 and 578.55 ± 5.22 MPa, respectively, as compared to 535.39 ± 6.25 MPa. In addition, the toughness of the films is greatly improved from 115 ± 2.16 MPa to 425.58 ± 4.18, 640.80 ± 5.71 and 580.57 ± 6.3 MPa, respectively. These results are advantageous in terms of proving that it is possible to alter the mechanical properties of polymeric films by the addition of functional groups.

El-Hadi and co-workers found that spherulite size affects the deformation characteristics of polymers. They found that polypropylene with larger spherulites (250 µm diameter) was more brittle than polypropylene with smaller spherulites (20 µm diameter) (El-hadi et al., 2002). The XRD data in Section 3.3.5 corroborates this finding because as the spherulite size increases, the films exhibit a more brittle mechanical behavior. In order of increasing brittleness, PCL has the lowest brittleness, PCL/CAP is more brittle than PCL due to the addition of the highly brittle polymer CAP. Thereafter NaOH, EDA and KOH-functionalized films are more brittle than the unfunctionalized films, followed by CAP as being the most brittle film. This is closely related to the spherulite sizes calculated in Section 3.3.5, with PCL having the smallest spherulite size (0.04 nm) and CAP having the largest spherulites (0.82 nm). The manual fabrication of the films is believed to be the cause of high standard deviations and is consistent with literature (Sun & Downes, 2009).

In conclusion, surface functionalization reduces the tensile strength of the films but improves the Young's modulus and toughness of the films. The tensile strength and Young's moduli of

samples were in-line with the mechanical requirements of nerve guidance conduits, proving their suitability in nerve tissue engineering in terms of mechanical integrity.

3.3.12 Determination of the hydrophilicity of the thin films by water contact angle measurements

Water contact angle measurements provide important information regarding the wettability or hydrophilicity of materials, which is important for cell-material interactions (Sun & Downes et al., 2009). Figure 3.27 represents the water contact angle values obtained from the analysis and draw a comparison between the hydrophilicity of the air and glass surfaces.

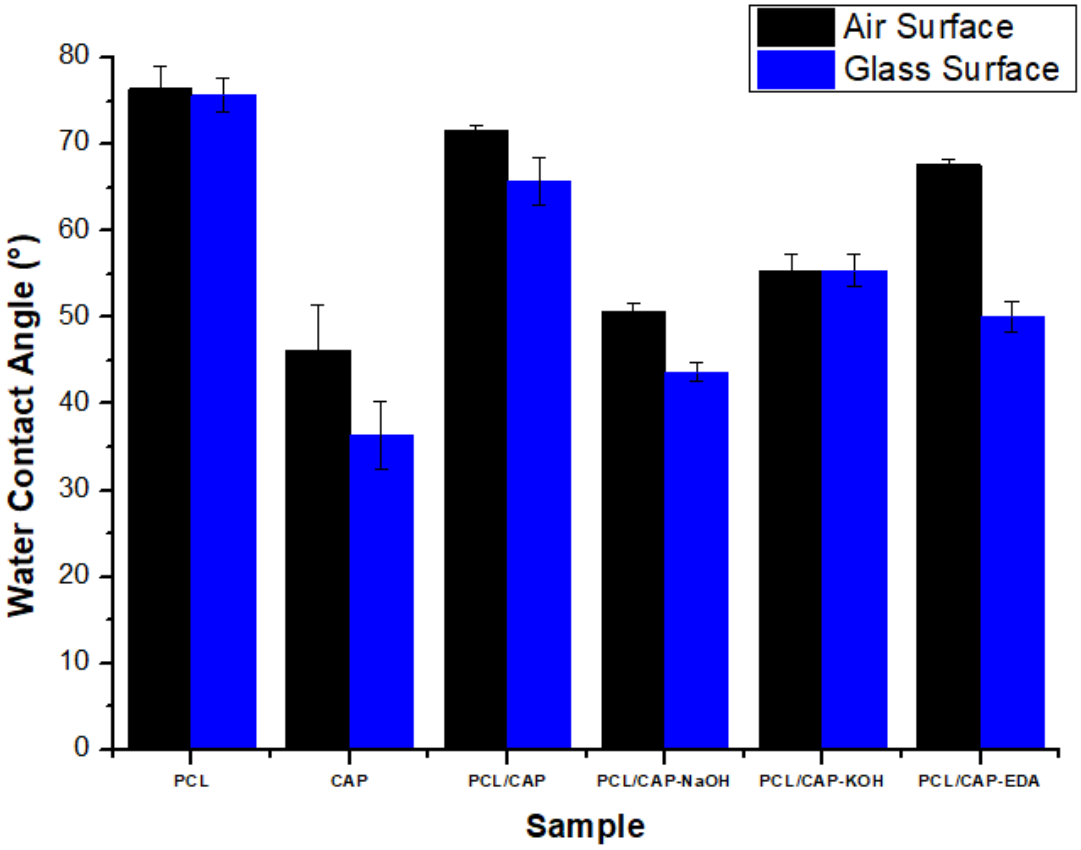


Figure 3. 27 Water contact angles of (PCL) polycaprolactone film, (CAP) cellulose acetate phthalate films, (PCL/CAP) polycaprolactone/cellulose acetate phthalate films, (PCL/CAP-NaOH) sodium hydroxide hydrolyzed films, (PCL/CAP-KOH) potassium hydroxide hydrolyzed films, (PCL/CAP-EDA) aminolyzed films.

Polycaprolactone is a hydrophobic polymer which is non-absorbent to water (Sousa et al., 2014), whereas cellulose acetate phthalate is known as a relatively hydrophilic polymer which has been used in blend formulations to improve the hydrophilicity of numerous hydrophobic synthetic polymers (Ali et al., 2014). Figure 3.27 shows that the addition of CAP to the PCL film reduces the water contact angle from 76.42° ± 2.64 to 71.60° ± 0.50, thereby increasing the hydrophilicity of the film. There is a slight decrease in water contact angle readings of the glass surfaces of the polymer films in comparison to the air surfaces. Factors such as surface roughness have an effect on the wettability of surfaces, with rougher surfaces often being less

hydrophilic than smoother surfaces (Sun & Downes, 2007). This is in alignment with the AFM data discussed in Section 3.3.8. The glass surfaces have lower surface roughness values than the air surfaces, therefore rendering the glass surface of the films more hydrophilic (Sun & Downes, 2009).

The treated surfaces (both air and glass surfaces) of the films are significantly more hydrophilic than the untreated counterparts. The NaOH-hydrolyzed films produce the lowest water contact angle measurements, followed by KOH-hydrolyzed films and EDA-aminolyzed films, which is in alignment with a similar study by Sun and Downes in 2009 (Sun & Downes, 2009). Figure 3.28 demonstrates how surface functionalization reduces the water contact angle of the films.

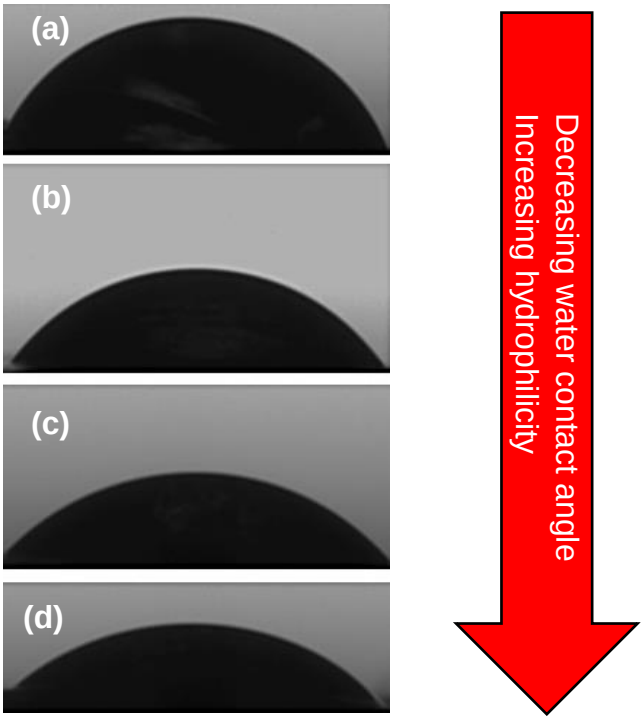


Figure 3. 28 Photographic images of water drops on (a) polycaprolactone/cellulose acetate phthalate film, (b) aminolyzed film, (c) potassium hydroxide-hydrolyzed film and (d) sodium hydroxide-hydrolyzed film.

To conclude, the unfunctionalized PCL/CAP films are relatively hydrophobic in nature, which may hinder cell attachment *In Vitro.* However, the surface hydrolysis and aminolysis treatments have the ability to enhance the hydrophilicity of the films, with the NaOH hydrolysis causing the highest increase in hydrophilicity, which are predicted to enhance cell-film interactions.

3.3.13 *In Vitro* degradation behavior of the thin films

The degradation rate of nerve guides is one of the important factors in the process of nerve regeneration though nerve guidance conduits (Siemionow et al., 2010). Non-biodegradable polymers should be avoided for nerve tissue engineering as they can lead to compression and inflammation *In Vivo* which can interfere with the regeneration of nerve fibers (Siemionow et

al., 2010). Therefore, current research has focused on biodegradable polymers for the fabrication of nerve guidance conduits. An ideal nerve guidance conduit should be composed of materials with a controlled degradation rate which will ensure that the structural stability of the conduit is upheld in accordance with axonal growth and maturation (Mohammadi & Mashayekhan, 2020). The conduit should gradually collapse until the regeneration process is complete (Mohammadi & Mashayekhan, 2020). The regeneration rate of nerves varies according to severity and location of the injury along the neuron (Ron et al., 2015). Proximal segments may increase two to three mm per day while more distal segments may progress at a rate of one to two mm per day (Ron et al., 2015). Polycaprolactone is characterized by a slow degradation rate occurring by hydrolysis, which leads to the formation of low molecular weight by-products (Pitt et al., 1981). These by-products are easily metabolised or expelled from the body, reducing the risk of foreign body reactions, making PCL an ideal biodegradable polymer for the fabrication of nerve guidance conduits (De Luca et al., 2014).

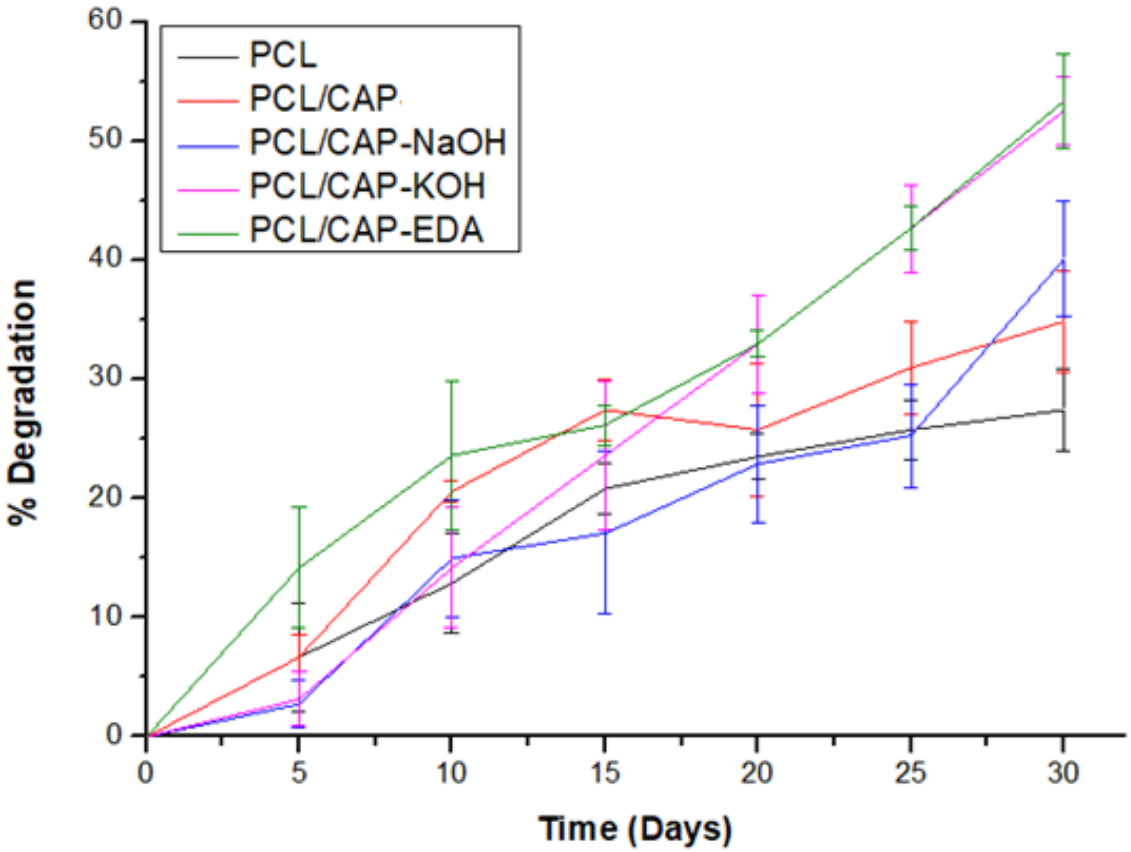


Figure 3. 29 Percentage degradation of the films over the 30-day period. (PCL) polycaprolactone film, (PCL/CAP) polycaprolactone/cellulose acetate phthalate film. (PCLCAP-NaOH) sodium hydroxide hydrolyzed film, (PCL/CAP-KOH) potassium hydroxide hydrolyzed film, (PCL/CAP-EDA) aminolyzed film.

The 3% w/v CAP film is not included in the *In Vitro* degradation and water-uptake studies as it completely dissolved in the PBS before the first time point. The degradation of polymeric films is controlled by numerous variables such as surface area, porosity and hydrophilicity (Elnaggar

et al., 2021). The aminolyzed films degrade the most over the 30 days, followed by PCL/CAP-KOH, PCL/CAP-NAOH, and PCL/CAP. The PCL films degrade the least over 30 days, degrading a total of 27.45% by the 30th day. The addition of CAP to the PCL films increases the percentage degradation, perhaps due to the enhanced hydrophilicity of the PCL/CAP films in comparison to the PCL films seen in Section 3.3.12 (Akhtar et al., 2017). The PCL/CAP films degrade a total of 34.89% by the 30th day. Previous reports have shown that as the hydrophilicity of a sample increases, the degradation and water-uptake rate increases (Akhtar et al., 2017).

Both hydrolysis and aminolysis surface treatments increase the degradation of the films over 30 days. The hydrolytic effect of NaOH and KOH treatment accelerates the degradation by introducing random scission to the polymer chains (Sun & Downes, 2009). Aminolysis reactions result in the cleavage of the ester bonds in the polymer chains which results in the simultaneous generation of amide bonds (Z Yang et al., 2013). This ester bond cleavage results in an accelerated degradation rate (Z Yang et al., 2013). The aminolyzed samples show the highest total percentage degradation (53.40%) as compared to the untreated samples. The NaOH and KOH hydrolyzed samples degrade a total of 40.11 and 52.56%, respectively over the 30-day period.

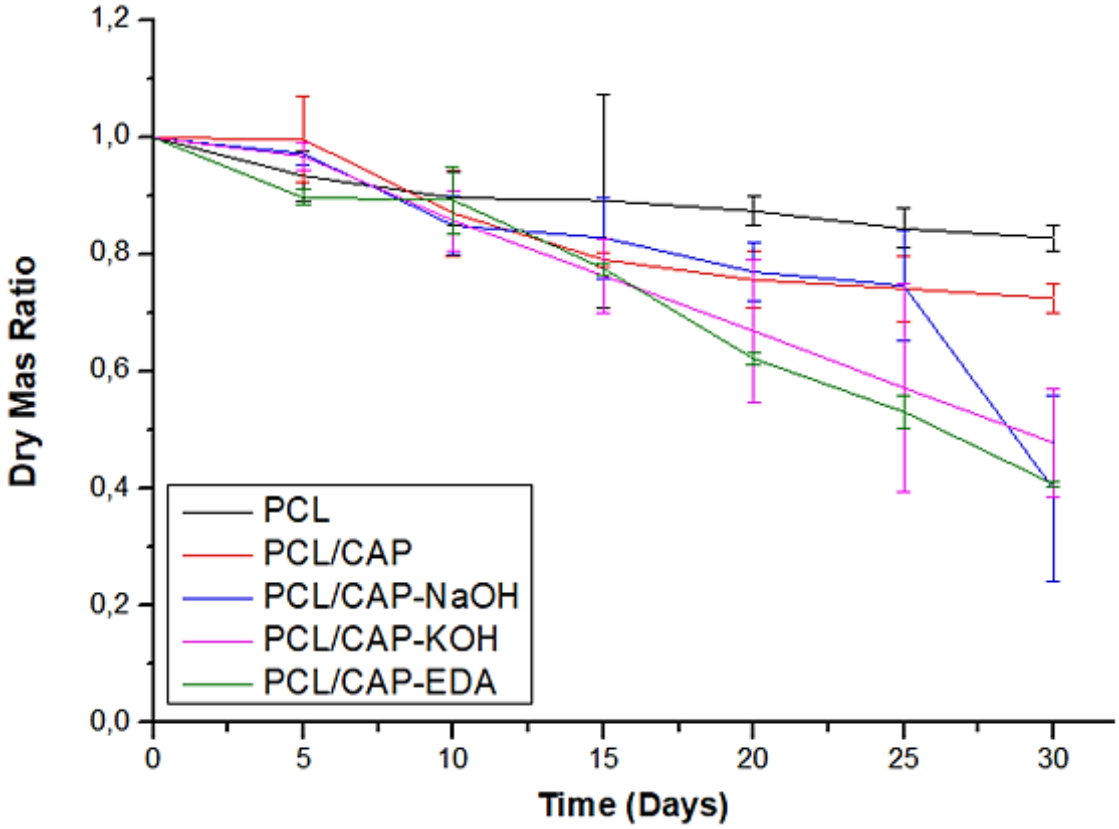


Figure 3. 30 *In Vitro* degradation rate of the film samples over the 30 day period. (PCL) polycaprolactone film, (PCL/CAP) polycaprolactone/cellulose acetate phthalate film. (PCLCAP-NaOH) sodium hydroxide hydrolyzed film, (PCL/CAP-KOH) potassium hydroxide hydrolyzed film, (PCL/CAP-EDA) aminolyzed film.

It has previously been found in a study by Ramburrun and co-workers, that a nerve repair device comprising a polysaccharide hydrogel conduit and intraluminal aligned nano-fibrous guidance cue implanted for a four week period showed sufficient support and biodegradability to produce an improved functional recovery and return of fine motor control in animals receiving implantation (Ramburrun et al., 2019). This indicates that a scaffold fit for neural tissue engineering should remain structurally intact for approximately four weeks (which could vary depending on the size of the nerve gap).

Despite the fact that the functionalized films did not completely degrade after the four week period in this study, they have all degraded over 40%, which indicates a significant loss in structural integrity and perhaps a loss in the ability to provide structural support to growing neuronal cells and tissue (Mohammadi & Mashayekhan, 2020). However, different sized nerve gaps and different degrees of damage require different biodegradation rates, depending on the time required to heal (Mohammadi & Mashayekhan, 2020).

It thus follows that depending on the specific clinical application, the film can be 'fine-tuned' to suit the clinical requirement. For example, a slower degradation rate could be achieved by (Mohammadi & Mashayekhan, 2020):

- Reducing the concentration of CAP in the film.
- Reducing the hydrolysis or aminolysis time.
- Reducing the concentration of NaOH, KOH or EDA.
- Reducing the functionalization temperature, or by
- Increasing the total polymer concentration.

However, it should be noted that these modifications would alter the other physio-chemical properties of the films, such as hydrophilicity and mechanical properties. The high standard deviation observed is proposed to be due to the manual fabrication of the films and is consistent with literature (Sun & Downes, 2007)

3.3.14 *In Vitro* water-uptake behavior of thin films

The water-uptake of a biomaterial is also an imperative factor which affects the type of biological response initiated by cells following its implantation into the body (Ramburrun et al., 2019). Water-uptake is influenced by surface area, porosity and hydrophilicity (Elnaggar et al., 2021).Table 3.16 highlights the total percentage water-uptake of each film on the 30th day.

The PCL/CAP composite film has a higher total water-uptake percentage compared to the pristine PCL film. In addition, surface hydrolysis and aminolysis reactions of the PCL/CAP films enhances the water-uptake capabilities of the films (Sun & Downes, 2009). The NaOH-

hydrolyzed PCL/CAP films show the highest total percentage water-uptake, followed by the KOH-hydrolyzed films and aminolyzed films. Previous reports have shown that as the hydrophilicity of a sample increases, the percentage water-uptake increases (Akhtar et al., 2017). Therefore, it is fitting that water contact angle measurements in Section 3.3.12 correspond to the total percentage water-uptake of each sample. The mean total percentage water-uptake values for each sample at day 30 are found in Table 3.16.

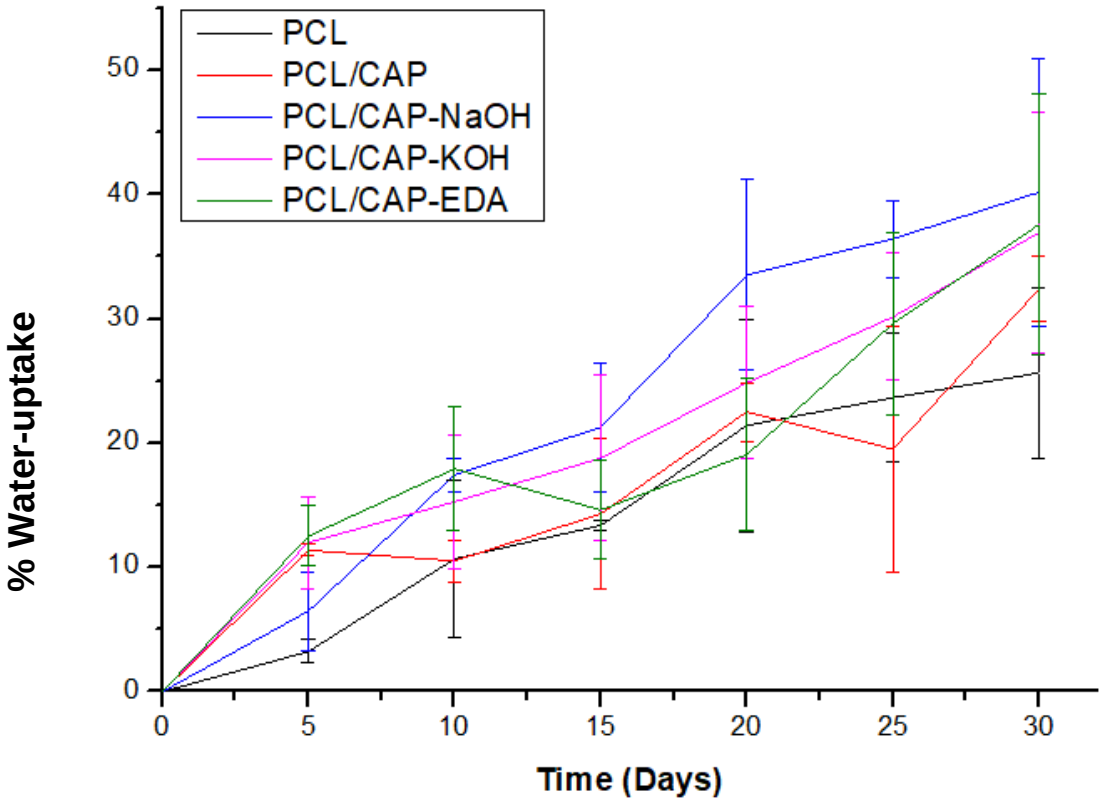


Figure 3. 31 *In Vitro* water-uptake behavior of (PCL) polycaprolactone film, (PCL/CAP) polycaprolactone/cellulose acetate phthalate film. (PCLCAP-NaOH) sodium hydroxide hydrolyzed film, (PCL/CAP-KOH) potassium hydroxide hydrolyzed film, (PCL/CAP-EDA) aminolyzed film.

Table 3. 16 representing total percentage water-uptake at day 30.

Sample	Water-uptake at day 30 (%)
Polycaprolactone film	25.67 ± 6.86
Polycaprolactpone/ cellulose acetate phthalate film	32.41 ± 2.67
Sodium hydroxide hydrolyzed film	40.20 ± 10.70
Potassium hydroxide hydrolyzed film	36.97 ± 9.70
Aminolyzed film	37.61 ± 10.44

In conclusion, the enhanced hydrophilicity of the functionalized samples enhances the water-uptake capabilities of the films. However, the water-uptake properties of the films may be altered by tuning the hydrophilicity of the films as discussed in Section 3.3.12. The high

standard deviation observed is proposed to be as a result of the manual fabrication of the films and is consistent with literature (Sun & Downes, 2007).

3.3.15 PC12 and A172 cell culture and cell viability quantification utilizing the XTT cytocompatibility assay

The cytocompatibility of the films is important to ensure that the cells can attach and survive on the film surface (Sun & Downes, 2007). Figure 3.32 represents the cell viability results from the XTT assay for the PC12 cell line.

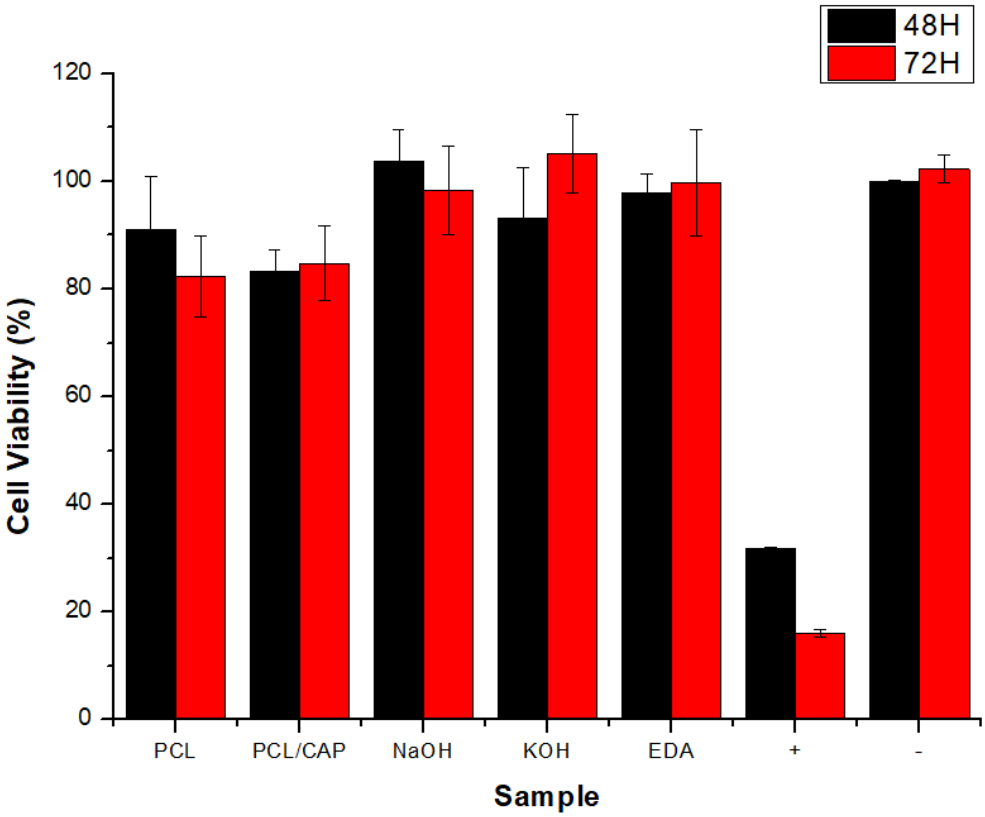


Figure 3. 32 PC12 cell viability results after 48 and 72 h of exposure to extraction media. (PCL) polycaprolactone film, (PCL/CAP) blend film, (NaOH) sodium hydroxide-hydrolyzed film, (KOH) potassium hydroxide-hydrolyzed film, (EDA) aminolyzed film, (+) positive control, (-) negative control. An unpaired, two-tailed student T-test was conducted comparing the cell viability obtained from the unfunctionalized sample and the functionalized samples, which showed statistical significance after the 48 h exposure of P=0.001, 0.16 and 0.002, respectively, and after 72 h exposure of P=0.073, 0.009 and 0.08, respectively.

The functionalized samples promote a higher cell viability in comparison to the untreated control. This indicates that a higher percentage of healthy, live cells are present in the wells containing the hydrolyzed and aminolyzed samples (Neu et al., 2009). A higher cell viability is indicative of a higher cellular activity (Neu et al., 2009). At the 48 h time-point, the only sample that presents a viability above the negative control is the NaOH-hydrolyzed sample, with 103.71%. The other samples are slightly below the negative control viability of 100.05%. In terms of the 72 h time point, the only sample that presents with a cell viability superior to that of the negative control (102.30%), is the KOH-hydrolyzed sample, having a viability of

105.12%. However, the other samples are all still above 80%. Another notable point is that the viability of the negative control has increased from 48 h to 72 h. However, the NaOH-hydrolyzed samples produce a reduced viability at 72 h in comparison to the 48 h viability. In other words, as time passes, the number of live cells present in the well plate decreases, perhaps due to the release of toxic by-products after 48 h (Boni et al., 2018). In addition, at the 48 h time point, the NaOH-hydrolyzed films produce a cell viability of 103.71%, and at the 72 h time point, the KOH-hydrolyzed samples have a viability of 105.12%, indicating that the cells are in a proliferative state (Boni et al., 2018). As time passes, the samples cause an increase in the number of live cells present in the well plate, indicating the proliferative properties of these samples (Boni et al., 2018). The P values computed indicate that the NaOH and EDA treated films produce a significant increase in cell viability in comparison to the untreated films at 48 h. Contrary to this, for the 72 h time point, the KOH-hydrolyzed sample is the one that produces a significant increase in cell viability in comparison to the untreated film. None of the films produce a significant decrease in cell viability. Figure 3.33 represents the cell viability results from the XTT assay for the A172 cell line.

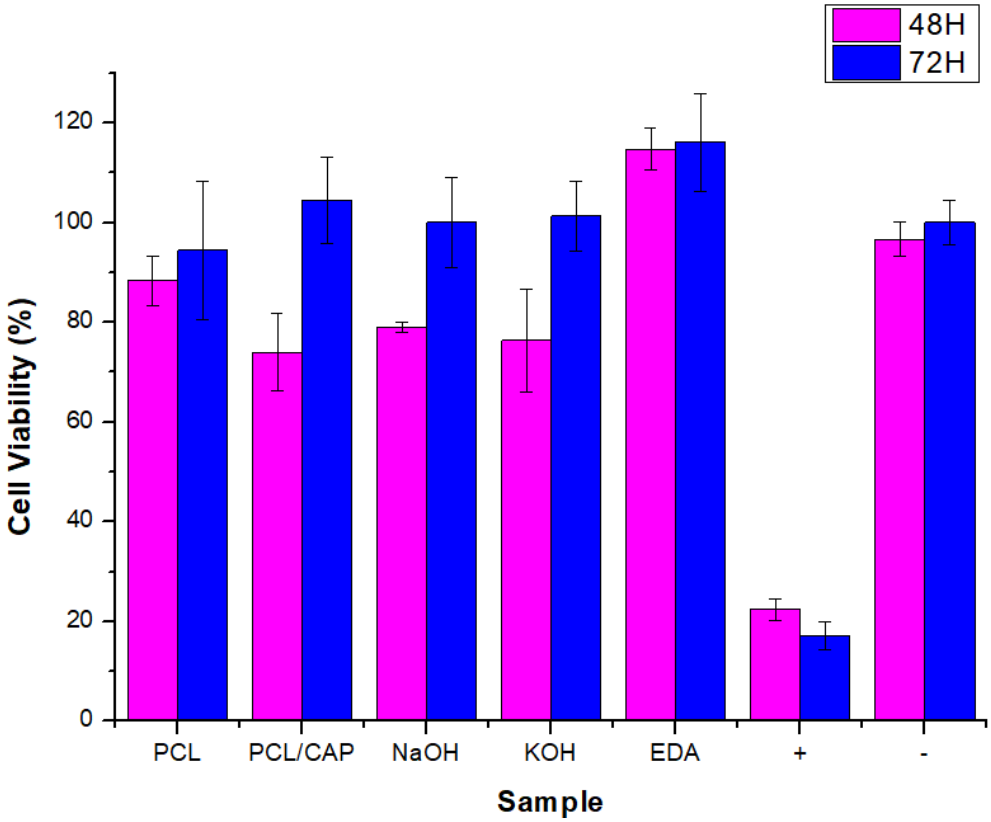


Figure 3. 33 A172 cell viability results after 48 and 72 h of exposure to extraction media. (PCL) polycaprolactone film, (PCL/CAP) blend film, (NaOH) sodium hydroxide-hydrolyzed film, (KOH) potassium hydroxide-hydrolyzed film, (EDA) aminolyzed film, (+) positive control, (-) negative control. An unpaired, two-tailed student T-test was conducted comparing the cell viability obtained from the unfunctionalized sample and the functionalized samples, which showed statistical significance after the 48 h exposure of P=0.56, 0.86, and 0.01, respectively, and after 72 h exposure of P=0.74, 0.79 and 0.42, respectively.

The functionalized films all display superior cell viabilities at the 48 h time point, with the aminolyzed film producing the highest increase in cell viability (114.75%). At the 72 h time point, the same result is found, where the functionalized samples enhance the cell viability, again with the aminolyzed film producing the highest improvement (116.16%). In contrast to the PC12 cell line, all the samples produce higher viabilities at the 72 h point in comparison to the 48 h point, indicating that as time passes, the samples enhance the number of live cells in the well plate, indicating their proliferative properties (Neu et al., 2009).The p values computed indicated that the aminolyzed films produced a significant increase in cell viability at 48 h. None of the samples produce a significant decrease in cell viability.

In conclusion, none of the films are cytotoxic (<80% cell viability) nor do they produce a significant reduction in cell viability in comparison to the control, indicating that the cells would possibly be able to attach to the films (Boni et al., 2018). The aminolyzed samples facilitate PC12 and A172 cell proliferation.

3.3.16 Qualitative assessment of cell attachment utilizing light microscopy

Light microscopy images were captured of the cells attached to the films in order to firstly prove that the cells are capable of attaching to the films, and to secondly assess whether the cells maintain their neuronal-like morphology while attached to the films. Figure 3.34 illustrates the natural morphology of live, healthy PC12 and A172 cells, demonstrating a neuronal-like morphology. Due to the intricate and branched/lamellar morphology of the film seen in Figure 3.35, differentiation between the films and the cells is challenging under light microscopy.

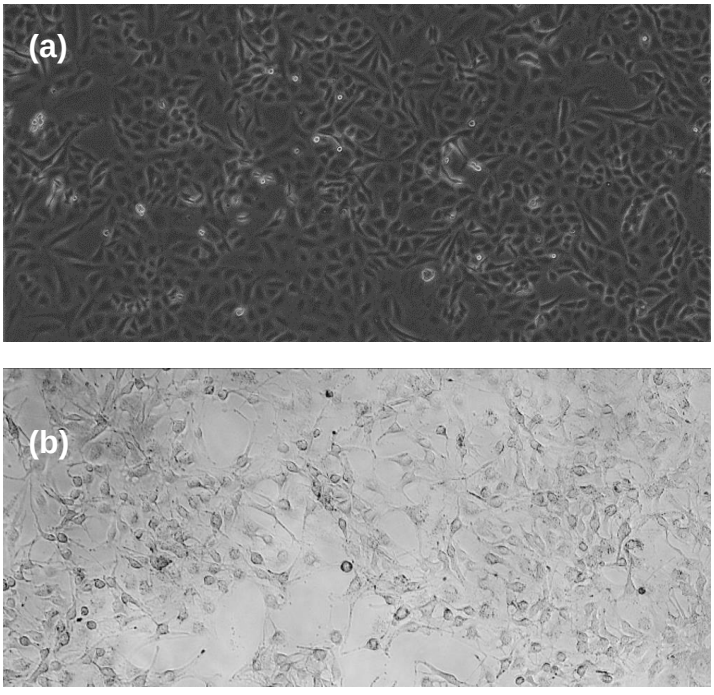


Figure 3. 34 Light microscopy images of confluent (a) PC12 and (b) A172 cells.

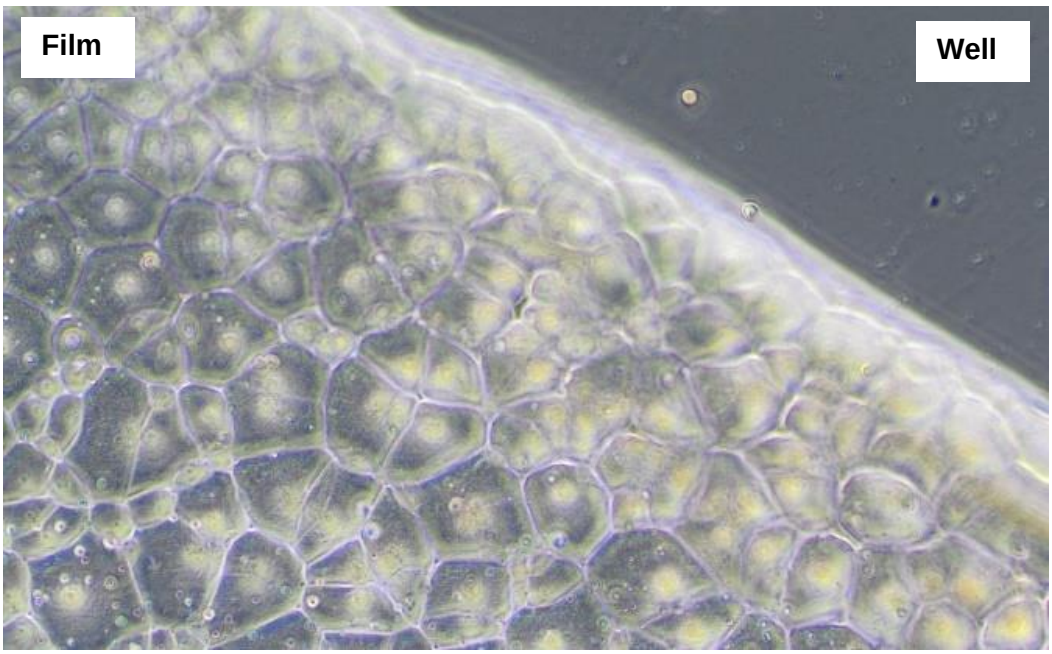


Figure 3. 35 Light microscopy image of the polycaprolactone/cellulose acetate phthalate film demonstrating the branched/lamellar-like morphology of the films which hinders the visualization of cell attachment.

Some cells were captured on the films, depicted in Figures 3.36 and 3.37 (highlighted in red), however, images were not obtained for all samples due to the morphology of the films obscuring the view.

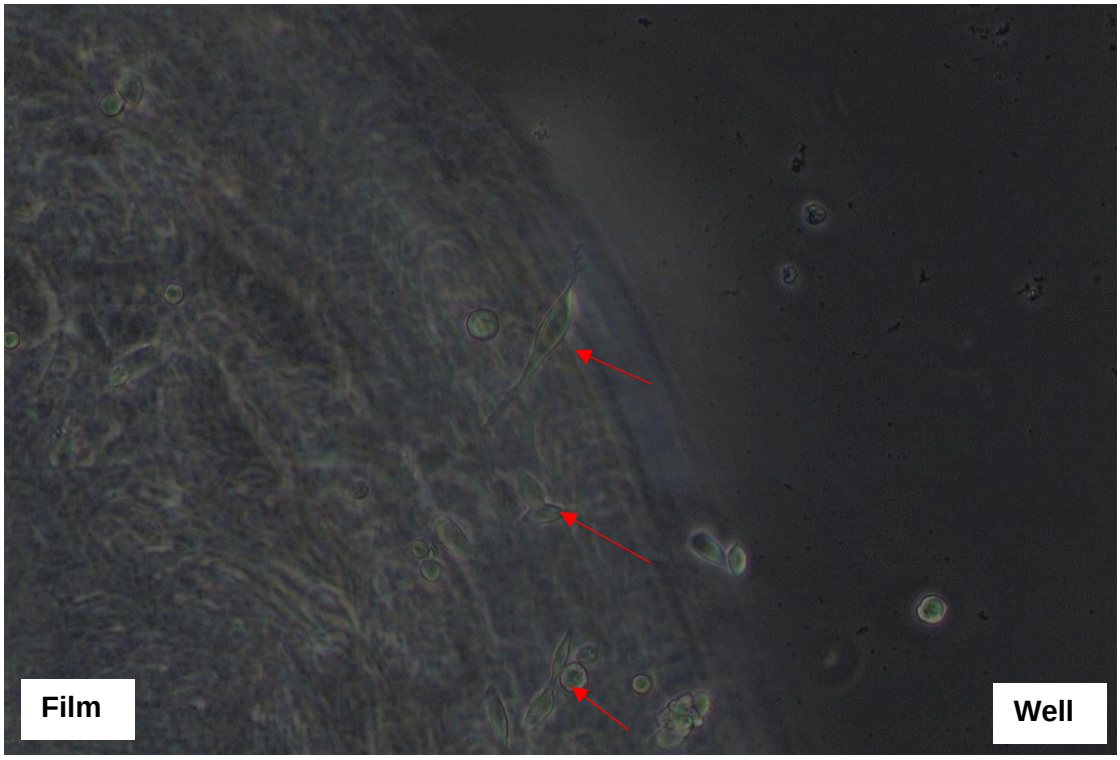


Figure 3. 36 PC12 cells attached onto the polycaprolactone/cellulose acetate phthalate film.

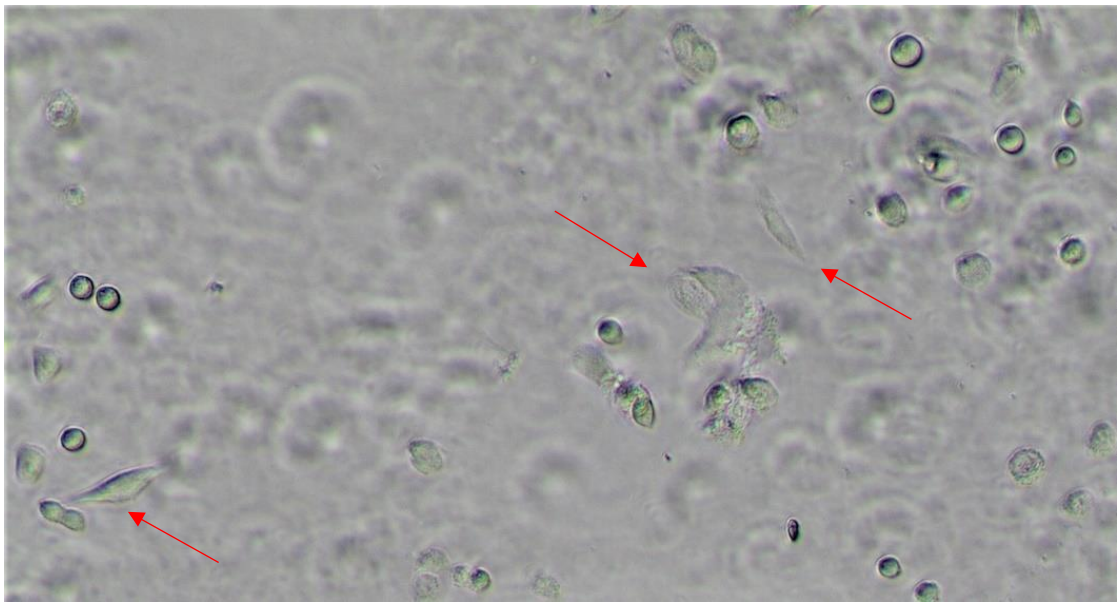


Figure 3. 37 PC12 cells attached onto polycaprolactone/cellulose acetate phthalate film.

In conclusion, this imaging confirmed that cells have the ability to attach to the films, indicating that the films are not cytotoxic. However, due to the limitation of not being able to differentiate between the films and the cells, a trypan blue exclusion method was employed in Section 3.3.17 to quantitatively determine if the films facilitated cell attachment.

3.3.17 Quantification of cell attachment using trypan blue exclusion method

The trypan blue exclusion assay provided a quantitative analysis of cells attached to the film (Liu et al., 2004). This is an important assay as it is a direct indication of the suitability of the films in neural tissue engineering (Liu et al., 2004). The higher the cell attachment to the films, the better the films perform *In Vitro*.

Figure 3.38 represents the PC12 cell attachment relative to the control (plasma treated cell culture well plates).The percentage of PC12 cells attached to the films are much lower in comparison to that of the plasma treated cell culture well plates (control). In terms of the PCL film, only 8.96% of cells are able to attach to the film. The reason for the low cell attachment could be the lack of cell-interactive moieties as well as a lack of topographical cues as seen in the SEM images of the PCL film in Section 3.3.7 (Sun & Downes, 2007). In terms of the PCL/CAP film, the cell attachment is 29.30%, which is higher than that of the PCL film, even though this sample also lacks cell-interactive functionalities. The higher cell attachment is likely due to the presence of topographical cues identified in Section 3.3.7 via SEM (Liu et al., 2004). This shows the importance of topographical cues in cell attachment (Liu et al., 2004). The hydrolyzed films show an improvement in cell attachment in comparison to the unfunctionalized film, each resulting in a 36.62 and 41.58% attachment.

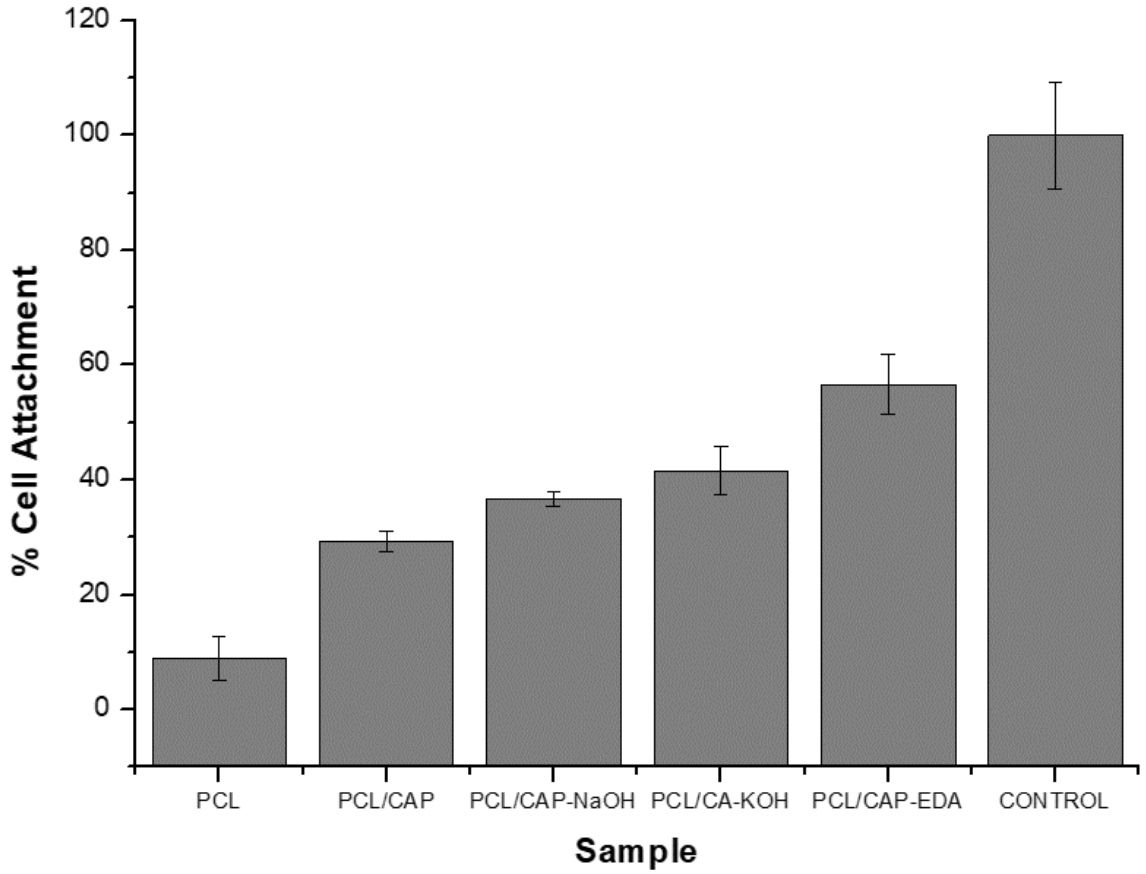


Figure 3. 38 Quantification of cell attachment of PC12 cells to the films. (PCL) polycaprolactone film, (PCL/CAP) polycaprolactone/cellulose acetate phthalate film. (PCLCAP-NaOH) sodium hydroxide hydrolyzed film, (PCL/CAP-KOH) potassium hydroxide hydrolyzed film, (PCL/CAP-EDA) aminolyzed film.

The aminolyzed film performs the best out of the functionalized films, increasing cell attachment to 55.44%. The possible reason for the aminolyzed films facilitating the highest cell attachment could be that amine groups generally promote cell adhesion due to the positive charges that have the ability to attract negatively charged cells in aqueous media at physiological pH (Gigout et al., 2011).

A similar finding is observed for the A172 cells (Figure 3.39) in comparison with the PC12 cells. The PCL film results in minimal cell attachment (9.60%), the PCL/CAP film results in an enhanced cell attachment (30.46%), and the functionalized films result in an even further enhancement of cell attachment (69.47, 46.76 and 48.96%, respectively). In this case, the NaOH hydrolyzed films perform the best out of the samples in comparison with the PC12 cell line, where the aminolyzed films perform the best. Similar to the PC12 cells, the well plates still have a higher cell attachment in comparison to the well plates.

In conclusion, the hydrolyzed and aminolyzed samples have the ability to enhance the neurocompatibility of the PCL/CAP films, however, none of the functionalized samples

outperform the plasma treated cell culture well plate control. The possible reason for this that the well plates are pre-treated via Nunclon Delta, which is a plasma gas surface modification that enhances the hydrophilicity of the well plate, which promotes maximum adhesion for a broad range of cell types (Thermofischer Scientific, n.d). These well plates are routinely used for cell culture as they encourage most adherent cells to grow healthily and reproducibly (Biomat, n.d). The resulting surface carries a net negative charge due to the presence of oxygen-containing functional groups such as hydroxyl and carboxyl (Perkin Elmer, n.d). The average water contact angle of a typical plasma-treated cell culture well plate is ~ 46° (O'Sullivan et al., 2020). Therefore, the results are fitting as the water contact angles for PCL, PCL/CAP, PCL/CAP-NaOH, PCL/CAP-KOH and PCL/CAP-EDA are 76.42, 71.6, 50.64, 55.37 and 67.68°, respectively (none of which are comparable to the well plates). Therefore, the hydrophilicity of the films needs to be enhanced further, so that they are more hydrophilic than the well plates.

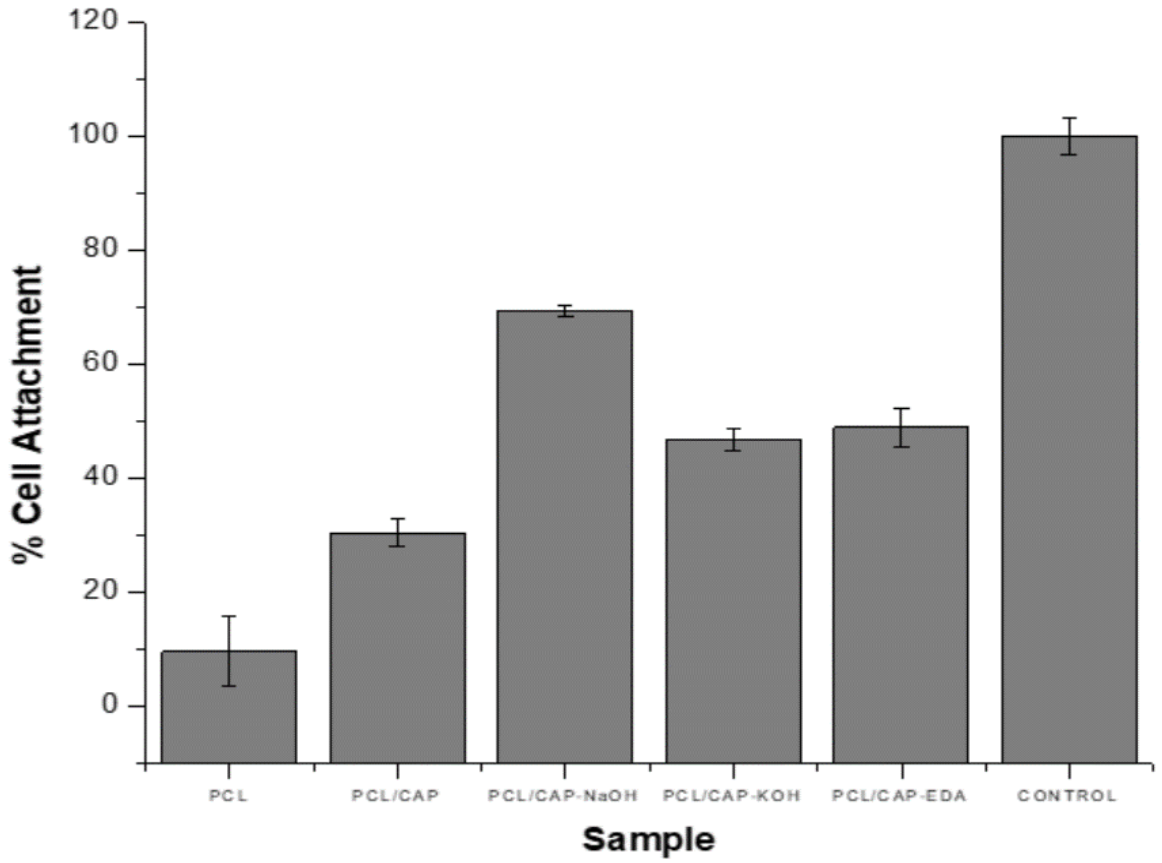


Figure 3. 39 Quantification of A172 cell attachment to the films. (PCL) polycaprolactone film, (PCL/CAP) polycaprolactone/cellulose acetate phthalate film, (PCLCAP-NaOH) sodium hydroxide hydrolyzed film, (PCL/CAP-KOH) potassium hydroxide hydrolyzed film, (PCL/CAP-EDA) aminolyzed film.

3.4 Concluding remarks

Chemical functionalization of the films has proven to be an effective manner of altering chemical, mechanical, porosimetric, topographical, degradation, morphological, as well as cell interactive properties. The performance of the composite PCL/CAP film has superseded that of the PCL film, proving that the addition of CAP to the formulation is advantageous. Further, it is evident from the studies conducted that the hydrolyzed and aminolyzed films outperform the unfunctionalized film, particularly in the *In Vitro* studies, which is a direct indication of neurocompatibility. In addition, the samples are non-cytotoxic to model neural cell lines. However, although good results were obtained throughout the study, the *In Vitro* trypan blue assay results demonstrate that the plasma treated plastic well plates are still superior in terms of cell attachment in comparison to all the film samples. While the results of both aminolysis and hydrolysis functionalization cannot supersede the plasma treated well plates *In Vitro*, they can enhance the neurocompatibility of the unfunctionalized films *In Vitro* in comparison to the unfunctionalized films. This study concludes that the chemical functionalization of thin polymeric films is an easy, cost-effective method to alter important properties of films to enhance their performance *In Vitro* in comparison to their unfunctionalized counterparts.

3.5 References

Akhtar, M. F., Ahmed, S., & Peerzada, S. (2017). Pharmaceutical technology effect of hydrophilic and hydrophobic polymer on In Vitro dissolution and permeation of bisoprolol fumarate through transdermal patch. Acta poloniae pharmaceutica, 74(1), 187-197.

Amores de Sousa, M. C., Rodrigues, C. A. V., Ferreira, I. A. F., Diogo, M. M., Linhardt, R. J., Cabral, J. M. S., & Ferreira, F. C. (2020). Functionalization of electrospun nanofibers and fiber alignment enhance neural stem cell proliferation and neuronal differentiation. Frontiers in bioengineering and biotechnology, 8.

Azioune, A., Chehimi, M. M., Miksa, B., Basinska, T., & Slomkowski, S. (2002). Hydrophobic protein-polypyrrole interactions: the role of van der Waals and Lewis acid-base forces as determined by contact angle measurements, 18(2), 1150-1156.

Azizi, S., Azizi, M. and Sabetzadeh, M. (2019). The role of multiwalled carbon nanotubes in the mechanical, thermal, rheological, and electrical properties of PP/PLA/MWCNTs nanocomposites. Journal of composites science, 3(3), 64.

Barrett, E., Joyner, L., & Halenda, P. (1951). The Determination of pore volume and area distributions in porous substances. Journal of the American chemical society, 73(1), 373-380.

Borschel, G.H., Kia, K.F, Kuzon, W.M. & Dennis, R.G. (2003). Mechanical properties of acellular peripheral nerve. Journal of surgical research, 114(2), 113-119.

Brien, F J O, Harley, B. A., Yannas, I. V, & Gibson, L. J. (2005). The effect of pore size on cell adhesion in collagen-GAG scaffolds, 26(4), 433-441.

Brunauer, S., Emmett, P. H., & Teller, E. (1936). Adsorption of gases in multimolecular layers. Journal of the American chemical society, 60(2), 309-319.

Brunetti, V., Maiorano, G., Rizzello, L., Sorce, B., Sabella, S., Cingolani, R., & Pompa, P. P. (2010). Neurons sense nanoscale roughness with nanometer sensitivity. Applied physical sciences, 8(14), 6264-6269.

Cao, M., Gu, F., Rao, C., Fu, J., Zhao, P. (2019). Improving the electrospinning process of fabricating nanofibrous membranes to filter. Science of the total environment, 20(666), 1011-1021.

Chang, S. & Hsiao, Y. (2017). Surface and protein adsorption properties of 316L stainless steel modified with polycaprolactone film. Polymers (Basel), 9(10), 545-551.

Chaturvedi, K., Kulkarni, A. R., & Aminabhavi, T. M. (2011). Blend microspheres of poly(3-hydroxybutyrate) and cellulose acetate phthalate for colon delivery of 5-fluorouracil. Industrial & engineering chemistry research, 50(18), 10414-10423.

Da Silva, K., Kumar, P., Vuuren, S. F. Van, Pillay, V., & Choonara, Y. E. (2021). Three-dimensional printability of an ECM-based gelatin methacryloyl (GelMA) biomaterial for potential neuroregeneration. ACS Omega, 6(33), 21368-21383.

Dash, T. K., & Konkimalla, V. B. (2012). Polycaprolactone based formulations for drug delivery and tissue engineering : a review. Journal of controlled release, 158(1), 15-33.

De Luca, A. C., Terenghi, G., & Downes, S. (2014). Chemical surface modification of polycaprolactone improves Schwann cell proliferation for peripheral nerve repair. Journal of tissue engineering and regenerative medicine, 8(2), 153-63.

Denis, P., Wrzecionek, M., Gadomska-Gajadhur, A., & Sajkiewicz, P. (2019). Poly(glycerol sebacate)-poly(l-lactide) nonwovens. Towards attractive electrospun material for tissue engineering. Polymers, 11(12), 2113-2116.

Dulnik, J., Denis, P., & Sajkiewicz, P. (2016). Biodegradation of bicomponent PCL/gelatin and PCL/collagen nanofibers electrospun from alternative solvent system. Polymer degradation and stability, 130(1), 10-21.

Elnaggar, M. A., El-fawal, H. A. N., & Allam, N. K. (2021). Materials science & engineering C biocompatible PCL-nanofibers scaffold with immobilized fibronectin and laminin for neuronal tissue regeneration. Materials science & engineering C, 119(4), 111550-111559.

Fukushima, K., Tabuani, D., Abbate, C., Arena, M., & Rizzarelli, P. (2011). Preparation, characterization, and biodegradation of biopolymer nanocomposites based on fumed silica. European polymer journal, 47(2), 139-152.

Gao, J., Niklason, L., & Langer, R. (1998). Surface hydrolysis of poly(glycolic acid) meshes increases the seeding density of vascular smooth muscle cells. Journal of biomedical materials research, 42(3), 417-424.

Garg, A., Rai, G., Lodhi, S., Jain, A. P., & Yadav, A. K. (2016). Hyaluronic acid embedded cellulose acetate phthlate core/shell nanoparticulate carrier of 5-fluorouracil. International journal of biological macromolecules, 87(2), 449-459.

Gigout, A, Ruiz, J., Wertheimer, M., Jolicoeur, M., & Lerouge, S. (2011). Amine-rich coatings to potentially promote cell adhesion, proliferation, and differentiation, and reduce microbial colonization: strategies for generation and characterization. Macromolecular bioscience, 11(8), 983-990.

Gonz, R., & Guti, I. (2009). A shrinking core model for the alkaline hydrolysis of PET assisted by tributylhexadecylphosphonium bromide. Chemical engineering journal, 146(2), 287-294.

Groen, J. C., Peffer, L. A. A., & Javier, P. (2003). Pore size determination in modified micro- and mesoporous materials. Pitfalls and limitations in gas adsorption data analysis, 60(1-3), 1-17.

Guo, X., Xia, B., Lu, X., Zhang, Z., Li, Z., Li, W., Deng, L., Tan, M., & Huang, Y. (2016). Grafting of mesenchymal stem cell-seeded small intestinal submucosa to repair the deep partial-thickness burns. Connective tissue research, 57(5), 388-397.

Hsiang, S.W., Lee, H.C., Tsai, F.J., Yao, C.H. & Chen, Y.S. (2011). Puerarin accelerates peripheral nerve regeneration. American journal of Chinese medicine, 39(6),1207-1217.

Karageorgiou, V. (2005). Porosity of 3D biomaterial scaffolds and osteogenesis. Biomaterials, 26(27), 5474-5491.

Khorramnezhad, M., Akbari, B., Akbari, M., & Kharaziha, M. (2021). Effect of surface modification on physical and cellular properties of PCL thin film. Colloids and surfaces B: biointerfaces, 200(3), 111582-111590.

Kotsilkova, R., Angelova, P., Angelov, V., Batakliev, T. (2019). Acid composite films with graphene and carbon nanotubes produced by solution blending and extrusion. Coatings, 9(6), 359-364.

Krithica, N., Natarajan, V., Madhan, B., Sehgal, P. K., & Mandal, A. B. (2012). Type I collagen immobilized poly(caprolactone) nanofibers: characterization of surface modification and growth of fibroblasts. Advanced engineering materials, 14(4),149-154.

Labet, M., & Thielemans, W. (2009). Synthesis of polycaprolactone : a review. Chemical society reviews, 38(12), 3484-3504.

Lee, S. J., Khang, G., Lee, Y. M., & Lee, H. B. (2002). Interaction of human chondrocytes and NIH/3T3 fibroblasts on chloric acid-treated biodegradable polymer surfaces. Journal of biomaterials science, polymer edition, 13(2), 197-212.

Levya-Porras, C., Cruz-Alcantar, P., Espinosa-Solis, V., Martinez-Guerra, E. (2020). Application of differential scanning calorimetry (MDSC) in food and drug industries. Polymers (Basel), 12(1), 5-9.

Liu, X., Poon, R. W. Y., Kwok, S. C. H., Chu, P. K., & Ding, C. (2004). Plasma surface modification of titanium for hard tissue replacements, surface & coatings technology, 186(4), 227-233.

Luo, Y., Wu, C., Lode, A., & Gelinsky, M. (2013). Hierarchical mesoporous bioactive glass/alginate composite scaffolds fabricated by three-dimensional plotting for bone tissue engineering. Biofabrication, 5(1), 15005-15008.

Ma, Z., Kotaki, M., Yong, T., He, W., & Ramakrishna, S. (2005). Surface engineering of electrospun polyethylene terephthalate (PET) nanofibers towards development of a new material for blood vessel engineering. Biomaterials, 26(15), 2527-2536.

Mailly, D., Chappert, C., Mathet, V., Warin, P., Chapman, J. N., Magn, T., Jian, B., Gong, P., & Katsuyama, Y. (2003). Double-network hydrogels with extremely high mechanical strength. Advanced materials,15(14),1155-1158.

Man, D., Eksridge, C., Strouse, B., Niamat, D. (2013). Electrospun fiber membranes enable proliferation of genetically modified cells. International journal of nanomedicine, 8(2), 855-864.

Mohammadi, M., & Mashayekhan, S. (2020). Conductive multichannel PCL/gelatin conduit with tunable mechanical and structural properties for peripheral nerve regeneration. Journal of applied polymer science, 137(40), 49219-49221.

Moussa, M., & Banakh, O. (2012). Focal adhesion of osteoblastic cells on titanium surface with amine functionalities formed by plasma polymerization. Japanese journal of applied physics, 51(8), 1134-1140.

Munhoz, M. R., Dias, L. G., Breganon, R., Sabino, F., Ribeiro, F., Fracaro, J., Gonçalves, D. S., Hashimoto, E. M., Elias, C., & Munhoz, M. R. (2020). Analysis of the surface roughness obtained by the abrasive flow machining process using an abrasive paste with oiticica oil. International journal of advanced manufacturing, 106(2), 5061-5070.

Murphy, C. M., & O'Brien, F. J. (2010). Understanding the effect of mean pore size on cell activity in collagen-glycosaminoglycan scaffolds. Cell adhesion and migration, 4(3), 377-381.

Neu, C., Arastu, H., Curtiss, S., & Reddi, A. (2009). Characterization of engineered tissue construct mechanical function by magnetic resonance imaging. Journal of tissue engineering and regenerative medicine, 3(6), 477-485.

Niemczyk-Soczynska, B., Gradys, A., & Sajkiewicz, P. (2020). Hydrophilic surface functionalization of electrospun nanofibrous scaffolds in tissue engineering. Polymers, 12(11), 1-20.

Nishida, H., & Tokiwa, Y. (1995). Confirmation of colonization of degrading bacterium strain SC-17 on poly(3-hydroxybutyrate) cast film. Journal of environmental polymer degradation, 3(4), 187-197.

O'Sullivan, D., O'Neill, L., & Bourke, P. (2020). Direct plasma deposition of collagen on 96-well polystyrene plates for cell culture. ACS omega, 5(39), 25069-25076.

Olaru, N., & Olaru, L. (2010). Electrospinning of cellulose acetate phthalate from different solvent systems. Industrial and engineering chemistry research, 49(4), 1953-1957.

Pan, Y., Liu, L., Zhang, Y., Song, L., Hu, Y., & Jiang, S. (2019). Effect of genipin crosslinked layer-by-layer self-assembled coating on the thermal stability, flammability, and wash durability of cotton fabric. Carbohydrate polymers, 15(206), 396-402.

Parak, A., Pillay, V., Choonara, Y., Du Toit, L., & Kumar, P. (2019). The effect of various chemical modifications on the physicomechanical properties of 3D bioprinted scaffolds for tissue engineering [Master of Pharmacy dissertation, The University of the Witwatersrand].

Peña, C., De, K., Eceiza, A., Ruseckaite, R., & Mondragon, I. (2010). Enhancing water repellence and mechanical properties of gelatin films by tannin addition. Bioresource technology, 101(17), 6836-6842.

Pitt, G. G., Gratzl, M. M., Kimmel, G. L., Surles, J., & Sohindler, A. (1981). Aliphatic polyesters II. The degradation of poly (d,l-lactide), poly (ε-caprolactone), and their copolymers In Vivo. Biomaterials, 2(4), 215-220.

Podgornik, B., & Viˇ, J. (2009). Influence of surface preparation on roughness parameters. Wear, 266 (3-4), 482-487.

Polini, A., Pagliara, S., Stabile, R., Netti, S., Roca, L., Prattichizzo, C., Gesualdo, L., & Pisignano, D. (2010). Collagen-functionalised electrospun polymer fibers for bioengineering applications. Soft matter, 6(1), 1668-1672.

Ramburrun, P., Kumar, P., Choonara, Y. E., du Toit, L. C., & Pillay, V. (2019). Design and characterisation of PHBV-magnesium oleate directional nanofibers for neurosupport. Biomedical materials, 14(6), 65015-65019.

Ravi, M., Song, S., Wang, J., Nadimicherla, R., & Zhang, Z. (2016). Preparation and characterization of biodegradable poly(ε-caprolactone)-based gel polymer electrolyte films. Ionics: international journal of ionics, the science and technology of ionic motion, 22(5), 661-670.

Ron, G., Menorca, B., S, T., Fussell, B., John, C., & Elfar, M. (2015). Peripheral nerve trauma: mechanisms of injury and recovery. Hand clinics, 29(3), 317-330.

Roux, S., & Demoustier-champagne, S. (2003). Surface-initiated polymerization from poly(ethylene terephthalate). Journal of polymer science part A-polymer chemistry, 41(9), 1347-1350.

Roxin, P., Karlsson, A., & Singh, S. K. (1998). Characterization of cellulose acetate phthalate (CAP). Drug development and industrial pharmacy, 24(11), 1025-1041.

Siemionow, M., Bozkurt, M., & Zor, F. (2010). Regeneration and repair of peripheral nerves with different biomaterials: review. Microsurgery, 30(7), 574-588.

Sing, K. S., Everett, D., Haul, R. A., Moscou, L., Pierotti, R., Rouquerol, J., & Siemieniewska, T. (1985). Reporting physisorption data for gas/solid systems with special reference to the determination of surface area and porosity. Pure and applied chemistry, 57(4), 603-619.

Sorkin, R., Greenbaum, A., David-pur, M., Anava, S., Ayali, A., Ben-Jacob, E., & Hanein, Y. (2009). Process entanglement as a neuronal anchorage mechanism to rough surfaces. Nanotechnology, 20(1), 15101-15108.

Su, T., Jiang, H., & Gong, H. (2008). Thermal stabilities and the thermal degradation kinetics of polycaprolactone. Journal of materials science, 44(1), 170-178.

Sun, M., & Downes, S. (2007). Solvent-cast PCL films support the regeneration of NG108-15 nerve cells. The international society for optical engineering, 6423(1), 1-8.

Sun, M., & Downes, S. (2009). Physicochemical characterisation of novel ultra-thin biodegradable scaffolds for peripheral nerve repair. Journal of materials science: materials in medicine, 20(2), 1181.

Svahn, F., Kassman-rudolphi, Å., & Wallén, E. (2003). The influence of surface roughness on friction and wear of machine element coatings. Wear, 254(2), 1092-1098.

Tang, Z. G., Black, R. A., Curran, J. M., Hunt, J. A., Rhodes, N. P., & Williams, D. F. (2004). Surface properties and biocompatibility of solvent-cast poly[ε-caprolactone] films. Biomaterials, 25(19), 4741-4748.

Tapia-Blácido, D.R., do Amaral Sobral, P.J., Menegalli, F.C. (2013). Effect of drying conditions and plasticizer type on some physical and mechanical properties of amaranth flour films. LWT-food science and technology, 50(2), 392-400.

Van De Velde, K., & Kiekens, P. (2002). Biopolymers: Overview of several properties and consequences on their applications. Polymer testing, 21(4), 433-442.

Vijayavenkataraman, S., Thaharah, S., Zhang, S., Lu, W. F., Ying, J., & Fuh, H. (2019). 3D-printed PCL/rGO conductive scaffolds for peripheral nerve injury repair. Artificial organs, 43(23), 515-523.

Wang, P., & Koberstein, J. T. (2004). Morphology of immiscible polymer blend thin films prepared by spin-coating. Macromolecules, 37(15), 5671-5681.

Woodruff, M. A., & Hutmacher, D. W. (2010). Progress in polymer science: the return of a forgotten polymer-polycaprolactone in the 21st century. Progress in polymer science, 35(1), 1217-1256.

Yang, S., Chen, G., Lv, C., Li, C., Yin, N., Yang, F., & Xue, L. (2018). Evolution of nanopore structure in lacustrine organic-rich shales during thermal maturation from hydrous pyrolysis, Minhe Basin, Northwest China. Energy exploration & exploitation, 36(6), 265-281.

Yang, Z, Zhengwei, M., & Changyou, G. (2013). Aminolysis-based surface modification of polyesters for biomedical applications. RSC advances, 3(2), 2509-2519.

Yang, Zhe, Peng, H., Wang, W., & Liu, T. (2010). Crystallization behavior of poly(ε-caprolactone)/ layered double hydroxide nanocomposites. Journal of applied polymer science, 116(5), 2658-2667.

Yannas, I. V. (1992). Tissue regeneration by use of glycosaminoglycan copolymer. Clinical materials, 9(3-4), 179-187.

Zhang, X. F., O'Shea, H., Kehoe, S., & Boyd, D. (2011). Time-dependent evaluation of mechanical properties and In Vitro cytocompatibility of experimental composite-based nerve guidance conduits. Journal of the mechanical behavior of biomedical materials, 4(7), 1266-1274.

Zhu, Y., Gao, C., Liu, X., & Shen, J. (2002). Surface modification of polycaprolactone membrane via aminolysis and biomacromolecule immobilization for promoting cytocompatibility of human endothelial cells. Biomacromolecules, 3(6), 1312-1319.

CHAPTER 4:
FABRICATION OF TWO-DIMENSIONAL BIOACTIVE THIN FILMS FOR ENHANCED NEUROCOMPATIBILITY

4.1 Introduction

Synthetic materials have excellent bulk and processing properties, however, their polymeric chains lack cell-interactive moieties and often under-perform during *In Vitro* studies, as observed in Chapter 3. The proposed reason for this is as follows: integrin receptors on cells bind to the extracellular matrix. More specifically, they recognize Arg-Gly-Asp amino acid (RGD) sequences in the extracellular matrix, making these binding sites paramount for cell adhesion, growth acceleration and providing an environment suitable for optimal cellular function (Dulnik et al., 2016). There are numerous natural polymers which contain these cell-interactive domains, such as collagen, laminin, fibronectin, gelatin, sodium alginate and elastin. However, they are limited by poor mechanical properties (Ikada, 1994; Ruoslahti, 1996). A simple solution to this dilemma is the biofunctionalization of synthetic polymers to provide these cell-platform interaction sites required for neuronal cell attachment, proliferation, differentiation, and migration (Bellis, 2011).

Collagen, gelatin, and sodium alginate were the biomolecules chosen to modify the films in this study based on their numerous advantages and wide range of application in neural tissue engineering. Collagen is a well-known, successful biomaterial in neural tissue engineering (Wangensteen & Kalliainen, 2010). Its success has prompted the commercial availability of collagen-based scaffolds such as NeuraGen® and Neuromax®, which have proved to be highly effective in nerve reconstruction in 43% of patients in a clinical trial (Wangensteen & Kalliainen, 2010). Collagen-based nerve conduits are the most biocompatible nerve guides currently available in clinical settings, and their efficacy is often comparable to the clinical gold standard, autologous nerve grafting (Boni et al., 2018). Gelatin is a denatured protein obtained by acid or alkaline hydrolysis of animal collagen and has a long history of safe use in pharmaceuticals, cosmetics, and food products due to its broad array of advantages, including low cost, high availability, high biocompatibility, and biodegradability (Pabari et al., 2011). As a denatured product, gelatin is less antigenic than collagen and its chemically modifiable structure allows modulation of cell adhesion and proliferation, improving the biological behavior of a polymeric device upon implantation (Su & Wang, 2015).Alginate is a naturally occurring anionic biopolymer usually obtained from brown seaweed (Lee & Mooney, 2012). Alginate has found growing interest in tissue engineering due to its excellent biocompatibility, low toxicity, low-cost, and unique gelation characteristics (Lee & Mooney, 2012). Alginate gels have been particularly useful for tissue engineering purposes, promoting the regeneration of blood vessels, bones, cartilage, muscle, pancreas, liver, and nerves. Studies have shown that

alginate gels promote nerve regeneration across gaps of a variety of sizes (Suzuki et al., 1999, Hashimoto et al., 2002).

Genipin is a naturally occurring cross-linking agent which is derived from the fruits *Genipa americana* and *Gardenia jasminoides* (Chiono et al., 2008). Genipin has the ability to covalently cross-link with amino acids or proteins to form dark blue pigments and is reported to be 5000-10000 times less cytotoxic than other frequently used cross-linking agents such as glutaraldehyde, which has streamlined its eminent use as a crosslinker for biomedical applications (Wang et al., 2013). Genipin has inherent anti-inflammatory and anti-angiogenic properties as it impedes lipid peroxidation and nitric oxide production (Nickerson et al., 2006). In addition, genipin has the ability to protect the hippocampal neurons from the toxicity of Alzheimer's amyloid beta protein (Manickam et al., 2014). Genipin has been approved for food use in Japan, Korea, Taiwan and South-Eastern Asia (Nickerson et al., 2006).

In conclusion, the biomolecules discussed above were chosen to modify the thin films, using genipin as the crosslinker. The addition of bioactive molecules to the thin films has been found to enhance cell-film interactions due to the presence of cell interactive RGD sequences on their backbones, which will provide a solution to the relatively low cell attachment observed for the non-bioactive thin films in Chapter 3.

4.2 Materials and Methods

SDS and PBS were purchased from Sigma-Aldrich (St. Louis, MO, USA). Ethanol was purchased from LabChem, Edenvale, Johannesburg, South Africa. Chloroform, acetone, DMSO and 2-propanol were purchased from Associated Chemical Enterprises, Southdale, Johannesburg, South Africa. NaOH and KOH pellets were purchased from Merck, Darmstadt, Germany. Millipore water was used for washing of preparations. DMEM, Trypan Blue, penicillin/streptomycin, cell culture treated well plates, flasks, DES, Cellcrown^{TM} Inserts and FBS were purchased from Sigma Aldrich, South Africa. The Ham's F12 Nutrient Mixture was purchased from Gibco (Thermo Fischer, South Africa). The Roche Cell Proliferation Kit II (XTT) was purchased from Sigma Aldrich, South Africa. The PC12 and A172 cells were purchased from Cellonex (Separations, South Africa). Genipin was purchased from Challenge Bioproducts Co. Ltd. (Yun-Lin Hsien, Taiwan). Gelatin (Bloom 160, type B) derived from bovine skin was purchased from Fluka (Steinheim, Germany). Collagen derived from bovine Achilles' tendon was purchased from Sigma-Aldrich (St Louis, MI, USA). Mammoth powerful grip double sided transparent tape was purchased from Builders Warehouse, South Africa. The bicinchoninic acid (BCA) protein kit was purchased from Pierce (Thermofischer, South Africa).

4.2.1 Method of bio-active thin film fabrication

The aminolyzed thin films from the Chapter 3 were used to facilitate the covalent attachment of collagen, sodium alginate, gelatin onto the surface of the films, using genipin as the crosslinker. The aminolyzed films were washed in deionised water and air-dried prior to use. A 0.5% w/v stock solution of collagen was prepared in 2% v/v acetic acid in distilled water. 0.5% w/v stock solutions of gelatin and sodium alginate were prepared in distilled water. All stock solutions were stored at 2-8 °C until further use. The aminolyzed films were immersed in 1 ml of each biomolecule stock solution in a glass vial for 24 h at 37 °C in an orbital shaker to allow for the electrostatic interaction between the films and the biomolecule. Thereafter, 1% w/v genipin solution was prepared in 50:50 ethanol: water solution. Thereafter, 1 ml of this genipin solution was added to each vial and allowed to cross-link for 5 days in an orbital shaker set at 37 °C. The films were then removed from the solutions and washed three times in deionised water to remove excess biomolecule and left to dry overnight. Method adapted from Chang (2009).

Control samples were prepared, which included aminolyzed PCL/CAP films (PCL/CAP-EDA) which were soaked in each biomolecule for five days, without the addition of the crosslinker. These films were merely coated with the biomolecules. Another control prepared was the aminolyzed films coated with genipin only, without the addition of the biomolecules. Table 4.1 summarises the various samples prepared.

Table 4. 1 Sample abbreviations and relative compositions.

Sample name	Composition
PCL/CAP-EDA	Aminolyzed polycaprolactone/cellulose acetate phthalate films.
PCL/CAP-EDA-GEN	Aminolyzed films coated with genipin.
PCL/CAP-EDA-COLL	Aminolyzed films coated with collagen.
PCL/CAP-EDA-GEN-COLL	Aminolyzed films crosslinked to collagen using genipin.
PCL/CAP-EDA-SA	Aminolyzed films coated with sodium alginate.
PCL/CAP-EDA-GEN-SA	Aminolyzed films crosslinked to sodium alginate using genipin.
PCL/CAP-EDA-GEL	Aminolyzed films coated with gelatin.
PCL/CAP-EDA-GEN-GEL	Aminolyzed film crosslinked to gelatin using genipin.

4.2.2 Method of chemical integrity characterization employing FT-IR spectroscopy

FT-IR spectroscopy was used to detect the molecular transitions and changes in crystallinity indices of the films arising from interactions between the films, the biomolecules and the crosslinker. Samples were analysed over wavelengths of 4000-600 cm^{-1} using a PerkinElmer

Spectrum 2000 ATR-FT-IR (PerkinElmer 100, Llantrisant, Wales, UK) spectrometer fitted with a single-reflection diamond MIRTGS detector.

4.2.3 Method of thermodynamic behavior analysis utilizing differential scanning calorimetry

DSC (Mettler Toledo, Schwerzernback, Switzerland) was used to reveal the thermal properties of the modified samples. Samples of 2-10 mg were sealed in aluminium crucibles and heated over a temperature range of 0 °C-300 °C, at a rate of 10 °C min^{-1}. DSC curves were obtained by plotting sample weight over sample temperature. Measurements were done in duplicate.

4.2.4 Method of phase transition assessment utilizing x-ray diffraction analysis

X-ray diffraction analysis was employed in order to determine the phase changes (crystallinity or amorphous) between the unmodified and modified films. This characterization technique was performed on the Rigaku MiniFlex 600 Benchtop X-ray Diffractometer (Rigaku Corporation, Tokyo, Japan). The film samples were secured on a sample holder and were scanned at a rate of 15° per min with a diffraction angle range of 05-90° 2Θ with a degree step of 0.02, a voltage of 40 kV and a current of 15 mA.

4.2.5 Method of thermal stability evaluation utilizing thermogravimetric analysis

The determination of change in sample weight as a function of temperature was performed using TGA (PerkinElmer, TGA 4000, Llantrisant, Wales, UK). Samples were heated at a rate of 10˚C/min from 0-900˚C under continuous nitrogen purging. Thermograms were generated as percentage weight vs. temperature and analysed using Pyris TM software (PerkinElmer, Llantrisant, Wales, UK). The derivative curves were plotted for each sample to accurately determine the temperature and weight loss of each degradation step.

4.2.6 Method of surface topography characterization utilizing scanning electron microscopy

Evaluation of surface morphology and image capturing of the thin films were performed under different magnifications using an FEI Nova NanoLab 600TM SEM (FEI Company, Hillsboro, OR, USA). Samples were fixed to aluminium stubs using double-sided adhesive carbon tape and then sputter coated with carbon and gold palladium for 120 s (SPI ModuleTM Sputter-Coater and Control Unit, West Chester, PA, USA).

4.2.7 Method of porosimetric and surface area characterization using Brunauer-Emmet-Teller (BET) analysis

The porosity and surface area of the samples were analysed using the Micromeritics Porositometer (Micromeritics ASAP 2020, Norcross, GA, USA). Surface areas, pore sizes,

shapes, and distributions were assessed according to the parameters presented in Table A4 in the appendix and analyzed. The samples were prepared by heating and simultaneously evacuating gas over the sample to remove impurities. The prepared samples were then cooled with liquid nitrogen and analyzed by measuring the volume of gas adsorbed at specific pressures. Nitrogen adsorption-desorption isotherms were generated for each sample and analyzed.

4.2.8 Method of mechanical characterizations using Texture Analyser analysis

The mechanical properties of the thin films were determined with a Texture Analyser (TA.XTplus Texture Analyser, Stable Microsystems, Surrey, UK) fitted with two clamps. The width, height, and length of the samples were measured with a digital Vernier calliper (Krafft, DV150GW, Schoellerstr Düren, Germany). Rectangular 40 x 15 mm strips of each sample were fixed at 20 mm between the two clamps. Tests were conducted at 0.167 $mm.s^{-1}$ while applying a 0.5 N trigger force.

4.2.9 Method of hydrophilicity characterization utilizing water contact angle measurements

The hydrophilicity of the films was evaluated using the Contact Angle Goniometer (DataPhysics Instruments, Germany), by measuring the water contact angle using the sessile drop method. The samples were secured on the stage with double sided tape. Subsequently, a Hamilton syringe was used to dispense 2 µl distilled water onto the surface at a dosing rate of 2 $\mu l.s^{-1}$ on three random positions on the films The images of the water droplet were recorded by camera software after the droplet was stable. Thereafter, the average water contact angle was measured using the SCA202 version 4.1.12 build 1019 software.

4.2.10 Method of *In Vitro* degradation analysis

The *In Vitro* degradation study was performed by submersing 0.5 cm x 3 cm film samples in 2 ml PBS pH 7.4 contained in 24-well plates (n=3). An orbital shaking incubator maintained at 37 °C and set at 50 rpm was used for sample agitation. The medium was replaced every alternate day. Samples were removed at predetermined time intervals. Samples were then placed in the oven at 40 °C for 48 h to dry, then weighed again. Equation 4.1 was used to calculate the percentage degradation.

Equation 4. 1 $\%\ \text{Degradation} = [(wi-wf)/wi] \times 100$

Where wi is the initial weight of the film samples, wf is the weight of the final oven-dried samples (Ramburrun et al., 2019).

4.2.11 Method of *In Vitro* water-uptake analysis

The water-uptake study was performed by submersing 0.5 x 3 cm film samples in 2 ml PBS pH 7.4 contained in 24 well plates (n=3). An orbital shaking incubator maintained at 37 °C and set at 50 rpm was used for sample agitation. Samples were removed at predetermined time intervals; excess moisture was carefully removed by blotting with tissue paper and the change in mass was measured for determination of moisture absorption using Equation 4.2 (Ramburrun et al., 2019).

Equation 4. 2 % Water-uptake= [(wh-wi)/wi] x 100

Where wh is the mass of the hydrated samples and wi is the initial weight of the samples.

4.2.12 Method of biomolecule attachment quantification using BCA protein assay

The quantification of each biomolecule was undertaken using the BCA protein assay. The samples were washed three times in PBS. The samples were cut to 20 x 20 mm strips using digital callipers and a scalpel. Thereafter, each sample was immersed in 2 ml SDS solution (1% w/v) in distilled water at 37 °C in an orbital shaker bath for 48 h to remove the immobilized biomolecules from the films. The films were removed from the SDS solutions, and these solutions were used for the quantification assay. The BCA assay was used to detect adsorbed biomolecules according to the standard test tube protocol with the ratio of Reagent A and Reagent B at 50:1, known as the 'working reagent'. Following this, 2 ml working reagent was added to 0.1 ml of each sample and incubated at 37 °C for 30 mins. Thereafter, the samples were cooled, and the absorbance was read at 562 nm. A calibration curve was made by diluting 5 mg/ml of each biomolecule to various concentrations outlined in the protocol. Thereafter, 0.1 ml of each dilution was added to 2 ml working reagent and incubated for 30 mins at 37 °C. The samples were cooled, and the absorbance was read at 562 nm. Method adapted from Masaeli (2014).

4.2.13 Method of PC12 and A172 cell culture and cell viability quantification utilizing the XTT cytocompatibility assay

PC12 cells were cultured in cell culture treated T-75 flasks using Ham's F12 Nutrient Mixture supplemented with 15% v/v DES, 2.5% v/v FBS and 1% v/v penicillin/streptomycin solution. A172 cells were cultured in cell culture treated T-75 flasks using DMEM supplemented with 10% v/v FBS and 1% v/v penicillin/streptomycin solution. Both cell lines were cultured in a humid 5% CO_2 atmosphere at 37 °C. The culture medium was replaced at 75% confluency every two days.

For the detection of cell proliferation and cyto-compatibility of the films, the Cell Proliferation Kit II (XTT) was utilized. Film strips (5 mg) were sterilised with 70% ethanol and rinsed three times in sterile PBS. Thereafter, 1 ml of the respective media was added to a 12-well plate containing the sterilised sample and incubated for 24 h at 37 °C, 5% CO_2 and 97% humidity. The resultant liquids were termed ‘extraction media’. PC12 and A172 cells were seeded into 96-well plates at a density of 25 000 cells/ml in 90 µl cell culture media and incubated for 24 h. Thereafter, the media was replaced with 90 µl extraction media. For the negative control, 10 µl fresh media was added to a cell-containing well. The positive control was prepared by adding 10 µl of DMSO to a cell-containing well. Thereafter, all wells were incubated for 48 and 72 h. At the respective time points, activated XTT solution was prepared by combining the 5 ml XTT Reagent and the 0.1 ml Activation Reagent. Thereafter, 50 µl of the activated XTT solution was added to each well and incubated for 4 h. The absorbance was read at 450 nm and 660 nm using a multiplate reader (BioTek, USA). Method adapted from Khorramnezhad (2021).

4.2.14 Method of cell attachment visualization utilizing light microscopy

To visualize the PC12 and A172 cells on the films, films were sterilised with 70% v/v ethanol: water and cut to 1 cm x 1 cm strips. The films were rinsed three times in sterile PBS. The samples were sterilized for 15 mins under UV light and transferred to 12-well plates and secured to the bottom of the plates using double-sided transparent tape to prevent the films from floating in the media. PC12 and A172 cells were separately seeded onto each film at a density of 500 000 cells/ml and incubated for 48 h. Thereafter, light microscopy images were taken of the cells attached to the films using the Olympus, DP 80, Tokyo, Japan, equipped with LCmicro Software.

4.2.15 Method of cell attachment quantification using the trypan blue exclusion method

Samples were cut to 3 cm x 3 cm strips and rinsed three times in sterile PBS. The samples (n=3) were then UV sterilised for 15 mins and transferred to 6-well plates. The samples were secured to the bottom of the wells using sterile CellCrown™ Inserts to prevent the films from floating in the media. PC12 and A172 cells were each seeded at a density of 500 000 cells/ml onto the samples and incubated for 48 h. The control included cells seeded onto the bottom of the well plate in the absence of any sample. Thereafter, the media was aspirated and discarded. The samples were removed from the plates and placed in new 6-well plates. The samples were then rinsed three times with sterile PBS and 200 µl trypsin was added to each sample to detach the cells. Following this, 500 µl media was added to stop the trypsinization and was placed in sterile centrifuge tubes and centrifuged for 10 mins at 5000 rpm. The supernatant was discarded, and the cells were re-suspended with 50 µl fresh media. Trypan blue (10 µl) was added to 10 µl of the cell suspension and cells were manually counted using a haemocytometer. The percentage cell attachment was calculated by expressing the total

number of counted live cells on each film as a percentage of live cells counted on the control using Equation 4.3.

Equation 4. 3 % Cell attachment= (live cells on sample/ live cells on control) x 100

Statistical analysis

All samples were analysed in triplicate and the mean and standard deviations were recorded as computed. Student T-tests we performed for statistical significance for *In Vitro* studies. Samples with P values of $P \leq 0.05$ were considered to have a significant effect on the variable being investigated. All statistics and calibration curves were analysed on Microsoft Excel. All graphs were plotted using OriginPro 8.5 Software.

4.3 Results and discussions

4.3.1 Visual appearance of the bio-active thin films

The hydrolyzed films from the Chapter 3 were excluded from this study as genipin did not crosslink to the samples, since it only has the ability to covalently cross-link with amine groups, amino acids, or proteins to form dark blue pigments (Wang et al., 2013). Photographic images were taken of the aminolyzed film, the genipin coated film and the biomolecule crosslinked films to qualitatively assess the successful immobilization of the biomolecules onto the films through the color change. The films were placed in 6-well plates and secured using CellCrown™ Inserts for ease of imaging illustrated in Figure 4.1.

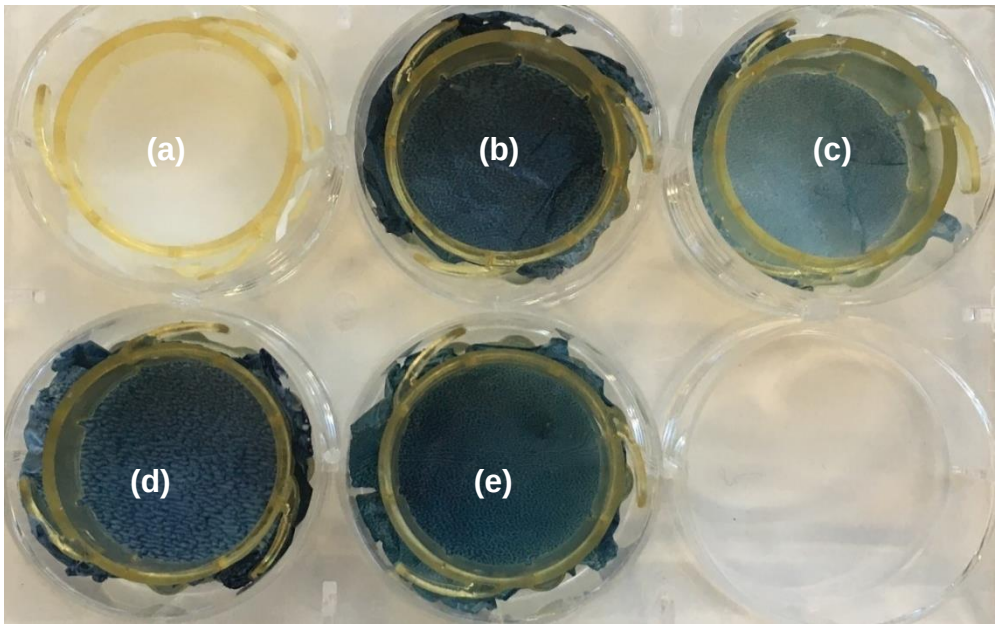


Figure 4. 1 Photographic image of the films secured in well plates (a) the aminolyzed film (b) the genipin crosslinked film, (c) the collagen crosslinked film, (d) the sodium alginate crosslinked film, (e) the gelatin crosslinked film.

The addition of genipin to the films changes the color from white to blue, indicating that effective crosslinking of the biomolecules has occurred onto the aminolyzed films (Nickerson et al., 2006), since genipin turns blue in the presence of primary amine groups (Wang et al., 2013). The biomolecule coated samples (PCL/CAP-EDA-COLL/SA/GEL), without genipin display no color change (not shown). To conclude, successful crosslinking was confirmed through the color change from white to blue.

4.3.2 Chemical integrity characterization of the thin films utilizing FT-IR

FT-IR was used to assess the chemical transition changes occurring upon biomolecule crosslinking and to evaluate whether successful crosslinking had occurred. Figure 4.2 represents the spectra obtained for the pristine biomolecule powders. Figure 4.3 highlights the spectra of genipin, collagen, sodium alginate and genipin.

Genipin (a) is characterized by a band at 984.95 cm^{-1} which corresponds to C-H ring out-of-plane bending, 1020 cm^{-1} which correlates to C-H ring in plane bending and 1617.65 cm^{-1} indicating C=C double bond ring stretch modes of the core genipin molecule (Kahoush et al., 2021). The band at 1678.37 cm^{-1} represents the carbonyl group of the ester in genipin (Arteche Pujana et al., 2013). The bands appearing at 3387.77 and 3204.18 cm^{-1} are due to the overlap of aromatic C-H and O-H vibrations (Arteche Pujana et al., 2013). The bands at 2948.90 and 2846.5 cm^{-1} are due to the C-H stretch vibration (Kahoush et al., 2021). The characteristic amide peaks in collagen (b) are detected at 3295 cm^{-1} corresponding to amide A and N-H stretching vibrations (Kahoush et al., 2021). This indicates hydrogen bonding between the two N-H groups. The band at 2928.42 cm^{-1} represents the amide B and asymmetric stretching of CH_2 (Kahoush et al., 2021). The band at 1627.9 cm^{-1} represents the amide I and C=O stretching vibrations (Kahoush et al., 2021). The band at 1547 cm^{-1} corresponds to amide II and N-H bending vibrations, and finally, the band at 1235 cm^{-1} represents amide III and C-H stretching (da Silva et al., 2021). Sodium alginate (c) shows important absorption bands regarding hydroxyl, ether, and carboxylic groups. Stretching vibrations of O-H bonds of alginate appear at 3288.16 cm^{-1} (Daemi & Barikani, 2012). Stretching vibrations of aliphatic C-H bands are observed at 2912 cm^{-1} (Daemi & Barikani, 2012). The peaks at 1598.37 and 1408.10 cm^{-1} are attributed to asymmetric and symmetric stretching vibrations of the carboxylate salt ion, respectively (Daemi & Barikani, 2012). The bands at 1087.44 and 943 cm^{-1} are attributed to the C-O stretching vibration of pyranosyl ring and the C-O stretching with contributions from C-C-H and C-O-H deformation (Daemi & Barikani, 2012). In terms of gelatin (d), two characteristic amide bands appear at 1630.96 cm^{-1} for amide I which are attributed to C=O stretching, and 1523.85 cm^{-1}, which is attributed to N-H bending for amide II (Rokhade et al., 2006). An N-H stretching band is observed at 3292.82 cm^{-1}. The peak at 2949.68 cm^{-1} is attributed to aliphatic C-H stretches (Rokhade et al., 2006). The peaks at 1445.35, 1338.24

and 1236.46 cm^{-1} represent C-H bending, C-H stretching and N-H bending (amide III), respectively (Rokhade et al., 2006).

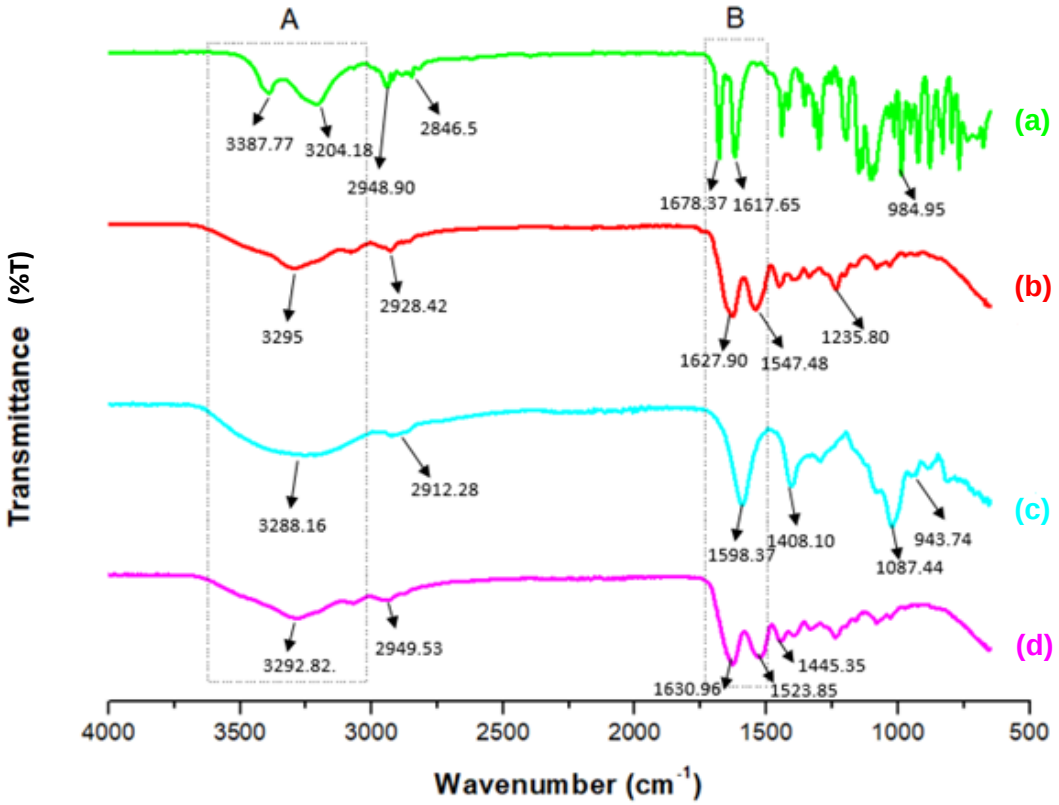


Figure 4. 2 Fourier-transform infrared spectra of (a) genipin, (b) collagen, (c) sodium alginate and (d) gelatin pristine powders showing two regions of interest: A and B.

The spectra in Figure 4.3 highlight two areas of interest: A and B, which compare the spectra of the aminolyzed film, the genipin coated film, and the biomolecule crosslinked films. The aminolyzed PCL/CAP films (black) display additional bands compared to the untreated PCL/CAP film as described in the preceding chapter. The band at ~1564.12 cm^{-1}, represents the N-H bending of the amide II group (Krithica et al., 2012). The smaller band at ~1585.8 cm^{-1} represents the C=O stretching of the amide I band (Krithica et al., 2012). These two peaks form part of one larger band. Further, the slight increase in intensity of the broad band at ~ 3500 cm^{-1} is due to the presence of a secondary amine group (Krithica et al., 2012). The addition of genipin to the aminolyzed films changes the chemical composition of the films as there is a relatively large increase in intensity of the peak at 3438.24 cm^{-1} in region A. In region B, there are two additional peaks at 1554.77 and 1640.71 cm^{-1}, corresponding to the amide I and amide II vibrations, respectively (Siritientong et al., 2013).These peaks are consistent with other FT-IR studies on genipin treated biopolymers (Sundararaghavan et al., 2008), confirming the crosslinking of genipin to the aminolyzed film. These features suggest that the carboxymethyl group of genipin reacts with the amino group of chitosan to form a secondary amide according to the literature (Dimida et al., 2017).

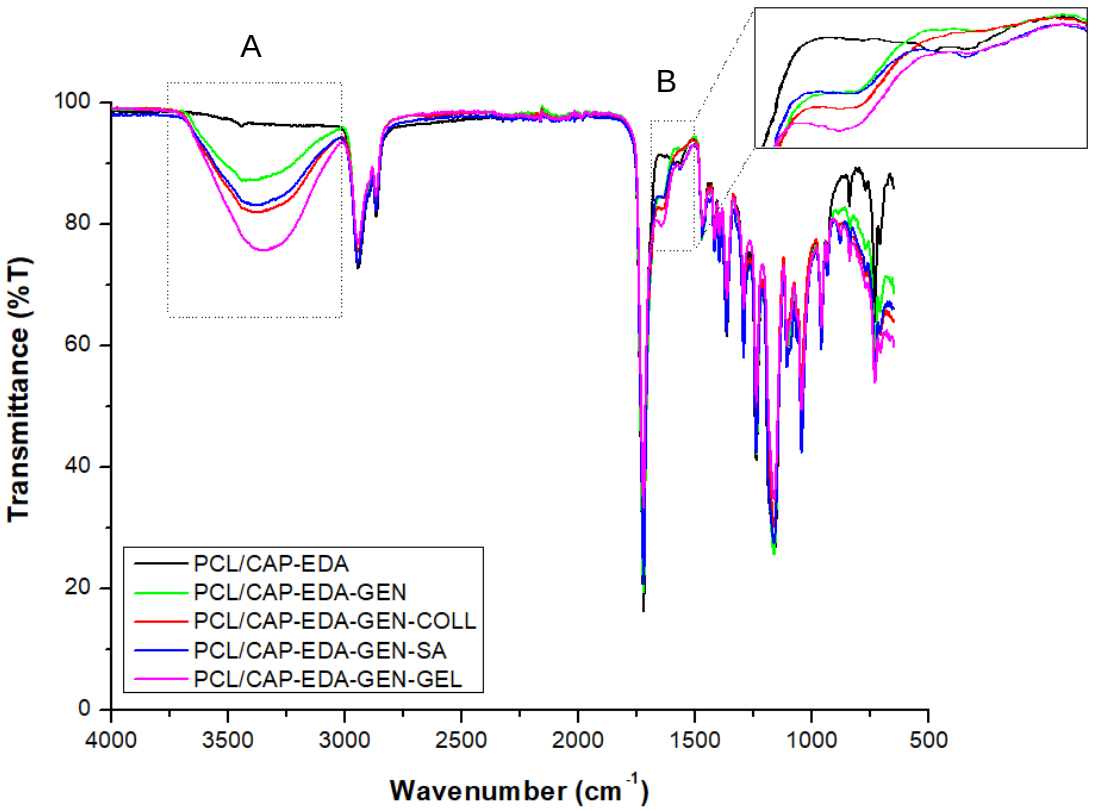


Figure 4. 3 Fourier-transfer infrared spectra of (PCL/CAP-EDA) aminolyzed film, (PCL/CAP-EDA-GEN) genipin crosslinked film, (PCL/CAP-EDA-GEN-COLL) collagen crosslinked film, (PCL/CAP-EDA-GEN-SA) so films, the genipin crosslinked films, the collagen crosslinked films, the sodium alginate crosslinked films and the gelatin crosslinked films.

The crosslinking mechanism between genipin and primary amines under basic conditions proceeds with the nucleophilic attack of genipin by the hydroxyl ions in aqueous solution, leading to a ring-opening reaction, and an intermediate aldehyde group is formed (Oryan et al., 2018). Subsequently, a Schiff reaction occurs between the terminal aldehyde groups on the polymerized genipin and the primary amines, forming a crosslinked network structure (Oryan et al., 2018; Yoo et al., 2011). Once collagen, sodium alginate and gelatin are immobilized on the films using genipin, there is an increase in the bands in region A, with sodium alginate causing the least increase in intensity compared to genipin and gelatin causing the highest increase in intensity. The reason for the increase in intensity of all three bands of the biomolecule-immobilized films is seen in Figure 4.2 (region A), where it can be seen that the pristine powders of collagen, sodium alginate and gelatin all have a relatively large band in the region (3500-3000 cm^{-1}). This corresponds to the N-H stretching of the NH_2 groups which confirms the successful immobilization of the biomolecules on the surface of the films (Mattanavee et al., 2009).

In region B, all the biomolecule-immobilized films have two distinct peaks in the same position as the PCL/CAP-EDA-GEN films (~ 1554.77 and 1640.71 cm^{-1}) yet are more intense. These bands correspond to protonated amine groups on the biomolecules (Kim et al., 2010;

Panzavolta et al., 2011) and their increase in intensity as compared to the aminolyzed films coated with genipin only, confirms their presence on the film surface (Krithica et al., 2012). Figures 4.4, 4.5 and 4.6 compare the FT-IR spectra of the biomolecule coated films (a) and the biomolecule crosslinked films (b).

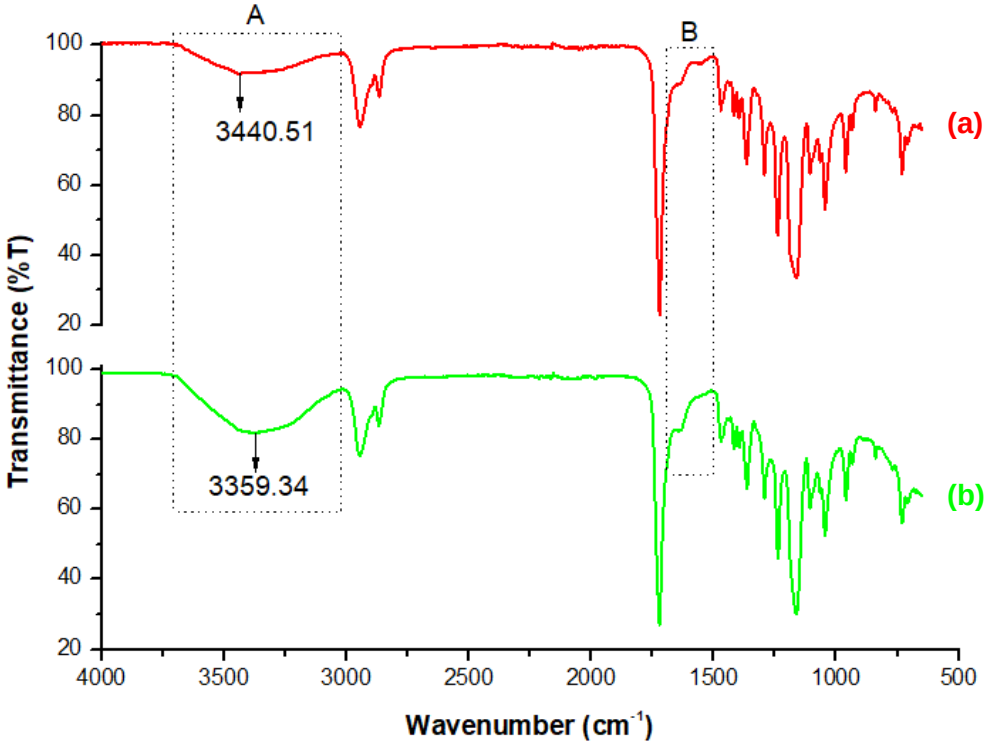


Figure 4. 4 Fourier-transform infrared spectra of (a) collagen coated and (b) collagen crosslinked films.

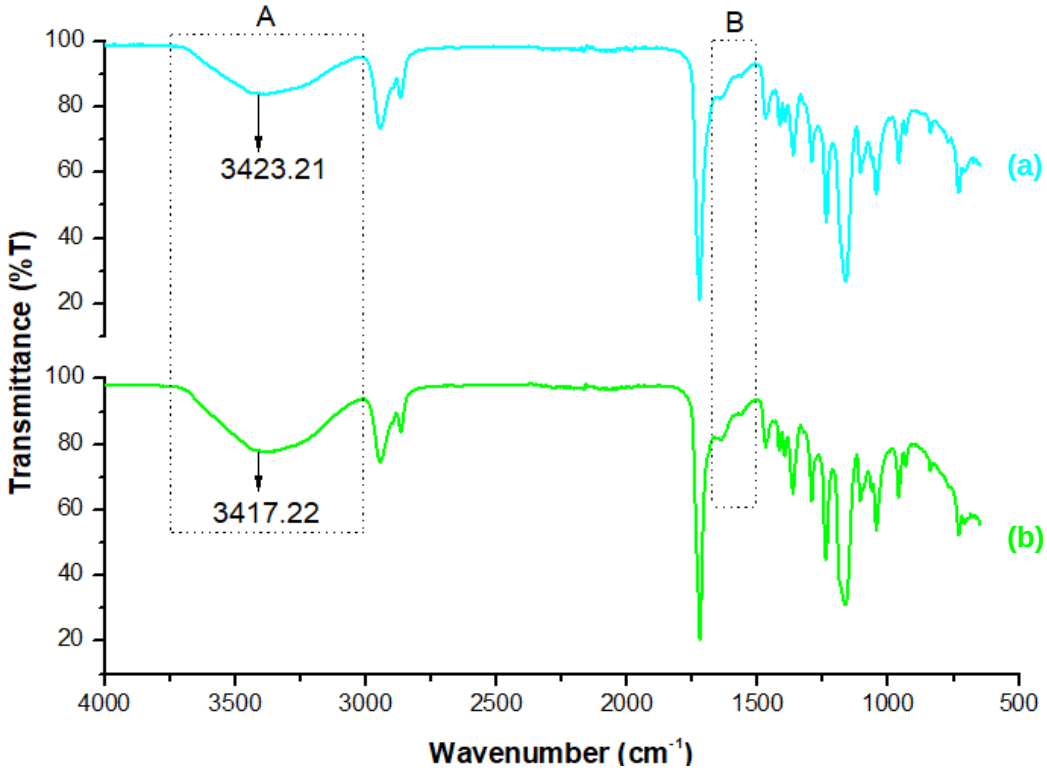


Figure 4. 5 Fourier-transform infrared spectra of (a) sodium alginate coated and (b) sodium alginate crosslinked film.

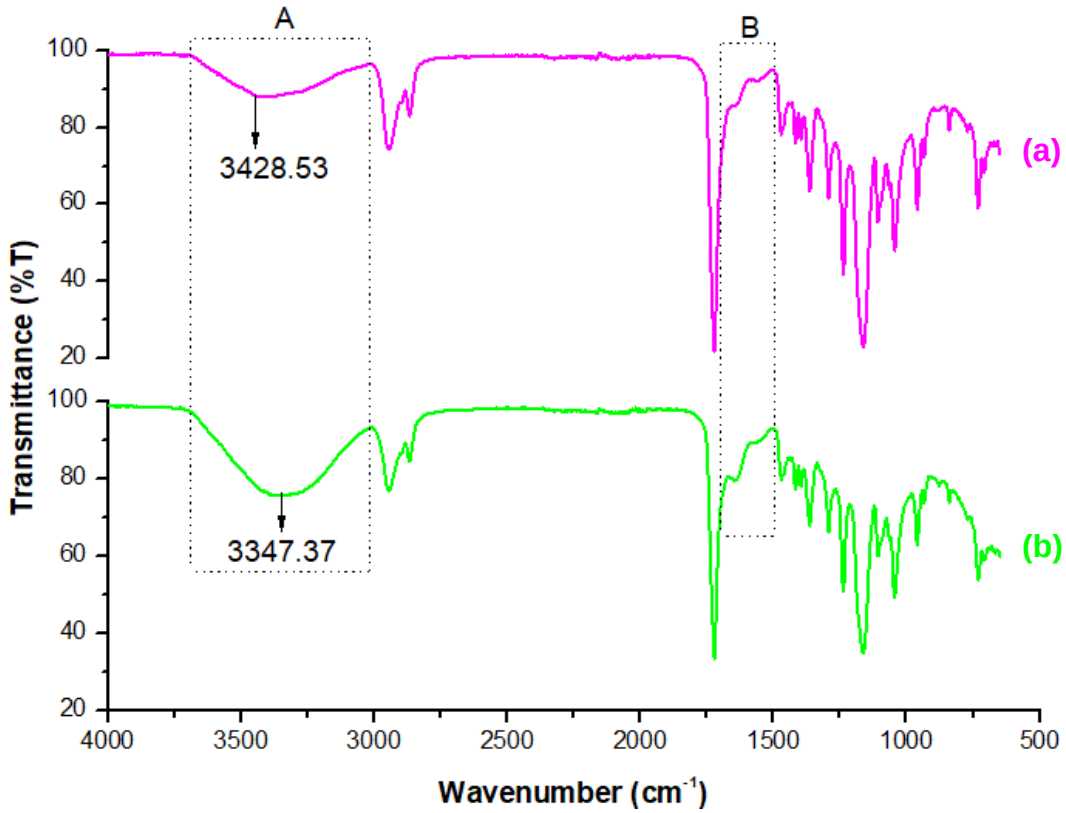


Figure 4. 6 Fourier-transform infrared spectra of (a) gelatin coated film and (b) gelatin crosslinked film.

Figures 4.4, 4.5 and 4.6 compare the biomolecule coated (a) and biomolecule crosslinked samples (b). Region A of each graph highlights that there is an increase in intensity of the spectra of (b) in comparison to (a). The amide A band of collagen, sodium alginate and gelatin (associated with the N-H stretching frequency) is usually found at 3325–3330 cm^{-1}. The broadening of the peak in (b) of Figure 4.4, 4.5 and 4.6 is possibly due to the hydrogen bonding associated with the biomolecules (Krithica et al., 2009). In terms of region B, the amide I band of the biomolecules is usually observed around 1650-1668 cm^{-1} and the amide II band of the biomolecules is centred in the range of 1530-1555 cm^{-1}, which corresponds to the N-H stretch coupled with C-N stretch (Kim et al., 2010; Panzavolta et al., 2011). Furthermore, there is a slight shift in wavenumber in (a) and (b) in region B, possibly due to the addition of the crosslinker, which contains O-H functional groups (Kosmala et al., 2017).

From this discussion, it is clear that the biomolecules have been successfully immobilized on to the aminolyzed films via genipin crosslinking (Kosmala et al., 2017; Krithica et al., 2012). Further, there is a clear difference between the biomolecule-coated samples and the biomolecule-crosslinked samples, highlighting that the biomolecules were indeed crosslinked to the films and not merely coated onto the films.

4.3.3. Analysis of the thermodynamic behavior of the thin films utilizing differential scanning calorimetry

DSC was conducted to evaluate the change of the thermal profiles of the samples following biomolecule modification. DSC thermograms were plotted and various parameters were calculated from them. The onset of melting, Tm, ∆hm, onset of degradation, Td and ∆hd were calculated to provide a detailed analysis on the changes that occurred following biomolecule modification and are presented in Table 4.2. The DSC thermograms of pristine genipin, collagen, sodium alginate and collagen are displayed in the Figure 4.7. Collagen, sodium alginate and gelatin exhibit a broad peak in the range of 25 to 125 °C, signifying the release of molecular water due to the rupturing of hydrogen bonds between the water molecules and the proteins around 88.98, 96.48 and 93.80 °C. respectively (Bozec & Odlyha, 2011; Samouillan et al., 2004). Thereafter, collagen and gelatin begin to degrade at 222.75 °C, representing the thermal degradation temperature of collagen and gelatin (Cui et al., 2007; Machado et al., 2002). The thermogram of sodium alginate depicts a sharp exothermic peak at ±239 °C which is related to its thermal decomposition (Rao et al., 2013). Genipin is characterized by a sharp endothermic peak at 123.11 °C, correlating to its melting temperature (Zu et al., 2014). Thereafter, genipin exhibits an exothermic peak at 252.4 °C, representing its thermal decomposition temperature (Zu et al., 2014).

Table 4. 2 Thermal profiles of the modified samples compared with the unmodified sample.

Sample	Onset of Melting (°C)	Tm[13] (°C)	∆hm[14] (mW .°C)	Onset of Degradation (°C)	Td[15] (°C)	∆hd[16] (mW.°C)
Aminolyzed films	34.36	60.34	128.38	353.85	406.89	507.74
Genipin crosslinked films	36.85	61.63	136.36	308.12	402.61	341.49
Collagen coated films	32.86	61.47	90.26	224.51	402.77	195.07
Sodium alginate coated films	34.53	61.15	67.12	315.60	405.88	384.96
Gelatin coated films	36.85	61.79	97.18	305.44	400.48	564.21
Collagen crosslinked films	36.19	62.27	120.86	351.36	403.58	461.76
Sodium alginate crosslinked films	40.99	60.83	52.49	331.75	405.73	257.02
Gelatin crosslinked films	41.65	61.15	81.23	337.23	404.42	384.08

[13] Melting temperature
[14] Enthalpy of melting
[15] Degradation temperature
[16] Enthalpy of degradation

Figures 4.8, 4.9 and 4.10 compare the DSC thermograms of the aminolyzed film, the genipin-coated film, the collagen-coated film, and the collagen crosslinked film using genipin. The onset of melting of the aminolyzed film occurs at 34.36 °C.

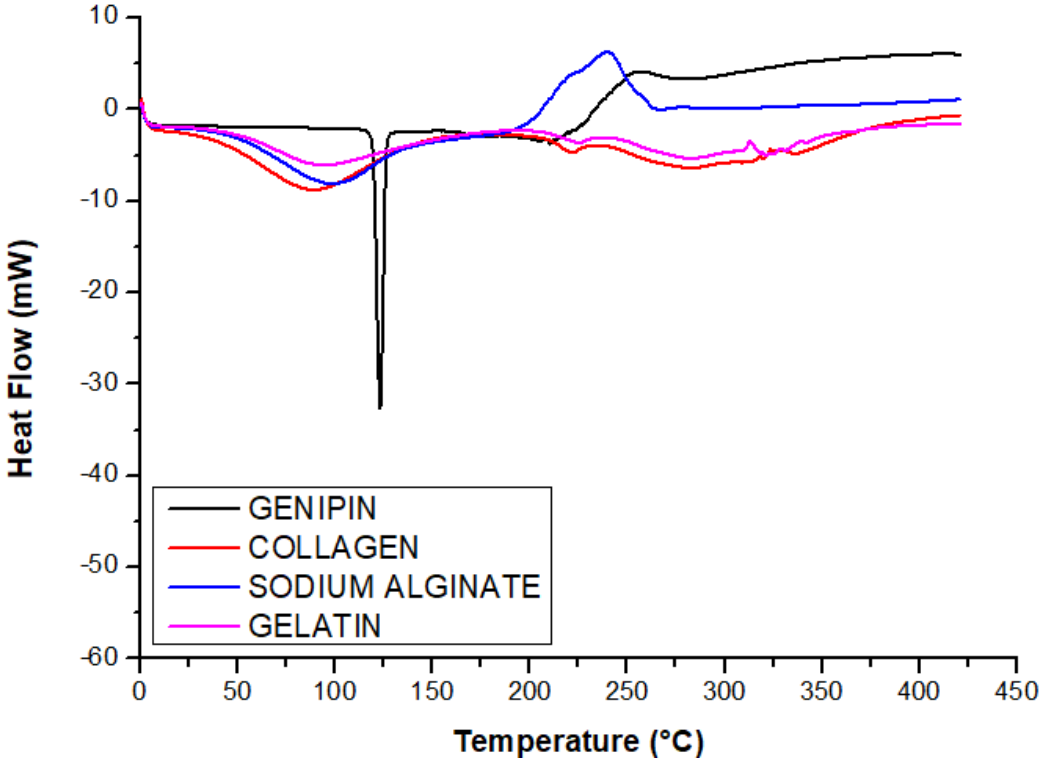


Figure 4. 7 Differential scanning calorimetry thermogram comparing pristine genipin, collagen, sodium alginate and gelatin.

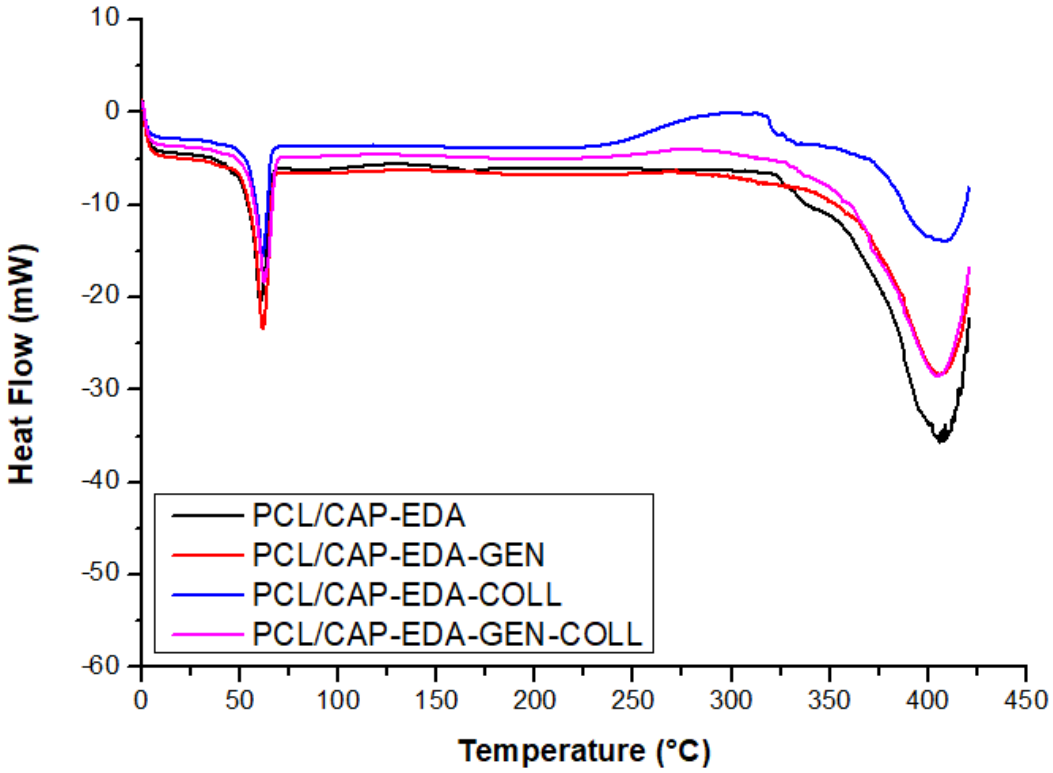


Figure 4. 8 Differential scanning calorimetry thermograms of (PCL/CAP-EDA) aminolyzed film, (PCL/CAP-EDA-GEN) genipin crosslinked film, (PCL/CAP-EDA-COLL) collagen coated film, (PCL/CAP-EDA-GEN-COLL) collagen crosslinked film.

The genipin coating increases the onset of melting to 36.85 °C, in addition to increasing in melting temperature, inferring an enhanced thermal stability during the onset of melting (Zu et al., 2014).The collagen coating increases the melting temperature to 61.47 °C. Finally, the collagen-crosslinked sample is compared to the collagen-coated sample to prove that there is a difference between the two and prove that the collagen crosslinked sample is crosslinked and not merely coated (Bruylants et al., 2020). The melting temperature is increased, as well as the onset of degradation, therefore indicating an enhanced thermal stability as compared to the collagen-coated film. This is also confirmed by TGA data in Section 4.3.5. This enhanced thermal stability is due to the presence of crosslinks, inferring that more energy is required to break the bonds (Bruylants et al., 2020; Vera-Graziano et al., 1995).

Figure 4.9 highlights that sodium alginate coating enhances the melting temperature of the sample in comparison to the aminolyzed sample, implying an increase in thermal stability (Bruylants et al., 2020). Sodium alginate crosslinking slightly reduces the melting temperature of the sample in comparison to the coated sample, however, the ∆hm and ∆hd of the crosslinked samples are reduced, indicating an enhanced thermal stability during melting and thermal degradation (Levya-Porras et al., 2020). The onset of degradation is increased from 315.6 to 331.75 °C, also inferring an enhanced thermal stability, proving the presence of crosslinks (Levya-Porras et al., 2020).

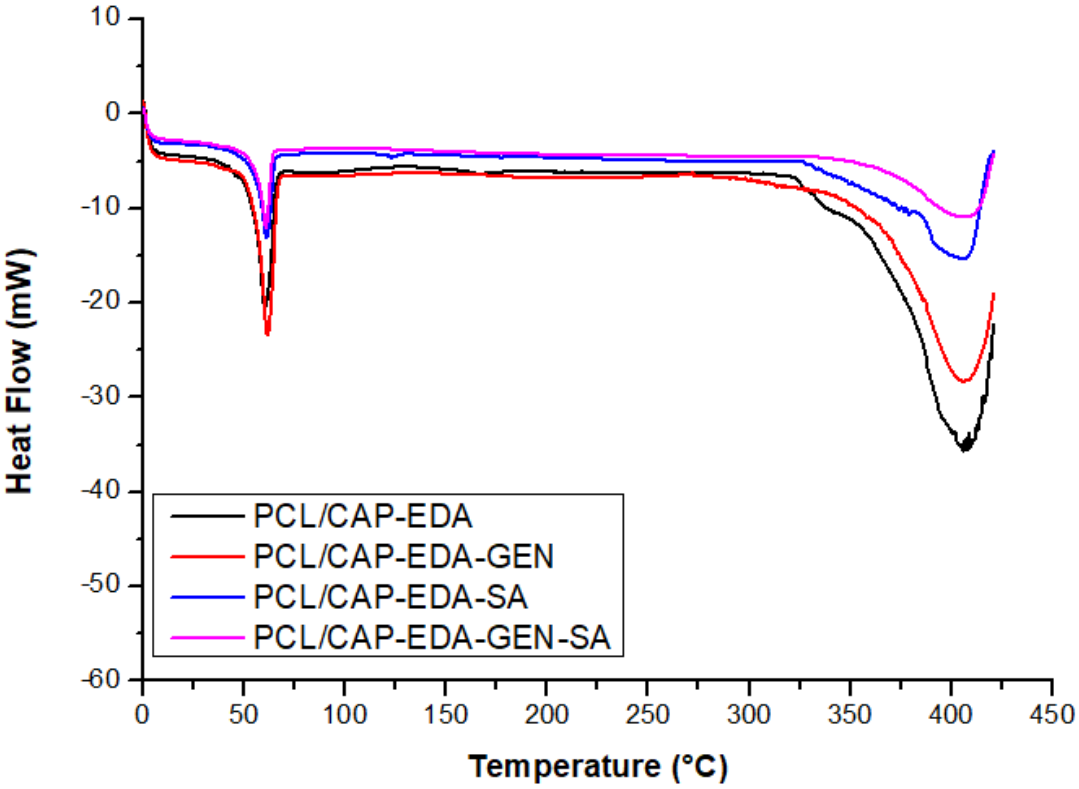


Figure 4. 9 DSC thermograms of (PCL/CAP-EDA) aminolyzed film, (PCL/CAP-EDA-GEN) genipin crosslinked film, (PCL/CAP-EDA-SA) sodium alginate crosslinked film, (PCL/CAP-EDA-GEN-SA) sodium alginate crosslinked film.

Figure 4.10 highlights that gelatin coating enhances the melting temperature of the aminolyzed sample, suggesting an enhanced thermal stability (Levya-Porras et al., 2020). The comparison of the gelatin-coated film and the gelatin crosslinked film indicates that the melting temperature of the crosslinked film is reduced, however, the onset of melting and degradation are enhanced in the crosslinked film. This relates to an enhanced thermal stability (Bruylants et al., 2020). Further, the ∆hm and ∆hd are both reduced, indicating an enhanced thermal stability as compared to the coated film (Bruylants et al., 2020).

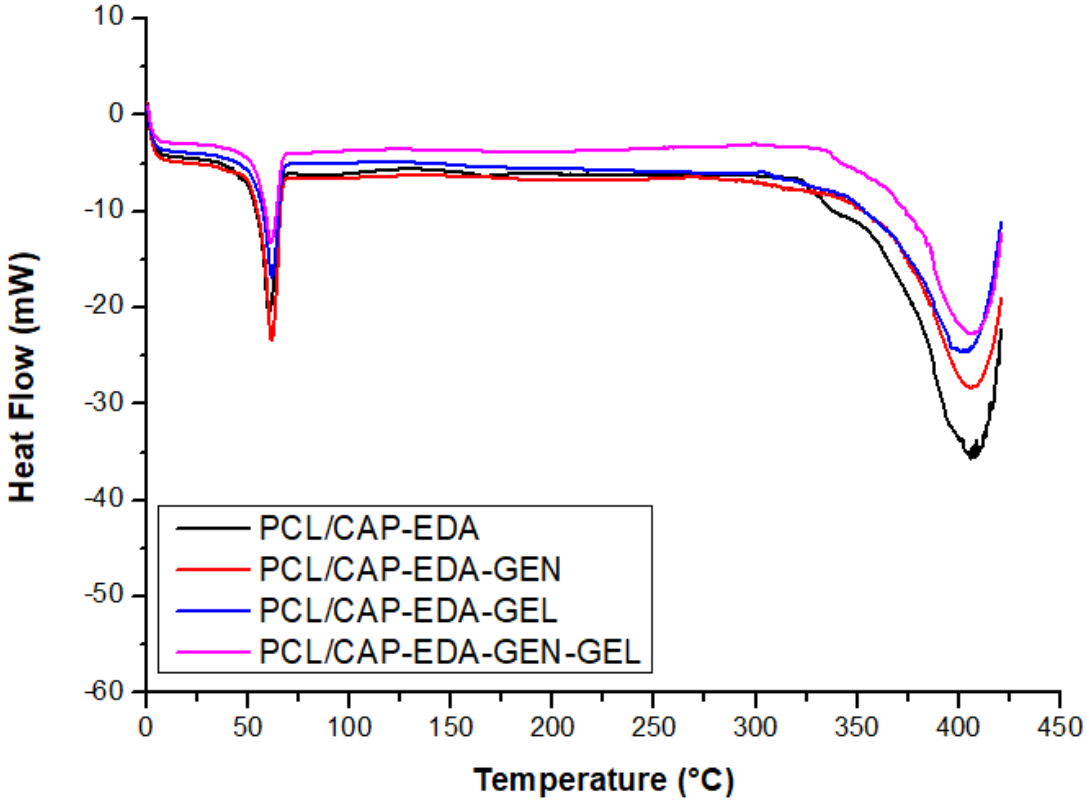


Figure 4. 10 DSC thermograms of (PCL/CAP-EDA) aminolyzed film, (PCL/CAP-EDA-GEN) genipin crosslinked film, (PCL/CAP-EDA-GEL) gelatin coated film, (PCL/CAP-EDA-GEN-GEL) gelatin crosslinked film.

In conclusion, the biomolecule coating on the samples enhances the thermal stability of the aminolyzed films. In addition, the films with crosslinked biomolecules demonstrate an enhanced thermal stability, which is due to the presence of the crosslinks.

4.3.4. Assessment of phase transitions of thin films utilizing x-ray diffraction analysis

X-ray diffraction characterizations were conducted to evaluate the microstructural modifications of the PCL/CAP films as a result of the surface and biomolecule modifications applied (Nagaraj et al., 2017). Morphological studies were performed to determine the phase transitions between the aminolyzed, the genipin coated, the biomolecule coated and the biomolecule crosslinked films. Table 4.3 highlights the differences in full width at half maximum (FWHM) values for the samples, which provides useful information regarding the degree of the

crystalline or amorphous nature of the films (Nagaraj et al., 2017). The higher the value, the broader the peak and the more amorphous/disordered the structure (Nagaraj et al., 2017).

Table 4. 3 representing the full width at half maximum values for the aminolyzed and modified samples.

Sample	Full width at half maximum value
Aminolyzed films	5.92
Genipin crosslinked films	0.59
Collagen coated films	3.42
Collagen crosslinked films	0.62
Sodium alginate coated films	0.54
Sodium alginate crosslinked films	1.24
Gelatin coated films	4.59
Gelatin crosslinked films	4.63
Pristine collagen	7.14
Pristine sodium alginate	10.66
Pristine gelatin	8.01

The XRD diffractograms of pristine collagen, sodium alginate and gelatin are presented in Figure 4.11. The XRD diffractograms of collagen and gelatin produce a characteristic broad, amorphous peak patten at ~ 22.12°, which is assigned to the triple-helical crystalline structure in collagen and gelatin (Peña et al., 2010; Yakimets et al., 2005). Sodium alginate produces three crystalline peaks at ~ 14, 21 and 37°, in alignment with literature (Dong et al., 2011).

The XRD patterns of all the films in Figure 4.12 show a sharp crystalline peak at a 2θ value of ~ 21.4° and a broad amorphous peak at ~ 22.04°, indicating the semi-crystalline nature of the films. The crosslinked samples should demonstrate the higher FWHM values in comparison to the coated samples since chemical crosslinking destroys the original hydrogen bonds that were beneficial to crystallization (Y. Liu et al., 2019), therefore are more amorphous, which can be used as one of the many indications that crosslinking took place. However, the collagen crosslinked samples present with a lower FWHM value in comparison to the collagen coated sample, but it is slightly enhanced in comparison to the genipin-coated sample (Y.Liu et al., 2019). This is not a conclusive measure of whether crosslinking took place, as the combination of FT-IR, TGA and DSC results led to the conclusion that collagen was crosslinked onto the film surface. Figures 4.12, 4.13 and 4.14 draw a comparison between the aminolyzed film, the genipin coated film, the collagen coated film and the collagen crosslinked film.

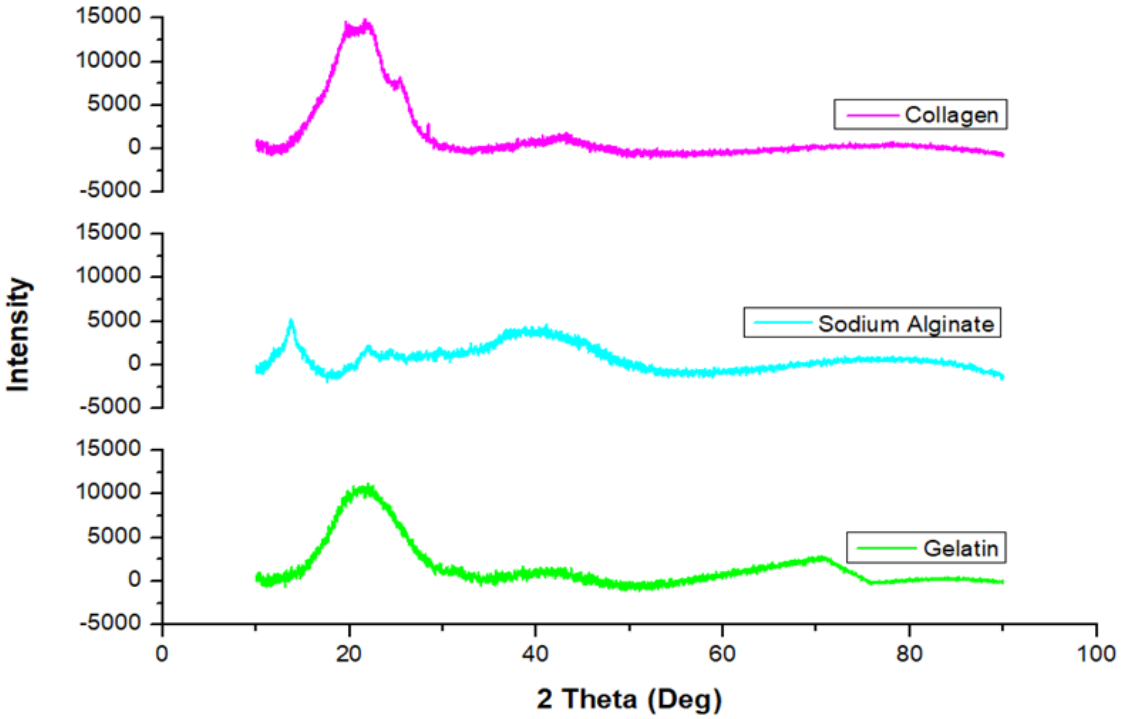


Figure 4. 11 X-ray diffraction pattern of pristine collagen, sodium alginate and gelatin.

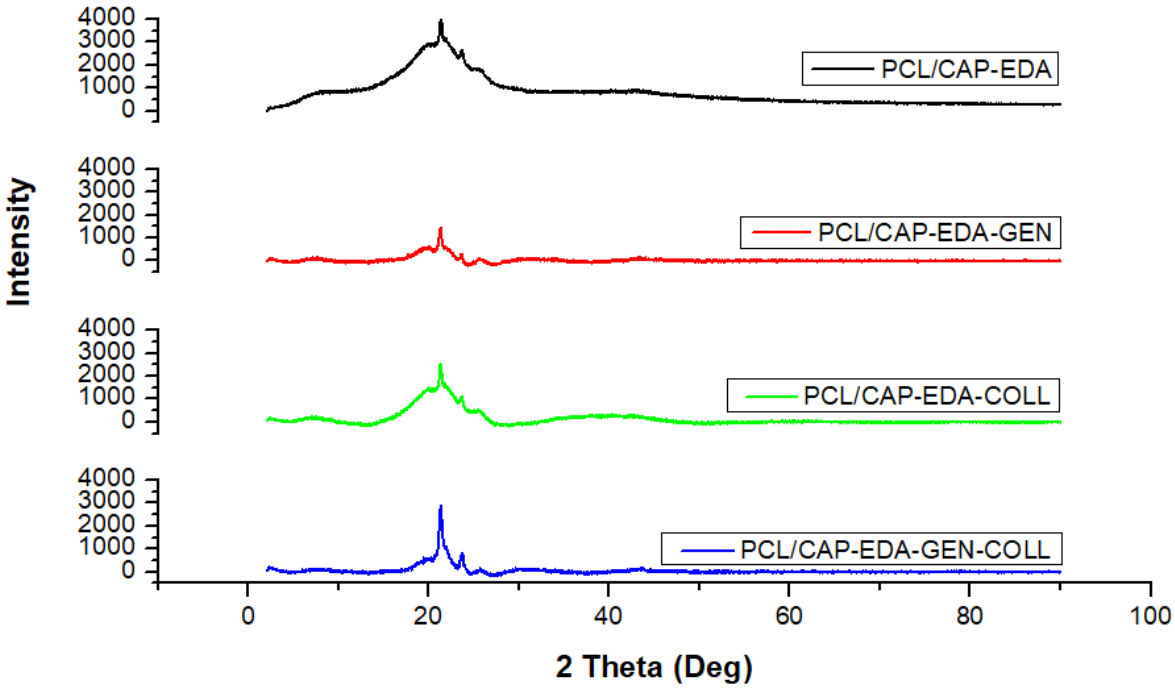


Figure 4. 12 X-ray diffraction pattern of (PCL/CAP-EDA) aminolyzed film, (PCL/CAP-EDA-GEN) genipin crosslinked film, (PCL/CAP-EDA-COLL) collagen coated film, (PCL/CAP-EDA-GEN-COLL) collagen crosslinked film.

Figure 4.13 draws a comparison between the aminolyzed film, the genipin coated film, the sodium alginate coated film and the sodium alginate crosslinked film. The FWHM value of the sodium alginate crosslinked sample in Figure 4.13 is significantly enhanced in comparison to the sodium alginate coated sample, indicating a reduction in crystallinity (Mateescu & Juha, 2002). This result is possibly attributed to the chemical crosslinking, which destroys the original

hydrogen bonds that are beneficial to crystallization, as described above (Mateescu & Juha, 2002), confirming the successful crosslinking of sodium alginate to the films.

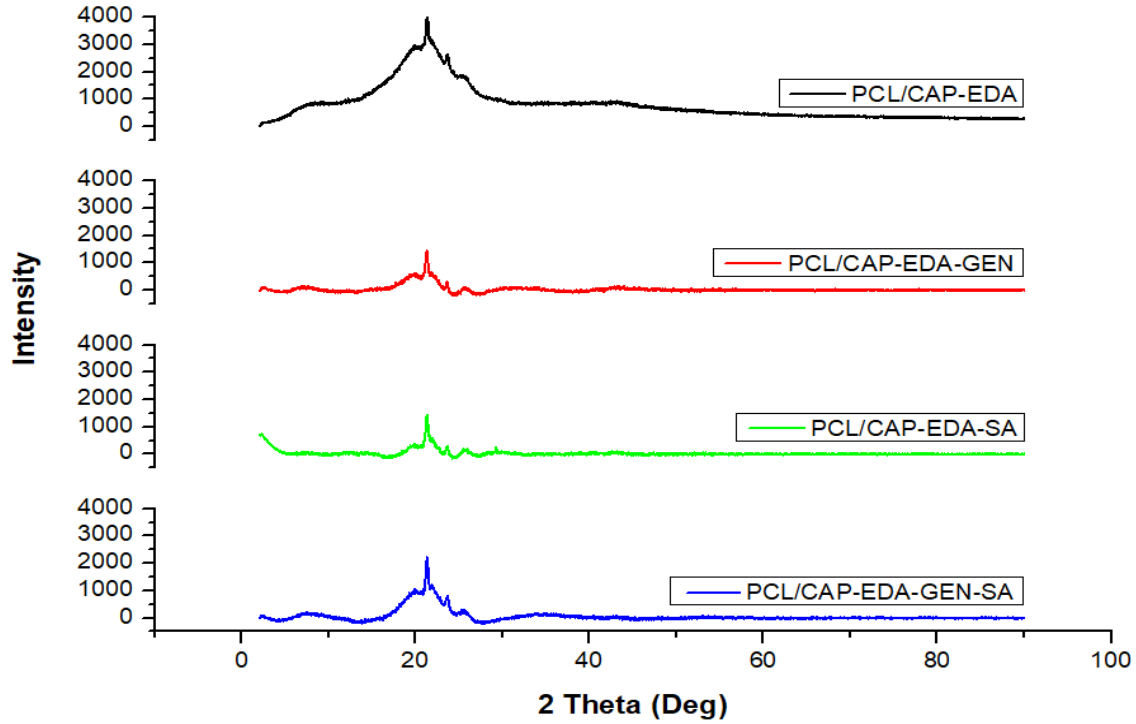


Figure 4. 13 X-ray diffraction patterns of (PCL/CAP-EDA) aminolyzed film, (PCL/CAP-EDA-GEN) genipin crosslinked film, (PCL/CAP-EDA-SA) coated film, (PCL/CAP-EDA-GEN-SA) sodium alginate crosslinked film.

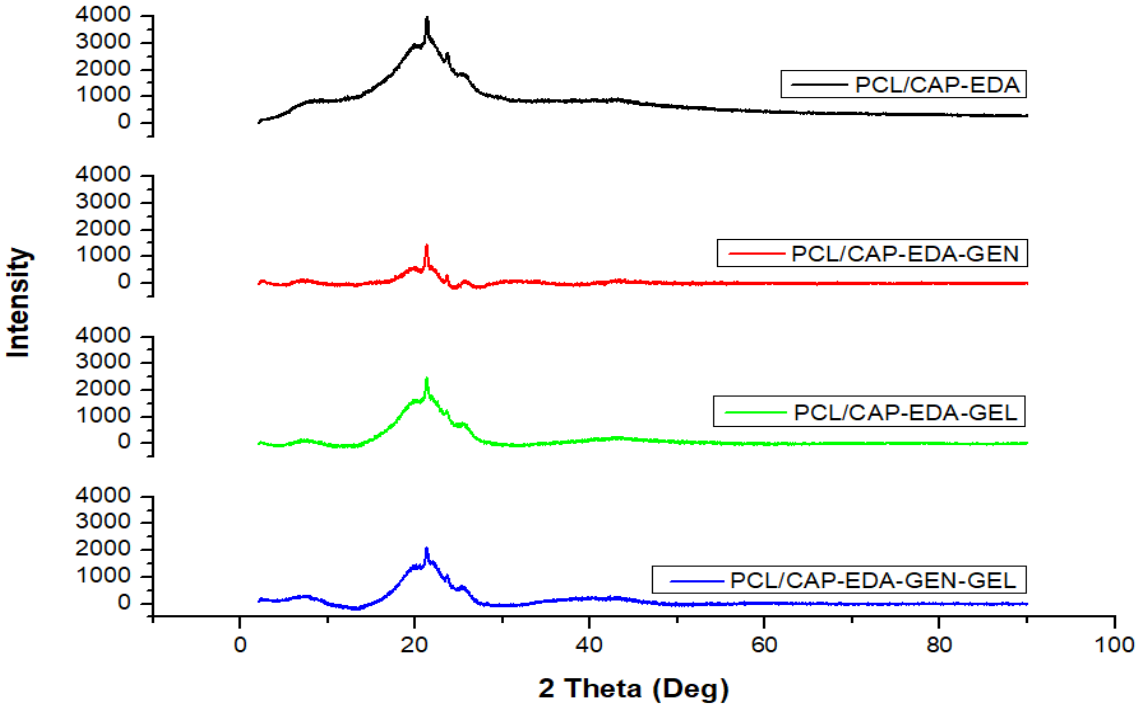


Figure 4. 14 X-ray diffractogram of (PCL/CAP-EDA) aminolyzed film, (PCL/CAP-EDA-GEN) genipin crosslinked film, (PCL/CAP-EDA-GEL) gelatin coated film, (PCL/CAP-EDA-GEN-GEL) gelatin crosslinked film.

In terms of the gelatin modified samples in Figure 4.14, the FWHM value for the gelatin crosslinked sample is slightly higher than that of the gelatin-coated sample. In addition, it is significantly higher than that of the genipin coated sample, which is a result of chemical crosslinking of the gelatin onto the film (Mateescu & Juha, 2002).

In conclusion, the XRD diffractograms are not significantly changed upon biomolecule modification, therefore it is evident that the semi-crystalline nature of the aminolyzed PCL/CAP film is maintained over the entire 2Θ angle range, which indicates that the genipin coating, biomolecule coating and biomolecule crosslinking to the sample does not significantly affect the profile (da Silva et al., 2021). The sodium alginate and gelatin crosslinked samples both display increased FWHM values compared to their coated counterparts, which is an indicator of successful crosslinking (Yakimets et al., 2005). However, this trend is not observed for the collagen crosslinked samples. The proposed reason for this is not known, however, it is to be noted that the combination of FT-IR, DSC and TGA draw the conclusion that all the biomolecules are successfully crosslinked to the films.

4.3.5. Thermogravimetric analysis for thermal stability evaluation of the thin films

Thermogravimetric analysis was conducted in order to evaluate the changes in thermal stability upon biomolecule modifications. TGA thermograms and corresponding derivatives were constructed and the respective $T_{5\%}$ and T_{max} values were calculated. Table 4.5 represents a comparison between the $T_{5\%}$ and T_{max} values for the biomolecule-modified samples and their respective controls. Figures 4.15, 4.17 and 4.19 represent the TGA thermograms of the biomolecule-modified films, as well as the pristine biomolecules. Each graph highlights three areas of interest: A, B and C. These sections are enlarged and discussed after each main graph.

The thermal degradation of genipin in Figure 4.15 indicates a two-step degradation mechanism with a $T_{5\%}$ of 207.5 °C and a T_{max} of 234.92 °C. The first degradation step is the major degradation step and results in a 46.75% mass loss, whereas the second degradation step results in a 28.83% mass loss, with a 24.42% residual content at 900 °C. Collagen degrades via a two-step mechanism and has a $T_{5\%}$ and T_{max} of 81.52 °C and 333.24°, respectively. The first degradation step results in a 13.03% mass loss whereas the major second step results in a 67.32% mass loss with a 19.78% residual content at 900 °C. PCL/CAP-EDA degrades via a four-step mechanism, with the third step occurring at 360.45 °C, resulting in the highest weight loss of the sample. Genipin coating on the PCL/CAP-EDA film increases the onset of degradation from 279.46 to 291.81 °C ,and the T_{max} from 360.45 to 414.03 °C, indicating that the genipin coating enhances thermal stability of the aminolyzed film, which is in accordance with literature (Pan et al., 2019)**.**

Collagen coating (Figure 4.15) further enhances the $T_{5\%}$ to 303.7 °C and the T_{max} to 415.58 °C, indicating that collagen coating enhances the thermal stability of the aminolyzed film, even further than that of the genipin coating. Collagen crosslinking to the aminolyzed film using genipin results in an enhanced T_{max} value to 394.69 °C, signifying an enhanced thermal stability in this range (Pan et al., 2019). In comparison with the genipin and collagen-coated samples, the collagen crosslinked sample displays reduced $T_{5\%}$ and T_{max} values, signifying a lowered thermal stability, a finding that presents an anomaly because a crosslinked system generally has a higher thermal stability (Roland, 2013). This finding may be a result of the crosslinking density causing the samples to become more brittle (Roland, 2013). Therefore, when the network structure begins to reach higher temperatures, the brittle structure collapses, and a reduced thermal stability is observed (da Silva et al., 2021). All the modified samples have an improved thermal stability in region A and B as compared to the aminolyzed sample.

Table 4. 4 $T_{5\%}$ and T_{max} values for each sample derived from individual TGA thermograms and derivative curves.

	Thermodynamic Property		
Sample	**Number of Degradation Steps**	**Temperature at initiation of degradation (°C)**	**Temperature of maximum decomposition rate (°C)**
Aminolyzed films	4	279.46	360.45
Genipin crosslinked films	2	291.81	414.03
Collagen coated films	2	303.7	415.58
Collagen crosslinked films	3	232.25	394.69
Sodium alginate coated films	2	315.79	359.003
Sodium alginate crosslinked films	3	307.86	404.36
Gelatin coated films	2	267.64	360.85
Gelatin crosslinked films	2	307.86	398.23

Region C in Figure 4.16 highlights that the genipin coated sample has the highest thermal stability in this temperature range. The collagen crosslinked sample has a thermal stability profile similar to that of the aminolyzed sample. Further, all the samples have very little to no residual content at 900 °C, whereas genipin and collagen still have a weight of 24.42% and 19.78%, indicating their superior thermal stability at very high temperatures, which could explain the trend in enhanced thermal stability of the coated films in comparison to the uncoated aminolyzed film (Roland, 2013).

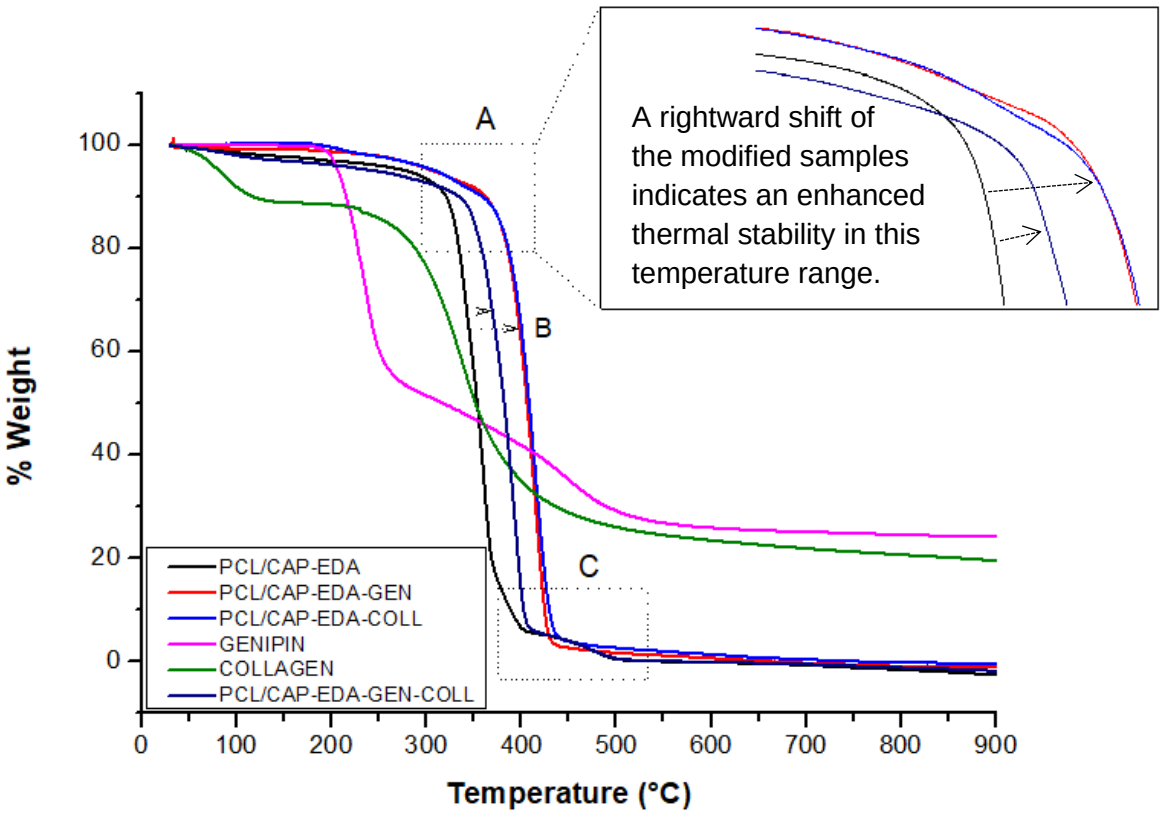


Figure 4. 15 Thermogravimetric analysis of (PCL/CAP-EDA) aminolyzed film, (PCL/CAP-EDA-GEN) genipin crosslinked film, (PCL/CAP-EDA-COLL) collagen coated film, (PCL/CAP-EDA-GEN-COLL) collagen crosslinked film.

Figure 4.17 compares the TGA thermograms of the aminolyzed sample, the genipin and sodium alginate coated sample, the sodium alginate crosslinked sample as well as pristine genipin and sodium alginate. The TGA thermodynamic profile of sodium alginate presents with a two stage degradation, where the initial step is due to water loss and the second step is due to the decarboxylation reaction of alginate, fracture of glycosidic bonds, and dehydration and decarboxylation of alginate (Soares et al., 2004).

Table 4.4 highlights that the sodium alginate coating enhances the $T_{5\%}$, which indicates an enhanced the thermal stability of the aminolyzed film (Roland, 2013), while the T_{max} remains unchanged. However, the sodium alginate crosslinking enhances the $T_{5\%}$ as well as the T_{max}, as compared to the aminolyzed film. The improvement of $T_{5\%}$ is more significant in the sodium alginate coated film rather than the crosslinked film. Region A in Figure 4.17 indicates an enhanced thermal stability of all the samples in comparison to the aminolyzed film due to the rightward shift of the curves (Soares et al., 2004). Region B indicates a significant improvement of the genipin coated sample, and the sodium alginate crosslinked sample as compared to the aminolyzed film. Region C in Figure 4.18 signifies the enhanced thermal stability at this temperature range of the genipin coated sample compared to all the other modified samples, with the sodium alginate coated sample displaying the lowest thermal stability in this range.

Figure 4.19 compares the TGA thermograms of the aminolyzed sample, the genipin and gelatin coated samples, the gelatin crosslinked sample as well as pristine genipin and gelatin.

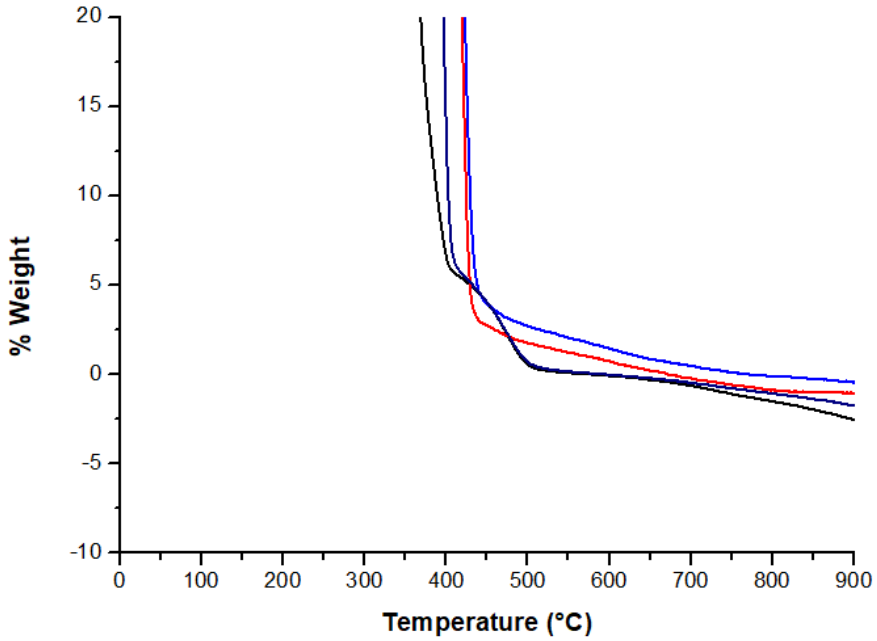


Figure 4. 16 Region C of Figure 4.15, highlighting the thermogravimetric analysis of the samples from 300-900 °C.

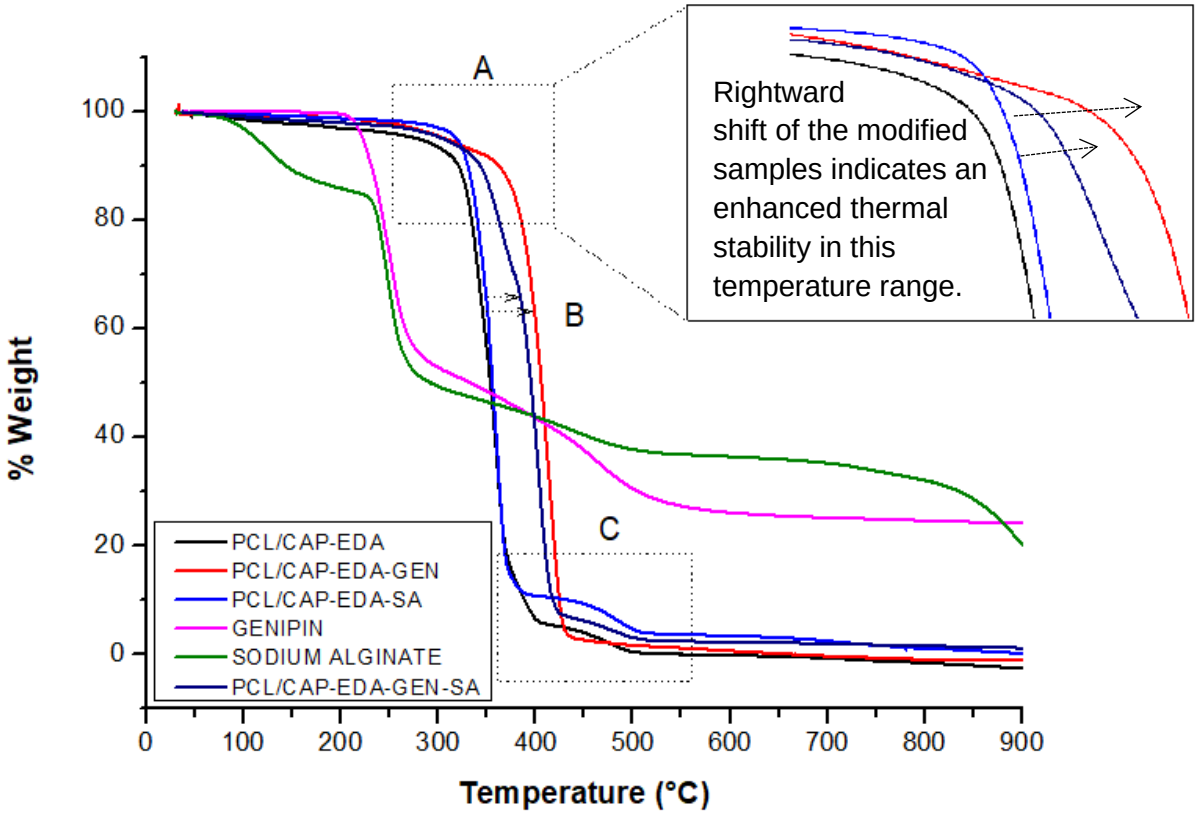


Figure 4. 17 Thermogravimetric analysis of (PCL/CAP-EDA) aminolyzed film, (PCL/CAP-EDA-GEN) genipin crosslinked film, (PCL/CAP-EDA-SA) sodium alginate coated film, (PCL/CAP-EDA-GEN-SA) sodium alginate crosslinked film.

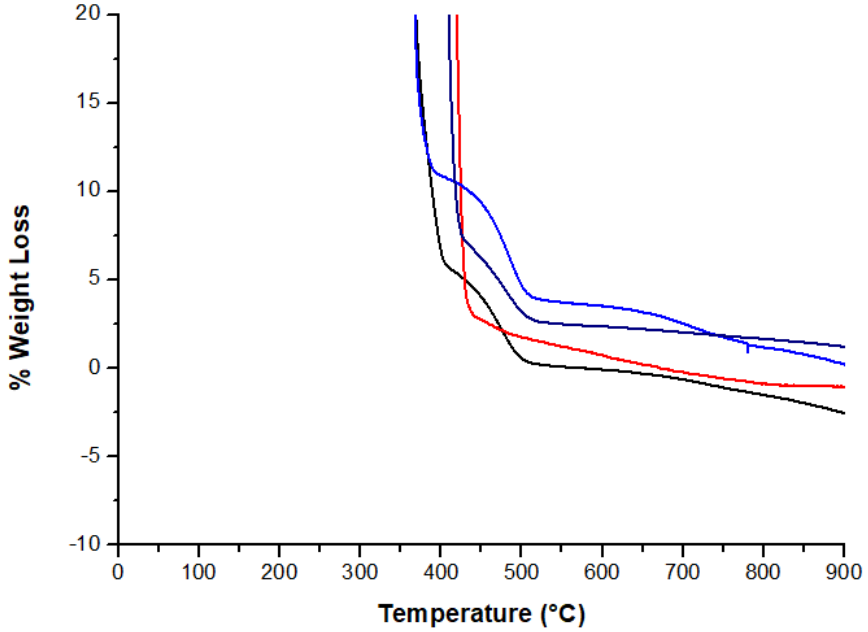


Figure 4. 18 Region C of Figure 4.17, highlighting the thermogravimetric analysis of the samples from 350-900 °C.

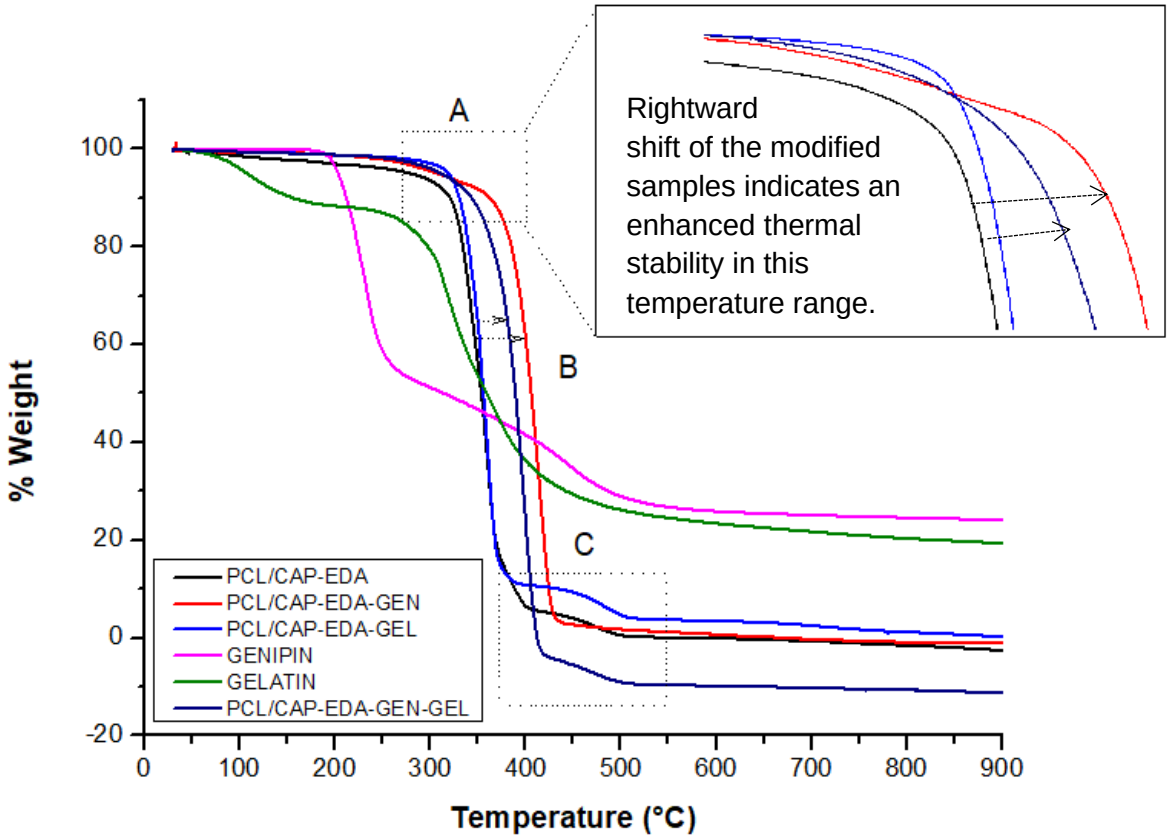


Figure 4. 19 Thermogravimetric analysis of (PCL/CAP-EDA) aminolyzed film, (PCL/CAP-EDA-GEN) genipin crosslinked film, (PCL/CAP-EDA-GEL) gelatin coated film, (PCL/CAP-EDA-GEN-GEL) gelatin crosslinked film.

The TGA thermogram of gelatin (Figure 4.19) shows two major weight loss steps. The first weight loss event results in a 11.34% loss, whereas the second results in a 68.74% weight loss due to the thermal decomposition of the gelatin network (Rodríguez-Baeza et al., 2003).

Table 4.4 reveals that the gelatin coating on the aminolyzed film has no effect on the T_{max} of the sample, whereas it reduces the $T_{5\%,}$ indicating a reduced thermal stability during the onset of degradation (Rodríguez-Baeza et al., 2003). Gelatin crosslinking significantly enhances the $T_{5\%}$ and T_{max} values compared to the aminolyzed film, highlighting its superior thermal stability (Rodríguez-Baeza et al., 2003). Region A of Figure 4.19 similarly shows a rightward shift of the modified samples from the aminolyzed sample, highlighting their superior thermal stability in this region. Region B also demonstrates a rightward shift of the modified samples, with the gelatin coated sample demonstrating a very weak rightward shift and the genipin coated and gelatin crosslinked samples demonstrating superior thermal stability (Soares et al., 2004). Region C in Figure 4.19 highlights that gelatin crosslinked sample shows the highest thermal stability of the films at high temperatures. Further, the residual content of the films is minimal, whereas genipin and gelatin have residual contents of 24.42% and 19.61%, respectively, highlighting their superior thermal stability at high temperatures.

In conclusion, the TGA data demonstrates that the biomolecule modifications significantly alter the thermal stability of the samples. The different regions of the thermograms indicate different thermal changes, however, region B highlights the rightward shift of the biomolecule-modified samples in relation to the aminolyzed sample, which indicates that the presence of the biomolecules on the films enhances the thermal stability.

4.3.6. Surface topography characterizations by scanning electron microscopy analysis

Scanning electron microscopy was undertaken in order to evaluate the changes that occurred to the surface morphology upon biomolecule crosslinking. The SEM morphology of the aminolyzed PCL/CAP films as well as the aminolyzed films with genipin-crosslinked biomolecules are depicted in Figure 4.20 (a-h).

The images reveal an increase in surface roughness after biomolecule immobilization (c-h). An increase in surface roughness is important in neural tissue engineering as it can improve cell attachment (Brunetti et al., 2010; Sorkin et al., 2009). In addition, this increase in surface roughness indicates that the biomolecules are present on the films (Brunetti et al., 2010). The films maintain their overall morphology with their lamellar-like structure and porous nature described in Chapter 3, proving that the crosslinking of biomolecules to the film surface does not alter the inherent desirable surface morphology of the films.

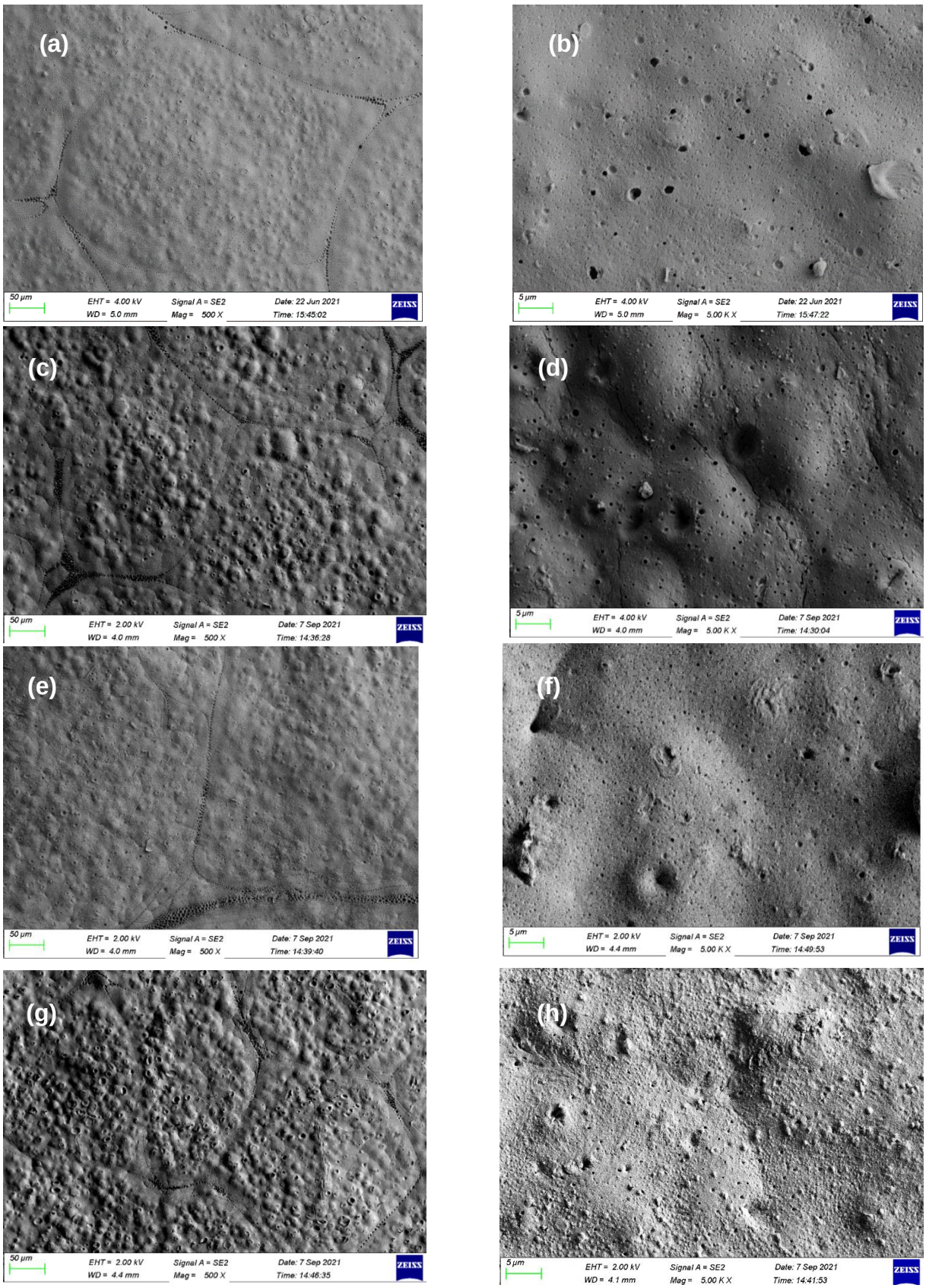


Figure 4. 20 Scanning electron microscopy of the aminolyzed films at (a) 500X and (b) 5000X, the collagen crosslinked films at (c) 500X and (d) 5000X, the sodium alginate crosslinked films at (e) 500X and (f) 5000X and the gelatin crosslinked films at (g) 500X and (h) 5000X.

4.3.7 Porosimetric and surface area analysis of the thin films using BET analysis

The porosimetric and surface area analysis was undertaken to evaluate the suitability of the biomolecule-modified films for neural tissue engineering. The effects of the presence of the biomolecules on the porosity and surface area was evaluated. Nitrogen adsorption-desorption isotherm plots were generated (A7 of appendix) and a detailed analysis on the pore sizes, volumes and surface areas were calculated. The isotherm plot for the aminolyzed sample is depicted in Figure 4.21. A representative isotherm plot for all the biomolecule-modified samples is depicted in Figure 4.22, as all the samples maintained the same general shape.

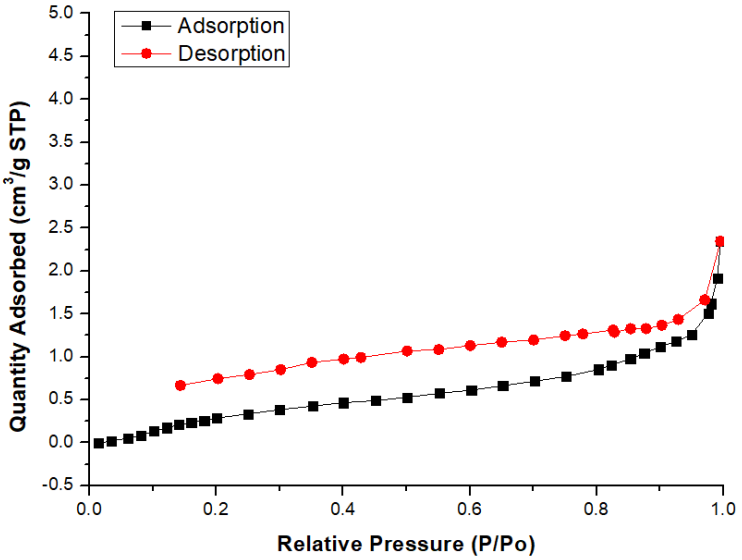


Figure 4. 21 Adsorption-desorption isotherm for the aminolyzed films.

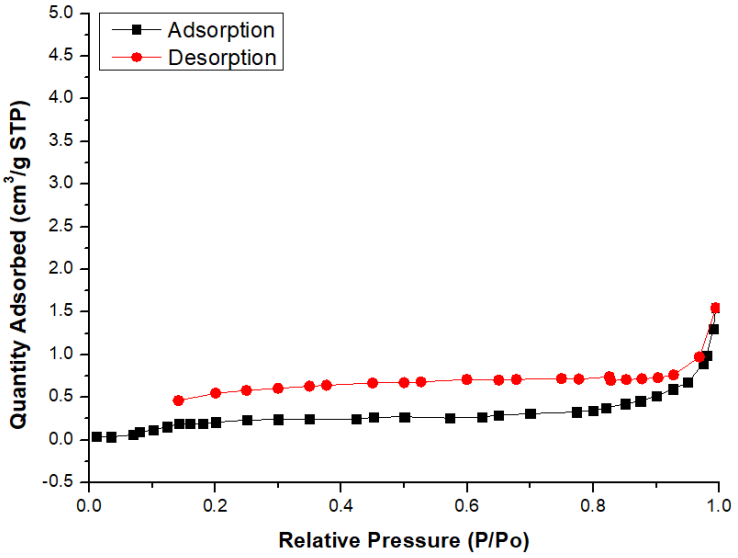


Figure 4. 22 Adsorption-desorption isotherm for the biomolecule-crosslinked films.

According to the IUPAC classification of gas adsorption isotherms defined in Chapter 3, the samples are all typical type II isotherms, indicating the development of a certain amount of mesopores (Ramburrun et al., 2019). There is no change in shape from the aminolyzed samples to the crosslinked samples, as seen in Figures 4.21 and 4.22, respectively. The average pore diameters all fall within the mesoporous range (2-50 nm), which is consistent with the isotherm plot predictions. The hysteresis loops are characteristic of shape H3 which relates to solids with a very wide distribution of pore size (Gregg et al., 1967). In terms of pore size and surface area, the effect of the immobilization of biomolecules onto the surface of the aminolyzed films is hallmarked by an increase in BET surface area in comparison to the aminolyzed films, from -4.05 to 0.24, 2.57 and 33.14 m^2/g, respectively. This is advantageous in tissue engineering as an enhanced surface area facilitates enhanced cell attachment and spreading *In Vitro* (Murphy & O'Brien, 2010). Another noteworthy effect on the porosity characteristics of the aminolyzed film is that the average pore volume of the samples is reduced upon biomolecule immobilization. The possible cause for this could be the embedding of the biomolecules within the pores, thereby reducing their apparent volume (Gregg et al., 1967).

To conclude, the immobilization of the biomolecules to the films enhances the surface area of the films, while maintaining the desirable mesoporous nature.

4.3.8 Determination of the mechanical properties of the thin films using Texture Analyser analysis

The mechanical properties of the thin films were evaluated in order to determine the effect of biomolecule immobilization on the tensile strength, Young's modulus, and toughness, as well as to evaluate the suitability of the modified films for neural tissue engineering. These parameters were calculated from the stress-strain curves generated for each sample. Figure 4.23 compares the stress-strain curves for the aminolyzed film and the biomolecule crosslinked films. The stress-strain curves represented in Figure 4.23 highlight that the mechanical properties of the aminolyzed films are significantly improved upon biomolecule crosslinking. Table 5.5 highlights the average values for tensile strength, Young's modulus, and toughness for all the samples, including the controls. The tensile strength of the aminolyzed film is 5.43 ± 0.27 MPa. It is evident from the graph that the crosslinking of the biomolecules to the film significantly enhances the tensile strength to 10.58 ± 0.65. 13.14 ± 4.84 and 8.92 ± 0.96 MPa for PCL/CAP-EDA-GEN-COLL, PCL/CAP-EDA-GEN-SA and PCL/CAP-EDA-GEN-GEL, respectively, which is consistent with literature (Frohbergh et al., 2012). The preceding chapter explored the effect of aminolysis on the tensile strength of the PCL/CAP films. It was found that it reduces the tensile strength, yet the immobilization of collagen, sodium alginate and

gelatin to the aminolyzed films assists in regaining the lost tensile strength. The Young's modulus of the aminolyzed film is 578.54 ± 7.22 KPa.

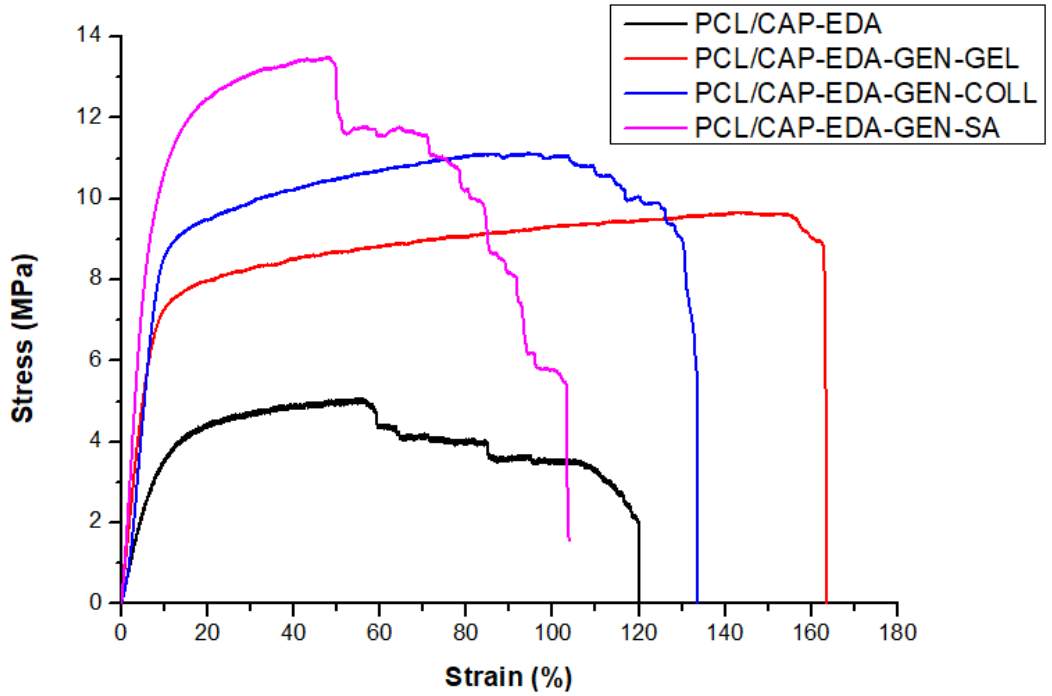


Figure 4. 23 Stress-strain curves comparing the aminolyzed films and the biomolecule-crosslinked films. (PCL/CAP-EDA) aminolyzed films, (PCL/CAP-EDA-GEN) genipin crosslinked films, (PCL/CAP-EDA-GEN-GEL) gelatin crosslinked films, (PCL/CAP-EDA-GEN-COLL) collagen crosslinked films, (PCL/CAP-EDA-GEN-SA) sodium alginate crosslinked films.

Following biomolecule crosslinking, the Young's modulus for PCL/CAP-EDA-GEN-COLL, PCL/CAP-EDA-GEN-SA and PCL/CAP-EDA-GEN-GEL is increased to 1183.83 ± 8.57, 1115.27 ± 6.85 and 1029.55 ± 6.57 KPa, respectively. All the biomolecule-modified films display a Young's modulus over two-fold above the aminolyzed film. The control groups (biomolecules coated on the film surface without the use of genipin) show a slight increase in tensile strength, Young's modulus, and toughness.

Table 4. 5 Average tensile strength, Young's modulus and toughness.

Average Sample	Tensile Strength (MPa)	Young's modulus (KPa)	Toughness ($J.m^{-3}$)
Aminolyzed film	5.43 ± 0.27	578.54 ± 7.22	580.57 ± 5.87
Collagen coated film	5.48 ± 2.11	571. 67± 5.44	587.56 ± 3.22
Sodium alginate coated film	5.62 ± 3.56	577.61 ± 1.46	573.34 ± 3.21
Gelatin coated film	5.34 ± 3.90	584.23 ± 3.41	592.90 ± 2.15
Genipin crosslinked film	7.99 ± 3.25	890.85 ± 3.41	932.19 ± 4.23
Collagen crosslinked film	10.58 ± 0.65	1183.83 ± 8.57	1417.72 ± 5.14
Sodium alginate crosslinked film	13.14 ± 4.84	1115.27 ± 6.85	1240.57 ± 11.47
Gelatin crosslinked film	8.92 ± 0.96	1029.55 ± 6.57	1455.88 ± 2.96

This is consistent with other works which involve the attachment of biomolecules to polymers using electrostatic attraction (Sadeghi-Avalshahr et al., 2020). However, the PCL/CAP-EDA-GEN sample show an increase in tensile strength, Young's modulus and toughness, which is also expected (Panzavolta et al., 2011).

In conclusion, the crosslinking of the biomolecules to the films significantly improves the tensile strength, Young's modulus, and toughness of the films, which is important in neural tissue engineering as it will aid the film in resisting pressure from the surrounding tissue as well as pressure from the regenerating nerve (Mathew et al., 2013). The improvement in Young's modulus is advantageous as it will impart more flexibility to the film which will enable it to move as the nerve tissue is regenerating. (Kim et al., 2010; Krithica et al., 2012; Mathew et al., 2013). The high standard deviation is proposed to be due to the manual fabrication of the films and is consistent with literature (Sun & Downes, 2007).

4.3.9 Determination of the hydrophilicity of the thin films by water contact angle measurements

Water contact angle measurements were done to assess the hydrophilicity of the samples after biomolecule modifications. Figure 4.24 highlights the changes in hydrophilicity upon biomolecule modification.

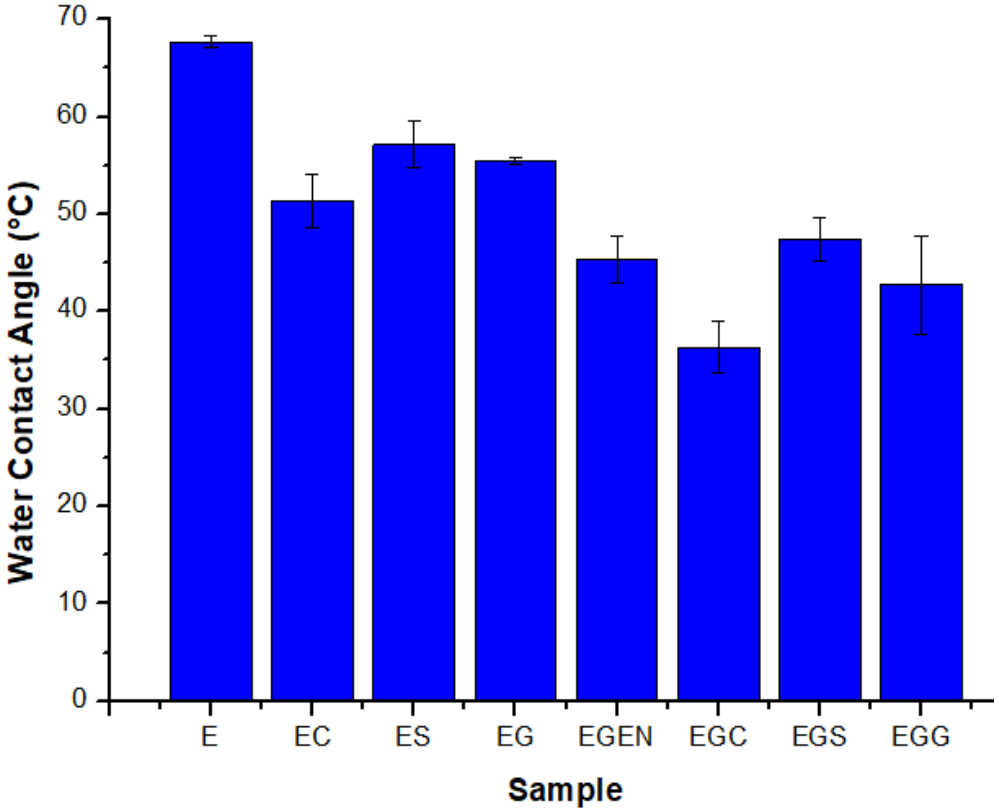


Figure 4. 24 Water contact angles for (E) the aminolyzed films, (EC) collagen coated films, (ES) sodium alginate coated films, (EG) gelatin coated films, (EGEN) genipin crosslinked films, (EGC) collagen crosslinked films, (EGS) sodium alginate crosslinked films, (EGG) gelatin crosslinked films.

The biomolecule coating reduces the water contact angle of the aminolyzed films from 67.68 ± 0.66° to 51.38 ± 2.72, 57.12 ± 2.36 and 55.46 ± 0.41°, respectively. This reason for this is that the coated biomolecules contain vast O-H groups, which reduces the water contact angle of the surfaces (Benykhlef et al., 2012; Meghdadi et al., 2019; Park et al., 2019). Further, the genipin coating also reduces the water contact angle to 45.33 ±2.45°, since it also contains O-H groups (Mu et al., 2013). The crosslinking of the biomolecules to the films using genipin results in an even further reduction in the water contact angle to 36.34 ± 2.58, 47.42 ± 2.22 and 42.74 ± 5.06°, respectively. It has been reported that the immobilization of biomolecules onto the surface of polymeric surfaces improves the hydrophilicity of the surfaces due to their inherent hydrophilic nature as discussed above illustrated in Figure 4.25.

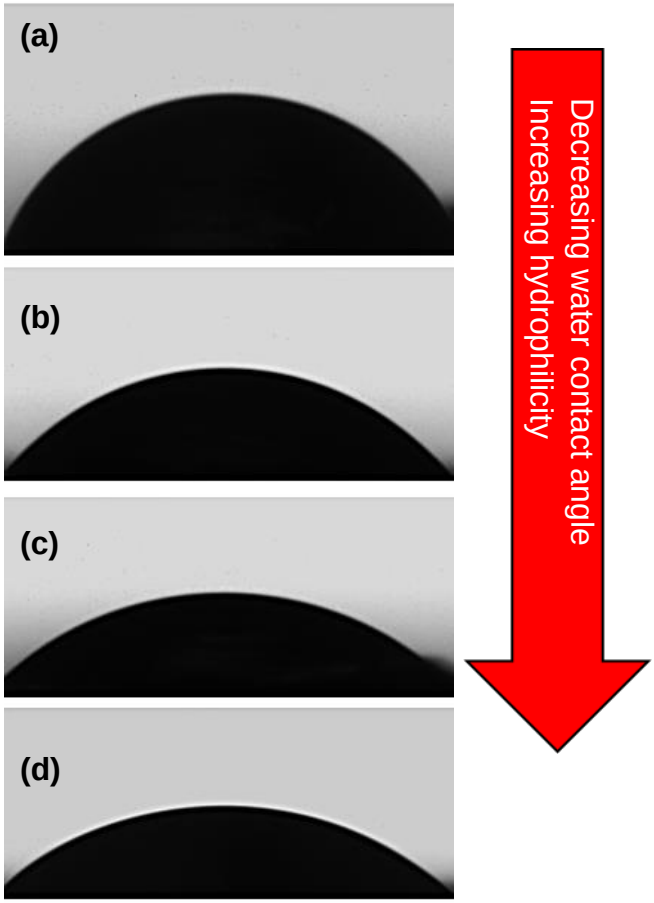


Figure 4. 25 Photographic image of water droplets on (a) the aminolyzed films, (b) the sodium alginate crosslinked films, (c) the gelatin crosslinked films and (d) the collagen crosslinked films.

To conclude, a homogeneous cell distribution and an ideal cell growth rate is facilitated by hydrophilic surfaces with appropriate cell interaction sites (Mirhosseini et al., 2016). Therefore, the reduction in hydrophilicity imparted by the biomolecule immobilization is predicted to be advantageous to cell attachment *In Vitro* (Mirhosseini et al., 2016).

4.3.10 *In Vitro* degradation study

The degradation rate of nerve guides is one of the most important factors in the process of nerve regeneration by nerve guidance conduits (Siemionow et al. 2010). Non-biodegradable polymers should be avoided for nerve tissue engineering as they can lead to compression and inflammation *In Vivo*, which can interfere with the regeneration of nerve fibers (Siemionow et al., 2010). Therefore, current research has focused on biodegradable polymers for the fabrication of nerve guidance conduits. An ideal nerve guidance conduit is composed of materials with a controlled degradation rate which ensures that the structural stability of the conduit is upheld in accordance with axonal growth and maturation (Mohammadi & Mashayekhan, 2020). The conduit should gradually collapse until the regeneration process is complete (Mohammadi & Mashayekhan, 2020). The regeneration rate of nerves varies according to severity and location of the injury along the neuron (Ron et al., 2015). Proximal segments may see an increase of two or three mm per day while more distal segments may progress at a rate of one or two mm per day. The graph in Figure 4.26 represents the degradation percentage over time of the aminolyzed samples and biomolecule-crosslinked samples.

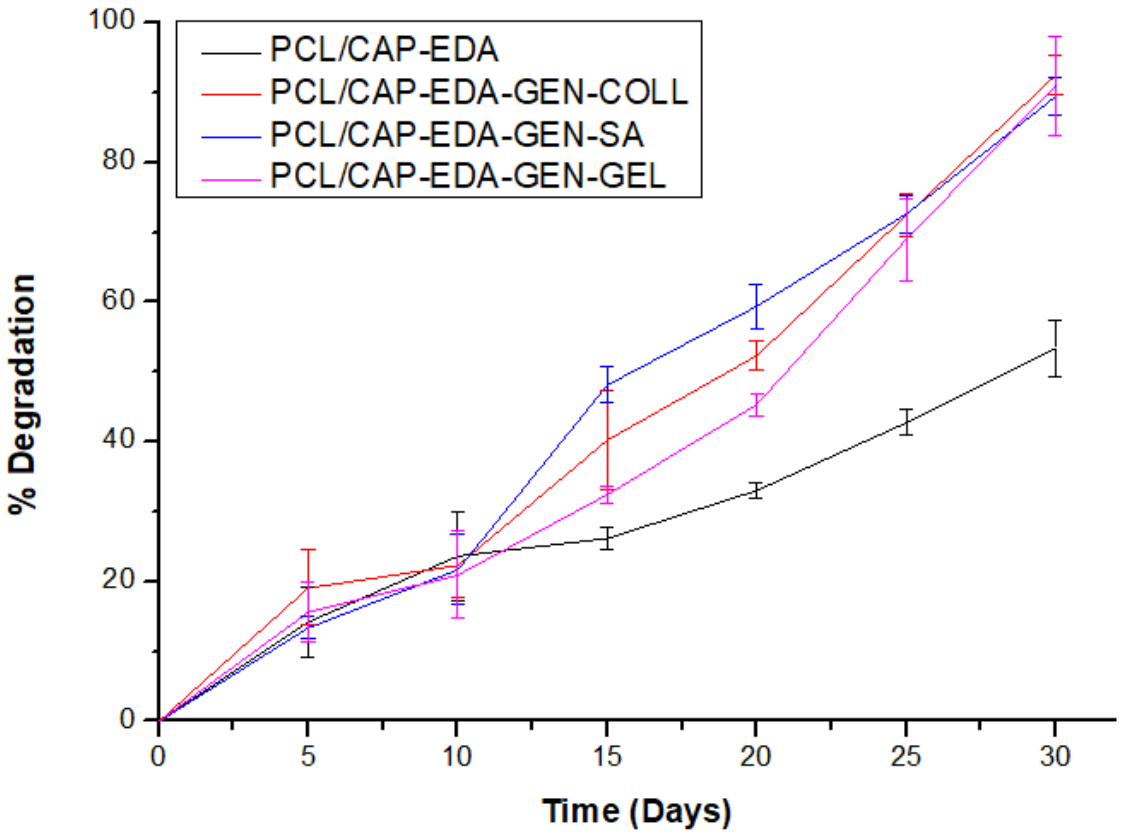


Figure 4. 26 *In Vitro* degradation behavior of the biomolecule-immobilized samples in comparison with the aminolyzed films. (PCL/CAP-EDA) aminolyzed films, (PCL/CAP-EDA-GEN) genipin crosslinked films, (PCL/CAP-EDA-GEN-GEL) gelatin crosslinked films, (PCL/CAP-EDA-GEN-COLL) collagen crosslinked films, (PCL/CAP-EDA-GEN-SA) sodium alginate crosslinked films.

From the graph in Figure 4.26, it is evident that the biomolecule-crosslinked samples show a higher degradation rate in comparison to the aminolyzed films. As the 25th day approaches, the biomolecule-crosslinked samples begin to break apart and on day 30, the samples are almost completely degraded. The samples that had broken apart were removed from their PBS and placed in a dry well plate and left to dry in the same conditions as the other samples. It has been found that biomolecules crosslinked to PCL conduits show higher weight loss compared to PCL controls, which is proposed to be attributed to physical changes that occur after biomolecule attachment such as increased hydrophilicity (dos Santos et al., 2018; Mondal et al., 2016). This is in-line with the water contact angle data found in Section 4.3.9 where the immobilization of each biomolecule to the aminolyzed films decreases the water contact angle, thereby increasing the hydrophilicity. It has previously been found in a study by Ramburrun and co-workers that a nerve repair device comprising a polysaccharide hydrogel conduit and intraluminal aligned nano-fibrous guidance cue implanted for a four-week period showed sufficient support and biodegradability to produce an improved functional recovery and return of fine motor control in animals receiving implantation (Ramburrun et al., 2019). This indicates that a scaffold fit for neural tissue engineering should remain structurally intact for approximately four weeks. The degradation results herein indicate that the addition of the biomolecules significantly increases the degradation rate, indicating a loss in structural integrity and a loss in the ability to provide structural support to growing neuronal cells and tissue. However, different sized nerve gaps and different degrees of damage require different biodegradation rates, depending on the time required to heal (Mohammadi & Mashayekhan, 2020).

It thus follows that, depending on the specific clinical application, the film can be fine-tuned to suit the situation. For example, the degradation rate can be reduced by:

- Enhancing the water contact angle.
- Reducing the concentration of the aminolysis agent.
- Reducing the aminolysis treatment time.
- Reducing the aminolysis treatment temperature.
- Reducing the concentration of genipin or by
- Reducing the crosslinking incubation time.

However, it should be noted that these modifications would alter the other physio-chemical properties of the films, such as hydrophilicity and mechanical properties.

4.3.11 *In Vitro* water-uptake study

Water-uptake of a scaffold is also one of the important factors to consider when designing neural guides and is affected by numerous characteristics of the scaffold such as hydrophilicity.

As mentioned previously, on day 25 of the degradation and water-uptake study, the biomolecule-crosslinked samples began to break apart, making it difficult to read the data as the tissue paper used to adsorb excess moisture stuck to the film pieces and broke the film even further. Therefore, there is no water-uptake data for day 30. Figure 4.27 highlights that the water-uptake of the films is significantly enhanced upon biomolecule crosslinking. The proposed reason for this is the enhanced hydrophilicity of the biomolecule-crosslinked films, as similarly discussed in Section 4.3.10 regarding the rate of degradation (dos Santos et al., 2018; Mondal et al., 2016). The high standard deviations observed for degradation and water-uptake studies is proposed to be as a result of the manual fabrication of the films and is consistent with literature (Sun & Downes, 2007).

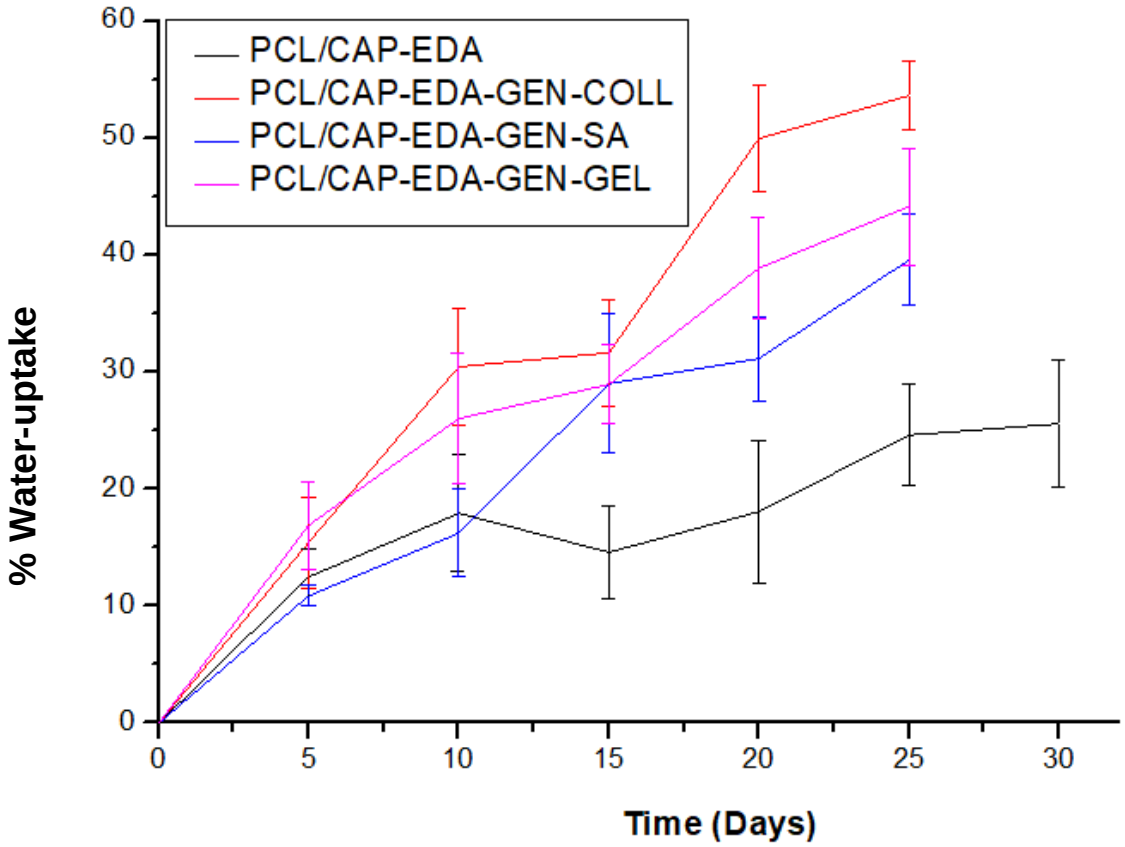


Figure 4. 27 Water-uptake behavior of the biomolecule-immobilized films compared to the aminolyzed films. (PCL/CAP-EDA) aminolyzed films, (PCL/CAP-EDA-GEN) genipin crosslinked films, (PCL/CAP-EDA-GEN-GEL) gelatin crosslinked films, (PCL/CAP-EDA-GEN-COLL) collagen crosslinked films, (PCL/CAP-EDA-GEN-SA) sodium alginate crosslinked films.

In conclusion, the films are highly adaptable scaffolds, therefore, if a reduced water-uptake is required for a specific clinical setting, various characteristics of the films could be altered to produce a faster or slower degradation rate by altering various characteristics of the films.

4.3.12 Quantification of biomolecule attachment onto the films utilizing the BCA protein kit

The quantification of crosslinked biomolecules was undertaken to firstly confirm the presence of biomolecules on the films and secondly, to determine the specific concentration of each biomolecule on the films. Figures 4.28-4.33 represent the calibration curves for each biomolecule as well as the corresponding concentration detected using the BCA protein assay. Figures 4.28, 4.30 and 4.32 are the calibration curves plotted for collagen, sodium alginate and gelatin, respectively. Figures 4.29, 4.31 and 4.33 represent the concentration of each biomolecule detected on the films during the BCA protein assay.

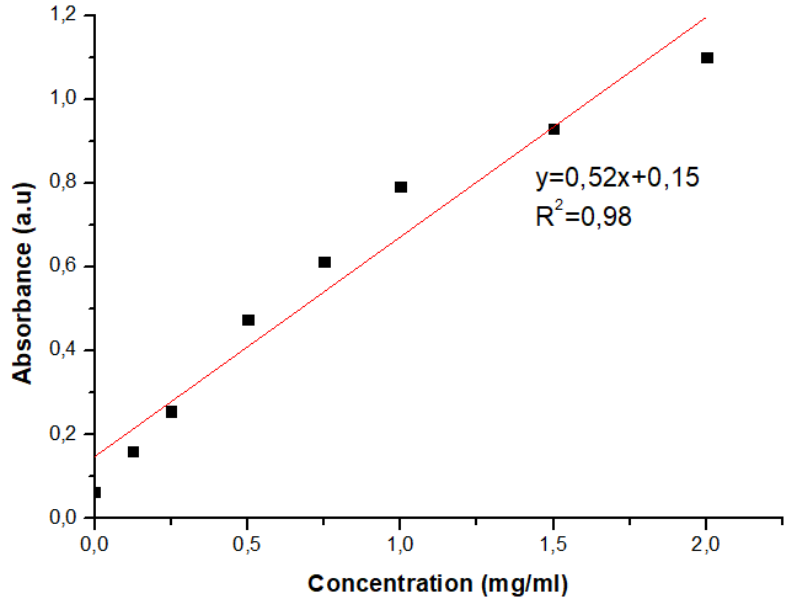


Figure 4. 28 Calibration curve used for the quantification of collagen on the films.

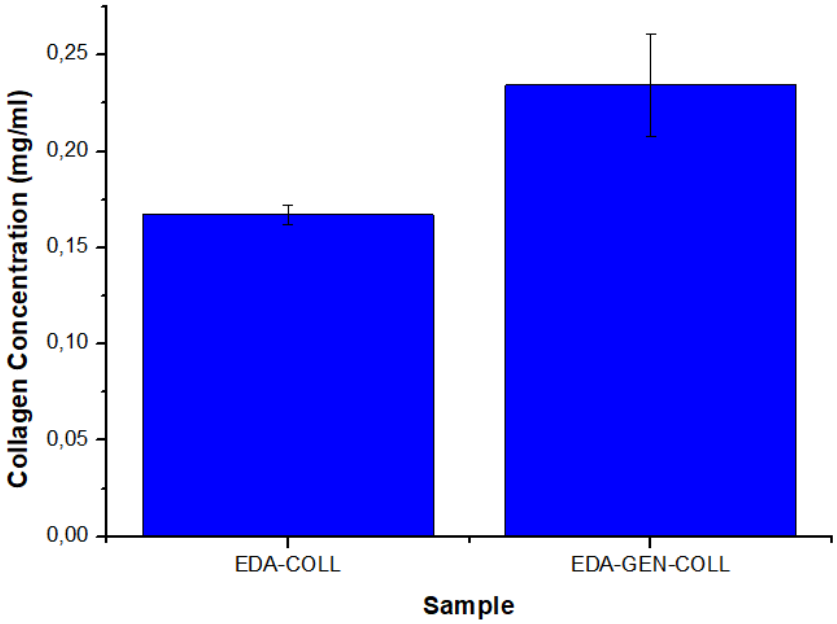


Figure 4. 29 Bar graph representing the collagen concentration detected on the surface of the (EDA-COLL) collagen coated films and the (EDA-GEN-COLL) collagen crosslinked films.

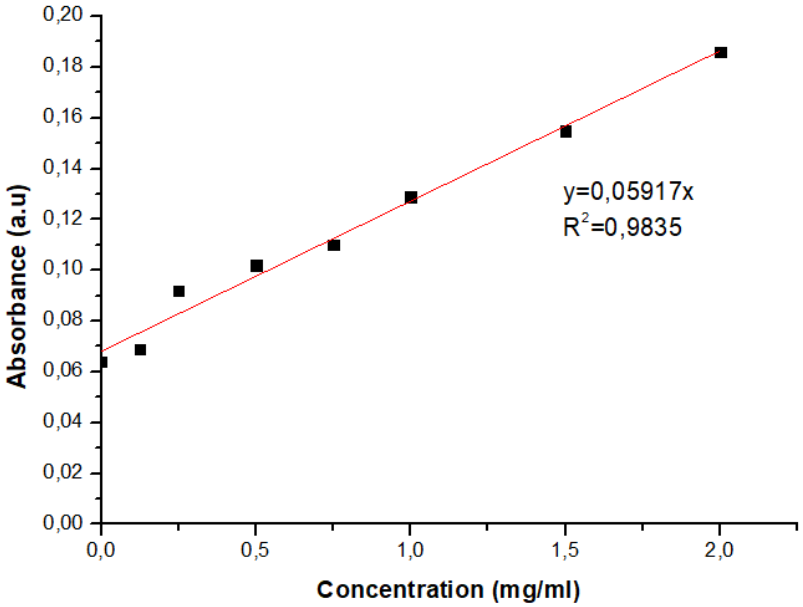


Figure 4. 30 Calibration curve used for the quantification of sodium alginate on the films.

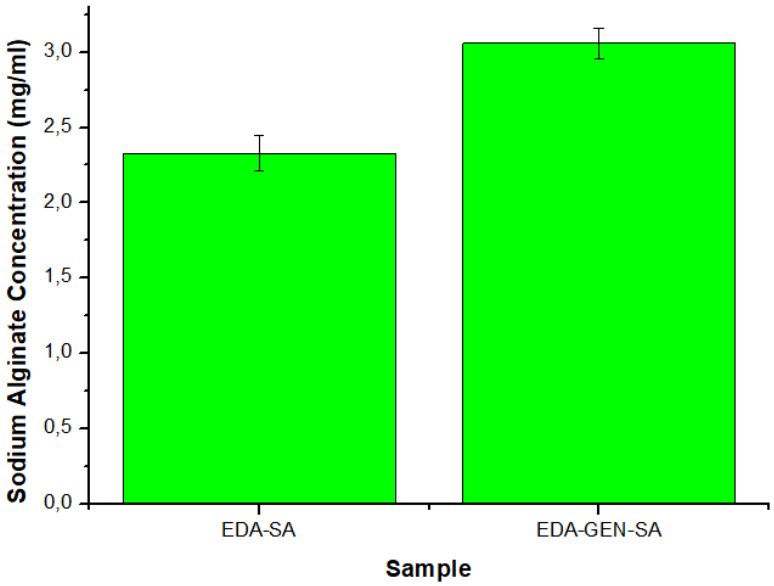


Figure 4. 31 Bar graph representing the concentration detected on the surface of the (EDA-SA) sodium alginate coated films and the (EDA-GEN-SA) sodium alginate crosslinked films.

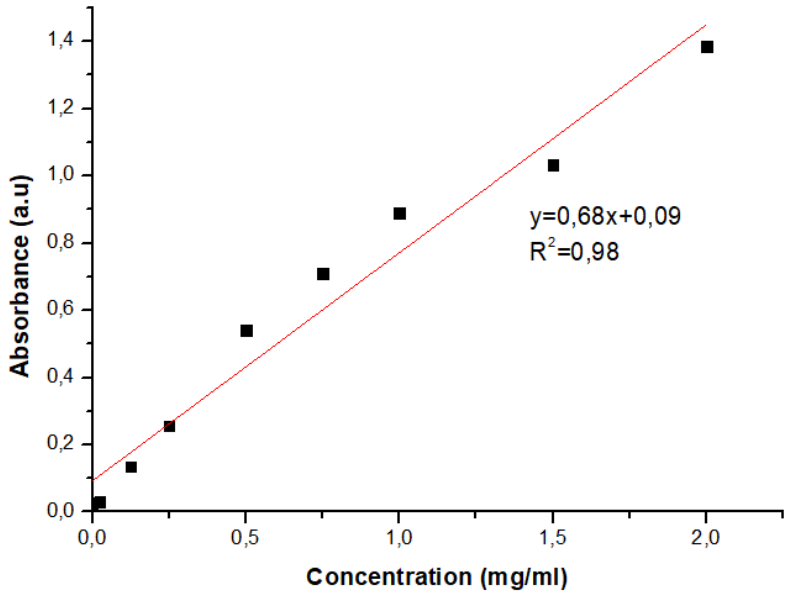


Figure 4. 32 Calibration curve used for the quantification of gelatin on the surface of the films.

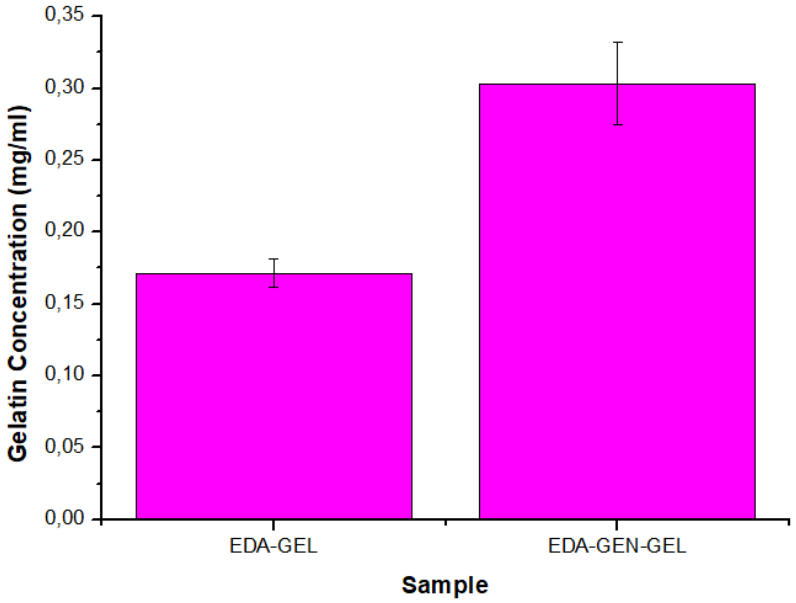


Figure 4. 33 Bar graph representing the concentration detected on the surface of the (EDA-GEL) gelatin coated films and the (EDA-GEN-GEL) gelatin crosslinked films.

The trend observed in Figures 4.28-4.33 is that the amount of each biomolecule detected on the crosslinked samples is higher than that on the biomolecule coated samples. This is possibly due to the crosslinks that have formed between the amine groups on the aminolyzed PCL/CAP film, and the amine groups present on each biomolecule. These crosslinks are stronger covalent bonds in comparison to the weaker electrostatic interactions between the films and the biomolecules in the coated samples, which do not have a crosslinking agent present (Atthoff & Hilborn, 2007; G. E. Park et al., 2005; Rentsch et al., 2009). Therefore, more biomolecule is retained on the sample after PBS washing, therefore a higher absorbance is detected for the crosslinked samples.

In conclusion, this assay confirms the presence of collagen, sodium alginate or gelatin on the films as well as quantified each biomolecule present and proves that the crosslinked samples retain more biomolecule due to the presence of the stronger crosslinks in comparison to weaker electrostatic forces present in the coated samples.

4.3.13 PC12 and A172 cell culture and quantification of cell viability utilizing the XTT cytocompatibility assay

The XTT cytocompatibility assay was performed to determine the cytocompatibility of the films with PC12 and A172 cell lines by quantifying the number of live cells present after exposure to the films. Figures 4.34 and 4.35 represent the cell viabilities detected for the PC12 and A172 cell lines, respectively after 48 and 72 h of exposure to the samples. The results indicate that at the 48 h time point, the viability for the aminolyzed samples is 97.75%, which is only slightly lower than that of the negative control (100.05%). Upon biomolecule coating with collagen, sodium alginate and gelatin, the viability is reduced to 84.86, 102.04 and 87.27%, respectively. This shows that the viability is reduced, except for the gelatin coated samples. However, upon biomolecule crosslinking, the viability is increased to 88.07, 96.64 and 94.65%, indicating that perhaps the presence of genipin aids the increase in cell viability. This is possibly due to the high cell viability of the genipin coated sample which is 101.53%. This is consistent with literature since it is known that genipin has neuroprotective effects and has a positive effect on cell viability (Di Giovanni et al., 2005; Hughes et al., 2014). The collagen crosslinked sample produces a significant decrease in cell viability in comparison to the aminolyzed sample ($P=0.03$), however, the PCL/CAP-EDA-GEN-SA and PCL/CAP-EDA-GEN-GEL samples do not significantly change the cell viability. After 72 h, the cell viability is slightly improved for most of the samples. However, the PCL/CAP-EDA-SA, PCL/CAP-EDA-GEN and PCL/CAP-EDA-GEN-SA percentage viability is slightly reduced in comparison to the 48 h viability, however, none of the samples are reduced below 90%. A comparison between the crosslinked samples indicates that the PCL/CAP-EDA-GEN-SA samples perform the best. At 72 h, none of the films significantly alter the cell viability in comparison to the aminolyzed sample.

With regards to the A172 cell line (Figure 4.35), the aminolyzed sample produces a 114.75% cell viability, which is higher than that of the negative control (96.70%). The coating of collagen, sodium alginate and gelatin onto the films reduces the viability to 80.06, 84.71 and 59.51%, respectively. The viability for the collagen and sodium alginate coated samples is still within the acceptable range but is much lower than the aminolyzed control (Boni et al., 2018).

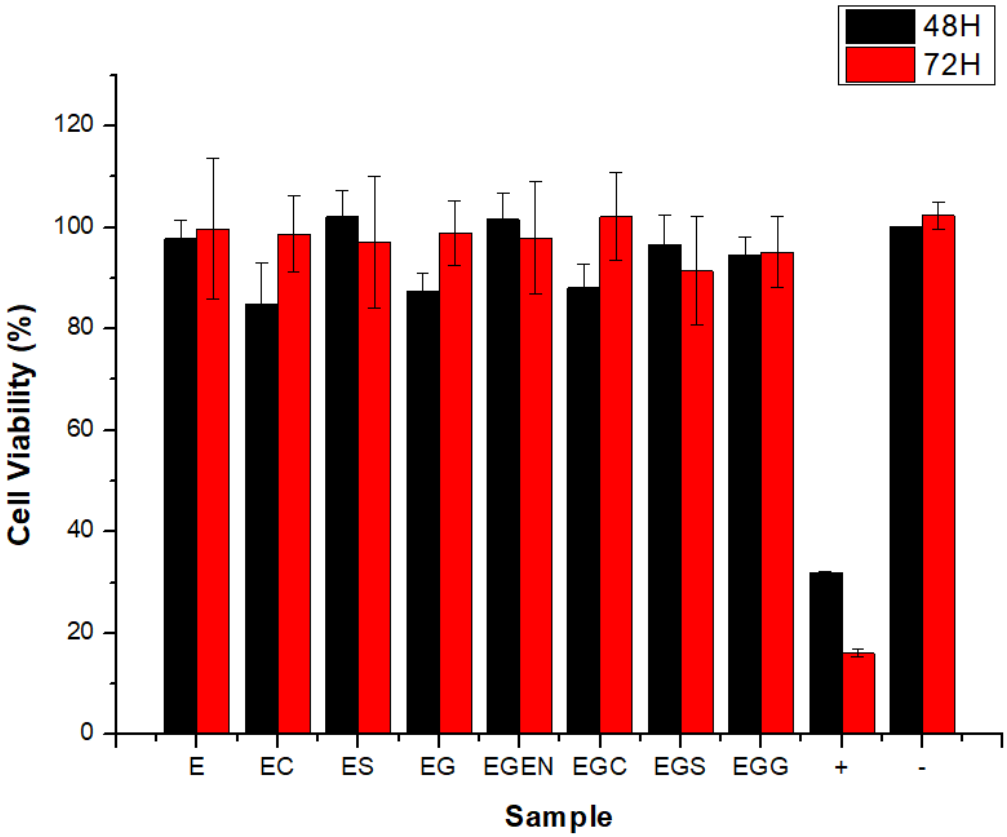


Figure 4. 34 Cytocompatibility results for PC12 cells after 48 and 72 h. (E) aminolyzed films, (EC) collagen coated films, (ES) sodium alginate coated films, (EG) gelatin coated films, (EGEN) genipin crosslinked films, (EGC) collagen crosslinked films, (EGS) sodium alginate crosslinked films, (EGG) gelatin crosslinked films, (+) positive control and (-) negative control. An unpaired, two-tailed student T-test was conducted comparing the cell viability obtained from the aminolyzed sample and the biomolecule crosslinked samples, which showed statistical significance after the 48 h exposure of P=0.03, 0.99 and 0.36, respectively, and after 72 h exposure of P=0.74, 0.31 and 0.52 respectively.

In addition, the gelatin coated samples significantly reduces the viability of the A172 cells, which is much lower than the acceptable standard (Boni et al., 2018). Genipin coating produces a viability of 103.87%, which is higher than that of the negative control. The biomolecule crosslinked samples all demonstrate viabilities above that of their coated counterparts, indicating the positive effects of the presence of genipin, as discussed above. The collagen crosslinked film significantly reduces the cell viability (P=0.007) in comparison to the aminolyzed sample.

After 72 h the viability of the cells exposed to all the samples are increased to over 100%, including the coated samples which demonstrate relatively poor results at 48 h. The possible reason for this could be that this cell line requires more time to enter a proliferative state. The biomolecule crosslinked samples all have p values higher than 0.05, indicating that they cause an insignificant alteration to the cell viability in comparison to the aminolyzed sample, except for the gelatin crosslinked sample at 48 h. None of the films produce a significant change in

cell viability at 72 h, indicating that none of the samples are cytotoxic (Neu et al., 2019).

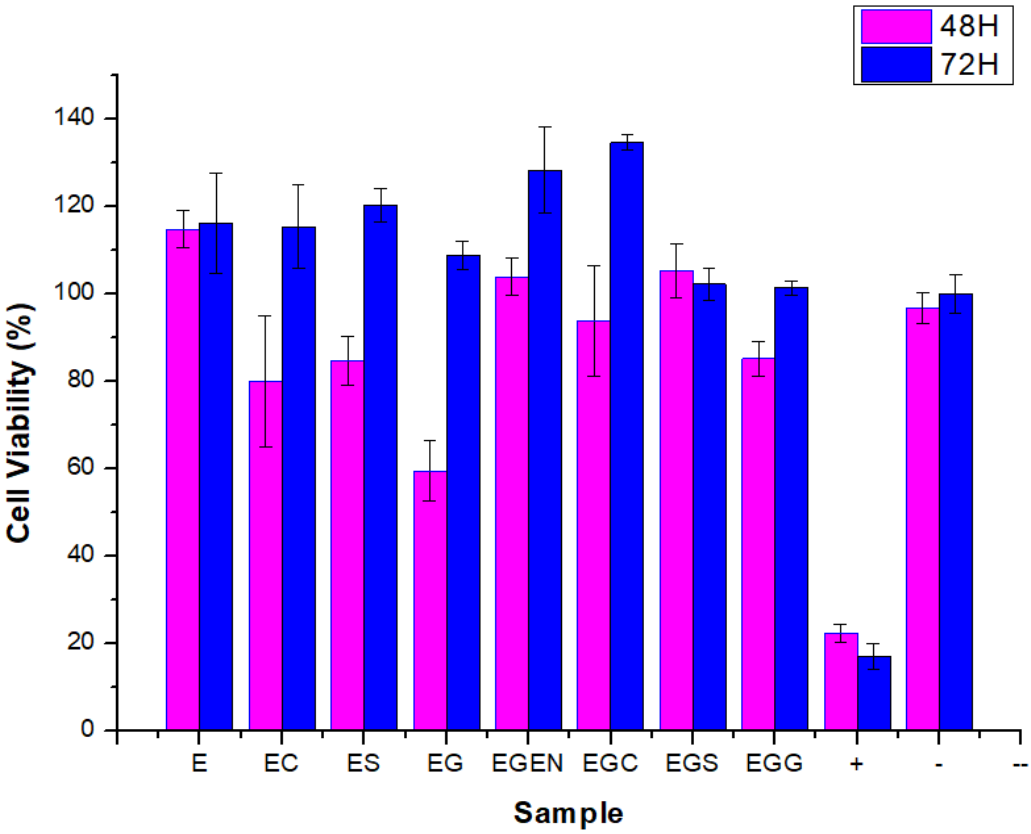


Figure 4. 35 Cytocompatibility results for A172 cells after 48 and 72 h. (E) aminolyzed films, (EC) collagen coated films, (ES) sodium alginate coated films, (EG) gelatin coated films, (EGEN) genipin crosslinked films, (EGC) collagen crosslinked films, (EGS) sodium alginate crosslinked films, (EGG) gelatin crosslinked films, (+) positive control and (-) negative control. An unpaired, two-tailed student T-test was conducted comparing the cell viability obtained from the aminolyzed sample and the biomolecule crosslinked samples, which showed statistical significance after the 48 h exposure of P=0.19, 0.27 and 0.007, respectively, and after 72 h exposure of P=0.14, 0.25 and 0.21, respectively.

In conclusion, none of the samples are cytotoxic, except for PCL/CAP-EDA-GEL at 48 h, however, this sample results in cell proliferation at 72 h, which proves that it is not cytotoxic (Neu et al., 2019). The comparison between the crosslinked samples indicates that at 48 h, the PCL/CAP-EDA-SA samples perform the best, whereas at 72 h, the PCL/CAP-EDA-GEN-COLL samples produce the best cell viability results.

4.3.14 Qualitative assessment of cell attachment onto the bioactive thin films utilizing light microscopy

Light microscopy images were taken of the cells attached to the films to prove that cells were capable of attaching to the films as well as to prove that they were healthy on the films by maintaining a neural-like morphology. The light microscopy images in Figures 4.36 and 4.37 depict PC12 cells attached to the films, proving that PC12 cells can adhere to the films and maintain their neural cell-like morphology. As discussed in Chapter 3, obtaining images of cells attached to the films was a limitation due to difficulty in differentiating between the film and the

cells due to the complex morphology of the film sample. Although pictures of cells are not captured for each sample due to the limitations already discussed, these images merely serve as proof that cells can attach to the films and maintain their normal neuronal morphology. The quantification of cell attachment will be assessed using the trypan blue exclusion assay, which is an accurate representation of how the cells interact with the films.

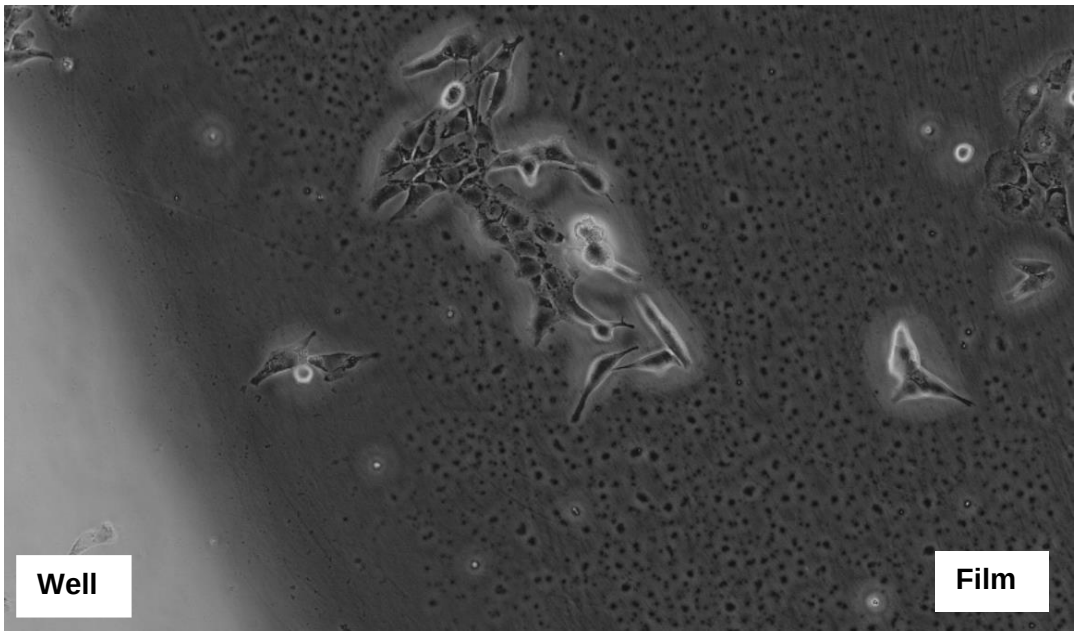


Figure 4. 36 PC12 cells attached to a collagen coated film.

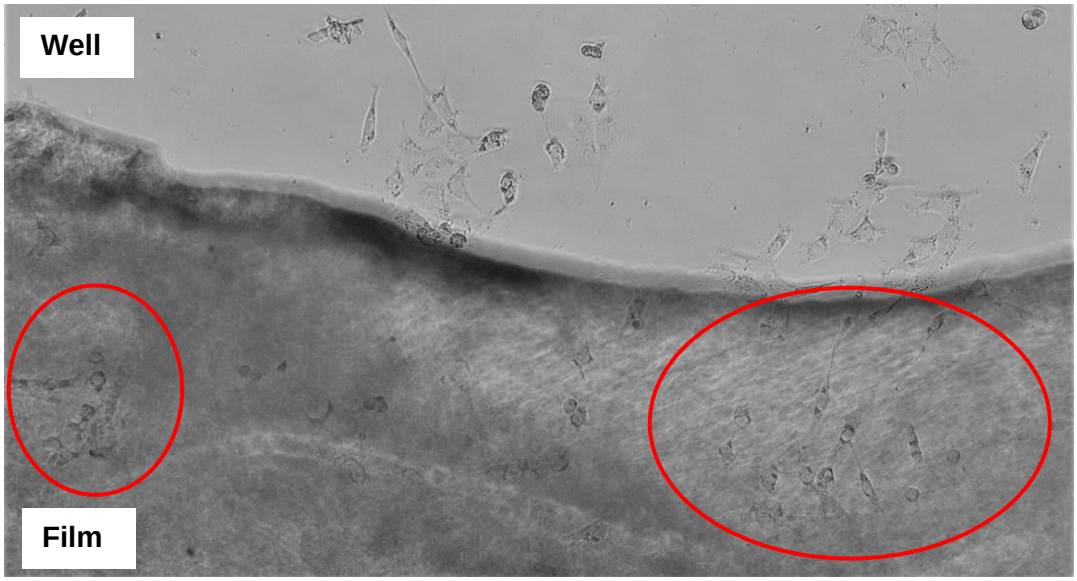


Figure 4. 37 PC12 cells attached to a gelatin crosslinked film circled in red**.**

4.3.15 Quantification of cell attachment using the trypan blue exclusion assay

The trypan blue exclusion assay provided a quantitative analysis of the percentage of cells that attached to the films. This was an important assay as it provided a direct indication of the suitability of the films in supporting cell attachment (Liu et al., 2004). The higher the cell

attachment to the films, the better the films performed *In Vitro* (Liu et al., 2004). Figure 4.38 represents the PC12 cell attachment relative to the control (plasma treated cell culture well plates).

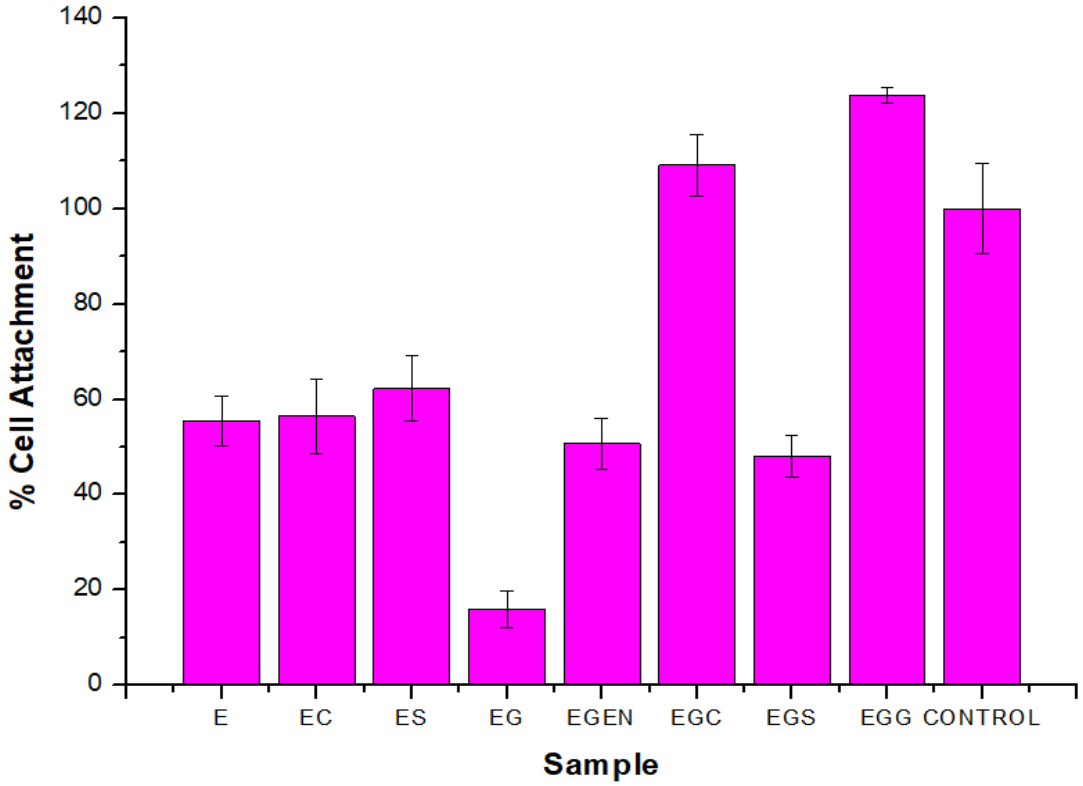


Figure 4. 38 Quantification of cell attachment of PC12 cells after 72 h incubation. (E) aminolyzed film, (EC) collagen coated film, (ES) sodium alginate coated film, (EG) gelatin coated film, (EGEN) genipin crosslinked film, (EGC) collagen crosslinked film, (EGS) sodium alginate crosslinked film, (EGG) gelatin crosslinked film.

The results in Figure 4.38 demonstrate that the collagen and sodium alginate coating slightly enhance the percentage cell attachment to the films from 55.43 to 56.45 and 62.31%, respectively. The gelatin coating only facilitates a 16% cell attachment, which is unusual since cytocompatibility tests show that these samples are not cytotoxic to PC12 cells. The genipin-crosslinked sample demonstrates a slightly reduced cell attachment in comparison to the aminolyzed sample. The collagen crosslinked sample shows a 109.07% cell attachment relative to the control. The gelatin crosslinked samples further increase the cell attachment to 123.72%. However, the sodium alginate crosslinked samples reduce the cell attachment to 48.11%, which is very poor (Boni et al., 2018). The reason for this was unclear.

The trypan blue exclusion assay results with A172 cells depicted in Figure 4.39 indicate that the aminolyzed film only enables a 48.95% cell attachment relative to the control. The coated films all improve cell attachment to 50.55, 52.94 and 56.02%, respectively. In comparison to the PC12 cell line, the PCL/CAP-EDA-GEL sample does not perform as poorly with the A172

cells. The genipin coated sample enhances the cell attachment in comparison to the aminolyzed sample, which is not the case found with the PC12 cells. The collagen and gelatin crosslinked samples both enhance the cell attachment to 116.62 and 127.96%, while the sodium alginate crosslinked samples only produce a cell attachment of 59.20%.

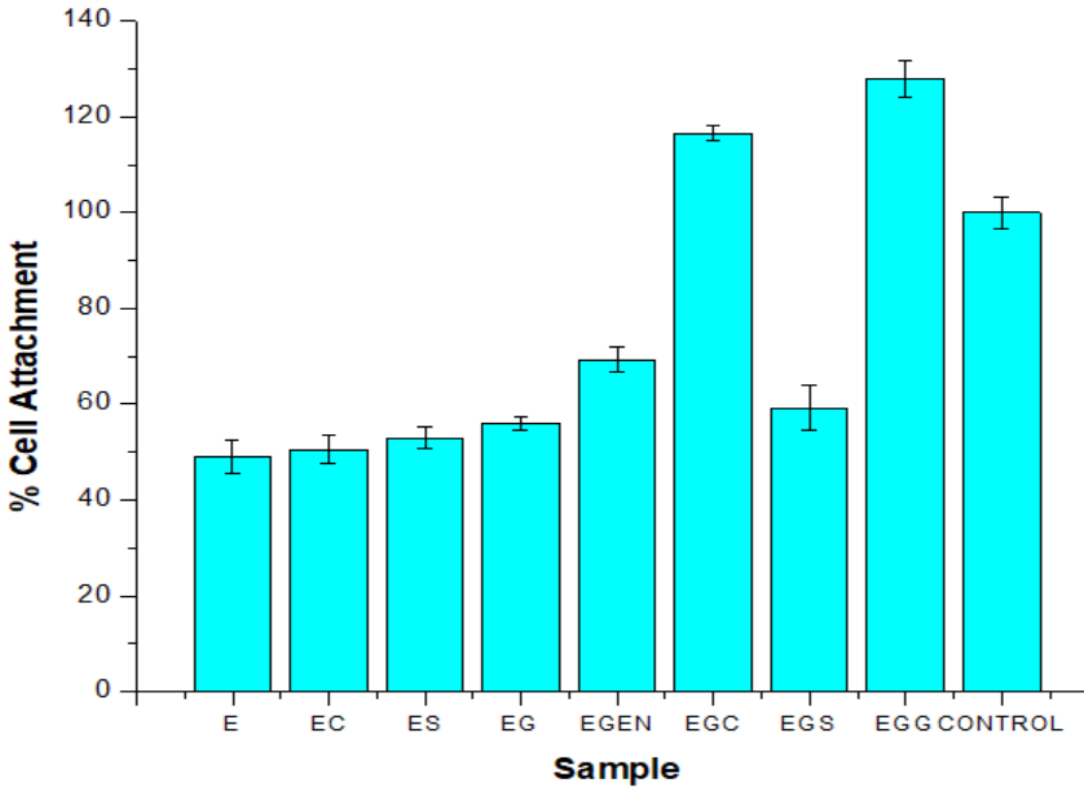


Figure 4. 35 Quantification of cell attachment results for A172 cells after 72 h incubation. (E) aminolyzed film, (EC) collagen coated film, (ES) sodium alginate coated film, (EG) gelatin coated film, (EGEN) genipin crosslinked film, (EGC) collagen crosslinked film, (EGS) sodium alginate crosslinked film, (EGG) gelatin crosslinked film.

To conclude, the XTT cell viability study uses 'extracts' of the sample which are only in contact with the media for 24 h, whereas this attachment assay involves the cells being in direct contact with the samples. Therefore, the trypan blue assay may produce a more accurate representation of cell-film interactions, therefore, the results of this assay are considered conclusive. This assay indicates that the biomolecule coated samples facilitate a higher cell attachment in comparison to the aminolyzed samples. In addition, the biomolecule crosslinked films facilitate an even higher cell attachment. Further, the collagen and gelatin crosslinked samples enable a superior cell attachment relative to the control, proving that the biomolecule crosslinked films possess enhanced neurocompatibility. (Liu et al., 2004).

4.4 Concluding remarks

Biomolecule immobilization has proven to be an effective modification technique to enhance the neurocompatibility of the aminolyzed PCL/CAP films. Further, various other characteristics

of the samples are also improved such as mechanical properties, BET surface area and hydrophilicity. In most cases, the biomolecule coated samples (without the genipin crosslinker) perform better than the aminolyzed sample. In addition, the biomolecule crosslinked samples supersede the performance of the coated samples, proving that the presence of genipin and the biomolecules enhances the properties of the thin films. In conclusion, the cell attachment quantification assay indicates that the cells preferentially attach to the collagen and gelatin-coated samples. The trypan blue exclusion assay is seen as the most accurate representation of cell attachment since the cells are in direct contact with the films, and this indicates that the biomolecule crosslinked samples are superior in comparison to the control. The cell attachment results of the crosslinked samples are far superior to those of the hydrolyzed and aminolyzed films in Chapter 3, proving the importance of biomolecules in neurocompatibility. Therefore, biomolecule immobilization, with or without the use of a crosslinker, is an appropriate and cost-effective method to enhance the neurocompatibility of polymeric thin films for neural tissue engineering applications.

4.5 References

Ansari, S., Diniz, I. M., Chen, C., Sarrion, P., Tamayol, A., Wu, B. M., & Moshaverinia, A. (2017). Human periodontal ligament- and gingiva-derived mesenchymal stem cells promote nerve regeneration when encapsulated in alginate/hyaluronic acid 3D scaffold. Advanced healthcare materials, 6(24), 10-15.

Archibald, S. J., Shefner, J., Krarup, C., & Madison, R. D. (1995). Monkey median nerve repaired by nerve graft or collagen nerve guide tube. Journal of neuroscience, 15(5), 4109-4123.

Arteche Pujana, M., Pérez-Álvarez, L., Cesteros Iturbe, L. C., & Katime, I. (2013). Biodegradable chitosan nanogels crosslinked with genipin. Carbohydrate polymers, 94(2), 836-842.

Atthoff, B., & Hilborn, J. (2007). Protein adsorption onto polyester surfaces: is there a need for surface activation? Journal of biomedical materials research-part B applied biomaterials, 10(1), 121-130.

Barrett, E., Joyner, L., & Halenda, P. (1951). The Determination of pore volume and area distributions in porous substances. Journal of the American chemical society, 73(1), 373-380.

Bellis, S. L. (2011). Advantages of RGD peptides for directing cell association with biomaterials. Biomaterials, 32(18), 4205-4210.

Bigi, A., Cojazzi, G., Panzavolta, S., Roveri, N., & Rubini, K. (2002). Stabilization of gelatin films by crosslinking with genipin. Biomaterials, 23(24), 4827-4832.

Boni, R., Ali, A., Shavandi, A., & Clarkson, A. N. (2018). Current and novel polymeric biomaterials for neural tissue engineering. Journal of biomedical science, 25(3), 90-94.

Bozec, L., & Odlyha, M. (2011). Thermal denaturation studies of collagen by microthermal analysis and atomic force microscopy. Biophysics, 101(1), 228-236.

Bozkurt, A., Claeys, K. G., Schrading, S., Rödler, J. V., Altinova, H., Schulz, J. B., Weis, J., Pallua, N., & Van Neerven, S. G. A. (2017). Clinical and biometrical 12-month follow-up in patients after reconstruction of the sural nerve biopsy defect by the collagen-based nerve guide Neuromatrix. European journal of medical research, 22(1), 1-12.

Bruylants, G., Wouters, J., & Michaux, C. (2020). Differential scanning calorimetry in life science : thermodynamics, stability, molecular recognition, and application in drug design. Current medicinal chemistry, 12(17), 2011-2020.

Cao, M., Gu, F., Rao, C., Fu, J., Zhao, P. (2019). Improving the electrospinning process of fabricating nanofibrous membranes to filter. Science of the total environment, 666(3),1011-1021.

Chang, C. (2009). Effects of nerve growth factor from genipin-crosslinked gelatin in polycaprolactone conduit on peripheral nerve regeneration In Vitro and In Vivo. Journal of biomedical materials research-part A, 91(2), 586-596.

Chiono, V., Pulieri, E., Vozzi, G., Ciardelli, G., Ahluwalia, A., & Giusti, P. (2008). Genipin-crosslinked chitosan/gelatin blends for biomedical applications. Journal of materials science: materials in medicine, 19(2), 889-898.

Cui, F., Xue, C., Li, Z., & Zhang, Y. (2007). Food chemistry characterization and subunit composition of collagen from the body wall of sea cucumber Stichopus japonicus. Food chemistry, 100(1), 1120-1125.

Da Silva, K. Da, Kumar, P., Vuuren, S. F. Van, Pillay, V., & Choonara, Y. E. (2021). Three-dimensional printability of an ECM-Based gelatin methacryloyl (GelMA) biomaterial for potential neuroregeneration. ACS Omega, 6 (33), 21368-21383.

Daemi, H., & Barikani, M. (2012). Synthesis and characterization of calcium alginate nanoparticles, sodium homopolymannuronate salt and its calcium nanoparticles. Scientia Iranica, 19(6), 2023-2028.

Di Giovanni, S., Movsesyan, V., Ahmed, F., Cernak, I., Schinelli, S., Stoica, B., & Faden, A. I. (2005). Cell cycle inhibition provides neuroprotection and reduces glial proliferation and scar formation after traumatic brain injury. Proceedings of the national academy of sciences of the United States of America, 102(23), 8333-8338.

Dimida, S., Barca, A., Cancelli, N., De Benedictis, V., Raucci, M. G., & Demitri, C. (2017). Effects of genipin concentration on cross-linked chitosan scaffolds for bone tissue engineering: Structural characterization and evidence of biocompatibility features. International journal of polymer science, 2017(1), 8410750.

Dong, Y., Dong, W., Cao, Y., Han, Z., & Ding, Z. (2011). Preparation and catalytic activity of Fe alginate gel beads for oxidative degradation of azo dyes under visible light irradiation. Catalysis today, 175(1), 346-355.

dos Santos, D. M., Leite, I. S., Bukzem, A. de L., de Oliveira Santos, R. P., Frollini, E., Inada, N. M., & Campana-Filho, S. P. (2018). Nanostructured electrospun nonwovens of poly(ε-caprolactone)/ quaternized chitosan for potential biomedical applications. Carbohydrate polymers, 186(11), 110-121.

Dulnik, J., Denis, P., & Sajkiewicz, P. (2016). Biodegradation of bicomponent PCL/ gelatin and PCL/ collagen nanofibers electrospun from alternative solvent system. Polymer degradation and stability, 130(2), 10-21.

Frohbergh, M. E., Katsman, A., Botta, G. P., Lazarovici, P., Schauer, C. L., Wegst, U. G. K., & Lelkes, P. I. (2012). Electrospun hydroxyapatite-containing chitosan nanofibers crosslinked with genipin for bone tissue engineering. Biomaterials, 33(36), 9167-9178.

Gregg, S., Sing, K., & Salzberg, H. (1967). Adsorption surface area and porosity. Journal of the electrochemical society, 114 (11), 279-285.

Hashimoto, T., Suzuki, Y., Kitada, M., Kataoka, K., Wu, S., Suzuki, K., Endo, K., Nishimura, Y., & Ide, C. (2002). Peripheral nerve regeneration through alginate gel: Analysis of early outgrowth and late increase in diameter of regenerating axons. Experimental brain research, 146(3), 356-368.

Hughes, R. H., Silva, V. A., Ahmed, I., Shreiber, D. I., & Morrison, B. (2014). Neuroprotection by genipin against reactive oxygen and reactive nitrogen species-mediated injury in organotypic hippocampal slice cultures. Brain research, 16(1543), 308-314.

Ikada, Y. (1994). Surface modification of polymers for medical applications. Biomaterials, 15(10), 725-736.

Kahoush, M., Behary, N., Guan, J., Cayla, A., Mutel, B., & Nierstrasz, V. (2021). Genipin-mediated immobilization of glucose oxidase enzyme on carbon felt for use as heterogeneous catalyst in sustainable wastewater treatment. Journal of environmental chemical engineering, 9(4), 0-2.

Kataoka, K., Suzuki, Y., Kitada, M., Hashimoto, T., Chou, H., Bai, H., Ohta, M., Wu, S., Suzuki, K., & Ide, C. (2004). Alginate enhances elongation of early regenerating axons in spinal cord of young rats. Tissue engineering, 10(3-4), 493-504.

Khorramnezhad, M., Akbari, B., Akbari, M., & Kharaziha, M. (2021). The effect of surface modification on physical and cellular properties of PCL thin film. Colloids and surfaces B:Biointerfaces, 200(1), 111582-11591.

Kim, M. S., Jun, I., Shin, Y. M., Jang, W., Kim, S. I., & Shin, H. (2010). The development of genipin-crosslinked poly(caprolactone) (PCL)/ gelatin nanofibers for tissue engineering applications. Macromolecular bioscience, 10(1), 91-100.

Kosmala, A., Fitzgerald, M., Moore, E., & Stam, F. (2017). Evaluation of a gelatin-modified poly(ε-caprolactone) film as a scaffold for lung disease. Analytical letters, 50(1), 219-232.

Krithica, N., Natarajan, V., Madhan, B., Sehgal, P. K., & Mandal, A. B. (2012). Type I collagen immobilized poly(caprolactone) nanofibers: Characterization of surface modification and growth of fibroblasts. Advanced engineering materials, 14(4), 149-154.

Lee, K. Y., & Mooney, D. J. (2012). Alginate: properties and biomedical applications. Progress in polymer science, 37(1), 106-126.

Liu, Y., Cai, Z., Sheng, L., Ma, M., Xu, Q., & Jin, Y. (2019). Structure-property of crosslinked chitosan/ silica composite films modified by genipin and glutaraldehyde under alkaline conditions. Carbohydrate polymers, 215(1), 348-357.

Machado, A. A. S., Martins, V. C. A., & Plepis, A. M. G. (2002). Thermal and rheological behavior of collagen chitosan blends. Journal of thermal analysis and calorimetry, 67(2), 491-498.

Manickam, B., Sreedharan, R., & Elumalai, M. (2014). 'Genipin'-the natural water-soluble cross-linking agent and its importance in the modified drug delivery systems: an overview. Current drug delivery, 11(1), 139-145.

Masaeli, E., Wieringa, M., Nasr-Esfahani, MH., Sadri, S., van Blitterswijk, C.A and Moroni, L. (2014). Peptide functionalized polyhydroxyalkanoate nanofibrous scaffolds enhance Schwann cells activity. Nanomedicine: nanotechnology, biology, and medicine 10(7),1559-1569.

Mateescu, M., & Juha, J. (2002). Structure, properties relationship in cross-linked high amylose starch cast films. Carbohydrate polymers, 50(4), 371-378.

Mathew, A. P., Oksman, K., Pierron, D., & Harmand, M. F. (2013). Biocompatible fibrous networks of cellulose nanofibres and collagen crosslinked using genipin: potential as artificial ligament/ tendons. Macromolecular bioscience, 13(3), 289-298.

Matsuura, S., Obara, T., Tsuchiya, N., Suzuki, Y., & Habuchi, T. (2006). Cavernous nerve regeneration by biodegradable alginate gel sponge sheet placement without sutures. Urology, 68(6), 1366-1371.

Meghdadi, M., Atyabi, S.-M., Pezeshki-Modaress, M., Irani, S., Noormohammadi, Z., & Zandi, M. (2019). Cold atmospheric plasma as a promising approach for gelatin immobilization on poly(ε-caprolactone) electrospun scaffolds. Progress in biomaterials, 8(1), 65-75.

Mirhosseini, M. M., Haddadi-Asl, V., & Zargarian, S. S. (2016). Fabrication and characterization of hydrophilic poly(ε-caprolactone)/ pluronic P123 electrospun fibers. Journal of applied polymer science, 133(17), 1-11

Mondal, D., Griffith, M., & Venkatraman, S. S. (2016). Polycaprolactone-based biomaterials for tissue engineering and drug delivery: current scenario and challenges. International journal of polymeric materials and polymeric biomaterials, 65(5), 255-265.

Mu, C., Zhang, K., Lin, W., & Li, D. (2013). Ring-opening polymerization of genipin and its long-range crosslinking effect on collagen hydrogel. Journal of biomedical materials research-part A, 101(2), 385-393.

Murphy, C. M., & O'Brien, F. J. (2010). Understanding the effect of mean pore size on cell activity in collagen-glycosaminoglycan scaffolds. Cell adhesion and migration, 4(3), 377-381.

Nickerson, M. T., Patel, J., Heyd, D. V., Rousseau, D., & Paulson, A. T. (2006). Kinetic and mechanistic considerations in the gelation of genipin-crosslinked gelatin. International journal of biological macromolecules, 39(4-5), 298-302.

Oland, C. M. (2013). Interpenetrating polymer networks (IPN): structure and mechanical behavior. In Kobayashi, S., Müllen, K. (eds). Encyclopedia of Polymeric Nanomaterials. Springer, Berlin, Heidelberg.

Oryan, A., Kamali, A., Moshiri, A., Baharvand, H., & Daemi, H. (2018). Chemical crosslinking of biopolymeric scaffolds: current knowledge and future directions of crosslinked engineered bone scaffolds. International journal of biological macromolecules, 107(A), 678-688.

Pabari, A., Yang, S. Y., Mosahebi, A., & Seifalian, A. M. (2011). Recent advances in artificial nerve conduit design. Journal of controlled release, 56(1), 2-10.

Pamula, E., & Menaszek, E. (2008). In Vitro and In Vivo degradation of poly(l-lactide-co-glycolide) films and scaffolds. Journal of materials science: materials in medicine, 19(5), 2063-2070.

Panzavolta, S., Gioffrè, M., Focarete, M. L., Gualandi, C., Foroni, L., & Bigi, A. (2011). Electrospun gelatin nanofibers: optimization of genipin cross-linking to preserve fiber morphology after exposure to water. Acta biomaterialia, 7(4), 1702-1709.

Park, B. U., Park, S. M., Lee, K. P., Lee, S. J., Nam, Y. E., Park, H. S., Eom, S., Lim, J. O., Kim, D. S., & Kim, H. K. (2019). Collagen immobilization on ultra-thin nanofiber membrane to promote In Vitro endothelial monolayer formation. Journal of tissue engineering, 10.

Park, G. E., Pattison, M. A., Park, K., & Webster, T. J. (2005). Accelerated chondrocyte functions on NaOH-treated PLGA scaffolds. Biomaterials, 26(16), 3075-3082.

Peña, C., De, K., Eceiza, A., Ruseckaite, R., & Mondragon, I. (2010). Enhancing water repellence and mechanical properties of gelatin films by tannin addition. Bioresource technology, 101(17), 6836-6842.

Ramburrun, P., Kumar, P., Choonara, Y. E., du Toit, L. C., & Pillay, V. (2019). Design and characterisation of PHBV-magnesium oleate directional nanofibers for neurosupport. Biomedical materials, 14(1), 65015-65019 .

Rao, K. M., Mallikarjuna, B., Rao, K. S. V. K., & Sudhakar, K. (2013). Synthesis and characterization of pH sensitive poly(hydroxy ethyl methacrylate-co-acrylamidoglycolic acid) based hydrogels for controlled release studies of 5-fluorouracil. International journal of polymeric materials and polymeric biomaterials, 62(11), 6-13.

Ray, W. Z., & Mackinnon, S. E. (2010). Management of nerve gaps: autografts, allografts, nerve transfers, and end-to-side neurorrhaphy. Experimental neurology, 223(1), 77-85.

Rentsch, B., Hofmann, A., Breier, A., Rentsch, C., & Scharnweber, D. (2009). Embroidered and surface modified polycaprolactone-co-lactide scaffolds as bone substitute: In Vitro characterization. Annals of biomedical engineering, 37(10), 2118-2128.

Rodríguez-Baeza, M., Neira A., Aguilera, C.J. (2003). Thermogravimetric study of the formation of cross-linked structures in the synthesis of poly(methylsiloxane). Journal of the Chilean chemical society, 48(2), 75-77.

Rokhade, A. P., Agnihotri, S. A., Patil, S. A., Mallikarjuna, N. N., Kulkarni, P. V., & Aminabhavi, T. M. (2006). Semi-interpenetrating polymer network microspheres of gelatin and sodium carboxymethyl cellulose for controlled release of ketorolac tromethamine. Carbohydrate polymers, 65(3), 243-252.

Ruoslahti, E. (1996). RGD and other recognition sequences for integrins. Annual review of cell and developmental biology, 12, 697-715.

Samouillan, V., Dandurand, J., Lacabanne, C., Sabatier, P., & Cedex, T. (2004). Effect of water on the molecular mobility of elastin. Biomacromolecules, 5(3), 958-964.

Sherman, V. R., Yang, W., & Meyers, M. A. (2015). The materials science of collagen. Journal of the mechanical behavior of biomedical materials, 52(11), 22-50.

Siritientong, T., Ratanavaraporn, J., Srichana, T., & Aramwit, P. (2013). Preliminary characterization of genipin-cross-linked silk sericin/poly(vinyl alcohol) films as two-dimensional wound dressings for the healing of superficial wounds. BioMed research international, 2013, 904314-904320.

Soares, J. P., Santos, J. E., Chierice, G. O., & Cavalheiro, E. T. G. (2004). Thermal behavior of alginic acid and its sodium salt. Eclética Química, 29(2), 53-56.

Su, K., & Wang, C. (2015). Recent advances in the use of gelatin in biomedical research. Biotechnology letters, 37(11), 2139-2145.

Sundararaghavan, H. G., Monteiro, G. A., Lapin, N. A., Chabal, Y. J., Miksan, J. R., & Shreiber, D. I. (2008). Genipin-induced changes in collagen gels: correlation of mechanical properties to fluorescence. Journal of biomedical materials research-part A, 87(2), 308-320.

Suzuki, Y., Tanihara, M., Ohnishi, K., Suzuki, K., Endo, K., & Nishimura, Y. (1999). Cat peripheral nerve regeneration across 50 mm gap repaired with a novel nerve guide composed of freeze-dried alginate gel. Neuroscience letters, 259(2), 75-78.

Vera-Graziano, R., Hernandez-Sanchez,F., Cauich-Rodriguez, J.V. (1995). Study of crosslinking density in polydimethylsiloxane networks by DSC. Journal of applied polymer science, 55(9), 1317-1327.

Wang, T., Ji, X., Feng, Z., Wu, J., Wang, H. and Xu, Z (2013). Fabrication and characterization of heparin-grafted poly-lactic acid-chitosan core-shell nanofibers scaffold for vascular gasket. ACS applied materials and interfaces, 5(9), 3757-3763.

Wangensteen, K. J., & Kalliainen, L. K. (2010). Collagen tube conduits in peripheral nerve repair: a retrospective analysis. Hand, 5(3), 273-277.

Yakimets, I., Wellner, N., Smith, A. C., Wilson, R. H., Farhat, I., & Mitchell, J. (2005). Mechanical properties with respect to water content of gelatin films in glassy state. Polymer, 46(26), 12577-12585.

Yao, Y., Cui, Y., Zhao, Y., Xiao, Z., Li, X., Han, S., Chen, B., Fang, Y., Wang, P., Pan, J., & Dai, J. (2018). Effect of longitudinally oriented collagen conduit combined with nerve growth factor on nerve regeneration after dog sciatic nerve injury. Journal of biomedical materials research-part B applied biomaterials, 106(6), 2131-2139.

Yi, B., Yu, L., Tang, H., Wang, W., Liu, W., & Zhang, Y. (2021). Lysine-doped polydopamine coating enhances antithrombogenicity and endothelialization of an electrospun aligned fibrous vascular graft. Applied materials today, 25(2), 101198-101201.

Yoo, J. S., Kim, Y. J., Kim, S. H., & Choi, S. H. (2011). Study on genipin: A new alternative natural crosslinking agent for fixing heterograft tissue. Korean journal of thoracic and cardiovascular surgery, 44(3), 197-207.

Zu, Y., Yu, X., Zhao, X., Wang, W., & Wang, K. (2014). Nano-crystallization of the pharmaceutically active agent genipin by an emulsion solvent evaporation method. Journal of nanomaterials, 2013(1-2), 1-13.

CHAPTER 5:
FABRICATION OF A TWO-DIMENSIONAL BIO-ACTIVE NANOFIBROUS PLATFORM FOR ENHANCED NEUROCOMPATIBILITY

5.1 Introduction

Nanofibers have the capacity to mimic the inherent nature of the fibrillar extracellular matrix and have featured extensively in the fabrication of nerve guidance conduits (Nagarajan et al., 2019). These conduits are aimed at the recapitulation of the essential biological and structural features of the native extracellular matrix to provide a viable environment to guide the regrowth or repair of transected nerves (Nagarajan et al., 2019). Furthermore, these fibrous structures are able to provide favourable topographical and chemical cues to neural cells in addition to providing a means for the influx of nutrients and efflux of waste (Valmikinathan et al., 2011). This feature provides electrospun nanofibers with an advantage over other materials such as non-fibrous structures such as films (Xie et al., 2014). Electrospinning has gleaned considerable interest in the production of nanofibers due to its appreciably efficient, reproducible, simple and highly adaptable nature (Doshi & Reneker, 1995). It involves the production of ultrathin fibers from a viscoelastic solution directed by a strong external electrical potential (Xiaoqiang Li et al., 2010). When the electric field comes into contact with the tip of the solution *In Situ*, the drop elongates to form a Taylor cone (Xiaoran Li et al., 2019). When the applied voltage exceeds the surface tension, charged jets of polymer solution are ejected from the solution reservoir onto the collector drum (Xiaoqiang Li et al., 2019). The solvent consequently evaporates, forming solidified nanofibers (Xiaoran Li et al., 2019). A collection of solidified nanofibers is formed over a period of time, in either an aligned or random orientation (Xie et al., 2014).

Electrospinning has been applied to a number of natural and synthetic polymers for application in neural tissue engineering, known for their exemplary inherent viscoelastic nature (Nagarajan et al., 2019). Natural polymers are innately bioactive, presenting vast domains of cellular interactive moieties on their backbones (Bhattarai et al., 2018). Nanofibers prepared from natural polymers exhibit a niche promotion of cell-platform interactions such as cell adhesion, proliferation, and differentiation, but are often limited by poor electrospinnability, poor processability, inadequate mechanical strength and rapid degradation (Bhattarai et al., 2018). Synthetic polymers have been used to great effect in neural tissue engineering due to their flexibility in processing, synthesis, modification and remarkable mechanical strength (Amani et al., 2019). Hydrophobicity and low surface energy are a few of the hallmark traits of most synthetic polymers, which often hinder cell attachment and proliferation on the nanofibrous platforms (Muthiah et al., 2011).

Regardless of their extracellular matrix mimicry, a significant push has been made towards improving the performance of nanofibrous platforms for neural tissue engineering *In Vitro* and *In Vivo*. The versatility of nanofibrous platforms allows for extensive modifications to further improve neurocompatibility, cell-platform interactions and neurite outgrowth by conferring surface functionalization, facilitating the surface attachment of drugs or biomolecules or enabling the transplantation and differentiation of stem cells (Zhan et al., 2012). Due to the simple and effective nature of the biomolecule immobilization process undertaken in the previous chapters, this same procedure will be utilized in this study for the bio-functionalization of the nanofibrous platforms.

5.2 Materials and Methods

PCL, CAP, EDA, SDS and PBS were purchased from Sigma-Aldrich (St. Louis, MO, USA). Ethanol (99% absolute) was purchased from LabChem, Edenvale, Johannesburg, South Africa. Chloroform, acetone, DMSO and 2-propanol were purchased from Associated Chemical Enterprises, Southdale, Johannesburg, South Africa. NaOH and KOH pellets were purchased from Merck, Darmstadt, Germany. Millipore water was used for washing of preparations. DMEM, Trypan Blue, penicillin/streptomycin, cell culture treated well plates, flasks, DES CellCrown^{TM} Inserts and FBS were purchased from Sigma Aldrich, South Africa. The Ham's F12 Nutrient Mixture was purchased from Gibco (Thermo Fischer, South Africa). The Roche Cell Proliferation Kit II (XTT) was purchased from Sigma Aldrich, South Africa. The PC12 and A172 cells were purchased from Cellonex (Separations, South Africa). Mammoth powerful grip double sided transparent tape was purchased from Builders Warehouse, South Africa. The BCA protein kit was purchased from Pierce (Thermofischer, South Africa).Genipin was purchased from Challenge Bioproducts Co, Ltd. (Yun-Lin Hsien, Taiwan). Gelatin (Bloom 160, type B) derived from bovine skin was purchased from Fluka (Steinheim, Germany). Collagen derived from bovine Achilles' tendon was purchased from Sigma-Aldrich (St Louis, MI USA).

5.2.1 Method of bioactive nanofibrous platform fabrication

5.2.1.1 Electrospinning of the polymeric solutions to form nanofibers

The film samples from Chapters 3 and 4 were used as a baseline for the development of the nanofibrous platform due to the novelty in neural tissue engineering, their desirable mechanical properties and cytocompatibility. Two composite solutions were formed to identify the optimal total polymer concentration for electrospinning. Briefly, 6% w/v and 4% w/v PCL solutions were made in chloroform and 3% w/v, and 2% w/v CAP solutions were made in acetone: ethanol (2:3). Thereafter, the corresponding PCL and CAP solutions were combined to form two composite polymer solutions consisting of PCL and CAP at a ratio of 2:1, with a total polymer concentration of 9% w/v and 6% w/v, respectively. The two solutions were electrospun

separately at the conditions outlined in Table 5.1 to form solidified nanofibers on the collector drum. Once a sheet of fibers was formed, the sheet was removed and dried under continuous airflow for 14 days to ensure complete solvent evaporation. The platforms were then rinsed three times in PBS and placed under continuous airflow at 25°C until further use.

Table 5. 1 Electrospinning conditions employed to fabricate the nanofibrous platforms.

Flow rate	Spinning distance (mm)	Rotations per min (rpm)	Voltage (V)	Stroke and velocity	Temperature (°C)	Relative Humidity (%)
8 µl/min	160 mm	120 rpm	11.5V	560	25 °C	41%

5.2.1.2 Method of determining the optimal total polymer concentration using scanning electron microscopy

The platforms were fixed to aluminium stubs using double-sided adhesive carbon tape and then sputter coated with carbon and gold palladium for 120 s (SPI ModuleTM Sputter-Coater and Control Unit, West Chester, PA, USA). Evaluation of surface morphology and image capturing of the nanofibrous platforms were performed under different magnifications using an FEI Nova NanoLab 600TM Scanning Electron Microscope (SEM) (FEI Company, Hillsboro, OR, USA).

5.2.1.3 Method of optimal aminolysis conditions determination utilizing scanning electron microscopy

The nanofibers were aminolyzed by immersing the platforms in 20% v/v ethylenediamine in isopropanol for increasing time intervals: 7.5; 15; 30; 60 and 90 mins in an orbital shaker bath at 37 °C. The samples were then rinsed three times in distilled water and left to dry overnight. The ideal aminolysis time was assessed by viewing the samples under SEM to determine the longest time interval that did not cause damage to the fibers. The aminolyzed samples were fixed to aluminium stubs using double-sided adhesive carbon tape and then sputter coated with carbon and gold palladium for 120 s. Evaluation of surface morphology and image capturing of the nanofibrous platforms were performed under different magnifications using an FEI Nova NanoLab 600TM SEM.

5.2.1.4 Method of biomolecule immobilization

A 0.5% w/v collagen stock solution was prepared in 2% v/v acetic acid in distilled water. Stock solutions of gelatin and sodium alginate (0.5% w/v) were prepared in distilled water. All stock solutions were stored at 2-8 °C until further use. The optimal aminolyzed nanofibrous platforms determined in 5.3.1.1 were immersed in 1 ml of each biomolecule stock solution in glass vials for 24 h at 37 °C in an orbital shaker to allow the biomolecule to attach to the nanofibers via electrostatic attraction. Thereafter, a 1% w/v genipin solution was prepared in a 50:50 ethanol:

water solution. Following this, 1 ml of this was added to each glass vial and left to cross-link for five days in an orbital shaker set at 37 °C. The films were then removed from the solutions and washed three times in deionised water to remove excess biomolecule and left to dry overnight. Method adapted from Chang (2009).

Table 5. 2 Abbreviations of all samples with their respective constituents.

Sample abbreviation	Sample constituents
PCL	Polycaprolactone nanofibrous platform.
PCL/CAP-EDA	Aminolyzed polycaprolactone/cellulose acetate phthalate nanofibrous platform.
PCL/CAP-EDA-GEN	Genipin coated aminolyzed nanofibrous platform.
PCL/CAP-EDA-COLL	Collagen coated aminolyzed nanofibrous platform.
PCL/CAP-EDA-GEN-COLL	Aminolyzed nanofibrous platform with collagen crosslinked to its surface using genipin.
PCL/CAP-EDA-SA	Sodium alginate coated aminolyzed nanofibrous platform.
PCL/CAP-EDA-GEN-SA	Aminolyzed nanofibrous platform with sodium aglinate crosslinked to its surface using genipin.
PCL/CAP-EDA-GEL	Gelatin coated aminolyzed nanofibrous platform.
PCL/CAP-EDA-GEN-GEL	Aminolyzed nanofibrous platform with gelatin crosslinked to its surface using genipin.

5.2.2 Surface topography mapping method by atomic force microscopy

AFM (Veeco CP2) was used to determine high-resolution surface mapping of the nanofibrous platforms as well as the aminolyzed nanofibrous platform in three dimensions providing rich data regarding the nanofibers' surface topography and surface roughness.

5.2.3 Method of chemical integrity characterizations employing FT-IR

FT-IR spectroscopy detected the molecular transitions and changes in crystallinity indices of the nanofibers arising from interactions between the samples and each of their constituents. Samples were analysed over an FT-IR spectra of wavelengths between 4000 and 600 cm^{-1} using a PerkinElmer Spectrum 2000 ATR FT-IR (PerkinElmer 100, Llantrisant, Wales, UK) spectrometer fitted with a single-reflection diamond MIRTGS detector.

5.2.4 Analysis of the thermodynamic behavior of the nanofibrous platforms utilizing differential scanning calorimetry

Differential scanning calorimetry (DSC) (Mettler Toledo, Schwerzernback, Switzerland) was used to reveal the thermal properties of the nanofibrous platforms and their constituents. Samples of 2-10 mg were sealed in aluminium crucibles and heated over a temperature range of 0-300 °C, at a rate of 10 $°C.min^{-1}$. DSC curves were obtained by plotting sample weight over sample temperature, and various parameters were obtained from the graphs using Origin Pro

8.5 software. These parameters included the temperature of onset of melting, the melting temperature (Tm), the enthalpy of melting (∆hm) as well as the onset of degradation.

5.2.5 Method of phase transition assessment utilizing x-ray diffraction analysis

X-ray diffraction was employed in order to determine the phase changes (crystallinity or amorphous) of the nanofibrous platforms and their constituents. This characterization technique was performed on the Rigaku MiniFlex 600 Benchtop X-ray Diffractometer (Rigaku Corporation, Tokyo, Japan). The nanofibrous samples were secured on a sample holder and were scanned at a rate of 15° per min with a diffraction angle range of 05-90° 2Θ with a degree step of 0.02, a voltage of 40 kV and a current of 15 mA.

5.2.6 Method of thermal stability analysis utilizing thermogravimetric analysis

The determination of change in sample weight as a function of temperature was performed using a Thermogravimetric analyser (PerkinElmer, TGA 4000, Llantrisant, Wales, UK). Samples were heated at a rate of 10 ˚C per min from 0-900˚C under continuous nitrogen purging. Thermograms were generated as percentage weight vs. temperature and analysed using Pyris TM software (PerkinElmer, Llantrisant, Wales, UK). The derivative curves were plotted for each sample to accurately determine the temperature of each degradation step.

5.2.7 Method of porosimetric and surface area characterization using BET analysis

The porosity and surface area of the samples were analysed using the Micromeritics Porositometer (Micromeritics ASAP 2020, Norcross, GA, USA). Surface areas, pore sizes, shapes, and distributions were assessed according to the parameters listed in A4 in the appendix and analysed.

5.2.8 Method of mechanical characterization using Texture Analyser analysis

The mechanical properties of the nanofibers were determined with a Texture Analyser (TA.XTplus Texture Analyser, Stable Microsystems, Surrey, UK) fitted with two clamps. The width, height, and length of the samples were measured with a digital Vernier calliper (Krafft. DV150GW, Schoellerstr Düren, German). Rectangular 40 x 15 mm strips of each sample were fixed at 20 mm between the two clamps. Tests were conducted at 0.167 $mm.s^{-1}$ while applying a 0.5 N trigger force.

5.2.9 Method of hydrophilicity characterization utilizing water contact angle measurements

The hydrophilicity of the nanofibers was evaluated with the DataPhysics Instruments contact angle goniometer by measuring the water contact angle using the sessile drop method. The samples were stuck on the stage using double-sided tape. A Hamilton syringe was used to

dispense 2 µl of distilled water onto the surface at a dosing rate of 2 $\mu l.s^{-1}$ in three random positions on the film surface. The images of the water droplet were recorded by camera software after the droplet was stable. Thereafter, the water contact angle was measured using the SCA202 version 4.1.12 build 1019 software and the averages calculated.

5.2.10 Method of biomolecule immobilization quantification using BCA protein assay

The quantification of each biomolecule was determined using a BCA protein assay. The samples were washed three times in PBS and cut to 20 x 20 mm strips using digital callipers and a scalpel. Thereafter, each sample was immersed in 2 ml SDS (1% w/v) in distilled water at 37 °C for 48 h in an orbital shaker bath to remove the adsorbed biomolecule from the films. The samples were removed from the SDS solutions, and the resultant SDS solutions were used for quantification. The BCA assay was used to detect adsorbed biomolecules according to the standard test tube protocol with the ratio of Reagent A and Reagent B at 50:1, known as the 'working reagent'. Thereafter, 2 ml working reagent was added to 0.1 ml of each sample and incubated at 37 °C for 30 min. The samples were cooled, and the absorbance was read at 562 nm. A calibration curve was plotted by diluting 5 mg/ml of each biomolecule (stock solutions prepared previously) to various concentrations outlined in the protocol. Thereafter, 0.1 ml of each dilution was added to 2 ml working reagent and incubated for 30 mins at 37 °C. The samples were cooled, and the absorbance was read at 562 nm. Method adapted from Masaeli (2014).

5.2.11 Method of PC12 and A172 cell culture and cell viability quantification utilizing the XTT cytocompatibility assay

PC12 cells were cultured in cell culture treated T-75 flasks with Ham's F12 Nutrient Mixture supplemented with 15%v/v DES, 2.5% v/v FBS and 1%v/v penicillin/streptomycin solution. A172 cells were cultured in cell culture treated T-75 flasks with DMEM supplemented with 10% v/v FBS and 1% v/v penicillin/streptomycin solution. Both cell lines were cultured in a humid 5% CO_2 atmosphere at 37˚C. The culture medium was replaced at 75% confluency every two days.

For the detection of cell proliferation and cyto-compatibility of the films, the Cell Proliferation Kit II (XTT) was utilized. Each sample (5 mg) was sterilised with 70% ethanol and rinsed three times in sterile PBS. Thereafter, 1 ml of the respective media was added to a 12-well plate containing the sterilised sample and incubated for 24 h at 37° C, 5% CO_2 and 97% humidity. The resultant liquids were termed 'extraction media'. PC12 and A172 cells were seeded into 96-well plates at a density of 25 000 cells/ml in 90 µl cell culture media and incubated for 24 h. Thereafter, the media was replaced with 90 µl extraction media. For the negative control, 10 µl fresh media was added to the well. For the positive control, 10 µl of DMSO was added to

the well and all wells were incubated for 48 and 72 h. At the respective time points, activated XTT solution was prepared by combining the 5 ml XTT Reagent and the 0.1 ml Activation Reagent. Thereafter, 50 µl of the activated XTT solution was added to each well and incubated for 4 h. The absorbance was read at 450 nm and 660 nm using a multiplate reader (BioTek, USA). Method adapted from Khorramnezhad (2021).

5.2.12 Method of cell attachment quantification using the trypan blue exclusion method

Samples were cut to 3 cm x 3 cm strips and rinsed three times in sterile PBS. The samples (n=3) were then UV sterilised for 15 mins and transferred to 6-well plates. The samples were secured to the bottom of the wells using sterile CellCrown™ Inserts. PC12 and A172 cells were each seeded at a density of 500 000 cells/ml onto the samples and incubated for 48 h. The control included cells seeded onto the bottom of the plasma treated well plate in the absence of any sample. Thereafter, the media was aspirated and discarded. The samples were removed from the plates and placed in new 6-well plates. The samples were then rinsed three times with sterile PBS. Following this, 200 µl trypsin was added to each sample to detach the cells. Following this, 500 µl media was added to stop the trypsinization and was placed in sterile centrifuge tubes and centrifuged for 10 mins at 5000 rpm. The supernatant was discarded, and the cells were re-suspended with 50 µl fresh media. Trypan blue (10µl) was then added to 10 µl of the cell suspension, and cells were manually counted using a haemocytometer under light microscopy. The percentage cell attachment was calculated by expressing the total number of counted live cells on each scaffold as a percentage of live cells counted on the control using Equation 5.1.

Equation 5. 1 % Cell attachment= (live cells on sample/ live cells on control) x 100

Statistical analysis

All samples were analysed in triplicate and the mean and standard deviations were recorded as computed. Student T-tests we performed for *In Vitro* studies for statistical significance. Samples that had p-values of $P \leq 0.05$ were considered to have a significant effect on the variable being investigated. All statistics and calibration curves were analysed on Microsoft Excel. All graphs were plotted using OriginPro 8.5 Software.

5.3 Results and discussions

5.3.1 Fabrication of the bioactive nanofibrous platforms

5.3.1.1 Determination of the optimal total polymer concentration using scanning electron microscopy

The optimal total polymer concentration was determined by viewing the sizes and morphology of the nanofibers under SEM. The SEM images in Figures 5.1, 5.2 and 5.3 represent the 9%

w/v PCL/CAP polymeric nanofibers which all have an extremely heterogenous matrix with large fiber diameter variability. Figure 5.2 highlights that some fibers have a diameter of up to 1.176 µm, which are then considered microfibers.

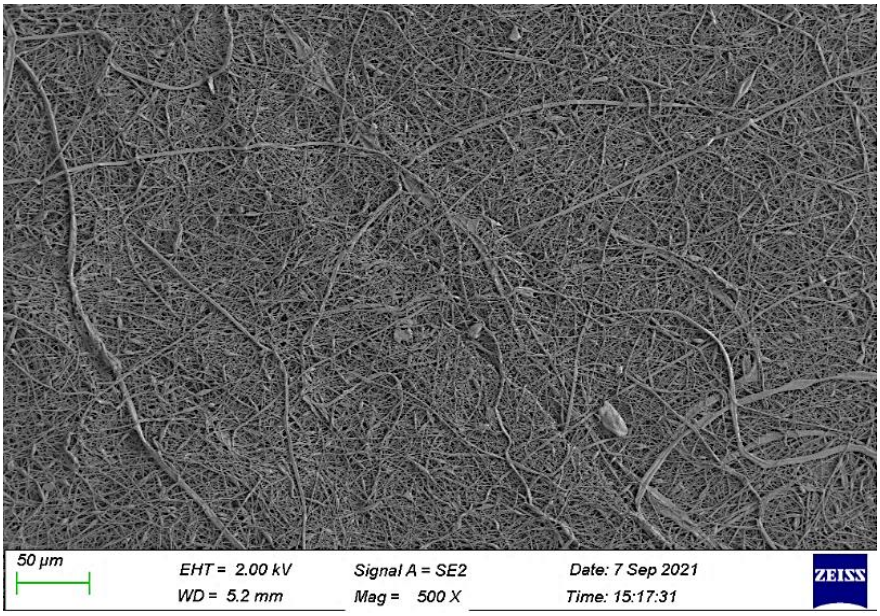


Figure 5. 1 Polycaprolactone/cellulose acetate phthalate (9% w/v) nanofibrous film showing a large variation in fiber diameter.

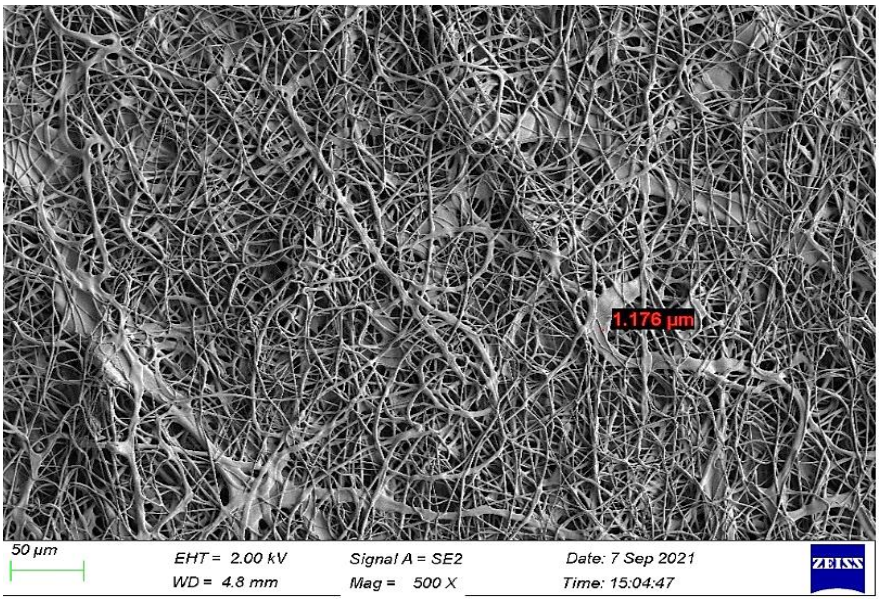


Figure 5. 2 Polycaprolactone/cellulose acetate phthalate (9% w/v) nanofibrous film showing a large variation in fiber diameter.

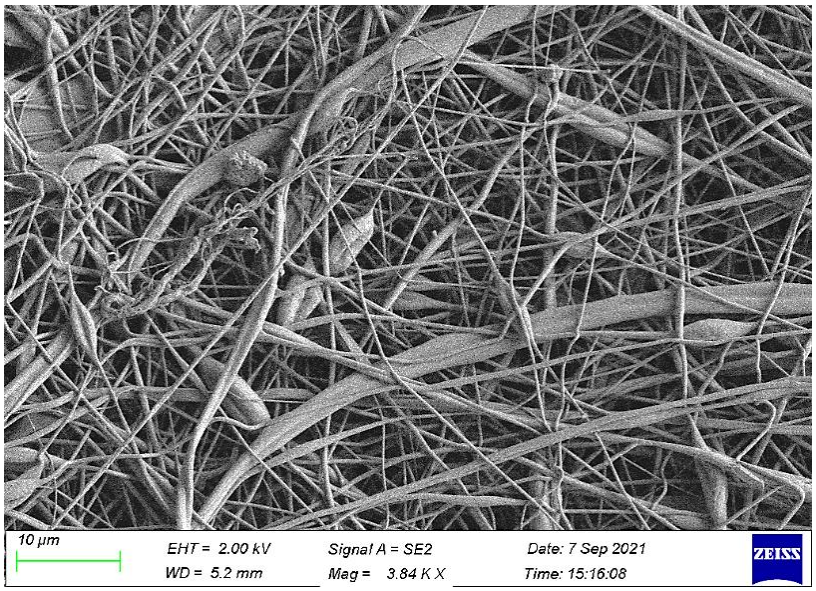


Figure 5. 3 Polycaprolactone/cellulose acetate phthalate (9% w/v) nanofibrous film showing a large variation in fiber diameter.

The ideal fiber diameter range described by He and co-workers is ± 500 nm for a nerve tissue engineering (He et al., 2010). Although some of the fibers in Figures 5.1, 5.2 and 5.3 may comply with this, there is a broad fiber diameter distribution, with many fibers in the micrometre range. Figure 5.4 illustrates the 6% w/v PCL/CAP nanofibrous platform with a more uniform fiber diameter distribution.

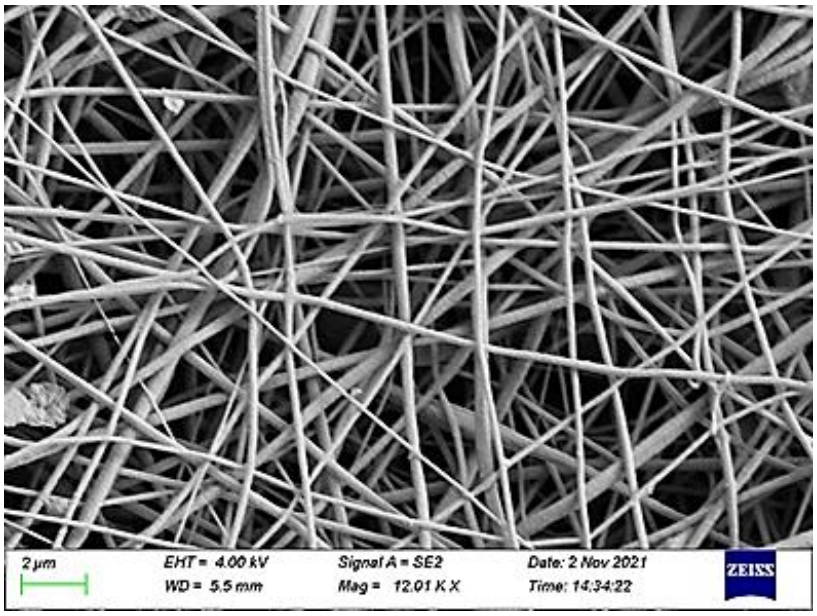


Figure 5. 4 polycaprolactone/cellulose acetate phthalate (6% w/v) nanofibers, showing a more uniform fiber diameter distribution.

The 6% w/v nanofibrous platform presents with a more uniform fiber diameter distribution and smaller fiber diameter in comparison to the 9% w/v nanofibrous platform. Therefore, the 6% w/v nanofibrous platform is chosen as the desirable concentration of the composite polymeric

solution for the fabrication of the fibers, due to smaller fiber diameters and enhanced fiber uniformity. The morphology of the nanofibrous platform shows a random fiber orientation which confers a 'branching' effect, with intersections creating a net-like structure resulting in porous features (You et al., 2006). This is important for achieving cell-cell contact by providing contact guidance and allowing cells to signal processes across multiple fibers (You et al., 2006).

The pristine PCL nanofibers (electrospun at the same conditions presented in Table 5.2) are depicted in Figure 5.5. The resultant fibrous mat contains many beads (clumps of polymer) and has a wide fiber diameter distribution. This illustrates that the addition of CAP to PCL produces more desirable fibers through electrospinning (You et al., 2006).

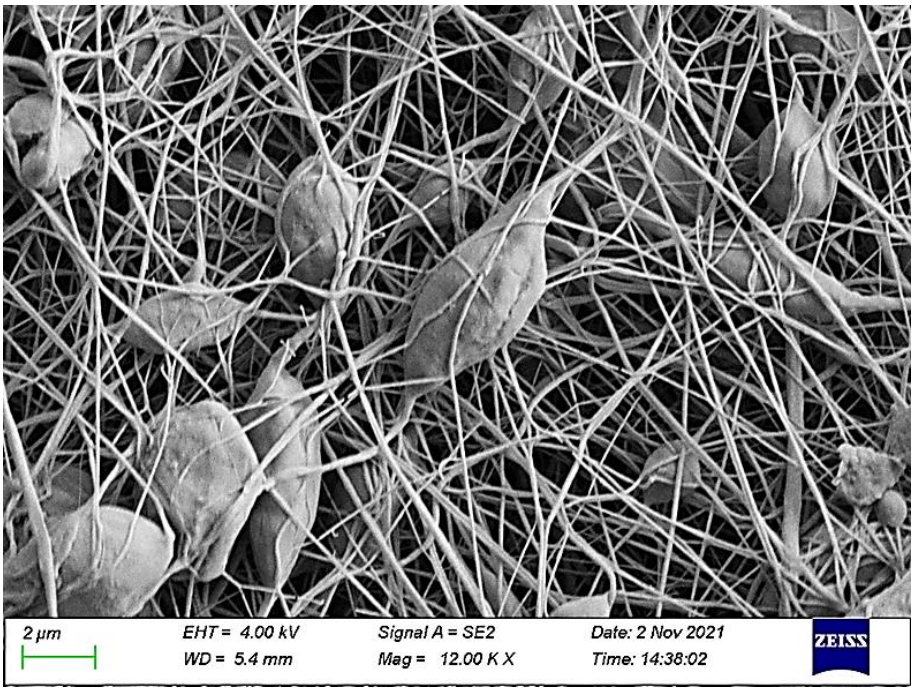


Figure 5. 5 Polycaprolactone (4% w/v) nanofibers (no cellulose acetate phthalate), showing the presence of many beads.

The SEM images prove that the lower polymer concentration (6% w/v) produces more desirable nanofibrous platforms at the same electrospinning conditions as the 9% w/v solution. The fibers are smaller in diameter and present with a more homogenous fiber diameter distribution, which is a well-noted result in literature (Amariei et al., 2017; Brown et al., 2007). The 6% w/v PCL control nanofibers are heterogenous and present with many polymer beads in the matrix, demonstrating the importance of CAP in the nano system.

5.3.1.2 Determining optimal aminolysis conditions using scanning electron microscopy

The fibers that were subjected to various aminolysis time intervals were viewed under SEM to qualitatively assess the morphology of the fibers to establish the longest aminolysis time that did not cause damage to the fibers.

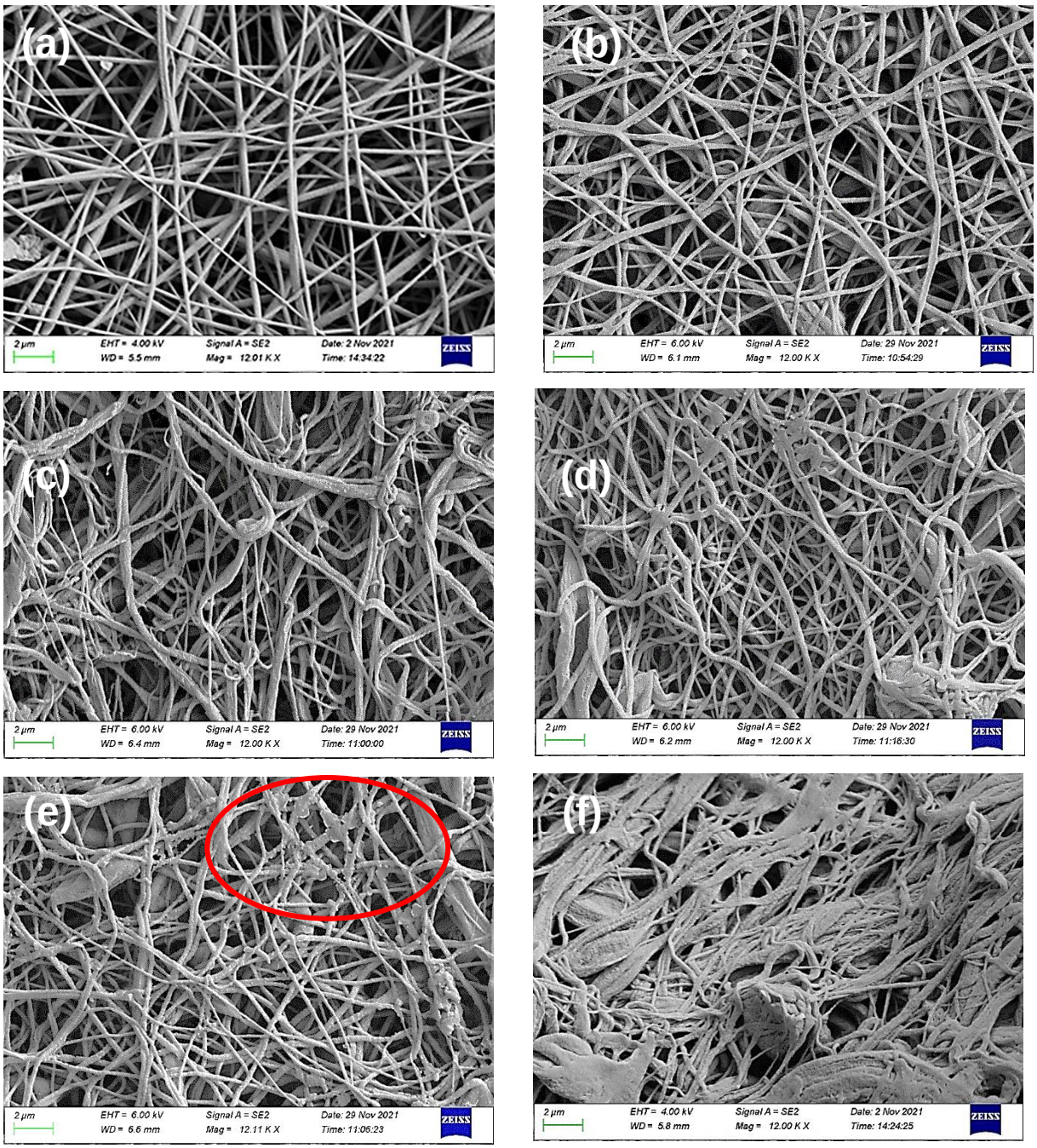


Figure 5. 6 Scanning electron microscopy images of polycaprolactone/cellulose acetate phthalate nanofibrous platforms aminolyzed for (a) 0, (b) 7.5, (c) 15, (d) 30, (e) 60 and (f) 90 mins.

The images in Figure 5.6 highlight that the ethylenediamine treatment time effects the morphology of the fibers. The maximum treatment time that does not cause damage to the fibers is 30 mins. The 60 min treatment time (e) causes damage to the fibers in one area highlighted in red. The 90 min treatment time (f) causes the fibers to fuse together and lose the nanofibrillar structure over the entire matrix. Therefore the 30 min treatment time is the optimal treatment time and is used in further investigations.

5.3.2 Surface topography mapping analysis by atomic force microscopy

Atomic force microscopy was conducted to evaluate the surface topographical cues of the nanofibers as well as to assess the surface roughness of the nanofibers following aminolysis. The results from the Image Rq values obtained from the AFM data indicate that aminolysis increases the surface roughness of the platform from 353 ± 12.73 to 448.33 ± 4.81 nm. According to previous studies, rougher surfaces promote neuronal adhesion, extension and proliferation (Brunetti et al., 2010; Sorkin et al., 2009). A noteworthy observation is that the nanofibrous platforms show a 10-fold increase in surface roughness when compared to the non-fibrous PCL/CAP films in Chapter 3 (35.43 ± 7.50 nm). Figures 5.7 and 5.8 show the 3D AFM images taken of the PCL/CAP and PCL/CAP-EDA samples, respectively, which highlighted the nanofibrous nature of the platforms.

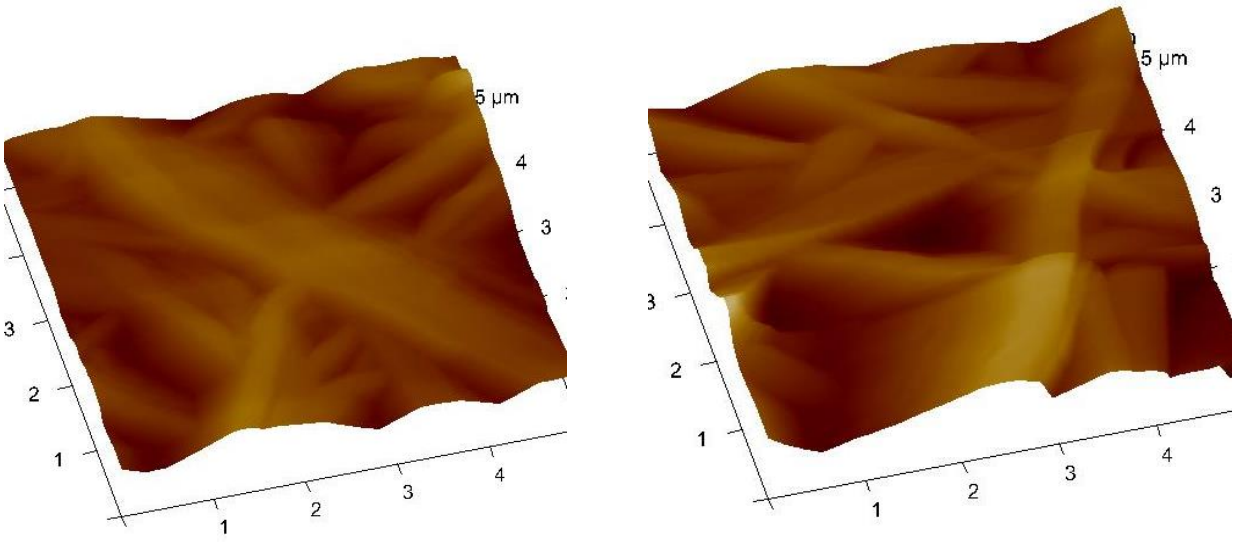


Figure 5. 7 3D atomic force microscopy images of polycaprolactone/cellulose acetate phthalate nanofibrous platforms showing the fibrillar surface topography of the platforms.

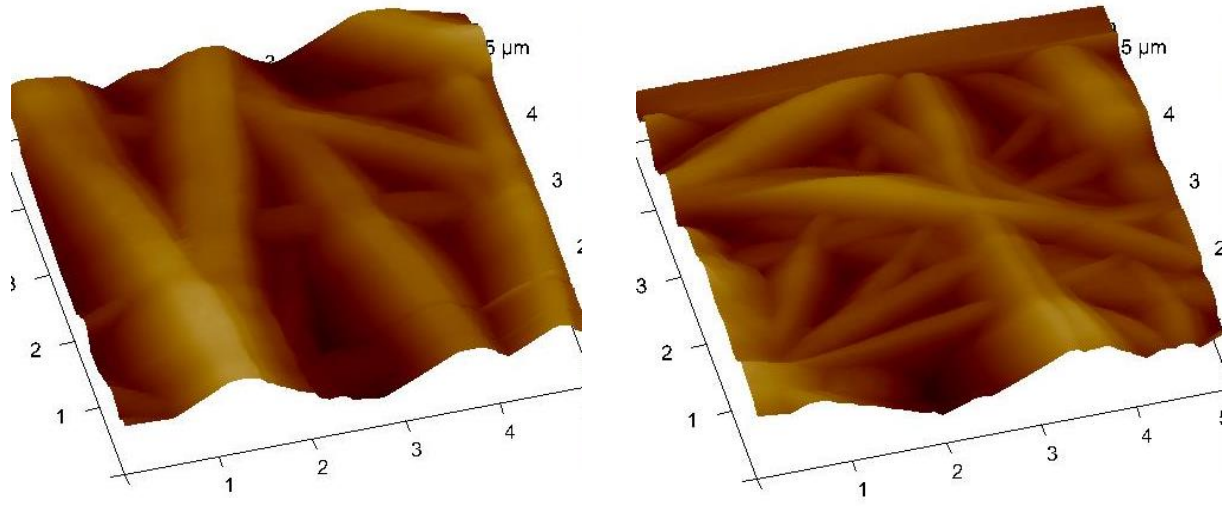


Figure 5. 8 3D atomic force microscopy images of aminolyzed nanofibrous platforms demonstrating the fibrillar nature of the surface.

In conclusion, the AFM images serve to confirm the nanofibrous nature of the platforms and confirm that the aminolysis of the nanofibrous platforms enhances the surface roughness, which is advantageous for cell attachment.

5.3.3 Chemical integrity characterizations of the nanofibrous platforms employing Fourier-transform infrared spectroscopy

FT-IR analysis was utilized to assess the chemical characteristics of the pristine polymers, the composite nanofibrous platform, as well as the aminolyzed and biomolecule-modified platforms. FT-IR also served to confirm that the nanofibers were successfully aminolyzed and that the biomolecules were efficiently crosslinked to their surface. Figure 5.9 highlights the increase in intensity of the peak in the range of 3000 cm^{-1} after electrospinning PCL. This peak is assigned to O-H stretching vibrations of the intermolecular and intramolecular hydrogen bonds in PCL (Mansur et al., 2008). Bounded water via hydrogen bonding in the microstructure of PCL chains and in the porous structure of electrospun PCL is the reason for the increase in the intensity (Mansur et al., 2008). Secondly, the overlapping of the graphs at 1264.91 cm^{-1} (which is enlarged in Figure 5.9), indicates a reduction of this peak upon electrospinning. This peak is attributed to the crystalline structure of PCL (Enyati et al., 2016). In fact, this peak is related to the symmetric C-C stretching mode or stretching vibration of the C-O of a portion of the chain where an intramolecular hydrogen bond is formed between two neighbouring O-H groups that are on the same side of the plane of the carbon chain (Mansur et al., 2008). The reduction of this peak indicates the reduction of crystallinity of PCL upon electrospinning due to partial replacement of intramolecular hydrogen bonding among PCL chains by hydrogen bonding between bounded water molecules and polymer chains (Mansur et al., 2008). This result is consistent with XRD data which suggests that the increase in FWHM upon electrospinning implies a reduced crystallinity of PCL in Section 5.3.5 (Enayati et al., 2016).

The FT-IR spectra in Figure 5.10 represent (a) pristine PCL pellets, (b) pristine CAP pellets and (c) the composite PCL/CAP nanofibrous platform. The FT-IR spectra in (a) shows characteristic peaks of PCL which include ~ 2945, 2866, 1720, 1239 and 1160 cm^{-1} which are assigned to C-H hydroxyl group asymmetric stretching, C-H hydroxyl group symmetric stretching, C=O stretching vibrations of the ester carbonyl group, C-O-C asymmetric stretching and C-O-C symmetric stretching, respectively (Pawlik et al., 2019). The spectrum in (b) shows characteristic peaks of CAP at ~ 735-770 cm^{-1} which are assigned to the ortho-disubstituted benzene ring, ~ 1034, 1223, 1369, 1719, 2942 and 3490 cm^{-1} which are characteristic bands corresponding to C-O-C stretching, the ester bond, methyl groups, the C=O carboxyl group, asymmetric and symmetric stretching of methyl C-H groups and O-H groups present in CAP, respectively. The bands at 1582 and 1598 cm^{-1} are attributed to cyclic alkene bonds in CAP (Gaurav et al., 2012).

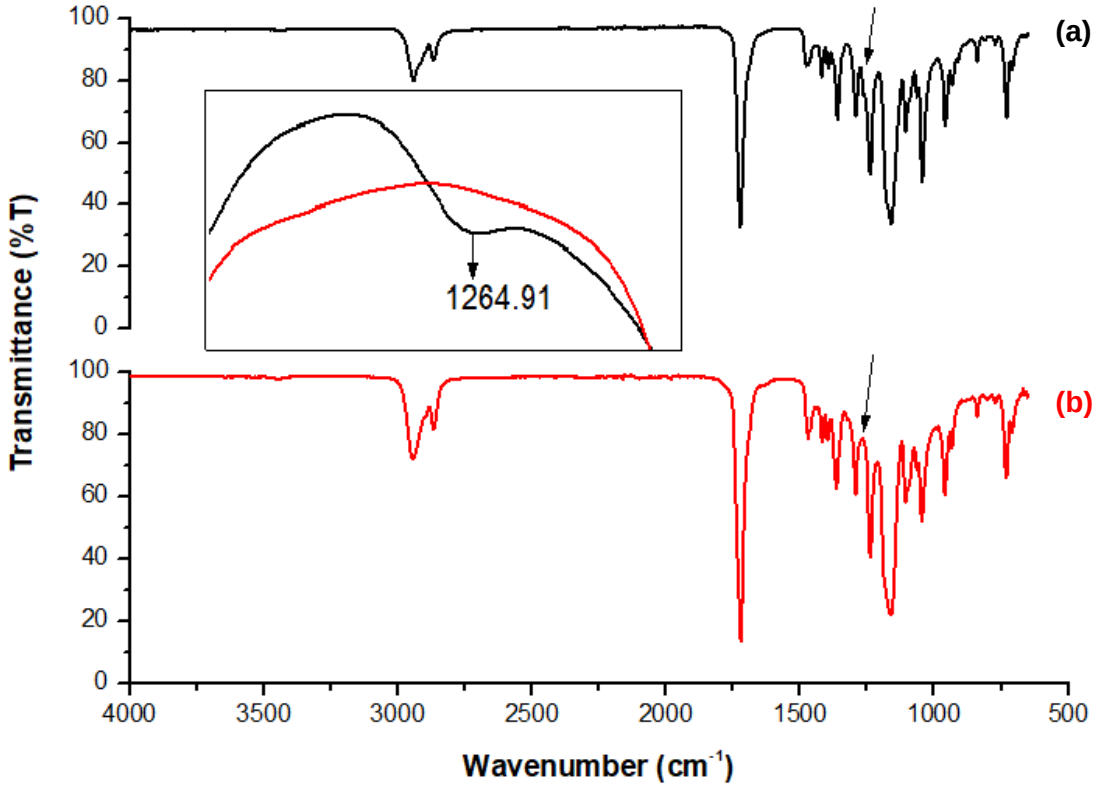


Figure 5. 9 Fourier-transform infrared spectra of (a) pristine polycaprolactone and (b) polycaprolactone nanofibrous platform.

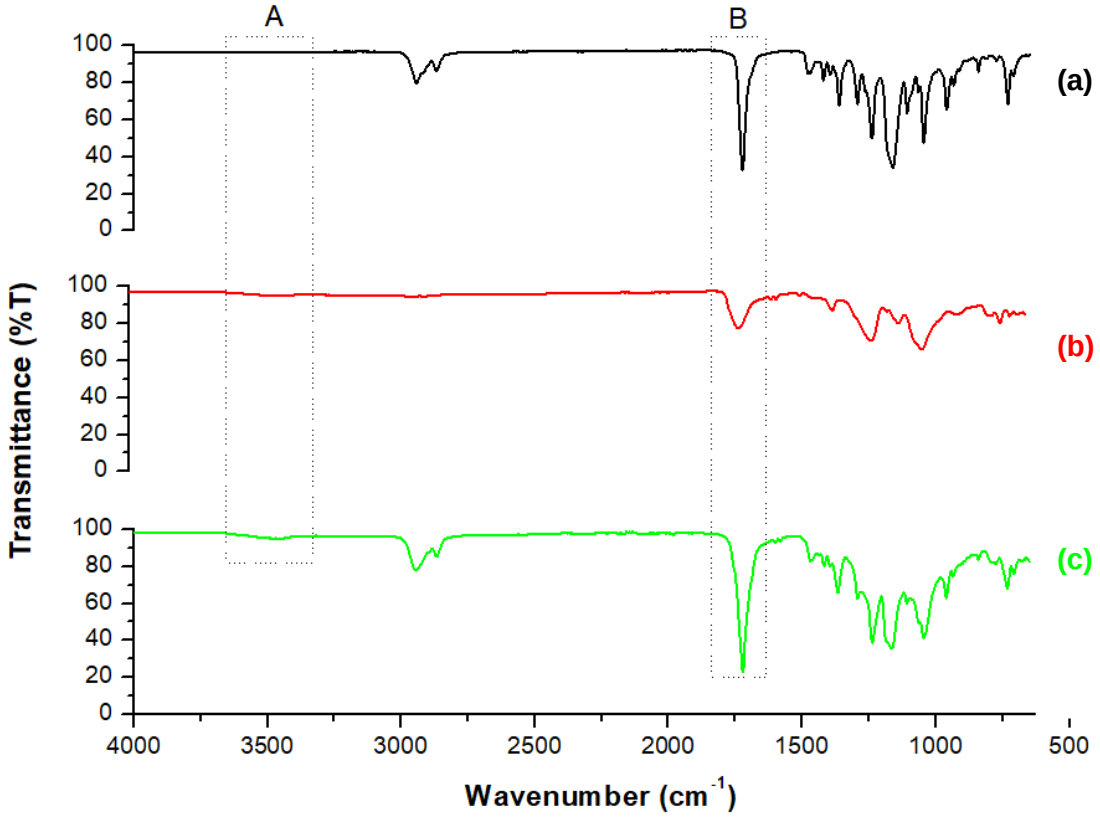


Figure 5. 10 Fourier-transform infrared spectra of (a) pristine polycaprolactone, (b) pristine cellulose acetate phthalate and (c) polycaprolactone/cellulose acetate phthalate nanofibrous platform.

The spectrum (c) in Figure 5.10 displays evidence of a blended formulation with a primarily PCL structure, which is a reasonable conclusion due to the relatively high concentration used (twice that of CAP) (Parak et al., 2019). This is confirmed by the presence of the PCL-related bands at ~ 2943, 2868, 1724, 1237 and 1160 cm^{-1} (Roxin et al.,1998). There are characteristic CAP bands present at ~ 3400, 1598, and 1369 cm^{-1} (Roxin et al., 1998). The slight change in shape of the bands at ~ 1164 cm^{-1} and ~ 1045cm^{-1} indicates overlapping bands from PCL and CAP. There is an increase in intensity of the peaks at ~ 1722, 1364, 1238, 1042 and 961 cm^{-1}, as a result of the additive effect of CAP to PCL. There are no new peaks formed in the FT-IR spectrum in (c), which proves the absence of any chemical boding formation between PCL and CAP (Parak et al., 2019). Figure 5.11 compares the FT-IR spectra of the PCL/CAP nanofibrous platform to the aminolyzed platform.

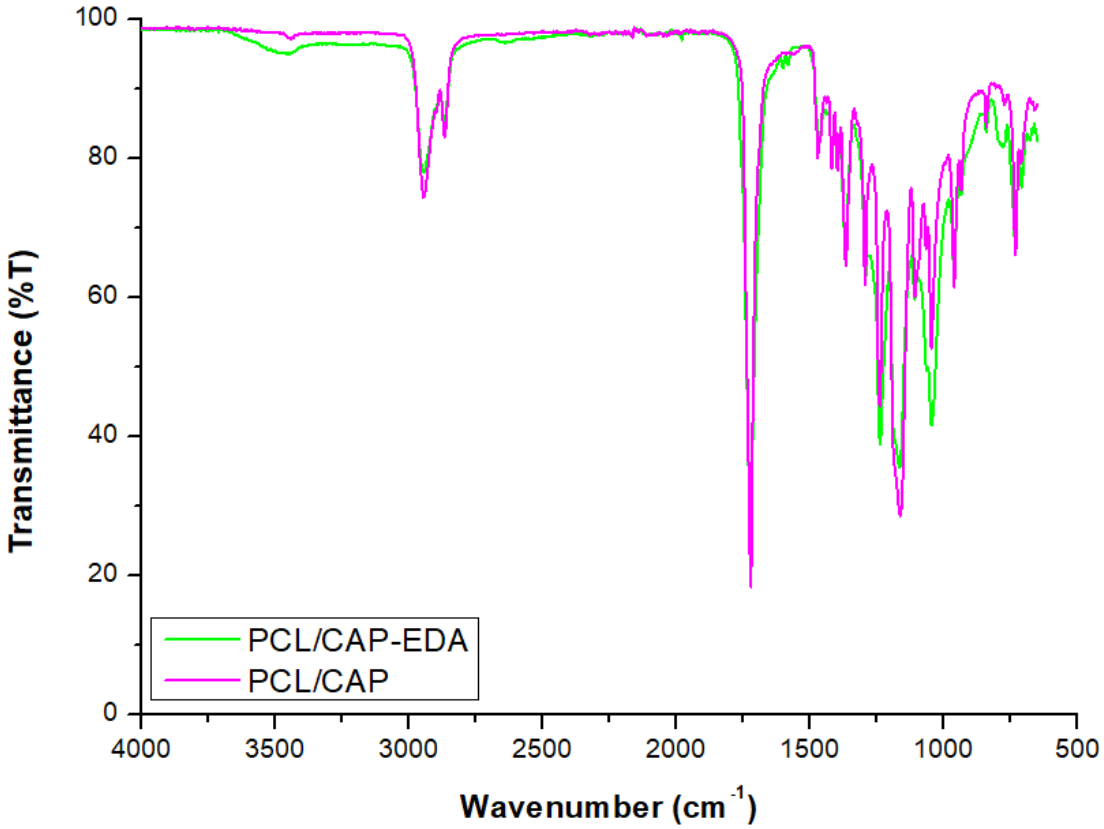


Figure 5. 11 Fourier-transform infrared spectra of (PCL/CAP) polycaprolactone/cellulose acetate phthalate and the (PCL/CAP-EDA) aminolyzed nanofibers using 20% v/v ethylenediamine for 30 mins.

Figure 5.11 proves that the nanofibrous films were successfully aminolyzed due to the appearance of an additional band at ~ 1566 cm^{-1}, representing the N-H bending of the amide II group (Krithica et al.,2012). Further, upon closer inspection, it can be seen that there is a smaller band at ~ 1640 cm^{-1} which represents the C=O stretching of the amide I band (Krithica et al., 2012). The broad band at ~ 3500 cm^{-1} is due to the presence of a secondary amine

group (Krithica et al., 2012). It should be noted that the change in spectra is much less intense than that in Chapter 3 since the EDA treatment time has been reduced from 90 mins to 30 mins. Figure 5.12 compares the Fourier-transform infrared spectra of the pristine biomolecule powders.

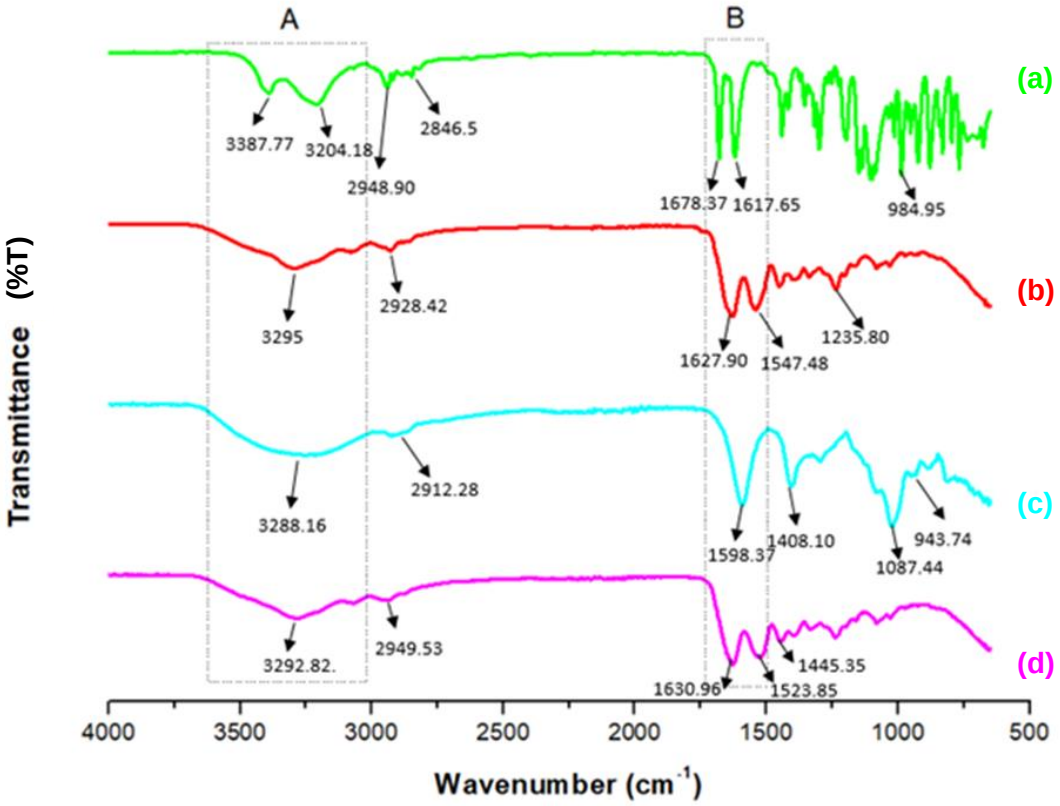


Figure 5. 12 Fourier-transform infrared spectra of pristine (a) genipin, (b) collagen, (c) sodium alginate and (d) gelatin.

Genipin (a) is characterized by a band at ~ 984.95 cm^{-1} which corresponds to C-H ring out-of-plane bending, 1020 cm^{-1} which correlates to C-H ring in plane bending and 1617.65 cm^{-1} which indicates C=C double bond ring stretch modes of the core genipin molecule (Arteche Pujana et al., 2013). The band at ~ 1678.37 cm^{-1} represents the carbonyl group of the ester in genipin (Arteche Pujana et al., 2013). The bands appearing at ~ 3387.77 and 3204.18 cm^{-1} are due to the overlap of aromatic C-H and O-H vibrations (Arteche Pujana et al., 2013). The bands at 2948.90 and 2846.5 cm^{-1} are due to the C-H stretch vibration (Kahoush et al., 2021).

The characteristic amide peaks in the collagen peptide (b) are detected at 3295 cm^{-1} corresponding to amide A and N-H stretching vibrations (Nagai, 2010). This indicates hydrogen bonding between the two N-H groups (Nagai, 2010). The band at 2928.42 cm^{-1} represents the amide B and asymmetric stretching of CH_2, the band at 1627.9 cm^{-1} represents the amide I and C=O stretching vibrations, the band at 1547 cm^{-1} represents amide II and N-H bending

vibrations and finally, the band at 1235 cm^{-1} represents amide III and C-H stretching (Nagai, 2010).

Characteristic peaks of sodium alginate (c) show characteristic absorption bands regarding hydroxyl, ether, and carboxylic groups. Stretching vibrations of O-H bonds of alginate appear at 3288.16 cm^{-1} (Daemi & Barikani, 2012). Stretching vibrations of aliphatic C-H are observed at 2912 cm^{-1} (Daemi & Barikani, 2012). Bands at 1598.37 and 1408.10 cm^{-1} are attributed to asymmetric and symmetric stretching vibrations of carboxylate salt ion, respectively (Daemi & Barikani, 2012). The bands at 1087.44 and 943 cm^{-1} are attributed to the C-O stretching vibration of pyranosyl ring and the C-O stretching with contributions from C-C-H and C-O-H deformation (Daemi & Barikani, 2012).

In terms of gelatin (d), two characteristic amide bands appear at 1630.96 cm^{-1} for amide I which is attributed to C=O stretching, and 1523.85 cm^{-1} which is attributed to N-H bending for amide II (Rokhade et al., 2006). An N-H stretching band is seen at 3292.82 cm^{-1}. The peak at 2949.68 cm^{-1} is attributed to aliphatic C-H stretches (Rokhade et al., 2006). The peaks at 1445.35, 1338.24 and 1236.46 cm^{-1} represent C-H bending, C-N stretching, and N-H bending (amide III), respectively (Rokhade et al., 2006). Figure 5.13 compares the spectra of the aminolyzed samples, the genipin coated sample as well as the three biomolecule-crosslinked samples.

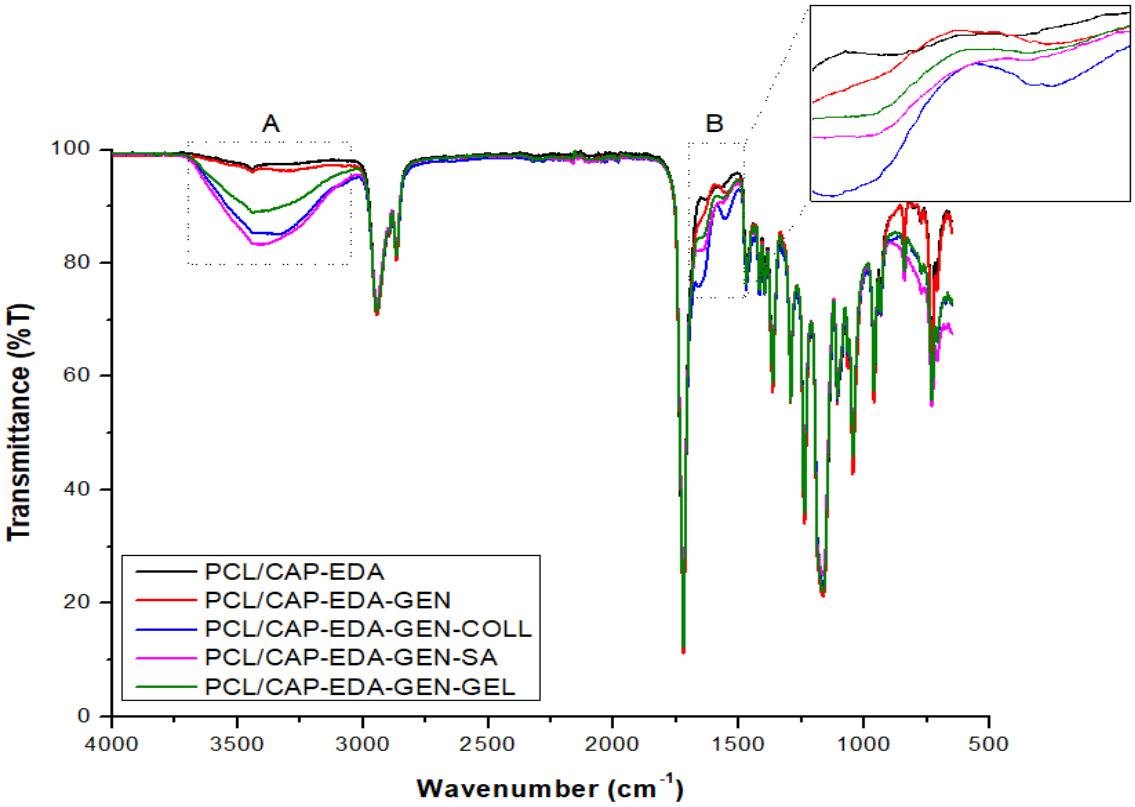


Figure 5. 13 Fourier-transform infrared spectra of (PCL/CAP-EDA) aminolyzed film, (PCL/CAP-EDA-GEN) genipin crosslinked film, (PCL/CAP-GEN-COLL) collagen crosslinked film, (PCL/CAP-EDA-GEN-SA) sodium alginate crosslinked film, (PCL/CAP-EDA-GEN-GEL) gelatin crosslinked film.

The genipin coated sample highlighted in Figure 5.13 (b), shows a relatively large increase in intensity of the peak at 3438.24 cm^{-1} in region A. In region B, two additional peaks appear at 1554.77 and 1640.71 cm^{-1}, corresponding to the amide I and amide II vibrations, respectively (Siritientong et al., 2013).These peaks are consistent with another FT-IR study on genipin-coated biopolymers (Sundararaghavan et al., 2008), which confirms the crosslinking of genipin to the aminolyzed film. These features suggest that the carboxymethyl group of genipin reacts with the amino group of chitosan to form a secondary amide according to literature (Dimida et al., 2017).The crosslinking mechanism between genipin and primary amines under basic conditions is as follows: the nucleophilic attack of genipin by the hydroxyl ions in aqueous solution leads to a ring-opening reaction, and an intermediate aldehyde group is formed. Subsequently, a Schiff reaction occurs between the terminal aldehyde groups on the polymerized genipin and the primary amines, forming a crosslinked network structure (Oryan et al., 2018; Yoo et al., 2011).

Once collagen, sodium alginate and gelatin are immobilized on the films using genipin, there is an increase in the intensity of the bands in section A in Figure 5.13, with sodium alginate causing the least increase in intensity compared to genipin and gelatin causing the highest increase in intensity. The reason for the increase in intensity of all three bands of the biomolecule-immobilized films is that the pristine powders of collagen, sodium alginate and gelatin all have a relatively large band in this region (3500-3000 cm^{-1}) (Mattanavee et al., 2009). This corresponds with the N-H stretching of the NH_2 groups which confirms the successful immobilization of the biomolecules on the surface of the nanofibers (Mattanavee et al., 2009).In region B, all the biomolecule-immobilized nanofibers have two distinct peaks in the same position as the PCL/CAP-EDA-GEN nanofibers (1554.77 and 1640.71 cm^{-1}) yet are more intense. These bands correspond to protonated amine groups on the biomolecules (Kim et al., 2010; Panzavolta et al., 2011) and their increase in intensity compared to the aminolyzed nanofibers coated with genipin confirms their presence on the nanofibrous surface (Krithica et al., 2012).

Figures 5.14, 5.15 and 5.16 compare the FT-IR spectra of the biomolecule coated nanofibers (a) and the biomolecule crosslinked nanofibers (b). Firstly, in the absence of genipin, small shifts in the wavenumber occur when comparing the biomolecule coated samples (a) and the genipin coated sample. This indicates that homogenous mixing occurs during the formulation resulting in the overlapping of the relevant wavenumber bands (Siritientong et al., 2013). An increase in intensity of the curves (b) as compared to curves (a) in Figures 5.14, 5.15 and 5.16 is observed. The amide A band of collagen, sodium alginate and gelatin (associated with the N-H stretching frequency) is found at 3325–3330 cm^{-1} (Siritientong et al., 2013).

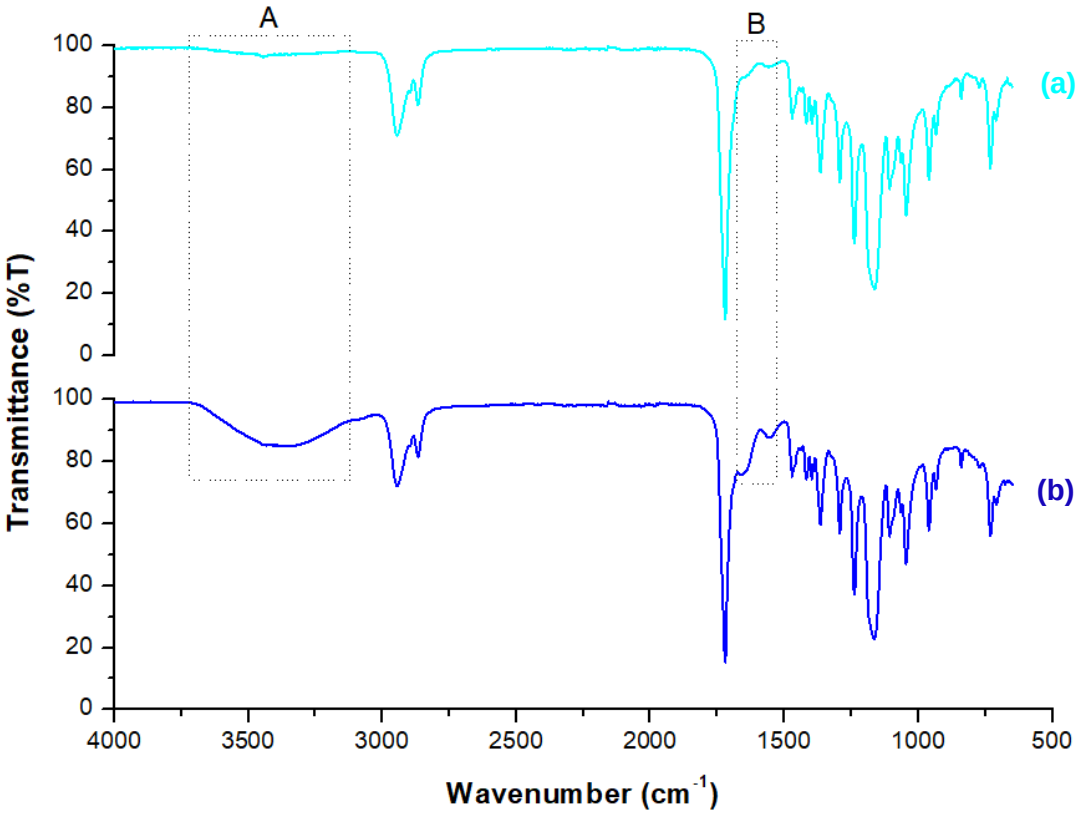


Figure 5. 14 Fourier-transform infrared spectra of (a) collagen coated nanofibers and (b) collagen crosslinked nanofibers.

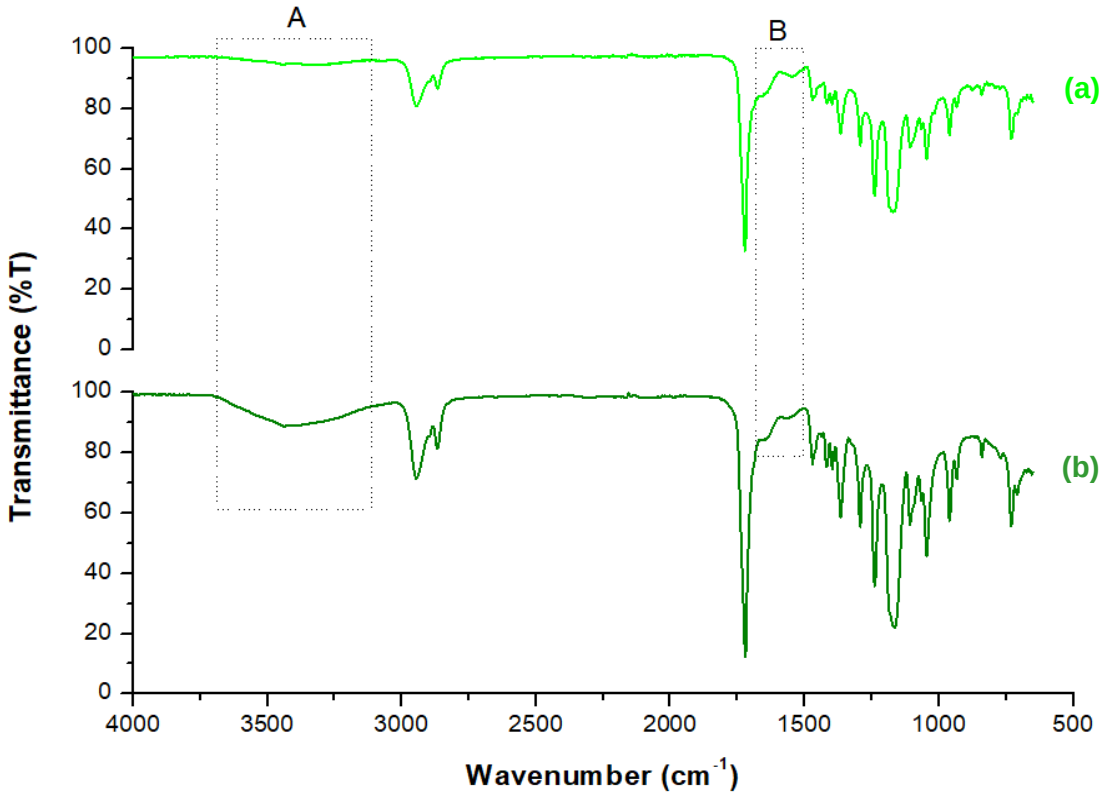


Figure 5. 15 Fourier-transform infrared spectra of (a) sodium alginate coated nanofibers and (b) sodium alginate crosslinked nanofibers.

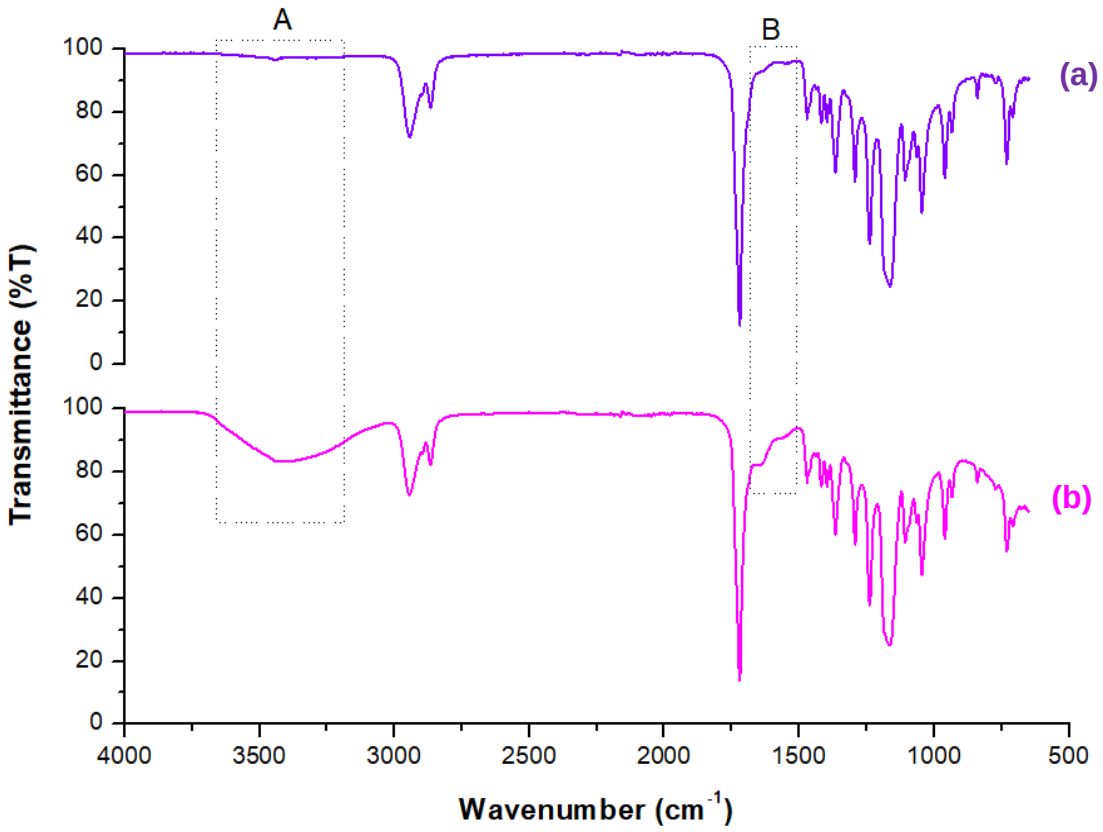


Figure 5. 16 Fourier-transform infrared spectra of (a) gelatin coated nanofibers and (b) gelatin crosslinked nanofibers.

The broadening of the peak in (b) of Figures 5.14, 5.15 and 5.16 represents the hydrogen bonding associated with the biomolecules (Kosmala et al., 2017). The amide I band of the biomolecules is usually observed around 1650-1668 cm^{-1} and the amide II band of the biomolecules is centred in the range of 1530-1555 cm^{-1}, which corresponds to the N-H stretch coupled with the C-N stretch (Kosmala at al., 2017). The spectrum in (b) of each Figure highlights that the amide I and amide II appear at 1661 and 1556 cm^{-1}, respectively (Krithica et al., 2012). Furthermore, there is a slight shift in wavenumber in (a) and (b) in section B, possibly due to the addition of the crosslinker, which contains O-H functional groups (Siritientong et al., 2013).

From this discussion, it is clear that the biomolecules are successfully immobilized on to the aminolyzed films via genipin crosslinking (Kosmala et al., 2017; Krithica et al., 2012).

5.3.4 Analysis of the thermodynamic behavior of the nanofibrous platforms utilizing differential scanning calorimetry

Differential scanning calorimetry was undertaken to examine the changes in the thermal profiles of the nanofibrous platforms following aminolysis and biomolecule modification (Levya-Porras et al., 2020). The onset of melting, Tm, Δhm and the onset of degradation were

calculated to give a more detailed analysis of the thermal changes that occurred (Levya-Porras et al., 2020). Table 5.3 represents the noteworthy DSC thermal profiles of the PCL nanofibers, the PCL/CAP nanofibers, the aminolyzed and biomolecule-modified samples**.**

The effect of the electrospinning process on pristine PCL is highlighted by the reduction in onset of degradation from 64.55 to 60.02 °C upon electrospinning. The onset of degradation is reduced from 331.12 to 325.81 °C. This concludes that the electrospinning process reduces the thermal stability of PCL (Nirmala et al., 2011). A reduction in the endothermic peak is also observed, which indicates that the crystalline microstructure of the electrospun fibers does not develop well, resulting in a reduced crystallinity of PCL upon electrospinning (Nirmala et al., 2011). However, the melting temperature is enhanced, which indicates an increased thermal stability during that temperature range, which is also confirmed by TGA data. The DSC curves in Figures 5.18, 5.19 and 5.20 compare the thermograms of the aminolyzed nanofibrous platform, the genipin coated platform, the collagen coated platform and the collagen crosslinked platform.

Table 5. 3 Differential scanning calorimetry profiles of samples.

Sample	Onset of Melting (°C)	Tm[17] (°C)	∆hm[18] (mw.°C)	Onset of Degradation (°C)
Pristine polycaprolactone	34.85	64.55	280.15	331.12
Polycaprolactone film	35.91	60.02	97.15	325.81
Polycaprolactone/cellulose acetate phthalate film	33.14	58.11	68.55	284.66
Aminolyzed film	33.06	61.48	152.70	286.38
Genipin crosslinked film	27.31	61.42	91.51	322.07
Collagen coated film	33.01	60.67	126.96	321.45
Collagen crosslinked film	29.28	61.35	106.24	307.47
Sodium alginate coated film	33.06	62.49	115.56	321.2
Sodium alginate crosslinked film	38.76	62.29	111.32	315.49
Genipin coated film	35.01	62.86	124.86	298.36
Genipin crosslinked film	32.28	60.95	63.49	324.39

[17] Melting temperature
[18] Enthalpy of melting

Figure 5.17 represents a comparison of the DSC thermal profiles of PCL nanofibers, PCL/CAP nanofibers and aminolyzed PCL/CAP nanofibers. The onset of melting, melting temperature and onset of degradation are all reduced upon addition of CAP to the electrospinning solution. This highlights that the addition of CAP to the electrospinning solution reduces the thermal stability of the sample. Upon aminolysis of the PCL/CAP nanofibrous platform, the onset of melting is not significantly altered.

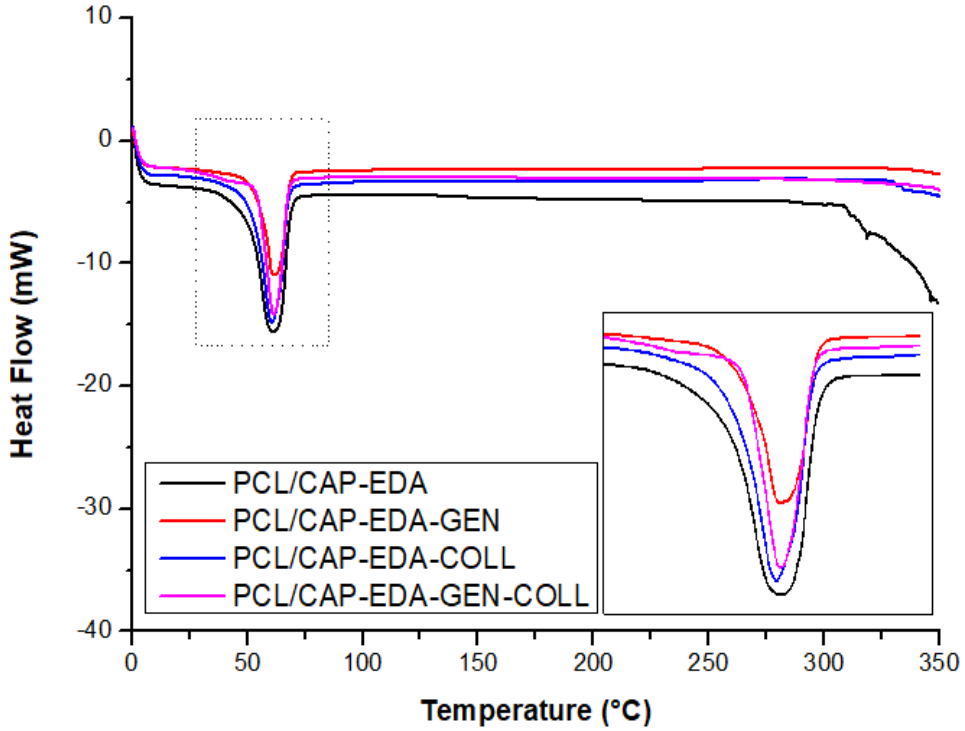


Figure 5. 17 Differential scanning calorimetry of (PCL) pristine polycaprolactone nanofibers, (PCL/CAP) polycaprolactone/cellulose acetate phthalate nanofibers and (PCL/CAP-EDA) the aminolyzed nanofibers.

The addition of genipin to the PCL/CAP-EDA sample reduces the ∆hm from 152.701 to 91.51 mW. °C, seen in Figure 5.18. This implies an increase in thermal stability during the melting phase transition. Further, the melting temperature and onset of degradation is increased from 286.38 to 322.07 °C, which also indicates an enhanced thermal stability. Collagen coating reduces the ∆hm to 126.957 mW.°C and increases the melting temperature and onset of degradation to 321.45 mW.°C, which both indicate an enhanced overall thermal stability. In comparison to the collagen coating, collagen crosslinking reduces the onset of melting and melting temperature. Figure 5.19 compares the DSC thermograms of the sodium alginate-modified samples. The sodium alginate coating in Figure 5.19 slightly increases the melting temperature and reduces the ∆hm. The onset of degradation is also increased, both of which indicate an enhanced thermal stability.

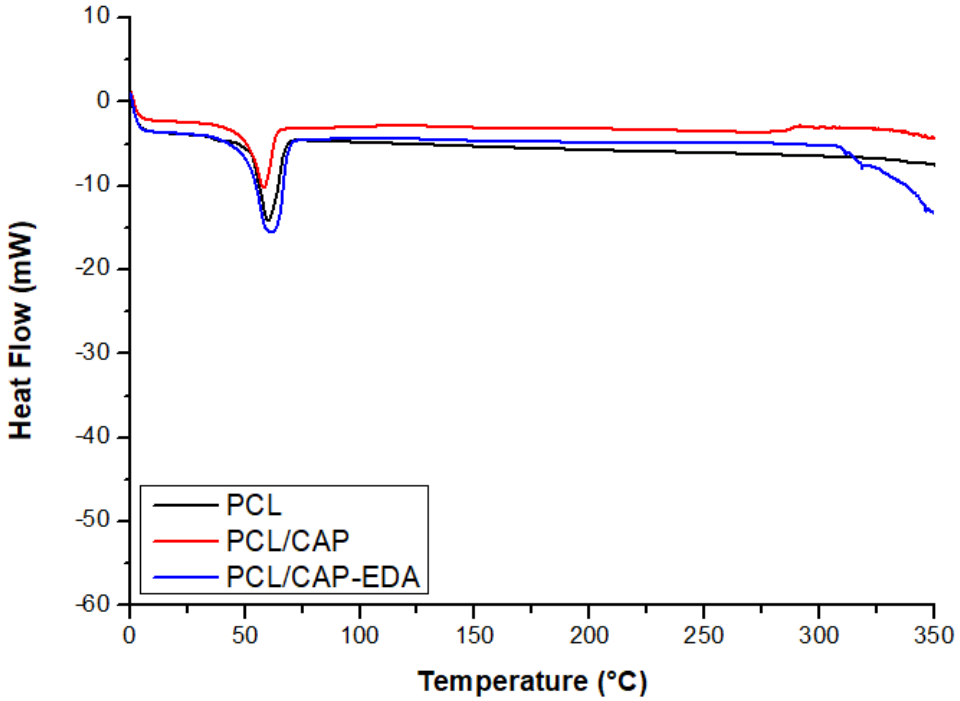


Figure 5. 18 Differential scanning calorimetry of (PCL/CAP-EDA) aminolyzed nanofibers, (PCL/CAP-EDA-GEN) genipin crosslinked nanofibers, (PCL/CAP-EDA-COLL) collagen coated nanofibers and (PCL/CAP-EDA-GEN-COLL) collagen crosslinked nanofibers.

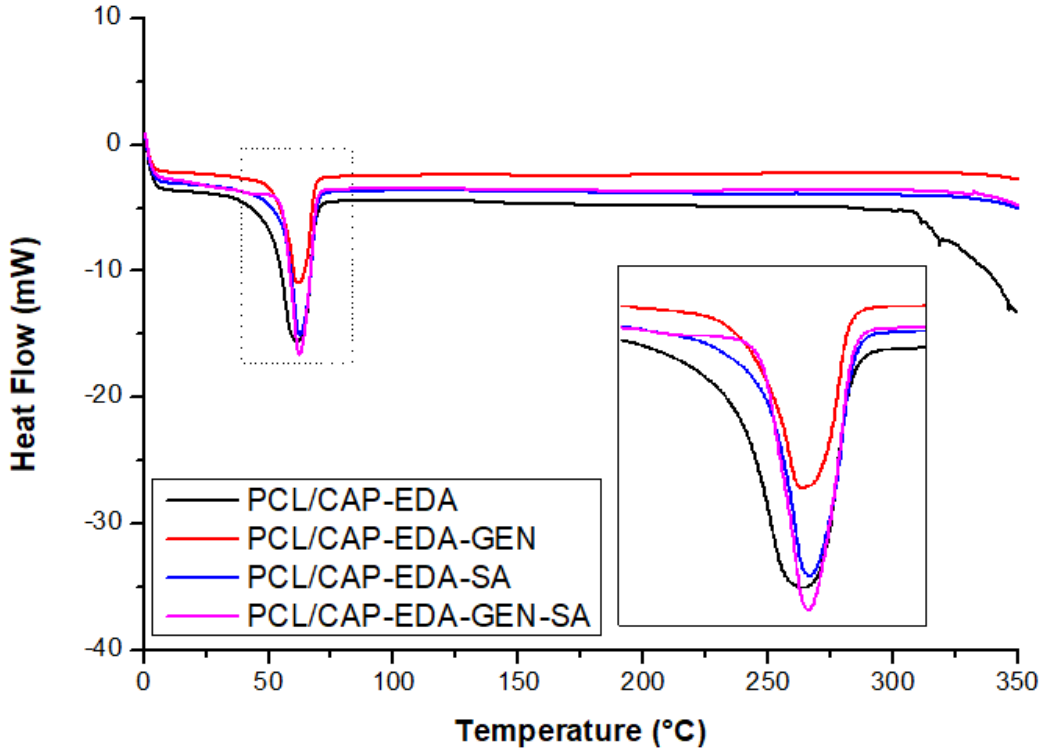


Figure 5. 19 Differential scanning calorimetry of (PCL/CAP-EDA) aminolyzed, (PCL/CAP-EDA-GEN) genipin crosslinked, (PCL/CAP-EDA-SA) sodium alginate coated, (PCL/CAP-EDA-GEN-SA) sodium alginate crosslinked nanofibers.

The sodium alginate crosslinking reduces the melting temperature in comparison to the sodium alginate coating, thereby reducing the thermal stability. Figure 5.20 compares the DSC

thermograms of the gelatin modified nanofibers. The gelatin coating increases the melting temperature and the onset of melting, while it reduces the ∆hm, thereby indicating an enhanced thermal stability. Further, the onset of degradation is enhanced. However, the gelatin crosslinking using genipin reduces the melting temperature and onset of degradation thereby reducing the thermal stability in comparison to mere gelatin coating.

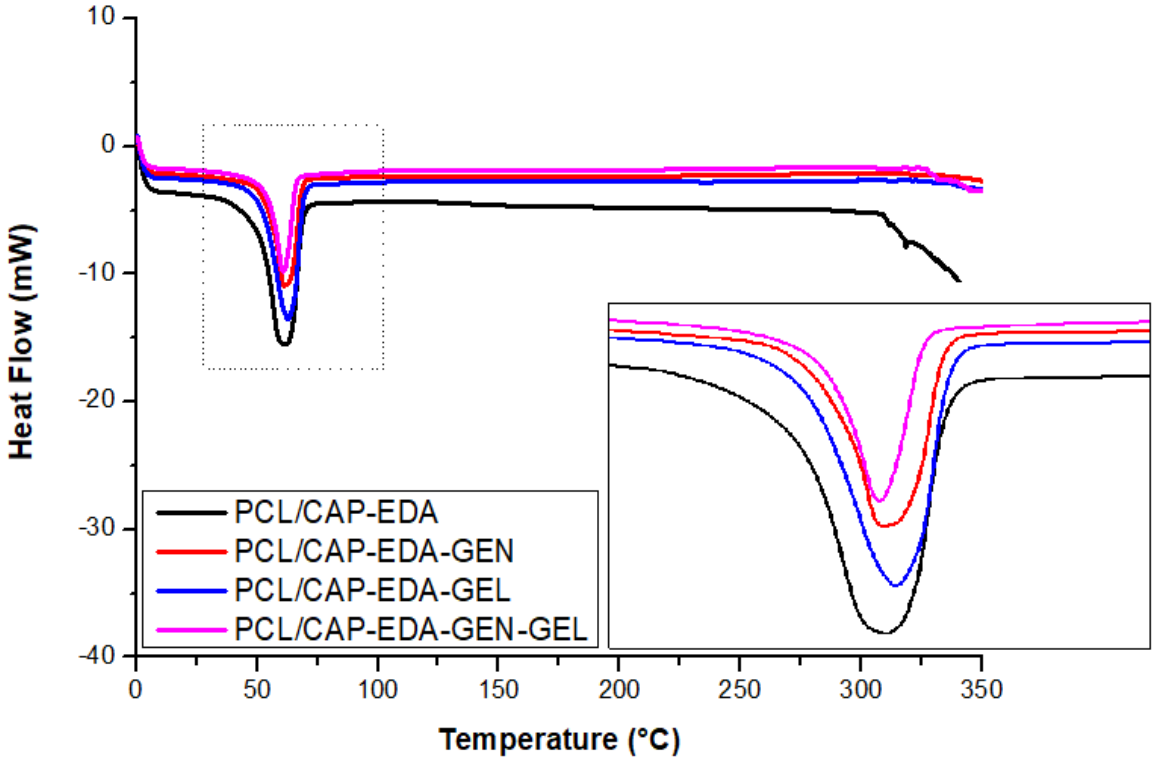


Figure 5. 20 Differential scanning calorimetry of (PCL/CAP-EDA) aminolyzed, (PCL/CAP-EDA-GEN) genipin crosslinked, (PCL/CAP-EDA-GEL) gelatin coated, (PCL/CAP-EDA-GEN-GEL) gelatin crosslinked nanofibers.

In conclusion, the genipin coating, the biomolecule coating as well as biomolecule crosslinking all alter the thermodynamic behaviors of the films in comparison to the aminolyzed nanofibrous platforms. There are marked differences between the biomolecule coated and the biomolecule crosslinked samples, confirming that effective crosslinking took place.

5.3.5 Assessment of phase transitions of nanofibrous films utilizing x-ray diffraction analysis

XRD analysis was undertaken to evaluate the phase transitions that occurred following nanofiber aminolysis as well as biomolecule modification. The FWHM values were calculated to quantitively assess the change in crystallinity of the samples. The higher the FWHM, the lower the crystallinity of the samples (Nagaraj et al., 2017).

Table 5.4 compares the FWHM values of the samples represented in the X-ray diffractograms in Figures 5.21-5.24.The FWHM values indicate that the addition of CAP to the PCL nanofibers

reduces the FWHM value and thereby reduces the crystallinity of the nanofibers (Bruylants et al., 2020). Upon aminolysis, the FWHM value is enhanced to 0.55, which indicates that aminolysis enhances the crystallinity of the nanofibers, which is consistent with the results in Chapter 3. The genipin coated sample enhances the FWHM, which indicates a reduction in crystallinity. This is expected since genipin crosslinked to the amine groups in the nanofibrous platform, which destroys the original hydrogen bonds that are beneficial to crystallization (Y.Liu et al., 2019). Following biomolecule coating and crosslinking, all the FWHM values are reduced slightly.

Table 5. 4 Full width at half maximum values for the samples.

Sample	Full width at half maximum
Pristine polycaprolactone	0.90
Polycaprolactone film	0.35
Polycaprolactone/cellulose acetate phthalate film	0.55
Aminolyzed film	0.61
Genipin crosslinked film	0.48
Collagen coated film	0.49
Collagen crosslinked film	0.41
Sodium alginate coated film	0.47
Sodium alginate crosslinked film	0.56
Genipin coated film	0.46

Figure 5.21 compares the XRD diffractograms for the PCL nanofibrous platform, the PCL/CAP nanofibrous platform and the aminolyzed nanofibrous platform.In Chapter 3, the FWHM value of the PCL solution cast film is 0.426. The electrospinning process increases this value to 0.90, indicating a reduced crystallinity, which is consistent with literature (Nirmala et al., 2011). The FWHM value upon addition of CAP to the electrospinning solution is reduced from 0.90 to 0.35, indicating an enhanced crystallinity (Garg et al., 2016). The PCL/CAP nanofibers present a sharp peak at a 2Θ value of ~ 21.4°, rendering the blended nanofibers semi-crystalline, imparted by the PCL component, which is typically semi-crystalline in nature (Ravi et al., 2016) and the CAP component, which is typically amorphous in nature (Garg et al., 2016). In terms of the aminolyzed films, the FWHM value is increased to 0.55, indicating an increase in disorder of its structure, and thereby its amorphous nature (da Silva et al., 2021). However, the diffraction pattern is similar to that of PCL/CAP, indicating that this change is minimal.

Figures 5.22, 5.23 and 5.24 illustrate the difference in crystallinity patterns between the aminolyzed PCL/CAP nanofibrous platforms, the genipin coated nanofibrous platforms, pristine biomolecule samples, the biomolecule coated nanofibrous platforms and the biomolecule crosslinked platforms. Figure 5.22 highlights that genipin coating increases the

FWHM value to 0.61, thereby slightly reducing the crystallinity of the aminolyzed sample, indicating that genipin forms crosslinks with the free amino groups on the fibers, which destroys the original hydrogen bonds that were beneficial to crystallization, as described above (Mateescu & Juha, 2002). The slight increase in the FWHM value of the collagen crosslinked sample in comparison to the collagen coated sample is due to the formation of crosslinks onto the nanofibers in the same mechanism as described above. Similarly, the sodium alginate crosslinked nanofibers presented in Figure 5.23 displays a slightly higher FWHM value in comparison to the sodium alginate coated samples, proving the presence of crosslinks in the PCL/CAP-EDA-GEN-SA sample (Mateescu & Juha, 2002).

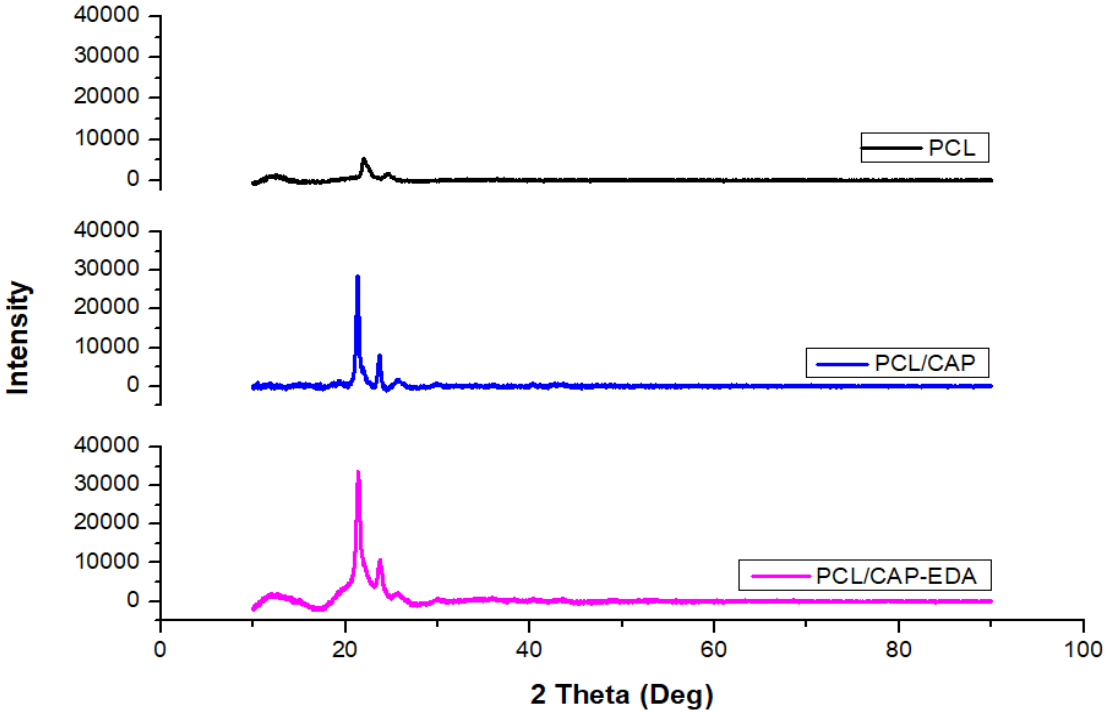


Figure 5. 21 X-ray diffraction patterns of (PCL) polycaprolactone nanofibers, (PCL/CAP) polycaprolactone/cellulose acetate phthalate nanofibers, (PCL/CAP-EDA) aminolyzed nanofibers.

The gelatin crosslinked samples (Figure 5.24) are expected to have a FWHM value higher than that of the gelatin coated samples as seen with the collagen and sodium alginate-modified samples. However, the converse is found, perhaps indicating that gelatin is not efficiently crosslinked onto the nanofiber surface, although the combination of FT-IR, DSC and TGA has proved the crosslinking of the biomolecules to the surface of the nanofibers.

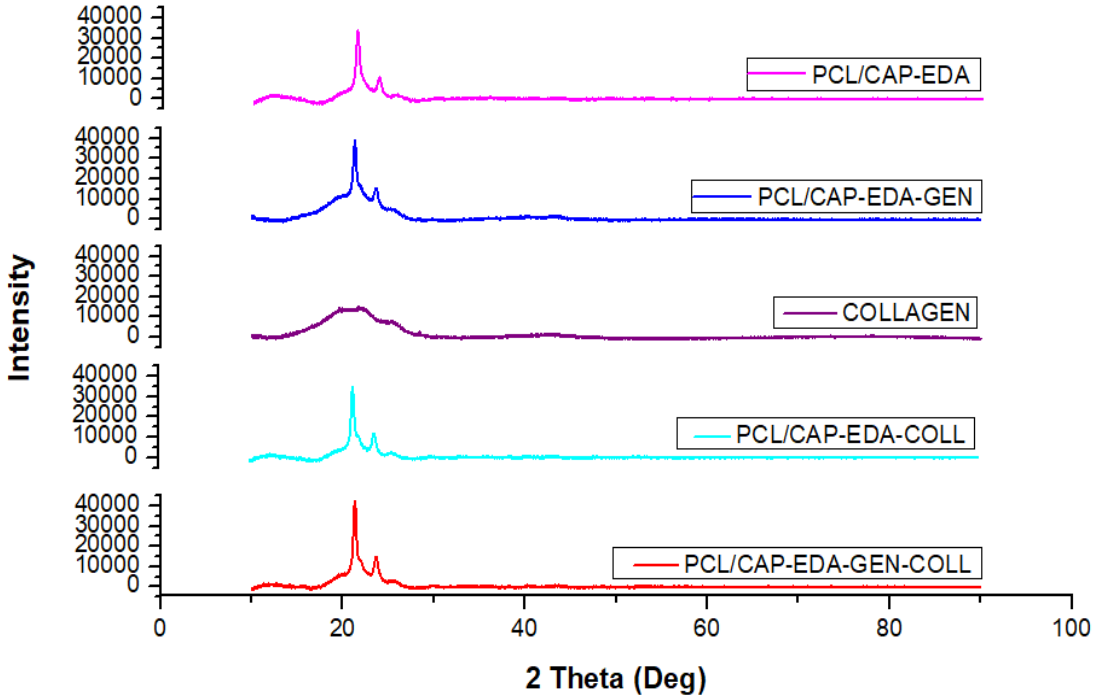


Figure 5. 22 X-ray diffraction patterns of (PCL/CAP-EDA) aminolyzed, (PCL/CAP-EDA-GEN) genipin crosslinked, (PCL/CAP-EDA-COLL) collagen coated, (PCL/CAP-EDA-GEN-COLL) collagen crosslinked nanofibers.

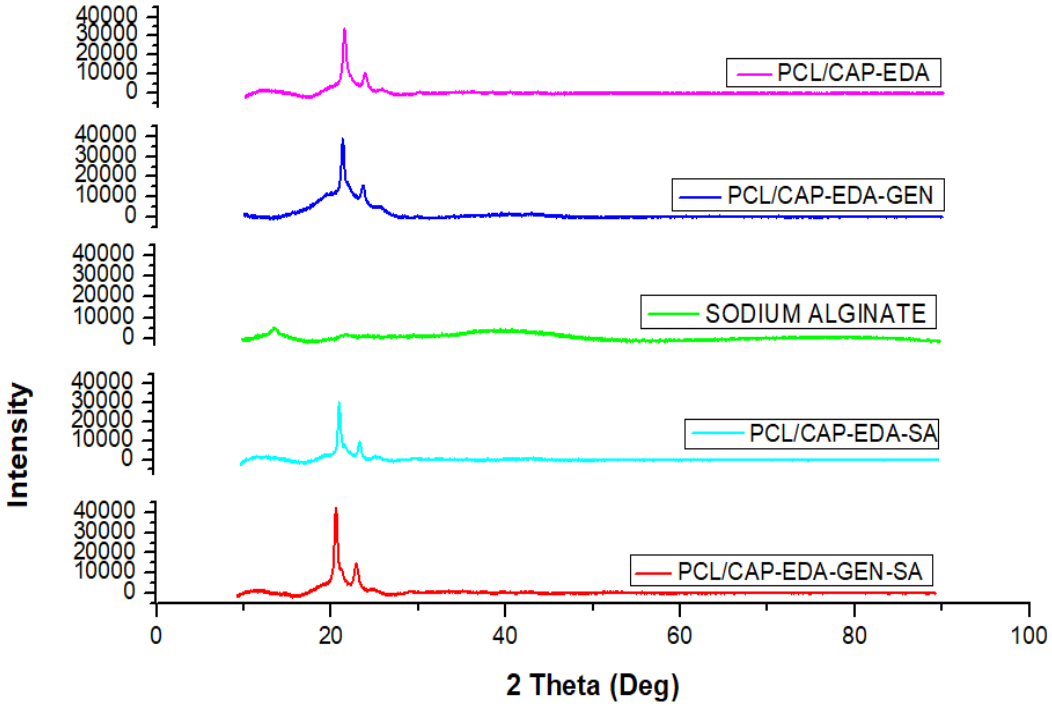


Figure 5. 23 X-ray diffraction patterns (PCL/CAP-EDA) aminolyzed, (PCL/CAP-EDA-GEN) genipin crosslinked, (PCL/CAP-EDA-SA) sodium alginate coated, (PCL/CAP-EDA-GEN-SA) sodium alginate crosslinked nanofibers.

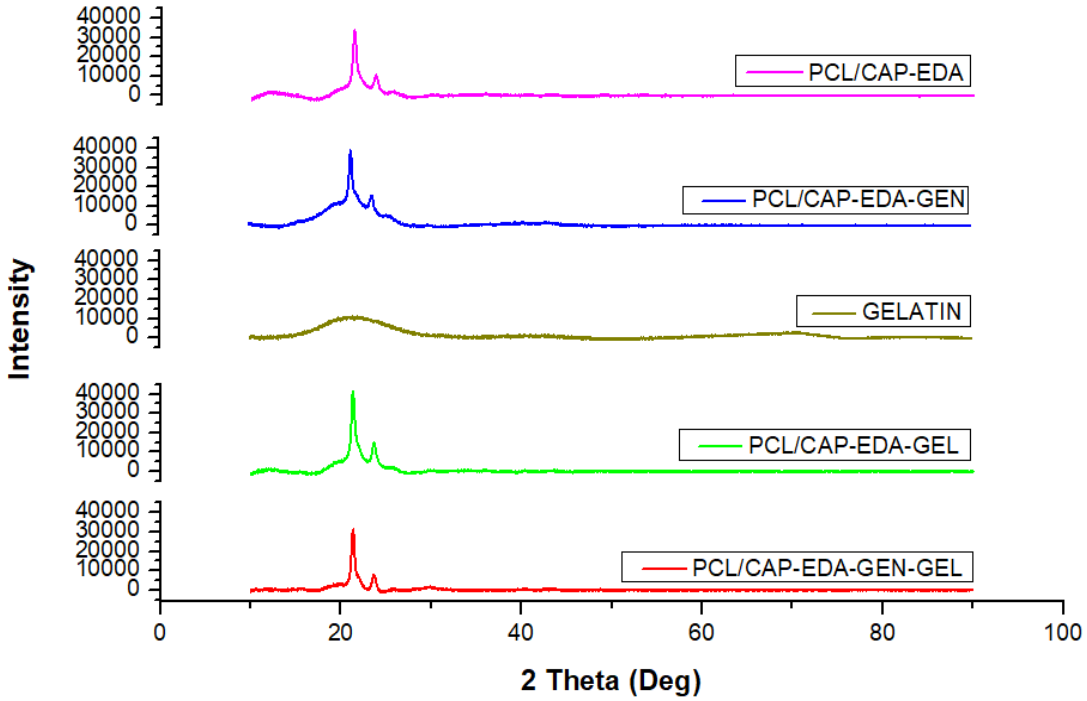


Figure 5. 24 X-ray diffraction patterns of (PCL/CAP-EDA) aminolyzed, (PCL/CAP-EDA-GEN) genipin crosslinked, (PCL/CAP-EDA-GEL) gelatin coated, (PCL/CAP-EDA-GEN-GEL) gelatin crosslinked nanofibers.

In conclusion, the genipin coating, biomolecule coating and biomolecule crosslinking all slightly alter the FWHM values derived from the XRD diffractograms. However, it is evident that the semi-crystalline nature of the PCL/CAP structure is maintained over the 2θ angle range, which indicates that the addition of the biomolecules to the nanofibers does not significantly affect the profile. In addition, the structure of the biomolecules differ, explaining the difference in FWHM values for the different biomolecule modified samples (Hussein et al., 2016).

5.3.6 Thermogravimetric analysis for thermal stability evaluation of the nanofibrous platforms

TGA analysis was performed to evaluate the effects of polymer blending, aminolysis and biomolecule modification on the thermal stability of the nanofibrous platforms. The individual thermograms were constructed to identify the $T_{5\%}$ and the derivative curves have been constructed to determine the T_{max} for each sample and are presented in A9 of the appendix. The respective $T_{5\%}$ and T_{max} values and number of degradation steps are displayed in Table 5.5. Figure 5.25 illustrates the difference between the thermal stability of the pristine PCL, CAP polymers, the PCL nanofibers, and the PCL/CAP nanofibers. Pristine PCL (Figure 5.25) presents a one-step degradation mechanism, corresponding to polymer pyrolysis (Pan et al., 2019). The $T_{5\%}$ occurs at ~ 368.97 °C and the T_{max} occurs at ~ 413.84 °C, which corresponds with literature (T. Su et al., 2008). Cellulose acetate phthalate degrades via a three-step mechanism. The first degradation step results in a 3.24% weight loss, followed by 45.81 and 44.65% weight loss in the second and third steps, respectively. The initiation of degradation

occurs at 195.12 °C. The T_{max} for each degradation step is 117.62, 274.90 and 359.83 °C, respectively. There is 6.3% residue remaining, which aligns with literature (Roxin et al., 1998).

Table 5. 5 T_{max} and $T_{5\%}$ for pristine polymers and nanofibers.

Thermodynamic Property			
Sample	**Number of Degradation steps**	**Temperature at initiation of degradation (°C)**	**Temperature of maximum decomposition rate (°C)**
Pristine polycaprolactone	1	368.97	413.84
Pristine cellulose acetate phthalate	3	195.12	359.83
Polycaprolactone nanofibers	1	381.90	419.75
Polycaprolactone/ cellulose acetate phthalate nanofibers	4	216.01	417.32

The T_{max} and $T_{5\%}$ values for PCL nanofibers are very similar to that of pristine PCL, indicating that the electrospinning process does not significantly affect the thermal stability of PCL (Pan et al., 2019). The major degradation step results in a 99.87% weight loss. In terms of the PCL/CAP nanofibers, Section A highlights a reduction in onset of degradation in comparison to PCL nanofibers, indicating that the addition of CAP reduces the thermal stability in this temperature range (Azizi et al., 2019). There is a 3.36% residue remaining at 900 °C, possibly due to the CAP, since PCL has very little residue. The PCL/CAP nanofibers degrade in four steps, each step resulting in 9.93, 6.21,13.35 and 67.29% weight loss, respectively. Following surface amination and subsequent biomolecule crosslinking, the TGA thermograms of the samples are altered, indicating a change in thermodynamic properties (Azizi et al., 2019).

The TGA thermograms are represented in Figures 5.27-5.30 which compare the thermal stability of the biomolecule modified samples relative to the unmodified samples. Figures 5.26, 5.28 and 5.30 compare the biomolecule-modified samples with controls. Each set of graphs highlights three areas of interest: region A, B and C, which are enlarged under each main graph and presented in Figures 5.27 and 5.29, respectively. Genipin degrades in two steps, with a $T_{5\%}$ of 207.5 °C and a T_{max} of 234.92 °C. The first degradation step results in a 46.75% mass loss and the second degradation step results in a 28.83% mass loss, with a 24.42% residual content at 900 °C. Collagen degrades in two steps and its $T_{5\%}$ and T_{max} values are 81.52 °C and 333.2 °C, respectively. The steps result in 13.03 and 67.32% mass loss, respectively with a 19.78% residual content at 900 °C. Region A (Figure 5.27) shows that surface amination of the PCL/CAP nanofibers reduces the onset of degradation. However, in the enlarged Section A (Figure 5.26), it is evident that there is a rightward shift of the PCL/CAP-EDA graph in comparison to the unfunctionalized sample, indicating an enhanced thermal stability at this temperature (Azizi et al., 2019).

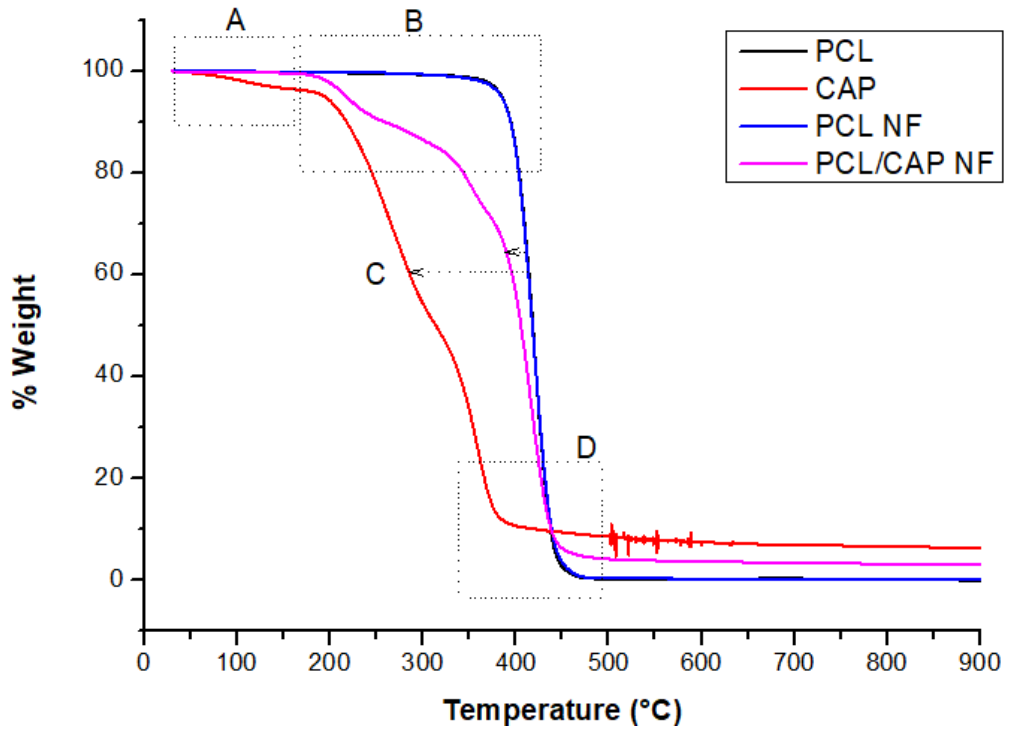


Figure 5. 25 Thermogravimetric analysis of (PCL) pristine polycaprolactone and (CAP) cellulose acetate phthalate, (PCL NF) polycaprolactone nanofibers and (PCL/CAP NF) polycaprolactone/cellulose acetate phthalate nanofibers.

Table 5. 6 T_{max} and $T_{5\%}$ for each sample.

Thermodynamic Property			
Sample	**Number Degradation steps**	**Temperature at initiation of degradation (°C)**	**Temperature of maximum decomposition rate (°C)**
Polycaprolactone/cellulose acetate phthalate nanofibers	4	203.24	420.07
Aminolyzed nanofibers	3	266.35	349.08
Genipin crosslinked nanofibers	2	319.08	410.74
Collagen coated nanofibers	2	354.47	417.32
Collagen crosslinked nanofibers	1	333.58	415.96
Sodium alginate coated nanofibers	1	346.54	410.06
Sodium alginate crosslinked nanofiber	1	319.00	413.85
Gelatin coated nanofibers	1	367.43	423.74
Gelatin crosslinked nanofibers	2	307.86	412.48

Region B (Figure 5.27) indicates a leftward shift of the aminolyzed sample from the unfunctionalized sample, indicating a reduced thermal stability from 350-450 °C (Azizi et al., 2019). Genipin coating on the aminolyzed film causes an enhanced onset of degradation in the range of 100-200 °C in comparison to the aminolyzed sample. Furthermore, there is a

rightward shift in region A, indicating an enhanced thermal stability (Azizi et al., 2019). Region B also demonstrates a strong rightward shift from the aminolyzed sample, indicating an enhanced thermal stability in the major degradation step of the samples (Azizi et al., 2019). Region C is analogous to this. This concludes that genipin coating enhances the thermal stability of the aminolyzed nanofibers. Collagen coating also shows similar rightward shifts in comparison to the aminolyzed nanofibers (Figure 5.26). However, the shifts are less drastic in comparison to the genipin coated nanofibers. This indicates that the collagen coating has an enhanced thermal stability in comparison to the aminolyzed nanofibers, yet a slightly decreased thermal stability in comparison to the genipin coated sample (Azizi et al., 2019). The collagen crosslinked sample presents with a very similar thermodynamic profile to that of the genipin coated sample. However, the rightward shift in regions A, B and C from the aminolyzed sample is more pronounced than that of the collagen coated sample, yet less than the genipin coated sample. This highlights that collagen crosslinking on the aminolyzed nanofibers enhances the overall thermal stability of the sample, more so than the collagen coating, but less than the genipin coating (Azizi et al., 2019). Figure 5.28 highlights the thermal stability of the sodium alginate modified samples.

Sodium alginate (Figure 5.28) degrades in two steps. The initial step is due to water loss and the second step is due to the decarboxylation reaction of alginate, fracture of glycosidic bonds, and dehydration and decarboxylation of alginate (Soares et al., 2004). Figure 5.29 shows enlarged images of region A, B and C in Figure 5.28. The onset of degradation of the sodium alginate coated sample is improved in comparison to the aminolyzed sample. Region A highlights a rightward shift of the sodium alginate coated sample from the aminolyzed sample, indicating an enhanced thermal stability in this range (Azizi et al., 2019). Furthermore, the sample shows an improved thermal stability in comparison to the genipin coated sample in the temperature range of 250-360 °C, as seen by the rightward shift of the graph.

Region B and C in Figure 5.29 indicate a rightward shift of the sample from the aminolyzed sample, also indicating an enhanced thermal stability in this range (Azizi et al., 2019). However, the sodium alginate coated sample presents with a reduced thermal stability compared to the genipin coated sample demonstrated by the leftward shift of the curve in region B and C (Azizi et al., 2019). The sodium alginate crosslinked sample also shows a rightward shift from the aminolyzed sample in all three regions, indicating an enhanced thermal stability in comparison to the aminolyzed sample. In region A, B and C, the crosslinked sample presents a rightward shift in comparison to the sodium alginate and genipin coated samples, indicating that it demonstrates the highest thermal stability at this temperature (Azizi et al., 2019).

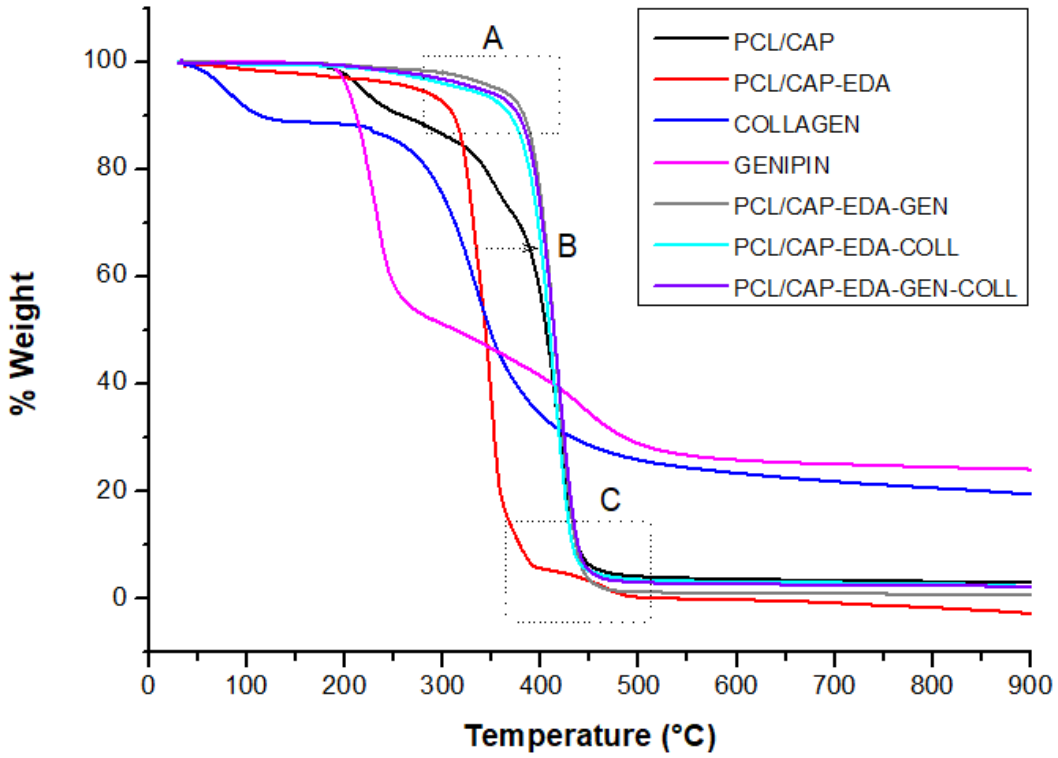


Figure 5. 26 Thermogravimetric analysis of (PCL/CAP) polycaprolactone/cellulose acetate phthalate, (PCL/CAP-EDA) aminolyzed nanofibers, pristine collagen, pristine genipin, (PCL/CAP-EDA-COLL) collagen coated nanofibers, (PCL/CAP-EDA-GEN) genipin crosslinked nanofibers and (PCL/CAP-EDA-GEN-COLL) collagen crosslinked nanofibers.

Figure 5.30 compares the thermal stability of the gelatin modified samples. The TGA thermogram of gelatin in Figure 5.30 shows two major weight loss steps. The first weight loss event results in a 11.34% weight loss, whereas the second results in a 68.74% weight loss due to the thermal decomposition of the gelatin network (Rodríguez-Baeza et al., 2003). The onset of degradation of the gelatin coated sample is higher than that of the aminolyzed sample (Azizi et al., 2019). Furthermore, in region A, B and C there is a rightward shift of the gelatin coated sample from the aminolyzed sample and the genipin coated sample. This indicates that the gelatin coated sample is more thermally stable in comparison to the aminolyzed sample and the genipin coated sample (Azizi et al., 2019).The gelatin crosslinked sample (Figure 5.30) shows a rightward shift in region A, B and C compared to the aminolyzed sample. However, the crosslinked sample presents a leftward shift from the gelatin coated sample and the genipin coated sample in region A, B and C, indicating that it is not as thermally stable as the latter two (Azizi et al., 2019). The conclusion drawn from all analyses on the different biomolecule modifications of the nanofibers is that the genipin coated sample is more thermally stable in comparison to the aminolyzed samples. The biomolecule coated samples and the biomolecule crosslinked samples are also more thermally stable than the aminolyzed sample, proving that the biomolecule modification of the aminolyzed samples enhances thermal properties, which is advantageous for tissue engineering purposes.

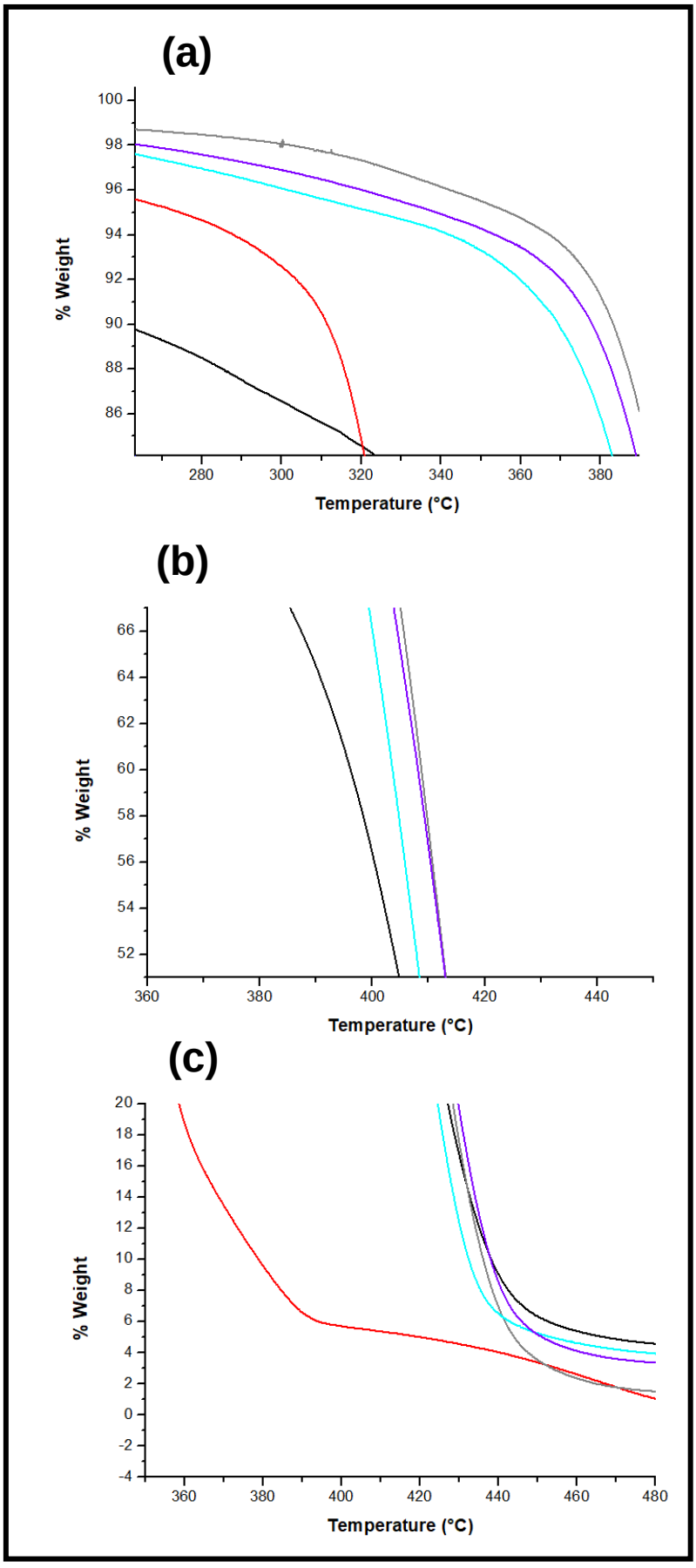


Figure 5.27 Thermogravimetric analysis of (a) region A, (b) region B and (c) region C of Figure 5.26.

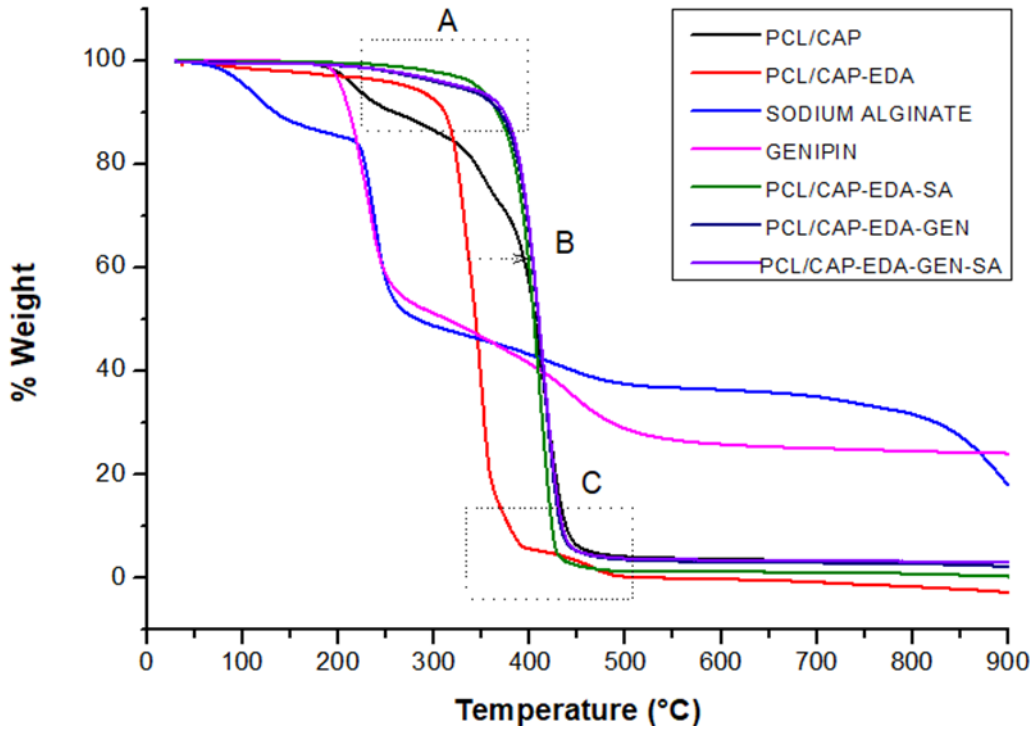


Figure 5. 27 Thermogravimetric analysis of (PCL/CAP) polycaprolactone/cellulose acetate phthalate nanofibers, (PCL/CAP-EDA) aminolyzed nanofibers, pristine sodium alginate, pristine genipin, (PCL/CAP-EDA-SA) sodium alginate coated nanofibers, (PCL/CAP-EDA-GEN) genipin crosslinked nanofibers and (PCL/CAP-EDA-GEN-SA) sodium alginate crosslinked nanofibers.

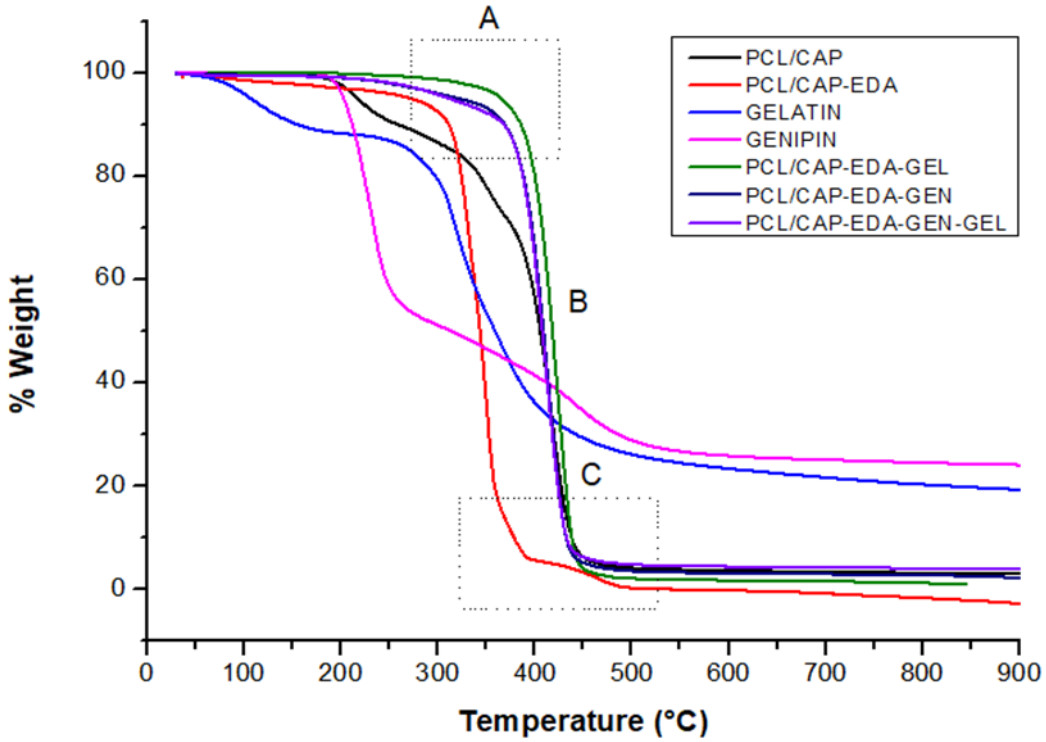


Figure 5. 30 Thermogravimetric analysis of (PCL/CAP-EDA) aminolyzed, (PCL/CAP-EDA-GEN) genipin crosslinked, (PCL/CAP-EDA-GEL) gelatin coated, (PCL/CAP-EDA-GEN-GEL) gelatin crosslinked nanofibers.

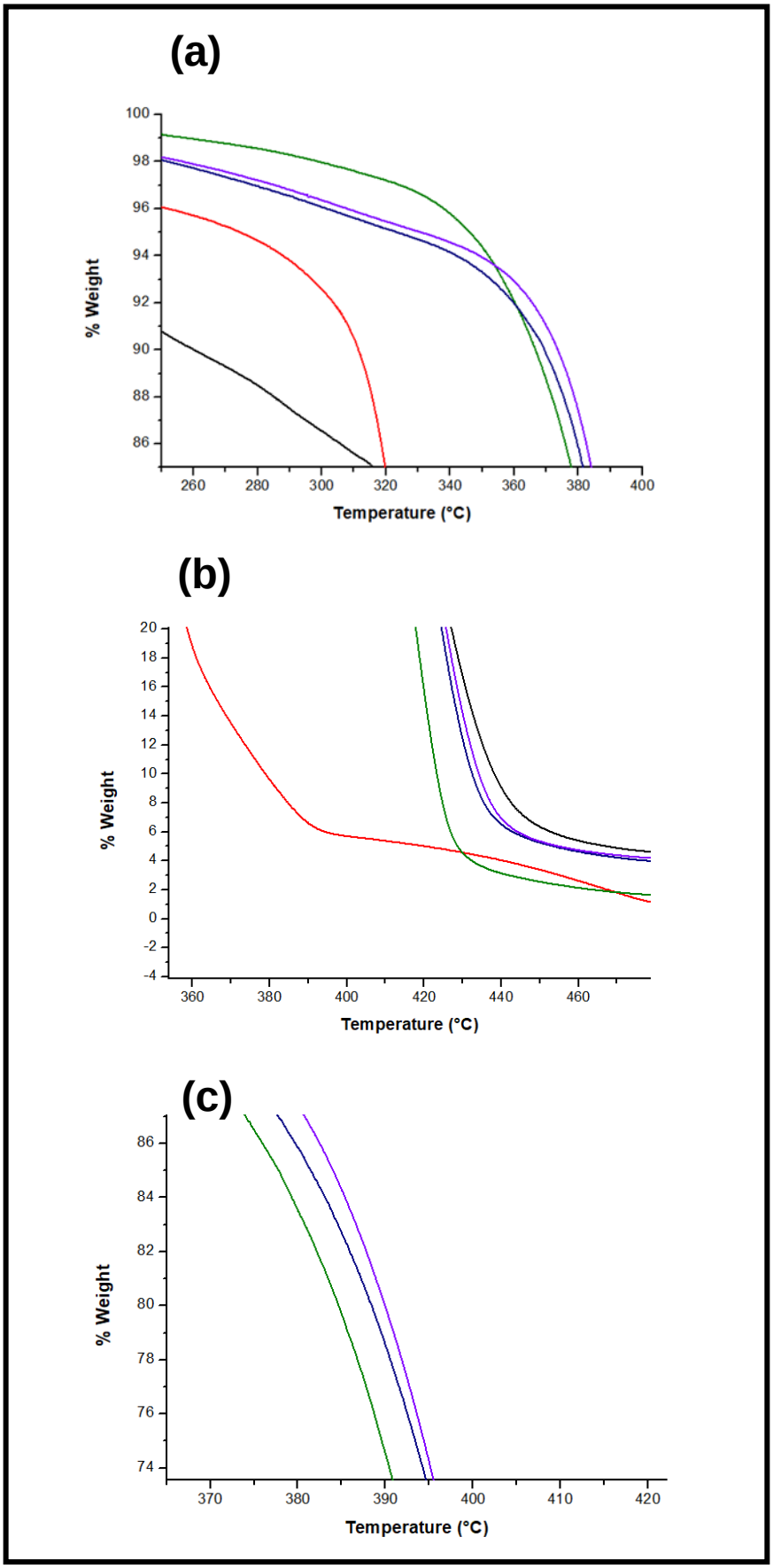


Figure 5. 29 Thermogravimetric analysis of (a) region A, (b) region B and (c) region C of Figure 5.28.

5.3.7 Porosimetric and surface area analysis of the nanofibrous platforms using BET analysis

The porosimetric and surface area analysis was undertaken to evaluate the suitability of the biomolecule-modified films for neural tissue engineering. The effects of the addition to CAP to the nanofibrous platform as well as the effect of aminolysis and biomolecule modification on the porosity and surface area was investigated. Nitrogen adsorption-desorption isotherm plots were generated (A9 in appendix) and a detailed analysis on the pore sizes, volumes and surface areas was undertaken.

A representative isotherm plot for all the nanofibrous platforms is depicted in Figure 5.31, as all the samples maintained the same general shape and classification. Porosity and surface area analyses are presented in Table 5.7, which highlights the difference between the PCL nanofibers and the composite PCL/CAP nanofibers. Firstly, the composite nanofibers produce a reduction in pore diameter and an increase in pore volume. This means that the pores, albeit smaller in diameter, occupy a larger depth in the nanofibrous platform (Sing et al., 1985). The pore size and volume reflect the cumulative surface area of pores on the sample where pores larger in diameter and depth contribute to a larger pore surface area. This means that the BJH cumulative volume of pores will increase as a result (as confirmed by the result in Table 5.7) (Ramburrun et al., 2019). The addition of CAP to the nanofibers enhances the BET surface area, which is advantageous as higher surface areas favor cell adhesion, proliferation, migration, and differentiation, all of which are highly desired properties for tissue engineering applications (Ma et al., 2005). Similarly, the effect of aminolysis on the PCL/CAP nanofibers is described by an increase in pore diameter and volume, thereby enhancing the BJH adsorption cumulative volume of pores. Furthermore, the BET surface area is enhanced which is due to the enhanced pore formation due to the aminolysis treatment (Y. Z. Zhang et al., 2006).The biomolecule immobilization on the surface of the nanofibers reduces the BET surface area and the pore volume, which is possibly due to the embedding of the biomolecule inside the pores, resulting in an apparent reduced pore volume and BET surface area. This finding is consistent with literature (Shabani et al., 2011). Pore sizes are categorized as micro- (<2nm), meso- (2-50nm) and macroporous (>50nm) (Gregg et al., 1967; Groen et al., 2003). According to this classification, the pore diameters of all the samples fall within the mesoporous range. The technique of nitrogen gas adsorption over a range of relative pressures for the determination of pore characteristics produce adsorption isotherms (Figure 5.31) which provide insightful information regarding the pore size and surface areas. It is to be noted that aminolysis, and biomolecule crosslinking did not alter the shape of the isotherms. The nanofibrous samples are classified as a type IV isotherm with a H3 hysteresis loop (Figure 5.32), according to the IUPAC classification of gas adsorption isotherms (Brunauer et al., 1936). This confirms their porous nature. The type IV isotherm is indicative of a multilayer material, which is appropriate

due to the multilayer positioning of individual fibers forming the nanofibrous platform (Groen et al., 2003). The hysteresis loops are characteristic of type H3 which relates to solids with a very wide distribution of pore size and is suggestive of complete pore filling including capillary condensation which occurs in the presence of mesopores (Gregg et al., 1967; Groen et al., 2003). The presence of a H3 hysteresis loop denotes an interconnected pore system of random distribution within the nanofibrous platform, with shapes of parallel, slit-like, and open-ended tubes (Sing et al., 1985). This is effective in the neural tissue engineering setting as it facilitates the permeability of the nanofibers for uninterrupted passage of cells, nutrients, and waste in the implant site (Groen et al., 2003). To draw a comparison between the non-fibrous PCL/CAP thin films in Chapter 3 and the PCL/CAP nanofibrous platforms presented here, the BET surface area has increased from -0.4 to 5.56 m^2/g, demonstrating a significant improvement in surface area, which is more fitting for the neural tissue engineering domain as the electrospun nanofibers more closely mimic the native extracellular matrix with its inherent high surface area and porosity (Shin et al., 2012).

Table 5. 7 Porosity analysis of the nanofibrous samples, comparing the effect of aminolysis and biomolecule crosslinking.

Property	Sample			
	PCL[19]	**PCL/CAP[20]**	**PCL/CAP-EDA[21]**	**PCL/CAP-EDA-GEN-BM[22]**
Surface Area				
BET[23] surface area (m^2/g)	5.01	5.56	16.33	11.97
BJH[24] adsorption cumulative surface area of pores diameter (m^2/g)	4.81	6.01	18.05	12.82
BJH desorption cumulative surface area of pores (m^2/g)	5.51	6.53	20.88	14.61
Pore Volume				
BJH Adsorption cumulative volume of pores (mm^3/g)	9.83	21.79	125.45	91.12
BJH desorption cumulative volume of pores (mm^3/g)	0.93	21.84	146.91	91.00
Pore Size				
Adsorption average pore width (4V/A by BET) (nm)	7.85	7.45	17.26	13.6
BJH Adsorption average pore diameter (4V/A) (nm)	21.63	14.50	27.79	28.44
BJH desorption average pore diameter (4V/A) (nm)	18.92	13.37	28.15	24.91

[19] Polycaprolactone nanofibers
[20] Polycaprolactone/cellulose acetate phthalate nanofibers
[21] Aminolyzed nanofibers
[22] Biomolecule crosslinked nanofibers
[23] Brunaeur-Emmet-Teller theory
[24] Barret-Joyner-Halenda theory

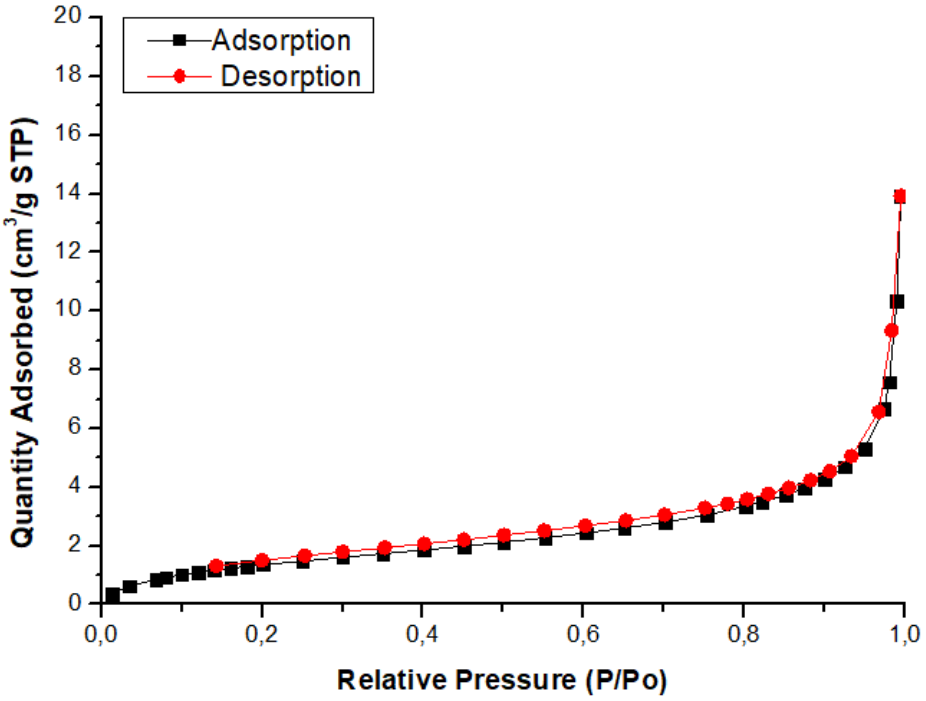


Figure 5. 31 Nitrogen adsorption-desorption isotherm for polycaprolactone/cellulose acetate phthalate nanofibrous platforms.

In conclusion, the nanofibrous platforms are well suited for neural tissue engineering as a result of their high surface area and interconnected mesoporous network to facilitate cell metabolism.

5.3.8 Determination of the mechanical properties of the nanofibrous platforms using Texture Analyser analysis

The mechanical properties of the nanofibrous platforms were assessed to evaluate their suitability for neural tissue engineering. Figure 5.32 represents the stress-strain curves generated to compare the mechanical properties of all the nanofibrous samples. Table 5.8 highlights the values calculated for the tensile strengths of the samples. The tensile strength upon addition of CAP to the electrospinning solution is reduced from 4.10 ± 0.58 to 2.86± 0.32 MPa. Furthermore, the aminolysis of the PLC/CAP nanofibrous platform results in a further reduction of tensile strength, which is expected since aminolysis is known to reduce the tensile strength of polymeric scaffolds (Jeznach et al., 2019). The crosslinking of genipin to the PCL/CAP nanofibers improves the tensile strength of the samples, possibly due to the formation of crosslinks, which is known to enhance the biomaterials' mechanical properties by increasing the intermolecular force in the material (Z. Wang et al., 2020). In addition, the crosslinking of the biomolecules to the surface of the films using genipin further enhances the tensile strength of the samples, which is consistent with literature (Frohbergh et al., 2012).

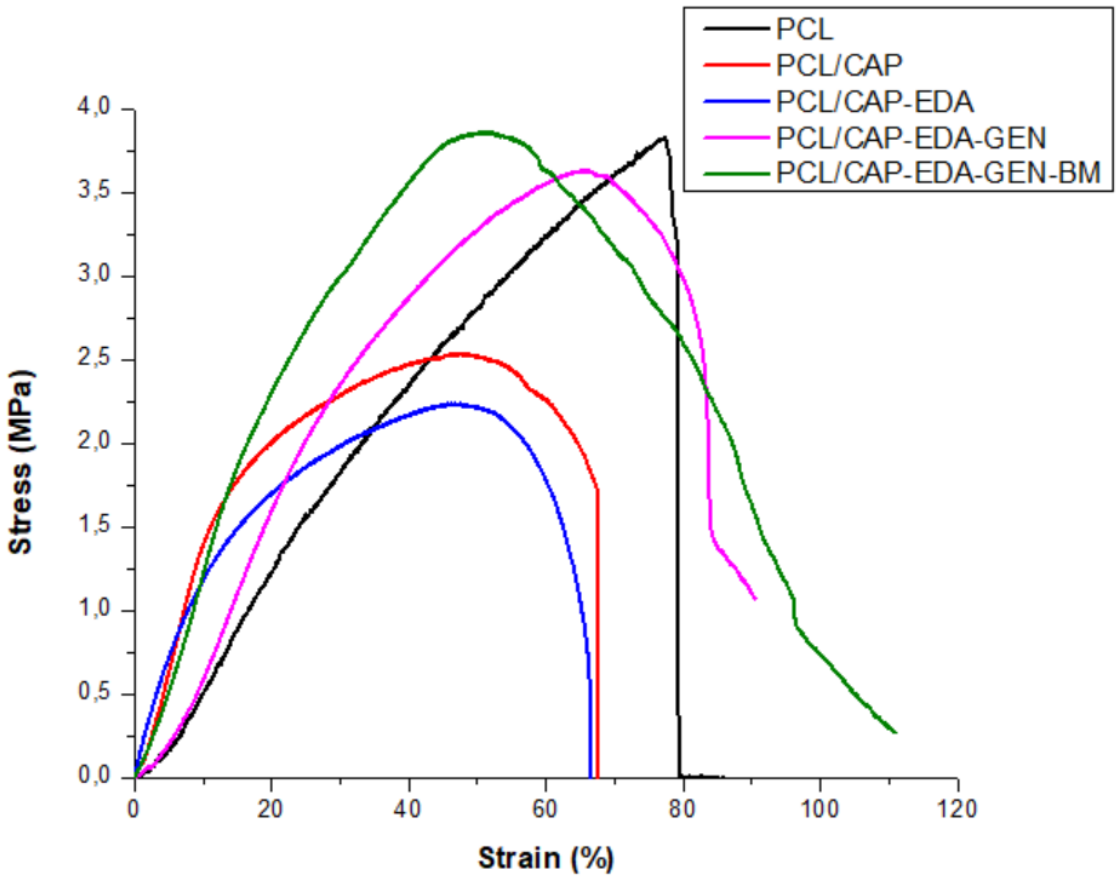


Figure 5. 32 Stress-strain curves generated to compare the mechanical properties of (PCL) polycaprolactone nanofibers, (PCL/CAP) polycaprolactone/cellulose acetate phthalate nanofibers, (PCL/CAP-EDA) aminolyzed nanofibers, (PCL/CAP-EDA-GEN) genipin crosslinked nanofibers and (PCL/CAP-EDA-GEN-BM) biomolecule crosslinked samples.

Table 5. 8 Comparison of the tensile strengths of the samples.

Sample	Tensile Strength (MPa)
Polycaprolactone nanofibers	4.10 ± 0.58
Polycaprolactone/cellulose acetate phthalate nanofibers	2.86 ± 0.32
Aminolyzed nanofibers	2.67 ± 0.25
Genipin crosslinked nanofibers	3.22 ± 0.49
Collagen crosslinked nanofibers	4.28 ± 0.53
Sodium alginate nanofibers	5.34 ± 0.47
Gelatin crosslinked nanofibers	4.73 ± 0.93

To conclude, Zhang and co-workers have observed that the ideal tensile strength for optimal mechanical performance in nerve tissue engineering (comparable to that of clinical materials such as Neurolac®) is 1-7 MPa (X. F. Zhang et al., 2017). All the samples fall within this range, therefore all present adequate tensile strength for neural tissue engineering.

5.3.9 Determination of the hydrophilicity of the nanofibrous platforms by water contact angle measurements

Water contact angle measurements were conducted to assess the hydrophilicity of the nanofibrous platforms, since the hydrophilicity of materials is important for cell adhesion and

spreading (Mirrhosseini et al., 2016). Figure 5.33 provides an illustration of the hydrophilicity of the nanofibrous platforms.

The water contact angle for pristine PCL nanofibers is 132.58 ± 1.33°. This is decreased to 128.37 ± 2.2° after the addition of CAP to the electrospinning solution. This is the predicted outcome since PCL is regarded as a relatively hydrophobic polymer and CAP is a relatively hydrophilic polymer (Xia et al., 2013). Upon aminolysis, the contact angle is reduced to 62.25 ± 1.03°. It is further reduced upon collagen, sodium alginate, gelatin and genipin coating to 63.07 ± 3.31, 53.47 ± 1.66, 58.73 ± 5.63 and 53.62 ± 3.02°, respectively. The contact angles are further reduced upon biomolecule crosslinking to 42.48 ± 2.43, 37.36 ± 3.59 and 50.63 ± 1.74°, respectively. From these results it is evident that aminolysis is an effective method to reduce the hydrophobic nature of PCL, which results in low cell attachment observed in Chapter 3. In addition, the coating of the aminolyzed surface with each biomolecule reduces the water contact angle even further. The crosslinked samples display the lowest water contact angles, indicating that they are the most hydrophilic samples. It has been reported that the immobilization of biomolecules onto the surface of polymeric surfaces improves the hydrophilicity of the surfaces due to their inherent hydrophilic nature (Benykhlef et al., 2012; Meghdadi et al., 2019; Park et al., 2019). Figure 5.34 illustrates how the crosslinking of biomolecules reduces the water contact angle, thereby enhancing the hydrophilicity.

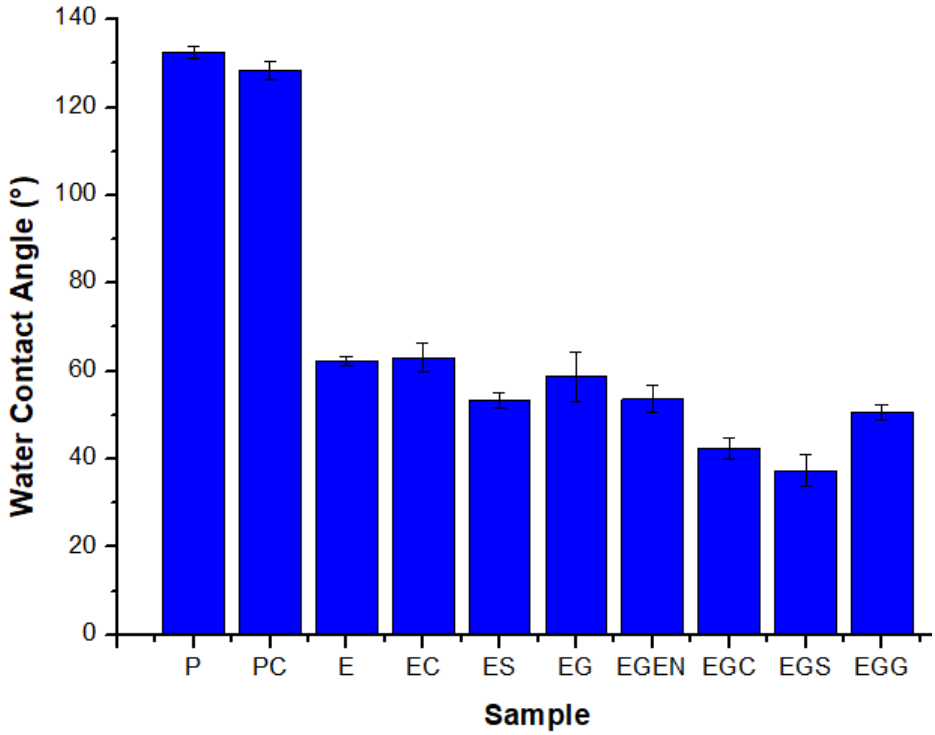


Figure 5. 33 Bar graph representing the water contact angle values of the nanofibrous platforms. (P) polycaprolactone, (PC) polycaprolactone/cellulose acetate phthalate, (E) aminolyzed, (EC) collagen coated, (ES) sodium alginate coated, (EG) gelatin coated, (EGEN) genipin crosslinked, (EGC) collagen crosslinked, (EGS) sodium alginate crosslinked, (EGG) gelatin crosslinked nanofibrous platforms.



Figure 5. 34 Water drop images on (a) polycaprolactone/cellulose acetate phthalate, (b) aminolyzed, (c) genipin crosslinked, (d) gelatin crosslinked, (e) collagen crosslinked and (f) sodium alginate crosslinked nanofibrous platforms.

The hydrophilic surfaces provide an ideal substrate for homogeneous cell distribution and an enhanced cell growth rate. The mechanism responsible for this is that the appropriate absorption or diffusion of cell culture medium into the scaffolds occurs due to the scaffolds hydrophilic nature, which then encourages cell attachment and spreading (Mirhosseini et al., 2016).

To conclude, aminolysis is an effective technique to improve the hydrophilicity of the nanofibrous platforms which are otherwise hallmarked by poor hydrophilicity. In Chapter 4, it is discussed that the films display a relatively poor PC12 and A172 cell attachment relative to the control (plasma treated well plates), which are reported to have a water contact angle of ~ 46° (O'Sullivan et al., 2020). The biomolecule crosslinked nanofibers have water contact angle values of 42.48, 37.36 and 50.63°. These results indicate that the collagen and sodium alginate nanofibrous platforms are more hydrophilic than the well plate control, therefore should have an improved cell attachment *In Vitro*.

5.3.10 Quantification of biomolecule attachment using BCA protein assay

The quantification of each biomolecule on the nanofibrous platforms was undertaken to firstly prove that the biomolecules were effectively immobilized on the surface, and secondly, to quantify the concentration of immobilized biomolecule. Figures 5.35-5.40 include the respective calibration curves and biomolecule quantification for the biomolecule coated and biomolecule crosslinked samples.

The trend observed is that the amount of each biomolecule detected on the crosslinked samples is higher than that on the biomolecule coated samples. This is possibly due to the crosslinks that have formed between the amine groups on the PCL/CAP film and the amine groups on the biomolecule. These crosslinks are stronger covalent bonds in comparison to the weaker electrostatic interactions between the films and the biomolecules in the coated samples, which did not have a crosslinking agent (Atthoff & Hilborn, 2007; G. E. Park et al., 2005; Rentsch et al., 2009). Therefore, more biomolecule is retained on the sample after PBS washing, therefore a higher absorbance is detected for the crosslinked samples.

To conclude, this assay proves the successful crosslinking of collagen, sodium alginate and gelatin to the nanofibers. It also proves that the crosslinked samples retain more biomolecule in comparison with their biomolecule coated counterparts.

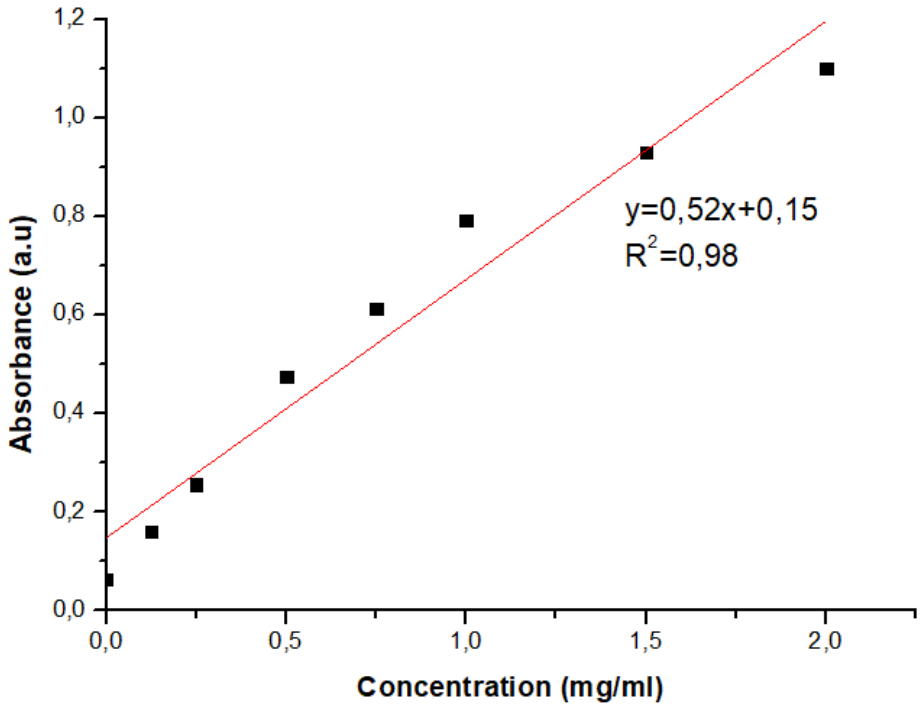


Figure 5. 35 Calibration curve used for the quantification of collagen on the nanofibrous surface.

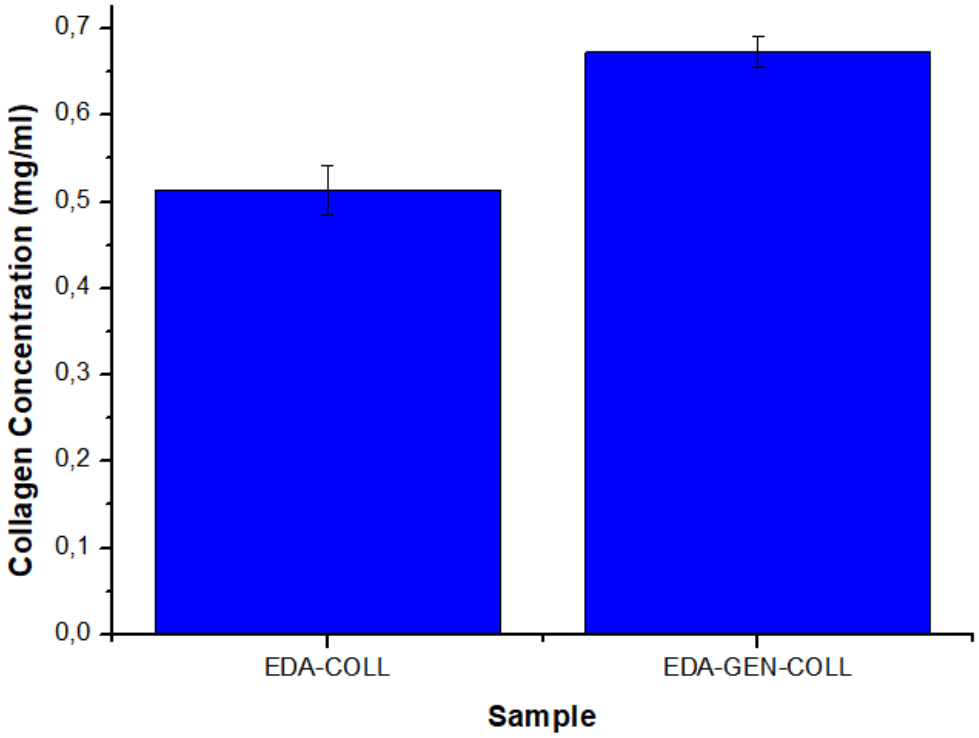


Figure 5. 36 Concentration of collagen detected on the nanofibrous surfaces of (EDA-COLL) collagen coated nanofibers and (EDA-GEN-COLL) collagen crosslinked nanofibers**.**

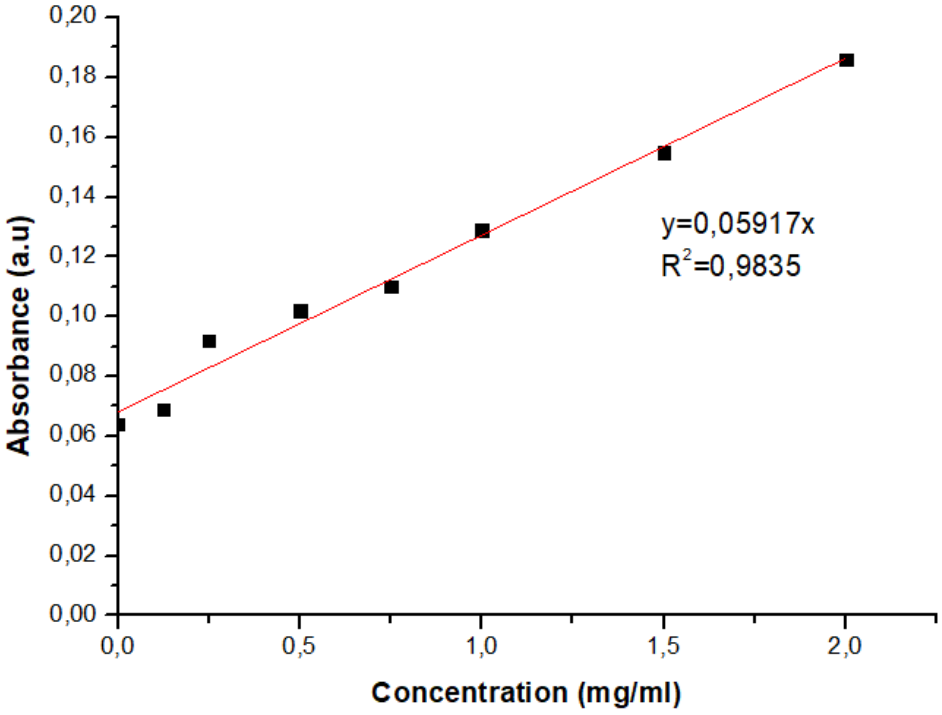


Figure 5. 37 Calibration curve used in the quantification of sodium alginate on the nanofibrous surface.

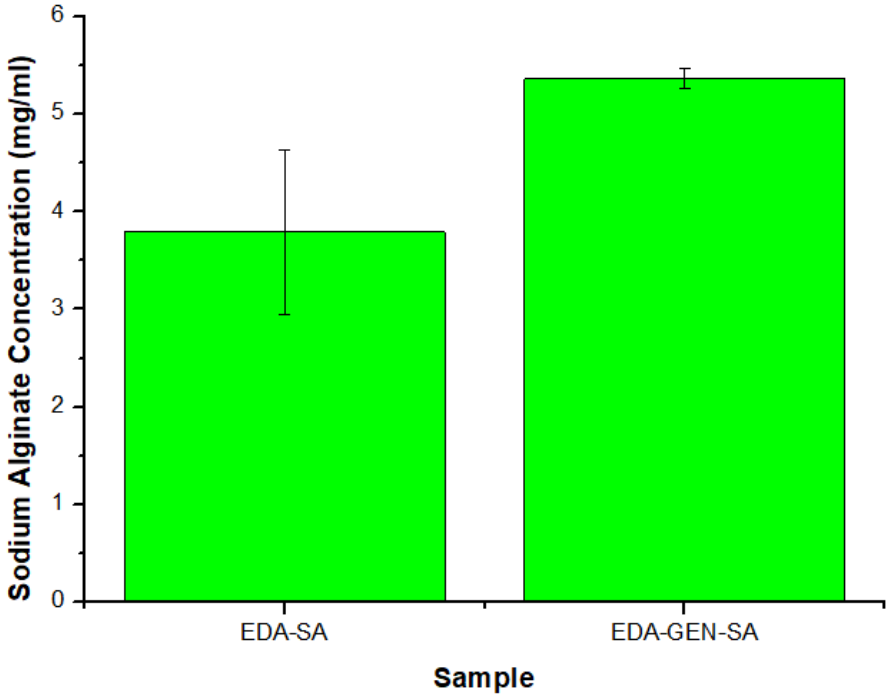


Figure 5. 3828 Concentration of sodium alginate detected on the surface of the (EDA-SA) sodium alginate coated nanofibers and (EDA-GEN-SA) sodium alginate crosslinked nanofibers.

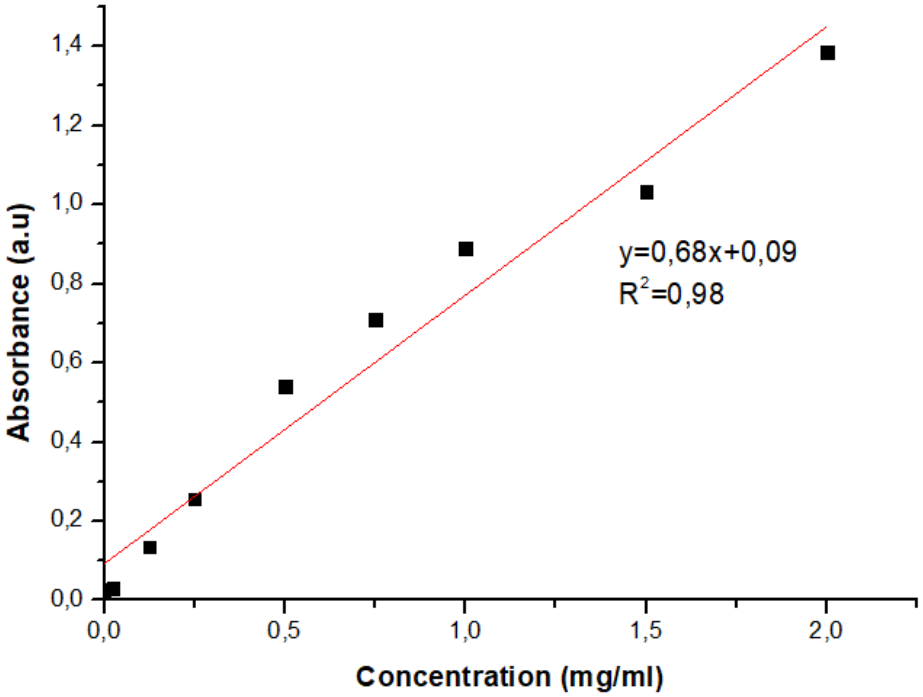


Figure 5. 39 Calibration curve used in the quantification of gelatin on the nanofibrous samples.

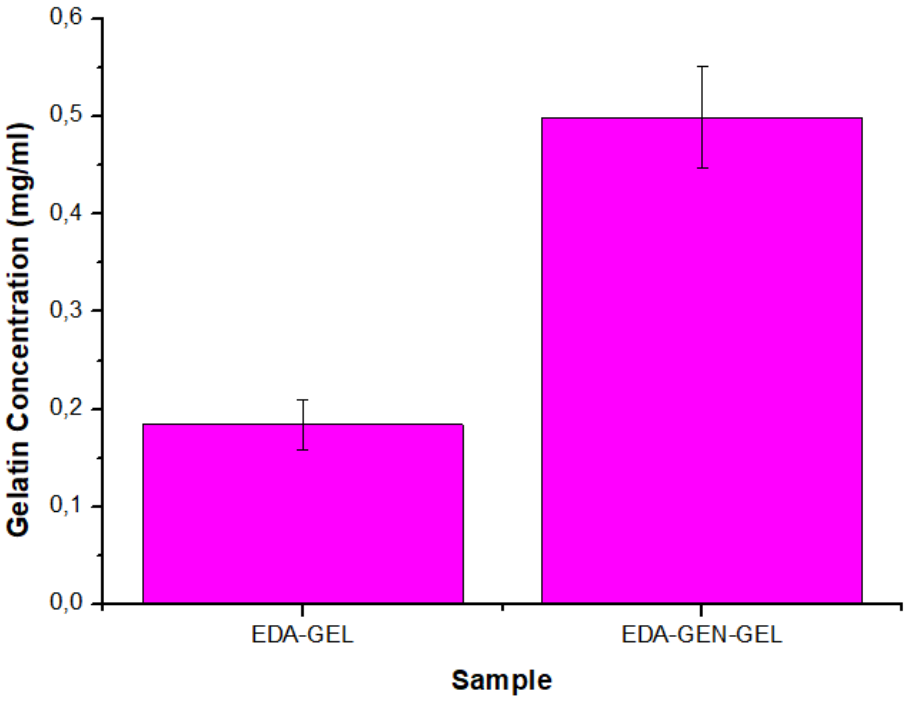


Figure 5. 40 Concentration of gelatin quantified on the nanofibrous surfaces of (EDA-GEL) gelatin coated nanofibers and (EDA-GEN-GEL) gelatin crosslinked nanofibers.

5.3.11 PC12 and A172 cell culture and quantification of cell viability utilizing the XTT cytocompatibility assay.

The XTT assay was performed to determine the cytocompatibility of the films with PC12 and A172 cell lines by quantifying the number of live cells present in the well plates after exposure to the films. Figure 5.41 represents the cell viability after 48 and 72 h exposure. The results presented in the XTT assay in Figure 5.40 illustrate that the 48 h time point, the cytocompatibility of the PCL/CAP nanofibrous platforms is higher than the PCL nanofibrous platform. Therefore, the addition of CAP is advantageous to cytocompatibility, possibly due to the increase in hydrophilicity it confers, determined in Section 5.3.9 (Boni et al., 2018). The aminolyzed film has a slightly lower cell viability compared to the unfunctionalized film of 94.46% (which is still relatively high in comparison to the negative control of 80.02%). The collagen and sodium alginate coating further reduces the viability to 87.48 and 79.22%, respectively, while the gelatin coating enhances the viability to 102.05%. Interestingly enough, the genipin coating reduces the cell viability to 62.09%, which is inconsistent with the genipin-coated films in Chapter 4 as well as literature, since genipin is known to have positive effects on cell viability (Di Giovanni et al., 2005; Hughes et al., 2014). The crosslinking of collagen, sodium alginate and gelatin to the films using genipin produces cell viabilities of 99.78, 89.34 and 93.92%, which are all higher than the negative control, although the sodium alginate and gelatin crosslinked samples have viabilities slightly lower than the aminolyzed samples (94.46%), which is unexpected since the sodium alginate nanofibers are the most hydrophilic,

therefore it was predicted that they would perform the best (Boni et al., 2018). None of the samples produce a significant change in cell viability in comparison to the unfunctionalized sample.

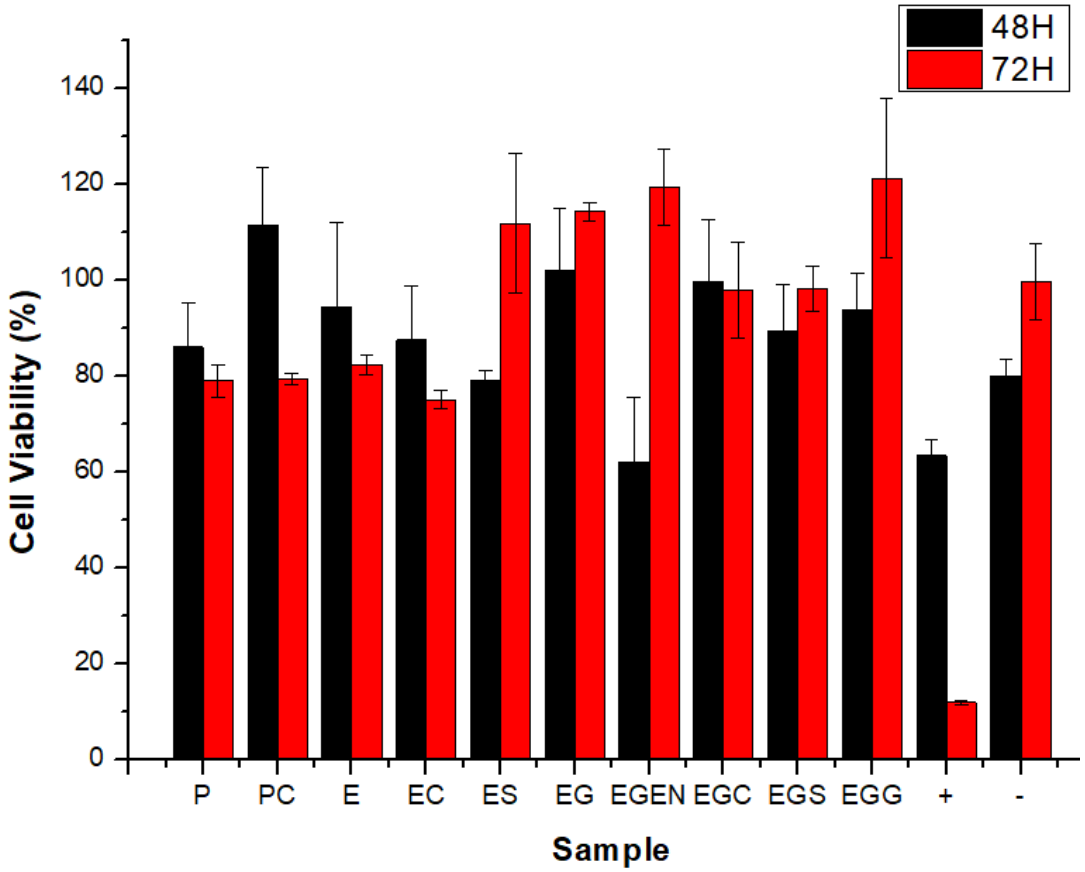


Figure 5. 41 PC12 Cytocompatibility results for 48 and 72 h for all the nanofibrous samples. (P) polycaprolactone, (PC) polycaprolactone/cellulose acetate phthalate, (E) aminolyzed, (EC) collagen coated, (ES) sodium alginate coated, (EG) gelatin coated, (EGEN) genipin coated, (EGC) collagen crosslinked, (EGS) sodium alginate crosslinked, (EGG) gelatin crosslinked, (+) positive control and (-) negative control. An unpaired, two-tailed student T-test was conducted comparing the cell viability obtained from the unfunctionalized sample, the aminolyzed sample and the biomolecule crosslinked samples, which showed statistical significance after the 48 h exposure of P=0.45, 0.51, 0.19 and 0.24, respectively, and after 72 h exposure of P=0.27, 0.14, 0.02 and 0.07, respectively.

After 72 h, the sodium alginate, gelatin and genipin coated samples, as well as the collagen and gelatin crosslinked samples all display cell viabilities over 100%, indicating cell proliferation (Boni et al., 2018). The only sample that has a viability less than 80% at this time point is the collagen coated samples, with a viability of 75.12%. This is more than 10% lower than the 48 h result. The large reduction in viability could possibly be due to residual acetic acid present in the collagen coating. However, this proposal is unlikely since the collagen crosslinked sample (which also involved the use of acetic acid during production) has a viability of 98.01% at 72 h. The sodium alginate and gelatin crosslinked samples both produce a significant increase in cell viability at 72 h. Overall, none of the samples demonstrate major

toxicity to the PC12 cells as none of the samples produce significant reduction in cell viability. An acceptable cell viability is over 80%, therefore only the sodium alginate coated sample at 48 h and the collagen coated sample at 72 h are below this threshold (Boni et al., 2018). All the biomolecule crosslinked samples demonstrate higher cell viabilities in comparison to their coated counterparts and none of the crosslinked samples display viabilities below 80%, in fact, they are all above 90%, indicating a high neurocompatibility with PC12 cells. Comparatively, the gelatin crosslinked sample performs the best in terms of cytocompatibility and proliferative effects.

In terms of the A172 cell line (Figure 5.42), at 48 h, the PCL nanofibers demonstrate a slightly better performance (107.34%) compared to the composite PCL/CAP nanofibers (100.03%). The aminolysis of the nanofibers results in a reduction in cell viability to 89.41%, which is contradictory to literature and the XTT assay in Chapter 3. The aminolyzed nanofibers are expected to enhance the cell viability (Krithica et al., 2019). The proposed reason for this is that there is residual ethylenediamine trapped inside the nanofibers, due to inefficient PBS rinsing or inadequate drying to allow for complete evaporation. Ethylenediamine has been found to have a high *In Vitro* cytotoxicity (Pantelić et al., 2014). The second proposed reason could be that the aminolysis treatment time is reduced for the nanofibers in comparison to the films, indicating that the concentration of free amines on the surface of the films is higher than that on the nanofibers, therefore resulting in a lower cell viability, since the presence of free amines on surfaces enhances cell attachment due to their positive charge (Jeznach et al., 2019).

The collagen coated sample produces a significant reduction in cell viability to 69.28% ($P=0.03$). The proposed reason for this is the possibility of residual acetic acid in the nanofibers (as discussed with the PC12 cells), which is also observed for the collagen crosslinked sample at 48 h. The sodium alginate and gelatin coated samples demonstrate an enhanced cell viability of 110.17 and 88.33%, respectively. Furthermore, the genipin coated samples have a viability of 91.77%, which is expected since genipin has a positive effect on cell viability (Hughes et al., 2014; Mu et al., 2013). The sodium alginate crosslinked sample is the only crosslinked sample to produce a higher cell viability in comparison to the aminolyzed sample. The aminolyzed samples, the genipin coated samples and the collagen and gelatin crosslinked samples all display viability values below that of the negative control. The collagen coated and crosslinked samples both produce viabilities below 80%, which indicates an unacceptable cell response (Boni et al., 2018). None of the samples (other than the collagen crosslinked sample) can produce a significant reduction in cell viability. At 72 h, it is to be noted that all the viabilities are improved in comparison to the 48 h time point, with most of them being over 100%, proving that the samples are conducive to cell proliferation. The collagen and gelatin coated and

crosslinked nanofibrous platforms perform the best out of all the samples. In this case, all the samples outperform the negative control. None of the samples produce a significant reduction in cell viability in comparison to the untreated sample.

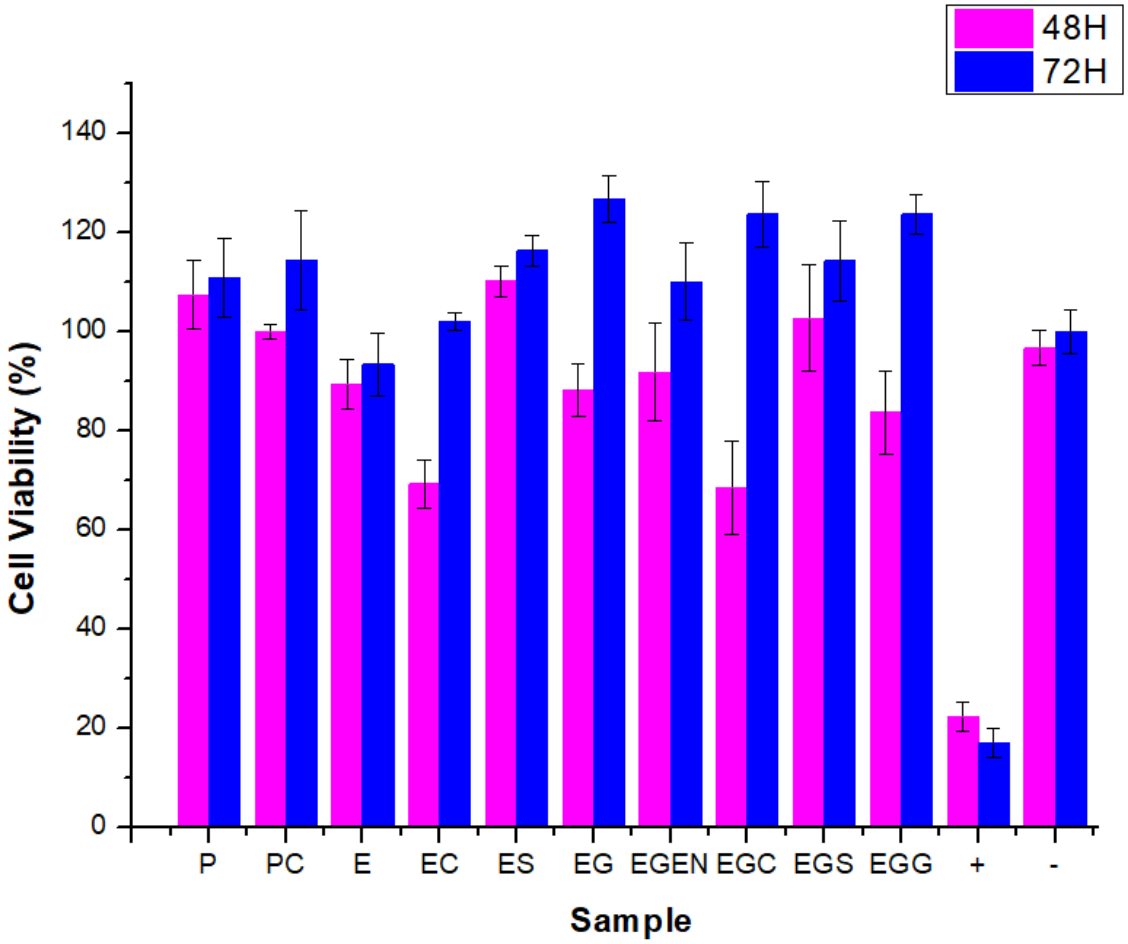


Figure 5. 42 A172 Cytocompatibility results for 48 and 72 h for all the nanofibrous samples. (P) polycaprolactone, (PC) polycaprolactone/cellulose acetate phthalate, (E) aminolyzed, (EC) collagen coated, (ES) sodium alginate coated, (EG) gelatin coated, (EGEN) genipin coated, (EGC) collagen crosslinked, (EGS) sodium alginate crosslinked, (EGG) gelatin crosslinked, (+) positive control and (-) negative control. An unpaired, two-tailed student T-test was conducted comparing the cell viability obtained from the aminolyzed sample and the biomolecule crosslinked samples, which showed statistical significance after the 48 h exposure of P=0.11, 0.03, 0.82 and 0.13, respectively, and after 72 h exposure of P=0.15, 0.48, 0.99 and 0.43, respectively.

In conclusion, none of the nanofibrous samples are cytotoxic to PC12 and A172 cells. The samples that produce a viability below 80% at 48 h are drastically increased at 72 h, therefore confirming that the samples are not cytotoxic. At 72 h, the gelatin coated, collagen crosslinked, and gelatin crosslinked samples cause the highest cell proliferation. Most of the samples have proliferatory effects on the cells, except for PCL/CAP-EDA and PCL/CAP-EDA-COLL.

5.3.12 Quantification of cell attachment utilizing trypan blue exclusion assay

The trypan blue exclusion assay provided a quantitative analysis of the cells attached to the film. This was an important assay as it provided a direct indication of the suitability of the nanofibers in supporting cell attachment (Liu et al., 2014). The higher the cell attachment to the films, the better the films performed *In Vitro* (Liu et al., 2014). Figure 5.43 represents the PC12 cell attachment relative to the control (plasma treated cell culture well plates).

The PCL nanofibers facilitate a relatively low cell attachment in comparison with the control (20.85%) which is improved upon addition of CAP to the nanofibers (35.61%). This is perhaps due to the hydrophobic nature of the PCL nanofibers determined in Section 5.3.9 (132.58°), since it has been found that more hydrophilic surfaces promote cell attachment (Webb et al., 1998). Therefore, the slight improvement in hydrophilicity of the PCL/CAP nanofibers to 128.37° through the addition of CAP facilitated a higher cell attachment. The aminolysis of the PCL/CAP nanofibers enhances the cell attachment to 39.66%. This is expected since the introduction of positively charged amine groups is known to enhance cell interactions with scaffolds (Jeznach et al., 2019). The coating of the samples with collagen and sodium alginate significantly enhances the cell attachment to 55.66 and 68.75%, respectively, which is expected as biomolecules have specific cell binding sites on their backbones, which are known to enhance cell attachment (Yabin Zhu et al., 2002).

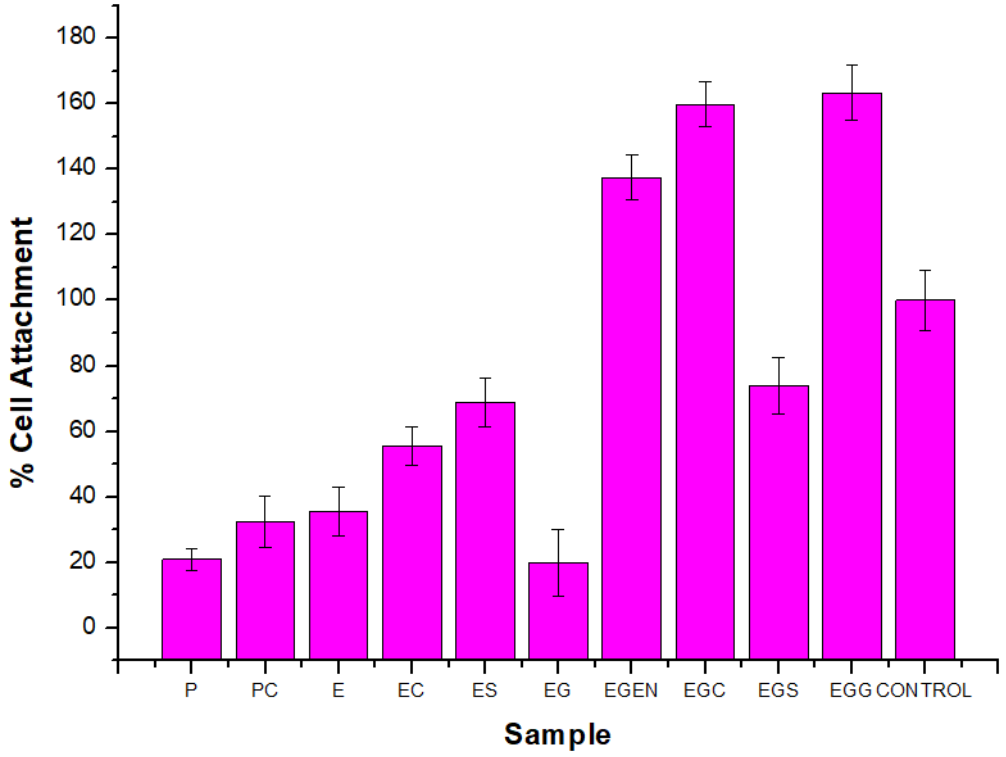


Figure 5. 43 Quantification of cell attachment for PC12 cells after 72 h. (P) polycaprolactone, (PC) polycaprolactone/cellulose acetate phthalate, (E) aminolyzed, (EC) collagen coated, (ES) sodium alginate coated, (EG) gelatin coated, (EGEN) genipin coated, (EGC) collagen crosslinked, (EGS) sodium alginate crosslinked, (EGG) gelatin crosslinked nanofibers.

However, the gelatin coating results in a reduced cell attachment of 19.94%. The proposed reason for this is unknown. The genipin coated nanofibers enhances the cell attachment to 137.4%, possibly due to the reduction in water contact angle to 53.62°, which promotes a higher cell attachment. In addition, studies have shown that the presence of genipin alone promotes cell attachment (Bellrichard et al., 2019).The collagen and gelatin crosslinked samples result in a drastic improvement of cell attachment to 159.77% and 157.28%, which are much higher than their coated counterparts. The proposed reason for this is that the crosslinking results in a higher amount of biomolecule present on the sample (which was confirmed in Section 6.4.9), thereby facilitating a higher percentage cell attachment due to an increase in specific cell binding RGD sites as well as an enhanced hydrophilicity (Yabin Zhu et al., 2002). In addition, the presence of the biomolecule and the genipin results in a higher cell attachment in comparison to the biomolecule alone. The sodium alginate crosslinked sample only results in a 74.03% cell attachment, which is similar to its coated counterpart. This is unexpected since this sample presents with a relatively low water contact angle of 37.36°, therefore is expected to have resulted in a higher cell attachment (Webb et al., 1998). Nonetheless, this sample outperforms the aminolyzed sample, proving that the presence of biomolecules enhances cell attachment. Figure 5.44 represents the quantification of cell attachment of the A172 cells on the nanofibrous platforms. Similar results to the PC12 cell line are observed for the A172 cell line. The same trend for all the samples is observed in this case.

In conclusion, the cell attachment quantification proves that the presence of biomolecules with cell-interactive domains plays an important role in promoting cell attachment. These biomolecule-modified samples perform better than the plasma treated cell culture well plate (except for the sodium alginate crosslinked sample). The proposed reason for this is the improved hydrophilicity of the samples in addition to the topographical cues imparted by the extracellular matrix-mimicking nature of the nanofibrous mesh (You et al., 2006). In addition, it is evident that the chemical modification of the samples through aminolysis enhances neurocompatibility demonstrated by the increase in cell attachment, although the cytocompatibility results are not in agreement with this. However, the cell quantification analysis using the trypan blue assay is seen as a more reliable result since the viability assay is an indirect method. This cell attachment quantification assay is a direct analysis of how many cells attached to the nanofibers, therefore is a more accurate representation of *In Vitro* results (Liu et al., 2004). It is evident that biomolecule immobilization on nanofibers enhances neurocompatibility and improves cell-platform interactions.

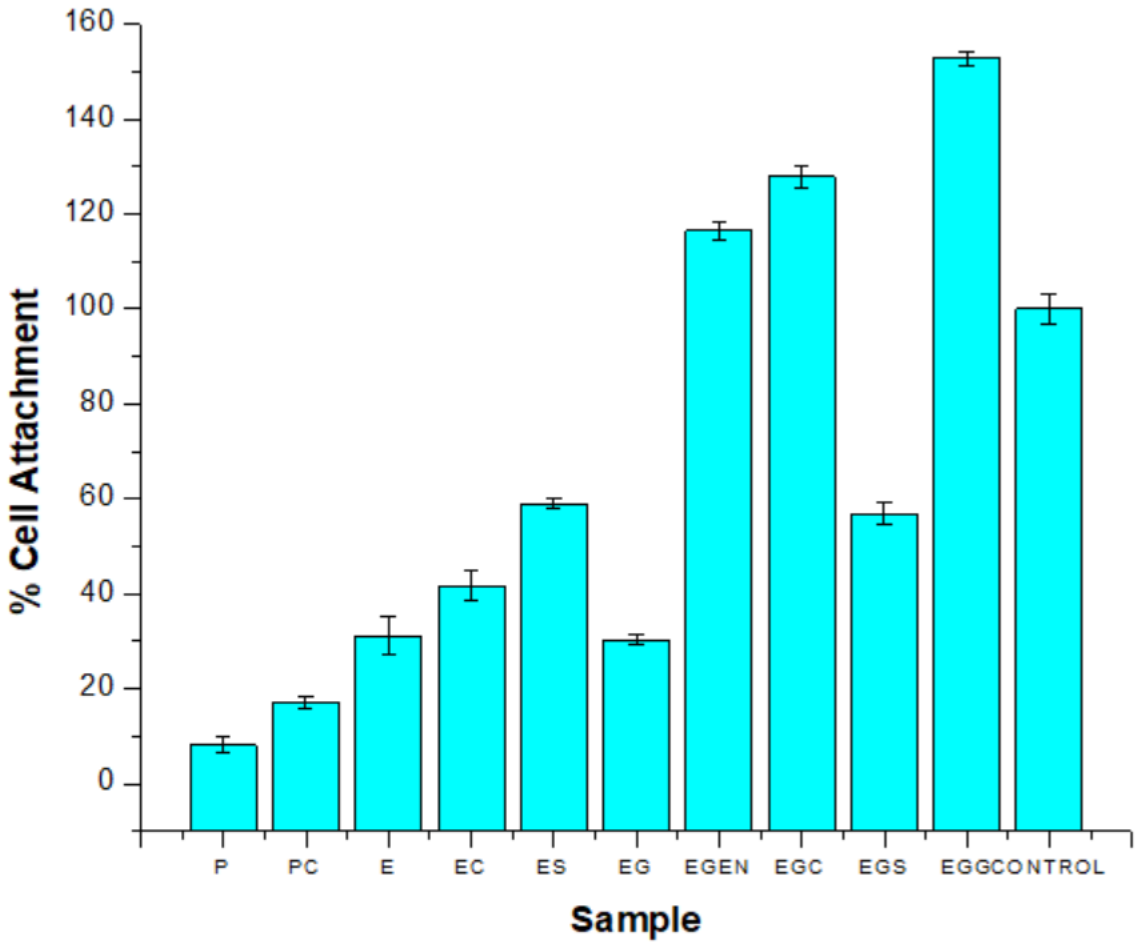


Figure 5. 294 Quantification of cell attachment results for A172 cells after 72 h. (P) polycaprolactone, (PC) polycaprolactone/cellulose acetate phthalate, (E) aminolyzed, (EC) collagen coated, (ES) sodium alginate coated, (EG) gelatin coated, (EGEN) genipin coated, (EGC) collagen crosslinked, (EGS) sodium alginate crosslinked, (EGG) gelatin crosslinked

5.4 Conclusion

Biomimetic aminolyzed and biomolecule-immobilized PCL/CAP nanofibers are fabricated via electrospinning. The chemical integrity and performance of the nano-systems are confirmed by detailed physicochemical and physio-mechanical studies. The scanning electron microscopy reveals the formation of a nanofibrous structure and BET analysis confirms an interconnected porous system to support nutrient, oxygen, and cell migration as well as to enable the integration of surrounding cells into the scaffold within the extracellular matrix of brain tissue (Bellis, 2011). *In Vitro* experimentation reveals that the aminolyzed nanofibers are slightly less neuro-compatible than their unfunctionalized counterparts, yet the biomolecule immobilized samples demonstrate cell viabilities of over 100%, indicating the proliferative effects of the biomolecules and genipin on PC12 and A172 cells (Boni et al., 2018). In terms of cell attachment, the biomolecule modified samples demonstrate a higher cell attachment in comparison to the samples without biomolecules, indicating the importance of the presence of the cell-interactive domains present in biomolecules. There is a direct link between the

hydrophilicity of the nanofibers and cell attachment, which is consistent with literature (Yabin Zhu et al., 2002). Overall, the results indicate that the biomolecule-modified nanofibrous system can be used to augment cell attachment and viability to facilitate neural repair.

In addition, a comparison between the non-fibrous films in Chapter 4 and the nanofibers highlights the importance of physical cues in cell interactions with scaffolds, since the nanofibrous samples outperform their film counterparts during *In Vitro* cell attachment quantification. This study concludes that it is possible to enhance the neurocompatibility of PCL/CAP films and nanofibers using relatively simple methods which include chemical surface functionalization and biomolecule immobilization.

5.5 References

Amani, H., Kazerooni, H., Hassanpoor, H., Akbarzadeh, A., & Pazoki-Toroudi, H. (2019). Tailoring synthetic polymeric biomaterials towards nerve tissue engineering: a review. Artificial cells, nanomedicine, and biotechnology, 47(1), 3524-3539.

Amariei, N., Manea, L.R., Bertea, A.P., Bertea, A., Popa, A. (2017). The influence of polymer solution on the properties of electrospun 3D nanostructures. IOP conference series material science engineering, 209, 12092-12099.

Arteche Pujana, M., Pérez-Álvarez, L., Cesteros Iturbe, L. C., & Katime, I. (2013). Biodegradable chitosan nanogels crosslinked with genipin. Carbohydrate polymers, 94(2), 836-842.

Atthoff, B., & Hilborn, J. (2007). Protein adsorption onto polyester surfaces: Is there a need for surface activation. Journal of biomedical materials research- part B applied biomaterials, 80(1), 121-130.

Barrett, E., Joyner, L., & Halenda, P. (1951). The determination of pore volume and area distributions in porous substances. Journal of the American chemical society, 73(1), 373-338.

Bellrichard, M., Snider, C., Dittmar, C., Brockman, J., Grant, D., & Grant, S. A. (2019). Genipin attachment of conjugated gold nanoparticles to a decellularized tissue scaffold. Applied sciences, 9(23), 5321-5330.

Benykhlef, S., Dulong, V., Bengharez, Z., Picton, L., Guemra, K., & Le Cerf, D. (2012). Alginate grafted with poly(ε-caprolactone): effect of enzymatic degradation on physicochemical properties. Polymer international, 61(9), 1456-1461.

Bhattarai, D. P., Aguilar, L. E., Park, C. H., & Kim, C. S. (2018). A review on properties of natural and synthetic based electrospun fibrous materials for bone tissue engineering. Membranes, 8(3), 62-69.

Brunauer, S., Emmett, P. H., & Teller, E. (1936). Adsorption of gases in multimolecular layers. Journal of the American chemical society, 60(2), 309-319.

Brown, P., Stevens, K. (2007). Nanofibers and nanotechnology. Textiles, 1, Elsevier, The Netherlands.

Cao, M., Gu, F., Rao, C., Fu, J., Zhao, P. (2019). Improving the electrospinning process of fabricating nanofibrous membranes to filter. Science of the total environment, 666(2), 1011-1021.

Da Silva, K. Da, Kumar, P., Vuuren, S. F. Van, Pillay, V., & Choonara, Y. E. (2021). Three-dimensional printability of an ECM-based gelatin methacryloyl (GelMA) biomaterial for potential neuroregeneration. ACS Omega, 6(33), 21368-21383.

Di Giovanni, S., Movsesyan, V., Ahmed, F., Cernak, I., Schinelli, S., Stoica, B., & Faden, A. I. (2005). Cell cycle inhibition provides neuroprotection and reduces glial proliferation and scar formation after traumatic brain injury. Proceedings of the national academy of sciences of the United States of America, 102(23), 8333-8338.

Frohbergh, M. E., Katsman, A., Botta, G. P., Lazarovici, P., Schauer, C. L., Wegst, U. G. K., & Lelkes, P. I. (2012). Electrospun hydroxyapatite-containing chitosan nanofibers crosslinked with genipin for bone tissue engineering. Biomaterials, 33(36), 9167-9178.

Fukushima, K., Tabuani, D., Abbate, C., Arena, M., & Rizzarelli, P. (2011). Preparation, characterization, and biodegradation of biopolymer nanocomposites based on fumed silica. European polymer journal, 47(2), 139-152.

Garg, A., Rai, G., Lodhi, S., Jain, A. P., & Yadav, A. K. (2016). Hyaluronic acid embedded cellulose acetate phthlate core/shell nanoparticulate carrier of 5-fluorouracil. International journal of biological macromolecules, 87(3), 449-459.

Gaurav, A., Ashamol, A., Deepthi, M. V, & Sailaja, R. R. N. (2012). Biodegradable nanocomposites of cellulose acetate phthalate and chitosan reinforced with functionalized nano clay : mechanical, thermal, and biodegradability studies. Journal of applied polymer science, 125(1), 16-26.

Gregg, S., Sing, K., & Salzberg, H. (1967). Adsorption surface area and porosity. Journal of the electrochemical society, 114(11), 279-285.

Groen, J. C., Peffer, L. A. A., & Javier, P. (2003). Pore size determination in modified micro- and mesoporous materials . Pitfalls and limitations in gas adsorption data analysis. Microporous and mesoporous materials, 60(3), 1-17.

He, L., Liao, S., Quan, D., Ma, K., Chan, C., Ramakrishna, S., & Lu, J. (2010). Synergistic effects of electrospun PLLA fiber dimension and pattern on neonatal mouse cerebellum C17.2 stem cells. Acta biomaterialia, 6(8), 2960-2969.

Hughes, R. H., Silva, V. A., Ahmed, I., Shreiber, D. I., & Morrison, B. (2014). Neuroprotection by genipin against reactive oxygen and reactive nitrogen species-mediated injury in organotypic hippocampal slice cultures. Brain research, 1543, 308-314.

Jeznach, O., Kolbuk, D., & Sajkiewicz, P. (2019). Aminolysis of various aliphatic polyesters in a form of nanofibers and films. Polymers, 11(10), 1169-1173.

Kahoush, M., Behary, N., Guan, J., Cayla, A., Mutel, B., & Nierstrasz, V. (2021). Genipin-mediated immobilization of glucose oxidase enzyme on carbon felt for use as heterogeneous catalyst in sustainable wastewater treatment. Journal of environmental chemical engineering, 9(4), 0-2.

Khorramnezhad, M., Akbari, B., Akbari, M., & Kharaziha, M. (2021). Effect of surface modification on physical and cellular properties of PCL thin film. Colloids and surfaces B: Biointerfaces, 200(5), 111-116.

Krithica, N., Natarajan, V., Madhan, B., Sehgal, P. K., & Mandal, A. B. (2012). Type I collagen immobilized poly(caprolactone) nanofibers: characterization of surface modification and growth of fibroblasts. Advanced engineering materials, 14(4), 149-154.

Li, Xiaoqiang, Su, Y., Liu, S., Tan, L., Mo, X., & Ramakrishna, S. (2010). Encapsulation of proteins in poly(l-lactide-co-caprolactone) fibers by emulsion electrospinning. Colloids and surfaces B: biointerfaces, 75(2), 418-424.

Li, Xiaoran, Chen, Z., Zhang, H., Zhuang, Y., Shen, H., Chen, Y., Zhao, Y., Chen, B., Xiao, Z., & Dai, J. (2019). Aligned scaffolds with biomolecular gradients for regenerative medicine. Polymers, 11(2), 341-350.

Ma, Z., Kotaki, M., Yong, T., He, W., & Ramakrishna, S. (2005). Surface engineering of electrospun polyethylene terephthalate (PET) nanofibers towards development of a new material for blood vessel engineering. Biomaterials, 26(15), 2527-2536.

Mansur, H. S., Sadahira, C. M., Souza, A. N., & Mansur, A. A. P. (2008). FTIR spectroscopy characterization of poly (vinyl alcohol) hydrogel with different hydrolysis degree and chemically crosslinked with glutaraldehyde. Materials science and engineering C, 28(4), 539-548.

Masaeli, E., Wieringa, M., Nasr-Esfahani, MH., Sadri, S., van Blitterswijk, C.A and Moroni, L. (2014). Peptide functionalized polyhydroxyalkanoate nanofibrous scaffolds enhance Schwann cells activity. Nanomedicine: nanotechnology, biology, and medicine, 10(2), 1559-1569.

Mateescu, M., & Juha, J. (2002). Structure-properties relationship in cross-linked high amylose starch cast films. Carbohydrate polymers, 323(1-4), 163-175.

Muthiah, P., Hoppe, S. M., Boyle, T. J., & Sigmund, W. (2011). Thermally tuneable surface wettability of electrospun fiber mats: Polystyrene/ poly(N-isopropylacrylamide) blended versus crosslinked poly[(N-isopropylacrylamide)-co-(methacrylic acid)]. Macromolecular rapid communications, 32(21), 1716-1721.

Nagai, T. (2010). Characterization of acid-soluble collagen from skins of surf smelt (Hypomesus pretiosus japonicus Brevoort). Food nutrition science, 1(3), 59-66.

Nagarajan, S., Bechelany, M., Kalkura, N. S., Miele, P., Bohatier, C. P., & Balme, S. (2019). Electrospun nanofibers for drug delivery in regenerative medicine. Applications of targeted nano drugs and delivery systems, 595-625.

Nirmala, R., Il, B. W., Navamathavan, R., El-Newehy, M. H., & Kim, H. Y. (2011). Preparation and characterizations of anisotropic chitosan nanofibers via electrospinning. Macromolecular research, 19(4), 345-350.

Oryan, A., Kamali, A., Moshiri, A., Baharvand, H., & Daemi, H. (2018). Chemical crosslinking of biopolymeric scaffolds: current knowledge and future directions of crosslinked engineered bone scaffolds. International journal of biological macromolecules, 107(6), 678-688.

Pan, Y., Liu, L., Zhang, Y., Song, L., Hu, Y., & Jiang, S. (2019b). Effect of genipin crosslinked layer-by-layer self-assembled coating on the thermal stability, flammability, and wash durability of cotton fabric. Carbohydrate polymers, 206(2), 396-402.

Pantelić, N., Zmejkovski, B. B., Stanojković, T. P., Jevtić, V. V., Radić, G. P., Trifunović, S. R., Kaluderović, G. N., & Sabo, T. J. (2014). Synthesis and high In Vitro cytotoxicity of some (S,S)-ethylenediamine-N, N'-di-2-propanoate dihydrochloride esters. Journal of the Serbian chemical society, 79(6), 649-658.

Park, B. U., Park, S. M., Lee, K. P., Lee, S. J., Nam, Y. E., Park, H. S., Eom, S., Lim, J. O., Kim, D. S., & Kim, H. K. (2019). Collagen immobilization on ultra-thin nanofiber membrane to promote In Vitro endothelial monolayer formation. Journal of tissue engineering, 10.

Ramburrun, P., Kumar, P., Choonara, Y. E., du Toit, L. C., & Pillay, V. (2019). Design and characterisation of PHBV-magnesium oleate directional nanofibers for neuro-support. Biomedical materials, 14(6), 65015-65018.

Ravi, M., Song, S., Wang, J., Nadimicherla, R., & Zhang, Z. (2016). Preparation and characterization of biodegradable poly(ε-caprolactone)-based gel polymer electrolyte films. Ionics: international journal of ionics, the science and technology of ionic motion, 22(5), 661-670.

Rokhade, A. P., Agnihotri, S. A., Patil, S. A., Mallikarjuna, N. N., Kulkarni, P. V., & Aminabhavi, T. M. (2006). Semi-interpenetrating polymer network microspheres of gelatin and sodium carboxymethyl cellulose for controlled release of ketorolac tromethamine. Carbohydrate polymers, 65(3), 243-252.

Shabani, I., Haddadi-Asl, V., Soleimani, M., Seyedjafari, E., Babaeijandaghi, F., & Ahmadbeigi, N. (2011). Enhanced infiltration and biomineralization of stem cells on collagen-grafted three-dimensional nanofibers. Tissue engineering- part A, 17(9-10), 1209-1218.

Shin, S. H., Purevdorj, O., Castano, O., Planell, J. A., & Kim, H. W. (2012). A short review: recent advances in electrospinning for bone tissue regeneration. Journal of tissue engineering, 3(1), 204-211.

Siritientong, T., Ratanavaraporn, J., Srichana, T., & Aramwit, P. (2013). Preliminary characterization of genipin-cross-linked silk sericin/poly(vinyl alcohol) films as two-dimensional wound dressings for the healing of superficial wounds. BioMed research international, 2013(1), 904-910.

Su, T., Jiang, H., & Gong, H. (2008). Thermal stabilities and the thermal degradation kinetics of poly(ε-caprolactone). Polymer plastics technology and engineering, 47(4), 398-403.

Sundararaghavan, H. G., Monteiro, G. A., Lapin, N. A., Chabal, Y. J., Miksan, J. R., & Shreiber, D. I. (2008). Genipin-induced changes in collagen gels: correlation of mechanical properties to fluorescence. Journal of biomedical materials research-part A, 87(2), 308-320.

Valmikinathan, C. M., Hoffman, J., & Yu, X. (2011). Impact of scaffold micro and macro architecture on Schwann cell proliferation under dynamic conditions in a rotating wall vessel bioreactor. Materials science and engineering C, 31(1), 22-29.

Wang, Z., Liu, H., Luo, W., Cai, T., Li, Z., Liu, Y., Gao, W., Wan, Q., Wang, X., Wang, J., Wang, Y., & Yang, X. (2020). Regeneration of skeletal system with genipin crosslinked biomaterials. Journal of tissue engineering, 29(1), 204-209.

Xie, J., Macewan, M. R., Liu, W., Jesuraj, N., Li, X., Hunter, D., & Xia, Y. (2014). Nerve guidance conduits based on double-layered scaffolds of electrospun nanofibers for repairing the peripheral nervous system. ACS applied materials and interfaces, 6(12), 9472-9480.

Yoo, J. S., Kim, Y. J., Kim, S. H., & Choi, S. H. (2011). Study on genipin: A new alternative natural crosslinking agent for fixing heterograft tissue. Korean journal of thoracic and cardiovascular surgery, 44(3), 197-207.

You, Y., Lee, S., Min, B.M., Park, W. (2006). Effect of solution properties on nanofibrous structure of electrospun poly(lactic-co-glycolic acid) nanofibers. Journal of applied polymer science, 99(1), 1214-1221.

Zhan, J., Singh, A., Zhang, Z., Huang, L., & Elisseeff, J. H. (2012). Multifunctional aliphatic polyester nanofibers for tissue engineering. Biomatter, 2(4), 202-212.

Zhang, Y. Z., Feng, Y., Huang, Z. M., Ramakrishna, S., & Lim, C. T. (2006). Fabrication of porous electrospun nanofibres. Nanotechnology, 17(3), 901-908.

CHAPTER 6:
CONCLUSIONS AND RECOMMENDATIONS

6.1 Conclusions

The dynamic and rapidly advancing realm of tissue engineering has given rise to numerous innovations, including two-dimensional thin polymeric films and nanofibrous platforms (Cao et al., 2019). The functional and structural tuning of polymeric thin films has caught the attention of many researchers in the field of tissue engineering due to the vast potential applications and wide range of adaptability (Jang et al., 2011). The design of thin films with precise control of their structures and properties for targeted biomedical applications has become important in recent years (Jang et al., 2011). Nanofibers have the capacity to mimic the inherent nature of the fibrillar extracellular matrix and have featured extensively in the fabrication of nerve guidance conduits (Nagarajan et al., 2019). These conduits are aimed at the recapitulation of the essential biological and structural features of the native extracellular matrix to provide a viable environment to guide the regrowth and repair of transected nerves (Nagarajan et al., 2019). Furthermore, these fibrillar structures are able to provide favourable topographical and chemical cues to neural cells in addition to providing a means for the influx of nutrients and efflux of waste (Valmikinathan et al., 2011).

This study explores the potential neurocompatibility and cell attachment efficiency of two systems, namely, polymeric thin films and electrospun nanofibers. The first component of this study involved the fabrication of mechanically suitable polymeric thin films from a novel combination of biodegradable polymers: polycaprolactone and cellulose acetate phthalate. The optimal concentrations and ratios were determined for optimal mechanical strength. These films were tested *In Vitro* to determine their cytotoxicity profile. The results indicated that the films facilitate very minimal neural cell attachment to the films, ascertained though a trypan blue exclusion assay which allowed the direct quantification of cell attachment on the surface of the films (Liu et al., 2004). However, the films were not cytotoxic, established through an XTT cell viability assay. This result is expected as most synthetic scaffolds for neural tissue engineering are limited by their poor *In Vitro* effectiveness in the support of neuronal cells (Valmikinathan et al., 2011).

To circumvent this issue, two methods of chemical functionalization were employed in an effort to enhance the neurocompatibility of the films: aminolysis and hydrolysis. Aminolysis introduces amine-functionalities onto the surface, while hydrolysis introduces hydroxyl functionalities, with the aim of hydrophilicity enhancement, which is known to improve cell attachment (Krithica et al., 2012). Extensive characterization of these modified samples highlighted the chemical transitions, thermal transitions, mechanical properties, porosity

characteristics, surface area, hydrophilicity, morphology, surface topography, *In Vitro* degradation, and water-uptake characteristics of the native materials, as well as the chemically functionalized films. Following this, *In Vitro* evaluations were undertaken of the chemically functionalized films. No evidence of cytotoxicity is observed, and the functionalized films are able to enhance cell attachment in comparison to the unfunctionalized films, proving that chemical functionalization enhances neurocompatibility of the films, without causing cytotoxic effects (Liu et al., 2004).

Although the cell attachment was improved, the results were still inferior to the control (plasma treated well plates). To circumvent this limitation, the films were further modified with the bioactive molecules (or biomolecules): collagen, sodium alginate and gelatin. The aminolyzed samples were coated and crosslinked with the biomolecules using genipin as the crosslinker. Extensive chemical, thermal, mechanical, hydrophilicity, porosimetric, surface area and morphological characterizations were undertaken to evaluate the changes after biomolecule immobilization. In addition, a biomolecule quantification assay was used to determine the concentration of each biomolecule on the films, which also served to confirm the presence of the biomolecules on the films (Masaeli et al., 2014). Subsequent to this, the films were evaluated *In Vitro* to evaluate if the presence of the biomolecules can enhance cell-surface interactions. It was found that the biomolecule-immobilized samples can significantly enhance cell attachment to the samples, most of which significantly out-perform the plasma treated plastic well plates. The sodium alginate-crosslinked samples demonstrate sub-par cell attachment (<80%) (Boni et al., 2018). The reason for this is unknown and it is recommended that this is further investigated, since these samples demonstrated sufficient mechanical strength, hydrophilicity and several other favorable characteristics that would otherwise facilitate cell attachment. Following the thorough investigation of the effectiveness of the bioactive polymeric thin films in tissue engineering, the scaffolds were further improved on through the development of a two-dimensional electrospun nanofibrous platform, utilizing the same polymers and surface modifications in the preceding chapters. The same characterization techniques were performed on the nanofibers as the thin films. The noteworthy observations are the significant enhancement of surface roughness, porosity, and surface area of the nanofibrous platforms in comparison to the thin films. These characteristics are highly advantageous in tissue engineering (Murphy & O'Brien, 2010; Brunetti et al., 2010; Sorkin et al., 2009). This was confirmed *In Vitro* through the enhanced cell attachment in the trypan blue exclusion assay.

In conclusion, the bioactive polymeric thin films and electrospun nanofibrous platforms are conceptually desirable for the neural tissue engineering application of traumatic brain injury in terms of mechanical properties, hydrophilicity, surface morphology and surface topography

(Murphy & 0'Brien, 2010; Brunetti et al., 2010; Sorkin et al., 2009; Yabin Zhu et al., 2002; Zhang et al., 2017 and Tang et al., 2004). In addition, the biomolecule-modified samples (collagen and gelatin) demonstrate an improved cell attachment in comparison to the control. This shows that the bioactive scaffolds have the ability to support neural cells *In Vitro*, which could then potentially proliferate, migrate, and differentiate. This could ultimately facilitate the regeneration of transected nerves *In Vivo* (Bellis, 2011). The enhancement of neurocompatibility of the samples throughout the progression of this study is observed and is illustrated in Figure 6.1.

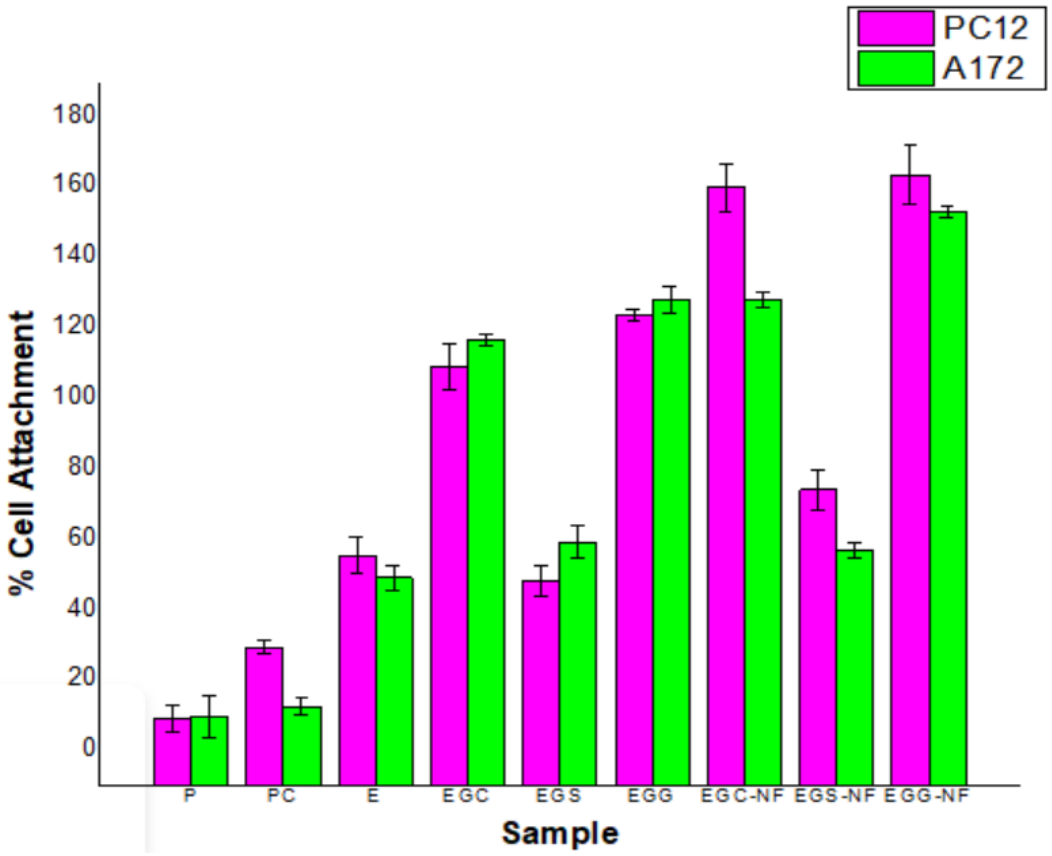


Figure 6. 1 Quantification of PC12 and A172 attachment on the (P) polycaprolactone, (PC) polycaprolactone/cellulose acetate phthalate, (E) aminolyzed, (EC) collagen coated, (ES) sodium alginate coated, (EG) gelatin coated, (EGEN) genipin coated, (EGC) collagen crosslinked, (EGS) sodium alginate crosslinked, (EGG) gelatin crosslinked nanofibers, to illustrate the enhancement of cell attachment throughout the progression of the chapters.

To this end, the main objective of the study is achieved as the scaffolds present an enhanced neurocompatibility throughout the progression of the chapters facilitated through surface hydrolysis, aminolysis, biomolecule immobilization as well as the fabrication of a bioactive nanofibrillar platform which closely mimicked the native extracellular matrix.

6.2 Limitations and recommendations

The process of chemical functionalization is complicated and relies on many variables to evaluate and ensure its success (Krithica et al., 2012). While this investigation highlights the

qualitative success of chemical functionalization of the thin films and electrospun nanofibers, the physiochemical and morphological results are consequently altered, most of which are positive and advantageous for neural tissue engineering. However, some have a negative impact on the scaffolds. For example, the enhancement of hydrophilicity of the samples due to chemical functionalization and subsequent biomolecule immobilization is advantageous *In Vitro*. However, this results in a significant enhancement of the biodegradation and water-uptake rate, to the extent that the biomolecule-immobilized samples completely disintegrated before 30 days. This may limit the scaffolds application in repairing larger nerve gaps *In Vivo*, since most larger nerve gaps require an in-tact structurally sound scaffold for a four-week period (Ramburrun et al., 2019). Therefore, it is recommended that the total polymer concentration is increased. Alternatively, the ratio of CAP, the functionalization time, concentration, or temperature could be reduced. In addition, the concentration of genipin, the crosslinking time or the concentration of the biomolecules could be reduced. These modifications can aid in reducing the biodegradation rate by increasing the weight of the scaffolds or by reducing the hydrophilicity of the scaffolds. However, all the scaffolds remained intact during *In Vitro* studies, therefore the evaluation of cytotoxicity and the quantification of cell attachment was possible. It is recommended that further studies be undertaken for various other chemical modifications to create a standard of functionalities that can be used to alter specific properties such as mechanical strength, hydrophilicity, degradation and water-uptake rate and porosity.

A major limitation of this study is the high standard deviation observed for the thin film samples during mechanical, degradation and water-uptake evaluation. This is believed to be as a result of the manual fabrication of the films, which is a reported result in literature (Sun & Downes, 2009), as discussed in each respective section. Therefore, it is recommended that the films be fabricated via a more robust technique such as spin-coating or via the use of an automated process.

During *In Vitro* investigations, the inability to view cells on the films and nanofibers due to the network-like morphology of the samples is a limitation. This limits the qualitative assessment of the morphology of the cells attached to the films. Although quantitative assessment was possible through the trypan blue exclusion assay, it is important to assess the morphology of the cells attached to scaffolds to assess whether they maintain their neural morphology and whether they begin to develop into neurites (Park et al., 2019). Although, some images were captured using light microscopy. These are not of a good scientific quality, and it is extremely difficult to identify the cells. Fluorescence microscopy was investigated as a method to overcome this challenge, wherein cells are seeded onto the samples and allowed to attach and grow, thereafter the cells are stained with 4′,6-diamidino-2-phenylindole and CellTracker

Red™, which selectively stains adenine-thymine-rich regions in DNA and the cell membrane, respectively (Combs & Shroff, 2017). However, the samples auto fluoresced during imaging, meaning that the samples also picked up the stain, making it impossible to view the cells on the films (Combs & Shroff, 2017). It is therefore recommended that other methods be investigated or developed to view cells on scaffolds with a network-like morphology.

During the XTT cytotoxicity evaluations, extracts were made by immersing the samples in cell culture media and then removing the samples from the media after incubation. These solutions were then used to evaluate the cytotoxicity of the samples, which is a well-known indirect method to evaluate cytotoxicity (Kuhn et al., 2003). However, this technique is limited as it is an indirect technique, which was clearly seen when comparing the XTT results to the cell attachment quantification. Therefore, it is recommended that a more direct and accurate method be used to investigate the long-term cytotoxicity of the samples. In addition, cellular migration could not be investigated due to the fact that it is not possible to view cells on the films, and most migration assays are dependent on this (Cory, 2011). It is thus recommended that a technique be investigated to investigate cellular migration on the samples. In addition, more advanced *In Vitro* studies should be undertaken as well as *In Vivo* trials to investigate the neural regenerating potential of the scaffolds after implantation.

6.3 References

Bellis, S. L. (2011). Advantages of RGD peptides for directing cell association with biomaterials. Biomaterials, 32(18), 4205-4210.

Boni, R., Ali, A., Shavandi, A., & Clarkson, A. N. (2018). Current and novel polymeric biomaterials for neural tissue engineering. Journal of biomedical science, 25(1), 90-94.

Brunetti, V., Maiorano, G., Rizzello, L., Sorce, B., Sabella, S., Cingolani, R., & Pompa, P. P. (2010). Neurons sense nanoscale roughness with nanometer sensitivity. Proceedings of the national academy of sciences of the United States, 107(14), 6264-6269.

Cao, M., Gu, F., Rao, C., Fu, J., Zhao, P. (2019). Improving the electrospinning process of fabricating nanofibrous membranes to filter. Science of the total environment, 666(3), 1011-1021.

Cory, G. (2011).Scratch-wound assay. Methods molecular biology, 769(2), 25-30.

Jang, Y., Park, S., & Char, K. (2011). Functionalization of polymer multilayer thin films for novel biomedical applications. Korean journal of chemical engineering, 28(5), 1149-1160.

Krithica, N., Natarajan, V., Madhan, B., Sehgal, P. K., & Mandal, A. B. (2012). Type I collagen immobilized poly(caprolactone) nanofibers: characterization of surface modification and growth of fibroblasts. Advanced engineering materials, 14(4),149-154.

Kuhn, D.M., Balk, J., Chandra, P.K., Mukherjee, M and Ghannoum, M.A. (2003). Uses and limitations of the XTT assay in studies of Candida growth and metabolism. Journal of clinical microbiology, 41(1), 506-508.

Liu, Y.X., Zhang, Y.R., Bogaerts, A., & Wang, Y.N. (2015). Electromagnetic effects in high-frequency large-area capacitive discharges: a review. Journal of vacuum science & technology A: vacuum, surfaces, and films, 33(2), 020801.

Masaeli, E., Wieringa, M., Nasr-Esfahani, MH., Sadri, S., van Blitterswijk, C.A and Moroni, L. (2014). Peptide functionalized polyhydroxyalkanoate nanofibrous scaffolds enhance Schwann cells activity. Nanomedicine: nanotechnology, biology, and medicine, 10(8),1591-1896.

Murphy, C. M., & O'Brien, F. J. (2010). Understanding the effect of mean pore size on cell activity in collagen-glycosaminoglycan scaffolds. Cell adhesion and migration, 4(3), 377-381.

Nagarajan, S., Bechelany, M., Kalkura, N. S., Miele, P., Bohatier, C. P., & Balme, S. (2019). Electrospun nanofibers for drug delivery in regenerative medicine. In applications of targeted nano drugs and delivery systems, 9(4), 595-626.

Park, B. U., Park, S. M., Lee, K. P., Lee, S. J., Nam, Y. E., Park, H. S., Eom, S., Lim, J. O., Kim, D. S., & Kim, H. K. (2019). Collagen immobilization on ultra-thin nanofiber membrane to promote In Vitro endothelial monolayer formation. Journal of tissue engineering, 10(2), 204-209.

Ramburrun, P., Kumar, P., Choonara, Y. E., du Toit, L. C., & Pillay, V. (2019). Design and characterisation of PHBV-magnesium oleate directional nanofibers for neuro-support. Biomedical materials, 14(6), 065015.

Combs, C.A., & Shroff, H. (2017). Fluorescence microscopy: a concise guide to current imaging methods. Current protocols in neuroscience, 79(5), 1-25.

Sorkin, R., Greenbaum, A., David-pur, M., Anava, S., Ayali, A., Ben-jacob, E., & Hanein, Y. (2009). Process entanglement as a neuronal anchorage mechanism to rough surfaces. Nanotechnology, 20(1), 15101-15108.

Sun, M., & Downes, S. (2009). Physicochemical characterisation of novel ultra-thin biodegradable scaffolds for peripheral nerve repair. Journal of materials science: materials in medicine, 20(5), 1181-1192.

Tang, Z. G., Black, R. A., Curran, J. M., Hunt, J. A., Rhodes, N. P., & Williams, D. F. (2004). Surface properties and biocompatibility of solvent-cast polycaprolactone films. Biomaterials, 25(19), 4741-4748.

Valmikinathan, C. M., Hoffman, J., & Yu, X. (2011). Impact of scaffold micro and macro architecture on Schwann cell proliferation under dynamic conditions in a rotating wall vessel bioreactor. Materials science and engineering C, 31(1), 22-39.

Zhang, K., Huang, D., Yan, Z., Wang., C. (2017). Heparin/collagen encapsulating nerve growth factor multilayers coated aligned PLLA nanofibrous scaffolds for nerve tissue engineering. Journal of biomedical materials research-part A, 105(1), 1900-1910.

Zhu, Y., Gao, C., Liu, X., & Shen, J. (2002). Surface modification of polycaprolactone membrane via aminolysis and biomacromolecule immobilization for promoting cytocompatibility of human endothelial cells. Biomacromolecules, 3(6), 1312-1319.

APPENDICES

A1: Published literature review

ARTICLE IN PRESS

Drug Discovery Today • Volume xxx, Number xx • xxxx 2022 REVIEWS

ELSEVIER

FOUNDATION (PURPLE)

Functionalizing nanofibrous platforms for neural tissue engineering applications

Michelle Lategan, Pradeep Kumar, Yahya E. Choonara *

Wits Advanced Drug Delivery Platform Research Unit, Department of Pharmacy and Pharmacology, School of Therapeutic Sciences, Faculty of Health Sciences, University of the Witwatersrand, Johannesburg, 7 York Road, Parktown 2193, South Africa

Over the past two decades, electrospun nanofibers have shown great promise in developing functional nerve constructs resembling the structural organization of the fibrillar extracellular matrix (ECM). However, these niche nanofibrous structures are often hindered by inadequate cell infiltration and poor mechanical strength. Further challenge is presented by the intricate nature of neural regeneration and repair processes. The versatility of electrospun nanofibers allows extensive modifications with the overarching aim of optimizing the neurocompatibility and neuroinductivity, in addition to enhancing cellular adhesion, proliferation, migration, differentiation, and neurite outgrowth. In this review, we provide a comprehensive overview of the various optimization techniques for electrospun nanofibrous platforms in neural tissue engineering (NTE), including surface modifications to enhance cell–platform interactions, and techniques to facilitate drug and biomolecule delivery applications.

Keywords: Electrospun nanofibers; Neural tissue engineering; Surface modifications; Drug delivery; Biomolecule delivery

Introduction

Neural damage from brain, spinal cord, or peripheral nerve injury can lead to permanent and incapacitating conditions, as a result of a lack of the innate ability to regenerate the nervous system.[1] This has inspired great interest in the NTE, which is streamlined by the use of polymeric-engineered nerve guidance conduits. These detour the limitations of conventional autologous and allogenic nerve grafts, such as the scarcity of donor nerves and the risk of immunological rejection, respectively.[2] Despite advances in this field, NTE still poses an immense challenge in tissue engineering as a result of the complex nature of the neural regeneration process.[3] As a result, initiatives in the fabrication of nerve guidance conduits have been widely explored, with the aim of improving biocompatibility, biodegradability, neuroconductivity, and neuroinductivity by optimizing biochemical, mechanical, electrical, and topographical signals, allowing for the regulation of cellular responses and ultimately promoting targeted neuron dendrite regeneration.[4]

Nanofibers have the capacity to imitate the inherent structure of the fibrillar ECM and have featured extensively in the fabrication of nerve guidance conduits.[5] These conduits aim to recapitulate the essential biological and structural features of the native ECM to provide a viable environment to guide the regrowth or repair of transected nerves.[5] Furthermore, these fibrillar provide favorable topographical and chemical cues to neural cells in addition to providing a means for the influx of nutrients and efflux of waste.[6–9] The collection of nanofibers created via the electrospinning process is henceforth referred to as 'NFPs'.

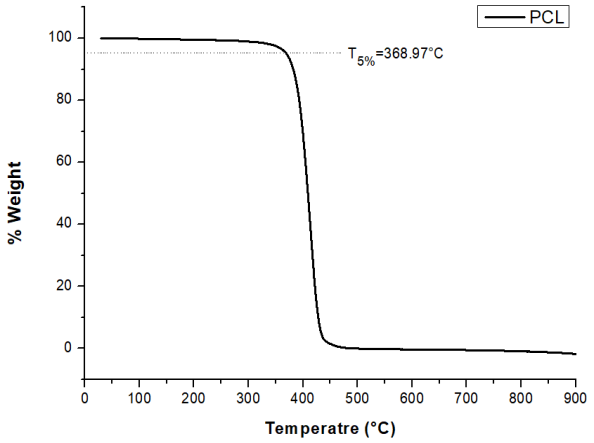
A host of natural and synthetic polymers have been electrospun for application in NTE, known for their inherent viscoelastic nature.[5] Natural polymers are innately bioactive, presenting vast domains of cellular interactive moieties on their back-

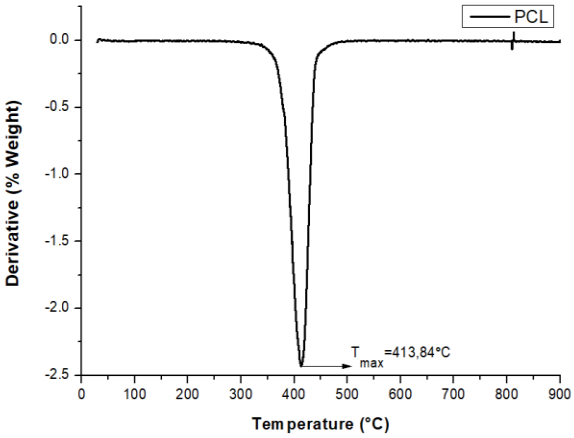
* Corresponding author:Choonara, Y.E. (yahya.choonara@wits.ac.za)

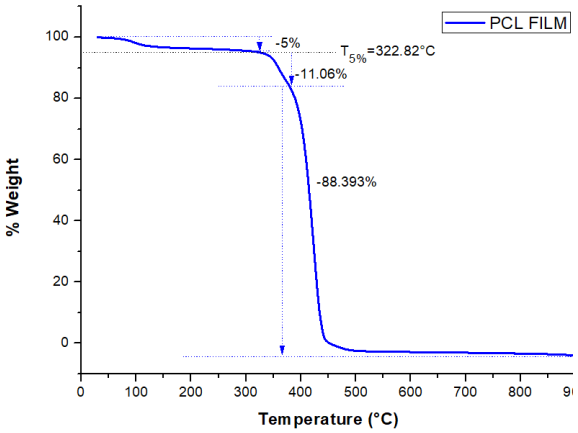
A2:Podium presentation

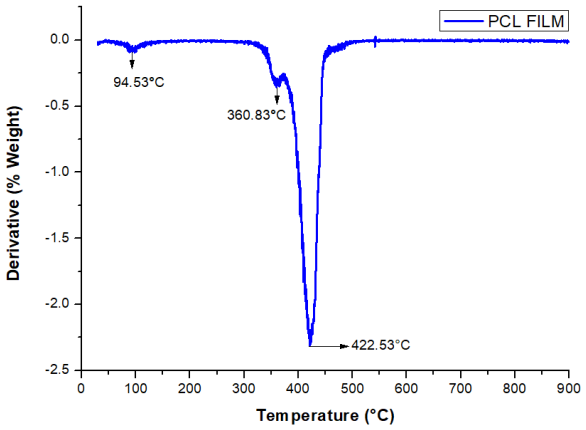


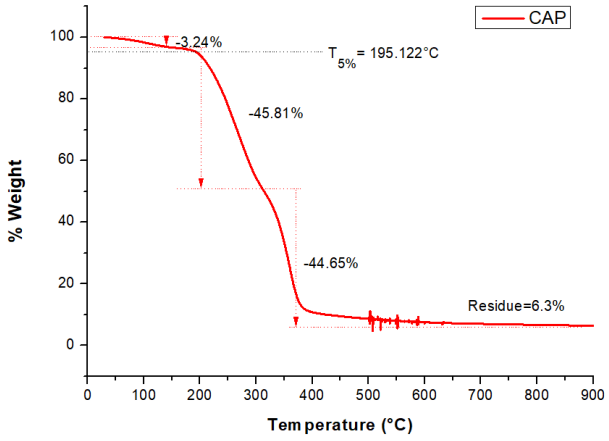
A3: Individual tga thermograms (Chapter 3)

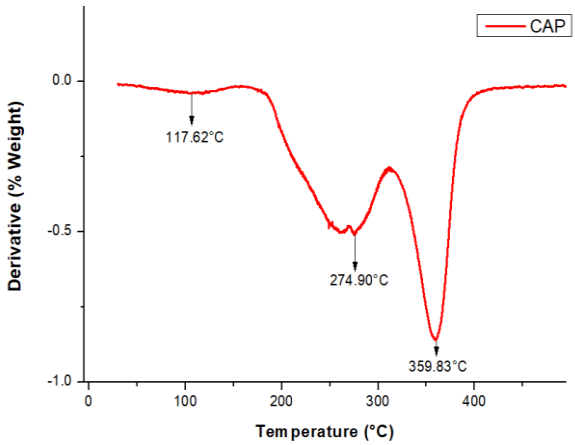


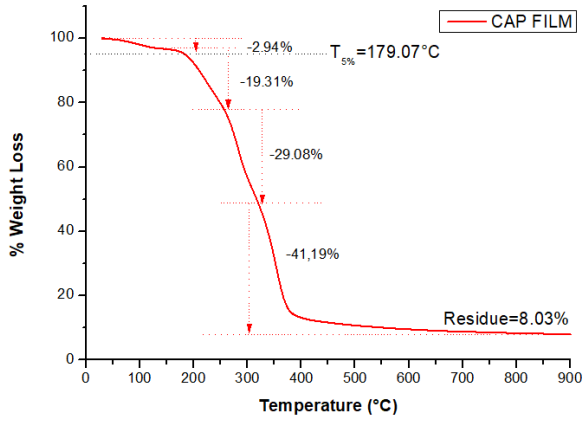


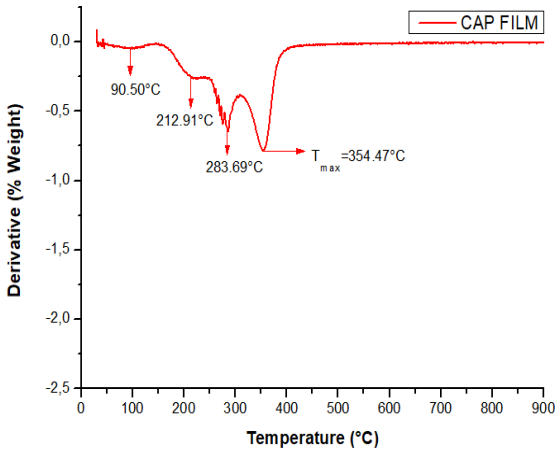


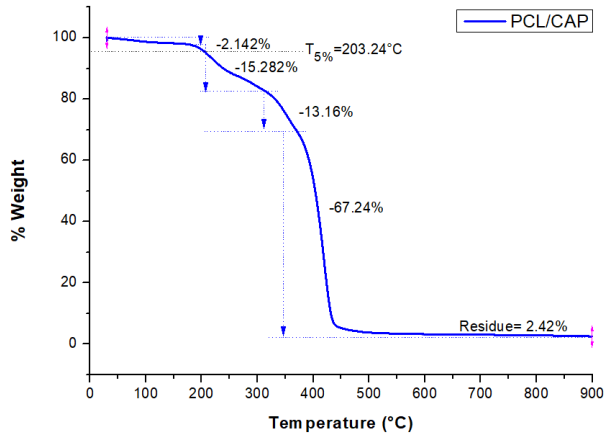


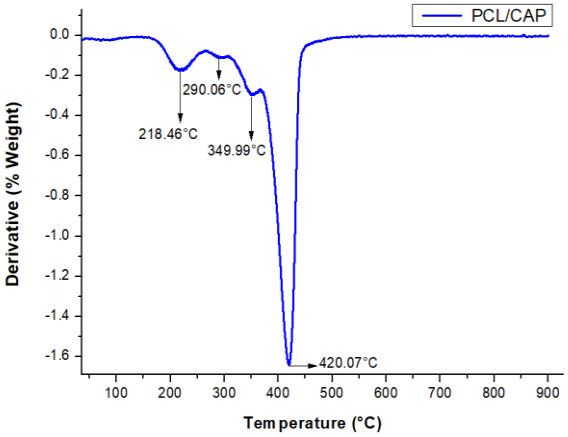


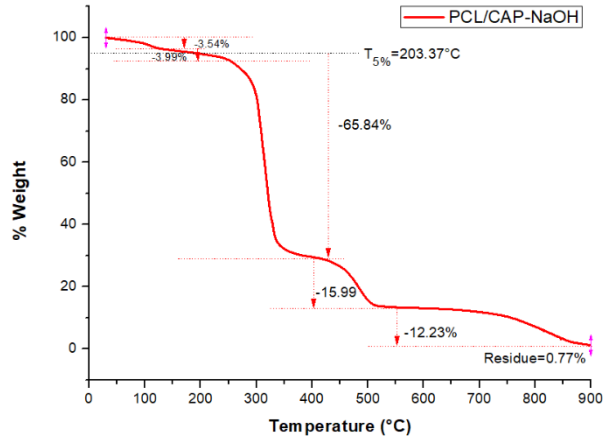


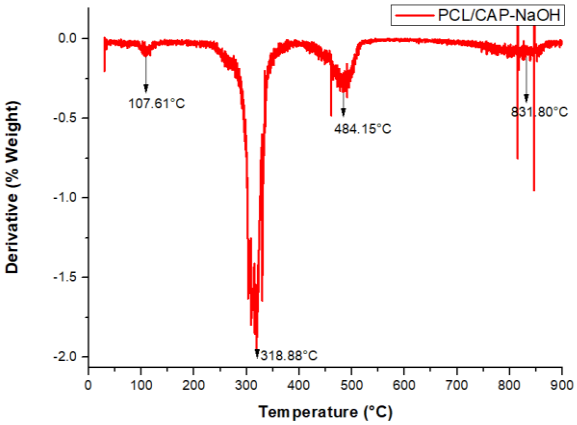

CAP FILM
-2.94%
$T_{5\%}$=179.07°C
-19.31%
-29.08%
-41,19%
Residue=8.03%
% Weight Loss
Temperature (°C)

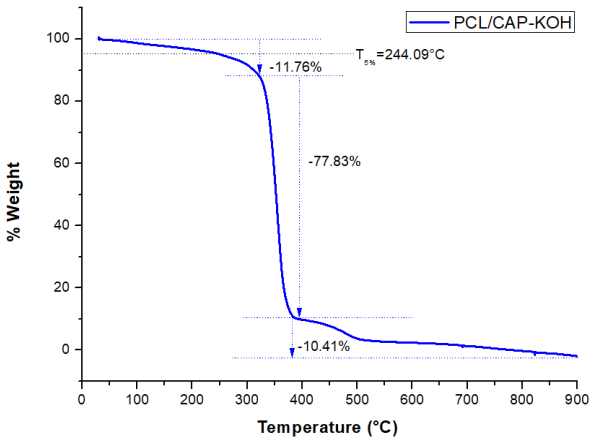

CAP FILM
90.50°C
212.91°C
283.69°C
T_{max}=354.47°C
Derivative (% Weight)
Temperature (°C)

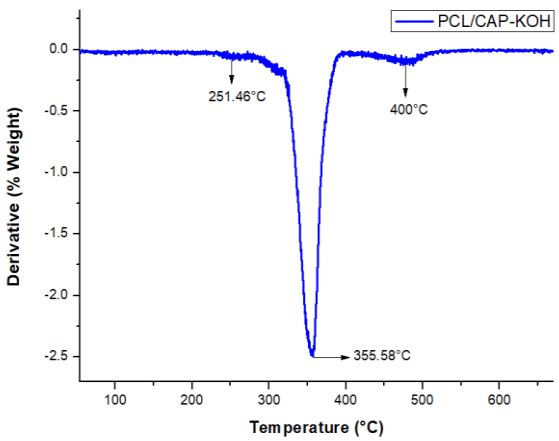

PCL/CAP
-2.142%
$T_{5\%}$=203.24°C
-15.282%
-13.16%
-67.24%
Residue= 2.42%
% Weight
Temperature (°C)

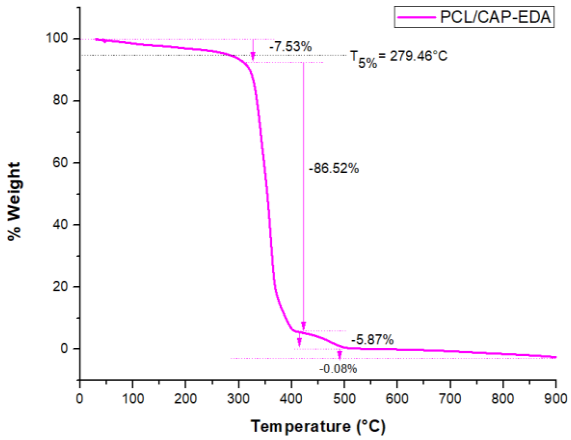

PCL/CAP
290.06°C
218.46°C
349.99°C
420.07°C
Derivative (% Weight)
Temperature (°C)

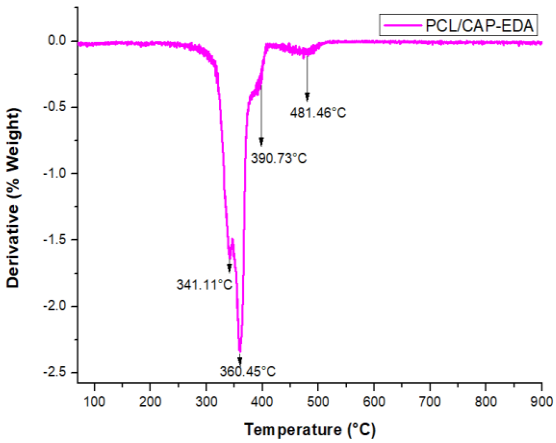

PCL/CAP-NaOH
-3.54%
-3.99%
$T_{5\%}$=203.37°C
-65.84%
-15.99
-12.23%
Residue=0.77%
% Weight
Temperature (°C)


PCL/CAP-NaOH
107.61°C
484.15°C
831.80°C
318.88°C
Derivative (% Weight)
Temperature (°C)


PCL/CAP-KOH
% Weight
Temperature (°C)
-11.76%
T5%=244.09°C
-77.83%
-10.41%


PCL/CAP-KOH
Derivative (% Weight)
Temperature (°C)
251.46°C
400°C
355.58°C


PCL/CAP-EDA
% Weight
Temperature (°C)
-7.53%
T5%= 279.46°C
-86.52%
-5.87%
-0.08%

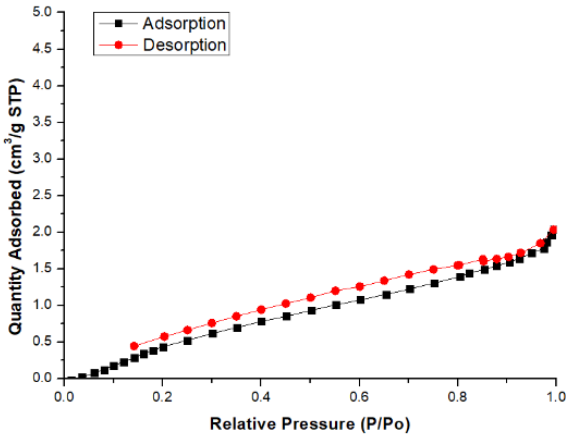

PCL/CAP-EDA
Derivative (% Weight)
Temperature (°C)
481.46°C
390.73°C
341.11°C
360.45°C

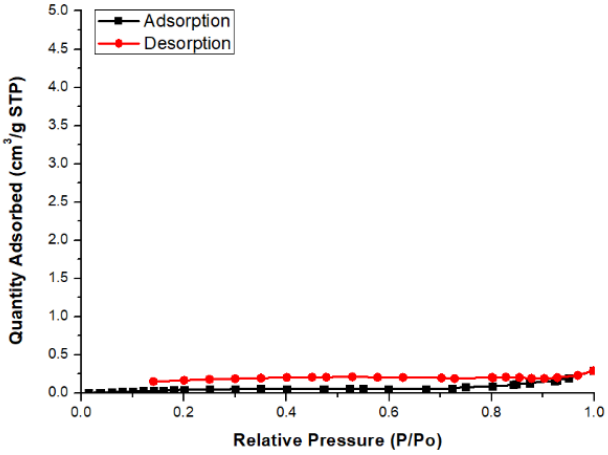
A4: Parameters employed during bet porosity and surface area analysis (all chapters)

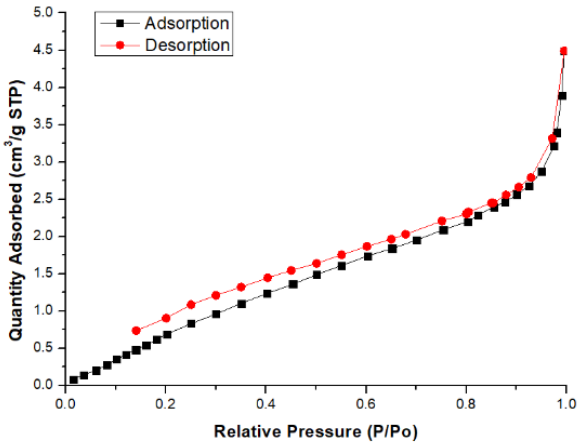
Table A4. Parameters employed during BET analysis

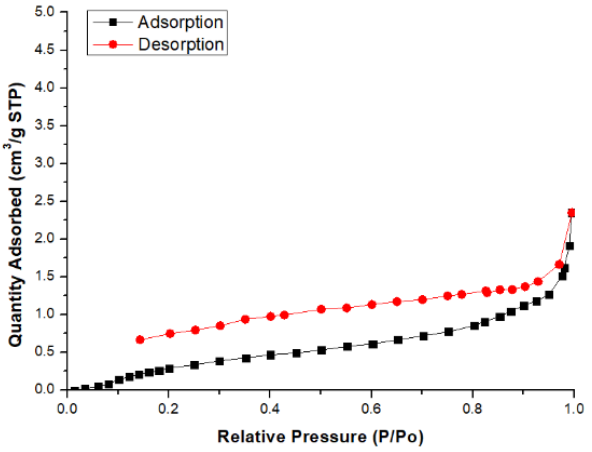
Sample Tube	Value
Warm free space	1 cm^3
Cold free space	1 cm^3
Non-ideality factor	0.0000620
Use isothermal jacket	Yes
Use filler rod	Yes
Vacuum seal type	Seal frit
Analysis conditions	
Preparation	
Fast evacuation	No
Evacuation from	5 mmHg
Vacuum set point	10 µmHg
Evauation time	0.1 h
Leak test	No
Use trans seal	No
Free space	
Free space type	Measured
Dewar for evacuation	Yes
Evacuation time	0.1 h
Outgas test	No
Po and temperature	No
Po and T type	Measure Po at intervals during analysis.
Measurement interval	120 min
Dosing	
Use first pressure fixed dose	No
Use maximum volume increment	No
Target tolerance	5% or 5 mmHg
Low pressure dosing	No
Equilibration time (P/Po = 1.000000000):	20 s
Minimum equilibration delay at P/Po > = 0.995	600 s
Sample Backfill	
Backfill at start of analysis	Yes
Backfill at end of analysis	Yes
Backfill gas	N^2
Adsorptive Properties	
Adsorptive	Nitrogen @ 77.35 K
Maximum manifold pressure	925 mmHg
Non-ideality factor	0.000062
Density conversion factor	0.0015468
Therm. tran. hard-sphere diameter	3.860 Å
Molecular cross-sectional area	0.162 nm^2
Inside diameter of sample tube	9.53 mm
Temperature Ramp Rate	10 °C/min
Target Temperature	30 °C
Evacuation Rate	50 mmHg/s
Restricted Evacuation from	30 mmHg
Vacuum Setpoint	500 µmHg
Evacuation Time	60 min
Heating Phase	
Ramp Rate	10 °C/min
Hold Temp	40 °C
Hold Time	250 min
Evacuation and Heating Phases	
Hold Pressure	100 mmHg

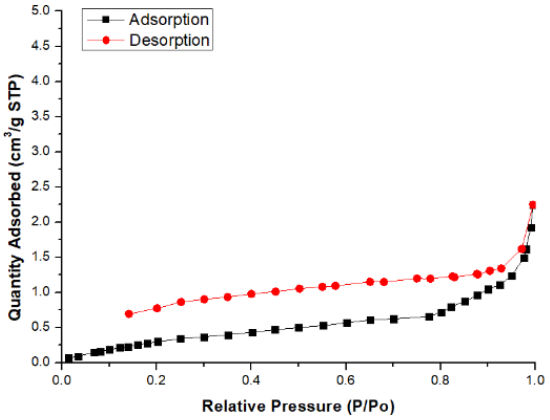
A5: Adsorption-desorption isotherms (Chapter 3)

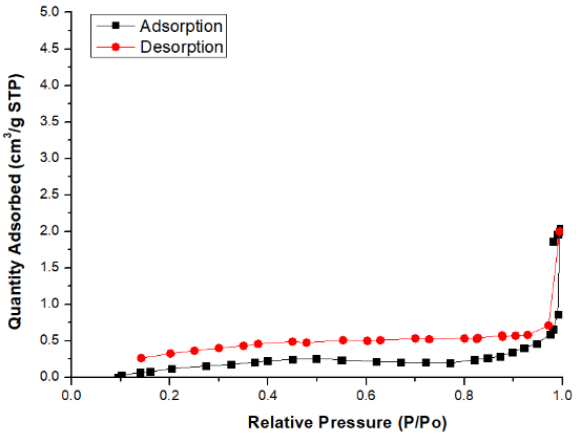




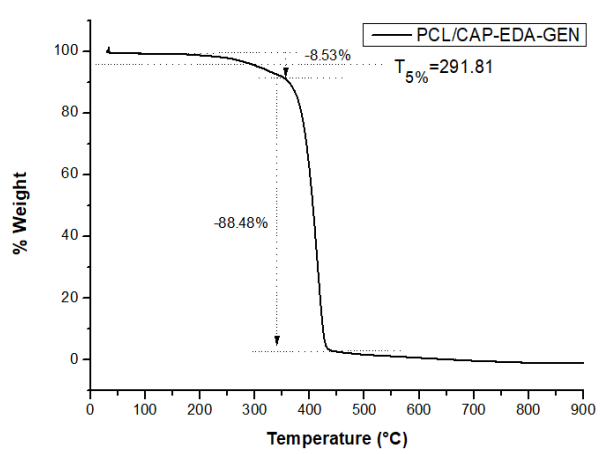


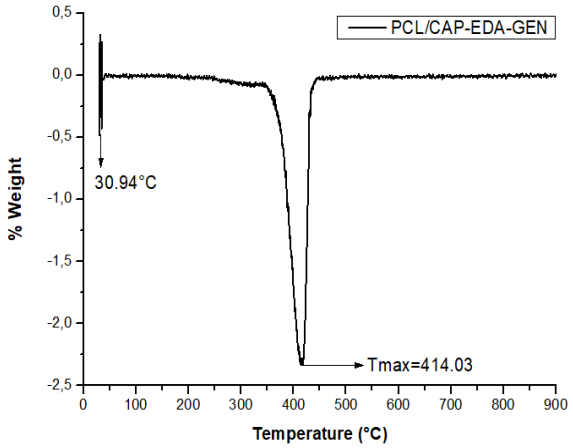


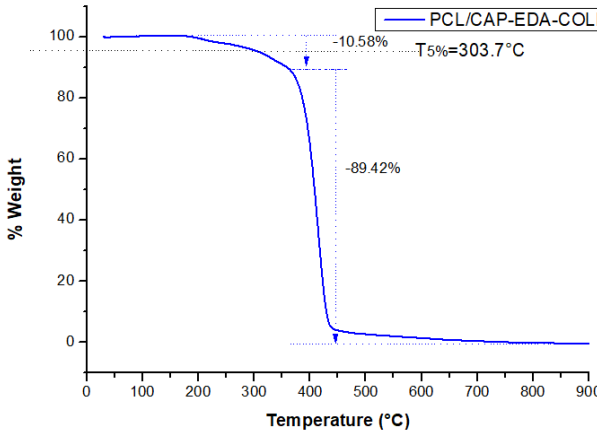


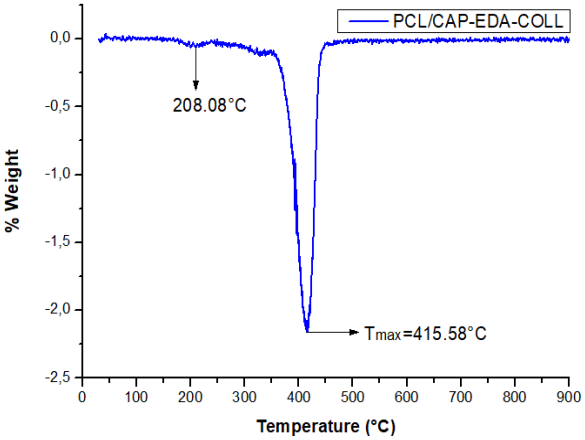


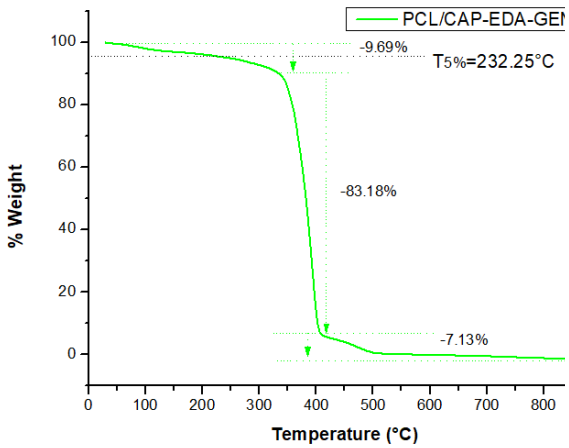
A6: TGA thermograms (Chapter 4)

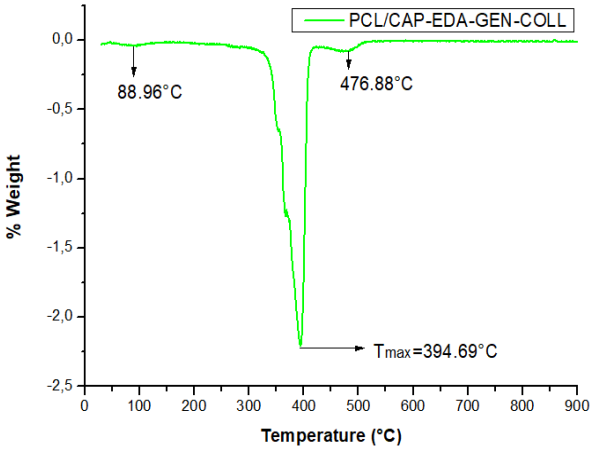


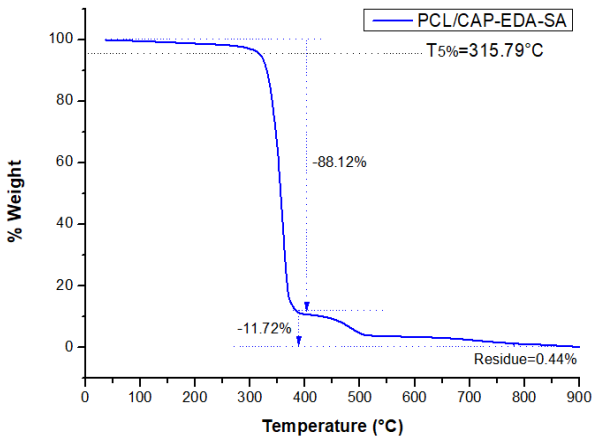


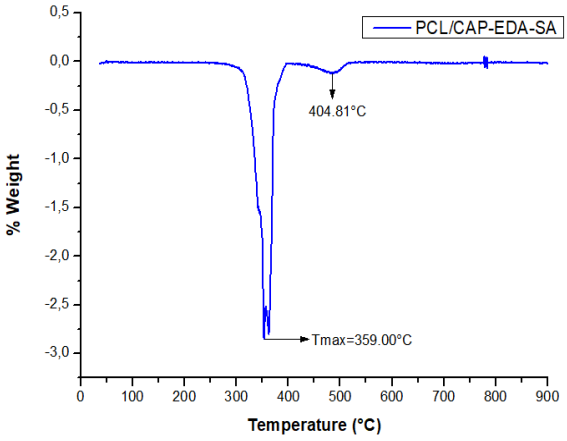


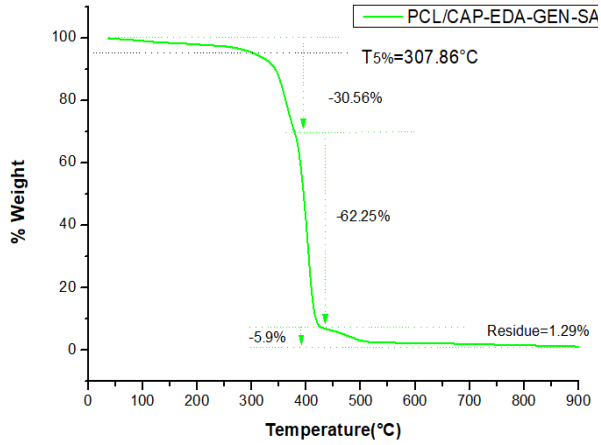


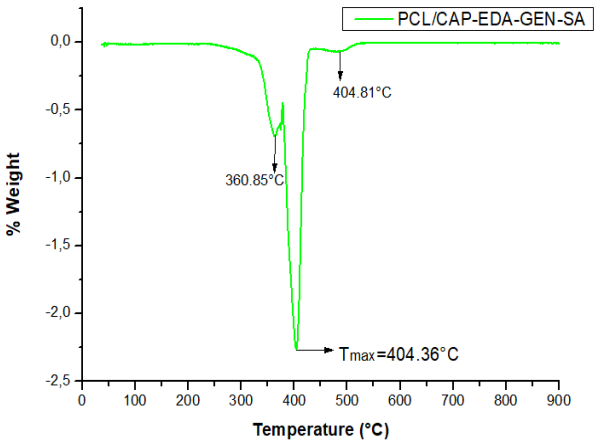


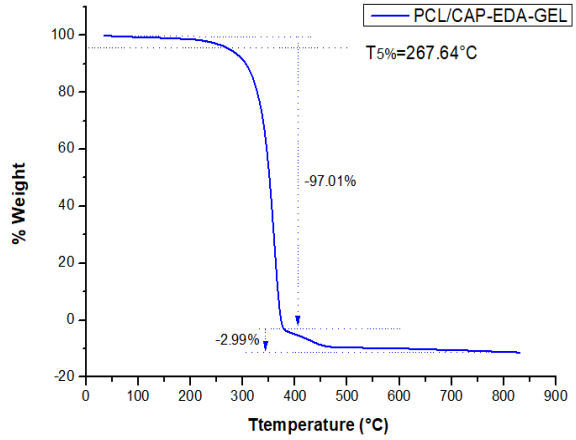


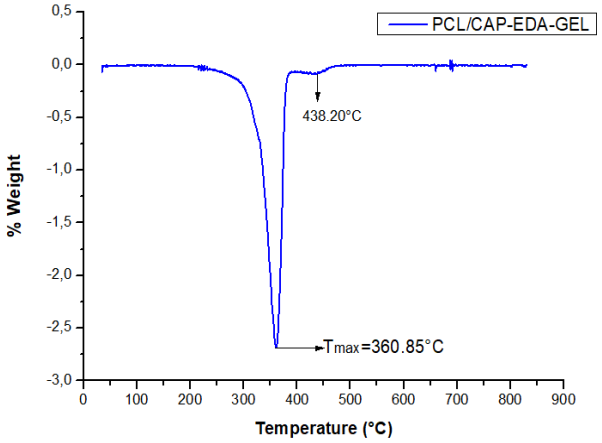

PCL/CAP-EDA-SA
T5%=315.79°C
-88.12%
-11.72%
Residue=0.44%
% Weight
Temperature (°C)

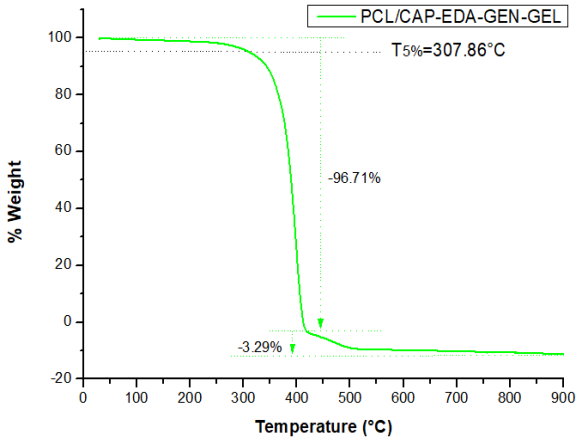

PCL/CAP-EDA-SA
404.81°C
Tmax=359.00°C
% Weight
Temperature (°C)

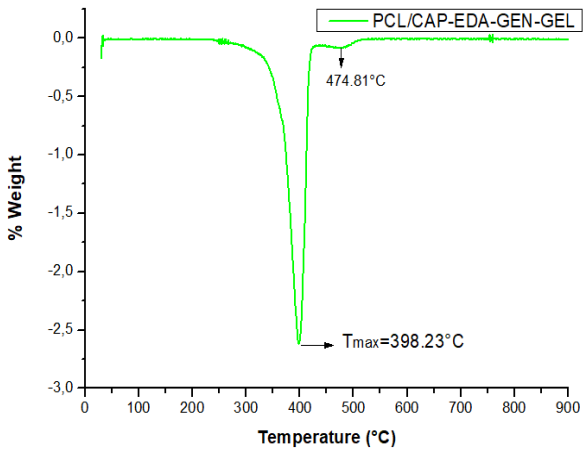

PCL/CAP-EDA-GEN-SA
T5%=307.86°C
-30.56%
-62.25%
-5.9%
Residue=1.29%
% Weight
Temperature(°C)


PCL/CAP-EDA-GEN-SA
404.81°C
360.85°C
Tmax=404.36°C
% Weight
Temperature (°C)

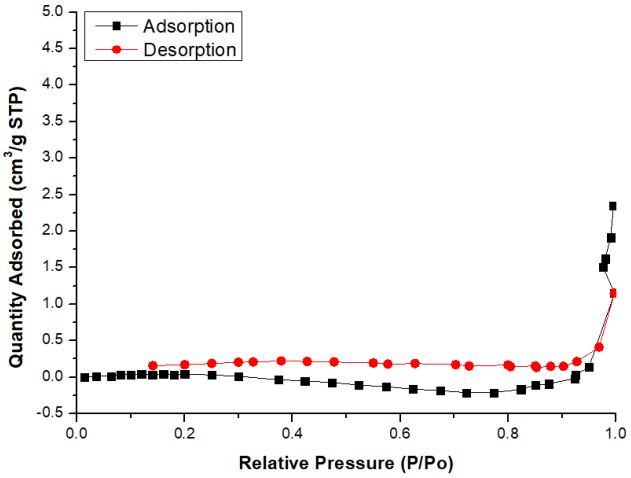

PCL/CAP-EDA-GEL
T5%=267.64°C
-97.01%
-2.99%
% Weight
Ttemperature (°C)

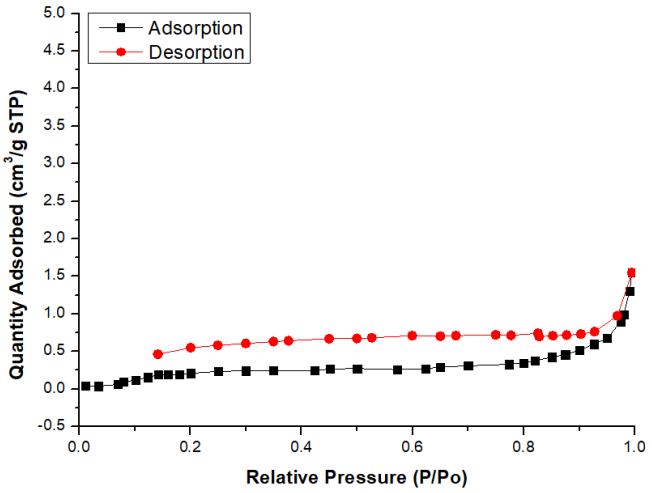

PCL/CAP-EDA-GEL
438.20°C
Tmax=360.85°C
% Weight
Temperature (°C)

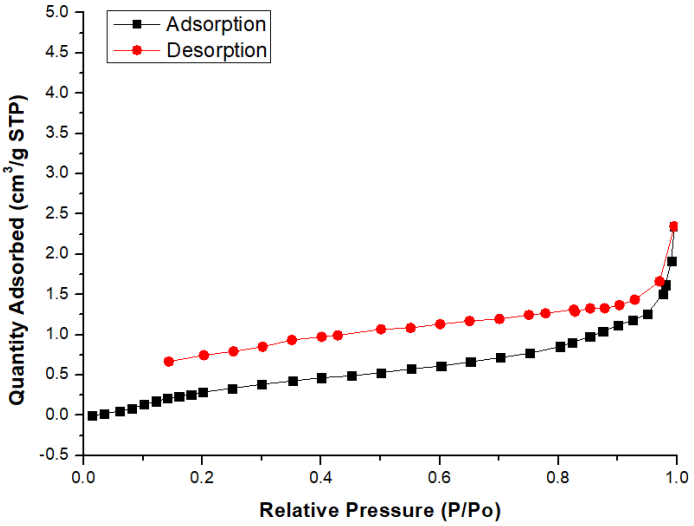

PCL/CAP-EDA-GEN-GEL
T5%=307.86°C
-96.71%
-3.29%
% Weight
Temperature (°C)


PCL/CAP-EDA-GEN-GEL
474.81°C
Tmax=398.23°C
% Weight
Temperature (°C)

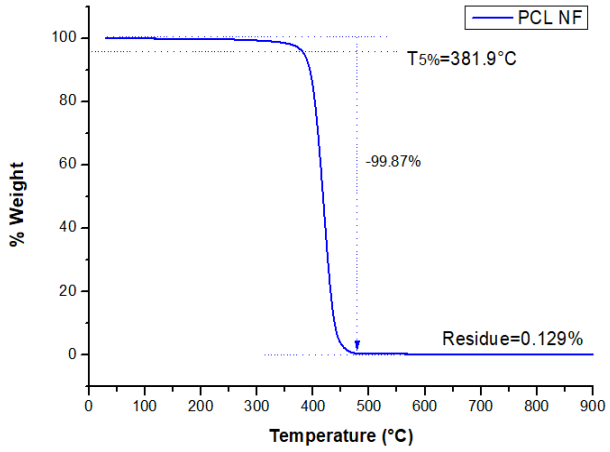
A7: Adsorption-desorption isotherms (Chapter 4)

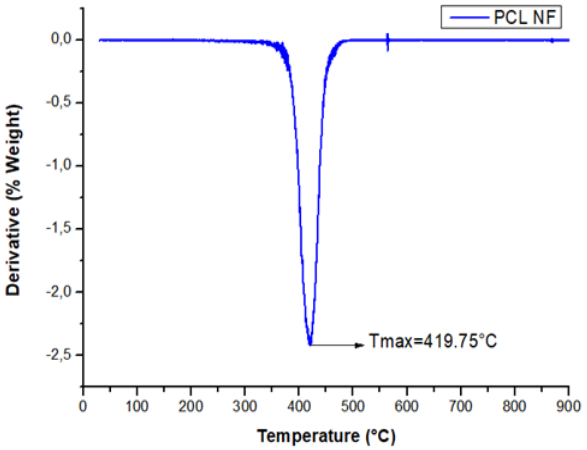


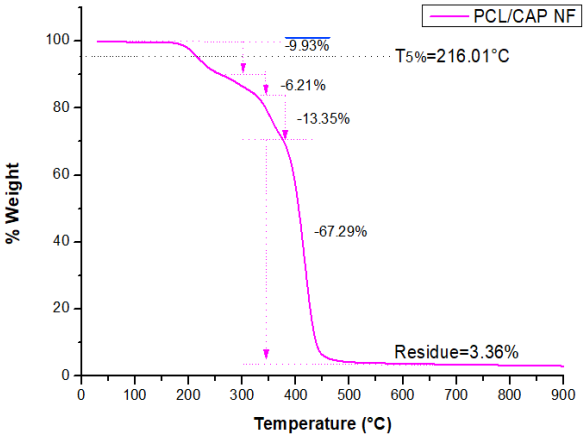


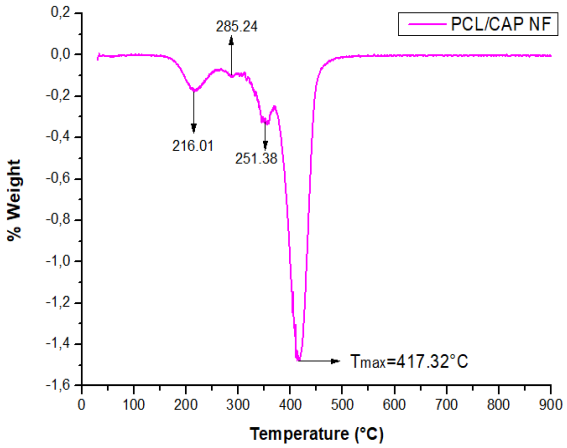


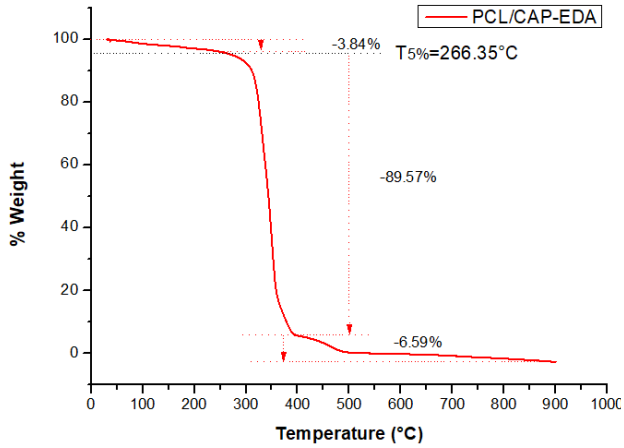
A8: TGA thermograms (Chapter 5)

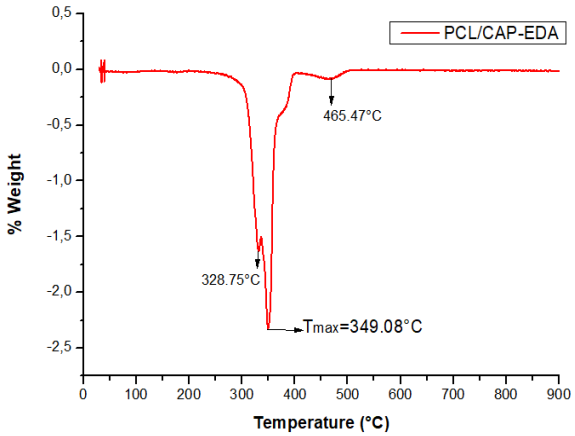


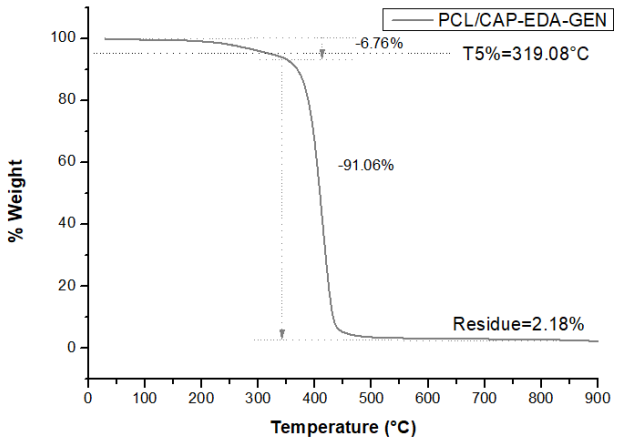


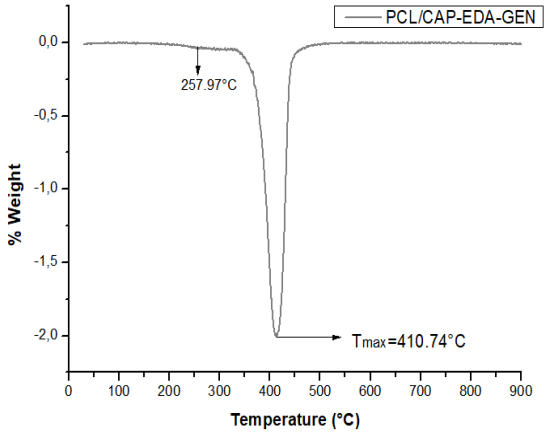


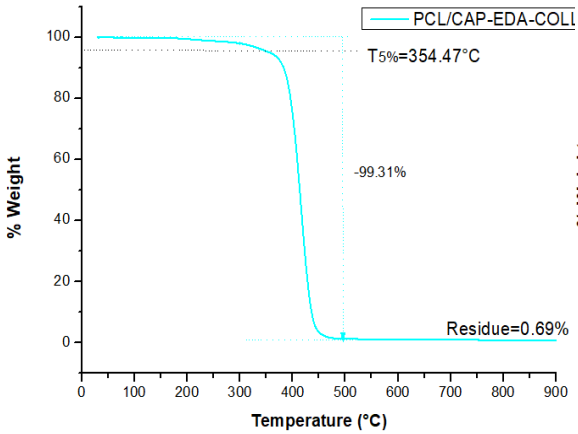


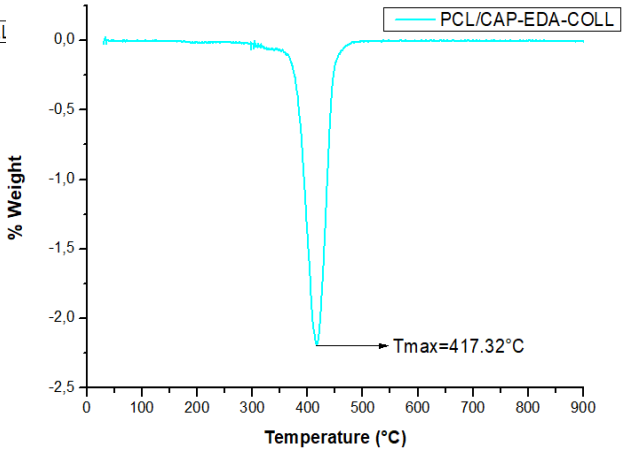


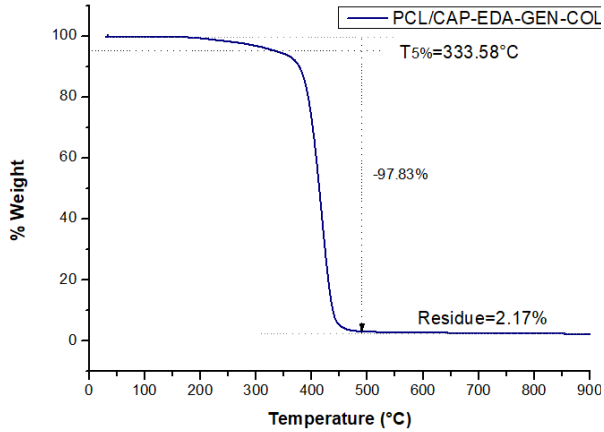


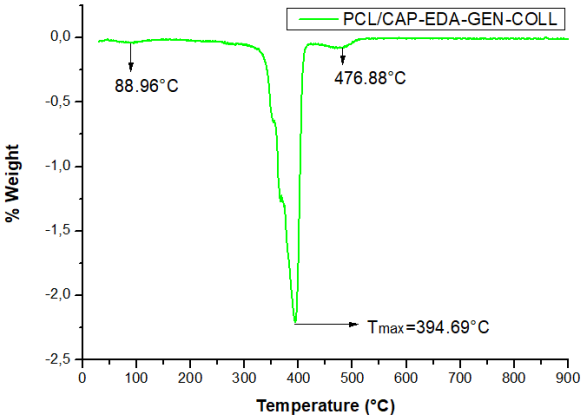

PCL/CAP-EDA-GEN
-6.76%
T5%=319.08°C
-91.06%
Residue=2.18%
% Weight
Temperature (°C)

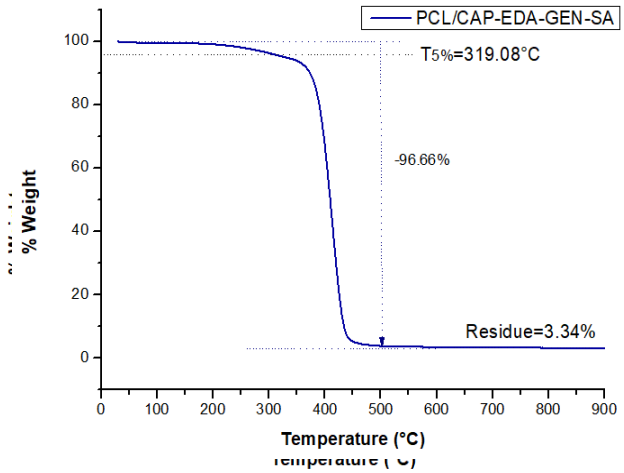

PCL/CAP-EDA-GEN
257.97°C
Tmax=410.74°C
% Weight
Temperature (°C)

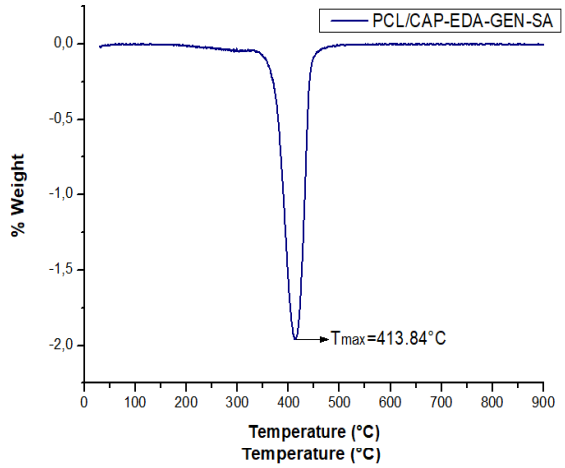

PCL/CAP-EDA-COLL
T5%=354.47°C
-99.31%
Residue=0.69%
% Weight
Temperature (°C)

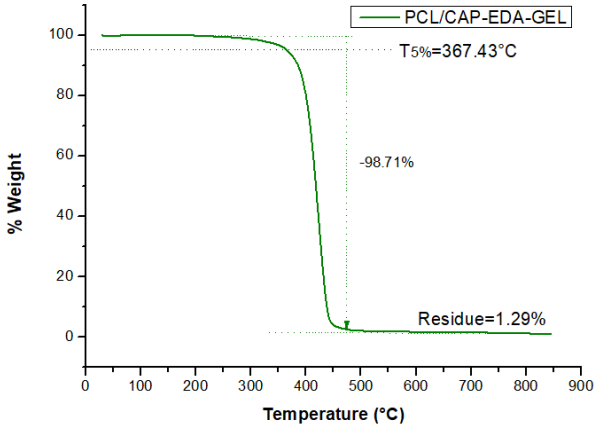

PCL/CAP-EDA-COLL
Tmax=417.32°C
% Weight
Temperature (°C)

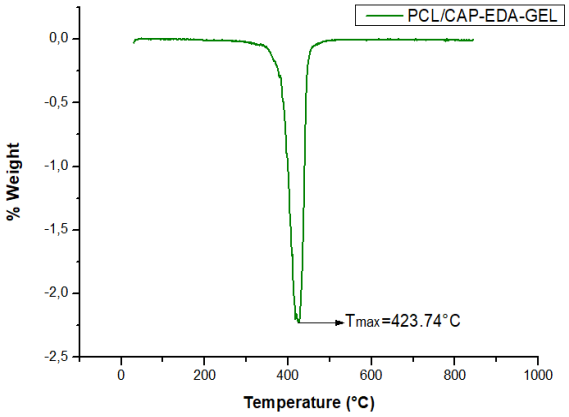

PCL/CAP-EDA-GEN-COL
T5%=333.58°C
-97.83%
Residue=2.17%
% Weight
Temperature (°C)

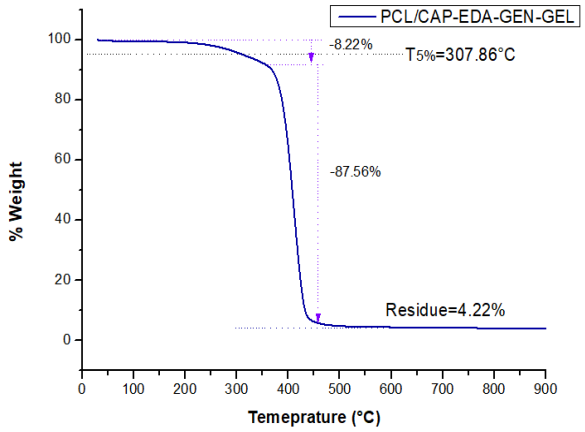

PCL/CAP-EDA-GEN-COLL
88.96°C
476.88°C
Tmax=394.69°C
% Weight
Temperature (°C)

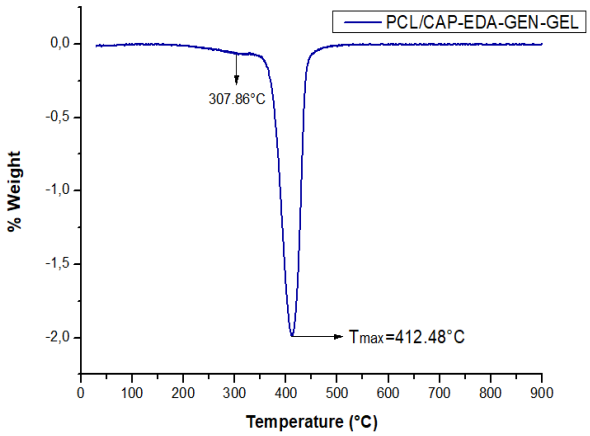

PCL/CAP-EDA-GEN-SA
T5%=319.08°C
-96.66%
Residue=3.34%
% Weight
Temperature (°C)


PCL/CAP-EDA-GEN-SA
Tmax=413.84°C
% Weight
Temperature (°C)


PCL/CAP-EDA-GEL
T5%=367.43°C
-98.71%
Residue=1.29%
% Weight
Temperature (°C)


PCL/CAP-EDA-GEL
Tmax=423.74°C
% Weight
Temperature (°C)


PCL/CAP-EDA-GEN-GEL
-8.22%
T5%=307.86°C
-87.56%
Residue=4.22%
% Weight
Temeprature (°C)


PCL/CAP-EDA-GEN-GEL
307.86°C
Tmax=412.48°C
% Weight
Temperature (°C)

A9: ADSORPTION-DESORPTION ISOTHERMS (CHAPTER 5)

